DEFENCE ACADEMY
OF THE UNITED KINGDOM

Cranfield UNIVERSITY

Defence College of Management and Technology

Department of Aerospace, Power and Sensors

PhD
2008

Peter Clement Wilkins

Some Unsteady Aerodynamics Relevant to Insect-inspired Flapping-wing Micro Air Vehicles

Supervisor: Professor Kevin Knowles

March 2008

Abstract

Flapping-wing micro air vehicles, based on insect-like flapping, could potentially fill a niche in the current market by offering the ability to gather information from within buildings. The aerodynamics of insect-like flapping are dominated by a large, lift-enhancing leading-edge vortex (LEV). Historically, the cause and structure of this vortex have been the subject of controversy. This thesis is primarily intended to provide insight into the LEV, using computational fluid dynamics coupled with validating experiments. The problem is simplified by breaking down the complex kinematics involved in insect-like flapping and examining only a part of these kinematics; firstly in 2D, before progressing to 3D sweeping wing motions. The thesis includes discussion of published literature in the field, highlighting gaps and inconsistencies in the current knowledge. Among the contributions of this thesis are: descriptions of the effects of changing Reynolds number and angle of attack for 2D and 3D flows; clarification of terminology and phenomenology, particular in the context of 2D flows; and detailed descriptions of the development and structure of the LEV in both 2D and 3D cases, including discussion of Kelvin-Helmholtz instability. The issues of Strouhal number, delayed leading-edge separation, dynamic stall and the Wagner effect are also considered. Generally, the LEV is shown to be unstable in 2D cases. However, in 3D cases the LEV is seen to be stable, even if Reynolds number is increased. The stability of the LEV is found to be critically dependent on wing aspect ratio.

Thanks...

To Prof. Kevin Knowles: for your invaluable advice, encouragement, patience, and practical help.

To Lis: for marrying me, and for everything you've done since and continue to do; and especially for more or less single-handedly arranging our house move whilst I was preoccupied with writing this.

To Chloe: for sleeping right through the night from the age of about six weeks.

To Mum and Dad: for bringing me up.

And to everyone else who's helped: in particular, Dr. Rafał Żbikowski (for hours of insightful discussion; and a special thanks for rescuing me from becoming a teacher); Dr. Alistair Saddington (for CFD advice); Dr. Salman Ansari (for running simulations, digging out old data, and teaching me LaTeX); Dr. Simon Ritchie, Dr. Mark Finnis and Dave Wasley (for help with experiments); Heather Athawes and Jilly Sellwood (for ensuring the smooth running of DAPS over the past 3.5 years); Andy Gittings (for making computers do what I wanted them to do); and the workshop, library, and computing services staff at DCMT.

Most importantly, thanks be unto God for his unspeakable gift. Now unto him that is able to do exceeding abundantly above all that we ask or think ... unto him be glory in the church by Christ Jesus throughout all ages, world without end.

Any errors or omissions within this thesis are solely my responsibility.

Peter Wilkins
March 2008

Preface

Motivation and scope

Flapping-wing micro air vehicles, based on insect-like flapping, could potentially fill a niche in the current market by offering the ability to gather information from within confined spaces such as buildings. The aerodynamics of insect-like flapping are dominated by the presence of a large leading-edge vortex which, it appears, enhances lift. This thesis is primarily intended to investigate, and provide insight into, this phenomenon.

The nature of the leading-edge vortex has historically been the subject of some controversy. There have been numerous attempts to investigate insect-like flapping using 2D models or experiments, and there have also been many attempts to investigate the problem using 3D models or experiments. However, little work appears to have been done to try and bridge the gap between these two approaches. Here, an attempt is made to remedy this shortfall.

In addition, the application of insect-like flapping to micro air vehicles has resulted in work being carried out in the field by both biologists and aerodynamicists. Though useful contributions have come from both communities, it is apparent that some of the disagreements and controversies are merely the result of terminology from one field being unfamiliar to those in the other. This thesis looks in detail at some of these disagreements.

This thesis forms part of a wider study of insect-like flapping, which has historically concentrated on analytical models, coupled with experimental validation. In this thesis, a computational fluid dynamics approach is used to complement past work. Experimental data are also presented to validate the computational results.

Contributions

The main contributions of this thesis are

- An introduction to and discussion of some current theories regarding the leading-edge vortex.
- A discussion of Strouhal number and its importance in the context of insect-like flapping.
- Analysis of the effects of changing Reynolds number (including discussion of Kelvin-Helmholtz instability), angle of attack, and aerofoil parameters for 2D flows.
- A detailed description and explanation of the process of vortex shedding for 2D cases, including discussion of delayed leading-edge separation, the Wagner effect, and the inappropriateness of the use of the term 'dynamic stall' in this field.
- Clarification of terminology and phenomenology, especially for 2D cases.
- Description of the impact of acceleration for 2D flows.
- Exploration of the fundamental difference between 2D flows and 3D sweeping wing motions and the reasons of these differences.
- Analysis of the structure and development of the leading-edge vortex in 3D sweeping wing motions.
- Descriptions of the effects of changing Reynolds number, angle of attack, wing planform, and wing aspect ratio for 3D flows.
- Analysis of the impact of wing-wake interaction for 3D cases.
- Quantification of the effect of using curved chords as opposed to flat chords.
- Discussion of the analytical model of Ansari and its benefits and limitations.

Thesis outline

This thesis is divided into two parts, each of which is sub-divided into a number of chapters, in order systematically to present the work included here. Part I covers introduction, background, and method, and sets the scene for the results, discussion and conclusion presented in Part II.

Chapter 1 gives the motivation for the research programme of which this thesis forms a part. The motivations for developing micro air vehicles are presented, some past attempts to design such vehicles are discussed, and the decision to concentrate of insect-like flapping as a basis for such a vehicle is justified.

Chapter 2 reviews in detail the existing literature relating more closely to the specific field of research of this thesis. Details of the current state of knowledge regarding insect flight and the phenomenology involved are given, as well as relevant research from other areas. In this chapter some current theories regarding the leading-edge vortex are discussed and some controversies and disagreements are explored.

Chapter 3 presents in more detail the aims of the current work and the objectives which were set to achieve these aims. This leads into Chapter 4, where the methods used to obtain the results presented in Part II of the thesis are presented and discussed, complemented by an appendix which gives further details of the CFD method used. Chapter 4 also explicitly states the assumptions made in the current work and the justification for these assumptions.

Part II commences with Chapter 5, in which the results relating to 2D flows are presented and discussed. Chapter 6 follows with results pertaining to 3D sweeping wing motions. These two chapters contain the bulk of the contributions of the thesis which were briefly outlined above.

Finally, Chapter 7 summarises the conclusions from the current work and suggests possible avenues for future research.

Contents

List of Figures

Nomenclature

Latin alphabet

a	Acceleration
A	Wing area
c	Chord length
$\overline{c}$	Mean aerodynamic chord
C_D	Drag coefficient
C_L	Lift coefficient
C_T	Torque coefficient
D	Drag force
f	Flapping frequency
f_{vs}	Vortex shedding frequency
Kn	Knudsen number ($=\lambda/l$)
l	Representative length
L	Lift force
p	Pressure
Re	Reynolds number ($=\rho V l/\mu$)
St	Strouhal number ($=f_{vs}l/V$)
t	Time
T	Torque
$\mathbf{u}$	Velocity vector
u	Velocity in x direction
v	Velocity in y direction
V	Aerofoil velocity
V_{tip}	Wing tip velocity
V_θ	Tangential velocity within vortex
V_Z	Axial velocity within vortex
w	Velocity in z direction
x	Coordinate on axis co-linear with chord
X	x/c
y	Coordinate on axis normal to chord and span
Y	z/c
z	Coordinate on axis co-linear with span
Z	z/c

Greek symbols

α	Angle of attack
λ	Molecular mean free path length
μ	Fluid viscosity
ρ	Fluid density
ω	Vorticity
ω	Vorticity vector
Ω	Angular velocity of 3D wing
Γ	Circulation

Acronyms/Abbreviations	
2D	Two-dimensional
3D	Three-dimensional
AR	Aspect ratio
CFD	Computational fluid dynamics
FMAV	Flapping-wing micro air vehicle
LEV	Leading-edge vortex
MAV	Micro air vehicle
PIV	Particle image velocimetry
RANS	Reynolds-averaged Navier Stokes
TEV	Trailing-edge vortex
UAV	Unmanned air vehicle

Part I

Introduction, Background, & Method

Chapter 1

Introduction

> *"Today about a billion billion insects are alive at any given time around the world. At nearest order of magnitude, this amounts to a trillion kilograms of living matter, somewhat more than the weight of humanity. Their species, most of which lack a scientific name, number into the millions."*
>
> — Edward O. Wilson

In this chapter, the motivation for developing micro air vehicles (MAVs) is explained; the required abilities and attributes for a successful MAV are discussed; details of some current and past MAVs are presented; and the advantages of an MAV based on insect-like flapping over alternative possible solutions are given.

1.1 The motivation for developing MAVs

World developments in recent years — particularly the events of September 11th 2001 and the resulting "War on Terror" — have seen a large increase in the use of unmanned aerial vehicles (UAVs). This increase has not only confirmed many of the advantages of UAV use over conventional manned platforms, but also highlighted some of the shortcomings of current systems and some new areas for research and development. With some analysts predicting a $54bn market for UAVs over the next ten years (Teal Group Corporation, 2006), it is not surprising that interest in

the field continues to grow.

Since UAVs were first extensively used in military action over Vietnam in the 1960s, research has generally concentrated on developing long-range surveillance UAVs — it was not until the beginning of the 21st century that the first UAV *specifically designed* for combat flew. This emphasis on surveillance was indicative of the fact that combat, for the most part, lay outside the capability of the available technology. The long range requirement stemmed from the belief of many military organisations of the time that future wars would be fought from a distance, without the close-in, man-to-man engagement of previous wars. This long-range surveillance requirement has led to an increase in the size of UAVs; Global Hawk, a modern high-altitude, high-endurance, long-range UAV, has a wing span of 35m, more than that of a Boeing 737.

However, recent experiences (particularly in Afghanistan and Iraq) have indicated that there will probably always be a need for 'boots on the ground' in many conflicts, and that most wars cannot be brought to a satisfactory conclusion using airborne assets alone. These 'boots on the ground' often have a requirement for comparatively short-range, 'over the hill'-type reconnaissance — using systems that can be carried by a single man and deployed at short notice. There are a number of systems currently on operational service or in development which are designed to meet this requirement — see e.g. the IAI Bird-Eye 400 (Israel Aerospace Industries, 2007). However, there are no current systems which are designed to carry out reconnaissance inside buildings and other confined spaces. Such an asset could be extremely valuable, not only to military organisations but also to paramilitary and civil organisations — for example, for search and rescue inside buildings, inspection of dangerous areas (e.g. the inside of a nuclear reactor), or building security. The most obvious criteria for such a system concerns size — a UAV suitable for flight in confined spaces must be small. Such vehicles are therefore called micro air vehicles, or MAVs.

1.2 Requirements for a successful MAV

One of the motivations for developing MAVs is their ability to fly in confined spaces. There is a niche in the current marketplace in this area (Żbikowski, 2002a), as generally speaking, current surveillance assets cannot obtain information from inside buildings. In order to fill this niche, any MAV needs to possess a number of attributes:

Small size. A 'micro air vehicle' has been generally, but fairly arbitrarily, defined as having a maximum dimension in any direction of $150mm$. However, recently this criterion seems to have been relaxed, and many aircraft that are termed MAVs have dimensions of up to $225mm$.

High efficiency. A small aircraft can only carry a limited amount of energy. This is one of the current major limitations on MAVs — power sources with the required energy density are not yet readily available.

Ability to carry at least one sensor. Inserting an MAV is only useful if the vehicle is able to return information to the operator.

High manoeuvrability at low speeds. Flying inside confined areas and through narrow openings is viable only if the aircraft is able to avoid collision. High speed flight is not required (or sensible) for indoor operation.

Vertical flight capability. In order to be able to (for example) fly up vertical shafts, the MAV needs to be able to sustain vertical flight. This is also required for vertical take-off and landing, so that the MAV can land in confined spaces.

Hover capability. Essential for surveying confined areas.

Stability when flying close to surfaces. An MAV must remain stable and controllable when flying close to walls, ceilings or floors.

High autonomy. The MAV needs to be able to sense and avoid obstacles. Although this might be possible if it were under direct human control, the

communications link could not always be guaranteed if the vehicle were inside a building or other structure. In addition, it would be difficult to enable the operator to manoeuvre the MAV accurately in tight spaces. For these reasons, a better solution is seen as making the vehicle fully autonomous and able to operate without direct supervision, although this solution is technically more complex.

Low aural and visual signatures. One of the potential roles for an MAV is the penetration of enemy held buildings. Thus, the MAV needs to be discreet to avoid detection.

High durability. Since the MAV is likely to fly in confined spaces, it may well be involved in collisions. The vehicle should be resilient, so that a collision need not necessarily terminate the mission.

Depending on the intended role of the MAV, there may be other attributes which might be required, and some of the above qualities may not be needed. As a simple example, an MAV that is intended to inspect the inside of a nuclear reactor dome needs to be unaffected by radiation, but need not be discrete.

1.3 Current (non-flapping-wing) MAVs

There are four vehicle types which might satisfy the above criteria:

- fixed-wing aircraft;
- rotary-wing aircraft;
- lighter-than-air aircraft;
- flapping-wing aircraft.

In this section some historical and current attempts to produce MAVs of the first three types are examined, and the shortcomings of each type are discussed. Flapping-wing MAVs (FMAVs) are then introduced, along with the justification for the choice to concentrate on this type of aircraft is given. Lastly, some of the

(a) *Black Widow* (b) *Wasp*

Figure 1.1: AeroVironment MAVs (Die Raven, 2005).

current attempts to build FMAVs are presented, and the particular type of FMAV which is of interest is identified.

1.3.1 Fixed-wing MAVs

The main advantage of fixed-wing aircraft is their simplicity, and it has been shown that MAV-sized fixed-wing aircraft are viable flying machines. In fact, almost all of the earliest MAVs were fixed-wing aircraft. AeroVironment, a US technology company, started development on their first MAV, the *Black Widow*, in 1996 (Figure 1.1(a)). Their efforts were (at least partially) funded by DARPA[1]. The aircraft weighed around $80g$, and measured $150mm$ in wingspan. At the conclusion of development in 2000, *Black Widow* was able to demonstrate automatic launch, followed by a flight of over 30 minutes, with a range of $1.8km$. Its maximum speed was around $20m/s$ (AeroVironment, Inc., 2007a). The aircraft was inaudible at $30m$ range and the pilot was able to fly most of the flights 'head-down', i.e. looking at the images from the video camera that was carried on the aircraft (Grasmeyer and Keennon, 2001; Keennon and Grasmeyer, 2003).

Using the experience and technology gained developing the *Black Widow*, AeroVi-

[1]The Defense Advanced Research Projects Agency — an agency of the United States Department of Defense. DARPA was instrumental in initiating research into MAVs in the early 1990s (see DARPA, 2000).

Figure 1.2: LS *MicroSTAR* (Die Raven, 2005).

Figure 1.3: Computer-generated image of ONERA *Mirador* (ONERA, 2004).

ronment went on to develop the *Wasp* (Figure 1.1(b)), starting in 1998. This was a larger aircraft with a wingspan of $410mm$ and a weight (without payload) of $275g$, and was developed in partnership with DARPA. A later version — the *Wasp II* — is now commercially available, and a modified version of *Wasp II* (named *Wasp III* or *BATMAV* — with a $420mm$ wingspan and an all-up weight of $450g$) appears to be in service with the US Air Force Special Operations Command (AeroVironment, Inc., 2007a,b; US Air Force Special Operations Command, 2007).

Another major player in the field was the Lockheed Sanders *MicroSTAR* (Figure 1.2), which was first demonstrated (after a 3-year development period) in 2000. It had a $225mm$ wingspan, a length of $150mm$, and a duration of $20-30$ minutes. A member of the design team commented that "We can make a 6-inch airplane fly. Getting it to be militarily useful was the part we had to work on — getting the airspeed, duration and stability to get something useful back." *MicroSTAR* was designed primarily for outdoor use and about 100 were built during development; there were a high number of crashes due to the operator losing sight of the aircraft. Despite promises from the manufacturers that *MicroSTAR* would "revolutionize future warfare" the project appears to have been shelved shortly after its first demonstration (Skeen, 2000; Lockheed Martin, 2000a,b). Though a reason for the decision to stop development was not given, it is reasonable to suspect that the company realised that outdoor flight was not feasible with such tiny aircraft.

The only real European challenger to the US monopoly on fixed-wing MAVs

came from the French aerospace research agency ONERA, who produced the *Mirador* (Figure 1.3). Apparently never intended to go into production, this 250mm long aircraft was built primarily to test miniature sensors. Details of the aircraft are somewhat scarce, but in 2002 *Mirador* was in development with a published weight of 90g — 50g of this being taken up by the propulsion system and power supply (Keuter et al., 2002; Goebel, 2006). Since then, little has been heard of it.

Contributions in this area have also come from the hobby community[2] — the most important coming from the US Company Plantraco. Their first product was the *Butterfly* (Figure 1.4(a)), a wood-and-tissue aircraft with a wingspan of 190mm and a flying weight of 3.8g. This was followed by the *Carbon Butterfly*, which was similar to the *Butterfly* but constructed from carbon fibre. The wingspan remained unchanged but the weight decreased to 3.6g. The *Micro Butterfly* (Figure 1.4(b)), a smaller version of the original Butterfly, was offered for sale in 2007. It has a wingspan of 114mm and a weight of 2.6g, earning it the title of the world's smallest and lightest radio-controlled model aircraft. Plantraco also produce the *MicroMAV* (Figure 1.4(c)), which is a flying wing with a wingspan of 114mm and a weight of 4g. All these aircraft are traditionally controlled by a human pilot, and it is doubtful that any of them could carry a camera or other payload. Video footage, available on Plantraco's website (Plantraco, 2007), shows that the larger *Carbon Butterfly* is the slowest-flying of the range, but even this flies at speeds which make indoor flight only just possible. In addition the duration of these aircraft is generally under 10 minutes, although Plantraco claim a record flight time of 24 minutes.

The basic problem for fixed-wing MAVs is one of wing loading. To be small enough for indoor flight, whilst still being able to carry a useful payload, the wing loading must be such that slow flight is difficult or impossible. They may be potentially useful for outdoor flight, but it is questionable whether small size is of much importance outdoors — 'man portable' is generally small enough, and there are already man-portable UAVs with wingspans of the order of feet rather than

[2] Although some might hesitate to denote these toys as MAVs, they can provide useful knowledge and new techniques for the construction and operation of 'serious' MAVs.

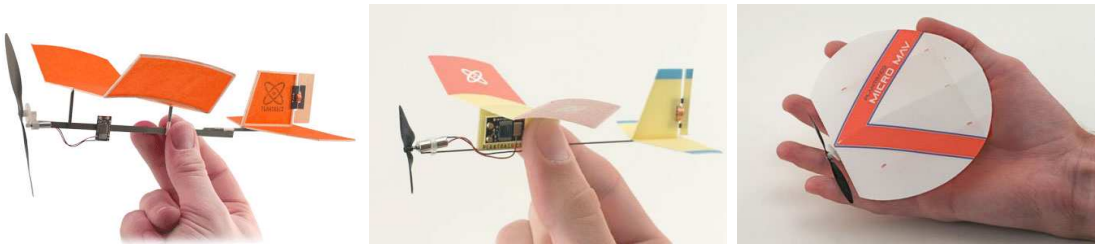

(a) *Butterfly* (b) *Micro Butterfly* (c) *MicroMAV*

Figure 1.4: Plantraco 'toy' MAVs (Plantraco, 2007).

centimetres. The advantages of decreasing size still further are few, except possibly the advantage of stealth. Another important disadvantage of fixed-wing MAVs is the lack of controlled hover ability, which almost automatically precludes their use in confined spaces. Some fixed-wing aircraft can be held in a hover by hanging from the propeller, but control is limited due to the lack of airflow over the control surfaces. In addition, unless the propeller is large, the efficiency of this mode of flight will be low.

1.3.2 Rotary-wing MAVs

The main advantage of rotary-wing aircraft over their fixed-wing counterparts is that the former can readily hover and their manoeuvrability improves at low speeds. Vertical flight is also simple. However, because rotary-wing aircraft are inevitably more complex than fixed-wing aircraft, development of rotary-wing MAVs has been comparatively slow. Most rotary-wing MAVs that have been designed so far have either used a ducted rotor or a ducted fan.

Among early contributors to this area were the US-based Lutronix Corporation. Their first MAV, the *Kolibri* (Figure 1.5), which appeared in 1997, is generally accepted as the world's first vertical-takeoff-and-landing (VTOL) MAV (Barrett et al., 2006). It was claimed to have an endurance of 30 minutes and was powered electrically or by a small diesel engine. Rumours exist that Lutronix developed 2nd- and 3rd-generation models, but Lutronix Corporation seems to have ceased to exist and further details of these models are unavailable (Goebel, 2006).

Micro Craft Inc., another US company, presented a ducted-fan MAV called

Figure 1.5: Lutronix *Kolibri* (Pines, 2007).

Figure 1.6: Micro Craft *iSTAR* (Lipera et al., 2001).

iSTAR (Figure 1.6) in 2000 (Lipera, 2000). It was 225mm in diameter, constructed largely of kevlar, and weighed 1.8kg — significantly heavier than the fixed-wing MAVs mentioned above. Flight testing was declared to be successful (Lipera et al., 2001), but Micro Flight, like Lutronix, seem now to have ceased to exist. The layout of this aircraft is similar to a current design by the US company Honeywell, which has a diameter of 325mm and a mass of around 6kg (Honeywell, 2004).

Stanford University (in the USA) started work on what they called the *Mesicopter* (Figure 1.7) in 1998, applying for $70 000 in funding from NASA's Institute for Advanced Concepts. *Mesicopter* was intended to be well below the MAV size criteria, at only 1cm across. The intention was that these tiny aircraft could be used in swarms, primarily for atmospheric studies — not only on Earth but on Mars. *Mesicopter* was designed with 4 rotors, one at each corner, for lift and manoeuver (Kroo and Kunz, 2001). It was claimed that rotor performance increased as Reynolds number decreased, and a demonstrator was constructed and was able to produce enough power to lift off. Each motor produced 700mg of lift, whereas the motor and rotor assembly had a mass of only 325mg. However this model did

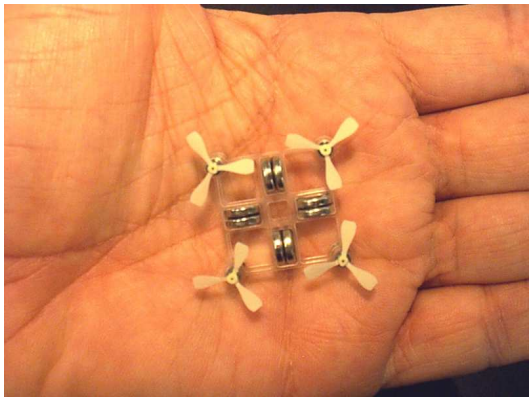

Figure 1.7: Stanford *Mesicopter* (Stanford University, 1999).

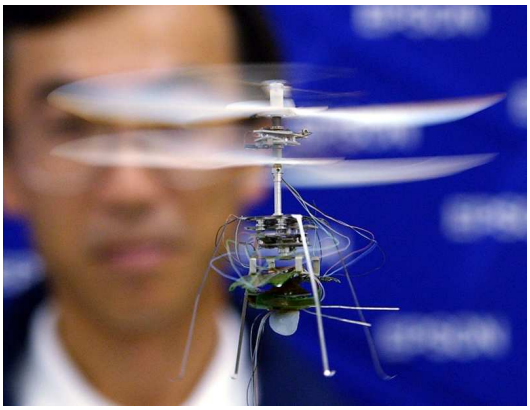

Figure 1.8: Epson μFR (Die Raven, 2005).

not carry its own power supply, being tethered to a ground source. Phase I of the project ended in 1999. A proposal was submitted for phase II of the project in order to obtain more funding, but it does not appear to have been successful and the project appears to have been shelved. At the very end, an independently-powered version of the *Mesicopter* was promised to be nearing its first flight, but it is unclear whether this ever occurred. It may be that the aircraft proved unable to lift its own power supply (Stanford University, 1999).

Epson — more commonly famed for their printers and other office equipment — started developing microrobots in the early 1990s. For 10 years, all of their products were ground-based, but in 2003 they produced what they called the Micro Flying Robot or μFR (Figure 1.8). This weighed $8.9g$ and had a pair of contra-rotating propellers of $130mm$ span, which were powered by a motor with the world's highest power to weight ratio. The μFR was developed mainly as a showcase to demonstrate Epson's micromechatronics technology and was never intended for production. It was rather uniquely controlled by shifting the centre of gravity of the helicopter rather than by a traditional cyclic control, but it did not carry its own power supply and was connected to a ground supply via a long cable. It was unable to carry any payload (Epson, 2003). However, Epson, a year later, followed this up with a new model, the $\mu FR-II$. This carried an internal battery, increasing its mass to $12.3g$, but thanks to improved motors and rotor blades the lift also increased to cope with the extra mass. The $\mu FR-II$ also carried a camera

Figure 1.9: Ikarus *Piccolo* (RC-Helicopters.net, 2004).

Figure 1.10: Silverlit *PicooZ* (Walker, 2007).

which could transmit images back to a ground station, and had some autonomous flight capability. Again, the $\mu FR-II$ was not intended for production, and in any case the limited flight time of around 3 minutes would probably have prevented it being operationally useful (Epson, 2004).

The hobby and toy industries have also contributed to this area, just as they have for fixed-wing MAVs. Commercially-available radio-controlled microhelicopters started to appear in 1999 with the release of the *Piccolo* (Figure 1.9) by the German company Ikarus. The *Piccolo* (still available in an updated version) had a rotor diameter of around $500mm$ and a flying weight of $280g$. It was powered by two electric motors — one for the main rotor, and an independent (and smaller) motor for the tail motor. It was a great success and other manufacturers quickly saw the potential for microhelicopters. The Czech company MS Composit released their first offering, the *Hornet*, around a year later. This was almost exactly the same size and weight, but was driven by only one motor — a shaft drive being used to take power from the motor to the tail rotor. It too attracted an enthusiastic following. Since then, the market for microhelicopters has undergone a huge expansion. However, most of those produced are too large to qualify as MAVs.

However, a private individual, Alexander Van de Rostyne, took the obsession with small size to extremes. Starting with the already-diminutive *Pixel I*, which had a rotor span of $370mm$ and a weight of $129g$, he progressed through *Pixel II*,

Figure 1.11: Van de Rostyne's *Piccolino* (Van de Rostyne, 2006).

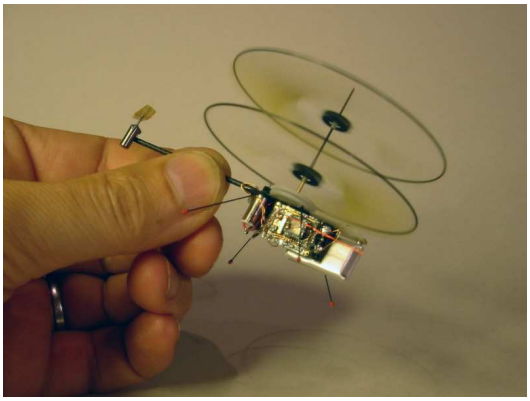

Figure 1.12: Muren's *Picoflyer* (Muren, 2005).

Pixel III, and *Pixel 2000* to the *Pixelito*, which had a rotor diameter of 148mm and a weight of 6.9g. The *Pixel 2000* led to a huge boost for Van de Rostyne, as the technology developed for it was used in a commercially available 'toy' helicopter, designed by Van de Rostyne and produced by the Chinese company Silverlit. This was called the *PicooZ* (Figure 1.10) and was released in the Summer of 2006. It had a rotor span of 130mm and a flying weight of 10g. It was sold for as little as $20 and was an enormous success. Presumably helped by the income produced by the *PicooZ*, Van de Rostyne produced the most recent version in the *Pixel* family, the *Piccolino* (Figure 1.11), in 2007. This has a rotor diameter of 63mm and a weight of 1.75g (Van de Rostyne, 2006). All of these fly via traditional human control — they are not autonomous, nor do they carry a useful payload. Flight time decreases with size; the Pixelito flies for around 3 minutes, the *Piccolino* presumably even less (at the time of writing, a flight time has not been published). Should it be argued that these 'toys' do not warrant attention, it should be noted that the *Pixelito* was suggested by NASA staff as a platform for the inspection of space vehicles during the pre-launch phase (Thirumalainambi et al., 2005).

Another private individual, Petter Muren, has developed a range of small rotary-wing aircraft, which are quite distinctively-designed and are generically called *Proxflyers*. Starting with the *Mosquito* in 2003 (rotor diameter 360mm, weight 110g), the size was gradually decreased through the *Microflyer* and *Nanoflyer* to the latest version — the *Picoflyer* (Figure 1.12), which has a rotor diameter of

60mm and a weight of 3.3g and was announced in 2005. The technology from these aircraft has also been licensed for use in commercially-available toys, though not as successfully as for the *Pixelito* above. The distinctive design has a number of advantages, including autostability, relative simplicity, and almost zero noise. On the other hand, *Proxflyers* cannot hover in even a small amount of wind, and can move only forwards (and only very slowly) — to change direction the pilot must rotate the craft in yaw until it is facing the direction he wants to move. Although the rotor system is claimed to be very efficient, flight times are still of the order of minutes — only 1 minute for the *Picoflyer* (Muren, 2005). It appears that no new models have been announced since 2005.

On the whole, then, rotary-wing MAVs have been even less successful than their fixed-wing counterparts. Perhaps this is inevitable due to the added complexity inherently involved in rotary-wing aircraft. In addition, if designing an MAV for outdoor use there seem few benefits in choosing a rotary-wing vehicle over a fixed-wing vehicle — the fixed-wing vehicle will almost inevitably be faster and more power-efficient, and will therefore have a longer range. Those companies who have proposed rotary-wing MAVs have emphasised the importance of VTOL and hover — the former for operation from unprepared land, and the latter to supply a stable platform for observation. But many (if not all) fixed-wing MAVs can be hand-launched, so VTOL is not important for most users. Also, with a modern, stabilised, gimballed camera, a stable view can be obtained even from a moving vehicle — although it may not be realistic to fit such a system to an MAV due to the small size of the vehicle. The major disadvantage of hover is that the vehicle becomes much more vulnerable to attack the moment it becomes stationary. The only conceivable potential benefit of a rotary-wing MAV for outdoor use is the ability to land and subsequently take off again autonomously — so that the MAV can "perch and stare."

Rotary-wing aircraft *are* more suited to the indoor flight niche than fixed-wing aircraft, primarily for reasons of manoeuvrability. However, the obvious size limitation for indoor flying also turns out, in the case of rotary-wing aircraft, to be a limit on efficiency, because as rotor diameter is decreased, efficiency drops,

Figure 1.13: Plantraco *Microblimp* (Plantraco, 2007).

even if disk loading is kept constant. This is due to Reynolds number effects — rotors operate best at higher Reynolds numbers. Rotary-wing aircraft also suffer from instability when flying close to walls and ceilings, due to recirculation effects. And finally, although the *Proxflyers* are apparently almost completely silent, rotary-wing aircraft in general have a high acoustic signature (because their acoustic output is concentrated at a single frequency — the main rotor blade-passing frequency) which may be a problem if the MAV is required to be discreet.

1.3.3 Lighter-than-air MAVs

Lighter-than-air machines can lift heavy payloads whilst requiring little power — in fact, once airborne, they can remain in flight without using any power whatsoever (if they are not required to move). However, since they rely on their displacement to produce lift, their size cannot be reduced without directly reducing the available lift. A $150mm$-diameter sphere ($150mm$ being the maximum dimension of the MAV) could produce an upthrust of around $0.02N$, so the total mass of the vehicle would have to be less than $2g$. The helium contained in the envelope would have a mass of around $0.3g$, leaving $1.7g$ for everything else. Given that a microhelicopter can fly with a weight of $1.75g$ (see *Piccolino*, §1.3.2) this target may not be as impossible as one might initially think. However, the envelope material would be very light and probably very fragile, and the MAV would be susceptible to gusts and air currents.

The smallest current lighter-than-air vehicle of which details are extant is the *Microblimp* (Figure 1.13), developed by Plantraco (mentioned in §1.3.1). The envelope has a diameter of around $500mm$ and the gondola has a mass of around $10g$ (Plantraco, 2007).

1.4 Flapping-wing MAVs

It seems that to design an aircraft for flight in confined spaces it is not sufficient simply to scale down existing aircraft. Due to the unique set of requirements for this type of aircraft — predominantly the need for extreme manoeuvrability and high power-efficiency at low speeds — a radical new concept is required. As often happens a possible solution is found in the world around us. There are already an enormous number of MAVs with amazing manoeuvrability (Żbikowski, 2004, 2002b) and outstanding efficiency — insects and birds. And despite the diversity in design and size, these MAVs all have one thing in common — they all fly using flapping wings. This suggests (if not proves) that flapping wings are an efficient form of propulsion and lift for aircraft at small scales, and, to confirm this suggestion, research has indicated that flapping-wing MAVs (FMAVs) should require less power at typical MAV (i.e. low) speeds than both rotorcraft and fixed-wing aircraft (Woods et al., 2001). So the required solution is not so radical or new after all, insects and birds having been around far longer than fixed- or rotary-wing aircraft. It is acknowledged, of course, that all potential types of MAVs have both positive and negative attributes, and that FMAVs may not be best suited to all potential situations. Fixed- and rotary-wing MAVs may also be useful tools in the future.

Insects and birds actually fly in quite distinct ways. Birds, which are, for the most part, optimised primarily for (relatively) high-speed forward flight rather than for hovering, generally move their wings approximately vertically up and down,

obtaining lift only on the downstroke[3]. Insects, which are optimised for extensive hovering, obtain lift from both downstroke and upstroke (Ellington, 2006).

As a result of these differences in flying technique, the performance of insects differs from that of birds. Generally speaking, insects can sustain hover — whereas birds cannot (with the exception of hummingbirds). Insects are more manoeuvrable than birds at very low speeds. In short, the capabilities of insects match the requirements of an MAV more closely than those of birds. However, historically, most man-made flapping-wing vehicles have been based on bird-like flapping.

Flapping-wing aircraft [often called ornithopters — from the Greek *ornithos* (bird) and *pteron* (wing)] are not a new idea. In fact, many of the earliest-designed (pre-1900) aircraft were designed to fly like birds, and the earliest recorded (unmanned) ornithopter flight occurred in 1870 in Paris. Since then, manned ornithopters have been developed and, in a few cases, flown. But in parallel with this, enthusiasts and hobbyists have developed a large range of smaller ornithopters for recreational purposes. Most of these have been rubber-band powered, with a few having electric motors and even fewer being fitted with internal-combustion engines. However, it was not until the late 1990s that the first ornithopters designed to carry a useful payload and perform a useful task were designed.

Ornithopters have generally been designed in one of three ways. Firstly, there are the original and authentic ornithopters that fly like birds. Secondly there are those that fly like insects, although these are less common and are occasionally called entomopters [from the Greek *entomo* (insect) and *pteron* (wing)]. Finally there are those which have flapping wings, but which do not fly like birds *or* insects. There are those that argue that basing an MAV on insect or bird flight may not be the optimum solution, because insects and birds may not actually be designed to perform the same functions as an MAV would be required to perform. There is also the argument that the optimum solution may not appear in nature; that perhaps it is possible to *improve* on what is achieved in nature using modern materials and

[3] The exception to this rule is the hummingbird, which could be described as a feathered insect because its wing kinematics (at least during hover) are very similar to those of insects. However, there are some indications that the aerodynamics of hummingbirds do differ from those of insects (Ellington, 2006).

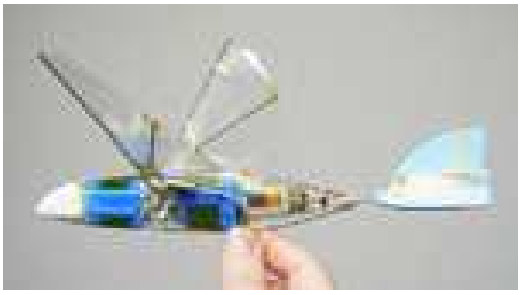

Figure 1.14: AeroVironment *Microbat* (Keennon and Grasmeyer, 2003).

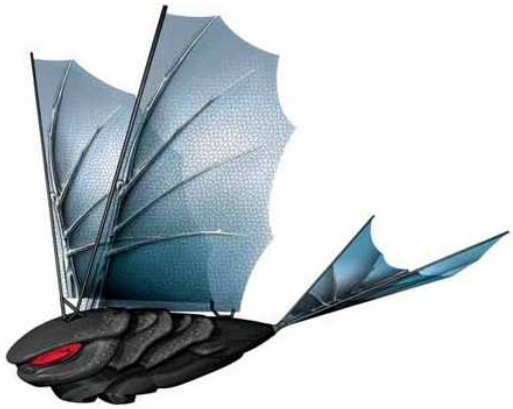

Figure 1.15: *i-Fly Vamp* (Thumbs Up (UK) Ltd, 2007).

manufacturing techniques.

1.4.1 Past and current FMAVs

It is generally accepted that the first 'serious' FMAV to fly was the *Microbat* (Figure 1.14), developed jointly by AeroVironment (see their fixed-wing MAVs, discussed in §1.3.1) and Caltech (California Institute of Technology). The first flight was in late 1998, but the aircraft was free-flight (i.e. not controllable) and had a maximum flight time of only 9 seconds. The next version doubled the maximum flight time but was still not controlled. A radio-controlled version first flew at the end of 2000 for 42 seconds, having a flying mass of $12.5g$ and a wingspan of $225mm$. *Microbat* has wing kinematics resembling those of a bat — closer to those of a bird than an insect — and the most recent version apparently has an endurance of 25 minutes (Keennon and Grasmeyer, 2003). However, the project now appears to have been shelved and no mention of the *Microbat* appears on AeroVironment's website (AeroVironment, Inc., 2007a).

Petter Muren (of *Proxflyer* fame, see §1.3.2) has recently turned his hand to flapping-wing aircraft, demonstrating a $10cm$-wingspan, $1g$-mass ornithopter. Details of this are scarce, but it appears that the technology in it has now been incorporated into a 'toy', the *i-Fly Vamp*, with a $300mm$ wingspan and a mass of around $12g$. The aircraft is rather unique in that all the control is carried out using the wings, whereas most other ornithopters (including the *Microbat*) use a

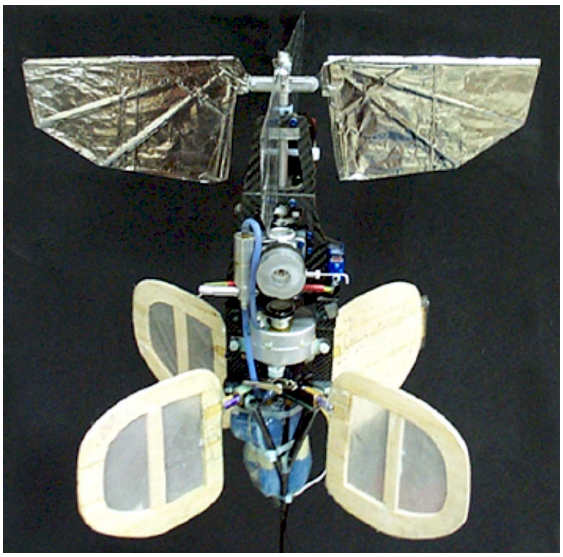

Figure 1.16: SRI International *Mentor* (Jones et al., 2004).

tail for control. It is not likely that hover is possible, given the kinematics of the wings, and it is unclear whether the aircraft has the potential to carry a payload. Like the *Microbat*, the *i-Fly Vamp* uses wing kinematics like those of a bird rather than an insect.

A US company, SRI International, worked in conjunction with the University of Toronto to produce the *Mentor* (Figure 1.16), an FMAV with a $360mm$ wingspan and a mass of around $500g$. It is notable that although the wingspan of the *Mentor* is similar to that of the *i-Fly Vamp*, the mass is very much greater. Two flying prototypes were produced — *SF-2.5* being powered by an internal-combustion engine, and *SF-3* by an electric motor. The design of the *Mentor* was fundamentally different to that of the *Microbat*. Instead of having a single pair of wings flapping in a vertical plane, the *Mentor* had four wings which flapped in a horizontal plane. The aircraft could hover, and tilting the whole aircraft allowed transition into forward flight; a similar approach to that used on helicopters. The *SF-2.5* carried sufficient fuel for only 6 minutes of hovering flight and the *SF-3* could fly for only 20s before a landing had to be made to allow the batteries to recover. Transition from hover to forward flight was demonstrated, but not *vice versa* (Zdunich et al., 2007). The kinematics of the *Mentor* are based on insect-like flapping but only on one particular aspect of it, the clap-and-fling (see §2.1.1). This technique produces

Figure 1.17: TUDelft *Delfly* (Roos, 2007).

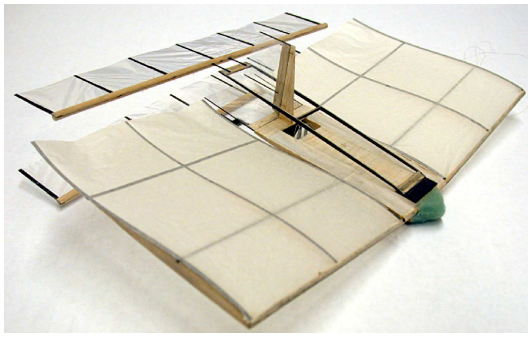

Figure 1.18: NPS' first flying model (Jones et al., 2004).

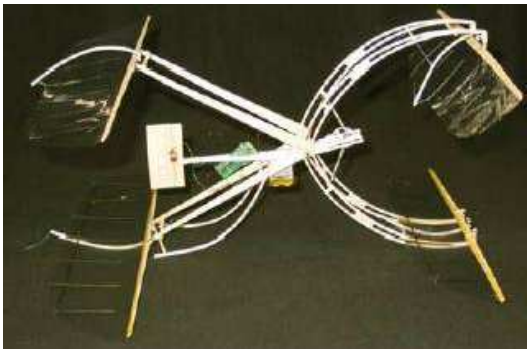

(a) Open

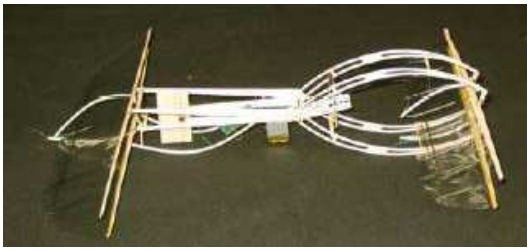

(b) Closed

Figure 1.19: NRL *BITE-Wing* (TechLink, 2006)

high lift but, from the flight times given, it appears it may not be particularly efficient, although the short flight times could also be a result of the comparatively high weight of the aircraft. The *Mentor* project appears to have ended in 2001 and again no mention of the project can currently be found on SRI International's website (SRI International, 2007).

At TUDelft (the Delft University of Technology, in the Netherlands), a project was commenced in January 2005 to design a $15g$ flapping-wing MAV capable of carrying a camera — named *Delfly* (Figure 1.17). Less than 10 working weeks later, the design team had decided on the final form of the aircraft, and by September 2005 a flying model had been produced. With a wingspan of $350mm$ and mass of $17g$, it could fly for up to 17 minutes. It had a similar layout to the *Mentor* (although the aircraft was very much lighter), with 4 wings flapping about a single point providing propulsion, and control provided by an inverted v-tail. Hover was achieved by rotating the craft nose-up, and videos of *Delfly* show that the aircraft

hovers in the same way that a fixed-wing aircraft can be made to hover, by simply pointing the nose vertically upwards and setting the thrust of the engine equal to the weight of the aircraft. *Delfly* in hover is not as stable as a rotary-wing aircraft in hover and appears to have been designed primarily for forward flight. In addition, its hover is inefficient, with the battery capable of powering only 8 minutes of hovering flight. The project was a success, and demonstrated some autonomous flight capability, being able to fly towards a target; but the electronics enabling this autonomy were not contained within the aircraft, as images from the onboard camera were transmitted back to a ground station, where they were processed and translated into commands, which were then transmitted back to the aircraft. So although the aircraft had some ability to fly without direct human control, it was not fully independent, as it was reliant on a remote ground control station (Mols, 2005).

Delfly II, which was first flown at the end of 2006 after a 1-year development period, is slightly smaller in size ($300mm$ maximum dimension, $16g$ mass) and has a different control system. Whereas *Delfly* was flown using a traditional radio-control transmitter, *Delfly II* has computerised flight control software which takes the pilot's input, compares it to the aircraft's current attitude using images from the onboard camera, and calculates the required steering inputs, transmitting these to the aircraft. Because of this system, it is claimed, *Delfly II* is very easy to fly. Flight time is slightly less than for *Delfly*, being limited to 15 minutes of forward flight or about half that time if hovering. Again, if the control link between ground station and aircraft were broken, *Delfly II* would be unable to fly. The latest stage of the *Delfly* project commenced in January 2007, called *Delfly NaNo*. The aim of this 4-year project is to build a *Delfly* with a wingspan of $5cm$. At present, a $10cm$ wingspan *Delfly* is being developed (Roos, 2007).

All of the above aircraft either fly like birds or utilise certain aspects of insect aerodynamics. However, researchers at the US Naval Postgraduate School (NPS) have taken another approach. They base their approach on the idea of going *beyond* what is seen in nature — taking inspiration from the flapping-wing creatures which surround us, but not attempting to reproduce them precisely. They started

by observing that birds often fly close to the surface of the earth or sea, taking advantage of the presence of the surface to increase efficiency. By utilising two wings, one above the other, moving vertically in opposition to each other (i.e. 'clapping'), each wing can theoretically experience 'ground effect' due to the presence of the other wing, as well as producing thrust *via* the Knoller-Betz effect (Jones et al., 1998). This is the basis of the NPS designs. Their first model flew in late 2002, and had a fixed wing in front of two 'clapping' wings (Figure 1.18). The span of the aircraft was $300mm$ and it had a mass of around $14g$. It proved virtually stall-proof, but was apparently not capable of hover. As of mid-2005, the design had been refined to give a $230mm$ span and a mass of $11g$, but hover was still not possible (although the minimum forward speed was only $2m/s$). Duration of flight was up to 20 minutes (Jones et al., 2001, 2003, 2004; Platzer and Jones, 2006).

A similar (but different) concept has been advocated by the US Naval Research Laboratory (NRL). Their craft — called the "Biplane Insectoid Travel Engine" (*BITE-Wing*) — has no fixed lifting surfaces (unlike the NPS designs above) and instead has a pair of clapping wings (Figure 1.19), with one pair at the front of the craft and the other pair at the rear. Most of the aircraft that have been built are between 400 and $500mm$ long and have a mass of between 20 and $30g$. Video of the aircraft in flight (TechLink, 2006) show that it is dynamically balanced, as claimed (US Naval Research Laboratory, 2007), leading to very smooth flight. However it appears that a payload is not carried at this stage, nor does hover seem possible. Details of the project are sketchy, but the concept has been patented (US Patent Office, 2004). It appears that the US Navy is currently seeking a partner to commercialise the concept for the hobby market (TechLink, 2006).

None of the above FMAVs fly exactly like insects. Some fly like birds: some fly using *some* of the techniques that insects use, but not exactly like insects: and there are others which do not fly like birds *or* insects. In fact, there are only a few organisations in the world which aim to reproduce the kinematics and flight dynamics of an insect in an FMAV. Perhaps the most prominent of these is the University of California, Berkeley (UCB). Since 1998, they have been working on the *Micromechanical Flying Insect (MFI)*, with a stated goal of developing a

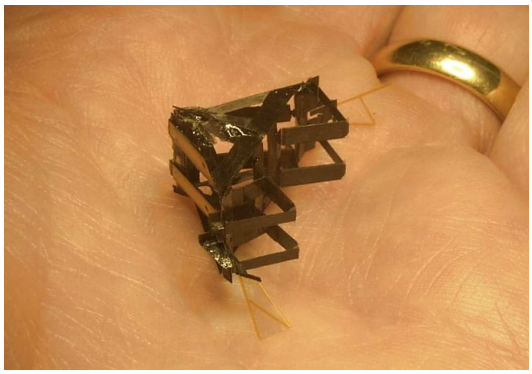

Figure 1.20: UCB *MFI* mock-up (Fearing, 2007).

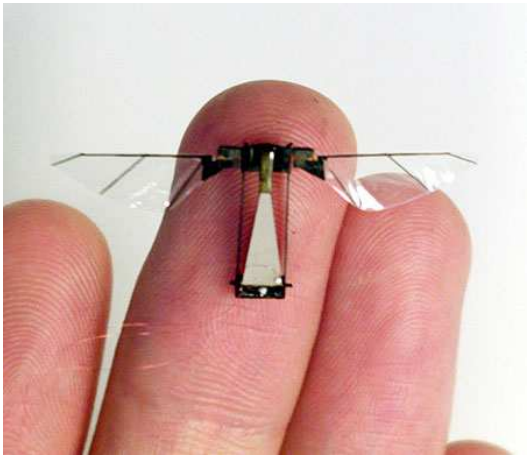

Figure 1.21: Harvard *FRI* (Harvard Microrobotics Laboratory, 2007).

$25mm$ wingspan vehicle with a mass of $0.1g$ (Fearing, 2007). Using state-of-the-art techniques for construction of their tiny mechanisms (Figure 1.20), they eventually 'broke even' (in terms of lift) in late 2003, when they measured $500\mu N$ of lift from a single wing, meaning that two wings would theoretically lift their $100mg$ target vehicle (Avadhanula et al., 2003). Gradual refinement followed until, by 2007, lift had increased to $1.4N$ per wing (Steltz et al., 2007). Rather uniquely, UCB intend the *MFI* to actually have sensors like those found on an insect, so that to all intents and purposes the *MFI* is, as it says, a mechanical insect. In September 2007 UCB were awarded almost $600 000 (US) in order to study progression from the current engineering models to flight-capable aircraft. The funding award runs until September 2010, indicating that a fully operational *MFI* may still be some years away.

A similar project is also underway at Harvard University, led by a former Berkeley PhD student. In 2007, they demonstrated a $30mm$ wingspan, $60mg$ *Flying Robotic Insect (FRI)* that was able to demonstrate lift-off (Figure 1.21). There was no control mechanism, so the aircraft was guided vertically up a pair of thin wires, and power was delivered to the aircraft through the same wires, but this does appear to the first device to actually lift its own weight (Wood, 2007; Harvard Microrobotics Laboratory, 2007).

Here in the UK, research into developing an FMAV based on insect-like flap-

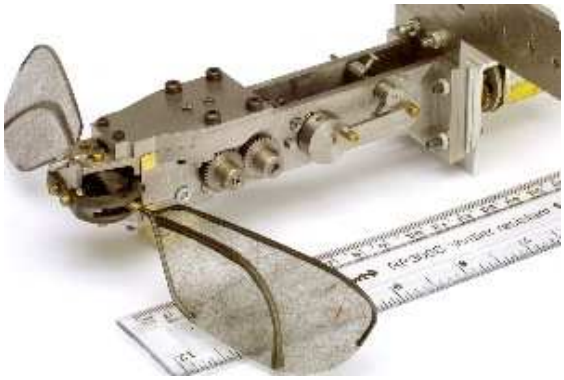

Figure 1.22: Cranfield flapping kinematics demonstrator (Żbikowski et al., 2005).

ping is predominantly being carried out by a small group of Universities. Cranfield University at the Defence College of Management and Technology, Shrivenham, (formerly the Royal Military College of Science) are carrying out research into the aerodynamics of insect-like flapping (Żbikowski, 2002a; Pedersen, 2003; Ansari, 2004; Ansari et al., 2006a; Wilkins et al., 2006; Wilkins and Knowles, 2007), developing mechanisms (Figure 1.22) to reproduce the kinematics required (Żbikowski et al., 2005; Galiński and Żbikowski, 2007), and working on materials which could be incorporated into FMAVs (Friend et al., 2003). At Cranfield University's campus in Bedfordshire, piezoelectric actuators are being developed that could have applications in MAVs (Duval et al., 2007). Engineers at Bristol University are also developing mechanisms (Conn et al., 2006, 2007) and zoologists at both Oxford and Cambridge Universities are applying their knowledge of insect aerodynamics to FMAVs (Ellington, 1999; Bomphrey et al., 2005).

1.4.2 Justification for an insect-like FMAV

Some justification must be given for the decision to concentrate on emulating insect-like flapping so precisely. There are those, as mentioned above, who advocate the view that it may be inadvisable to attempt to mimic insects exactly, because it is not necessarily true that insect-like flapping is the optimum solution for an MAV. This is certainly true for some MAVs. For example, an MAV designed to fly outdoors in all weather might be more likely to be a success if it were *not* based on insect-like flapping. But there are a number of reasons why, for the

particular application that is envisaged here, insect-like flapping is a plausible solution. As mentioned above, a major motivation for developing MAVs is their ability to operate in confined spaces. The small number of fixed-wing MAVs that have flown have proved that such craft are of limited value for indoor flight. Rotary-wing aircraft are more suitable in terms of manoeuvrability, but small rotors are inefficient (Ramasamy et al., 2007). Flapping wings do seem therefore to be the best (or at least a viable) solution. The ingenious 'clapping-wing' craft of the NPS and NRL do not have the ability to hover. Bird-like ornithopters (e.g. *Microbat*) are designed primarily for forward flight and again do not have the required hover ability. And the 'quasi-insect' flappers (e.g. *Mentor*, *Delfly*) are also unsuitable for hover — again, being primarily designed for forward flight. None of these designs have been able to get even close to what can be observed in insects. For an indoor MAV, insect-like flapping does appear to be the optimum solution.

That is not to say that it is definitely necessary to reproduce insect-like flapping *precisely* in an FMAV — there may well be some simplifications that can be made without affecting performance. But before it is possible to know what these simplifications are, it is necessary to understand what techniques and phenomena insects use to stay aloft, and have some idea of the relative importance of those techniques. This is the aim of current work at Shrivenham, of which this thesis forms a part.

Chapter 2

Literature survey

> *"Of making many books there is no end; and much study is a weariness of the flesh."*
>
> — Ecclesiastes ch.12, v.12

In this chapter, the currently-extant literature relating to insect-like flapping is examined, starting by looking at work pertaining to the kinematics of insects, before moving on to look at some of the aerodynamic phenomena produced by these kinematics. Some past attempts to analyse insect-like flapping are discussed, including experimental, analytical, and computational approaches. Finally, some literature relating to general low Reynolds number aerodynamics is reviewed.

2.1 Insect flight kinematics and aerodynamics

2.1.1 The kinematics of insect-like flapping

The human eye is not fast enough to capture the kinematics of insect flight in any great detail. Marey (1868) was one of the first researchers to try to overcome this problem. He took a sheet of paper which was covered in a black substance, and held an insect using forceps so that the tip of one wing brushed against the paper. As the insect flapped, the pattern of its wing tip was traced out on the paper by the removal of the black substance. Marey was not satisfied with this arrangement, as he realised that the friction between the wing tip and the paper resulted in a change

in the insect's flapping motion — slowing down the frequency of flapping — and therefore it was not possible to be confident that the results were the same as they would have been had the insect been flying freely. He therefore tried a different method; coating the wing tip of an insect with a thin layer of gold, he then shone a ray of sunlight onto the insect as it flew. The wingtip left behind a luminous trace, visible to the naked eye, due to the high flapping frequency (Marey tried the same technique with birds but the flapping frequency was too low for a trace to be visible). This trace took the form of an extended figure of eight — perhaps the first indication that insect-like flapping was not simply a matter of direct up-and-down motion. Marey later constructed a 'mechanical insect' to illustrate what he had found (Braun, 1995).

By the 1920s, the advent of cinematography meant that it was easier to capture the motion of insect wings and the novel and ingenious methods of Marey were no longer needed. However, the next problem that presented itself was the question of keeping insects still for long enough to film them. In the 1930s Magnan (1934), who originally worked on birds (Magnan, 1922), extended his studies to include insects and used high-speed cinematography to observe insects during free flight, concluding (like Marey) that generally the wing tips moved in a figure-of-eight. However, most researchers continued to tether insects in some way to make observation easier. As mentioned above, early researchers simply held the unfortunate insects in forceps. By the 1940s, however, questions were starting to arise over how this method (and similar methods) might affect the insects and more specifically how tethering might affect their wing motions.

Hollick (1940) stated that "diverse methods have been employed in the past for mounting insects which were to be held stationary. It has long been recognised that the legs should remain free, and that wing movements normally cease if the tarsi make contact with any support." In other words, insects generally do not flap their wings if their feet are touching anything. It was generally accepted that insects should therefore be mounted from above, using rods attached to the upper thorax or abdomen. Exactly where these rods should be attached was a matter for much discussion — but it was accepted that insects needed to be constrained in

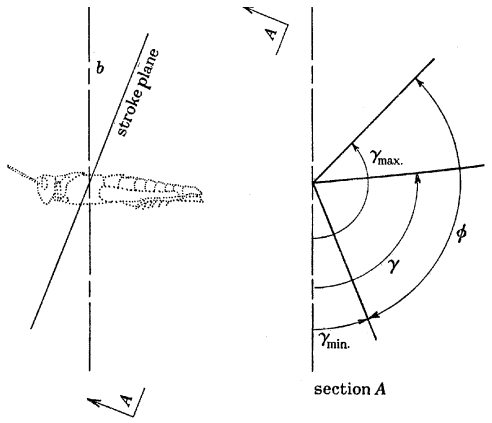

Figure 2.1: Wing stroke parameters, from Weis-Fogh and Jensen (1956).

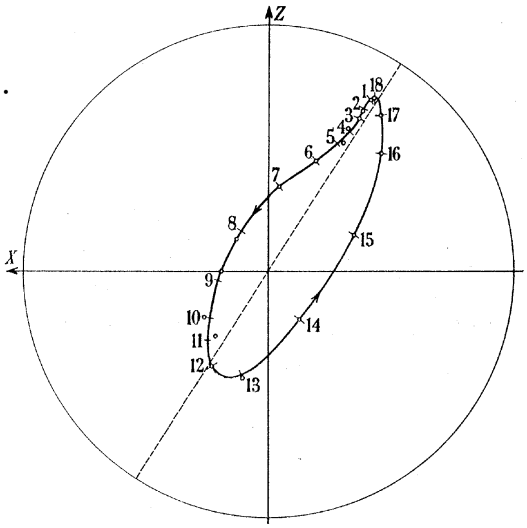

Figure 2.2: Example of locust wing kinematics, from Jensen (1956). The insect lies at the origin and is flying forwards in the direction of X, with Z being vertically upwards. Only one wing is shown.

some way, and that filming them in free flight was impractical. However, Hollick (1940) carried out experiments in which an insect [the Dipterous[1] fly *Muscina stabulans* (Fallén)] was mounted on a trolley, accelerated to a certain speed, and then suddenly released. A camera was focussed on the area through which the insect would be expected to fly, so that the insect was captured in free flight. It was concluded that insects generally did not change their body orientation on being released. Insects were also studied whilst being held stationary in a stream of air, and Hollick concluded that "there are good grounds for believing that the living insect held stationary in an appropriate stream of air closely resembles in essentials the system in free flight and is therefore suitable for further study of flight." He also reported that the wing tip path was not a figure-of-eight when the insect was hovering (it was instead a distorted ellipse) but that as airspeed increased a crossover was introduced and a figure-of-eight was formed.

Weis-Fogh and Jensen (1956) examined the problem of determining the kine-

[1]That is, having only one pair of functional wings. The work of which this thesis forms a part has concentrated on insects with one pair of wings, as they generally have the ability to hover and are highly manoeuvrable.

matics of insect-like flapping in some detail and commented that the flapping of an insect's wing can be reasonably described by three variables: firstly, the frequency of flapping f (which, it has been subsequently determined, is roughly inversely proportional to the size of the insect — as low as $5Hz$ for large insects and as high as $1\,000Hz$ for the smallest); secondly, the angle of the stroke plane to the vertical (b in Figure 2.1) and, thirdly, the positional angle of the wing along the stroke plane (γ in Figure 2.1). They noted that the frequency of flapping was almost always determined in studies of insect flapping; the stroke plane angle was sometimes recorded; but that the variation in positional angle of the wing in time was rarely studied, a sinusoidal oscillation being assumed in most cases. Weis-Fogh and Jensen also noted that in order to understand insect flight comprehensively, data were needed on wing twist and angle of attack, as well as any motion of the wing perpendicular to the stroke plane. They concluded that at that time the kinematics of insect-like flapping were not "sufficiently well known to permit a theoretical treatment of the energetics of natural flapping flight." As part of the same body of work, Jensen (1956) used a stroboscope and slow-motion film to capture images of locusts as they 'flew' whilst tethered in a wind tunnel. He stated that the insects "flew under nearly the same conditions as during natural forward flight" and presented data for stroke frequency, stroke angle and middle angular position (for both pairs of wings) and flying speed. He also presented detailed plots of wingtip positions for complete strokes (see Figure 2.2 for an example plot), for both forewing and hindwing. All this work was carried out with locusts (*Schistocerca gregaria*), which are incapable of hovering flight and also possess two pairs of wings; some of their results, therefore, may not be relevant to the case of two-winged hovering insects.

Vogel (1967a) photographed fruit flies (*Drosophila virilis*) that were tethered in a wind tunnel. He reported that wing beat frequency was almost constant, and that wing pitch angle was dependent only on the position of the wing within the stroke, suggesting that wing pitch was not actively controlled (during strokes) by the insect but was set by the structural characteristics of the insect. Vogel postulated that control was primarily effected by varying body angle, and that

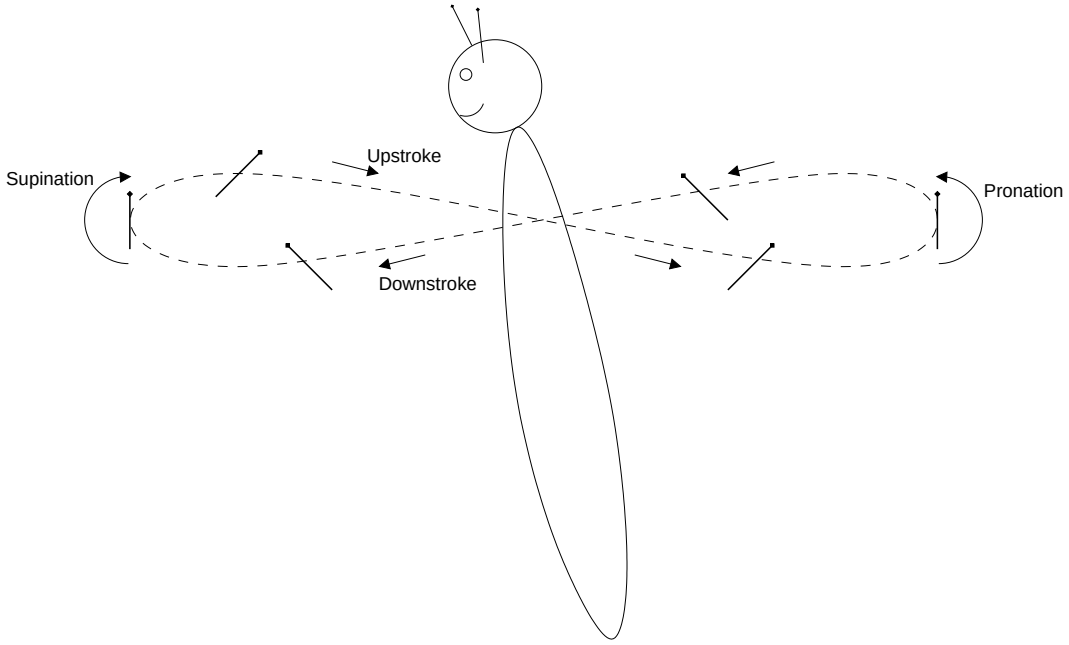

Figure 2.3: Typical insect wing kinematics. The wing tip is shown moving in a figure-of-eight pattern about a horizontal stroke plane. The leading edge of the wing is marked by the black circle.

this was done using the hind legs as 'elevators'. But it was also concluded that this was not be the only means of changing body angle, since specimens that had had their legs removed continued to fly in normal fashion. According to Vogel, the results suggested that "the flight machinery of fruit flies is considerably simpler than that of larger flying animals" (Vogel, 1967a, p. 391).

By this time it was generally accepted that insects moved their wings in a complex and variable manner, but that generally (at least for many insects, and for the case of hover) each wingtip traced a figure-of-eight. The entire wing cycle, it was seen, could be broken down into four sections (to be defined below) — downstroke, supination, upstroke, and pronation — and this breakdown has subsequently been shown to be reasonable. The downstroke commences with the wing tip above the insect's body. The wing then sweeps forwards and downwards (travelling, typically, around 4 chord lengths at the mid-span location), coming to rest below the insect's body. The wing then rotates in pitch (angle of attack) through a large angle (typically around 120°) — this is termed *supination*, and results in the leading edge from the downstroke being also the leading edge for the upstroke. The

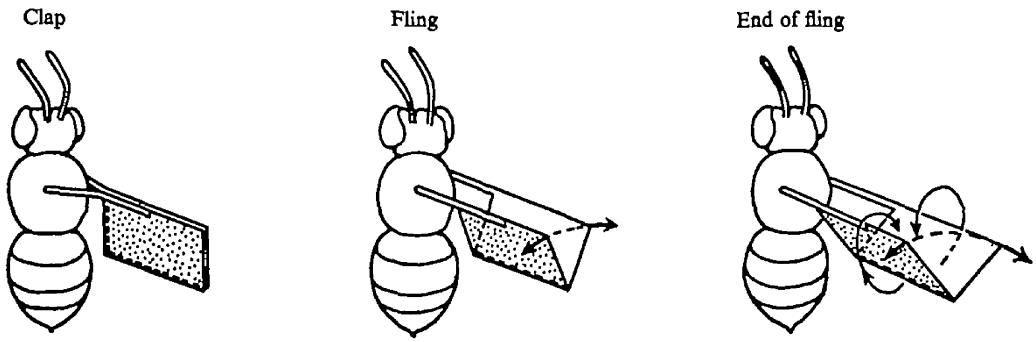

Figure 2.4: Clap and fling mechanisms, from Weis-Fogh (1973, Figure 21).

upstroke then begins, being an approximate 'mirror-image' of the downstroke. At the top of the upstroke the wing rotates again, in the opposite direction (this is termed *pronation*), ready to start the next downstroke. This process is illustrated in Figure 2.3. Further research was needed, though, to investigate the role of each of these four phases in producing lift; at this point it was generally thought that the lift was produced during the upstroke and downstroke, and that the pronation and supination phases were only necessary to prepare the wing for the next stroke.

Weis-Fogh (1973), again using slow-motion film of free-flying insects, confirmed that the exact motion of an insect's wings depends on the flight speed of the insect — so that insects in fast forward flight tend to flap their wings in a vertical plane, whereas in the hover the stroke plane is more horizontal. Weis-Fogh also identified extreme elastic deformation of the wings of some insects in flight, and, most importantly, identified some novel aspects of flapping in some cases — the clap (where the wings are brought together at the end of stroke), the fling (where the opposed wings are flung open like a book, both wings rotating about their trailing edges), and the flip (where a wing is pitched rapidly through about 180°). The clap and fling mechanisms — which usually occur together — are shown in Figure 2.4. Weis-Fogh suggested that these were mechanisms of lift augmentation, and that some insects (generally small insects, such as the wasp *Encarsia formosa*) depend almost entirely upon these mechanisms to remain aloft — thus going against the then-accepted opinion that pronation and supination did not contribute to the lift. Lighthill (1973) later carried out some analysis on the clap-and-fling, calling it

the "Weis-Fogh mechanism of lift generation," and others tested the mechanism experimentally and reported that it could indeed produce large circulations and hence large lifts (Bennett, 1977; Maxworthy, 1979).

So, accurate descriptions of the kinematics of insect-like flapping began to appear in the middle of the 20th century; but even by 1984 one prominent researcher noted that "relatively few such descriptions [of the kinematics of insect wings] can be found in the literature" (Ellington, 1984c, p. 43). As part of a seminal series of papers, Ellington (1984a,b,c,d,e,f) then gave detailed descriptions of the kinematics of a wide range of insects in unconstrained flight, concentrating on hover. He found that for most insects the flapping motion of the wing differed only slightly from a sinusoidal motion — so that the displacement of the wing tip could be approximated by a sinusoidal function of time. However it was also noted that wing kinematics varied widely between species and often within species — some species had a detectable 'general' wing tip path whilst others showed "such a large individual variation that no general path [could] be detected" (Ellington, 1984c, p. 63). Some insects used figure-of-eight tip paths, whilst others did not. Ellington postulated that the exact form of the wing path might not be very important in flight and that it was unnecessary to attach too much significance to it — suggesting that the general form of wing motion might be more important than the details specific to each species of insect. He also looked further at the unsteady mechanisms of lift proposed by Weis-Fogh (1973), and postulated that the 'fling' mechanism would generate circulation which would persist for the following half-stroke, and that this circulation would generate sufficient lift for flight (Ellington, 1984d, p. 101). Ellington also proposed a number of other 'special' aerodynamic mechanisms which could enhance lift — such as isolated rotation of a wing and flexing of a wing during rotation, although it was confessed that these proposed mechanisms were "highly fanciful and speculative" (Ellington, 1984d, p. 106) and that the deductions in the paper were "too tentative even to consider them as 'conclusions'" (Ellington, 1984d, p. 109). It was beginning to become clear that unsteady mechanisms did play an important part in the flight of at least some insects, and that (contrary to the assertion of Vogel (1967a)) insects did actively

rotate their wings (in pitch) during flight.

The series of papers of Ellington seems to have stimulated a growth in interest into insect flight. Ennos (1989b) used high-speed film of Dipterous flies in free flight, and noted that some insects hovered with a horizontal stroke plane, and others used an inclined stroke plane — the difference being that a horizontal stroke plane was more efficient but less stable and manoeuvrable. He proposed that insects manoeuvred by tilting the force vector from their wings, and stated that this did not usually involve tilting the stroke plane, but that insects adjusted the timing of pronation and/or supination in order to change the relative lift produced by the upstroke and downstroke. Clap-and-fling was widely used to allow vertical takeoff. Ennos bemoaned the fact that there was no reliable way of measuring the angle of attack of an insect's wings in free flight and that therefore the timing and speed of rotations could only be estimated. At any rate, it was becoming clear that insect-like flapping was more complex than scientists had thought, making use of novel methods of lift augmentation.

It would be unfair not to mention the work that at this time was simultaneously being carried out in what was then the USSR. Unfortunately all of the early work was published in Russian and has therefore remained relatively unknown to most of the wider research community (see e.g. Antonova et al., 1981; Brodsky and Ivanov, 1984). Later on, some work began to appear in English — Brodsky (1991) described his work on tethered butterflies, but again there is no discussion of how the tethering itself (nor the smoke that was used for visualisation) might affect the insect.

Götz (1987) tethered flies (the Dipterous *Drosophila melanogaster*) in a 'flight simulator', where (by measuring the stroke amplitude of each wing) it was estimated when the insect was trying to turn and in which direction, and the surrounding objects in the simulator were rotated, to give the fly the impression it was flying freely. High speed photography was obtained of the clap-and-fling mechanism. Götz commented that the wings on a particular fly, after about 23 million clap-and-flings, showed no evidence of any wear or tear and concluded that, in the particular species under investigation, the lift-enhancing effect of the vigorous 'clap

and fling' seemed to be essential for the support of the body weight of the hovering fly. This was more evidence that unsteady aerodynamics plays a vital role in the flight of insects. Dickinson et al. (1993) found that some insects actively regulate the timing of wing rotations to manoeuvre, and suggested that this explained how they could change the direction of wing forces without changing stroke plane angle. Dickinson (1994) later estimated the speed of rotation during pronation and supination to be as high as $5 \times 10^5\ deg/s$ — equivalent to around $83\,000\,rpm$.

Srygley and Thomas (2002) investigated the flight of butterflies and reported that they use a "variety of unconventional aerodynamic mechanisms to generate force." They concluded that there "seems to be no one 'key' to insect flight; instead insects rely on a wide array of aerodynamic mechanisms to take off, manoeuvre, maintain steady flight, and for landing" but also said that "the situation may not be as complex as it first seems, because inspection of the flow visualisation videos suggests that [butterflies switch] between different aerodynamic mechanisms through rather simple changes in wing-beat kinematics" — so force production can be varied by simple changes in wing motion.

The kinematics of insect-like flapping have now been relatively well established and it has been demonstrated that many insects depend on unsteady effects to augment lift. Any FMAV will have to reproduce these complex kinematics in some way, although it is not yet clear which aspects of the motion are the most important.

2.1.2 Mechanical 'flappers'

As has been seen, the efforts to determine the kinematics of insect wings have generally been useful, and have resulted in a good understanding of what exactly insects do with their wings. However, this in itself, though vital, does not help to answer the more fundamental question of how it is that insects actually fly — that is, how is the motion of their wings converted into a lift force? In order to address this question it is arguably vital to have some idea of what an insect wing does to the air it moves through. At the most fundamental level, a force on a wing is caused by a pressure difference between its lower and upper surfaces, but how does

an insect produce this pressure difference, and what aspects of insect wing motion are the most important in doing so?

Visualising the flow around real insects is challenging due to their small size. Some researchers have sought to circumvent this problem by building mechanical insects ('flappers') which reproduce insect-like flapping but on a much larger scale and at much lower flapping frequencies. This combination makes visualising the flow much easier. There are three main contributors to this area — Ellington (at Cambridge University), Dickinson (at the California Institute of Technology) and most recently Leishman (at the University of Maryland). The former two have taken the approach of scaling up an insect quite significantly — with Ellington choosing a scale factor of around 10 (Ellington et al., 1996) and Dickinson (who based his 'flapper' on a smaller insect) around 200 (Dickinson et al., 1999). The mechanism of Leishman is comparatively small and is not based on a specific insect but, rather, a prototype FMAV (Ramasamy and Leishman, 2006). Another important difference is that Dickinson's 'flapper' operates in oil, whereas the other two operate in air.

These models have provided significant insight into some aspects of the aerodynamics of insect-like flapping, as is shown later. However, the mechanism of Dickinson et al. (1999) is designed to represent a fruit fly with a wing span of 2.5mm. The mechanism itself has a span of 60cm and therefore flaps much more slowly than the real insect (at about $5Hz$). The scaling is such that Reynolds number is kept constant. However, some have expressed concerns that other dimensionless parameters may not have been preserved and that this may mean that results from these mechanisms are unreliable (see e.g. Galiński and Żbikowski, 2007).

Appendix A explores these issues and shows that Reynolds number *is* the only parameter of importance when scaling up insect-like flapping. It is shown that the frequency of vortex shedding is dependent on two factors — kinematics (which affects the frequency of forced shedding) and Reynolds number (which affects the frequency of both forced and free shedding). Therefore, provided that kinematics and Reynolds number are preserved when moving from insect to 'flapper', the

Parameter	Value
Wing length	$112.5mm$
Mean chord	$66.67mm$
Flapping frequency	$12Hz$
Stroke amplitude	$120°$
Wing offset	$37.5mm$

Table 2.1: Wing parameters for an 'optimised' FMAV (from Ansari (2004, §7)). Wing offset is the distance from the wing root to the rotation axis.

dynamics of the flow and the force coefficients will also be preserved.

2.1.3 Insect flight aerodynamics

One of the first differences between insects and more-conventional 'aircraft' concerns size. Insects are almost without exception smaller than any man-made fixed- or rotary-wing aircraft, and therefore operate at extremely low Reynolds numbers[2]. To give one example, one of the smallest flying insects, the fairy fly (*Alaptus magnanimus*) has a wingspan of only 0.2mm (Natural History Museum, 2005). If it is assumed that it flaps its wings at around 1 000 strokes per second (i.e. 500 complete upstroke-downstroke cycles per second), and that each wing travels through 180° per stroke, the average tip speed will be approximately $0.3m/s$. This gives a Reynolds number of $O(1)$. Admittedly, most flying insects are larger than this extreme example: Vogel (1994) gives the Reynolds number of the smallest flying insects as of $O(30)$ (Vogel, 1994, table 5.1). This is still extremely low in the context of a typical passenger jet, which might operate at wing chord Reynolds numbers of $O(10^7)$ (see Figure 2.5). For this reason alone, perhaps it is not surprising that attempts to analyse insect flight using ideas and techniques that were developed for much higher Reynolds numbers have often failed, as is shown later.

Any FMAV is likely to be larger than a typical insect (though fossils have been

[2]Reynolds number (Re) is given by

$$Re = \frac{\rho V l}{\mu}, \tag{2.1}$$

where ρ and μ are fluid density and viscosity respectively. In this thesis, for 2D cases, l is wing chord and V is wing velocity; for 3D cases, l is wing mean aerodynamic chord and V is mean wing tip velocity.

found of much larger insects than those alive today — see below), so it is useful to gain an understanding of the Reynolds number at which an FMAV is likely to operate. To do this, the wing parameters for an 'optimised' FMAV given by Ansari (2004) are used. The parameters needed are given in Table 2.1. Reynolds number in this case is based on mean tip velocity and mean aerodynamic chord. The mean tip velocity can be found from the wing length, flapping frequency and stroke amplitude. The distance travelled by the wingtip per stroke can be found by:

$$\begin{aligned} d &= \frac{120}{360} \times 2 \times \pi \times r \\ &= \frac{120}{360} \times 2 \times \pi \times (112.5 + 37.5) \\ &= 314.2mm, \end{aligned}$$

and it travels through this distance 24 times per second (as flapping frequency is for a complete downstroke-upstroke cycle), giving a mean tip speed of:

$$\begin{aligned} V &= 0.3142 \times 24 \\ &= 7.540m/s. \end{aligned}$$

Reynolds number can therefore be calculated (using ISA sea level values for density and viscosity):

$$\begin{aligned} Re &= \frac{\rho V l}{\mu} \\ &= \frac{1.225 \times 7.540 \times 0.06667}{1.7894 \times 10^{-5}} \\ &\approx 34\,000. \end{aligned}$$

So an FMAV is likely to operate at Reynolds numbers around 3 orders of magnitude larger than the smallest insects, although some current insects do operate at Reynolds numbers of $O(10^4)$. As already mentioned, the fossil record reveals that there have at times existed much larger insects than those seen today — including dragonfly-like creatures with wingspans of up to $70cm$ (Dudley, 1998). Appar-

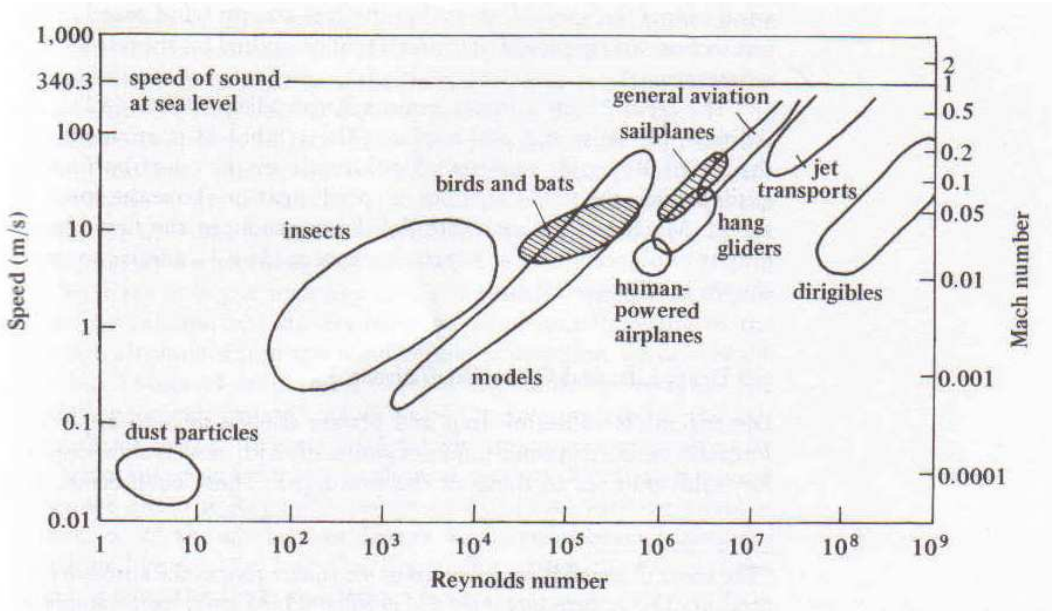

Figure 2.5: Approximate Reynolds number ranges for a variety of aerodynamic objects, from Wegener (1997, Figure 6.3). Reynolds numbers are given as a function of Mach number and speed.

ently, then, insect-like flight is possible at larger scales than that of present-day insects. But what difference does the size of the 'aircraft' make to their efficiency of flight? Did the large size of these insects lead to a drop in efficiency and therefore their eventual extinction? And to what extent can the techniques designed for 'conventional' aircraft be used to analyse the flight of FMAVs — which operate at Reynolds numbers which (although high compared to those at which most present-day insects fly) are still extremely low compared to conventional aircraft?

Figure 2.5 shows that an FMAV which uses the 'optimised' parameters in Table 2.1 will operate at Reynolds numbers lower than those for bats and birds and in the same range as model aircraft. In addition to this Reynolds-number-related issue, the aerodynamics of insect-like flapping differ from those of more conventional aircraft in 4 key ways:

- An insect wing stops and starts at the end of each stroke (i.e. when the 'aircraft' is *in flight*), unlike the wings on rotary- or fixed-wing aircraft.
- An insect wing passes through its own wake, which produces complex interactions between the wake and the aerofoil. This happens with a rotary-wing

aircraft, but to a much lesser degree.

- The angle of attack of an insect wing is often much higher than would normally occur on conventional aircraft (often in excess of 45°). Despite this "flagrant disregard [for] sound aerodynamic design" (Dickinson, 2006), there seems to be no catastrophic 'stall'.

- Insects use various specialised techniques (such as the 'clap-and-fling,' mentioned above) which, it appears, enhance the lift that their wings produce. Ellington (1984d) gives good descriptions of many of these techniques.

Because of these differences, there are a number of aerodynamic effects that may be important for insect flight. Most of these effects either do not occur (or occur to such a small extent that they can be ignored) when the flight of more-conventional aircraft is considered. Some of these phenomena are now discussed in detail.

2.1.3.1 Wake capture

When a wing is translated, it leaves behind a *wake* — a region of disturbed air. Fixed-wing aircraft generally move rapidly away from their wake, so that the effect of the wake can be ignored. The wake is sometimes ignored in rotary-wing aircraft analysis (see e.g. Leishman, 2000, §2.2), although this is less justifiable.

During flapping flight, however, the wings frequently reverse direction and pass directly through the wake from previous strokes. The potential benefits of this were described by Dickinson, who stated that "the flows generated during one stroke and rotation can increase lift production in the subsequent stroke" (Dickinson, 1994, p. 205); this research was, however, 2D in nature and (as is shown later) would therefore not have captured all the features of full insect-like flapping. The idea that wake capture could enhance lift had been suggested by Ennos (1989a), and the importance of wake capture was later emphasised by Dickinson et al. (1999) and Sane and Dickinson (2001), where wake capture was again presented as a *lift-enhancing* phenomenon. For some years this was generally accepted as true, and it does seem logical that (firstly) a wing undergoing insect-like flapping will

interact with its own wake to a large extent and that (secondly) this interaction will affect the forces experienced by the wing. However it is shown later that there is a fundamental difference between 2D and 3D flows — 2D flows produce a vortex street-like wake whereas for 3D flows the leading-edge vortex (see §2.1.3.4) is not shed (at least if the aspect ratio of the wing is low enough; see §6.8).

Sun and Tang (2002), however, who used a CFD approach, stated that "the wake from the previous stroke does not increase the lift [for the current stroke] and...the large [lift] peak at the beginning of a stroke is due to the rapid acceleration of the wing" (Sun and Tang, 2002, p. 67). They suggested that the results of Dickinson (1994) were unhelpful because they were 2D and therefore predicted vortex shedding where in a 3D case it might not occur — a suggestion which the results presented in this thesis certainly support.

At around the same time, Ramamurti and Sandberg (2002), also using a CFD model, produced results which were consistent with the results of Dickinson et al. (1999). However, they did not seek to explain the source of the force peaks that they discovered, only concluding that they were probably due to either wake capture or what they called 'rotational circulation'. Srygley and Thomas (2002) listed wake capture among the unconventional aerodynamic mechanisms that butterflies use to generate force, and suggested that in successive wing-beats, some butterflies can choose to use, or not use, wake capture to enhance force production, though they did not explain how this could work in practice. They relied on flow visualisation data for their conclusions.

Birch and Dickinson (2003) studied the subject in detail and examined the suggestion of Sun and Tang (2002) that the force peaks at flow reversal were due to wing acceleration rather than wake capture. Birch and Dickinson conceded that an accelerating wing did produce a force peak, but they also claimed "forces created by identical kinematics in the presence of a wake are unequivocally higher" (Birch and Dickinson, 2003, p. 2271). But to complicate things further, Wu and Sun (2005) studied the effect of the wake — again using a CFD approach — and concluded that the wake from previous strokes had a *detrimental* effect, *reducing* the mean lift by $6 - 18\%$. Aono and Liu (2006) carried out a CFD study into

insect-like flapping and implied that wake capture did not "prominently" increase the lift produced. Consensus on this point is lacking, though the majority opinion remains that wake capture enhances lift.

2.1.3.2 Added mass

To accelerate a body of mass $1kg$ at a rate of $1m/s^2$ in a vacuum, a force of $1N$ will be required. However, to obtain the same acceleration in air (or any fluid), $1N$ will not be sufficient. The reason for this lies in the fact that the fluid that surrounds the body has its own inertia, and thus a force must be supplied not only to accelerate the body, but also the fluid that lies around it. The difference between the force required in a vacuum and the force required in a fluid is termed the *added-mass* force[3]; because it requires more force to accelerate the object in the fluid, it appears that the object's mass is higher in the fluid than in the vacuum. The magnitude of the added-mass force is dependent only on the size, shape, and acceleration of the body and the density of the fluid (the viscosity of the fluid has no effect).

The wings of conventional aircraft do not generally accelerate and decelerate rapidly, so added-mass forces can generally be ignored. Insects wings, however, are rarely found *not* to be accelerating. Osborne (1951) suggested that these added-mass forces might play a key role in insect flight, but this was judged not to be the case by Ellington (1984d), who stated that "none of the virtual mass [added-mass] forces will significantly alter the mean lift of the wing," (Ellington, 1984d, p. 96) although he accepted that they would affect *instantaneous* values. This view (that added-mass forces do not contribute significantly to the mean lift) was also expressed by Sunada and Ellington (2000). However, added-mass forces do affect the power required for (and therefore the efficiency of) flapping flight, and so cannot be completely ignored.

[3]The term 'virtual mass' is also sometimes used, but strictly speaking this is the combined mass of the body itself and the added mass (Massey and Ward-Smith, 1998). 'Apparent mass' is also used in place of 'virtual mass'.

2.1.3.3 The Wagner effect

The Wagner effect is considered later (see p. 57) and so only a brief overview will be given here. The effect occurs whenever a wing accelerates or decelerates, as well as when a wing undergoes an increase in angle of attack, and explains why it is that the lift in such cases does not instantaneously change. The effect is of little or no importance when considering fixed-wing aircraft, which do not stop and start in flight, although it is important in understanding the aerodynamics of rotary-wing aircraft in forward flight (Leishman, 2000). The effect cannot be neglected when considering insect flight.

2.1.3.4 The leading-edge vortex

The flow around an aerofoil at low angle of attack is relatively simple. Flow travels smoothly around the leading edge, runs down the upper surface and separates at the trailing edge. However, if the angle of attack of an aerofoil is increased beyond a critical value, the flow will separate at some point on the aerofoil's upper surface. This separation is usually associated with a dramatic loss of lift, called stall, although the extent and nature of this lift change depends on the type of stall that occurs (McCullough and Gault, 1951). Most common low-speed aerofoils stall at an angle of attack of around 15°, but the stall angle depends on the shape of the aerofoil, particulary the shape of the leading edge; aerofoils with sharp leading edges stall at lower angles of attack than those with rounded leading edges.

Insect wings typically operate at angles of attack of up to 45°. Vogel (1967b) proposed that insects avoid separation by the morphology and structure of their wings (in particular, by the presence of small hairs on the wing surface), although he acknowledged that "the precise mechanism and structural basis of stall prevention [had] yet to be determined." However, this idea quickly fell out of favour, and it is now indisputable that separation *does* occur on insect wings. However, rather than this separation leading to a loss of lift, insects actually seem to benefit from it. There are a number of suggestions as to how this benefit is obtained, all of them centring in a *leading-edge vortex* (LEV). The separated flow forms a vortex above the wing, and as this vortex is an area of low pressure it enhances lift. It is

now universally accepted that this LEV exists, but opinion remains divided as to the exact nature of the LEV.

Maxworthy (1979) was the first to report the presence of an LEV lying above the wing, fed by separation from the leading edge. However, it was not until the 1990s that the potential importance of the LEV began to be recognised, with some researchers reporting that its presence resulted in "an 80% increase in lift" (Dickinson and Götz, 1993, p. 45). It soon began to be seen as a major candidate for the high lift produced by insect wings. Ellington et al. (1996) used a mechanical model of a hawkmoth (*Manduca sexta*) wing to study the LEV, and reported that it was stable, conical in shape, and contained significant spanwise flow (from root to tip). They postulated that this spanwise flow was responsible for the stability of the vortex, as it extracted vorticity from its core[4]. Later, Willmott et al. (1997) found that a stable LEV also formed on real hawkmoths.

It is important to emphasise at this point what is meant by 'stable'. Some researchers have used the word 'stable' to describe an LEV that remains attached for an entire upstroke or downstroke. However, it is suggested here that this is misleading. The definition of 'stable' is generally considered to be 'not likely to move' or 'firmly fixed' (Hawker and Soanes, 2005). Here, a stable LEV is defined as one which remains attached to the wing for all time; that is, no matter how far the aerofoil or wing travels, the LEV never sheds, but remains in a fixed position relative to the aerofoil or wing. It is important to realise that for an FMAV, the LEV does not necessarily *need* to be stable by this definition; it merely needs to remain attached for the time it takes the wing to complete a half-stroke. But since it is the phenomenon of the LEV which is of interest, the aim is to determine whether it is stable (by the definition used here) and, if not, whether it remains attached for long enough to be of any value for an FMAV.

van den Berg and Ellington (1997a) suggested a link between the LEV formed during insect-like flapping and the LEVs formed over the leading edges of delta wings at high angles of attack, noting "clear similarities" between the flow pat-

[4]The same effect can be used to stabilise leading-edge vortices on fixed wing aircraft by blowing air from the root of the wing towards the tip (see e.g. Rossow, 1978).

terns. They also postulated that the mechanism for the formation of the LEV was dynamic stall (sometimes called delayed stall), an idea which has been restated by others (Ellington, 1995; Dickinson, 1996; Willmott et al., 1997), sometimes with a high degree of certainty — for example, Ellington et al. state unequivocally that "the vortex is created by dynamic stall" (Ellington et al., 1996, p. 626). However, dynamic stall, as originally defined, occurs when a wing simultaneously translates and pitches up (see the main discussion of dynamic stall on p. 52). An aerofoil which is *purely translating* at a constant high angle of attack and constant speed may (and indeed, most probably will) experience separation at the leading edge, but it is not appropriate to call this dynamic stall; it is simply separation, leading to a vortex. Until this vortex has shed from the upper surface of the wing, it enhances lift because it is an area of low pressure (McCroskey, 1981) — this is discussed in detail on page 171. In any case, an insect wing is usually pitching *down* as it begins a stroke (see Figure 2.3). Therefore dynamic stall should not be used to describe the mechanism for the *formation* of the LEV. It is simply flow separation.

Others have expressed doubts about the LEV being caused by dynamic stall (Żbikowski, 2002a; Ansari, 2004) by pointing out that a dynamic-stall vortex usually sheds almost immediately (McCroskey, 1981) rather than remaining stable. The usual counter-argument to this is that because insect wings move only short distances with each stroke, the LEV does not have time to break away before stroke reversal takes place. Wang (2000) claims that the vortex that is formed when leading-edge separation takes place on a 2D wing is not completely shed from the aerofoil until about 4 chords have been travelled; and the wings of many insects travel less than 4 chords between stroke reversals (Wang et al., 2004; Weis-Fogh, 1973). However, even if this is true (and it is shown later that the current results — and the results of others — suggest that in fact 2D LEVs are shed after less than *two* chords of travel) it does not alter the fact that it is inappropriate to call this dynamic stall because the wing is generally not being pitched up as it is translated at the start of a stroke (as the LEV is forming).

In any case, the word *stall* is usually used to refer to a situation where the

wing has reached its maximum possible lift coefficient. The stall angle is usually identified by plotting lift against angle of attack and locating the point of maximum lift. In the case of insect wings, it is known that they produce *high* lift, but it is obviously not true that their wings *always* operate at the point of *maximum* lift. The wings of an insect in the hover cannot be said to be stalled, because they are not operating at the maximum possible lift; if they were, the insect would be unable to ascend. It may be accurate to say that the presence of the LEV does *delay stall* — that is, the maximum lift when an LEV is present is higher than when there is no LEV. In practice, however, creating a situation where no LEV exists would be impossible, as the LEV cannot be 'turned on and off' at will; it is simply a result of the high angle of attack at which insect wings operate.

In a computational study, Liu et al. (1998) found an LEV which they stated was responsible for enhancing lift production. Again, this LEV was stable, and the assertion that spanwise flow was responsible for the stability of the LEV was generally accepted for a time. However, Birch and Dickinson (2001) tested this hypothesis using 2D particle image velocimetry (PIV, see Raffel et al. (1998)) and reported that "at the Reynolds numbers matching the flows relevant for most insects, flapping wings do not generate a spiral vortex akin to that produced by delta-wing aircraft." They stated, "limiting spanwise flow with fences and edge baffles does not cause detachment of the leading-edge vortex," and suggested an alternative explanation for the LEV's stability — that "downward flow induced by tip vortices limits the growth of the leading-edge vortex" (Birch and Dickinson, 2001, p. 729) — referring to the shed tip vortices from previous strokes, not the tip vortex of the current stroke. In other words, the suggestion was that some form of wake capture was responsible for the LEV's stability. Later on, Birch et al. (2004) conceded that "spiral flow [within the LEV] is a conspicuous feature of flapping wings at Reynolds numbers (Re) of 5 000" but also stated that "similar experiments at $Re = 100$ failed to identify a comparable structure" (Birch et al., 2004, p. 1063), suggesting that the phenomenology involved in the LEV varies with Reynolds number. Birch and Dickinson (2001) had previously suggested that the effectiveness of the LEV as a lift-enhancing mechanism might depend on Reynolds

number. Using a rotating (sweeping — not flapping) wing, they found lower lift coefficients at higher Reynolds numbers compared to those at lower Reynolds numbers.

In contrast to this, Nolan (2004), who also studied rotating wings (in this case using stereoscopic (3D) PIV) in order to elucidate the structure of the LEV, reported spanwise flow within the LEV at all Reynolds numbers from 140 up to 6 500 and postulated that this flow was driven by a pressure gradient caused by the sweeping motion of the wing. Some changes in the flow were noted as Reynolds number was increased but spanwise flow was evident over the whole range of Reynolds number. Nolan proposed two reasons why this spanwise flow was not seen in the experiments of Birch and Dickinson (2001): firstly, it was suggested that Birch and Dickinson simply did not see the spanwise flow, although it was there (because it was concentrated in a small area which their PIV data 'missed', or because the spanwise velocity was too low for their PIV to capture); and secondly, there may have been other failings in the way they carried out their experiments and analysed their data. Nolan also made the point that 2D PIV is not a satisfactory technique with which to study these highly-3D flows.

Wang (2005) suggested that the LEV is stable because the "vortex line is pinned to the root and cannot shed" due to the fact that the velocity is zero at the root. However this does not address the issue of the effects of Reynolds number or aspect ratio. In any case, for many of the experimental 'flappers' that have shown a stable LEV, the velocity at the root is not zero because the wing root is mounted at some distance from the point of rotation.

Ramasamy and Leishman (2006), from results of experiments with a mechanical 'flapper', concluded that the LEV was *not* stable — despite containing significant spanwise flow (of the same order of magnitude as wing tip velocity). They suggested that the LEV *did* shed from the wing (like a dynamic stall vortex) but that another LEV took its place, meaning that lift remained high. However, the wing used in their experiments did not translate at an exactly constant angle of attack, and it is difficult to isolate the effects of the pitch changes which occurred during the translational phases of motion, which were up to 10° in magnitude. In addition

they failed to disclose the relationship between sweep position and wing angular velocity. It is possible that the shedding of the LEV in their case was due to changes in angle of attack or angular velocity as the wing swept.

Lu et al. (2006), again using a mechanical 'flapper', examined the flow around dragonfly wings and noticed a co-rotating *pair* of LEVs near the leading edge. Similar structures can appear on delta wings, but Lu et al. were unable to conclusively answer the issue of what caused the formation of the dual-LEV structure. Nor did they give details of the stability of the vortex pair. They suggested that this dual-LEV structure was not noted in previous studies due to either inadequate visualisation techniques or (in the case of CFD studies) inadequate mesh resolution, and that the dual-LEV system might be a "basic flow structure" of flapping wings. The current results, when compared with theirs, indicate that the second LEV might simply be a result of Kelvin-Helmholtz instability in the leading-edge vortex sheet (see §5.3.3.1).

Poelma et al. (2006) used Dickinson's 'flapper' to produce a detailed 3D 'map' of the flow around a flapping wing. They found that an impulsively-started wing produced a vortex around its edges. The vortex at the trailing edge separated, whilst the vortex at the leading edge remained attached to the wing and remained connected to the trailing-edge vortex by the tip vortex. After around 90° of sweep (at constant velocity and angle of attack) they found a pair of counter-rotating tip vortices — a phenomenon that had not been noticed before. One of the tip vortices combined with the stable LEV, whilst the other combined with a stable TEV. It is not clear how this TEV came to exist, given that the TEV created during early stages of motion was said to separate almost immediately. At this point the flow field became stable and neither the LEV or TEV grew further. They stated that there was no spanwise flow within the LEV but they did identify a large area of spanwise flow behind the wing, induced by the pair of tip vortices. They stated that this spanwise flow drained circulation from the wing and balanced the production of circulation at the leading edge. This was at a comparatively low Reynolds number of 256 (based on maximum wingtip velocity and maximum wing chord). It was not made clear how spanwise flow *behind* the LEV could possibly

extract vorticity *from* the LEV.

Most recently, Hamamoto et al. (2007) used a computational approach and noted the presence of a distinct and obvious LEV above the leading edge of the wing. However, their results did not indicate whether or not this LEV was stable. Meanwhile, Muijres et al. (2008) discovered LEVs attached to the wings of bats and stated that their presence increased lift by as much as 40%.

It is practically indisputable that the LEV exists, and that it is a lift-enhancing mechanism. It is also virtually certain that it is a stable vortex, despite the anomalous results of Ramasamy and Leishman (2006). However a couple of important questions remain unresolved. Firstly, what is the reason for the stability of the LEV — and, secondly, does the stability of the LEV depend on Reynolds number? There are also a number of questions relating to the precise structure of the LEV. Of course, the reason why these questions need to be answered is to help us answer the most important question of all — will a stable, lift-enhancing LEV still exist if insect-like flapping is scaled up to FMAV sizes?

2.1.3.5 Rotational effects

Given that an insect's wing kinematics can be divided into translational and rotational phases (see Figure 2.3 on p. 31), it might appear logical to attempt to separate the forces that are produced during flapping into those produced by rotation and those produced by translation. This approach has been taken by, for example, Ellington (1984d) and Dickinson et al. (1999). An insect wing does not, however, translate at a fixed angle of attack, then rotate without translating for a time, and then translate again. Instead, translation and rotation occur simultaneously during much of the motion. For this reason there has been some confusion in the literature over what forces should be called 'translational' and what forces should be called 'rotational'. The fundamental question is this — are the rotational phases of wing motion mere inconveniences that are necessary to prepare the wing for the next stroke, or actual lift-enhancing mechanisms in themselves? As mentioned above, Weis-Fogh (1973) was among the first to suggest that the latter might be the case, but since then there has been much confusion regarding

the distinction between translational and rotational forces.

Ellington (1984d) looked in detail at this area, and suggested that the rotational phases of flapping could be useful in "delaying stall" during the translational motions. If an aerofoil is translated whilst having its angle of attack increased, it will stall at a higher angle of attack than if it were translated at constant angle of attack. In other words, if the static stall angle for an aerofoil is 15°, it may be possible to delay stall (and obtain a higher lift coefficient) until an angle of attack of (perhaps) 20° by pitching the wing up as it is translated. This is the Kramer effect, also known as dynamic stall, and is discussed in more detail below (p. 52). However, as mentioned above (p. 45), insect wings are generally pitching *down* as they begin translation, and thus dynamic stall (as originally defined) will not occur.

Later, it was suggested that the rotational phases not only enhanced lift during the subsequent stroke but also generated lift themselves. Dickinson et al. (1999) found a force peak at the end of each half stroke, which they postulated might be connected to the Magnus effect[5]. However, their procedure for separating translational and rotational forces was rather unsatisfactory. In their case the flow was fully 3D. In order to estimate the forces solely due to translation, Dickinson et al. swept a wing through 180° at constant angle of attack and velocity and measured the lift produced. However, in order to obtain a mean value they averaged the measured lift coefficient over an interval of around 1 second. This interval was taken *after the wing had swept for some distance*, so that the mean value captured did not incorporate the large force peak that was observed at the start of sweeping motion (Dickinson et al., 1999, Fig. 2A). Subtracting this mean value from the total force produced by a wing undergoing flapping motion meant, unsurprisingly, that a large peak was left at the start and end of the translational phases of motion. Dickinson et al. concluded that these peaks were due to what they called 'rotational forces', but in fact the peak *could* have been merely due to the large forces that occur when a wing starts motion, which were excluded from the subtracted mean value. Sane and Dickinson (2002) simply described the forces as rotational

[5]See Houghton and Carpenter (2003, p.135)

forces, and did not mention the Magnus effect, and Sun and Tang (2002) sought to show that the Magnus effect alone cannot explain the large force peaks that occur during wing rotation.

The Magnus effect is most commonly mentioned in relation to spheres or cylinders that are rotating as they translate. The effect explains why a football can be made to curve through the air by imparting a measure of spin to it during the kick. On one side of the ball — where the surface of the ball is travelling in the *same direction* as the oncoming air — skin friction results in the air being *accelerated* due to the movement of the ball surface. On the opposite side of the ball, the surface of the ball will be moving in the *opposite* direction to the oncoming air, and skin friction will result in the air on this side of the ball being *decelerated*. The difference in velocity leads to a difference in pressure, and therefore a force on the ball which acts in a direction perpendicular to the direction of motion. It is important to realise that the velocity difference only comes about because of the no-slip condition on the surface of the ball. Another way of looking at the phenomenon is to consider that by rotating the ball circulation is imparted to the air through which it is passing, which leads to a force on the ball normal to the direction of flight.

In the case of an insect wing, the only surfaces capable of imparting this velocity difference to the air are the aerofoil leading and trailing edges — where the direction of motion of the surface (due to the rotation of the aerofoil) is perpendicular to the wing chord. However, insect-like aerofoils are extremely thin. It seems therefore highly unlikely that spinning a thin flat plate as it is translated can produce a Magnus effect — the flow would not stay attached *to the relevant surface* for long enough to be either accelerated or decelerated by skin friction. Of course, rotating an insect wing *will* produce a force in some direction (if the rotation point is not at the mid-chord), but this is not due to the Magnus effect, because this force would be produced whether the wing were translating or not. In addition, the Magnus effect cannot explain why the peaks in lift force that occur during rotation are accompanied by a large drag peaks (Sun and Tang, 2002).

Walker (2002) presented a detailed study of the so-called rotational forces, and

stated that "comparisons of the rotation-dependent force component with the Magnus effect... are misleading" (Walker, 2002, p. 3791). He concluded that rotational forces are "caused by the same fluid-dynamic mechanism that occurs during wing translation" (Walker, 2002, p. 3783), much the same as argued above.

Further support for this reasoning came from Sane (2003), who stated that "the mechanism of Magnus force applies only in relation to cylinders, spheres and blunt objects," (Sane, 2003, p. 4203) and presented the *Kramer effect* as the *only* rotational force involved in insect-like flapping. He called the Kramer effect a "rotational force," postulating that when a wing rotates whilst in motion, the separation point moves away from the trailing edge. In order to return the separation point to the trailing edge, additional circulation is produced which results in additional lift. Whether this description of what happens during wing rotation is accurate or not, this is not the Kramer effect as originally defined (Kramer (1932a), translated as Kramer (1932b)). The Kramer effect is actually the same thing as dynamic stall (as noted by Ellington (1984d, p. 99), Dudley (1999, p. 129), and Leishman (2000, p. 379)). Some researchers have categorised dynamic stall (or the Kramer effect) as a translational lift mechanism, whereas others have categorised it as a rotational mechanism. The reason for the confusion is clear — dynamic stall applies only when an aerofoil is both translating *and* rotating, so it is both translational and rotational.

Lehmann (2004) stated that there are two possible sources of rotational forces — firstly, rotational circulation (although he explained that this is not, strictly speaking, related to the Magnus effect (Lehmann, 2004, p. 113)) and secondly, the Kramer effect. Again, the link between the Kramer effect and dynamic stall is not made; Lehmann discusses dynamic stall in some detail and then presents an entirely separate section on the Kramer effect. Having emphasised the importance of 'dynamic stall', Lehmann goes on to say "whether the Kramer effect is of functional significance for flapping insect wings still remains unclear" (Lehmann, 2004, p. 115). All this, despite the fact that Kramer's original paper (Kramer (1932a), translated as Kramer (1932b)) actually describes his experiments in which stall was delayed (i.e. the maximum lift coefficient was increased) when a wing was

rapidly pitched up past the steady-state stall angle of attack by a gust. His paper was entitled "Increase in the maximum lift of an airplane wing due to a sudden increase in its effective angle of attack resulting from a gust," and he concluded that the reason for the increase in this maximum lift was that the flow does not immediately separate from a wing or aerofoil when the angle of attack is suddenly increased.

Ansari et al. (2006a), in agreement with Sane (2003), implied that the Kramer effect is the only rotational effect of importance, neglecting to discuss the Magnus effect entirely. Ansari et al. (2006a) described the Kramer effect as the change (positive or negative) in lift caused by the wing pitching (upwards or downwards) as it ends or begins a stroke. Again, this is not the Kramer effect as originally defined. Because insect wings generally rotate in pitch about a point *ahead* of the mid-chord, a downward pitching (i.e. angle of attack decreasing) motion will produce a downward force, because the area of the wing that is moving upwards (the area *behind* the pitch axis) is larger than the area that is moving downwards (the area *ahead* of the pitch axis). Conversely, an upward pitching motion will produce an upward force. It is not necessary to invoke the Kramer effect — or indeed *any* unconventional aerodynamic effect — to explain this.

Aono and Liu (2006), using a CFD model, investigated the vortical structures formed around the hawkmoth *Manduca sexta* during flapping motion and related these structures to the forces produced. They concluded that their results seemed "not able to support the conclusion of Dickinson et al. (1999) that...[the] rotational circulation mechanism [produces] prominent augment of aerodynamic force production" [*sic*], and suggested that the leading-edge vortex was the dominant mechanism of lift production; their model predicted only small forces during the rotational phases of motion.

Another aspect of the rotational parts of insect-like flapping is that, during these phases of motion, the wings can be close together, and the flow around one wing can be affected by the flow round the other. Weis-Fogh (1973) was the first to propose this as a possible mechanism of lift-enhancement — he identified some novel kinematics such as the clap-and-fling, discussed above (p. 32). These

mechanisms (particularly the clap-and-fling) have since been the subject of scrutiny (Lighthill, 1973; Bennett, 1977; Maxworthy, 1979) and it is generally accepted that they are involved in lift production, particularly in small insects, although some large insects use the technique when carrying loads (Marden, 1987) and even the wings of some birds (e.g. pigeons) make an audible clapping sound on takeoff. Marden (1987) calculated a maximum lift force per unit muscle mass of $63N/kg$ for flying animals, *except* for animals using the clap-and-fling technique, where muscle mass-specific lift increased by about 35% to $86N/kg$. The CFD results of Sun and Yu (2006) supported this result; they estimated that clap-and-fling resulted in a 30% increase in mean lift coefficient compared to the case of flapping without clap-and-fling. More recently, Lehmann and Pick (2007) (using a mechanical 'flapper') found that the lift augmentation due to wing-wing interaction ranged from $1.4 - 17\%$, depending on the exact kinematics of the flapping motion.

It seems that there is some confusion regarding, firstly, how to defined a "rotational force" and, secondly, which "rotational forces" are relevant to insect-like flapping. This supports the suggestion made above that perhaps it is not sensible to attempt to categorise the forces produced during insect-like flapping in this way. It is also clear that there is some difficulty in defining the terminology that should be used to refer to the forces produced. 'Dynamic stall' should not be referred to as a rotational effect, and the only effects discussed above which could strictly be defined as 'rotational' are the Magnus effect and the effects due to wing-wing interaction. Clearly it is necessary to use the term 'rotational forces' with care (if it is used at all).

2.2 Modelling insect flight

This section looks at some of the attempts that have been made to analyse insect (or insect-like) flight. These can be divided into two categories — analytical (which category can be subdivided into quasi-steady and unsteady approaches) and computational.

2.2.1 Analytical approaches

2.2.1.1 The quasi-steady approach

Many early researchers assumed that the instantaneous lift produced by an insect's wing was dependent only on the wing's instantaneous speed and angle of attack. This approach is denoted *quasi-steady* — it does not assume completely steady motion, and is able to take into account the complex kinematics of insect-like flapping. It does, however, make the assumption that the lift produced by the wing at a given instant is not affected by the wing's previous motion — so, for example, the phenomena of wake capture and the Wagner effect (see p. 57) are not captured. It was this approach that led Magnan (1934) to make his now-infamous statement; "*I have applied the laws of air resistance to insects, and have arrived... at the conclusion that their flight is impossible.*"

Osborne (1951) was the first to make a major contribution in this area. He used a quasi-steady approach, in conjunction with blade element theory[6], in order to find required values of average lift coefficient. Based on these findings, Osborne concluded that "insects must utilise some special mechanism in flight not present in conventional aerodynamic phenomena."

Weis-Fogh and Jensen (1956) carried out a 'critical review' of work done in the field. They concluded that the then-current understanding of insect flight was unsatisfactory, but proposed that this was more likely to be due to faulty methods and data rather than any failing in the quasi-steady approach itself. Later on, however, Weis-Fogh found that the forces required for insect flight were higher than those that were produced by insects' wings under steady conditions (Weis-Fogh, 1972, 1973), and conceded that it was necessary to take unsteady aerodynamic effects into account in order to analyse insect flight fully, especially hovering insect flight.

Ellington, in his seminal series of papers in the Philosophical Transactions of the Royal Society, concluded that "most, if not all, hovering animals do not rely on quasi-steady aerodynamics" (Ellington, 1984f, p. 178). Later, Dudley and

[6] Blade element theory is often used for helicopter rotor analysis — see Leishman (2000, §3), and, in relation to its use for insect flight analysis, Ansari (2004, §3.2).

Ellington (1990) showed that, according to quasi-steady predictions, Bumblebees are unable to fly at any speed. Support for the quasi-steady approach has now fallen and there is now wide-spread agreement that, especially when analysing hovering flight, it is essential to include unsteady effects. Quasi-steady methods *can* provide useful results when analysing insects in fast forward flight (see e.g. Willmott and Ellington, 1997; Sane and Dickinson, 2002), when unsteady effects are less dominant.

One way in which these quasi-steady models can be made more accurate is to introduce empirical corrections. Among the first to attempt this approach were Walker and Westneat (2000), who formulated a quasi-steady model but included apparent mass effects and the Wagner function (see p. 57). They validated their model against experimental data and reported good agreement. Later, Walker (2002) used the model to investigate the issue of the Magnus effect (see p. 49). He reported that the importance of the Magnus effect was minimal and that, in fact, the rotational forces were primarily due to conventional circulatory forces and/or forces due to attached vortices.

Sane and Dickinson (2002) presented a quasi-steady model, but incorporated the effects of wake capture empirically. This provided some insight into the relative importance of each source of lift associated with insect-like flapping flight, but cannot reasonably be used to predict the forces due to wake capture for a given wing and kinematics because the effect of wake capture was inserted empirically using previously-obtained data from a mechanical 'flapper'.

Traub (2004) formulated a (semi-empirical) model which was designed to estimate the lift on a flapping wing in the hover. Polhamus' leading edge suction analogy[7] was used to estimate the lift due to the leading-edge vortex, and Traub used data from Weis-Fogh (1973) to determine an empirical value which was used in calculating the lift on the wing. The model was able to give some idea of the rel-

[7]Polhamus' leading-edge suction analogy (see Polhamus (1966, 1971)) is a method of estimating the force due to a leading-edge vortex. It assumes that the leading-edge separation causes a total loss of leading-edge suction, and that a force is produced by the LEV which is equivalent in magnitude but acts normal to the wing surface. Although the method is very simple, it has been shown to be accurate in predicting the non-linear lift on delta wings due to the leading-edge vortex.

ative important of the leading-edge vortex lift compared to the lift due to attached flow, and Traub also concluded that wake capture was an important lift-producing mechanism which should be accounted for.

2.2.1.2 Unsteady aerodynamics

The four most important ways in which insect flight fundamentally differs from fixed- or rotary-wing aircraft flight have been presented on p. 39. It is these differences which result in the increased importance of unsteady effects when insect flight is compared to the flight of either of the more-conventional aircraft types.

As already mentioned, the quasi-steady approach makes the assumption that the lift on an aerofoil at a given time is dependent only on the aerofoil's current angle of attack and speed. All real flows are to some extent unsteady, but for the flows associated with conventional fixed-wing aircraft, the unsteadiness is often sufficiently small to be negligible — most attempts to analyse fixed-wing flight make this assumption. The first important attempt to analyse any kind of unsteady aerofoil motion was made by Wagner (1925). He considered a comparatively simple case — that of an aerofoil at a small angle of attack, originally at rest, being impulsively started and then moving at constant speed. This is analogous to an aerofoil in steady motion undergoing a step change in angle of attack.

When the speed of an aerofoil is impulsively increased, or when the angle of attack on an aerofoil in a flow is suddenly increased, the lift does not change instantaneously. The Wagner function gives a *theoretically* exact description of how the lift grows. There is an "infinite pulse in the lift" (Leishman, 2000, p. 325) to half of the (new) steady state value. Thereafter the lift increases at a decreasing rate, tending towards its final value. In theory it will never reach its final value, but in practice, after a distance of only a few tens of chords has been moved, the lift reaches 99% of the steady-state lift. The Wagner function is shown in Fig. 2.6.

Although the Wagner function is known exactly, the exact formulation is not convenient for analysis, and an approximation is usually used. One of the most

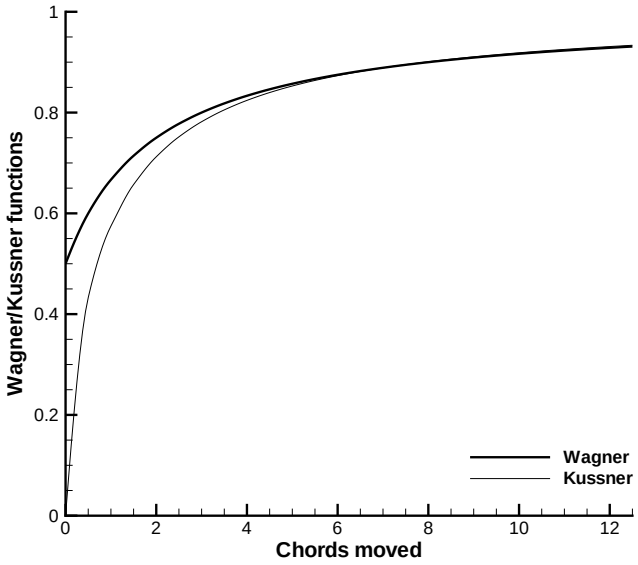

Figure 2.6: Wagner and Küssner functions.

famous is that attributed to R. T. Jones:

$$\phi(s) = 1.0 - 0.165e^{-0.0455s} - 0.335e^{-0.3s},$$

where $\phi(s)$ is the value of the Wagner function after the aerofoil has travelled s semi-chord lengths.

Later on, Küssner (1936) considered a similar problem — that of an aerofoil at zero angle of attack penetrating a sharp-edged gust[8]. The Küssner function predicts that the lift on an aerofoil entering such a gust will increase from zero (when the aerofoil is outside the gust) to its steady-state value. Fig. 2.6 shows the Küssner function. It is notable that the steady-state value is not reached as soon as the aerofoil is fully immersed in the gust — the aerofoil will be fully immersed in the gust when it has travelled one chord, but at this point, according to the prediction, the lift will have reached only around 60% of its final value.

As with Wagner's function, Küssner's function is known exactly, but is usually

[8] An error in his work was later corrected by von Kármán and Sears (1938).

approximated with an exponential function such as:

$$\psi(s) = 1 - 0.5e^{-0.13s} - 0.5e^{-s}, \tag{2.2}$$

where $\psi(s)$ is the value of the Küssner function after the aerofoil has travelled s semi-chord lengths.

The problem of unsteady aerodynamics began to receive more attention in the 1930s, when wing flutter was beginning to become a problem due to the increasing speeds of aircraft[9]. Glauert (1929) was among the first to attempt to analyse the lift produced by an oscillating aerofoil, but the problem was properly solved by Theodorsen (1935), who, using a velocity potential approach, was able to produce equations to find the lift and moment on an aerofoil undergoing sinusoidal oscillations in either angle of attack (pitch) or vertical motion (plunge). The approach Theodorsen used, and the resulting equations, are presented in Leishman (2000). This approach has been extended (e.g. Garrick, 1937; van der Wall and Leishman, 1994) to account for, among other things, variations in incident velocity.

More research in this field has come from those involved in the analysis of rotorcraft. A rotor blade is regularly affected by the wake from other blades in the same rotor, and this can affect the performance of the rotor as a whole. Loewy (1957) extended Theodorsen's theory to account for the wakes from previous rotor blades, representing these wakes by vortex sheets below the aerofoil.

Theodorsen's work, along with the various extensions to it, could potentially be helpful when analysing insect flight. After all, an insect wing is simply a wing which stops, starts, pitches, plunges, and sweeps — motions which the models above can analyse (at least in principle). However, high accuracy would not be expected if this approach were used, because Theodorsen made a number of assumptions. Most importantly, he assumed a flat wake (i.e. that shed vortices do not move relative to the freestream air) and also used small angle approximations — approximations that will be inaccurate if applied to insect flight, which involves large angles of

[9]Flutter is when a wing oscillates due to fluctuations in the lift it is producing. The oscillation of the wing leads to further fluctuations in lift, and if these oscillations occur at the natural frequency of vibration of the wing, they can increase in magnitude until structural failure occurs. The phenomenon was responsible for many early aeroplane accidents.

attack. In addition, it is not possible to account for the leading-edge vortex using this approach — although it is possible to account for the leading-edge vortex separately.

Such an approach was taken by Pedersen and Żbikowski (2006) (full details in Pedersen (2003)), as suggested by Żbikowski (2002a). They analysed the total lift on a flapping aerofoil using an additive approach — using a velocity potential approach to find the added-mass and quasi-steady forces, Polhamus' leading-edge suction analogy[10] to find the 'extra' lift due to the leading-edge vortex, and the Wagner and Küssner functions (along with a modified form of the method of Loewy (1957)) to find the effect of the wake. The results were somewhat mixed, but did show some promise — when compared with experimental results, the model "underpredicted the average lift by only 9%" (Pedersen, 2003). The model is discussed in more detail in §3.1.1.

The velocity potential approach (which was used by all the above analyses) brings with it an inevitable complexity. It is not easy to relate the equations to physical realities — Morris (1937), after some complicated mathematics, conceded that "the general formulae we have now obtained are rather too complex to convey directly an idea of their physical significance." In other words, although it may be possible to analyse unsteady aerodynamics using this approach, the results are not transparent and therefore not very helpful in increasing understanding of the causes of the forces on an aerofoil in unsteady motion. In addition, the assumptions made in these approaches mean that, although they may be adequate for analysing situations such as flutter, they cannot be expected to be satisfactory at analysing insect flight without substantial and complicated revision.

The seminal paper of von Kármán and Sears appeared in 1938. In it, they took a step back from the unwieldy and complicated equations of those who had gone before, and analysed the problem from a radically different perspective, starting by considering the origin of lift. Their approach was circulation based (rather than a velocity potential approach). Arguably the most important result of their work was that the lift on an unsteady aerofoil can be thought of as being the sum of

[10] See footnote, p. 56.

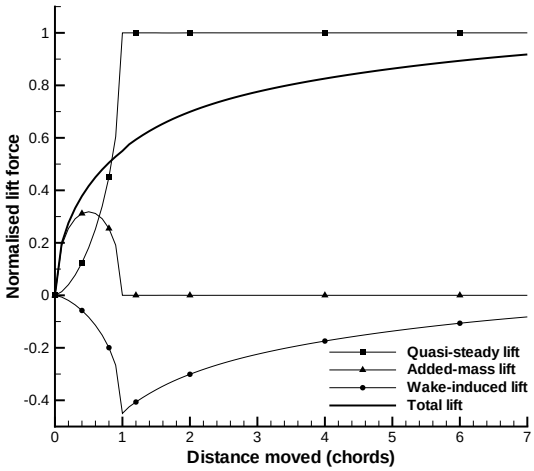

Figure 2.7: The three components of lift, and the total lift, on an aerofoil at zero angle of attack entering a sharp-edged gust. The horizontal axis is in terms of chord lengths, so that at 0 the leading edge is about to enter the gust, and at 1 the trailing edge has just entered the gust. The vertical axis is normalised with respect to the eventual steady value of the lift.

three components:

The quasi-steady lift — this is the lift that would be calculated if standard quasi-steady methods (for example steady thin aerofoil theory) were used. This component of the lift depends on the aerofoil's current speed, angle of attack, and size.

The added-mass lift — as mentioned previously, this is the lift force on the aerofoil due to the inertia of the surrounding fluid that is being accelerated. This force depends on the aerofoil's current acceleration and size.

The wake-induced lift — this is the 'lift' (which in many cases is often negative) due to the presence of the wake. It is this last component that is responsible for the fact that the lift on an impulsively-started aerofoil does not increase instantaneously to its final value — see Fig. 2.6 This component depends not on the aerofoil's *current* speed, angle of attack, etc., but on the aerofoil's motion history.

To visualise these three components, Figure 2.7 shows the three components of lift, and the total lift, on an aerofoil entering a sharp-edged gust. It can be

seen that the added-mass and wake-induced lift components have a large impact on the total lift. The added-mass lift component increases until half of the aerofoil is immersed in the gust, and then decreases to zero when the entire aerofoil is immersed. The wake-induced lift is negative — indicating that the effect of the wake is to decrease the total lift on the aerofoil. The total lift can be seen to have reached about 90% of its final value when the aerofoil's leading edge is 7 chord lengths from the edge of the gust.

Using their approach, von Kármán and Sears (1938) were able to confirm the results of Wagner, Küssner, and Theodorsen. Although von Kármán and Sears' theory proved to be very versatile, and greatly simplified understanding of unsteady aerodynamics, it was still a linear theory[11], and as such was only suitable for cases "in which the wake produced is approximately flat, i.e. in which the movement of the airfoil normal to its mean path is small" (von Kármán and Sears, 1938, p. 379). This made it eminently suitable for many problems — for example when examining aeroelasticity — but unsuitable for problems involving severe manoeuvre, in which the wake will distort. In addition, von Kármán and Sears took no account of any leading-edge vortex. Their model, in its basic form, is therefore unsuitable for analysing insect flight.

Scott (1987) was among the first to try to create a non-linear version of von Kármán and Sears' theory (i.e. a version in which the small-angle approximations are removed and the wake is allowed to distort). It transpired that much of von Kármán and Sears' work could be carried over into the non-linear version. Scott's work was later extended by others at the same institution (Lam (1989); Tavares (1990); Lee (1991)), and a summary of all four theses is given by McCune and Tavares (1993). One interesting result is that, in the nonlinear theory, the lift can be thought of as being made up of *four* components. The first three of these have the same physical meaning as the three linear terms, whilst the fourth is an "*explicit nonlinear term*," and vanishes in the linear limit (McCune and Tavares, 1993, p. 553). In a related study, Tavares and McCune (1993) modified the theory

[11]Linear, because von Kármán and Sears made the assumption that the wake remained flat behind the aerofoil and did not distort.

further (in relation to unsteady motion of delta wings), allowing two separation points — at both the trailing and leading edges of the aerofoil.

Most attempts to analyse insect flight using unsteady aerodynamics are based on at least some of this earlier work from outside the field. Azuma (1992), using earlier work by Theodorsen (1935) and Garrick (1937), attempted to calculate the thrust produced by oscillating wings in forward flight. However, it was assumed that the oscillations would never be extreme enough to produce separation at the leading edge, and therefore no account was taken of any leading-edge separation. The method is not suitable for analysing insect flight where the oscillations are very severe. In a later publication by Azuma et al. (2001), the idea is extended somewhat, but the possibility of leading-edge separation is still ignored. Wu (2001) used a somewhat similar approach, utilising the results of Theodorsen (1935), Wagner (1925), von Kármán and Sears (1938), McCune et al. (1990) and Tavares and McCune (1993). However, again, it was assumed that separation occurred only at the trailing edge.

Minotti (2002) used a different approach, making use of conformal transformation and the circle theorem of Milne-Thomson (see Milne-Thomson, 1973). Minotti accounted for leading-edge separation, but validated his model against experimental data (from Dickinson et al. (1999)) in order to assess the 'best' location to place the leading-edge vortex. This somewhat arbitrary placement of the leading-edge vortex is a disadvantage of the approach, but Minotti reported good agreement between data from his model and experimental data from Sane and Dickinson (2001). However, the model is unable to include the effects of wake capture.

Another important approach, although it is again not suitable for analysing insect flight, was that of Jones (2003). He used a boundary integral representation of the velocity field and assumed separation from both the leading edge and trailing edge of the aerofoil. On first glance the method seems similar to that of Ansari (2004), but a number of important differences mean that the model of Jones (2003) cannot analyse the interaction of the wing with its wake — meaning that analysing insect flight is not possible.

Pullin and Wang (2004) presented both a theoretical approach and a CFD

approach to the problem of a 2D wing being impulsively started. Their theoretical approach used conformal mapping to produce an equation for the force on an aerofoil. They then used an approximation to this equation (in order to make it solvable). This approximation meant that the model was only valid for situations in which the aerofoil moved a short distance — less that half a chord length. Pullin and Wang (2004) also presented an alternative analytical method, and compared results to their own CFD data[12]. Again, the model did not include the effects of wake capture, meaning it is of little use in analysing insect-like flapping.

Yu et al. (2003) formulated a fully analytical model, which was based loosely on the approach suggested by Żbikowski (2002a). The method was similar in some respects to that employed by Ansari (2004), including the effects of both leading- and trailing-edge separation. Some of their findings were similar to those of Ansari (2004), and their model compared favourably to experimental data from Dickinson and Götz (1993).

Żbikowski (2002a) suggested a number of ways in which the modelling of insect flight could be attempted. One of these concentrated on the use of a circulation-based approach — drawing heavily on the work of von Kármán and Sears (1938), along with the nonlinear extensions due to Lam (1989), Tavares (1990), Lee (1991) and Tavares and McCune (1993). Using these, and with significant further extensions to the theory of von Kármán and Sears, Ansari et al. (2006b,c) (full details in Ansari, 2004) were able to formulate a nonlinear, unsteady, aerodynamic model for insect-like flapping wings in the hover, along the lines suggested by Żbikowski (2002a). When compared to experimental data, the results were good, despite the model being essentially inviscid. In addition, the model is reasonably transparent, and can produce visualisation of the flow to increase understanding of the phenomena involved. However, because of the blade-element nature of the model, it cannot take into account spanwise flow within the LEV. Further discussion of Ansari's model can be found in §3.1.2.

One of the problems that researchers have faced is the lack of experimental data

[12] The CFD model had been compared previously to experimental data (see Wang et al., 2004), albeit with mixed results.

against which models can be validated. This is due to the obvious difficulties in measuring the forces on insect wings — as highlighted by Sane (2003). There are two methods by which this problem can be overcome. The first involves designed and constructing mechanical 'flappers' with which forces can be measured more easily and flow can be visualised (as discussed in §2.1.2). This has been carried out by, for example, Dickinson and Götz (1993), Ellington et al. (1996), and Dickinson et al. (1999). Many, if not most, of the unsteady analyses that have been presented here have been validated against data from these mechanical 'flappers'.

The other approach that has been used is to conduct computational fluid dynamics simulations of flapping insect wings, from which the forces on the wings can be extracted relatively simply[13]. The next section looks at some of these computational approaches.

2.2.2 Computational approaches

It is only comparatively recently that computational power has increased to a level where it is possible to analyse insect-like flapping. One of the first attempts was by Liu and Kawachi (1998), who modelled the morphologically coupled forewing and hindwing of the moth *Manduca sexta* using a time-accurate solution of the three-dimensional, incompressible, laminar Navier-Stokes equations. They compared their results with 3D flow visualisation and 2D force data, and reported encouraging agreement. They also noticed the spiral-structured LEV which had earlier been seen in experimental work (see §2.1.3.4). Liu et al. (1998) discussed this phenomenon in detail and concluded that the LEV was responsible for enhancing lift production.

A few years later, Sun and his co-workers developed a similar code which reproduced insect-like flapping by fluctuating the background flow whilst keeping the wing stationary. Sun and Tang (2002) modelled the flight of the fruit fly *Drosophila*

[13] One disadvantage of CFD approaches, however, is that it is not possible to break down forces to analyse, for example, what proportion of the lift comes from the leading-edge vortex. Also, the CFD model must be validated (by comparing results to experimental data) before it can be relied upon, and even when validated, it is not possible to be certain that the CFD model is capturing all the important aspects of the flow.

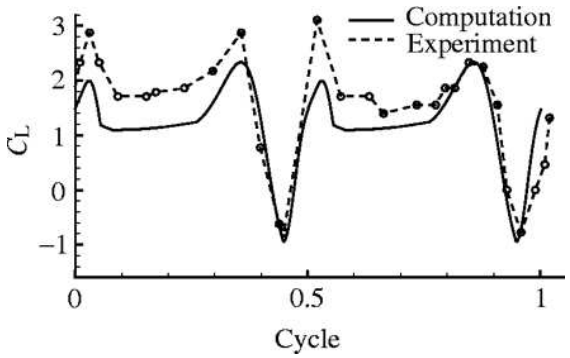

Figure 2.8: Comparison of the CFD results of Sun and Tang (2002) and the experimental results of Dickinson et al. (1999).

melanogaster and validated the model against experimental results from Dickinson et al. (1999) and Sane and Dickinson (2001). Agreement was good, as shown in Figure 2.8, and the model has subsequently been used to investigate the aerodynamics of various insects both in hover and in forward flight (Sun and Tang, 2002; Sun and Wu, 2003; Sun and Lan, 2004; Wang and Sun, 2005). A review of much of this work can be found in Sun (2005). Sun and Xiong (2005) even used the model to assess the stability of a bumblebee, but the assumptions made in the analysis limit the usefulness of the results.

Ramamurti and Sandberg (2002) used a finite-element flow solver to compute the flow around a three-dimensional insect wing (again, based on the wing of *Drosophila melanogaster*) undergoing flapping motion. They compared their results with the experimental results of Dickinson et al. (1999) and reported good agreement. Ramamurti and Sandberg also studied the effect of advancing wing rotation (i.e. starting rotation of the wing earlier in the translational stroke) and visualised the leading-edge vortex, which was found to contain considerable spanwise flow, though they did not specify the exact magnitude of this spanwise flow.

Miller and Peskin (2004) used a CFD model to investigate the flow around a 2-dimensional wing undergoing flapping motion. They found a transition point between $Re = 32$ and $Re = 64$ — above the higher value, the wing shed vortices alternately from the leading and trailing edges. Below $Re = 32$, these vortices formed but remained attached to the wing. They suggested that this transition

was significant for lift generation in tiny insects. It is well-known that attached vortices do form on spheres and cylinders at low Reynolds number (see §2.3 below) and Miller and Peskin suggested that this occurs for flat plates at high angles of attack. The lack of vortex shedding was reported to reduce lift.

Kurtulus et al. (2007) used a CFD approach, again to investigate a 2D aerofoil at high angle of attack, but at a higher Reynolds number of 1 000. Once again, vortex shedding took place and dominated the time-evolution of aerodynamic forces. However, they did not extend their study to consider 3D flows. A similar kind of study was carried out by Tang et al. (2008) at Reynolds numbers between 75 and 1700; again, they limited their investigation to 2D cases and restated the (probably mistaken — see §2.1.3.4) idea that delayed stall is relevant to insect-like flapping, saying "the delayed-stall mechanism is mainly responsible for generating most of the lift force" (Tang et al., 2008, p. 973). They conceded that there were "important three-dimensional aspects" that were not addressed in their work, but did not discuss these effects further (or their potential impact on the flow). Their main findings were that the exact kinematics of flapping "strongly influences the specific physical mechanisms present in lift enhancement" and that Reynolds number is an important parameter for this type of flow.

Shyy and Liu (2007) attempted to shed light on the controversy regarding the stability of the LEV. They used a 3D RANS CFD model to compare the flows around a thrip wing at $Re = 10$, a fruit fly wing at $Re = 120$, and a hawkmoth wing at $Re = 6000$. Their results indicated that although an LEV was formed for each case, the detailed phenomenology of the LEV changed as Reynolds number was increased. However, it is difficult to draw any definite conclusions from their work because when Re was changed, the wing planform was also changed. It is therefore not possible to accurately isolate the effect of increasing Re.

2.3 Low Reynolds number aerodynamics

As mentioned above, insect wings operate at much lower Reynolds numbers than those of conventional manned aircraft (see §2.1.3). Current understanding of flow

characteristics at these very low Reynolds numbers is limited by a lack of experimental data in this area. It is known that, because of the high angles of attack at which insect wings operate, a major feature of the flow is separation from the leading edge — a phenomenon that is generally avoided for fixed- and rotary-wing aircraft (with the exception of delta-wing aircraft at high angles of attack and certain helicopter rotor blade tip profiles). This separation leads to the shedding of vortices, at least in the 2D case, as is shown later. This section, then, presents a brief overview of the current state of knowledge in the field of vortex shedding and flow separation, particularly concentrating on the flow around flat-plate aerofoils at low Reynolds numbers.

Until the early 20th century, understanding of the reasons for flow separation was for the most part lacking. The theory of potential (or ideal) flow (that is, the flow of an inviscid fluid) was well developed, the process having been started by Euler in the 1700s who first applied Newton's laws of motion to a fluid. However, potential flow is unable to represent separation of the fluid from, for example, a sharp edge. This leads to the paradox of d'Alembert (1844) — potential flow around a finite body can produce no force on the body. In the early 1900s more understanding was gained — a notable contributor being Prandtl. Eventually this led to Prandtl's boundary layer theorem (Prandtl, 1928) which was able to explain why it was that flow separated.

The development of boundary layers is now well understood — see e.g. Houghton and Carpenter (2003, §6) or Street et al. (1996, §7). It is also known that the precise characteristics of the boundary layer will depend predominantly on the Reynolds number of the flow. Low Reynolds number flows are dominated by viscous forces — these will separate less easily than high Reynolds number flows, which are dominated by their inertia and thus cannot negotiate sharp corners successfully. For the shapes under consideration here — to all intents and purposes, flat plates — separation will occur at both edges for all except the very lowest Reynolds numbers, as is shown later.

This assertion — that high Reynolds number flows separate more readily than low Reynolds number flows — needs some explanation, because it is generally

understood that the opposite is true. There is potential for confusion here, because turbulent boundary layers (which occur at higher Reynolds numbers) separate less readily than laminar boundary layers. Therefore separation will occur more readily for a laminar flow than for a turbulent flow. However, the Reynolds numbers of interest here are so low that transition and turbulence will not occur in the boundary layer (boundary layer transition occurs at Reynolds numbers of $O(10^6)$ (Massey and Ward-Smith, 1998)). The statement above — that separation occurs more readily at higher Reynolds numbers — is true only if the boundary layer remains laminar.

It is possible to gain some insight into the process of separation by examining the flow around a sphere or a circular cylinder. This area has received considerable attention in the last 100 or so years — among the first to study this type of flow was Strouhal (1878).

The nature of the flow around a cylinder is now relatively well understood, largely through the important work of Roshko (1955). Houghton and Carpenter (2003, §6) identify six 'types' of flow, classified by Reynolds number. These are illustrated in Fig. 2.9.

For very low Reynolds numbers ($Re < 1$), flow is 'creeping' — that is, there is no separation and the fluid simply flows around the body. The flow is therefore steady, and symmetrical fore and aft. Above $Re = 1$ a slight asymmetry develops fore and aft, which grows as Reynolds number is increased up to $Re = 5$.

At $Re = 5$, the flow on the rear section of the cylinder is unable to remain attached to the surface of the cylinder due to the adverse pressure gradient. It therefore separates, forming a closed area of circulation behind the cylinder — however, no vortices are shed. Hence the flow remains steady. This phase continues up to $Re = 40$, with the closed wake gradually extending in length as Reynolds number is increased within this range.

When a Reynolds number of 40 is exceeded, vortices begin to form in the wake, meaning that the flow becomes unsteady. These vortices are shed alternately from each side of the cylinder, those from one side rotating in one direction, those from the other rotating in the opposite direction, but do not form until relatively far

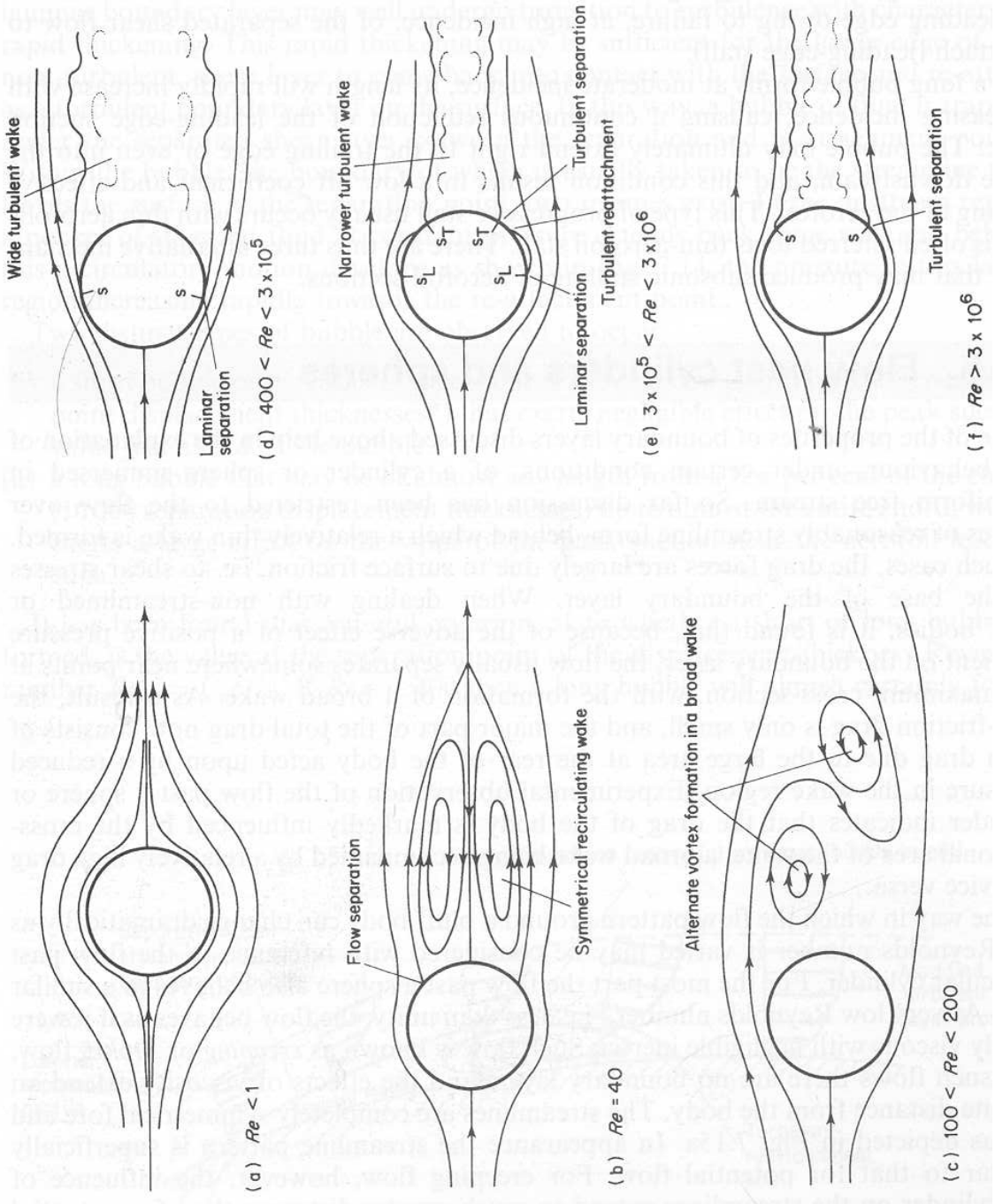

Figure 2.9: 'Stages' of flow around a cylinder, from Houghton and Carpenter (2003). The Reynolds numbers quoted are approximate; the exact values at which changes occur will vary according to the free-stream turbulence level.

downstream in the wake. The formation point of these vortices moves upstream with increasing Re until, at around $Re = 100$, the vortices form directly after the flow has separated and remain attached to the cylinder until they increase in size sufficiently to be shed. The frequency of vortex shedding increases with Reynolds number up to a Reynolds number of about 500, after which it remains more or less constant. The vortex structure seen in the wake of the body is known as a von Kármán street.

Because of this periodic formation of vortices from the cylinder, the cylinder experiences an oscillating net circulation around itself, which leads to an oscillating force on the body normal to the freestream flow direction. If the cylinder is not completely rigid it will oscillate, which will affect the frequency of shedding, which can lead to a phenomenon known as 'lock-on', where the frequency of oscillation matches the frequency of vortex shedding (see e.g. Sarpkaya, 1979). This can lead to the magnitude of the oscillations increasing, which in turn can lead to catastrophic structural failure. This is of particular concern to those involved with designing tall chimney stacks or similar structures. It can also affect slender structures such as bridges, and it is possible that it occurs in insect-like flapping and increases efficiency — perhaps the shedding of vortices from an insect wing creates an oscillating force on the wing that augments the force actually provided by the insect's flight muscles.

If Reynolds number exceeds 200, the wake transitions to a turbulent flow, although transition occurs far downstream of the cylinder. The transition point moves upstream (as do the separation points) as Reynolds number is increased until, at $Re \approx 1 \times 10^6$ (Singh and Mittal, 2005), transition occurs close to the separation points, which, by this time, have moved to the front half of the cylinder. Transition re-energises the boundary layer, causing re-attachment and leading to a separation bubble. The re-attached boundary layer (now turbulent) remains attached to the cylinder until further downstream, leading to a narrower wake and decreased pressure drag.

If Reynolds number is increased above 3×10^6, the separation bubbles disappear and the boundary layer becomes turbulent close to the stagnation point on the front

of the cylinder. Fig. 2.9 illustrates these 6 stages.

Although this study of the flow around cylinders may offer some insight into the types of flows of interest here, it is important to bear in mind that the shapes of interest here (i.e. flat-plate aerofoils) are much more slender than cylinders. Do these six stages still occur with an aerofoil-like shape or a flat plate? If so, how are the Reynolds numbers at which the changes occur affected?

These questions are somewhat difficult to answer because it appears that little work has been done — or at least published — involving flat plates at incidence at low Reynolds numbers, although some work has been done at higher Reynolds numbers (see e.g. Fage and Johansen, 1927). This is no doubt mainly due to the fact that, until recently, the area of very low Reynolds number external aerodynamics has been of relatively little interest. It has only been with the fairly recent increased interest in MAVs that research into very low Reynolds number external flows has become of any value. Another factor is the difficulty of obtaining these very low Reynolds numbers experimentally.

Most of the early work in this field was related to model aircraft and dealt with minimum Reynolds numbers of $O(10\,000)$. Schmitz (1940, translated 1967), in an experimental study, found that at Reynolds numbers below 40 000, a flat plate had superior lifting performance compared to a more-conventional streamlined aerofoil. This was later confirmed by Sunada et al. (1997), who found that a flat plate also outperformed a conventional aerofoil at $Re = 4\,000$.

Research did not really begin to accelerate until the early 1980s, when papers specifically dealing with low Reynolds number aerofoils began to appear. Among the important contributions made at this time were those of Mueller and Batill (1982). However the definition of a low Reynolds number was still somewhat higher those of interest here — for example Mueller and Batill (1982) investigated what they called 'low' Reynolds numbers between 40 000 and 400 000, O'Meara and Mueller (1987) between 50 000 and 200 000, and Hsiao et al. (1989) between 300 000 and 774 000. By contrast, this work is interested in Reynolds numbers from $O(1)$ to $O(10\,000)$ (see §2.1.3). During insect-like flapping the wings repeatedly come to rest, so individual wing sections frequently operate at effective Reynolds

numbers close to zero.

Carmichael (1982) presented an in-depth review of the field of low Reynolds number aerofoils in 1982. Although he concentrated mainly on the Reynolds number range 20 000 to 200 000, he also looked briefly at lower Reynolds numbers ($Re < 150$), but only mentioned the flow around cylinders. Jones (1990) briefly reviewed low Reynolds number aerofoil theory, but again did not consider Reynolds numbers below 40 000. He noted that the "behaviour of airfoils, especially in the range of low Reynolds numbers, depends on the persistence and stability of laminar flow" (Jones, 1990, p. 46). However for the Reynolds numbers under consideration here, laminar flow is almost certain to persist until the flow is well aft of the aerofoil — as Ellington (1984d) noted, "it is doubtful whether one can speak of transition in the separated boundary layer at these low Re" ($Re = 10^4$). Much of the literature, for this reason, is irrelevant, as it assumes transition occurs somewhere in the boundary layer on the surface of the aerofoil.

In any case, almost all of the above research was carried out at low angles of attack — separation was limited in most cases to separation bubbles, and vortex shedding was not addressed to any great extent. Insects, however, have been shown to take advantage of flow separation from the leading edge of their wings.

Ohmi et al. (1990, 1991) studied the flow around an aerofoil at Reynolds numbers as low as 1 500 and angles of attack as high as 45°. However, they oscillated their aerofoil in pitch as they translated it. They noted large-scale vortex shedding from the leading and trailing edges of the aerofoil, and suggested that this pattern of shedding was insensitive to changes in Reynolds number in the range $1\,500 \leq Re \leq 10\,000$. However, their results must be treated with care because they conclude that the phenomenology of the flow is dramatically affected by the frequency of pitch oscillation. It is not possible to isolate the effects of this oscillation from the effects of simple translation.

Chang et al. (1993) investigated the flow around an aerofoil at a low angle of attack and a Reynolds number of 5 000. However, due to the low angle of attack, separation occurred only at the trailing edge, and Chang et al. were concerned primarily with the starting vortex and its effect on lift production. Later, Katz

et al. (1996) used a CFD method to model an aerofoil at a higher angle of attack of 10° and $Re = 12\,000$. Although the angle of attack was still relatively low, leading-edge separation was observed, but not until the aerofoil had travelled two chord lengths. Trailing-edge separation, on the other hand, was seen almost immediately (after around 0.02 chords of travel). The LEV that was formed enhanced lift whilst it remained above the aerofoil, but was quickly shed, and periodic vortex shedding ensued.

Later, Huang et al. (2001) studied the flow around an aerofoil at Reynolds number between 1 200 and 2 400 and angles of attack of up to 90°. Once again, they observed large scale vortex shedding at high angles of attack, but did not measure lift on the aerofoil and did not speculate on how the shedding of an LEV might affect lift. They identified 5 regimes of flow. At low angles of attack (2°), the flow remained attached to the aerofoil and no vortex shedding occurred (apart from the initial starting vortex). If angle of attack was increased slightly (to 7°), a vortex formed above the upper surface of the wing, although it did not appear to form close to the leading edge. This vortex was eventually shed and subsequently periodic vortex shedding occurred. If angle of attack was increased further (to 15°), separation occurred at the leading edge and an LEV was formed which grew and was then shed into the wake. A similar flow pattern was seen at an angle of attack of 30°. At 90° angle of attack, separation occurred simultaneously at both edges of the plate and a pair of large counter-rotating vortices formed behind the plate. This work (and the work of Ohmi et al. (1990, 1991)) gives some idea of the difficulties involved in carrying out experiments at these low Reynolds numbers.

Although the above research does provide insight into the phenomenology of the flow around an aerofoil at high angle of attack and relatively low Reynolds number, it does not tell us much about how the vortices that form affect the lift on the aerofoil. In an attempt to address this deficiency, Dickinson and Götz (1993) studied the simple but important case of a flat-plate aerofoil accelerating from rest to a constant velocity at fixed angle of attack. They noted that there was very little data for Reynolds numbers between 10 and 1 000, and therefore concentrated on increasing understanding in this area. Most of their experiments,

which were physical rather than computational, were at a Reynolds number of 192 (based on chord length and velocity). They found that at angles of attack above 13.5°, a leading edge vortex was formed which, they postulated, enhanced lift production. They noted also the formation of a von Kármán street as vortices were shed alternately from leading and trailing edges. However, because their experiments were designed to be 2D, they were unable to investigate the importance of spanwise flow, though they suggested that spanwise flow may be important in stabilising the leading-edge vortex in 3D cases. They also implied, however, that for some insects the leading-edge vortex may not need to be completely stable because the wings move only a few chords per stroke so that the vortex would not have time to shed.

Sun and Boyd (2003, 2004) also investigated this field, concentrating on even lower Reynolds number right down to $Re = O(1)$. They noted that there were "very few computations and experiments for aerodynamics of airfoils at Reynolds number below 1 000" (Sun and Boyd, 2004, p. 199), and used a hybrid continuum-particle computational approach. They found that at $Re \approx 140$ the flow separated from the leading edge once angle of attack exceeded 20°. However, when they studied flow at $Re \approx 14$, they noted "several new effects" (Sun and Boyd, 2003, p. 8). Firstly, separation at the leading edge was delayed beyond an angle of attack of 40°, and when it did occur it was fundamentally different to the separation that was seen at higher Reynolds numbers — the flow rounds the leading edge without separation, but then leaves the top surface at around 25% chord. At $Re \approx 1$, they found no separation at all even at an angle of attack of 50° (Sun and Boyd, 2004, p. 203). They also found changes in the boundary layer profile as Reynolds number was decreased (Sun and Boyd, 2004, p. 201), including the breakdown of the no-slip condition (at $Re < 50$) on the aerofoil surface. They suggested that flow at very low Reynolds numbers could not be assumed to be incompressible, claiming that density can vary by as much as 15% of the freestream value (Sun and Boyd, 2004, p. 206). They concluded that "the aerodynamic characteristics of the micro-scale airfoil at low Reynolds number flows are very different from those at high Reynolds numbers" (Sun and Boyd, 2003, p. 8). However, their results

are not directly comparable to those presented here, because they dealt with very small aerofoils — with chord of 30 microns. At these very small scales, continuum approaches (such as the one used in the current study) are not accurate because rarified effects become important. This could account for the two effects they discovered (slip at the solid boundary and compressibility).

Despite the helpful contributions discussed above, a full and coherent understanding of the flow around flat-plate aerofoils at these low Reynolds numbers ($O(1) - O(10\,000)$) and high angles of attack ($\alpha \geq 45°$)) is still lacking.

2.4 Summary

It has been shown that, thanks largely to work from the zoological research community, there now exists a comparatively good understanding of what insects do with their wings, and it is clear that insect-like flapping involves complex kinematics — it is not simply a matter of pure up-and-down motion. Because of this complex wing motion, insect flight involves some highly unsteady aerodynamics and some novel phenomena that are not seen (or at least not to such an extent) in the cases of fixed- or rotary-wing aircraft. Efforts to explain insect flight using familiar terminology (e.g. dynamic stall, the Magnus effect, and so on) have tended to produce more confusion than insight, and current understanding of the aerodynamics involved in insect-like flapping is still imperfect. As a result of this imperfection, many past efforts to model insect flight have proved inadequate. 2D models are, by definition, too simple and fail to reflect the fact that insect-like flapping appears to produce highly-3D flows. Until the aerodynamics involved at the very low Reynolds numbers under consideration here are better understood, it is hard to see how future analytical models can capture all of the relevant phenomena.

Based on the preceding review of the literature, it is evident that consensus is lacking on some rather fundamental points relating to the aerodynamics of insect-like flapping. One of the aims of the current work is to provide further insight into these types of flows in order to try and answer some of the unanswered questions; for example, why does the LEV appear to be stable for 3D flows when for 2D flows

it is unstable? The other aim relates to the existing analytical models which have been developed at Shrivenham. These aims, and the objectives relating to them, are described in more detail in §3.

Chapter 3

Aims and objectives

Broadly speaking, there are two primary aims for this project. The first relates to existing analytical models developed by Cranfield University at Shrivenham. The second is more fundamental, and relates to certain aspects of the phenomenology of the flow around a wing undergoing insect-like flapping. The present project aims to address both of these using a primarily-computational approach, to complement the analytical work carried out within Cranfield and elsewhere, and the experimental work carried out elsewhere. Some experiments have also been carried out to validate the results of the CFD work and to gain further insight into the flow.

3.1 Cranfield analytical models

The first of the aims of this thesis relates to the Cranfield analytical models for flapping wings. These models and some of their findings will now be outlined briefly by way of introduction to the first set of objectives, which are described in §3.1.3.

3.1.1 Pedersen's model

Two analytical models have been developed by Cranfield University using two different approaches, which were originally suggested by Żbikowski (2002a). The first approach is based on the idea of velocity potential (Pedersen and Żbikowski

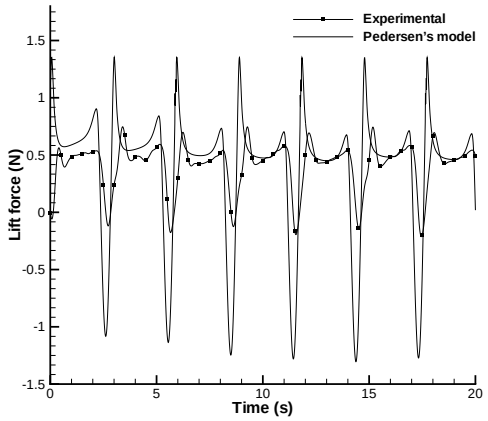

Figure 3.1: Comparison of measured lift force for Dickinson's 'flapper' (priv. comm.) with data from Pedersen's model.

(2006); full details in Pedersen (2003)). This idea goes back many years and is the foundation of much work on wing flutter (Wagner, 1925; Theodorsen, 1935).

Pedersen's model involves dividing the wing (which is assumed rigid and infinitely thin) into chordwise elements (with each slice running from leading to trailing edge). The lift on each element is then calculated and the lift on the whole wing is calculated by summing the effect of each slice — i.e. a modular, quasi-3D approach is used. For each 2D slice, the quasi-steady forces are calculated using the velocity potential approach; Polhamus' leading-edge suction analogy[1] is used to calculate the 'extra' force due to the LEV; the Wagner and Küssner functions (along with a modified form of the method of Loewy (1957)) are used to account for the effect of the wake from previous strokes; and finally added-mass forces are incorporated. The total force on the wing is then calculated by summing all the slices. The model has the advantage of being simple and fast. In addition, the net force on the wing at a given time can easily be broken down into the constituent parts (added-mass forces, forces due to the LEV, etc), thus, in principle, providing useful insight.

Comparisons made by Pedersen (2003) of his predicted lift and drag forces with measured forces from Dickinson's 'flapper' (Dickinson, priv. comm.) are shown

[1]See footnote, p. 56. The implicit assumption is that the LEV formed on an insect wing is similar in structure and in effect to the LEV formed over a delta wing at high angle of attack. This assumption may or may not be valid.

in Figure 3.1. Pedersen (2003) noted that his model predicted a mean lift force of $0.37N$, whereas the measured lift force was $0.40N$ — a difference of only 9%. However, the average error in the predicted lift force (i.e. error at each time step, averaged over all time steps) was $0.3N$ or around 81% of the average measured lift force, whilst the median error was $0.11N$ or 27% of the average measured lift force. In addition, the predicted mean drag force was $1.52N$, which, when compared to the measured mean drag force of $0.60N$, showed a difference of 153%. Pedersen gave a number of possible reasons for this discrepancy, related to the assumptions made in the formulation of the model. Most importantly, the LEV was assumed to dissipate immediately when shed, the wake was assumed not to deform, and the added-mass forces were based only on the motion of the wing (i.e. they were calculated without taking into account the wake from previous strokes). The other major simplification was the 2D nature of the model, which meant that spanwise flow was not captured. The main conclusion of the project was that the model as it stood was over-simplified, and did not capture the physics of the flow with sufficient accuracy.

3.1.2 Ansari's model

The second analytical model developed by Cranfield University is that of Ansari. The model uses a circulation-based approach, essentially using the technique introduced by von Kármán and Sears (1938) (after extensive modification to remove small angle approximations and allow wake deformation). The wing is divided into an array of 2D sections, each running from the leading to the trailing edge of the wing. These sections are curved (rather than straight, as in Pedersen's model), in order to try and capture the fact that the wing is sweeping about its root; but it is shown later (§6.10.1) that this change does not make much of a difference to the final force predictions.

For each 2D section, the wing is represented by a continuous distribution of bound vorticity, and separation is enforced at the leading and trailing edges, leading to a pair of vortex sheets in the wake. The flow is assumed inviscid, but the effects of viscosity are introduced directly though the imposition of flow separation at the

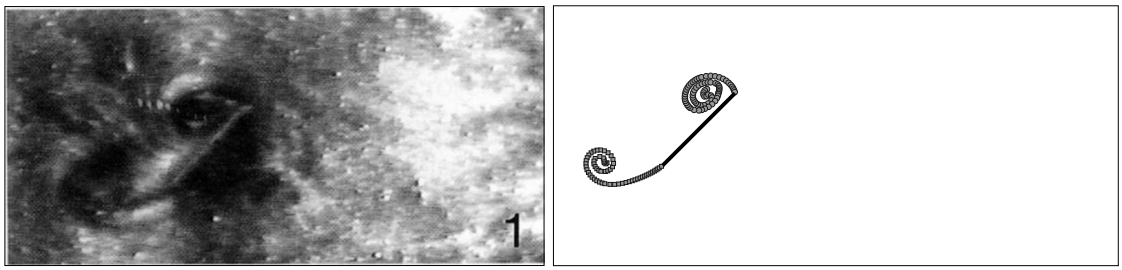

(a) After 1 chord travelled

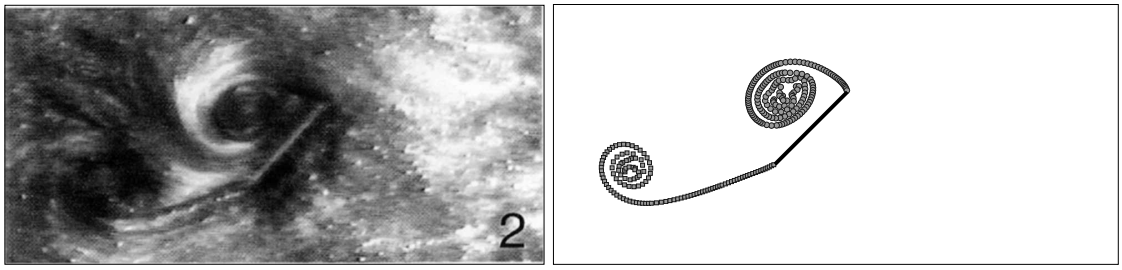

(b) After 2 chords travelled

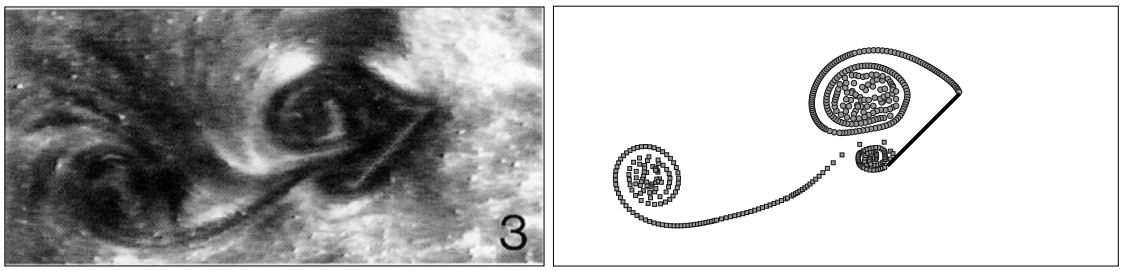

(c) After 3 chords travelled

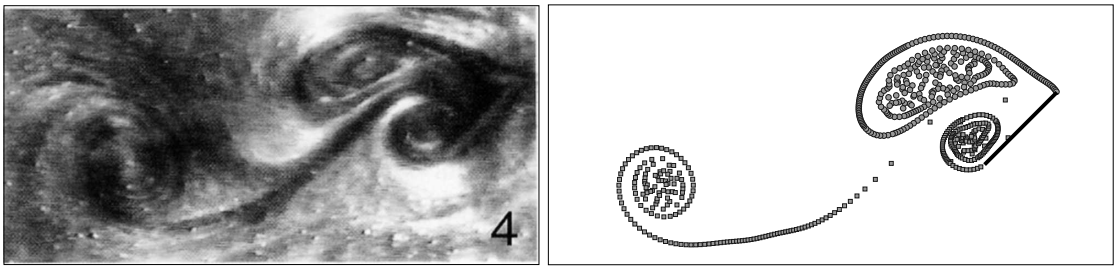

(d) After 4 chords travelled

Figure 3.2: Comparison of experimental flow visualisation from Dickinson and Götz (left) with flow visualisation from Ansari's model (right) for a uniformly-accelerated, flat-plate aerofoil at 45° angle of attack (Dickinson and Götz, 1993; Ansari, 2004).

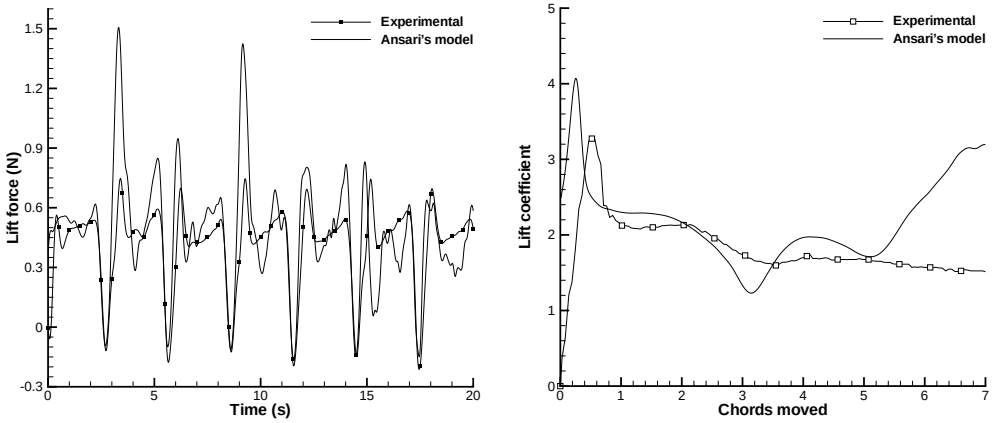

(a) 3D; experimental data as in Figure 3.1

(b) 2D; the aerofoil is a thin flat plate and is translated (after an impulsive start) at an angle of attack of 45°. $Re = 192$ for the experimental case.

Figure 3.3: Comparison of data from Dickinson's 'flapper' (priv. comm.) (left) and Dickinson and Götz (1993) (right) with data from Ansari's model.

edges of the aerofoil. These wakes are allowed to deform and the resulting flow is solved by ensuring that the net circulation in the system remains zero, there is no flow through the aerofoil, and separation always occurs at the leading and trailing edges.

Ansari's model is more general and more logical (and generally more accurate) than that of Pedersen, and also has another significant advantage over Pedersen's model; it is able to produce flow visualisation. This is extremely useful in identifying, for example, the reason for the force peak at a given time. However, a number of important assumptions were still made to simplify the formulation of the model. The most important of these are: the wing is assumed rigid; the flow is assumed inviscid (although the *effect* of viscosity — separation — is included, as mentioned above); only one wing is modelled (so wing-wing interactions such as the clap-and-fling cannot be modelled); and no interaction is allowed between different spanwise locations (i.e. there is assumed to be no spanwise flow within the LEV, and no tip vortex).

The model has been validated using 2D flow visualisation and force data from Dickinson and Götz (1993) and with 3D force data from Dickinson's 'flapper' (Dick-

inson, priv. comm.). It has proved extremely accurate when compared to the 2D flow visualisation data (see Figure 3.2) and also remarkably accurate (considering the essentially-2D nature of the model) when compared to the 3D force data (see Figure 3.3(a)). In the 3D case, the average predicted lift force was $0.457N$, which when compared to the average measured lift force of $0.403N$ gives an error of around 13%. The average error in the predicted lift force was $0.15N$, or around 37% of the average measured lift force (much better than for Pedersen's model above), whilst the median error was $0.09N$ or 23% of the average measured lift force (slightly better than for Pedersen's model). Much of this improvement is probably due to the more accurate phasing of the lift peaks (compare Figures 3.1 and 3.3(a)). It has been suggested by Ansari et al. (2006c) that the experimental setup may not have captured the true magnitude of the positive lift peaks due to bandwidth limitations, but no other suitable flapping-wing force data exist to compare against.

When compared to the force measurements from the 2D experiments of Dickinson and Götz (1993), the correlation is poor (see Figure 3.3(b)), despite the close agreement with the flow visualisation data from the same experiments. Ansari proposed two possible reasons for this. Firstly, his model is essentially inviscid, and viscosity may play a major part in the flow at the low Reynolds number ($Re = 192$) at which the experiments of Dickinson and Götz took place (but the Reynolds number of Dickinson's 'flapper' was even lower at $Re = 160$, and for that case Ansari's model predicted the forces very accurately). Secondly, Ansari questioned the quality and reliability of the experimental results. It is shown later that the second of these two reasons seems to be the more likely source of the difference.

A final point about Ansari's model is that, when compared to 3D flow visualisation, results are poor. There has been speculation that this is because 3D flow visualisation generally plots results on a 2D straight plane, whereas Ansari's model produces flow visualisation on cylindrical surfaces. The validity of this speculation is examined in §6.10.1.

3.1.3 Aim and objectives of the current work regarding the two present models

Ansari's model has proved the more accurate and useful of the two analytical models developed by Cranfield. Therefore, in this project, more attention has been paid to Ansari's model than to Pedersen's. This is not to say that Pedersen's model is useless; in fact with some refinement there is no reason why the approach taken by Pedersen could not be more successful. But, as Pedersen's model stands, it is not so helpful for gaining *insight* into the phenomenology of the flow around a flapping wing (although it does give useful information about the relative contributions of the lift mechanisms modelled) whereas Ansari's model produces helpful flow visualisation (which is consistent with experimental observations). The comments regarding the existing models will therefore be primarily concerned with Ansari's; but many of the conclusions will also apply to Pedersen's. Other analytical models have been developed elsewhere (some of which were discussed in §2.2.1.2) but none has proved more successful than that of Ansari. Ansari et al. (2006a) review many of these other models.

The two models described above have one thing in common — they are both essentially two-dimensional. The wing is divided into a number of chordwise elements and the total force on the wing is found by summing the contribution from each element. The validity of this approach is questionable, given that insect-like flapping has been shown to produce highly-3D flows. However, it is undeniable that Ansari's model does produce remarkably good results when used to analyse insect-like flapping. This is surprising, given the inviscid, 2D nature of the model. The primary aim of the current work with regard to Ansari's model is to investigate some of the possible limitations of Ansari's model, especially the effect of the assumption of 2D inviscid flow. To fulfil this aim, a number of objectives are defined: first, the role of spanwise flow is investigated; secondly, the role of the tip vortex; and, thirdly, the role of Reynolds number and viscosity.

Flow visualisation from Ansari's model compares unfavourably to that from 3D experiments. Another question that the thesis aims to answer, relating to this, is

whether this difference can be explained by considering the 'curved chords' that Ansari's model uses — flow visualisation from 3D experiments is generally captured over flat surfaces whereas Ansari's model produces flow visualisation results over curved (cylindrical) surfaces.

A final aim is to conclude whether, in general, it is reasonable to use 2D models to investigate 3D flows — in other words, to ascertain whether spanwise flow occurs during the particular phase of flapping under examination here, and, if so, what impact it has. This will enable future models to prioritise the phenomena more accurately in order to determine which should be included in the model, and which can justifiably be left out.

3.2 Insect-like flapping

In addition to the aim and objectives listed above regarding the current analytical models, this work also has a more general aim: to gain insight into the flow around a wing undergoing insect-like flapping. Most of the early CFD work in this regard, as was seen in §2, concentrated on precisely reproducing insect-like flapping in the CFD domain (see e.g. Liu and Kawachi, 1998). The data obtained could then be compared to the results from mechanical flappers, but insights into the phenomenology involved were few and far between — the words of F. W. Lanchester, quoted on p. 303, seem entirely applicable to this kind of approach. More recently, some CFD work has concentrated on 2D flows (see e.g. Miller and Peskin, 2004; Kurtulus et al., 2007; Tang et al., 2008), but little attention appears to have been paid to the fact that, when considering insect-like flapping, 2D and 3D flows are fundamentally different — as is shown later. The current study aims to build understanding of the flow involved in insect-like flapping by first looking at 2D flows and then progressing to 3D flows. By examining the differences, the thesis will attempt to explain some of the disagreements that have taken place in the literature, as well as show the effects of various relevant parameters.

Another way in which insight can be gained is to try and break down the complex flapping kinematics of an insect wing into more manageable components.

It has already been noted that insect-like flapping consists of rotation phases and translational phases. Up to 90% of such flapping motion simply involves the wing sweeping about its root (pronation and supination comprise only around 10% of the motion in terms of time) (Ellington, 1984c). In addition, the results of Aono and Liu (2006) suggest that only small forces are produced during the rotational phases of motion, and that most of the lift force is produced during the upstroke and downstroke. So the current work has concentrated on this phase of the motion — the part that lies between the pronation and supination phases.

The objectives of the current work can be divided into 2 categories — 2D (i.e. those objectives which relate to the flow around aerofoils or chordwise elements of wings) and 3D (those objectives which relate to 3D wings). These will now be discussed in detail.

3.2.1 2D flows

Specific questions to be addressed, in the context of 2D flows relevant to insect-like flapping, are described below. Answering these questions provides the objectives for this part of the work.

- How does Strouhal number fit into current understanding of insect-like flapping? Some have proposed that "Strouhal number may be a more important parameter than the Reynolds number for these kinds of flows" (Ansari et al., 2006a, §4.3). The thesis aims to cast some light on the physical meaning of Strouhal number and in particular its relationship to Reynolds number.

- What is the effect of Reynolds number on the kind of flows under examination here? It has already been noted that any FMAV will operate at a higher Reynolds number than that of most current insects. What difference does this make and how can that difference be explained?

- How much of an impact does changing the aerofoil section (including section shape and section thickness) have on the aerodynamic forces?

- What is the impact of changing angle of attack for these 2D flows? Is there an 'optimum' angle of attack?
- How important are the kinematics of the aerofoil? How much of a contribution do added-mass forces make to the total force? And what difference does acceleration make to vortex shedding frequency?

3.2.2 3D flows

The thesis aims to address the following questions, which provide further objectives, this time in the context of 3D flows relevant to insect-like flapping.

- What are the effects of moving from a 2D aerofoil to a purely-translating 3D wing, i.e. a wing which is not sweeping?
- What is the result of the switch from a 3D translating wing to a 3D rotating wing (i.e. a wing which sweeps about its root)?
- Is the LEV stabilised by the sweeping motion of the wing, and if so, why?
- How is the flow affected by Reynolds number?
- What is the effect of changing the planform of the wing?
- What impact does angle of attack have for these 3D flows?
- Why does a stable LEV not form on helicopter rotor blades; is this because of the high aspect ratio of these blades, or because of the high Reynolds number at which they operate?

3.3 Summary of aims and objectives

The two primary aims of this thesis are to examine the validity of some of the assumptions made in Ansari's model, and to provide further insight into aerodynamics relevant to insect-like flapping. The principle objectives, relating to these two aims, are to investigate the role of Reynolds number for both 2D and 3D flows;

to examine the stability of the LEV in both 2D and 3D cases; and to quantify the effect of the various relevant parameters (e.g. angle of attack, wing aspect ratio).

The chief aim of the current project is to gain *insight*. Previous work has concentrated on producing models which can be used to predict the forces on an insect or FMAV wing. Here an attempt is made to take a step back, and look more closely at what actually happens during insect-like flapping. To this end, a progressive approach is used. Rather than simply producing a 3D CFD model of full insect-like flapping, and then comparing the results of it to experimental data, the work has built up from 2D flows to 3D flows, trying to get maximum value out of the results obtained.

The remainder of this thesis is laid out as follows. Chapter 4 examines the assumptions made in the formulation of the CFD model, describes the CFD model itself (further details of which are contained in Appendix B), and outlines the experimental work that was carried out. Results and discussion (including results relating to the validation of the CFD model) are divided into two chapters: Chapter 5 presents those results relevant to 2D flows, and Chapter 6 presents results relating to 3D wings. Finally, the findings of the current work are summarised and avenues for further investigation are suggested in Chapter 7.

Chapter 4

Primary assumptions & method

"Everything should be made as simple as possible, but not simpler."

— Albert Einstein

This chapter covers briefly the methods that have been used to obtain the results presented in this thesis. First, though, some of the definitions and terminology used in the thesis are briefly reviewed. Subsequently, the assumptions that were made in formulating the CFD model are discussed, along with the justification for these assumptions. The CFD model itself is then presented (further details of the CFD model are contained in Appendix B), and finally the methods used to produce the experimental results (with which the CFD model is compared later) are detailed.

4.1 Definitions and terminology

The definitions given are divided into two sections; firstly, the more general terms, and secondly those relating more specifically to the field of insect-like flapping.

4.1.1 General terminology

4.1.1.1 Navier-Stokes Equations

The Navier-Stokes equations are the governing equations of fluid flows. They can be stated in various forms, as discussed in §4.3.1.1 below.

4.1.1.2 Kelvin-Helmholtz instability

Kelvin-Helmholtz instability (KHI) is a type of instability to which vortex sheets are prone. It involves the formation of discrete vortices within the sheet, and is discussed in detail in §5.3.3.1.

4.1.1.3 Vortex

A flow with closed streamlines, where fluid rotates around its own centre.

4.1.1.4 Vortex sheet

A surface of discontinuity of velocity in a fluid, which may be regarded as formed by vortex filaments oriented normal to the shear vector across the surface.

4.1.1.5 Vorticity

A vector measure of local rotation in a fluid flow, defined mathematically as the curl of the velocity vector ($\nabla \times \mathbf{u}$).

4.1.1.6 Vorticity balance

A method for analysing the evolution of vorticity in a given flow. The method uses the vorticity transport equation (Panton, 1996);

$$\frac{D\omega}{Dt} = \omega \cdot \nabla \mathbf{u} + \frac{\mu}{\rho}\nabla^2\omega. \tag{4.1}$$

It is interesting to note the link between this equation and the vorticity-based formulation of the Navier-Stokes equations (Equation 4.7 below). The term on the LHS is the rate of change of vorticity of a given particle with respect to time. The last term on the RHS is the net rate of viscous diffusion of vorticity. Vorticity diffuses through a flow by viscous action, as momentum does. This explains how vorticity is generated at a surface and then passes into the wake, as will be seen later; this is the only method by which vorticity can enter a flow.

The first term on the RHS represents the generation or destruction of vorticity by the stretching or turning of vortex lines. Stretching a vortex line produces an

increase in vorticity in much the same way as stretching a material line produces an increase in length. For 2D flows, this mechanism is absent and Equation 4.1 is simplified by the removal of the first term on the RHS. In these cases, the rate of change of vorticity for a given particle is simply equal to the net rate of viscous diffusion for that particle.

The key principle behind the idea of vorticity balance is that the rate of accumulation of vorticity within a flow can simply be calculated by subtracting the rate at which vorticity is being extracted from the flow (by diffusion) from the rate at which it is being added to the flow (by generation within the boundary layer attached to a surface in the flow) (Reynolds and Carr, 1985). Generally speaking, turbulence also has an impact on this process, but as only laminar flows are considered in this thesis, it can be ignored.

4.1.2 Terminology relating to insect-like flapping

4.1.2.1 Added mass

When a body is accelerated in a fluid, an 'extra' force is required in order to accelerate the mass of fluid around the body. Therefore it appears as if the body has 'extra' mass. This extra mass is termed added mass. Added mass is discussed in §2.1.3.2.

4.1.2.2 Dynamic or delayed stall

Dynamic stall is discussed extensively in §2.1.3.4. Historically it refers to the fact that if a wing is simultaneously translated and pitched up, higher lift coefficients can be achieved than if the same wing is translated at constant angle of attack. However, many authors have attributed the generation of the leading-edge vortex seen during insect like flapping to dynamic or delayed stall. The discussion in §2.1.3.4 and the results presented in §5 show that this is inappropriate and leads to confusion, and that the LEV is simply formed by flow separation at the leading edge.

4.1.2.3 Delayed leading-edge separation

Delayed leading-edge separation is discussed later in §5.4. The term is defined to describe the fact that when an aerofoil is impulsively started at high angle of attack, separation occurs immediately at the trailing edge, but does not occur at the leading edge until some time later. This is important in explaining the development of the lift force on 2D aerofoils.

4.1.2.4 The leading-edge vortex

The leading-edge vortex (LEV) is an important phenomena in insect-like flapping. The vortex is formed above the wing due to flow separation at the leading edge and enhances lift. The LEV is discussed in §2.1.3.4. In this thesis an LEV is defined as stable if it eventually remains in a fixed position relative to the moving aerofoil or wing.

4.1.2.5 Wake capture

Wake capture was discussed in §2.1.3.1. It refers to the interaction between a wing undergoing insect-like flapping and its wake from previous strokes. It is a misleading term because the wake is not actually 'captured' by the wing; the wing simply passes through the wake. Therefore, the term 'wake capture' generally means the same as 'wing-wake interaction'.

4.1.2.6 The Wagner effect

The Wagner effect is discussed on p. 57. It accounts for the fact that when the velocity or angle of attack of an aerofoil in motion is changed, the lift force does not immediately change to the new steady state value, and is important in explaining the development of the lift force on 2D aerofoils.

4.2 Discussion of assumptions

Some of the assumptions that have been made in the course of this work have already been mentioned. A summary of these assumptions and discuss the justifi-

cation for them is now given.

4.2.1 Laminar flow

The assumption that flow is fully laminar is also made in all of the CFD studies of insect flight that are extant (see e.g. Liu et al. (1998); Sun and Tang (2002); Kurtulus et al. (2007); Tang et al. (2008)). However, this of itself is no evidence that the assumption is reasonable. Ellington (1984d) postulated that turbulence "cannot occur" at wing chord Reynolds numbers of 200 and expressed doubt that transition would occur even at Reynolds numbers of the order of 10^4, and Katz et al. (1996), carrying out CFD analysis at a wing chord Reynolds number of 12 000, stated that "at this low Reynolds number, unknowns associated with the modeling of turbulence are avoided," again implying that transition is not possible at these orders of Reynolds numbers. However, this is in direct contrast with what was seen in §2.3, where it was stated that transition in the wake of a circular cylinder occurs even at Reynolds numbers as low as 200. How can this apparent discrepancy be accounted for?

Boundary layer transition occurs at a critical Reynolds number, which depends on various factors such as pressure gradient, free-stream turbulence level, and surface roughness, but a quick review of the literature shows that some authors report this critical Reynolds number to be as low as 385 000 (Lawson, 2001) and others as high as 5 000 000 (Massey and Ward-Smith, 1998) (based on the free-stream velocity and the streamwise distance from the start of the boundary layer).

It has been seen that even the largest insects — and indeed FMAVs — operate at mean wing chord Reynolds numbers of no higher than $O(10^4)$. Therefore, at no point would transition be expected within the boundary layer attached to the insect's wings. However, it is equally clear that at some point the boundary layer will become detached from the wing, if only at the trailing edge, and is then termed a free shear layer. In fact, as has been seen, insect wings generally translate at high angles of attack and separation occurs at both the leading and trailing edges. The von Kármán street that is formed in the wake is essentially a pair of free shear layers that roll up into discrete vortices, as shown in Figure 2.9c.

The flow around a flat plate at high angle of attack is not as well documented as, for example, the flow around a cylinder. However, the principles involved in the latter should apply to the former. As discussed in §2.3, the flow around a cylinder first becomes *unsteady* at $Re = 40$, when vortices begin to be shed alternately from the sides of the cylinder, leading to a von Kármán street in the wake. This structure continues to persist even if Reynolds number is increased to $Re = 270\,000$ (Williamson, 1996), but at higher Reynolds numbers the shear layers which emanate from the body will become turbulent rather than laminar at some point downstream. The Reynolds number at which this transition occurs is not precisely defined. Some have identified the onset of transition in the shear layer at Reynolds numbers as low as 350, whilst others claim it first appears at Reynolds numbers of 1900 (Singh and Mittal, 2005). Reynolds numbers quoted in the context of cylinder flows are usually based on free-stream velocity and cylinder diameter.

There are two important Reynolds numbers for a given flow — the *critical* Reynolds number, at which the flow becomes unstable, and the *transition* Reynolds number, at which the flow becomes turbulent. The former is lower than the latter, so that a flow will become unstable before transition occurs. For example, the boundary layer on a flat plate becomes *unstable* at $Re \approx 10^5$, but *transition* does not occur until $Re \approx 10^6$ (Versteeg and Malalasekera, 2007). In the case of a free shear layer, instability is part of the process that leads to turbulence (Dong et al., 1997), with the free shear layer rolling up into discrete vortices (due to Kelvin-Helmholtz instability) before transition to turbulence occurs. Therefore, the actual transition to turbulence will not occur until the free shear layer is some distance downstream. This is the crucial point — that transition will not occur either in the boundary layer or in the immediate vicinity of the aerofoil. The point at which the instability occurs does move upstream as Reynolds number is increased (Singh and Mittal, 2005), and the transition point would therefore move closer to the aerofoil, but for a cylinder case the transition point does not actually reach the surface of the cylinder until $Re \approx 10^6$ (Singh and Mittal, 2005). For Reynolds numbers of up to 30 000, transition should only occur in the free shear

layers well aft of the aerofoil, and therefore it has been assumed transition will have a negligible impact on the flow in the immediate vicinity of the aerofoil. Further experimental work is needed to prove or disprove the validity of this assumption.

4.2.2 Incompressibility

The assumption that the air around an insect's wings is effectively incompressible is generally considered to be reasonable, and, again, is made in all of the computational and analytical studies made so far. It has long been accepted that compressibility only becomes important if the local Mach number at any point in the flow exceeds a value of around 0.3 (Houghton and Carpenter, 2003). This is invariably the case when considering insect-like flapping, where Mach numbers certainly do not exceed 0.1 (based on the tip speed for the 'optimum' FMAV calculated in §2.1.3). Despite this, ignoring compressibility will introduce some errors — around 2% at $M = 0.3$ (Houghton and Carpenter, 2003).

However, there has been some suggestion that the impact of compressibility also depends on Reynolds number, with very low Reynolds numbers leading to quite high variations in density. Sun and Boyd (2004) state that density variation can be as high as 16% when $Re = 1$. However, this result is likely to be due to the fact that Sun and Boyd were analysing very small-scale flows, with aerofoils of chord length $30\,\mu m$. The assumption that the fluid is a continuum (instead of the collection of molecules which it is in reality) is invalid at these very small scales.

The non-dimensional parameter that is used to assess the validity of the continuum assumption is the *Knudsen number* (Kn). This is defined by

$$Kn = \frac{\lambda}{l}, \tag{4.2}$$

where λ is the mean free path of the molecules and l is a representative length. In order for the flow to act as a continuum, Kn must be less than some critical value, which has been defined by some authors as 0.01 (Duncan et al., 1970) and by others as 0.1 (Schetz and Fuhs, 1999; Bird, 1994) — the reason for the disparity is not clear. It can be shown that Kn is of the same order of magnitude as M/Re,

where M is Mach number. Therefore rarified effects would be expected to become important only when Mach number is equal to around 1% of Reynolds number.

If a Mach number of 0.1 is assumed (which is probably much higher than would occur in reality) the Reynolds number would have to be as low as 10 in order to achieve a Knudsen number of 0.01. In the current case, though, Reynolds number and Mach number are directly related, so that if Re is as low as 10, M will be much lower than 0.1.

Another way of looking at it is to use Equation 4.2 to calculate what L would need to be to produce a Kn of 0.01. λ, the molecular mean free path length, is around $8 \times 10^{-8}\,m$ for sea-level air, so to obtain a Kn of 0.01 or greater, L would have to be $8\,\mu m$ (i.e. $0.008\,mm$) or less, or around 1/25 of the wingspan of the smallest insects. Certainly for an FMAV Kn will be less than 0.01.

In conclusion, it seems reasonable, when considering likely practical FMAVs, to assume that the flow is a continuum and therefore can be assumed to be incompressible.

4.2.3 Other assumptions

It is assumed that the aerofoil or wing is fully rigid. In fact, insect wings are quite flexible and certainly deform quite significantly during flight — see, for example, the photographs of Brackenbury (1995). However, aeroelastic analysis of insect-like flapping is impossible without some knowledge of the forces that apply and the source of those forces.

The other important assumption, which comes about because of the modular approach which has been taken, is that only one wing is studied. It has been noted that interaction between wings does seem to be a method of lift enhancement in many insects. In the current study, though, only a very specific part of insect-like flapping is studied; namely, the translational, constant-angle of attack motion that occurs between pronation and supination. Further development of the CFD models used could in theory shed light on the interaction between wings, but this is beyond the scope of the present study.

4.3 Computational method

This section discusses, firstly, the general method by which CFD operates. It then continues to justify the choice of CFD model used and to discuss the specific method used for the current study.

4.3.1 CFD modelling

4.3.1.1 Governing equations

Using Newton's second law of motion it is possible to state that for a fluid, the rate of change of momentum is equal to the applied force. This applied force is composed of three types of force — firstly, body forces (which act on the body of fluid as a whole, for example gravity, and are often negligible); secondly, pressure forces; and thirdly, viscous forces. Pressure forces can be calculated using Newton's second law of motion. Viscous forces are more complex to calculate but there are constitutive laws that allow this to be done. In using these laws the assumption is made that the fluid is a continuum.

Using these laws, it is possible to derive the Navier-Stokes equations in velocity-pressure form (for derivation, see Houghton and Carpenter, 2003, S 2). Here, body forces are ignored:

$$\rho \frac{D\mathbf{u}}{Dt} = -\nabla p + \mu \nabla^2 \mathbf{u} \tag{4.3}$$

$$\therefore \quad \frac{\partial \mathbf{u}}{\partial t} + \mathbf{u} \cdot \nabla \mathbf{u} = -\nabla p + \frac{1}{Re} \nabla^2 \mathbf{u}. \tag{4.4}$$

Here, $\mathbf{u}$ is the velocity vector, p is pressure, t is time, ρ and μ are the density and dynamic viscosity of the fluid respectively, and Re is Reynolds number. What this equation means is that, for an element of fluid, the rate of change of momentum in the x direction (for example) is equal to the sum of the forces acting on the fluid in the x direction.

Another important equation is the continuity equation, which states that the volume of fluid flowing into an elemental area must be equal the volume of fluid

flowing out of it:

$$\nabla \cdot \mathbf{u} = 0. \tag{4.5}$$

Here it has been assumed that the fluid is incompressible. This is generally accepted as a reasonable assumption provided that the velocity of the flow is low relative to the speed of sound. For insect-like flapping, this is invariably the case. It has been suggested that the assumption of incompressibility is actually unreasonable at very small scales (Sun and Boyd, 2004, see e.g.), and the validity of this assumption is investigated later.

Another equation that is often mentioned in this context is the energy equation, which states that the total energy is conserved. However, this is only required in cases where the flow is compressible and/or where heat transfer is involved. In the cases under consideration here, because of the low speeds involved, the flow is assumed to be incompressible; the same assumptions is made by many others working in this area (see e.g. Liu and Kawachi, 1998; Sun and Tang, 2002).

Having made these two assumptions, the result is a system of four simultaneous equations (the three Navier-Stokes equations and the continuity equation) with four unknowns (u, v, w and p), because ρ and μ have been assumed to be constant. It should be noted that often the whole system of equations (Navier-Stokes, continuity, and energy) are often improperly called the 'complete Navier-Stokes equations', particularly in the context of CFD.

In order to solve the above set of equations, it is necessary to provide an initial condition and boundary conditions. For this formulation of the Navier-Stokes equations, this is relatively simple; and this is a particular attraction of the velocity-pressure formulation. The initial and boundary conditions for the situations under investigation here are discussed in §4.3.3.

However, it should be noted that the above (velocity-pressure) formulation of these equations is only one of four that are commonly used (Rempfer, 2006). A second formulation can derived from the first by taking the divergence of Equation 4.4 and substituting into Equation 4.5. This yields the Poisson equation:

$$\nabla^2 p = -\nabla \cdot (\mathbf{u} \cdot \nabla \mathbf{u}) \,. \tag{4.6}$$

This equation, in conjunction with Equation 4.4, is known as the pressure-Poisson equation (PPE) formulation of the Navier Stokes equation. The advantage of this formulation is that Equation 4.6 is an explicit equation for pressure p. However, Equation 4.5 is a first-order equation, whereas the Poisson equation is second-order. It is therefore necessary to provide an addition boundary condition; the most convenient way to do this would be to specify the pressure at the boundary of the computational domain. Unfortunately this is not always easy and this means that the PPE formulation is generally a less convenient formulation than the velocity-pressure formulation.

The two other generally-used forms of the governing equations are vorticity based, as opposed to the two forms above, which are both velocity-based. The motivation for producing vorticity-based formulations is to remove the pressure term from the equations, and one way to do this is by taking the curl of Equation 4.4 to yield

$$\frac{\partial \omega}{\partial t} + \mathbf{u} \cdot \nabla \omega = \omega \cdot \nabla \mathbf{u} + \frac{1}{Re} \nabla^2 \omega, \tag{4.7}$$

where ω is the vorticity vector ($\omega = \nabla \times \mathbf{u}$). This equation can be used in conjunction with

$$\nabla^2 \mathbf{u} = -\nabla \times \omega, \tag{4.8}$$

which is derived from the definition of ω, to form the vorticity-transport formulation of the governing equations. However, a similar problem occurs as with the PPE formulation above — the order of the system has been increased and so an additional boundary condition is required, preferably in terms of the vorticity at the boundary. Obtaining this condition is often difficult.

The final form of the governing equations is the vorticity-stream function formulation. In this case, the two governing equations are

$$\frac{\partial \omega}{\partial t} + \mathbf{u} \cdot \nabla \omega = \frac{1}{Re} \nabla^2 \omega, \tag{4.9}$$

and

$$\nabla^2 \psi = \omega. \tag{4.10}$$

This formulation is generally used only for 2D flows, as stream function ψ is generally not defined for 3D flows. ω is therefore defined as the only component of vorticity that can appear in a 2D flow. Just as for the vorticity-transport formulation, in order to solve these equation it is helpful to define boundary conditions in terms of vorticity.

It is important to emphasise that all four of these formulations essentially come from the same basic principles. Which formulation is most suited for a given problem will depend on the problem. The current work exclusively uses the velocity-pressure formulation, for reasons which will be discussed later.

4.3.1.2 Boundary conditions

The governing equations presented above 'govern' the flow of fluid, whether over the wing of an aircraft or an insect. The flows in different cases will of course be completely dissimilar. This is due to the *boundary conditions* — those known factors (e.g. the shape of any bodies in the flow) which determine where the fluid flows and in what directions. In the current case, the boundary conditions concern the motion of the aerofoil or wing and its physical dimensions. The latter will determine how the fluid flows around the wing — the fluid cannot be allowed to flow through the wing, and the non-slip condition must apply on the wing's surface. Basically, if the wing is stationary with the fluid moving past it then $u = v = w = 0$ at the surface of the wing.

If the boundary conditions are known, along with the laws that govern fluid flow, this is all the information required to predict exactly which path the fluid will take by solving the above equations. If this were possible, closed-form expressions for u, v, w and p in terms of x, y and z would be obtained, so that the pressure at any location in the flow could be calculated and (for example) by integrating over the wing's surface, the force on the wing could be obtained. Unfortunately, because of the coupled nature of these non-linear partial differential equations, finding a closed-form solution is in general impossible for all but the most simple flows, and certainly there is no known general solution.

4.3.1.3 Discretisation

Expanding Equation 4.3 gives

$$\begin{aligned}
\rho\left(\frac{\partial u}{\partial t}+u\frac{\partial u}{\partial x}+v\frac{\partial u}{\partial y}+w\frac{\partial u}{\partial z}\right) &= \rho g_x-\frac{\partial p}{\partial x}+\mu\left(\frac{\partial^2 u}{\partial x^2}+\frac{\partial^2 u}{\partial y^2}+\frac{\partial^2 u}{\partial z^2}\right),\\
\rho\left(\frac{\partial v}{\partial t}+u\frac{\partial v}{\partial x}+v\frac{\partial v}{\partial y}+w\frac{\partial v}{\partial z}\right) &= \rho g_y-\frac{\partial p}{\partial y}+\mu\left(\frac{\partial^2 v}{\partial x^2}+\frac{\partial^2 v}{\partial y^2}+\frac{\partial^2 v}{\partial z^2}\right),\\
\rho\left(\frac{\partial w}{\partial t}+u\frac{\partial w}{\partial x}+v\frac{\partial w}{\partial y}+w\frac{\partial w}{\partial z}\right) &= \rho g_z-\frac{\partial p}{\partial z}+\mu\left(\frac{\partial^2 w}{\partial x^2}+\frac{\partial^2 w}{\partial y^2}+\frac{\partial^2 w}{\partial z^2}\right).
\end{aligned}$$

From this it can be seen that the governing equations for fluid motion are made up of a number of variables (velocities, pressure, etc) as well as the partial derivatives of those variables. As such they cannot be directly solved by a computer, and must instead be *discretised*. Essentially, this involves replacing the differential terms with numerical approximations.

One approach — the finite difference approach — is based on the Taylor series expansion. For example, for a variable ϕ which varies with respect to t, the Taylor series expansion can be written as

$$\phi(t+\Delta t) = \phi(t)+\Delta t\frac{d\phi}{dt}+\frac{1}{2}(\Delta t)^2\frac{d^2\phi}{dt^2}+\frac{1}{6}(\Delta t)^3\frac{d^3\phi}{dt^3}+\ldots \tag{4.11}$$

$$\phi(t-\Delta t) = \phi(t)-\Delta t\frac{d\phi}{dt}+\frac{1}{2}(\Delta t)^2\frac{d^2\phi}{dt^2}-\frac{1}{6}(\Delta t)^3\frac{d^3\phi}{dt^3}+\ldots, \tag{4.12}$$

where Δt is a small change in t.

Adding these two equations together:

$$\begin{aligned}
\phi(t+\Delta t)+\phi(t-\Delta t) &= 2\phi(t)+(\Delta t)^2\frac{d^2\phi}{dt^2}+O\left((\Delta t)^4\right)\\
(\Delta t)^2\frac{d^2\phi}{dt^2} &= \phi(t+\Delta t)+\phi(t-\Delta t)-2\phi(t)+O\left((\Delta t)^4\right)\\
\frac{d^2\phi}{dt^2} &= \frac{1}{(\Delta t)^2}\left[\phi(t+\Delta t)-2\phi(t)+\phi(t-\Delta t)\right]+O\left((\Delta t)^2\right),
\end{aligned} \tag{4.13}$$

where the nomenclature $O\left((\Delta t)^2\right)$ means terms of the order of $(\Delta t)^2$ or higher do exist but are ignored (since Δt is in practise very small, terms of the order of $(\Delta t)^2$

will be negligible).

Similarly be subtracting Equation 4.12 from Equation 4.11:

$$\begin{aligned}
\phi(t+\Delta t)-\phi(t-\Delta t) &= 2\Delta t\frac{d\phi}{dt}+\frac{1}{3}(\Delta t)^3\frac{d^3\phi}{dt^3}+O\left((\Delta t)^5\right)\\
2\Delta t\frac{d\phi}{dt} &= \phi(t+\Delta t)-\phi(t-\Delta t)-\frac{1}{3}(\Delta t)^3\frac{d^3\phi}{dt^3}+O\left((\Delta t)^5\right)\\
\frac{d\phi}{dt} &= \frac{1}{2\Delta t}\left(\phi(t+\Delta t)-\phi(t-\Delta t)\right)+O\left((\Delta t)^2\right). \qquad (4.14)
\end{aligned}$$

The result is expressions for the first and second derivatives of ϕ with respect to t in terms of the values of ϕ now, a short time ago, and a short time in the future. Both of these equations are approximations, as terms of order $(\Delta t)^2$ and above are ignored, but providing Δt is small the error introduced will be minor. Equations 4.13 and 4.14 are classified as central-difference, 2nd-order equations — central-difference because the equation involves the value of $\phi(t+\Delta t)$ as well as $\phi(t-\Delta t)$ and 2nd-order because terms of order $(\Delta t)^2$ and above are neglected. Often, a CFD solver allows the user to specify the order of the discretisation equations — higher-order equations require greater computational power or more run-time but may produce more accurate results. Higher-order equations may also be more unstable (i.e. may not converge so readily); as a result, it is common to start a simulation using first-order approximations and then switch to second-order once a degree of convergence has been achieved. However, in the current work, second-order schemes were consistently used (as mentioned in Appendix B) and no problems with divergence were encountered.

The above process can be carried out for the rate of change of each quantity with respect to space and, for unsteady simulations, time, and the approximations which are produced can be used to convert the governing partial differential equations into numerical approximations. These approximations will vary according to the point at which the process is carried out — so that a set of equations will be formed for each point within the computational domain. The partial differential equations that were valid for the entire domain (the governing equations) have been converted into a number of equations that give the relationships between the variables at certain points within the domain (Shaw, 1992). It can be seen that the

value of a variable at a point p within the domain will be calculated by referring to the values of that variable at the points adjacent to p. It is essential, therefore, to have a *grid* — a network of points within the domain — to allow this process to be carried out. Producing grids (or *meshing*) can be one of the most time-consuming parts of running a CFD simulation. The meshing process for the current work is described later in this chapter.

The discretisation of the Navier-Stokes equations is in two domains; both in space, and in time. The issue of convergence of these discretised solutions is an important one and must be considered for both domains. Convergence in the space domain is usually investigated by carrying out mesh-sensitivity tests; these are described in §4.3.4 below. In the time domain, it is necessary to investigate the sensitivity of the results to changes in the time step used during simulations. For the cases investigated here, the time step was chosen to ensure acceptably-quick convergence at each time step; further details are given in Appendix B. Due to the low Reynolds numbers of the flows considered here, the simulations were insensitive to changes in time step, providing the magnitude of the step was kept small — the values used ranged from $0.0001s$ for the highest Reynolds number 2D cases to around $0.04s$ for the lowest Reynolds number 3D cases.

The CFD software used here (*Fluent 6*) is based on a finite volume method. This technique is similar to the finite difference approach demonstrated above but also incorporates aspects of the finite element method (which is well-known in relation to stress analysis). The approach involves applying the integral form of the conservation equations to each cell in the mesh to ensure that the net volume flow into each cell is zero; in other words, mass is automatically conserved (as the fluid is assumed incompressible).

4.3.1.4 Solving the discrete governing equations

It has been seen that it is possible to approximate partial differential equations by discrete numerical equations. The next step of the CFD process is to solve these discrete equations to produce values for the dependent variables at points within the domain. There are two fundamental ways of doing this — *segregated* and

coupled[1]. Both processes are iterative, and both require a set of 'initial conditions' to be supplied, so that the solver has a 'starting point'. For a transient problem like ours, these initial conditions will usually be set to assume a uniform flow — in other words, flow as though the aerofoil or wing were no present. The simulation will then progress as though the aerofoil or wing has suddenly been placed in the flow. In other words, it is as if the aerofoil or wing has been impulsively started.

The coupled approach was originally designed for high-speed compressible flows and involves solving the momentum and continuity equations simultaneously (i.e. coupled together) (Fluent Inc., 1998). This process requires more much more memory than the segregated approach (Pascua et al., 1996), and for the types of flow of interest here (i.e. low-speed incompressible flows) is unlikely to provide any performance benefit. A segregated approach has therefore been used throughout this work, despite the performance benefit that can be achieved using a coupled approach. A quick comparison of the two approaches has indicated that this benefit is negligible in any case, probably due to the comparatively small meshes used.

A segregated approach takes the linearised continuity and momentum equations and solves them sequentially. The pressure field is used to calculate an updated velocity field, and the momentum equation is used to correct this velocity field. An updated pressure field is then produced, and the process is repeated until convergence is achieved (i.e. until the solution stabilises and does not change significantly with each iteration). The exact procedure for solving the system of equations, using a Gauss-Seidel method, is covered in Shaw (1992); Patankar (1980); Fluent Inc. (1998).

In summary, CFD works by taking the governing equations of fluid flow (the Navier-Stokes equations and the continuity equation), discretising them, and then solving them iteratively based on the known boundary conditions. Further details of this process and of the software used can be found in Shaw (1992); Patankar (1980); Fluent Inc. (1998). The next section examines the justification for the choice of the specific model used. After this follows a more specific description of

[1]In later versions of the Fluent CFD software used in the current work, these were renamed *pressure-based* and *density-based* — see Appendix B

how the CFD results presented in this thesis were produced. Further details of the CFD model are contained in Appendix B.

4.3.2 Justification for the choice of CFD model used

RANS CFD models of the type used here have been historically shown to be applicable to a wide range of flows. However, in vortex-dominated flows like those under consideration in the current work, such models can suffer from excess numerical dissipation of vorticity due to the primitive variable (velocity-pressure) form of the Navier-Stokes equations used (Brown and Line, 2005). There are three main reasons why this is thought unlikely to be a problem in the current work. Firstly, the Reynolds numbers under consideration are very low in absolute terms. Therefore, viscosity is likely to be comparatively dominant and the amount of numerical dissipation is therefore likely to be low when compared to the amount of 'natural' dissipation due to viscosity.

Secondly, for the majority of the work in this thesis, the aerofoil or wing does not pass through its own wake. As the wake moves away from the aerofoil or wing, the vortices within it will become more dissipated, particularly as the mesh is coarsened far from the aerofoil or wing; but this is unlikely to have a noticeable impact on the phenomenology of the flow close to the aerofoil or wing. It is the phenomenology of the flow close to the aerofoil or wing which is of most interest. Some cases do involve the wing passing through its own wake (see §6.9) and this issue is discussed in more detail there.

Thirdly, the amount of dissipation will increase as time progresses, so that if the simulations are short in duration, the resulting errors will be small. For most of the results presented here, the simulations were run for only a few chord lengths of travel (for 2D cases) or less than a single revolution (for 3D sweeping cases). Therefore the amount of numerical dissipation will be small. This conclusion is supported by the validation work that has been carried out.

The final reason for the use of a velocity-pressure formulation lies in the ease of application of relevant boundary conditions, as discussed in §4.3.1.1 above. The boundary conditions used are discussed below.

In addition to the above reasoning, it is of value to investigate the type of RANS CFD models used here in order to ascertain whether this type of approach can reasonably be used to model the types of flow under consideration. The results of the validation work described in §5.1 and §6.1 go some way towards confirming that RANS CFD codes can be usefully applied to flows of this type.

4.3.3 Boundary conditions

This section summarises the boundary conditions used in the CFD model (full details are contained in Appendix B). Aerofoils and wings were set as walls, with the no-slip condition enforced on the surfaces. The boundaries of the computational domains were set as velocity inlets. For 2D cases the velocity of the aerofoil was imposed at these boundaries. For 3D cases the velocity at all the boundaries (including the boundaries in the positive and negative z directions) was set to zero and the motion of the wing was imposed using a rotating reference frame.

It is important to consider the impact of the wake of the aerofoil crossing the boundary of the computational domain. This will introduce an error into the simulation, as the velocities at the boundaries are assumed constant. However, provided the boundaries are sufficiently far from the aerofoil or wing, the effect of this error on the flow near the aerofoil or wing will be small. Later, the effect of changing this distance is investigated in order to ascertain the minimum distance at which increasing the distance further has negligible impact on the forces on the aerofoil.

4.3.4 Meshing

As already mentioned, the process of discretisation involves dividing the domain of interest into a finite number of cells. For each of these cells only one value of the dependent variables will be stored — in other words, the pressure and velocity components are assumed constant throughout a cell. In reality, of course, this will not be the case; so a CFD model cannot be expected to produce exact results. But the errors can be reduced by intelligent placing of the cells, so that in areas

where the dependent variables might be expected to change rapidly the cells are very small. Conversely, in areas where the flow can be expected to be uniform, the mesh can be coarsened without this having too dramatic an effect on the accuracy of the results. The size of mesh cells should also be dependant on the local Reynolds number; the usual parameter used to assess this is cell Reynolds number, which is Reynolds number based on local velocity and cell size.

For many CFD problems, the overall cost of the analysis can be dominated by the cost of mesh generation (Shaw, 1992). Here, the domain is fairly simple — meshing the domain around a flat plate is evidently much simpler than meshing the domain around an aircraft or car. However it is still important to think about where the *critical areas* are; the areas where the gradients of the variables might be highest and therefore where the mesh needs to be most dense. The only object in the flow is the aerofoil or wing, and the main focus of interest is the flow close to it. Therefore as a general rule the mesh should be most dense near the aerofoil and can be more coarse at a distance from it. More specifically, the flow will be most dramatically affected near the leading and trailing edges of the wing or aerofoil, so mesh cells should be finest there.

Usually in a CFD analysis, mesh cells are concentrated near surfaces to capture the boundary layers. Here, though, the vortical structures that occur outside the boundary layer are of more interest than the boundary layer itself, so capturing the boundary layer accurately is not so important as in, for example, the case of flow over a conventional aircraft. However, the area of the domain near the surface of the wing does need to be highly resolved in order to capture the separation points. At high angles of attack the separation points will be constrained to the leading and trailing edges of the aerofoil. Mesh density therefore needs to be highest in these areas.

Another point to bear in mind is that for much of the analysis that follows, it is the region of the wake close to the aerofoil which is of interest, so that it is not necessary to resolve the wake with great accuracy far downstream. Some analysis does involve a returning wake (i.e. the wake that leaves the computational domain downstream of the aerofoil is re-introduced on the upstream boundary) and here

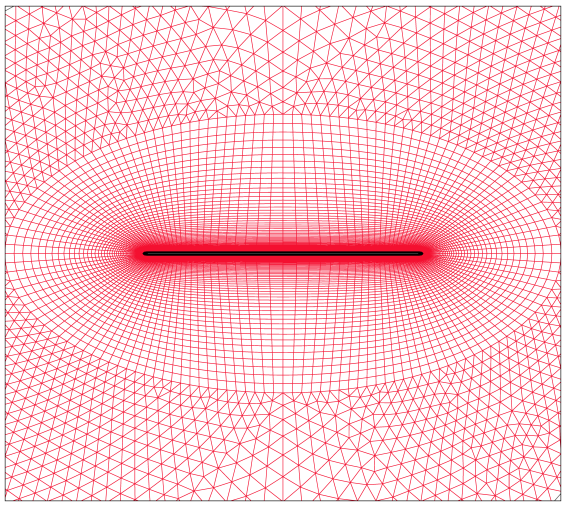

Figure 4.1: Grid for aerofoil of finite thickness. This is a fairly coarse grid that was used during the mesh sensitivity analysis — grids used to obtain the final results were much more refined, particularly close to the aerofoil. The transition point between the O-grid and the unstructured triangular grid is evident.

care must be taken not to coarsen the mesh far from the aerofoil to the extent that the wake is not captured in sufficient detail — this is discussed in §6.9.1.

However, bearing all the above in mind, it appears that mesh production should not be dominant in this analysis; the shapes involved are simple, the flow is not too unpredictable, and in most cases only the area close to the wing is of interest. All meshing was carried out using the commercial grid-generating software *Gambit 2*.

4.3.4.1 2D meshes

Full details of the meshes used are contained in Appendix B. For 2D cases, four different sections have been used. These are: a flat plate of zero thickness; a full ellipse of thickness to chord ratio 1%; a flat plate with elliptical leading and trailing edges (each edge being one half of an ellipse with length:thickness ratio 4:1); and a flat plate with semicircular leading and trailing edges. Both of these latter shapes were defined to have the same cross-sectional area as the ellipse. A number of other ellipses were also studied in order to assess the effect of aerofoil thickness. The mesh for these takes the same basic form as the mesh for the 1% thick ellipse.

For aerofoils of finite thickness, an O-grid was used close to the aerofoil surface,

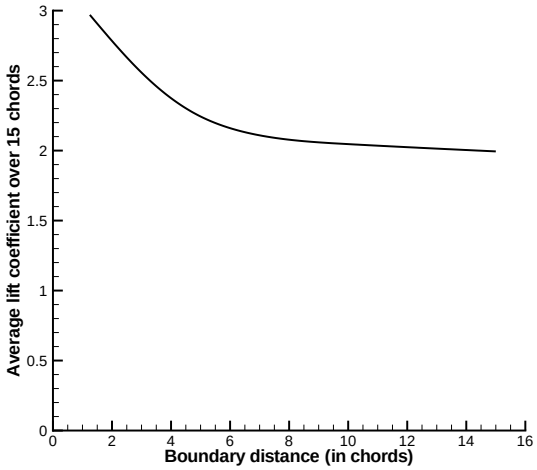

Figure 4.2: Boundary distance sensitivity results. The lift coefficient on an aerofoil at 45° fluctuates widely, as is shown later. This figure compares the average lift coefficient over 15 chords of travel for different boundary distances.

with an unstructured triangular grid in the far field. An example of this type of grid is shown in Figure 4.1. For the central O-grid portion, there are a number of parameters to be selected — the number of nodes around the aerofoil itself, their distribution, and the first cell thickness and growth ratio. It would be unreasonably time-consuming to attempt to find the optimum parameter for each of these individually, so a compromise mesh sensitivity analysis was used. The number of nodes placed around the aerofoil's surface was chosen as the primary measure of mesh density, and the other parameters were either scaled in proportion with this or kept constant.

Boundary distance The computational domain must have edges. At these outer boundaries, it is assumed that the flow is unaffected by the presence of the aerofoil or wing, so that the velocities at the boundaries are equal to the freestream velocities. In theory, it is the case that the aerofoil will have an impact on the flow at any distance from it — so that introducing fictitious 'boundaries' in this way will introduce an error. As a result, it is important that care is taken as to the location of these boundaries to ensure that the error introduced is small.

In subsonic flows such as those under consideration here, disturbances due to the presence of a body in the flow can be far reaching in all directions (Anderson,

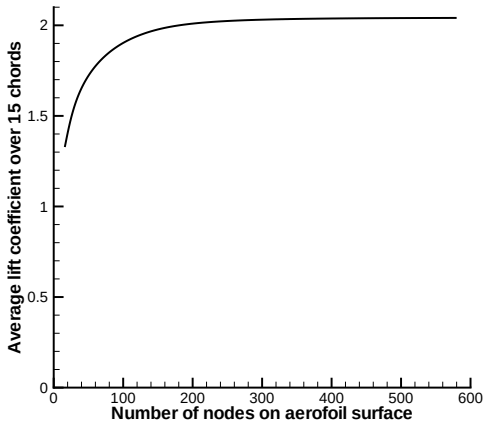

Figure 4.3: Mesh sensitivity results. Again, the figure compares the average lift coefficient over 15 chords of travel, but in this case for different grid densities.

1995). In order to assess the sensitivity of the present model to the position of the outer boundaries, simulations were run with the boundaries set at different distances from the aerofoil; the results are shown in Figure 4.2. It is clear that the solution becomes almost boundary-distance independent once the boundary is around 8 chords away; increases beyond this do not lead to large changes in the average lift coefficient, nor (as inspection of the resulting data confirms) in the phenomenology of the flow. In the 2D model, a boundary distance of 10 chords in all directions has been used.

Mesh sensitivity The aerofoil section used for the mesh sensitivity analysis described here was the flat plate with elliptical ends. The baseline case had 290 cells placed on the aerofoil's surface; full details are in Appendix B. The thickness of the first layer of cells was kept constant and the growth factor as cells moved away from the aerofoil was varied such that the number of layers within the O-grid varied with the same scale factor as the number of nodes around the aerofoil. So, for example, the baseline case of 290 nodes had around 75 layers in the O-grid portion of the grid, and the most refined grid (with 580 nodes around the aerofoil) had double this. The results of the mesh sensitivity analysis are shown in Figure 4.3, and it can be seen that the average lift stabilises when the number of nodes on

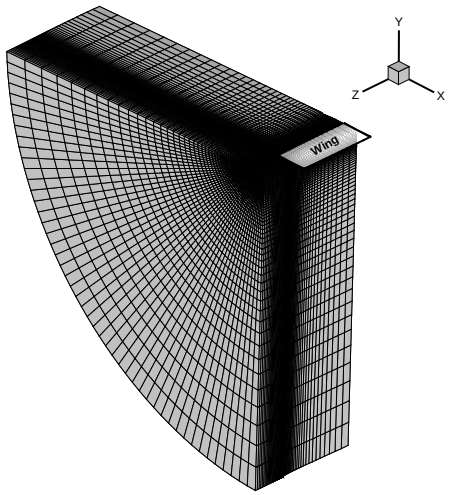

Figure 4.4: Example 3D mesh. One quarter of the mesh is shown: the complete domain is a cylinder.

the aerofoil surfaces reaches around 200. Examination of the lift/time history and the resulting flow-visualisation data confirms that the differences between the 290- and the 580-node cases are negligible.

4.3.4.2 3D meshes

As will be discussed later, for 3D cases, the most simple wing planform and section possible has been used — a rectangular, infinitely-thin, flat wing. It might be objected that this shape is rather unlike those seen on real insects. However, this is quite intentional. As has already been emphasised, the primary aim of the current study is to gain insight into the phenomena that occur during insect-like flapping, and the phenomenon that seems to be of greatest importance is the leading-edge vortex. Using a rectangular wing should isolate any effects that might occur due to the relatively complex shapes of insect wings. In any case, the shapes of insects' wings vary widely (see e.g Ellington, 1984b). It is important to avoid limiting the study to one or two particular wings shapes and thereby obtaining information about the flow around the wings of a particular species of insect, rather than gaining broader and more generally-applicable insights into the types of flows that occur.

When defining 3D meshes it would be sensible to use as much information

as possible from the investigation of the 2D meshes, for example regarding mesh sensitivity and boundary distances. With this in mind, 3D meshes have simply used extrusions of a 2D mesh. So, to create 3D wings, a 2D mesh for an infinitely thin section is 'stretched' in the direction out of the plane of the 2D mesh. In doing this, it has been assumed that the boundary distance sensitivity tests carried out above for the 2D case will also apply to the 3D case. Having determined that a boundary distance of 10 chords was sufficient in the 2D case, the same distance has been used when drawing 3D meshes — at least in the X and Y directions (X and Y being the two axes which lie in the plane of 2D meshes). In the Z direction, further tests have been carried out to determine, firstly, the number of cells that should lie along the wing from root to tip (this defines the total number of cells which make up the mesh), and secondly the distance between the tip of the wing and the boundary of maximum Z coordinate.

The root of the wing is actually at the boundary of the computational domain. There are two reasons for this. Firstly, it removes the complication of a returning wake — if the domain extended inboard of the root, the wing would to some extent interact with its own wake. This is a complication that it was important to remove, though the issue of wing-wake interaction is discussed later. In addition, because inboard sections are moving very slowly (due to the sweeping motion of the wing) the proximity of the inboard boundary to the root of the wing has only a small impact on the overall lift produced by the wing. The results of the validation process (see §6.1) support this view.

3D Mesh sensitivity Because of the extruded-2D nature of the mesh, the mesh took the form of a number of 'slices' in the Z direction, as in Figure 4.4. The slices near the tip were defined to be thinner (in the Z direction) than those nearer the root (so that the mesh density was highest near the tip) in order to capture the tip vortex with high resolution.

In order to assess how many of these slices were needed, simulations were run for different numbers of slices, and the results are shown in Figure 4.5(a). The simulation becomes grid-independent once the total number of cells exceeds around

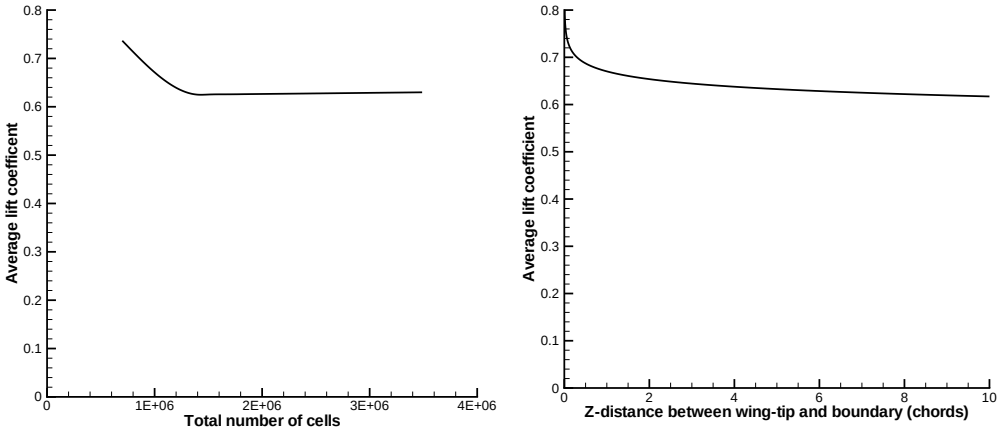

(a) (b)

Figure 4.5: Mesh sensitivity results. The figure compares the average lift coefficient over the first 270°of sweep for different grid densities (Figure 4.5(a)) and different z-distances between the wingtip and the mesh boundary (Figure 4.5(b)).

1.5×10^6; this corresponds to around 40 slices in the z direction. Examination of the resulting data revealed that the phenomena involved did not change when the mesh density was increased beyond this point, and again, it is phenomena that are of most interest in rather than supremely accurate force predictions.

z-boundary distance As mentioned above, the boundaries in the x and y directions were placed 10 chords away from the aerofoil, as for the 2D cases. However, because of the nature of the flow, it was thought that to place the z-boundary 10 chords away from the wing tip would lead to a great number of 'wasted' cells — that is, cells whose removal would not affect the simulation apart from to decrease the run time.

In fact, as Figure 4.5(b) shows, the results of the simulation were relatively insensitive to changes in this parameter once the distance between the wing tip and the boundary exceeded around 1 chord. Further increases in this distance did lead to a small further decrease in the force predictions (the graph gives an average lift coefficient of 0.68 for the 1-chord distance case and a corresponding figure of 0.64 for the 10-chord case). However, examination of the resulting data showed no change in the flow phenomena, and increasing the z-boundary distance even to two chords led to an increase in simulation run time of around 20%. Since the run

time was already measurable in weeks rather than hours, this was an unacceptable time penalty for such a small accuracy increase.

The fact that increasing z-boundary distance tended to decrease average lift coefficient is interesting in itself and gives some indication that the role of the tip vortex is to decrease lift. This will be confirmed in §6.4.6.

4.4 Force calculations

Much of the following work involved comparing forces on aerofoils and wings in different cases. Lift is defined as the force normal to the freestream, and drag as the force parallel to it. For 2D cases, lift and drag are both non-dimensionalised with respect to chord length and freestream flow velocity to produce lift and drag coefficients. In 3D cases, lift is non-dimensionalised with respect to wing area and wing tip velocity, and instead of drag, torque is examined, which is defined as the moment about the axis about which the wing is sweeping. Torque is non-dimensionalised with respect to wing area, wing tip velocity and wing mean aerodynamic chord.

Forces are calculated from the CFD data by integrating pressure and viscous forces for each mesh face on the aerofoil or wing surface and summing these forces. Thus it is possible to calculate the pressure force, the viscous force, and (by summing these) the total force.

4.5 Experimental work

The main aims of the experimental work involved in this project were to validate the results of 2D simulations; to verify the existence of spanwise flow within the 3D LEV; and to investigate the lift produced by a 3D wing over a range of Reynolds numbers, in order to gain evidence about the susceptibility of the LEV to changes in Reynolds number.

4.5.1 Flow visualisation

After experimenting with various methods of flow visualisation (including releasing dye from holes in the wing or aerofoil, using tufts attached to the wing to indicate local flow direction, and blowing compressed air from holes in the wing or aerofoil) the most useful method was found to be the hydrogen bubble technique. First used in the 1950s for visualising boundary layers (Geller, 1955), it has since been used in a variety of flows, such that it is now "one of the most ... successful methods for flow visualization in water" (Johnson, 1998, p. 38.37). It relies on the fact that if a current is passed between two electrodes in water, hydrogen bubbles are given off at the cathode and oxygen bubbles at the anode. Because the hydrogen bubbles are smaller and more numerous than the oxygen bubbles, the hydrogen bubbles are used to visualise the flow (Merzkirch, 1987).

The size of the bubbles depends on a number of factors; most importantly, the diameter of the wire used for the cathode. The applied voltage also has an impact on the size and quantity of the bubbles. In this work, stainless steel wire of $0.05mm$ diameter was found to produce bubbles that were large enough to be visible but small enough to have a sufficiently low buoyancy. Experiments with tungsten wire of $0.01mm$ diameter were unsuccessful — the resulting bubbles were too small to be clearly seen.

The applied voltage was $15V$ for most experiments. Reducing the voltage tended to decrease the size of the resulting bubbles, and was necessary during some of the low Reynolds number 3D experiments, as larger bubbles tended to rise too quickly and distort the apparent structure of the flow.

4.5.2 2D experiments

The main aim of the 2D experiments was to validate the predictions of the CFD model regarding the shedding of vortices. A wing was translated through a tank of water, with hydrogen bubbles being released at the leading edge in order to capture the structure of the LEV. The experimental setup is shown in Figure 4.6, and in diagrammatic form in Figure 4.7.

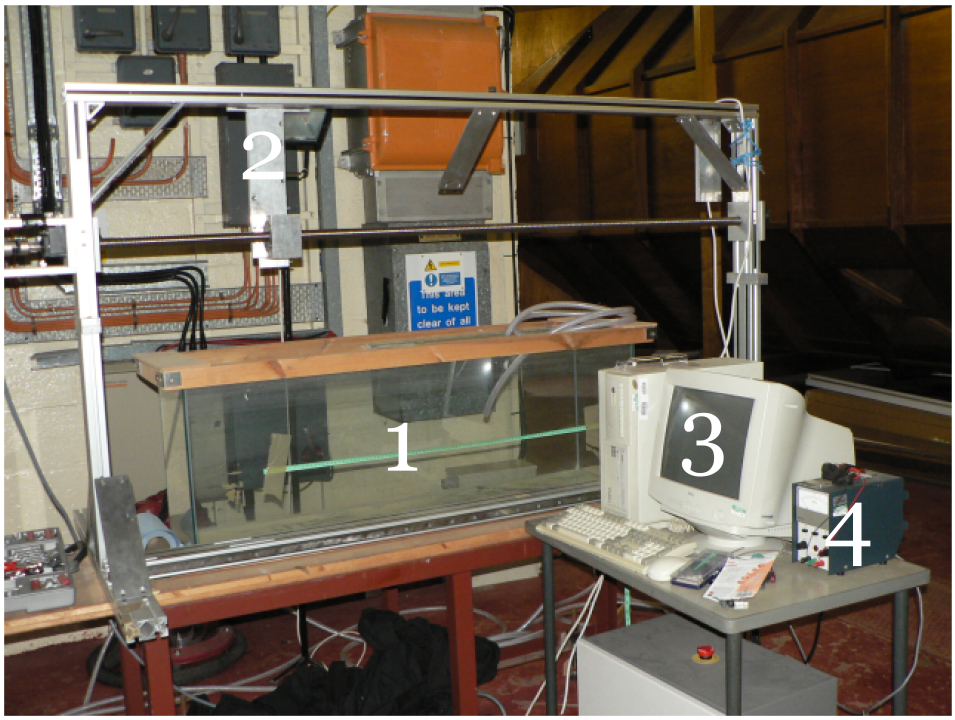

Figure 4.6: Setup for 2D experiments.

The glass tank is labelled **1** in Figure 4.6. Its dimensions were $1200mm(L) \times 300mm(W) \times 460mm(H)$. The wing used was a stainless steel flat plate of span $300mm$ (so that it spanned the entire width of the tank) and chord of $50mm$. The plate used was $2mm$ thick, giving a thickness/chord ratio of 4%.

The wing was driven by a traverse mechanism, labelled **2** in Figure 4.6. The traverse was controlled by the computer labelled **3** using in-house software (developed by Dr. M. V. Finnis). The maximum speed of the traverse was $600mm/s$ (though this was not measured) and the desired acceleration was set at the maximum allowable: $100\,000mm/s^2$. Although the actual acceleration rate is not known, the start of motion was rapid enough to be considered 'impulsive', so as to match the CFD results. The Reynolds number was varied by changing velocity; the maximum chord Reynolds number was therefore approximately 30 000.

Flow visualisation used the hydrogen bubble technique, described above. The power supply for the bubble system is labelled **4** in Figure 4.6. It supplied $15V$ across the anode and cathode. The anode was a piece of aluminium plate which was suspended in the tank. For the cathode, thin tape was attached to the leading

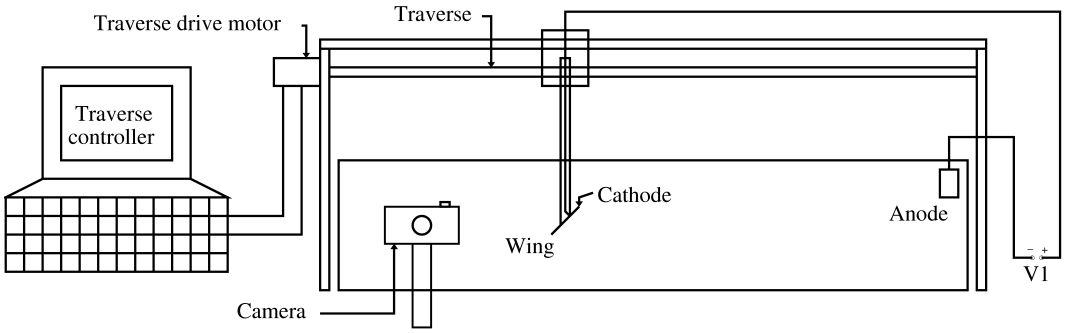

Figure 4.7: Diagram of setup for 2D experiments.

edge of the wing and $0.05mm$ stainless steel wire was taped on top of this (this was necessary to isolate the wing from the cathode). It is well known that increases in surface roughness (or the attachment of a wire or other protuberance to a surface) can trip the boundary layer (that is, cause it to transition to turbulent flow) but this should only occur at Reynolds numbers much higher than were used here. In addition, the wire was mounted on the leading edge of the wing; as this surface was only 2mm long, it is highly unlikely that attaching a wire to the leading edge will have much of an impact on the attached boundary layer.

Flow visualisation images were captured using a Panasonic DMC-FZ5 digital camera. Results are shown in Figure 5.5 on p. 135.

4.5.3 3D experiments

The 3D experiments had three purposes. Firstly, to establish the existence of a stable LEV; secondly, to establish the existence of spanwise flow within this LEV; and thirdly, to capture force measurements to compare to the 3D CFD results.

The experimental setup is shown in Figure 4.8, with a schematic in Figure 4.9. The glass tank, (**1** in Figure 4.8) had dimensions of $600mm(L) \times 600mm(W) \times 600mm(H)$. A pair of wings were mounted on a driveshaft in the centre of the tank and the dimensions of the wings were chosen to match those used in the CFD model. Wings were constructed from $2mm$ thick transparent styrene acrylonitrile (SAN), cut to shape using in-house machining facilities.

The driveshaft was driven by a motor/gearbox combination (Bosch part no.

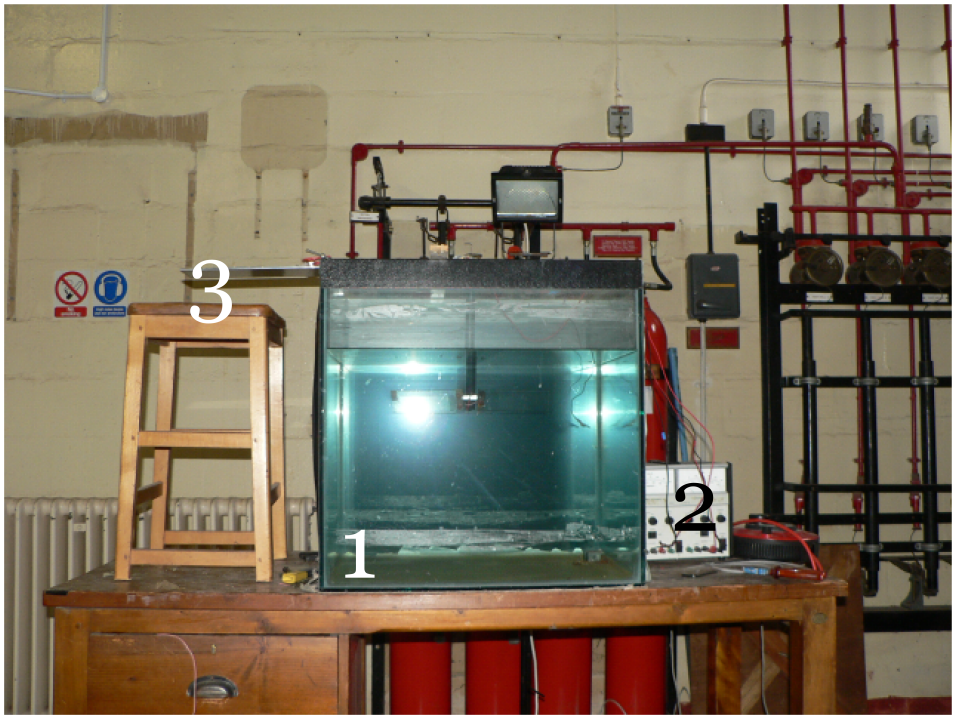

Figure 4.8: Setup for 3D experiments.

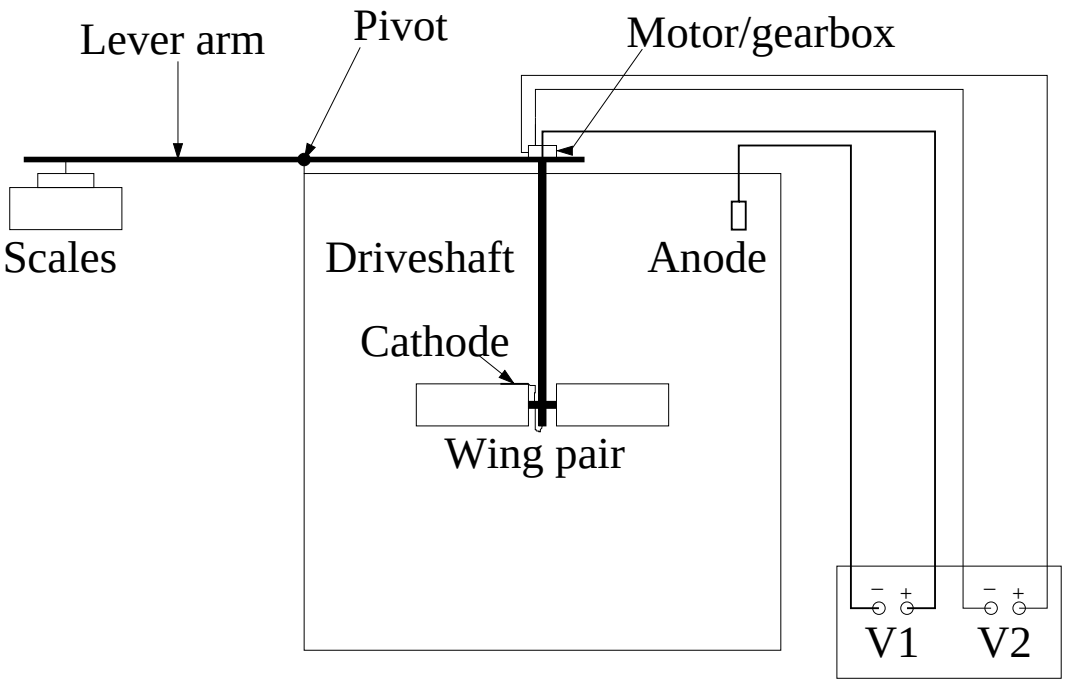

Figure 4.9: Diagram of setup for 3D experiments.

0 132 801 346), capable of an output speed of up to around $1.6 rad/s$. This translates to a maximum 3D Reynolds number (based on tip velocity and mean chord) of around 17 000. The minimum output speed at which the speed remained smooth was around $0.3 rad/s$, equating to a 3D Reynolds number of around 3 000. The rotational speed of the driveshaft was measured using a Metravi DT2236B contact tachometer, accurate to $0.01 rad/s$ — around 3% at the lowest speeds used. This results in an error in Reynolds number of ± 50.

The motor and flow visualisation system were supplied by a variable dual DC power supply (**2** in Figure 4.8). The minimum supply voltage for smooth operation was $6V$; for maximum speed, the supply voltage was $30V$. The flow visualisation system was the same as for the 2D experiments described above, with the cathode taped to the leading edge of one of the wings.

In order to capture force measurements, the motor/gearbox was mounted on one end of lever arm, consisting of an aluminium plate. The other end of this lever arm can be seen projecting from the side of the tank (**3** in Figure 4.8) and was located on a set of Mettler PL200 digital scales. The arm was pivoted in the middle so that an upward force provided by the wings produced a downward force on the scales. A similar system was used by Usherwood and Ellington (2002a), although they used strain gauges in place of scales. The use of scales rather then strain gauges meant that it was not possible to produce a force/time history, but as is shown later this is unimportant because the lift produced by a 3D wing eventually stabilises (see §6.1.1). The minimum reading was $0.9g$, and the scales were accurate to $\pm 0.001g$ — around 0.1% of the lowest reading.

Part II

Results, Discussion, & Conclusions

Chapter 5

2D Results

"Essentially, all models are wrong, but some are useful."

— George E. P. Box

As already mentioned, in this thesis results from the current model are divided into two sections; firstly, in this chapter, those relating to 2D flows (aerofoils, or chordwise elements of wings) and secondly (in §6) those relating to 3D flows (entire wings). In this 2D results section results are presented to show the validation process that was applied to the CFD model. The effects on 2D flows of Reynolds number, angle of attack, aerofoil shape and thickness, and aerofoil acceleration, are examined. The issue of Strouhal number is also discussed.

5.1 Comparison with existing data

CFD is an extremely powerful tool, and can produce vast quantities of data. In order to assess whether these data are reliable — in other words, whether what the model *predicts* will happen correlates with what *actually* happens 'in real life' — it is necessary to compare results from the model with physical experiments. This is somewhat difficult in this particular field; as has already been mentioned, there are very few experimental data extant at the very low Reynolds numbers which are modelled here. Interest in Reynolds numbers of the order of 100 has grown recently, due to the fact that *aerodynamicists* have begun to study insect

flight with a view to designing FMAVs. Of course, *zoologists* have always been interested in insects, but traditionally have been more interested in the physical characteristics of insects rather than their aerodynamics.

The main source of validation data is the experiments of Dickinson and Götz (1993). Firstly, the present CFD results are compared with their experimental results. They produced both force measurements and flow visualisation data, but the latter are of poor quality and so new experiments have been carried out to produce better flow visualisation data. The present CFD results are compared with the experimental results second.

Thirdly, the computational results of Sun and Boyd (2003) are used. Their computation model is entirely different to the RANS code used here, so the comparison may prove useful. However it must be borne in mind that, firstly, their model has not been validated itself (and therefore agreement with it is not *in itself* proof of accuracy) and secondly their model is designed for tiny aerofoils of chord length 30 microns. The continuum assumption used here is not valid at these small scales, so some differences between current results and theirs should be expected.

Finally, results from the current model are compared to those from the model of Ansari (2004), as this model has been shown to be accurate when compared to 3D experimental results.

5.1.1 Comparison with the results of Dickinson and Götz (1993)

As mentioned in §2.3, Dickinson and Götz (1993) concentrated on increasing understanding of the flow around a flat plate at high angles of attack at Reynolds numbers of $O(100)$. Mounting a thin wing on a traverse and moving it through a fluid, they captured flow visualisation of the resulting vortical structures and measured the forces produced by the aerofoil. Their experiments were intended to be two-dimensional — baffles were placed at both ends of the wing in an attempt to prevent spanwise flow. However, adding baffles is unlikely to create a fully-2D flow and their results must be examined with this in mind. The wing used was a

(a) After 1 chord travelled

(b) After 2 chords travelled

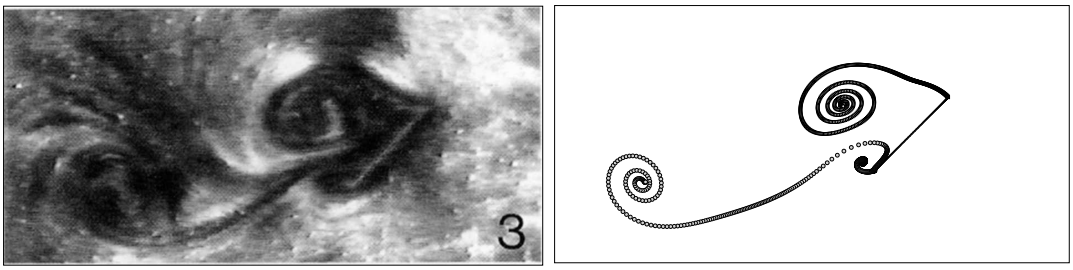

(c) After 3 chords travelled

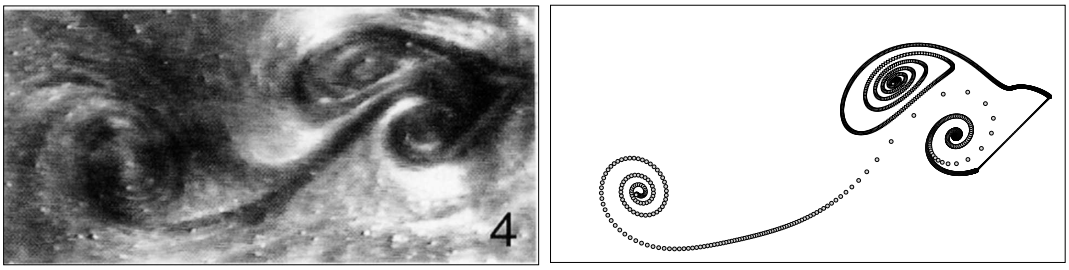

(d) After 4 chords travelled

Figure 5.1: Comparison of flow visualisation from Dickinson and Götz (1993) (left) with that from the present model (right) for uniformly-accelerated flat plate. For the CFD case, the vortical structures are visualised by particles released from the leading and trailing edges and moving with the flow. For the experimental case, the aerofoil was moving through a mixture of sucrose solution and fine aluminium shavings, which was illuminated by a light sheet to allow flow visualisation. Angle of attack is 45° and $Re = 192$ (based on final velocity and aerofoil chord).

thin flat plate and it was accelerated over the first 0.5 chords of travel at a rate of $0.625 m/s^2$. Reynolds number, based on chord and final velocity, was 192 for the results presented here.

The flow visualisation results of Dickinson and Götz are compared to those from the present CFD model in Figure 5.1. The experimental results are somewhat unclear, as mentioned above, but it can be seen that the basic structure of the flow is very similar for both cases. The comparison at four chords of travel is particularly encouraging, with the 'squashed' shape of the leading-edge vortex being clearly visible in both images. The shape of the trailing edge vortex sheet is also very similar for both cases.

Dickinson and Götz also measured the lift and drag produced by their aerofoil over a range of angles of attack. Figure 5.2 compares the lift and drag predictions from the current CFD model with some of these measurement. For all cases, there is a discrepancy in the initial 'peak'. The starting kinematics (i.e. the rate of initial acceleration) in both cases were carefully matched, so there must be some other cause for this difference. It is suggested here that the difference is due to the inertia of the components used in the experiments. Forces were measured, in the experimental case, using strain gauges. This type of system predicts the forces on the wing using the minute displacements due to those forces, and so it is apparent that, if the wing possessed significant inertia, there would have been some limitation in measuring instantaneous force changes. Conversely, in the CFD case, forces are predicted by integrating pressure and skin-friction forces around the aerofoil, so that any change in force is immediately detected. It should be noted that this inertia-caused discrepancy will only occur when the forces on the aerofoil change rapidly; and forces do change extremely rapidly when a body is accelerated. It is suggested here that this effect is responsible for the differences in initial peaks.

It is important to realise that this effect is different to the 'inertial forces' that are mentioned by Dickinson and Götz which they state they have accounted for. In that case, the emphasis is on the inertia of the force transducer and sting, which can be accounted for by subtracting the forces produced when the wing is *not*

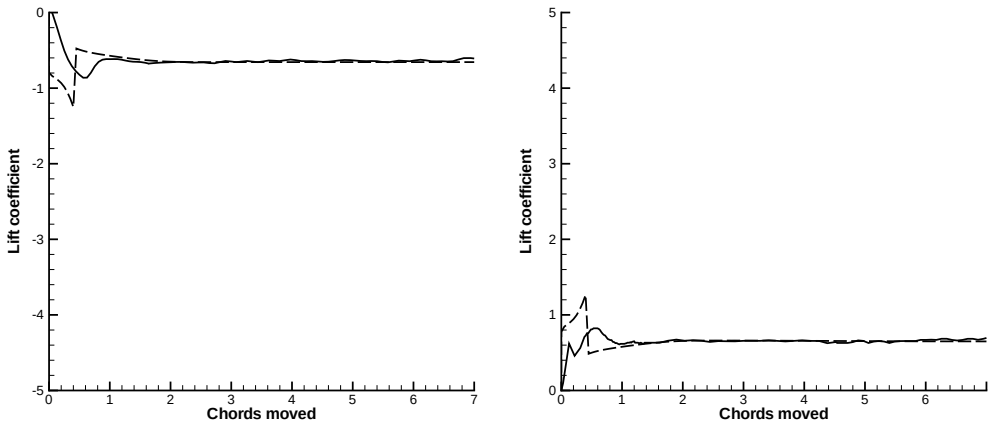

(a) $-9°$ (b) $9°$

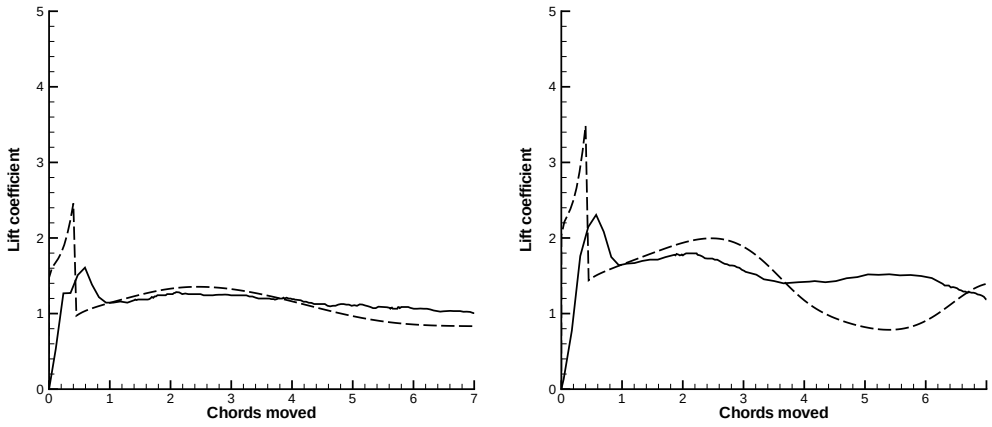

(c) $18°$ (d) $27°$

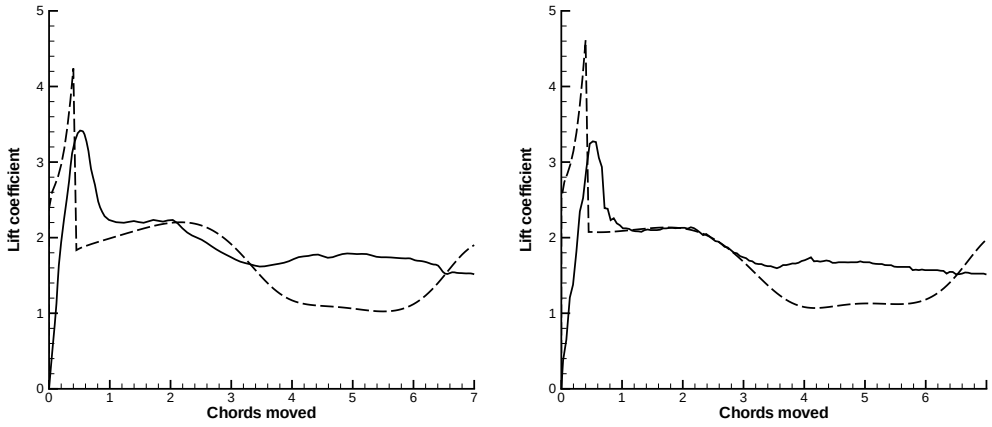

(e) $36°$ (f) $45°$

Figure 5.2: Comparison of CFD lift predictions (dashed lines) with measurements from Dickinson and Götz (1993) (solid lines) for a uniformly-accelerated flat-plate aerofoil at various angles of attack.

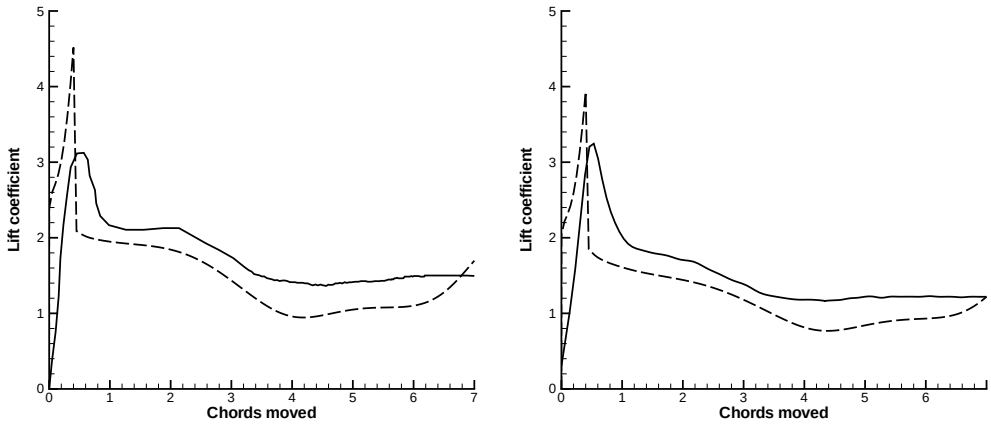

(g) 54° (h) 63°

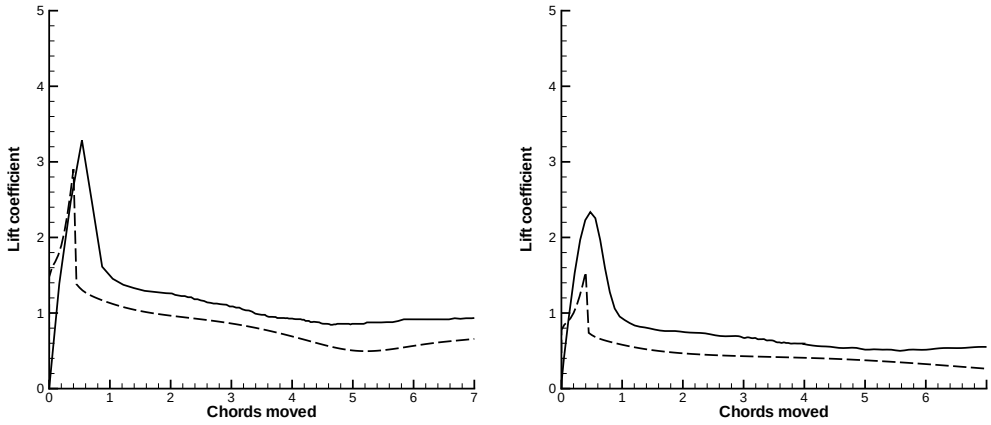

(i) 72° (j) 81°

Figure 5.2: Comparison of CFD lift predictions (dashed lines) with measurements from Dickinson and Götz (1993) (solid lines) for a uniformly-accelerated flat-plate aerofoil at various angles of attack (continued).

attached from the forces produced when the wing is *present*. In the current case, it is not the accelerations that are due to the motion of the wing in the *horizontal* direction (as the wing is driven through the fluid) which are under consideration, but those accelerations that occur *perpendicular* to the wing's direction of motion due to lift forces.

To illustrate this problem, consider the added-mass forces that were discussed in §2.1.3.2. No matter what acceleration profile is used, it is clear that it is possible to pinpoint an instant in time when the wing starts accelerating — an infinitesimal time before this, the wing was stationary, but it is now in motion. This change may actually cause a relatively large increase in force, as highlighted in the discussion of the Wagner effect on p. 57, but unless the wing has zero inertia it will not *instantaneously* move in response to this force peak and therefore the strain gauges attached to the wing will not instantaneously register this force peak. This explains why, in the CFD case, a force is detected *as soon as motion starts* (i.e. there is a lift force present even when the wing has moved zero chords) whereas in the experimental case the lift force increases gradually from the origin of the graph. Similarly, at the end of the acceleration phase of motion (after 0.5 chords of travel), the CFD results show an instantaneous drop in lift as the added-mass forces cease to exist. It is proposed here that such a force drop would also have occurred in the experimental case — but the strain gauges could not detect such a change in force because the wing would not instantaneously change position in response to it.

Dickinson and Götz state that "the inertial force resulting from the rapid acceleration of the wing model and added mass can be clearly seen as a sharp transient force peak at the start of each trace which decays after about 0.7 chord lengths of travel." They do not address why the initial force peak decays *gradually* when the acceleration phase of the motion actually ends *suddenly*. It is clear that if this force peak is due to the accelerating motion of the wing, the peak ought to disappear *instantaneously* when the acceleration stops. It is notable that in the experimental case, the initial peak *starts to decrease* at around the same time as the CFD results predict the added-mass forces disappearing. The fact that it does not disappear instantaneously indicates some limitation in the force measuring technique. This

limitation is inevitable when using any force measurement technique that measures the *displacement* of a body in order to determine the forces on it.

It is interesting to note that the model of Ansari (2004) predicts an initial peak which is very similar to the prediction from the current CFD model (compare Figures 5.2 above and 3.3(b) on p. 83) . This supports the assertion that the experiments of Dickinson and Götz (1993) failed to capture this peak, even though it was almost certainly present.

Bearing this concern in mind, it is clear that at low angles of attack (i.e. $\pm 9°$), where there is no leading-edge separation and the flow eventually stabilises (examination of the CFD flow visualisation confirms these two conditions), the CFD model predicts the steady lift value remarkably well. The low-amplitude fluctuations in the experimental lift measurements at these low angles of attack are almost certainly due to either mechanical or electrical 'noise' entering the system.

As the angle of attack increases, other discrepancies appear between the two sets of results. For example, at 27°, the CFD results show (after the initial 'added mass' peak) a gradual lift peak followed by a gradual trough. The experimental results do show a smaller peak, but the subsequent trough occurs much sooner (at around 3.5 chords of travel as opposed to around 5 for the CFD case) and is much less pronounced. It is followed by another very mild peak. Since these force changes occur very gradually, it is not reasonable to blame the inertia of the wing in this case.

At 36°, the first broad peak is similar when the two sets of results are compared. However, the CFD results once again show a broad, gentle, and flat-bottomed trough that is deeper and more pronounced than in the experimental data. A similar effect is seen at 45°. It is notable that the graphs match fairly well over the first 4 chords of travel, and this is as would be expected because it has already been seen that the flow-visualisation results match very well (Figure 5.1). However after 4 chords of travel the CFD results show a trough, which is much shallower in the experimental case. This is followed in the CFD case by a sharp increase in lift, which again does not appear in the experimental case.

It is shown later that this trough is the result of the initial leading-edge vortex

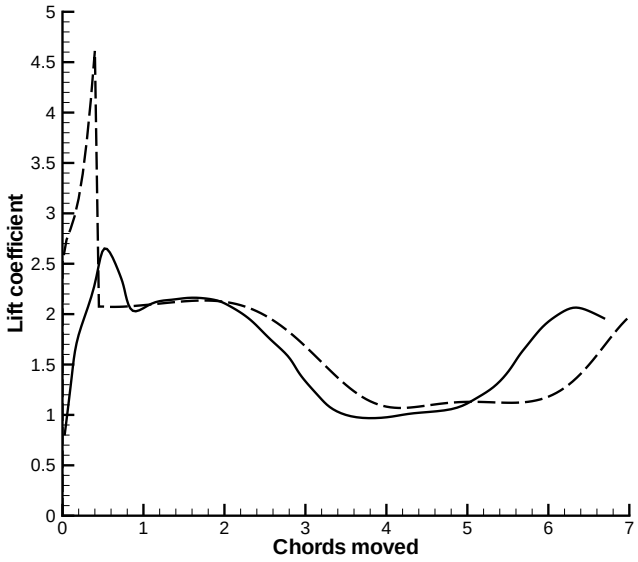

Figure 5.3: Comparison of 2D CFD lift prediction from current work (dashed line) with 2D CFD prediction from Miller and Peskin (2004) (solid line) for a flat-plate aerofoil at 45° angle of attack. Kinematics are identical to those of Dickinson and Götz (1993).

(LEV) being shed, and the sharp increase in lift which follows it is due to the formation of another LEV. In the experimental case, the trough is much shallower and the subsequent peak is not present. It appears that the cycle of vortex growth and shedding was different for the experimental case than for the CFD case. Other experimental results show a continuing cycle of vortex growth and shedding, as is seen in the CFD results as well as in the experimental results of others (see e.g. Gustafson and Sethian, 1991, p. 73). It is possible that the discrepancy is due to some vibration (due to the fact that the traverse used a stepper motor) having an impact in the experimental case of Dickinson and Götz, but it is not possible to postulate as to how this might affect the vortex shedding pattern. Without flow visualisation data, the source of the apparent difference in shedding pattern is impossible to determine. This difference was also noted by Ansari (2004).

Miller and Peskin (2004) also used a 2D CFD model, and they also validated it using the data of Dickinson and Götz (1993). It is interesting to note that their findings closely match those from the current model — see Figure 5.3. They noted the obvious discrepancies and proposed that they could probably be due

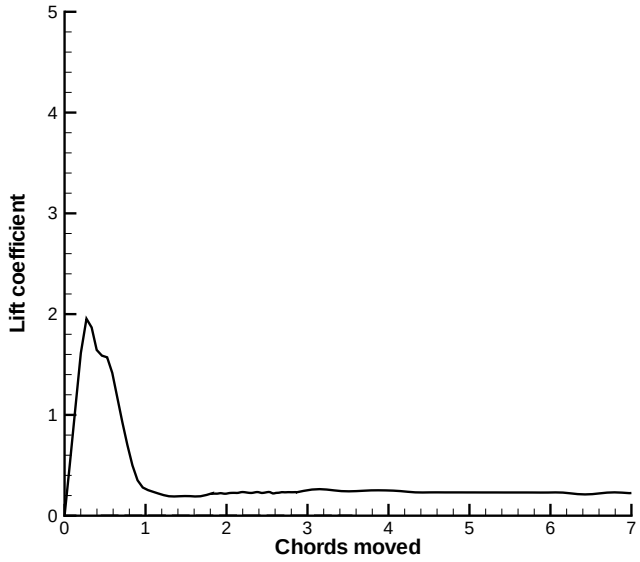

Figure 5.4: Experimental lift measurements from Dickinson and Götz (1993) for a uniformly-accelerated flat-plate aerofoil at 90° angle of attack. The CFD model predicts a constant zero lift at this angle of attack.

partially to numerical error in the simulation and experimental error in the results of Dickinson and Götz (1993). They also postulated that 3D effects might have occurred in the experiments. It is interesting to note that the agreement between the current CFD model and theirs is relatively good. There is a difference in the initial peak, with the results of Miller and Peskin not predicting an instantaneous force (i.e. as soon as motion starts) as the current CFD model does — the results of Miller and Peskin therefore match the experimental results more closely than results from the current model. The reasons for this are unclear because Miller and Peskin do not discuss this phase of motion.

The final discrepancy between the two sets of results (i.e. the present CFD results and the experimental results of Dickinson and Götz (1993)) appears most obviously at very high angles of attack. From 54° to 81° the *shapes* of the graphs correlate well, but it appears that there is a small offset — the experimental results indicating an extra lift coefficient increment of about 0.3. The reason for this becomes clear when the results of Dickinson and Götz for the case of 90° angle of attack are introduced (Figure 5.4). Dickinson and Götz appear to have measured an eventual stable lift coefficient of around 0.25 *even though* the aerofoil was appar-

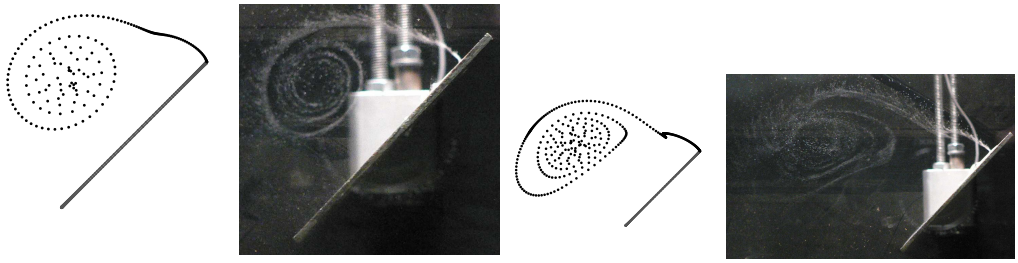

(a) After 2 chords of travel (b) After 4 chords of travel

Figure 5.5: Comparison of CFD flow visualisation (left) with that from current experiments (right). The impulsively-started, flat-plate aerofoil is moving left to right at an angle of attack of 45°. The leading-edge vortex sheet does not appear to be emanating from the leading edge in the experimental case because of perspective. $Re = 500$.

ently set at 90° angle of attack. In addition there is a large positive lift peak at the start of motion. An aerofoil at 90° angle of attack can produce a force normal to the direction motion if vortex shedding occurs asymmetrically, but there certainly should not be a lift peak as measured by Dickinson and Götz, and it seems unlikely that vortex shedding could occur in such a way as to produce a positive lift force for over 7 chords of travel.

It appears, then, that inconsistencies are undeniably present in the experimental results, and it might be natural to ask whether validating a CFD model against them is meaningful. There are two answers to this. Firstly, as has already been said, there is no alternative — experimental data for these low Reynolds numbers are extremely rare, due to the practical difficulties involved in working at these very low Reynolds numbers (as mentioned in §2.3). Secondly, despite these discrepancies, the results of Dickinson and Götz do give us some indication of whether the current CFD model is producing the right *kind* of results; they give us some idea whether the CFD results are what should be expected. On this basis, the CFD results do look (at least) *reasonable* — in some points, they look *good* — and it is plausible to use the model to gain further insight. In §7.4 the need to gather more experimental data is mentioned; this is beyond the scope of the current work.

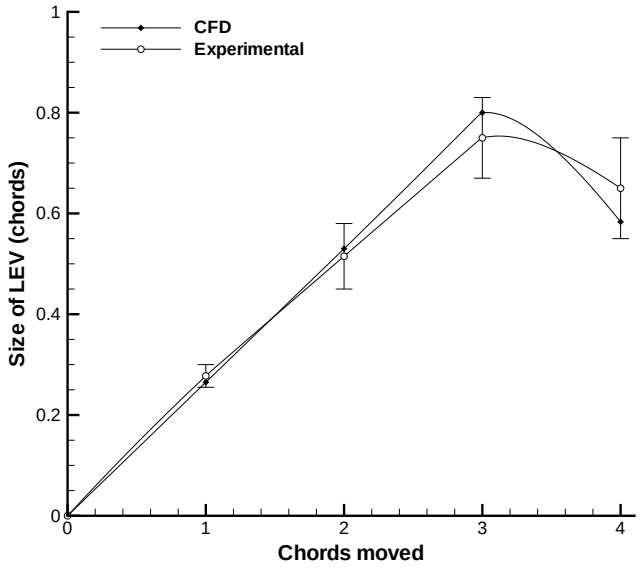

Figure 5.6: Comparison of LEV size vs. distance moved for experimental case and current CFD model predictions. Wing is moving as in Figure 5.5. The size of the LEV is the distance across it (i.e. from the vortex sheet on one edge to the vortex sheet on the other edge) in a direction normal to the aerofoil's chord. The error bars for the experimental case result from measurement uncertainty due to diffusion of the flow-visualisation bubble traces.

5.1.2 Comparison with current flow-visualisation results

Using the procedure outlined in §4.5, experimental flow-visualisation data were obtained for an impulsively-started, flat-plate aerofoil translating at an angle of attack of 45° and Reynolds number of 500. These data are compared with results from the current CFD model in Figure 5.5. For clarity, only the LEV is visualised. The agreement is very good. At 2 chords, the CFD model predicts an LEV of the right size and position, and at 4 chords the 'squashed' shape of the LEV is apparent in both cases. Also apparent is the fact that at 4 chords a second LEV is just beginning to form in both experimental and CFD cases. Beyond 4 chords, the flow field became periodic, as was demonstrated by Gustafson and Sethian (1991).

Figure 5.6 shows that both the CFD model's prediction of the size of the LEV matches the experimental results closely, particularly over the first 2 chords of travel. The reason for the errors at later stages could lie in the fact that the bubbles used to visualise the experimental flow tend to drift upwards due to their

buoyancy. This error would become larger as the experiment progressed; hence the difference between the two cases would tend to increase as the experiment continued. However, even at the later stages the CFD prediction still lies within the error bars for the experimental results.

5.1.3 Comparison with the results of Sun and Boyd (2003, 2004)

Sun and Boyd investigated the flow over micro-scale aerofoils. They state that this is "in order to understand the aerodynamic issues related to micro air vehicle design and performance" (Sun and Boyd, 2003), but the aerofoil they analyse has a chord length of only 30 microns[1] — smaller by far than the wings of any viable MAV (at least in the foreseeable future). Because their aerofoil is so small they state that continuum approaches (like the one used in the current study) are invalid, and they instead use a hybrid continuum-particle approach. The computational domain is divided into two areas — one where the continuum assumption is made, and the other where the fluid is treated as a collection of particles. The position of the interface between these two domains is set using a continuum breakdown parameter. However, as Sun and Boyd (2003) state, "there is no theory that indicates the cutoff value for the continuum breakdown parameter," and it appears that they simply choose "a small number" to define the position of the boundary. It is not clear what effect the choice of this parameter has.

Because their approach is statistical and numerically expensive, it is not possible to obtain data showing the force/time history (Sun, priv. comm., 2006). Instead, Sun and Boyd appear to *assume* that flow *must* be steady, even when flow-visualisation data from their model indicate that large-scale vortex shedding is occurring (see e.g. Sun and Boyd, 2004, Figure 4e). It is not clear what form this assumption of steadiness takes, but it is clear that an unrealistic situation is being created. It is not specified whether the lift and drag forces they present are instantaneous or time-averaged; it appears that no account whatever of the un-

[1] Indeed, their computational domain has a radius of only 150 microns — or $0.15mm$.

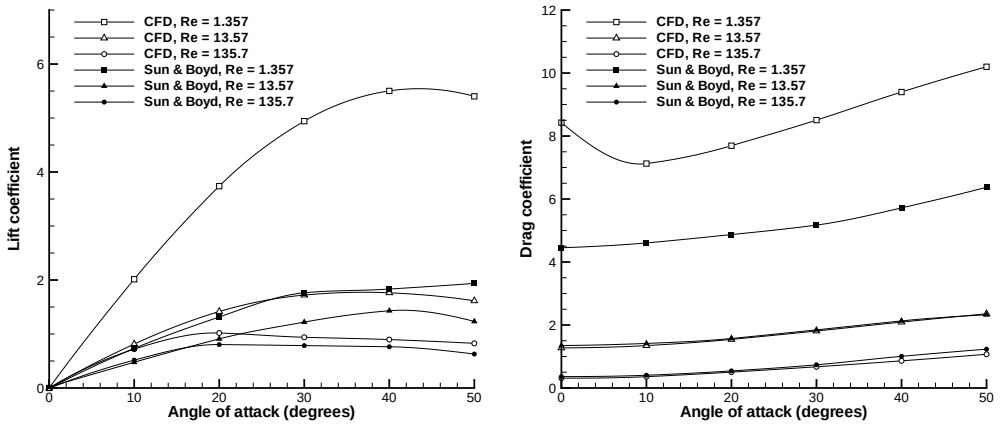

(a) Lift (b) Drag

Figure 5.7: Comparison of CFD results with results from Sun and Boyd (2004) for an infinitely-thin flat-plate aerofoil in steady motion at various angles of attack.

steady nature of the flow has been taken. In order to compare the current model with theirs, it is necessary to create a similar artificial situation; the flow must be forced to be steady when in reality it will not be. What this means physically is unclear, but in practice it simply involves running the CFD simulation and forcing it to find some 'steady state' situation for each case. Of course, in some cases, the steady state will be entirely realistic — for example, if the aerofoil is at 0° angle of attack, no vortex shedding occurs and the flow really *is* steady. But in other cases, where the angle of attack/Reynolds number combination are high enough to produce vortex shedding, the 'steady state' picture that emerges from the simulation is entirely unrealistic — in reality, the flow would not be steady.

It could perhaps be argued that comparing unrealistic results from one model with unrealistic results from another is unlikely to yield useful insights. However, it is also possible to argue that, although *some* of the results themselves *may be* unrealistic, examining whether the two models produce the same results might be helpful. In particular more insight into the effect of Knudsen number might be gained.

Figure 5.7 compares the two sets of results. The first thing that is immediately obvious is that both models predict very poor aerodynamic performance at these very low Reynolds numbers, as is confirmed by Figure 5.8. In particular, for the

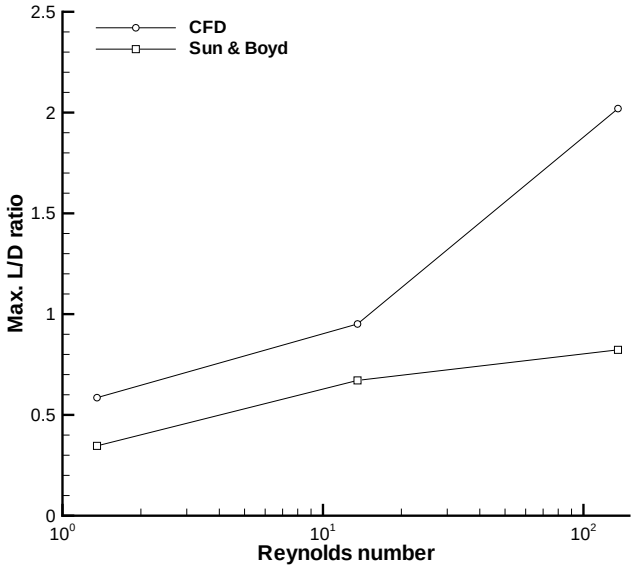

Figure 5.8: Comparison of maximum lift/drag ratio vs. Reynolds number for results from CFD model and the model of Sun and Boyd. Results relate to an infinitely-thin flat-plate aerofoil in steady motion at an angle of attack of 45°. Note the log scale on the x-axis.

$Re = 1.357$ and $Re = 13.57$ cases, at no point does the lift/drag ratio exceed 1. This is due to the dominance of viscosity; at $Re = 1.357$ separation does not occur at the leading edge and fluid flows straight down the upper surface of the aerofoil — hence skin-friction drag is high. At higher Reynolds numbers a separation bubble is created (see §5.3 below) and as a result skin-friction drag is reduced. Of course, the poor lift/drag ratio may not matter for flapping-wing flight, where wing motion can be such that drag force contributes to vertical lift.

There are marked discrepancies between the current results and those of Sun and Boyd, and the differences become more prominent as Reynolds number is decreased. This is as would be expected. As was noted earlier, the method of Sun and Boyd assumes that the flow does not act as a continuum in certain regions of the flow. At high Reynolds numbers, these non-continuum areas will be very small (if they exist at all) and the two models should converge. However, at low Reynolds numbers the non-continuum areas could be relatively large. Because the CFD model assumes continuum behaviour everywhere, differences are bound to occur at lower Reynolds numbers. In fact, the average difference in lift coefficient

between the two models (as a percentage of the CFD values) is 52% at $Re = 1.357$, 16.4% at $Re = 13.57$, and 16.9% at $Re = 135.7$. The reason for the small increase in average percentage difference between the latter two Reynolds numbers is unclear; what is important is the dramatic decrease in average percentage error between the lower two Reynolds numbers.

At the lowest Reynolds number tested here ($Re = 1.357$) the differences between the two models are extremely large. The CFD model predicts much higher lift and drag forces. Perhaps this is explained by what Sun and Boyd refer to as "velocity slip." In the CFD case, the flow is brought to a stop at the surface of the aerofoil due to skin friction between the fluid and the surface. In the results of Sun and Boyd (2003), this is not the case — in fact, for the $Re = 1.357$ case, the velocity of the fluid on the surface was predicted to be around 30% of the freestream velocity. It is evident that this would cause a change in skin-friction drag, and because skin-friction drag is more dominant at low Reynolds numbers, the results becomes more disparate as Re is decreased.

An unusual characteristic in the $Re = 1.357$ case is the decrease in drag coefficient between the angles of attack of zero and ten degrees, which does not occur in the data of Sun and Boyd. Separating out the drag due to pressure and that due to viscosity reveals that, for the two higher Re cases, the skin-friction drag decreases between 0 and 10°, but the pressure drag rises to compensate for it, leading to a smooth rise in total drag from 0 to 50°angle of attack. In the $Re = 1.357$ case, the pressure drag does not rise sufficiently to compensate for the decrease in skin-friction drag, so that the total drag falls. Again, this seems likely to be due to the high skin-friction drag at these very low Reynolds numbers.

The present CFD model and the model of Sun and Boyd agree very closely in their predictions of drag at the two higher Reynolds numbers. However, the CFD model consistently predicts a higher lift that the model of Sun and Boyd, although the difference becomes smaller as Re is increased. It is difficult to determine the precise reason for this difference. Sun and Boyd (2003) note that their model predicts relatively large variations in density even at $Re = 135.7$ and this could well be responsible for this difference — the CFD model assumes incompressible

flow.

Note that it is not possible from these comparisons to determine whether the assumption of continuum flow is valid. It is clear that making the assumption has an effect, but what is not known is whether *in reality* the assumption is reasonable or not. Based on the discussion of Knudsen number earlier (§4.2.2) the assumption would be expected to hold. Gathering experimental data at these low Reynolds numbers is extremely difficult but may prove necessary if this question is to be answered more conclusively.

Finally, at $Re = 135.7$ the angle of attack for maximum lift is around 20° for both models. The experiments of Dickinson and Götz (1993) found that at $Re = 192$, maximum average lift occurred at an angle of attack of around 36°. The computational model of Pullin and Wang (2004) found that an angle of attack of around 52° produced maximum average lift at a similar Reynolds number. It seems likely that the value obtained by Sun and Boyd and the value obtained using the current model are unrealistically low, and this is probably because of the artificial assumption of flow steadiness which was discussed above. It is postulated here that the assumption of flow steadiness is unrealistic at $Re = 135.7$ for angles of attack of 20° or higher. In other words, provided the angle of attack is below 20°, the flow is in reality steady (for this Reynolds number). If the angle of attack exceeds this value, the flow in reality would be unsteady. It should be noted that the present CFD model does not make this assumption (that the flow is steady) generally — only for the purposes of this comparison.

5.1.4 Comparison with results of Ansari's model

Ansari's analytical model (which was discussed in §3.1.2) is essentially inviscid, with the effects of viscosity introduced by the imposition of separation at the leading and trailing edges. This separation cannot be imposed using CFD, but because CFD can model viscosity the separation should occur naturally. However, the essentially-inviscid nature of Ansari's model does bring problems when trying to compare the two techniques. The issue becomes evident when Reynolds number is considered. Because Ansari's model essentially assumes that viscosity is zero, the

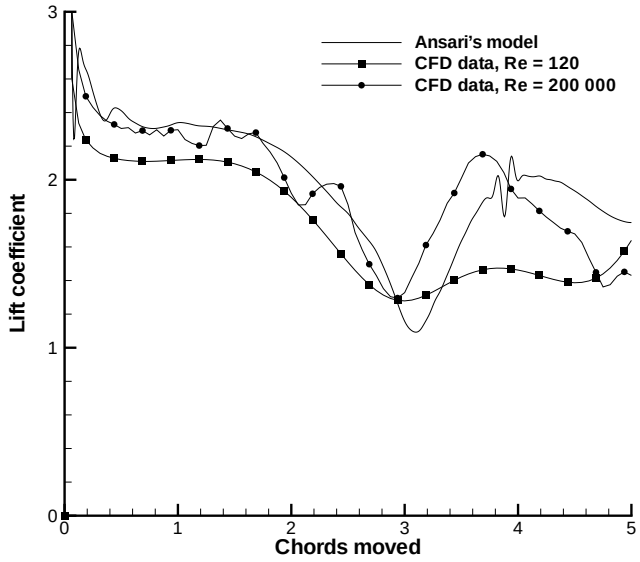

Figure 5.9: Lift prediction from Ansari's model (Ansari, priv. comm., 2006) compared with that from current CFD model for an impulsively-started, infinitely-thin, flat plate at an angle of attack of 45°.

model is Reynolds number-independent. The question is, therefore, what Reynolds number should be used when obtaining CFD data to compare with this model?

Figure 5.9 shows data from Ansari's model (Ansari, priv. comm., 2006) compared with CFD data. For the reasons given above, CFD data are given for two Reynolds numbers. The effect of increasing Reynolds number is immediately apparent, but at this stage it is the agreement between the two models that is under consideration.

As already mentioned, Ansari's model was designed to model low Reynolds number flows. Comparison with the CFD data for $Re = 120$ shows encouraging agreement between the two techniques. Both the magnitudes of the predicted forces and the shapes of the graphs (especially during the first 3 chords of motion) are similar. However, the graphs diverge after 3 chords of travel — this is when the initial leading-edge vortex has been shed from the aerofoil, leading to a drop in lift. Ansari's model shows a rapid climb in lift and a prominent peak at around 4 chords travelled, whereas the CFD results for $Re = 120$ show an earlier and less pronounced peak. It is likely that this difference is due to the essentially-inviscid nature of Ansari's model (see §3.1.2).

The forces from the CFD data for $Re = 200\,000$ seem to confirm this. At this higher Reynolds number, the CFD results show a peak at around 4 chords of travel which is of a much higher magnitude and is much more pronounced. However, at this higher Reynolds number, the force/time history can be seen to have a higher degree of unsteadiness. Since these higher-frequency fluctuations are not captured by Ansari's model, it is logical to assume that they are the results of the inclusion of viscosity. These high-frequency fluctuations are discussed in more depth in §5.3.3.1. It might be thought that if these fluctuations are the result of viscosity, they should appear more readily at the lower Reynolds number, where viscosity should be more dominant. This argument is simplistic, however; instead it is suggested that these fluctuations only occur when viscosity is included, but that at low Reynolds number the dominance of viscosity leads to the fluctuations being 'damped out'.

It is also possible to compare the flow visualisations from the two models, as in Figure 5.10. As might be expected, the basic flow pattern is the same in both cases. One slight difference is that Ansari's model predicts the flow leaving the leading edge at a slightly different angle to that seen in the CFD data and hence the leading-edge vortex appears to form nearer the leading edge. Another is that the CFD model seems to predict the second trailing-edge vortex forming earlier than Ansari's data — it has started to form after two chords of travel in the CFD data, but not in Ansari's data. Apart from these two small differences, the flow patterns are very similar. It should be noted that both models visualise the flow by releasing particles from the leading and trailing edges, but the rate at which these particles are released differs between the models, so that vortices appear more dense in one case than in the other. This is merely an anomaly of the visualisation process, not a physical reality — the way to compare the two sets of images is to examine the relative positions and overall sizes of the vortices.

5.1.5 Conclusions

Data from the current CFD model have been compared to three other data sets and, on the whole, the comparisons have yielded encouraging results. The most im-

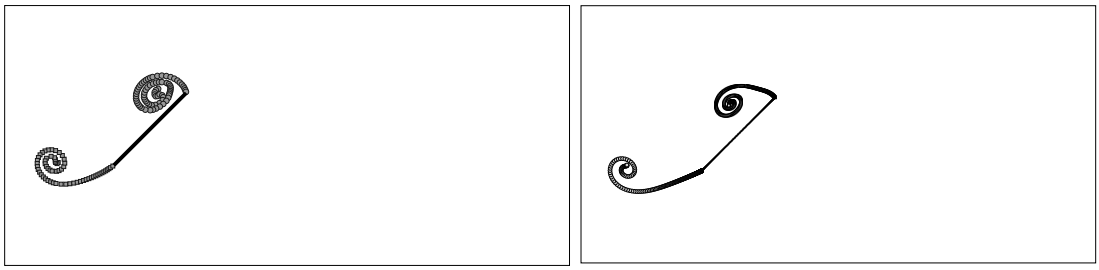

(a) After 1 chord travelled

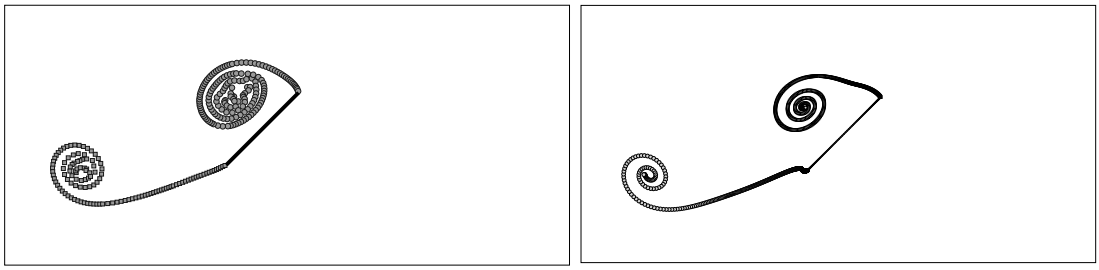

(b) After 2 chords travelled

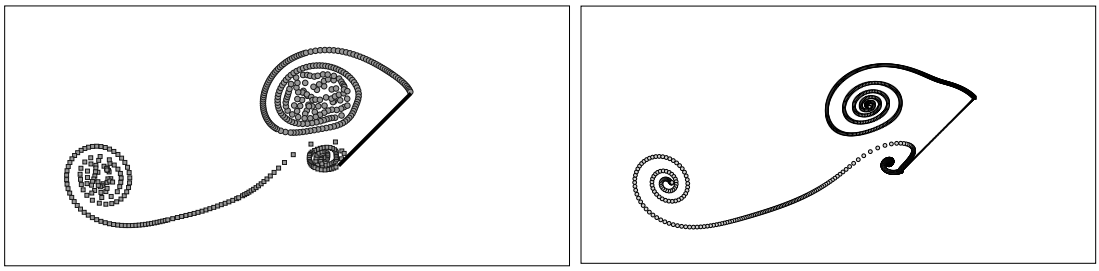

(c) After 3 chords travelled

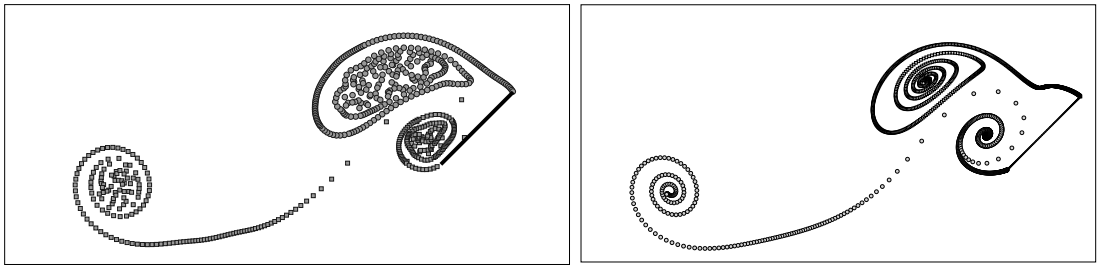

(d) After 4 chords travelled

Figure 5.10: Comparison of flow visualisation from Ansari's model (left) with that from the present CFD model (right) for uniformly-accelerated flat plate. For both cases, the vortical structures are visualised by particles released from the leading and trailing edges and moving with the flow. Angle of attack is 45° and (for the CFD case) $Re = 192$ (based on final velocity and aerofoil chord).

portant comparison was with the experimental data of Dickinson and Götz (1993). Here some discrepancies between the CFD results and the experimental results were noted, but on the whole the agreement was good, particularly when the flow visualisation results were compared. The differences in the force/time histories are, for the most part, minor, and can be explained by careful analysis of the experimental results and the method used to obtain them.

The current CFD results were also compared to the results of Sun and Boyd (2003, 2004). Here, more significant discrepancies were found, but, as has been explained, this is exactly what should be expected, and the comparison highlighted the importance of Knudsen number. It must also be borne in mind that there are certain questions relating to the method of Sun and Boyd that remain unanswered. In particular, their model is designed for rarified gas flows, and divides the domain into regions where the continuum assumption is made and regions where the fluid is not treated as a continuum. As mentioned above, the boundary between these two domains *appears* to be quite arbitrarily placed, and this may have some impact on their results. In any case, their results and the current CFD results appear to converge as Reynolds number is increased, and this is precisely what should be expected.

Finally, current CFD data have been compared with data from the model of Ansari (2004). Once again, the comparison of flow visualisation gave encouraging results, and the comparison of force/time histories was also good. The differences between the two sets of results are easily explicable by considering the differences in approach between the two models.

In conclusion, it is clear that the current CFD model produces results which agree with expectations. Although there is a need for more experimental data to be gathered at these low Reynolds numbers (as noted in §7.4), it is still possible to proceed with confidence in the CFD model.

5.2 Strouhal number and its (un)importance

Strouhal number (St) is a non-dimensional parameter which is often mentioned in the context of insect flight, and is a non-dimensional frequency of vortex shedding. It is calculated using the equation

$$St = \frac{f_{vs} l}{V}, \tag{5.1}$$

where f_{vs} is the frequency of vortex shedding, V is the velocity of the aerofoil and l is the aerofoil's chord length.

Because insect flight involves the shedding of vortices, Strouhal number is thought by some to be an important parameter. Even so, many authors ignore it altogether — neither Sane (2003) or Wang (2005) even mention the term in their reviews. Ansari et al. (2006a), on the other hand, infer that the "Strouhal number may be a more important parameter than the Reynolds number for these kinds of flows" (Ansari et al., 2006a, §4.3).

However, Ansari et al. (2006a) (along with many others), when considering Equation 5.1, substitute f (the wing flapping frequency) for f_{vs} (the frequency of vortex shedding). This introduces a possible source of confusion, because Strouhal number was originally defined in relation to the vortex shedding which occurs behind bodies such as spheres. This vortex shedding occurs 'naturally' — that is, it is only the physics of the flow itself that determines when a vortex will be shed. In the case of insect flapping, the value of f is in effect constrained because a vortex is shed whenever the wing reverses direction.

To illustrate this, consider a flat plate being moved through a fluid at 45° angle of attack. It will shed vortices, forming a von Kármán street-like structure. The frequency at which they will be shed will be the 'natural' frequency. If the flat plate is now 'flapped' at twice that frequency, vortices will be shed twice as frequently. Is it correct to interpret this as a doubling of Strouhal number? If so, any desired value of Strouhal number can be obtained, simply by varying flapping frequency. The traditional understanding of Strouhal number is that it "depends only on the Reynolds number" (Lugt, 1995, p. 103), but in this case it has been detached from

Reynolds number entirely — no matter what the Reynolds number is, any Strouhal number can be obtained.

The zoological community has done a great deal of research in the area of flapping flight (see e.g. Taylor et al., 2003) and has also used Strouhal number, again defining it using f (flapping frequency). It seems, then, that there exist two understandings of Strouhal number — one concerned with the *natural* frequency of vortex shedding (the aerodynamicist's view), and one with the frequency of flapping, or the *forced* frequency of vortex shedding (the zoologist's view). In this thesis, Strouhal number (St) refers to the former meaning.

This thesis does not deal with all the kinematics of flapping-wing flight — stroke reversal is not included (see §3.2). In the 2D case, the apparently-simple case of an aerofoil at high angle of attack in a flow is considered. Strouhal number then is in terms of the natural vortex shedding frequency.

What, then, is the importance of Strouhal number in these 2-dimensional flows? Is it dependent solely on Reynolds number? In order to assess this, three simulations were run, with different values of V and l such that, in each case, the product Vl was the same. Since ρ and μ were kept constant, this meant that for each case the Reynolds number was 500.

Figure 5.11 shows the results. Each peak in the lift coefficient C_L relates to a vortex being shed, as is shown later. The taller peaks relate to a leading-edge vortex being shed, the smaller peaks to a trailing-edge vortex.

For case 1 (the line with no markers) 3 leading-edge vortices are shed in just over 3 seconds, giving a time between vortices of 1.02s. This equates to a shedding frequency of $1/1.02 = 0.98$ Hz. The equivalent figures for the second (solid markers) and third (hollow markers) cases are 3.92 Hz and 0.25 Hz respectively. Using the values of V and l used for each simulation, the Strouhal number for each case can

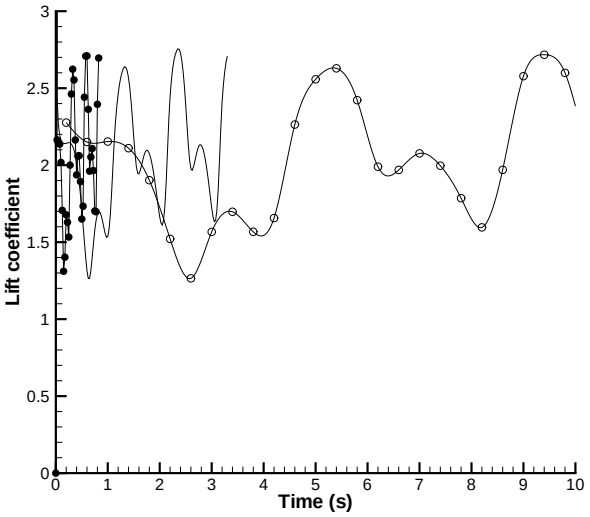

Figure 5.11: Lift coefficient vs. time for three different combinations of V and l. The line with unfilled markers is for a case with low velocity but large chord length, whereas the line with filled markers relates to a case with small chord length but high velocity. In each case chord Reynolds number is 500. 1% thick elliptical aerofoil.

be calculated:

$$\begin{aligned} St_1 &= \frac{0.98 \times 0.04}{0.182592} = 0.22, \\ St_2 &= \frac{3.92 \times 0.02}{0.365184} = 0.22, \\ St_3 &= \frac{0.25 \times 0.08}{0.091296} = 0.22. \end{aligned}$$

This result can be confirmed visually by plotting C_L against chords travelled, as in Figure 5.12. The result in itself is not surprising; indeed, it would only be a sign of numerical problems if the resulting Strouhal numbers were not equal. Therefore, this result will seem trivial to those who are familiar with the aerodynamicist's view of Strouhal number; it may not be so trivial to those who think of Strouhal number in terms of flapping frequency.

These results show that, as would be expected, it makes no difference *how* a Reynolds number is obtained — Strouhal number is always dependent on it. For example, if three simulations are run, using *(a)* a fluid with the density and viscosity of air, *(b)* a fluid with density and viscosity of 10 times the values for

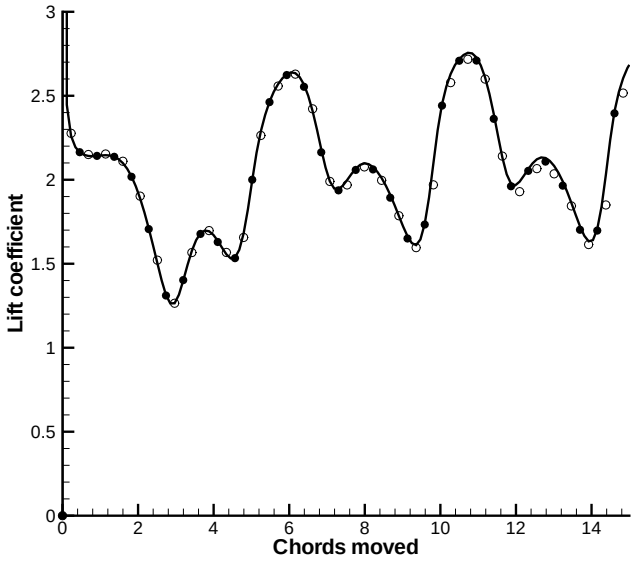

Figure 5.12: Lift coefficient vs. aerofoil distance moved (in chords) for the three cases shown in Figure 5.11.

air, and *(c)* a fluid with density and viscosity one tenth of the values for air, the Strouhal number will be the same in each case. Non-dimensionalised vortex shedding frequency is determined by Reynolds number alone (for a certain object at a certain incidence). This conclusion is supported by the dimensional analysis work presented in Appendix A.

5.3 The impact of Reynolds number

As has already been emphasised, Reynolds number is a most important parameter when considering this (or indeed any) type of flow. Osborne Reynolds (1842-1912) proposed the number as a means of determining (to quote the title of his paper) "whether the motion of water shall be direct or sinuous" (Reynolds, 1883). A high Reynolds number indicates that inertial forces will dominate the flow, whereas a low Reynolds number indicates that viscous forces will dominate, as can be seen from the mathematical formulation of Reynolds number:

$$Re = \frac{\rho V l}{\mu}, \tag{5.2}$$

where ρ and μ are the density and dynamic viscosity of the fluid respectively, and for these 2D cases V is the velocity of the aerofoil and l is the aerofoil's chord length.

Reynolds number can therefore be changed in more than one way. In physical experiments, it is usually varied by changing V or l. But in fact, as demonstrated above, the *effect* of changing Reynolds number is the same, no matter *how* Reynolds number is changed. Any steady flow can be defined using only Reynolds number, aerofoil section, and angle of attack — at least providing that Mach number is less than around 0.3 (so that the flow can be assumed incompressible) and gravity is ignored.

It has already been noted that an FMAV will probably operate at a significantly higher Reynolds number than is currently found in insect flight. The effects of this have not been extensively considered in the literature. This section examines the effect of Reynolds number on an aerofoil at high angle of attack. To do this, both flow visualisation and force data will be compared.

The flow is categorised according to Reynolds number in the following way. 'Low' Reynolds numbers are defined as those less than 25. 'Medium' Reynolds numbers are those between 25 and 1 000; 'high' Reynolds numbers are those above 1 000. The reasons for these divisions will become clear and are discussed in §5.3.5.

5.3.1 Low Reynolds numbers ($Re < 25$)

For an extremely viscous fluid, where $Re \ll 1$ (or for an inviscid fluid), separation will not occur (Houghton and Carpenter, 2003, p. 399). This situation can be simulated using the Hele-Shaw analogy — see e.g. Van Dyke (1982, p. 9). In this case, there will be no circulation and hence no lift (or pressure drag), as predicted by D'Alambert's paradox. This type of flow is not seen here for even the lowest Reynolds numbers tested; even at $Re = 1$ the flow separates at the trailing edge of the aerofoil rather than flowing around it.

However, for very low Reynolds numbers ($Re \leq 5$), separation does not occur at the *leading* edge, even at very high ($> 45°$) angles of attack. Instead, fluid flows around the leading edge and down the upper surface of the aerofoil. This is shown

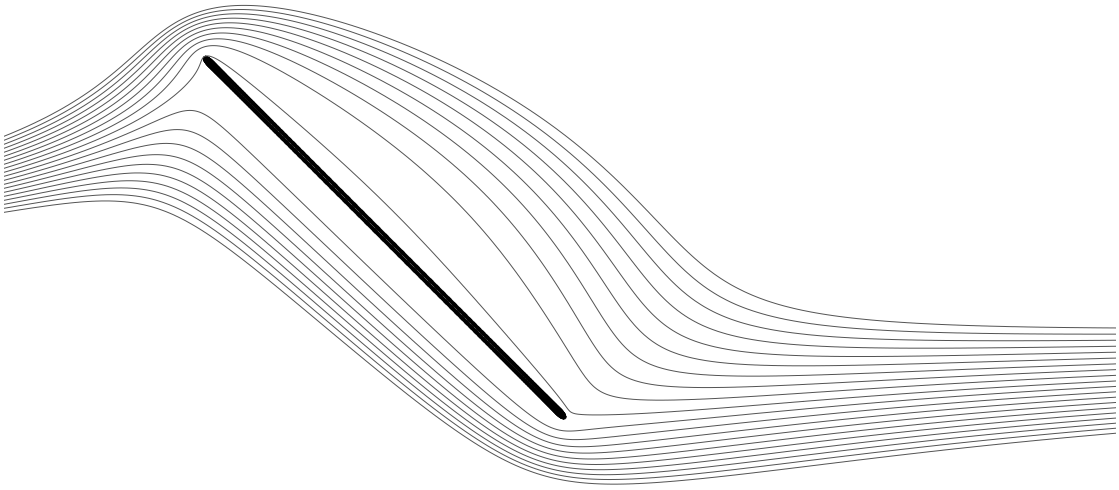

Figure 5.13: Streamlines for $Re = 5$ steady-state flow. Flow is from left to right. 1% thick elliptical aerofoil.

for an $Re = 5$ case in Figure 5.13. In this situation the flow eventually becomes steady, and, once the initial starting vortex has been shed, no further leading- or trailing-edge vortices are seen. The force produced by the aerofoil, therefore, eventually stabilises. This kind of flow pattern is observed when conventional aerofoils translate at low angles of attack.

Figure 5.14 shows that at these low Reynolds numbers, pressure forces always increase both lift and drag, whereas viscous forces reduce lift whilst increasing drag. The reason for this is clear from Figure 5.13; fluid flows from the leading to the trailing edge on both the upper and lower surfaces, leading to a viscous force which acts parallel to the aerofoil and in the direction of the trailing edge. Figure 5.15 shows that at a Reynolds number of around 20, the magnitude of the average viscous lift is around 25% of the magnitude of the average total lift. This supports the assertion of Kundu and Cohen, who state that "in a low Reynolds number flow, the pressure forces are of the order of the viscous forces" (Kundu and Cohen, 2004, p. 302).

As Reynolds number is increased within the range 5 to 25, there is a sharp decrease in the magnitude of both the pressure and viscous forces. The magnitudes of the pressure and viscous forces drop by almost 50% and by more than 75% respectively. As a result, there is a dramatic decrease in the relative importance

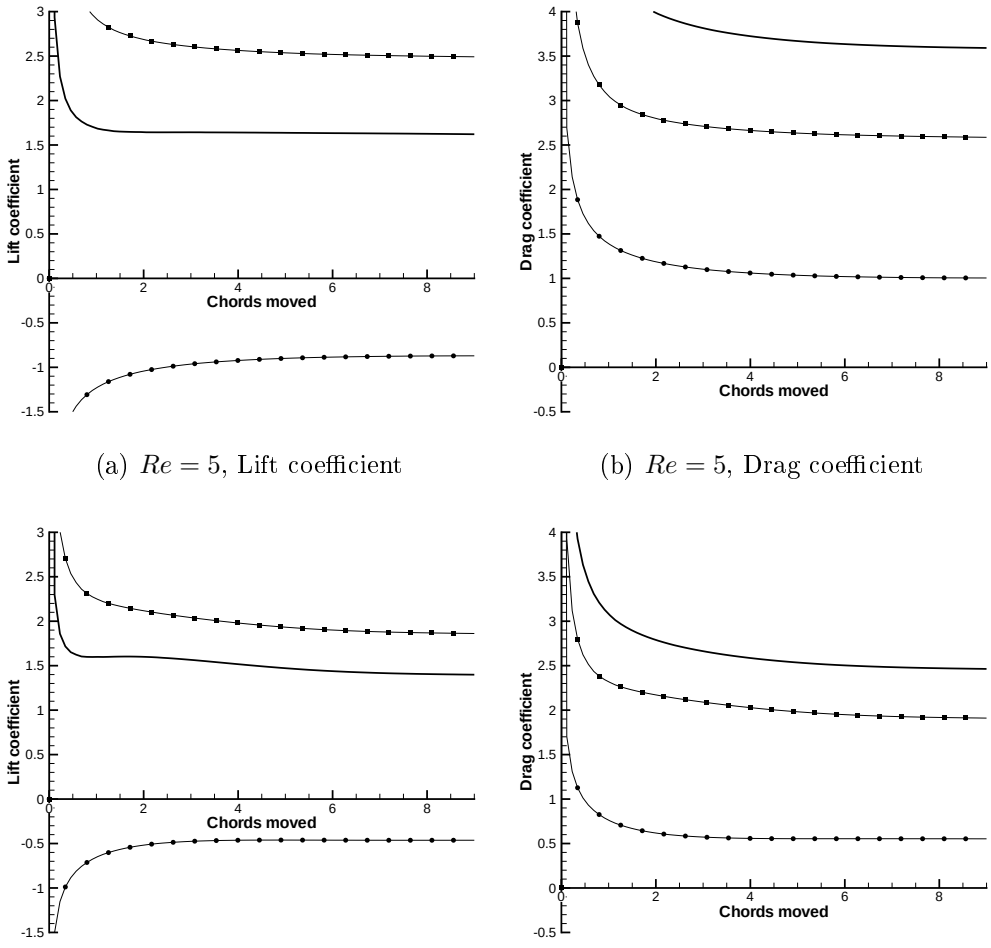

(a) $Re = 5$, Lift coefficient

(b) $Re = 5$, Drag coefficient

(c) $Re = 10$, Lift coefficient

(d) $Re = 10$, Drag coefficient

Figure 5.14: Pressure, viscous, and total lift and drag coefficients for various Re. Pressure coefficients are marked with square symbols; viscous coefficients have round symbols; total coefficient is thick line. Angle of attack is 45° in each case and 1% thick elliptical aerofoil is impulsively started.

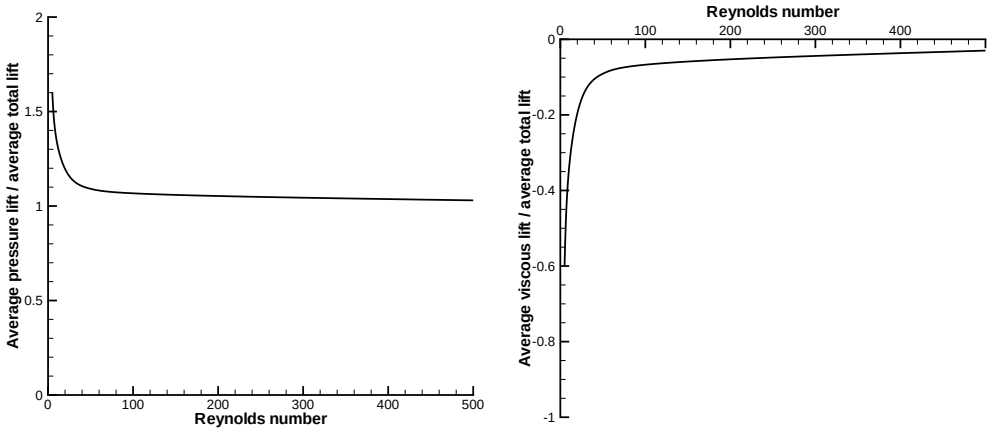

(a) Pressure (b) Viscous

Figure 5.15: Average pressure and viscous lift forces as proportions of average total lift force. Averages are taken over the 9 chords of travel shown in Figure 5.14, but the initial peak is excluded. 1% thick elliptical aerofoil.

of viscous forces. For example, at $Re = 5$ viscous drag accounts for over 25% of the total drag, whereas at $Re = 25$ the corresponding figure is around 15%. This change is partly due to the natural decrease in the dominance of viscosity which occurs as Reynolds number is increased but also partly due to changes in the phenomenology of the flow which will be discussed shortly.

Figure 5.16 collates the data from Figure 5.14 and shows clearly the decrease in lift coefficient that occurs during this phase. Thus it might intuitively be supposed that smaller insects are more efficient because their wings operate at lower Reynolds numbers and therefore produce more lift, but this would be misguided. The eventual drag coefficient is around twice as high at $Re = 5$ than at $Re = 25$, so that in fact the lift to drag ratio *rises* by about 60% as Re is increased from 5 to 25, as shown in Figure 5.17. It is evident that if there were no viscous forces, the lift/drag ratio would be 1 at 45° angle of attack (because the net pressure force acts normal to the chord of the aerofoil), so this drop in lift/drag ratio at low Re simply confirms the importance of viscous forces as Reynolds number decreases. Figures 5.15 and 5.16 show the inapplicability of the assumption of inviscid flow at low Reynolds numbers. Since many of the analytical models that have been formulated assume inviscid flow, this places a limitation on their use.

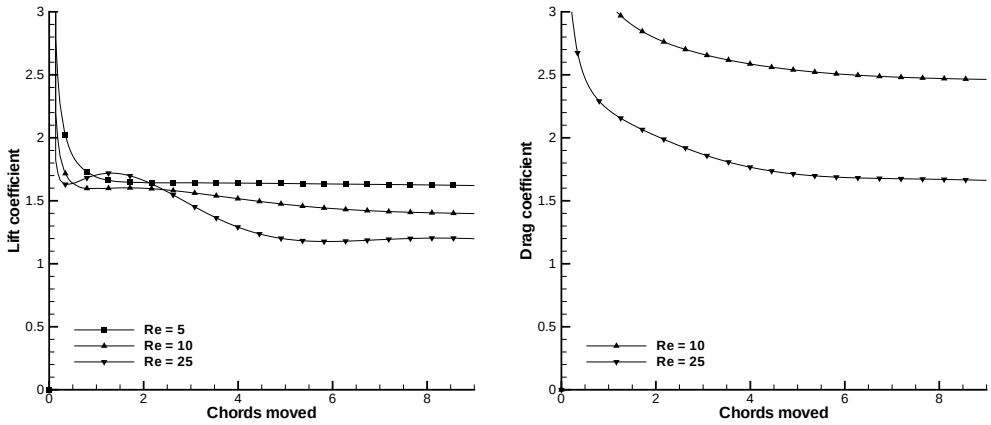

(a) Lift (b) Drag

Figure 5.16: Lift and drag coefficients vs. chords moved for a 1% thick elliptical aerofoil for a range of low Reynolds numbers. Angle of attack is 45°. In (b) the plot for $Re = 5$ lies off the graph. 1% thick elliptical aerofoil.

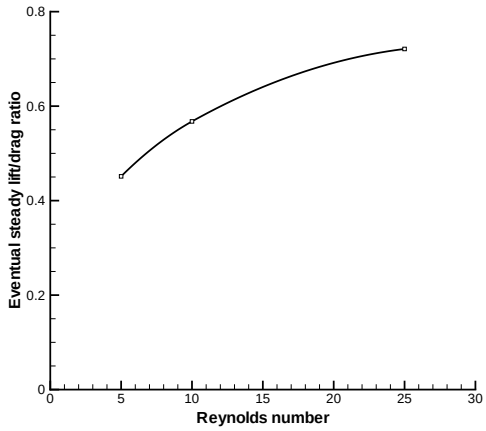

Figure 5.17: Eventual steady lift/drag ratio vs. Reynolds number for 1% thick elliptical aerofoil at low Reynolds numbers. Angle of attack is 45°.

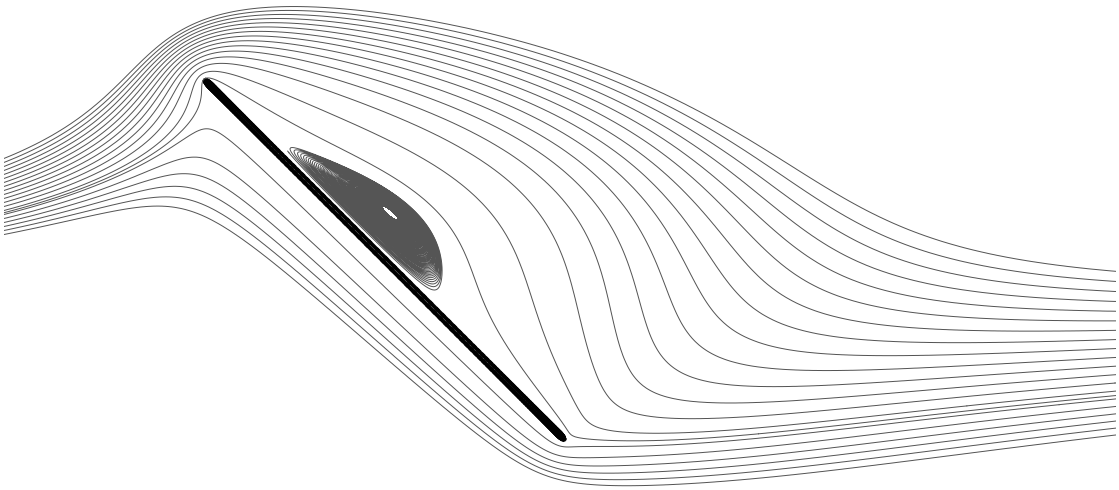

Figure 5.18: Streamlines for $Re = 10$ steady-state flow. 1% thick elliptical aerofoil.

If the Reynolds number exceeds $Re = 10$, the flow does not quite succeed in making its way round the leading edge, and it separates. However, separation does not occur until the flow is almost completely around the leading edge, so the angle between the separated flow and the aerofoil's upper surface is very acute. This is illustrated in Figure 5.18. The separation leads to a 'bubble' of recirculating flow above the aerofoil; the flow actually reattaches to the aerofoil's upper surface aft of this bubble. This phenomenon can be seen in the computational results of Sun and Boyd (2004), also at very low Reynolds numbers. The separation bubble (or vortex) grows until it reaches a steady-state condition, shown in Figure 5.18 — so it is still the case that (apart from the starting vortex) no vortices are shed and the force on the aerofoil eventually stabilises (see Figure 5.16). However, it is obvious that this bubble will cause a reduction in skin-friction (viscous) drag, because now the flow on the upper surface is not universally towards the trailing edge. This contributes to the decrease in viscous drag which was noted above.

LEVs are known to enhance lift, as has already been mentioned. These results show that one of the ways in which they do this is to induce flow on the upper surface of the aerofoil which is toward the leading edge, thus leading to a positive viscous lift force on that portion of the upper surface. However, this effect will only be important at very low Reynolds numbers. At higher Reynolds numbers, viscous forces are insignificant compared to pressure forces (see Figure 5.40 on p. 191), so

any change in viscous lift will be practically unnoticeable.

The evolution of any vortex can be understood using a vorticity balance approach. Vorticity is a measure of the amount of fluid particle rotation in a region[2], and a vortex is an area of concentrated vorticity. If vorticity is fed into a vortex, the vortex will become stronger. Conversely, if vorticity is extracted by some means, the vortex will weaken. This vorticity balance approach is discussed in §4.1.1.6 and has been extensively used in research on delta-wing leading-edge vortices (see e.g. Lee and Ho, 1990). A good explanation and review is given by Reynolds and Carr (1985).

Vorticity is generated by the interaction of the fluid with the aerofoil. At the leading edge, a line of vorticity is generated — a leading-edge vortex sheet — which concentrates into a spiral. Because vorticity continues to be fed from the leading-edge vortex sheet into the vortex, it will tend to increase in strength and grow. However, vorticity will also be diffused out of the vortex due to viscosity, tending to make the vortex weaken and shrink.

Thus the development of any 2D LEV will follow one of three patterns. Either

(A) the rate of vorticity production will be *higher* than the rate of diffusion, in which case the LEV will strengthen and grow; or

(B) the rate of vorticity production will *equal* the rate of diffusion, which case the size and strength of the LEV will remain constant; or

(C) the rate of vorticity production will be *lower* than the rate of diffusion, in which case the LEV will weaken and shrink.

The rate of diffusion will depend on the size and strength of the vortex (with more diffusion occurring in larger and stronger vortices than in smaller, weaker vortices) and on the Reynolds number of the flow, with lower Reynolds numbers leading to more diffusion. Thus if vorticity is fed into a vortex, it will strengthen

[2]The mathematical definition for vorticity ω is

$$\omega = \frac{\partial v}{\partial x} - \frac{\partial u}{\partial y}.$$

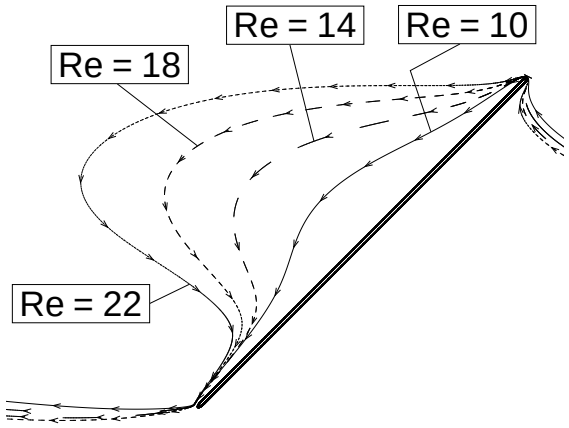

Figure 5.19: Separation bubbles for range of low Reynolds numbers (shown by bubble's bounding streamline for each case). All four cases shown here are steady. 1% thick elliptical aerofoil is moving from left to right at angle of attack 45°.

and grow — but as it does so, the rate of diffusion will increase. If the rate of diffusion increases to a point where it matches the rate of vorticity *addition*, the vortex will stabilise and vortex growth will cease.

Based on the reasoning above, there should be a maximum value of Reynolds number at which case (B) can occur — above this Reynolds number, viscous effects become too weak (relative to inertial effects) to stop the LEV strengthening and case (A) will occur. The present CFD results indicate that this critical value of Re is around 25 (for an angle of attack of 45°). Up to this point, a stable separation bubble is created. As expected, this bubble grows as Reynolds number is increased (see Figure 5.19) until at $Re = 25$ the bubble becomes unstable and is shed.

Laminar separation bubbles, like those seen here, have been observed in physical experiments at Reynolds numbers of around 10 000 (see e.g. Van Dyke, 1982, p. 26), but little work seems to have been carried out at these very low ($O(10)$) Reynolds numbers (at least in relation to flat plates), a notable exception being the work of Sun and Boyd (2003, 2004), whose computational results closely resemble those seen here.

It is known that at certain Reynolds numbers, the flow around a circular cylinder will separate from the cylinder's surface but vortices will not be shed. Instead, a "closed wake of recirculating flow" is produced (Houghton and Carpenter, 2003,

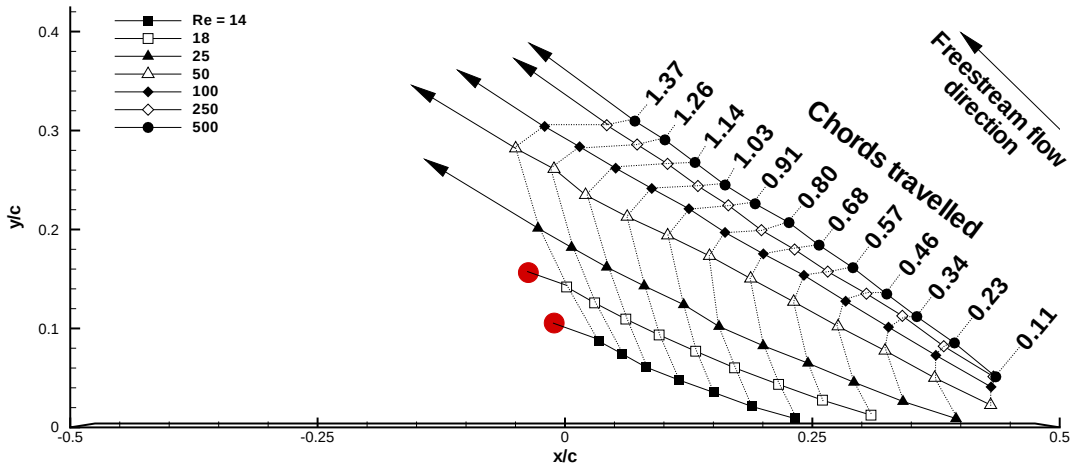

Figure 5.20: Path of LEV centre for range of Reynolds numbers and angle of attack 45°. The aerofoil's upper surface is the thick black line just visible above the x-axis. The dotted lines indicate the number of chords moved since an impulsive start. For the $Re = 14$ and $Re = 18$ cases, the LEV eventually stabilises (indicated by the red dot); for all other cases, the LEV continues to grow and is shed (indicated by the arrows). 1% thick elliptical aerofoil.

p. 401) (see Figure 2.9 on page 70). The Reynolds number at which this phenomenon is first seen depends on the curvature of the body at the sides (Batchelor, 2000) — so that the appearance of the separation bubble would be expected to depend on angle of attack as well as Reynolds number. In fact, this is exactly what is seen — the Reynolds number at which the bubble appears decreases as the angle of attack is increased. Again, this is in agreement with the results of Sun and Boyd (2003, 2004), who found that at $Re \approx 100$ a separation bubble appeared when angle of attack was 20° or more, whereas at $Re \approx 10$ the bubble did not appear until the angle of attack exceeded 40°.

So it seems that the separation bubble seen here is analogous to the closed wake that occurs in the lee of a circular cylinder at low Reynolds numbers. If this is true, the bubble should grow as Reynolds number is increased further. This is in fact what happens — as Reynolds number is increased, the size of the stable separation bubble increases until, as Re approaches 25, it covers the whole chord of the aerofoil (see Figure 5.19).

It is in the range of $5 \leq Re \leq 25$, therefore, that one of the most dramatic

changes in the phenomenology of these 2D flows is seen. At $Re = 5$, no leading-edge vortex (LEV) is formed. At $Re = 10$, what could be described as an LEV is seen, but could also be called a separation bubble. This is formed, as has been said, because the flow separates from the leading edge, but at a very acute angle. As Re is increased beyond 10, this separation angle increases so that the separation bubble grows. To demonstrate this, Figure 5.20 plots the path of the centre of the leading-edge vortex against time. It can be seen that for lower Reynolds numbers, the LEV initially forms fairly near the quarter-chord point of the aerofoil, and takes some time to form; for the $Re = 14$ case the LEV is first seen after the aerofoil has travelled over 0.5 chords. For higher Reynolds number the LEV forms near the leading edge soon after the impulsive start. The path of the LEV also changes as Re is increased, but the change in the LEV's path between $Re = 250$ and $Re = 500$ is much smaller than the change that occurs between $Re = 10$ and $Re = 250$; as Reynolds number increases, the effect on the LEV path per unit change in Reynolds number decreases.

Figure 5.20 shows that if $Re > 25$, the LEV forms very close to the leading edge. It then grows until it eventually sheds from the aerofoil. The flow then becomes unsteady, with LEVs being shed regularly, as will be seen later. This type of transition — from steady to unsteady flow — was noted by Miller and Peskin (2004). They also used a 2D CFD model, and found that for $Re \geq 64$, vortices were shed alternately from the leading and trailing edges, whereas for $Re \leq 32$ the vortices remained attached. They postulated that this transition (somewhere between $Re = 32$ and $Re = 64$) was significant for the flight of tiny insects, but did not investigate the effects of the 3D nature of real insect-like flapping. Nor did they specify the exact transition point — they merely said that vortices are shed at $Re = 64$ but not at $Re = 32$. These results suggest that vortices are shed when $Re \geq 25$; close to the transition point which they found. The difference can probably be explained by considering that they were dealing with full insect-like flapping (though still in two dimensions) and therefore their kinematics differed from those used here.

5.3.2 Medium Reynolds numbers ($25 \leq Re \leq 1\,000$)

It has been noted that, in the range of low Reynolds numbers, an important change occurs in the phenomenology of the flow. At $Re = 5$, there is no separation at the leading edge. At $Re = 10$, there is, and a separation bubble forms. As Re is increased further, this bubble grows until at $Re = 25$ it becomes unstable at the lower end of the range of Reynolds numbers which is here defined as 'medium' ($25 \leq Re \leq 1\,000$). This, then, is how the distinction between 'low' and 'medium' Reynolds numbers is defined — low Reynolds number flows are stable, whereas medium Reynolds number flows are unstable.

Comparing Figures 5.14 and 5.21 shows the results of the flow instability. At $Re = 10$, as has been discussed, the flow eventually becomes stable — no vortices are shed — and therefore both lift and drag coefficients also become stable (Figure 5.14). At $Re = 25$, however, vortices are shed, and the forces become unstable (although this is not obvious in Figure 5.21 for the $Re = 25$ case). The pattern of vortex shedding is now examined in an attempt to relate this to the force/time histories shown in Figure 5.21.

5.3.2.1 The pattern of vortex shedding

When $Re \geq 25$ and the initial LEV sheds, a new trailing-edge vortex forms. This is due to the effect of the initial LEV on the flow at the trailing edge. The process is shown in Figure 5.22. When the initial LEV is small, the flow that separates at the leading edge flows around the LEV and reattaches to the aerofoil. It then flows smoothly aft to the trailing edge (Figure 5.22(a)). Once the LEV reaches a certain size, however, the flow that separates from the leading edge does not reattach, and the LEV induces flow at the *trailing* edge which is towards the *leading* edge (as can be deduced from Figure 5.22(b)). The influence of the LEV causes the fluid to flow *around* the trailing edge so that separation does not occur there. As the LEV moves away, the flow begins to separate at the trailing edge once more before turning and heading towards the leading edge. A new trailing edge vortex is created, which can be seen at the trailing edge in Figure 5.22(c) at a very early stage of its development. This second TEV is eventually also released into the

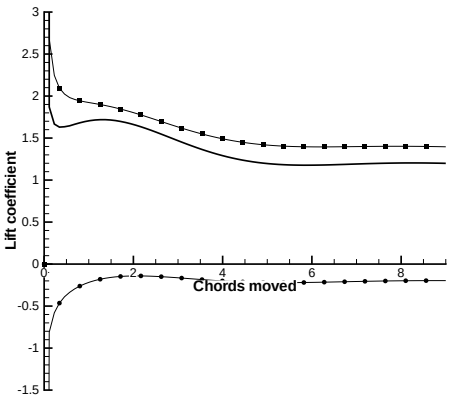

(a) $Re = 25$, Lift coefficient

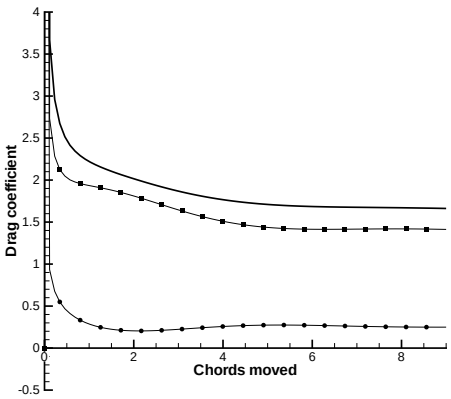

(b) $Re = 25$, Drag coefficient

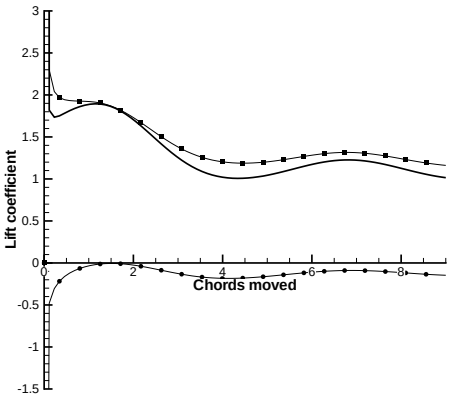

(c) $Re = 50$, Lift coefficient

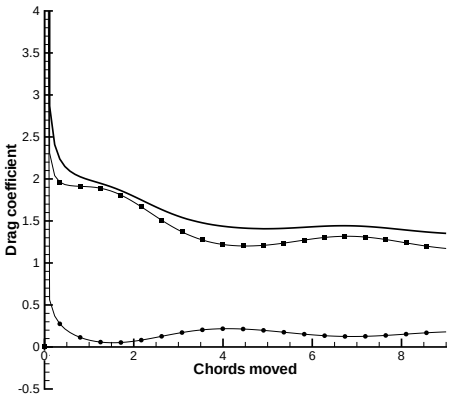

(d) $Re = 50$, Drag coefficient

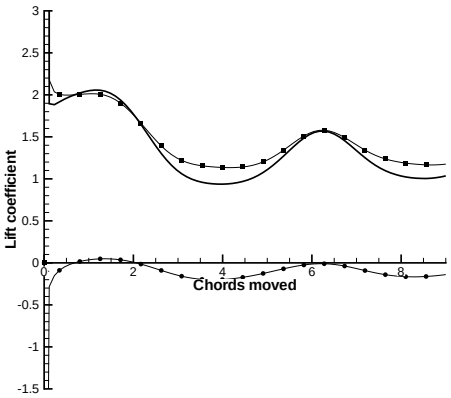

(e) $Re = 100$, Lift coefficient

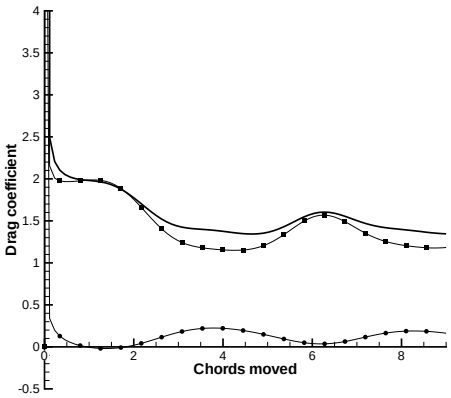

(f) $Re = 100$, Drag coefficient

Figure 5.21: Pressure, viscous, and total lift and drag coefficients for various Re. Pressure coefficients are marked with square symbols; viscous coefficients have round symbols; total coefficient is thick line. Angle of attack is 45° in each case and 1% thick elliptical aerofoil is impulsively started.

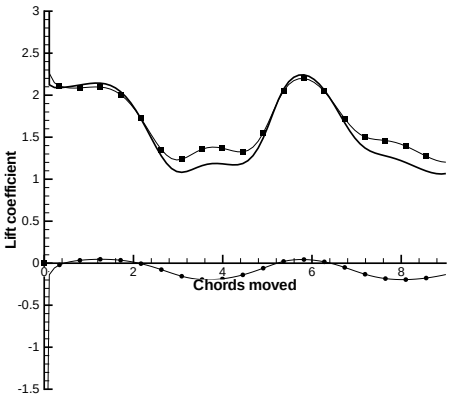

(g) $Re = 250$, Lift coefficient

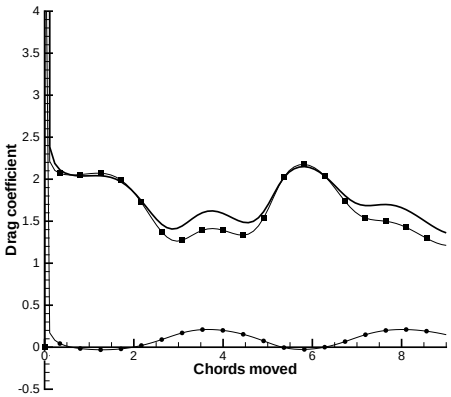

(h) $Re = 250$, Drag coefficient

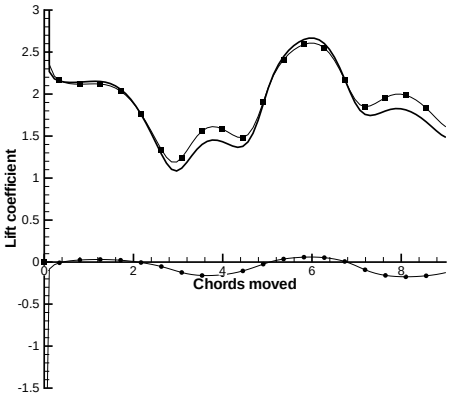

(i) $Re = 500$, Lift coefficient

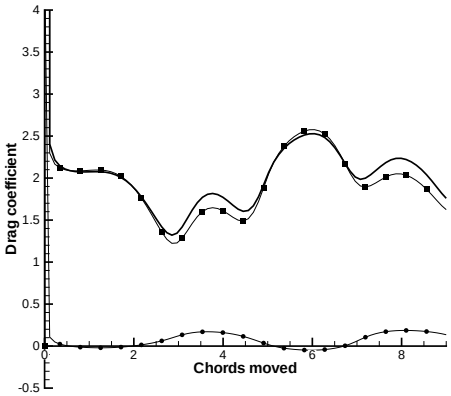

(j) $Re = 500$, Drag coefficient

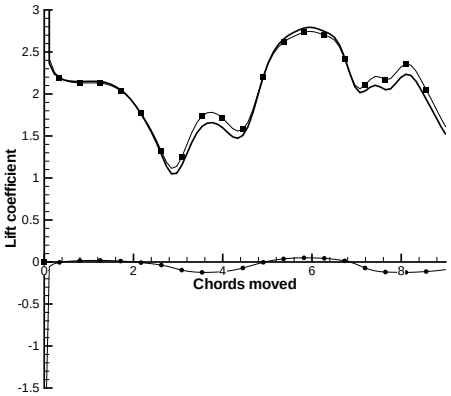

(k) $Re = 1\,000$, Lift coefficient

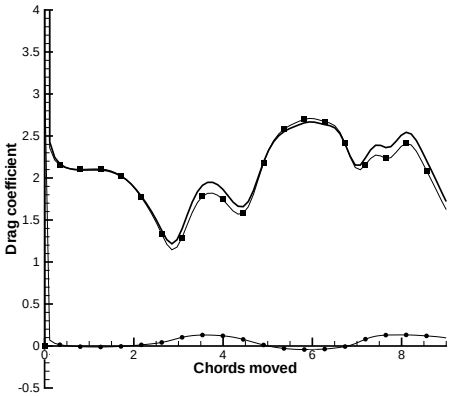

(l) $Re = 1\,000$, Drag coefficient

Figure 5.21: Pressure, viscous, and total lift and drag coefficients for various Re. Pressure coefficients are marked with square symbols; viscous coefficients have round symbols; total coefficient is thick line. Angle of attack is 45° in each case and 1% thick elliptical aerofoil is impulsively started (continued).

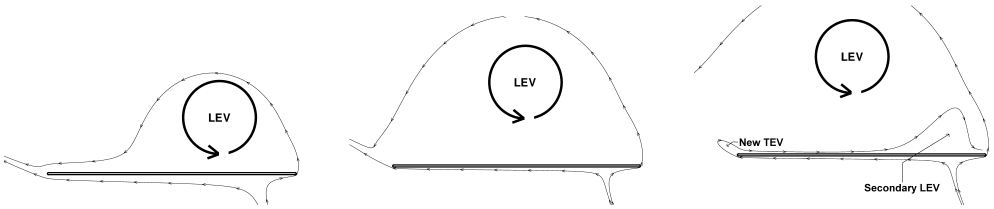

(a) (b) (c)

Figure 5.22: Evolution of flowfield in time showing formation of 2nd TEV (see text). Angle of attack is 45°, and $Re = 500$. 1% thick elliptical aerofoil has travelled approximately 1 chord (since impulsive start) in (a), 1.4 chords in (b), and 1.8 chords in (c).

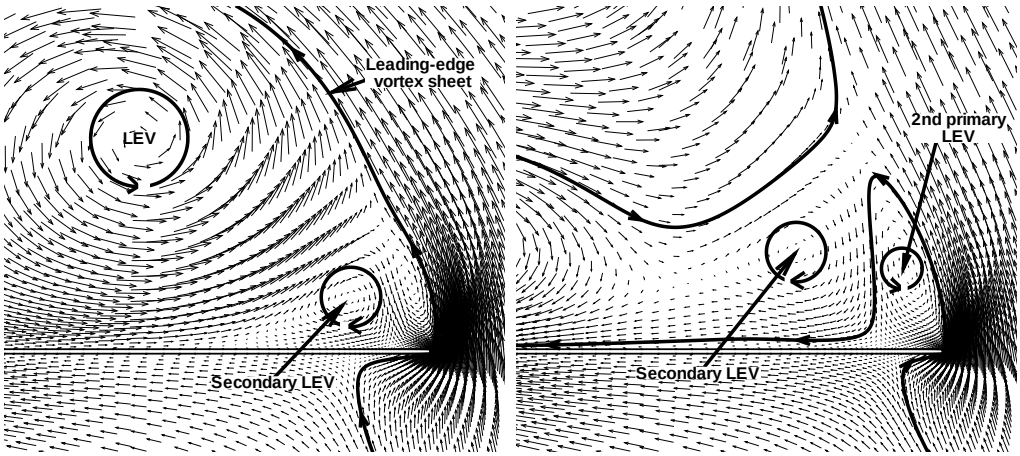

(a) (b)

Figure 5.23: Secondary leading-edge vortex and 2nd primary LEV formation. Visualised by instantaneous vectors. Freestream flow is from bottom right, angle of attack is 45°, and $Re = 500$. 1% thick elliptical aerofoil has travelled approximately 1 chord since impulsive start in (a) and approximately 3.5 chords in (b).

wake.

Also in Figure 5.22(c) it is noticeable that the streamline that originates at the trailing edge and then flows forwards (under the LEV) separates from the aerofoil's surface near the leading edge and then reattaches. This is due to another vortex that is formed in the corner of fluid between the leading-edge vortex sheet and the aerofoil itself. It is well known that when a vortex is adjacent to a trapped area of fluid, another vortex (known as a *secondary vortex*) is created in the trapped area of fluid — see, for example, Van Dyke (1982, Figure 61) or Moffatt (1964). In the current case, the area of fluid is 'trapped' by the aerofoil and the leading-edge

vortex sheet. The secondary leading-edge vortex is visible in Figure 5.23(a). It is evident that the secondary vortex is caused by viscosity — if the fluid were inviscid, no secondary vortex would occur. It is caused by the fact that the flow induced by the primary LEV is unable to negotiate the sharp corner at the leading edge (formed between the aerofoil and the leading-edge vortex sheet) and so separates from the surface aft of the leading edge, leaving a closed volume of fluid. The induced velocity of the primary LEV then causes this volume of fluid to rotate and it becomes what has been denoted a secondary LEV. It is shown later that this secondary LEV becomes important as Reynolds number is increased further. Note the terminology — a secondary LEV is one that is created by a primary LEV. The word 'LEV' in this thesis refers to a primary LEV. There are also secondary TEVs, created by the influence of the primary TEVs; but these do not have as much influence on the flow as secondary LEVs because the primary TEVs do not remain above the trailing edge of the wing long enough for the secondary TEVs to strengthen. They are more significant at higher Reynolds numbers, as is shown later.

The formation of a new TEV causes fluid to flow forward from the trailing edge, underneath the primary LEV. This causes the primary LEV to lift off from the surface of the aerofoil. It is at this point, perhaps, that the LEV could be defined as having been 'shed'. As the LEV sheds, the secondary LEV merges with the 2nd TEV (which lies just off to the left of Figure 5.23(b)) and the combined vortex sheds from the aerofoil. A 2nd primary LEV is then formed which LEV grows, eventually causing another TEV, and the cycle repeats.

Once the flow has reached this stage, the process described above repeats and the familiar von Kármán street wake formation is seen (Figure 5.24). The shed vortices are weak and indistinct at $Re = 25$ but become stronger and more obvious at higher Reynolds numbers. Because the flow is now unsteady (vortices are shed alternately from leading and trailing edges) the force produced by the aerofoil is also unsteady. However, at $Re = 25$ the shed vortices are weak, and they have little impact on the force produced by the aerofoil (see Figure 5.16). It is only when Reynolds number is increased to 100 that significant fluctuations in lift coefficient

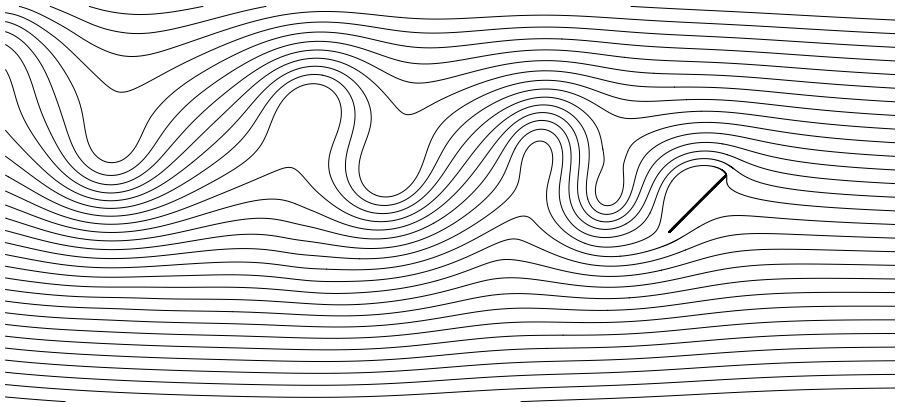

Figure 5.24: von Kármán street behind aerofoil at 45° angle of attack. Visualised by instantaneous streamlines. Flow is from right to left and $Re = 500$.

begin to be seen as vortices are shed (after the initial LEV is shed).

Figure 5.25(a) shows the lift on an aerofoil against chords travelled for a variety of Reynolds numbers of $O(10)$, $O(100)$, and $O(1\,000)$. It is important to note the discussion regarding numerical dissipation in §4.3.2 at this point; it is maintained here that the cell Reynolds numbers are still low enough to avoid this become a problem, even at the highest Reynolds numbers tested, for the reasons presented there. It can be seen that the force/time history differs from that seen at low Reynolds numbers (i.e. Reynolds numbers less than 25) in that the force is unsteady. It is also clear that as Reynolds number is increased, the amplitude of the force peaks also increases. However, providing that Reynolds number is within the range $250 \leqq Re \leqq 1\,000$, the basic *shape* of the graph does not change radically. It is possible to explain the shape of the graph by considering what is happening in the flow.

5.3.2.2 Force on the aerofoil and the link with circulation

Figures 5.26 and 5.27 allow us to examine the dynamic lift force and pitching moment and attempt to relate these to the vortices that are shed from the aerofoil. After the initial peak, which is due to added-mass forces, both of the two components of lift remain almost constant until the aerofoil has moved about 1.5 chords. This is a little unusual, because the circulation bound to the aerofoil (and hence the lift) would normally be expected to rise gradually during this period, due to

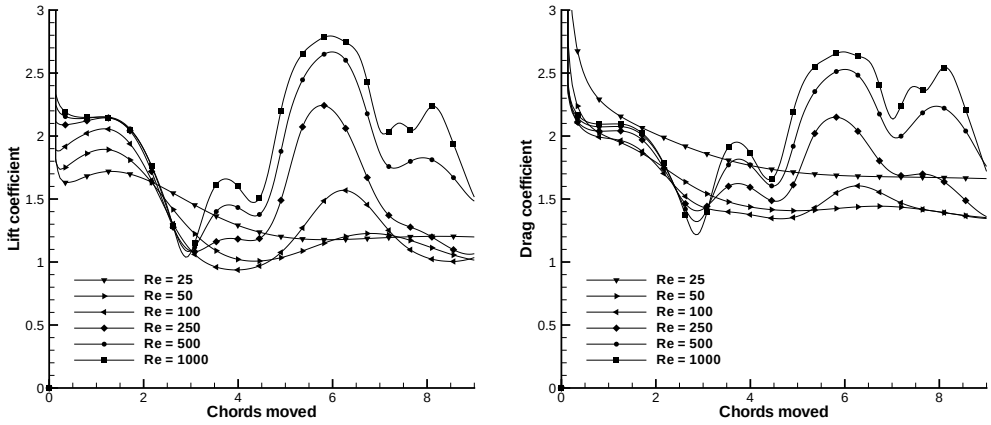

(a) Lift (b) Drag

Figure 5.25: Lift and drag coefficients vs. chords moved for an impulsively-started, 1% thick elliptical aerofoil for a range of medium Reynolds numbers. Angle of attack is 45°.

the Wagner effect (see page 57).

The Wagner effect as originally defined applies to aerofoils at low angles of attack, and therefore only includes separation at the trailing edge. The Wagner effect predicts that as soon as an aerofoil (at a low angle of attack) is impulsively started, the lift 'jumps' to half of its steady state value, indicating that a positive circulation is *immediately* (i.e. an infinitesimal time after motion starts) created around the aerofoil. In order to satisfy the requirement that the net circulation in the flow must remain zero (assuming that the flow was originally at rest), there must be an equal but opposite circulation shed into the wake — the starting vortex. So separation occurs at the trailing edge *immediately*.

In the case under consideration, there is obviously an instantaneous 'jump' in bound circulation. Figure 5.26 shows that after the added mass peak, the lift coefficient is around 2.2. If the angle of attack were 90°, a lift coefficient of zero would be expected and vorticity would be shed from the leading and trailing edges at an equal rate (at least initially). The fact that for this 45° angle of attack case the lift coefficient is initially positive indicates that, at the same time as the wing starts to move, more vorticity is shed from the trailing edge than from the leading edge. The resulting bound circulation will be denoted the 'initial bound

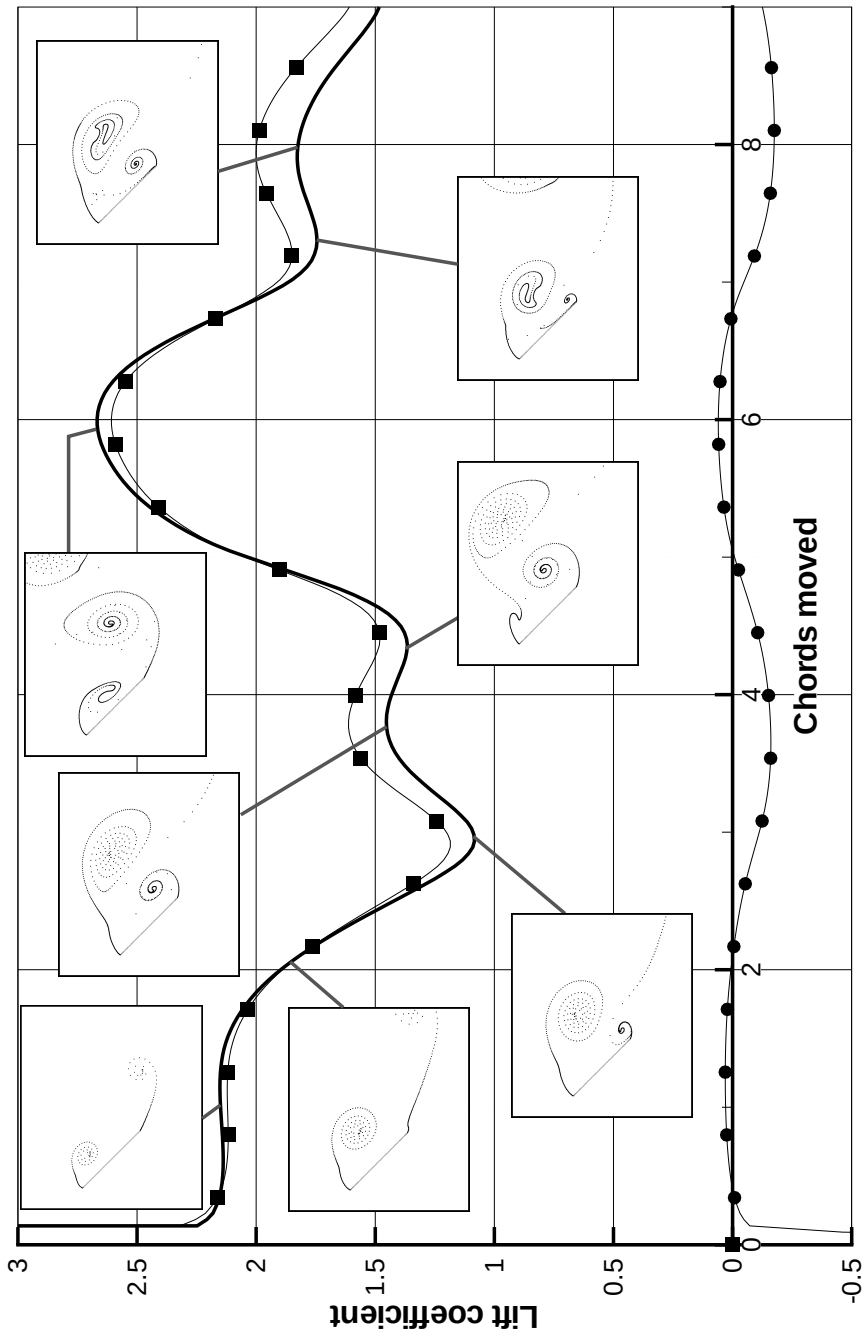

Figure 5.26: Pressure (square markers), viscous (round markers), and total (thick line) lift coefficients vs. chords moved for an impulsively-started, 1% thick elliptical aerofoil at $Re = 500$ and angle of attack 45°, showing vortical structures at points of interest. The structures are visualised by particles which are periodically released from the leading and trailing edges and then move freely with their local flow velocity — in effect, this is equivalent to releasing dye into the flow.

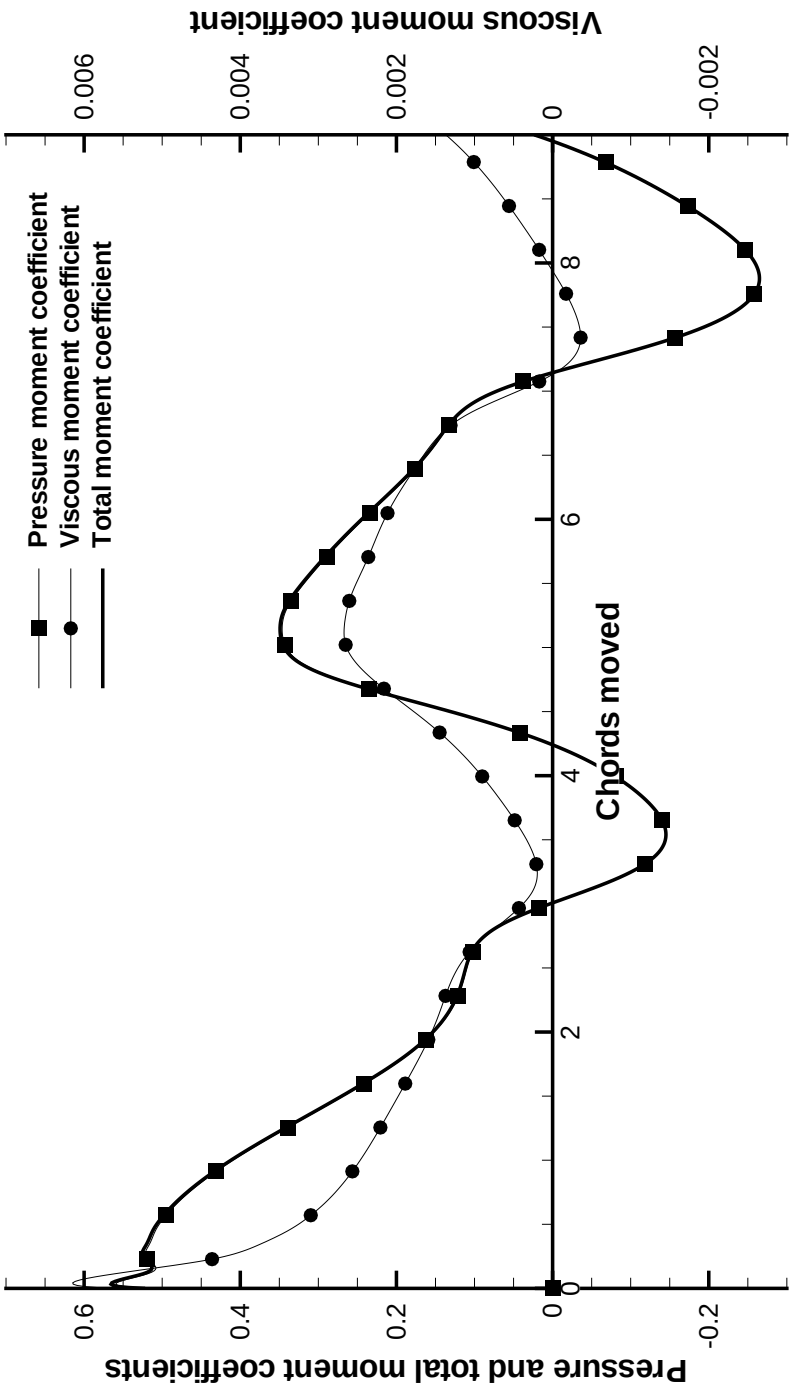

Figure 5.27: Pressure, viscous, and total moment coefficients (about the midchord) vs. chords moved for an impulsively-started, 1% thick elliptical aerofoil at $Re = 500$ and angle of attack 45°. Note that the viscous pitching moment (right-hand scale) is generally about 1% of the total pitching moment (left-hand scale). Leading edge upwards pitching is positive.

circulation', as it exists *as soon as* motion starts.

Separation would be expected to occur (and a vortex would be expected to form) more readily at the trailing edge, because the angle through which the flow has to turn to follow the aerofoil surface is larger there. The results above, for very low Reynolds numbers, support this view; at $Re = 5$, separation occurs at the trailing edge but not at the leading edge (see Figure 5.13 on p. 151). This view is also supported by the experimental results of Ohmi et al. (1990); Huang et al. (2001) and the CFD results of Katz et al. (1996), where the starting vortex (TEV) is seen to form almost as soon as the aerofoil starts motion, whereas the LEV starts to form a short time afterwards. Huang et al. (2001, Figure 7) appears to show the LEV beginning to form after around 0.25 chords of travel. This will be denoted 'delayed leading-edge separation' — note that this is *not* the same as delayed or dynamic stall. However, 'delayed leading-edge separation' may have some role in delayed stall — if the angle of attack of an aerofoil is increased whilst it is in motion, separation will occur at the trailing edge more readily than at the leading edge. The trailing edge is moving in a direction (due to the rotation) which *increases* the effective velocity of the oncoming flow there. Conversely, the leading edge is moving (due to the rotation) in a direction which tends to *reduce* the velocity of the oncoming flow at the leading edge. Thus vorticity will be shed at the trailing edge more readily than at the leading edge, leading to a rise in the lift-producing circulation bound to the aerofoil and a corresponding rise in lift.

So, for a short time after the aerofoil has started motion, separation occurs only at the trailing edge. Only a trailing-edge vortex is shed and the Wagner effect initially operates as for lower angles of attack — there is an 'initial jump' in the lift as the 'initial bound circulation' is created. However, in the current case the lift coefficient then remains roughly constant for around 1.5 chords of travel. Over this period circulation is being shed into both the leading- and trailing-edge vortex sheets, but the lift on the wing is constant.

Shedding circulation into the leading-edge vortex sheet will tend to decrease the lift on the wing (because circulation shed into the LEV will be positive and so the bound circulation will therefore *decrease*) whereas shedding circulation into

the trailing-edge vortex sheet will tend to increase the lift on the wing (because circulation shed into the TEV will be negative and so the bound circulation will therefore *increase*). It might therefore be concluded that vorticity is being shed into the two vortex sheets at the same rate in order to keep the circulation bound to the wing constant. However, this view is simplistic, and does not take account of the fact that the LEV *itself* augments the lift on the wing by its presence, as is discuss shortly.

To summarise: negative circulation is being created at the trailing edge and fed into the TEV, leading to a rise in positive circulation bound to the aerofoil (the Wagner effect, as traditionally understood) but at the same time positive circulation is being fed into the LEV. At the same time the growing LEV itself is enhancing the lift on the aerofoil because of its position. The combination of these effects is such that the actual lift on the aerofoil remains constant.

This initial lift plateau was noted by Dickinson and Götz. They said that it was unexpected, and stated "the cause of this discrepancy is unclear" (Dickinson and Götz, 1993, p. 57). Dudley commented that "few experimental data exist on the magnitude of the Wagner effect for wings at the Re and kinematic profiles appropriate to insect flight" (Dudley, 1999, p. 128), implying that the Wagner effect may not exist due to the low Reynolds number and high angle of attack. It is suggested here that the Wagner effect does in fact *exist*, but that it is 'cancelled out' — at least in this 45° angle of attack case — by the presence of separation at the leading edge, which means that the rise in bound circulation (due to the Wagner effect) is counteracted by the shedding of this bound circulation into the LEV sheet. In §5.4 the effect of changing the angle of attack of the aerofoil is investigated; this sheds further light on this phase of the wing motion.

During these first two chords of motion, there is a strong positive pitching moment due to the formation of the LEV over the leading edge of the aerofoil. This pitching moment decreases as the leading-edge vortex moves aft. At about 2 chords travelled, the LEV lies almost directly above the midchord, and thus would not be expected to produce a pitching moment at all. The pitching moment that *does* exist at this point is a result of the low pressure area that is due to the

secondary LEV.

The fact that LEVs enhance lift is almost universally accepted, but little attention has been paid to the question of how this works in practice. It has already been seen that at very low Reynolds numbers, LEVs enhance lift by increasing the lift due to viscous forces. This effect still occurs for the $Re = 500$ case, as is shown in Figure 5.26, but the viscous lift is small compared to the pressure lift, and there are also large peaks in pressure lift. It is not possible, therefore, to attribute the lift-enhancement due to an LEV entirely to the fact that LEVs increase *viscous* lift.

Some authors (see e.g. van den Berg and Ellington, 1997a; Muijres et al., 2008) have asserted that the LEV enhances lift because it is 'bound to the aerofoil' and therefore its circulation can be thought of as bound circulation. In other words, if an LEV is present, the aerofoil's bound circulation is effectively increased by an amount exactly equal to the circulation within the LEV. The main problem with this proposal is that, for 2D flows at least, any LEV is eventually shed into the wake. At what point does the circulation within the LEV change from being 'bound to the aerofoil' to being in the wake? If there is such a point, an instantaneous drop in lift would be expected, when the LEV circulation goes from being 'bound' to being 'shed'. No such drops are shown in the current CFD data or indeed in the experimental data of Dickinson and Götz (1993).

Based on the logic above (that the leading-edge vortex enhances lift because it is 'bound to the aerofoil'), some have gone so far as to calculate the circulation within the LEV from flow-visualisation data and have then used the equation $L = \rho V \Gamma$ to calculate the lift that is contributed by the LEV. van den Berg and Ellington followed this process and concluded that "the leading-edge vortex can supply up to two-thirds of the required lift during the upstroke" (van den Berg and Ellington, 1997a, p. 335). It is suggested here that this view is simplistic. Γ, in the equation just quoted, is the circulation *bound* to the aerofoil. Just because a vortex is *close to* the aerofoil, it is not possible to conclude that its circulation can be simply added to the wing's bound circulation. It is suggested here that in reality and by definition, any circulation that is within the LEV is *not* bound to

the wing. Therefore the conclusion of van den Berg and Ellington is unwarranted and possibly misleading.

The presence of an LEV does enhance lift, and therefore the LEV appears to increase the *circulation* bound to the aerofoil. What has not been proved is that this increase in circulation is *exactly equal* to the circulation of the LEV, and indeed there is no reason why this should be the case. In other words, if at a given time the circulation bound to the aerofoil is Γ_a and the circulation in the LEV is Γ_b, it does not immediately follow that the lift produced by the aerofoil will be equal to $\rho V (\Gamma_a + \Gamma_b)$. More reasonably, it could be the case that the lift produced will be equal to $\rho V (\Gamma_a + k\Gamma_b)$, where k is a constant whose value depends on the exact location of the LEV.

To back up this suggestion, consider the case of a cylinder in a flow. It is well-known that if the Reynolds number exceeds a certain value, vortices will be shed alternately from the sides of the cylinder, and this will lead to a fluctuating force normal to the freestream flow direction. While a vortex is attached, a circulation will be present about the cylinder and attached vortex and hence a force will occur. But it is not necessarily true that the net circulation can be calculated simply by summing the circulation bound to the cylinder and the circulation within the vortex. If this were the case it would be necessary to pinpoint when the vortex was no longer attached. In reality, as a vortex moves away from the cylinder, its influence will reduce gradually — there will not be a point at which it suddenly becomes detached. Whether or not a vortex is 'attached' is hard to determine — for example, the first flow-visualisation image in Figure 5.26 shows an LEV which most people might call 'attached', but in the second image it is not so clear-cut.

As another illustration, consider the case of a delta wing at a high angle of attack. It is well known that a pair of vortices will be formed above the wing in such a case, which augment lift. It appears that there is some increase in the circulation about the wing due to the presence of these vortices. But if the structure of the flow is considered, it is clear that much of the circulation in the two vortices is in a direction which is normal to the direction of the (lift-producing) circulation about the wing. It seems to make little sense to add these two circulations and

state that this circulation is bound to the wing.

Instead of the view proposed above, it is more accurate to carefully state that the presence of a vortex close to a body can produce 'extra' force, but that the magnitude of this extra force depends on a number of factors; not only the circulation of the vortex, but also its position, and (for 3D cases) its orientation. This view is in accordance with that of Walker and Westneat, who stated that pressure differences (due to the presence of a vortex) on either side of an aerofoil "distort the flow in a way that *creates the appearance* of a bound circulation superimposed over the freestream" (Walker and Westneat, 2002, p. 1036, emphasis added). In other words, the presence of a vortex in close proximity to the aerofoil creates extra lift, and therefore it *appears* as though the aerofoil has 'extra' bound circulation. However, it is important to reiterate the fact that the magnitude of this 'extra' bound circulation may not be the same as the magnitude of the circulation in the vortex.

At around 1.5 chords of travel (referring back to Figure 5.26), the lift starts to decrease. At this point, the rate at which negative circulation is being fed into the TEV is reducing (as occurs with the traditional Wagner effect), but the positive circulation bound to the wing is continuing to be shed from the wing into the LEV. At the same time the LEV is moving further away, meaning that its lift-enhancing effect is reducing. Note that this is a smooth reduction — there is not a point at which the LEV suddenly goes from being 'attached' to being 'shed', with a corresponding sudden drop in lift.

An intuitive way of looking at the flow from this point onwards is to think in terms of pressure (as opposed to thinking in terms of circulation). Because of the relatively high velocities within a vortex, it is an area of low pressure. The actual pressure within a vortex is inversely proportional to its strength, so that as the strength of a vortex increases, the pressure at its core drops (Bartol et al., 2003). Therefore, if a vortex exists — no matter in which direction it is rotating — above the aerofoil, it will cause 'extra' lift to be produced. Thinking in this way helps to avoid the confusion mentioned above.

At around 3 chords moved, the drop in lift caused by the detachment of the

first LEV is halted by the production of a TEV. It is immediately evident that there is a difference between this second TEV and the first TEV (the starting vortex). Whereas the first TEV moves immediately away from the aerofoil, the second TEV is 'sucked' forward by the influence of the first LEV, and eventually lies directly above the aerofoil. As mentioned, the TEV is an area of low pressure, and therefore it causes lift to start to rise again. It seems that the first LEV is now far enough away that its influence is negligible, and the fact that it continues to move further away does not have any effect on the lift produced by the aerofoil.

This second TEV also produces a strong negative (leading edge down) pitching moment, as would be expected due to its location above the trailing edge, but as it moves away from the trailing edge its effect is diminished and at the same time the second primary LEV is starting to form above the leading edge, leading to a sharp increase in clockwise pitching moment which peaks at around 5 chords of travel — about 1 chord before the lift force peaks due to the LEV.

The fact that TEVs enhance lift would be counter-intuitive if the reasoning that attached LEVs directly augment circulation were followed. The direction of circulation for a TEV is in the opposite direction to that of an LEV and it might be expected, therefore, that an attached TEV would *reduce* lift. The fact that this is *not* the case adds extra weight to the assertion that the reasoning described above is too simplistic. Those who have followed the reasoning above have often found themselves in difficulty. For example, Miller and Peskin state that "the shedding of the LEV reduces lift while the shedding of the [TEV] augments lift" (Miller and Peskin, 2004, p. 3085). This implies that while an LEV is attached it will enhance lift, whereas when a TEV is attached it will decrease lift, whereas the current results indicate that *both* enhance lift. Miller and Peskin base their reasoning on the fact that when vortices are shed from a cylinder, the 'lift' force fluctuates from positive to negative as vortices are shed alternately from each side. However, in the case of a cylinder, half of the vortices form on the geometrically-upper side of the cylinder, whilst half form on the lower side. Therefore the two types of vortex would be expected to produce forces in opposing directions. Here, however, both LEVs and TEVs form above the upper surface of the aerofoil and therefore both

produce an 'extra' force in the same (upwards) vertical direction. As has been said, the effect of a vortex depends not only on its sign and strength, but also its location.

Referring back to Figure 5.26, the next prominent feature is now considered. It has been noted that between about 1.5 and 3 chords, the lift is dropping as the first LEV is moving away from the aerofoil. At just less than 3 chords, the lift starts to rise again due to the presence of the newly-formed second TEV. This rise is short-lived, because, as can be seen in Figure 5.26, this second TEV moves away from the aerofoil more quickly than an LEV. For about a chord of travel, the TEV grows and spreads over the aerofoil's upper surface, but by around 3.7 chords of travel, this TEV has moved away from the aerofoil and its effect starts to wane, so that lift starts to decrease once more. Lift decreases until about 4.5 chords have been travelled, at which point the second LEV starts to form.

The second LEV is, again, an area of low pressure, and it enhances lift. It grows until it spreads over practically the entire upper surface of the aerofoil (at around 6 chords travelled). The effect of this second LEV is significantly more pronounced than the effect of the second TEV, for the simple reason that it remains over the aerofoil for longer; firstly, because it starts further forward (being formed at the leading edge rather than the trailing edge) and secondly because the effect of the second TEV is to force the second LEV downwards onto the aerofoil's surface, resulting in the 'squashed' form of the second LEV seen in Figure 5.26 at about 6 chords travelled. At this point the pitching moment is decreasing as the LEV moves aft (Figure 5.27).

Why is a plateau in lift for the second and subsequent TEV/LEV pairs not seen, as it was for the first pair? The answer lies in the fact that during the impulsive start, separation occurs almost instantly at the trailing edge but not so at the leading edge, as described above. During the subsequent constant-speed motion, delayed leading-edge separation does not occur; separation is *always* occurring at the leading edge.

At this point, the flow becomes periodic. The second LEV produces a third TEV which causes the second LEV to shed, and the third LEV forms; the third

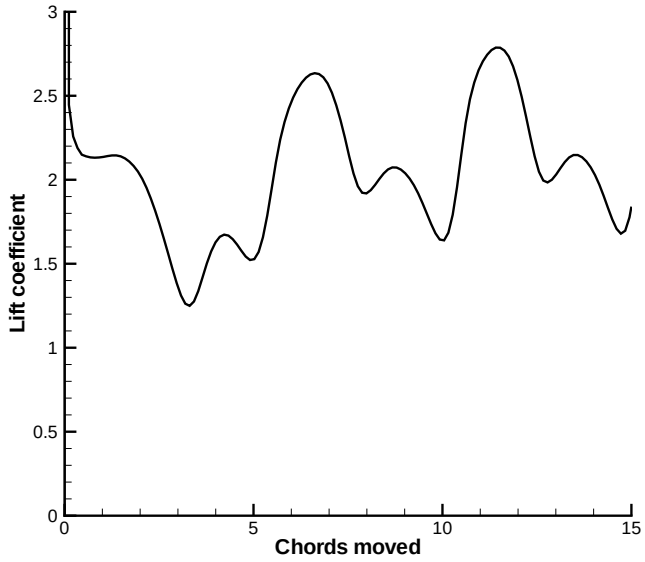

Figure 5.28: Extended time-history of lift coefficient vs. chords moved for an impulsively-started 1% thick elliptical aerofoil at $Re = 500$ and angle of attack 45°.

LEV produces the fourth TEV which results in the fourth LEV; and so on. Inspection of the resulting force data reveals that this also becomes periodic, as would be expected. Figure 5.28 shows that the height of the peaks relating to the shed vortices does increase for the third cycle relative to the second[3] but the periodicity of the force/time history is clear.

Figure 5.26 also gives further insight into the contributions of viscous and pressure forces at this Reynolds number. It was noted that for the low Reynolds numbers discussed above (§5.3.1), the viscous force always reduces the net lift force whilst increasing the net drag force. In this case, however, the viscous lift force fluctuates and for a significant proportion of the time is slightly positive. Examining the corresponding vortical structures reveals that LEVs rotate in a direction which induces a flow on the upper surface towards the leading edge. Thus the viscous force — at least over a portion of the upper surface — acts in a direction parallel to the aerofoil and towards the leading edge (thus contributing to lift). TEVs have the opposite effect, causing a flow on the upper surface which is

[3]This seems likely to be due to subtle changes in the shape of the shed vortices — compare the shape of the first and second LEVs in Figure 5.26, for example.

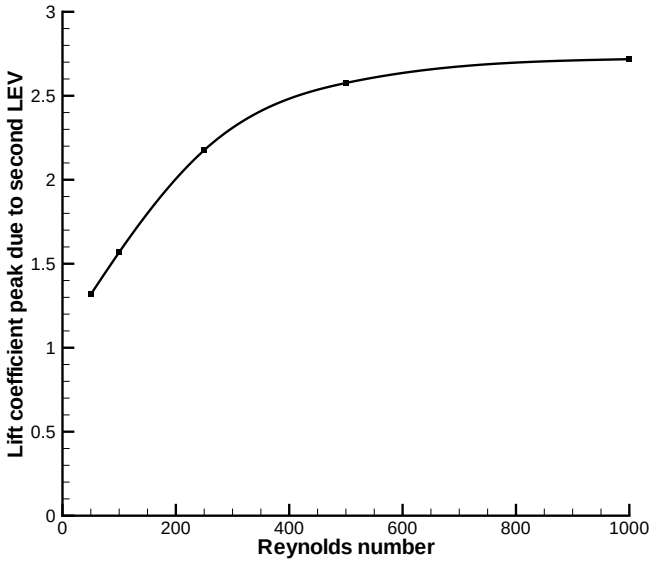

Figure 5.29: Peak lift coefficient due to second LEV vs. Reynolds number; angle of attack 45°. 1% thick elliptical aerofoil is impulsively started.

towards the trailing edge and therefore a viscous force which reduces lift.

Figure 5.26 is for a Reynolds number of 500. Referring back to Figure 5.25, for Reynolds numbers lower than this, the effect of the shed vortices is much reduced; and for Reynolds numbers higher than this, the effect of the shed vortices is increased, up to a point. This can be explained by considering the link between the strength of the shed vortices and the Reynolds number of the flow. At low Reynolds numbers, viscosity tends to 'damp out' any shed vortices, and limits their strength and therefore their lift-enhancing effect. In fact, at $Re = 100$, the second and subsequent TEVs do not produce a lift peak at all, whereas they do for higher Reynolds numbers. The effect of Re on the lift peaks can be visualised by plotting the value of the peak due to the second LEV against Reynolds number; see Figure 5.29. The magnitude of the peak increases up to about $Re = 1\,000$ at which point it levels off and remains roughly constant, although it is shown later (§5.3.3.1) that identifying a peak due to a specific LEV becomes more difficult at higher Reynolds numbers due to high-frequency fluctuations in lift force.

Shed vortices would be expected to strengthen as Reynolds number is increased — Mittal et al. state that "as the Reynolds number increases, the vortices that

roll up tend to be of higher strength...Thus, as the Reynolds number increases, the magnitude of the suction pressure increases" (Mittal et al., 2004, p. 168). The strength of a vortex at a given time is defined by the *net* rate at which vorticity has been fed into it in the past. At low Reynolds numbers, this net rate is diminished because of the large amount of vorticity diffusion. As Reynolds number is increased, the rate of diffusion will decrease, so that, at a given time, the shed vortices will be stronger at higher Reynolds numbers than at lower Reynolds numbers. However, the rate of increase diminishes as Re is increased, so that the effect of increasing Re from (say) 50 to 200 is much greater than the effect of increasing Re from 500 to 2000. This is because the impact of changing Re *decreases* as Re is *increased*; so that a change in Reynolds number when Reynolds number is low has a larger impact than a change *of the same magnitude* when Reynolds number is high.

5.3.3 High Reynolds numbers ($Re > 1\,000$)

5.3.3.1 The occurrence of Kelvin-Helmholtz instability

In Figure 5.25 for the $Re = 1\,000$ case, an interesting feature is seen in the force/time history between around 7 and 8 chords moved. Whereas for the $Re = 500$ case the lift fluctuations remain smooth and low-frequency, at $Re = 1\,000$ a certain amount of higher-frequency fluctuation is seen, particularly in the later stages of the lift/time history.

Figure 5.30 shows that these high-frequency fluctuations in lift become more severe and more dominant, and that they occur earlier in the development of the flow, as Reynolds number is increased further. At $Re = 15\,000$ the high-frequency fluctuations occur immediately after the aerofoil has started motion.

Examining the flow field reveals the reason for this increasing unsteadiness. As Reynolds number increases, the vortex sheets becomes less stable. This is illustrated in Figure 5.31, which compares the evolution of the flow field for two Reynolds numbers (500 and 5 000). The flow at $Re = 500$ is as just described — a TEV has been shed immediately on the aerofoil starting, and an LEV builds up gradually and smoothly, fed by the leading-edge vortex sheet. The flow at

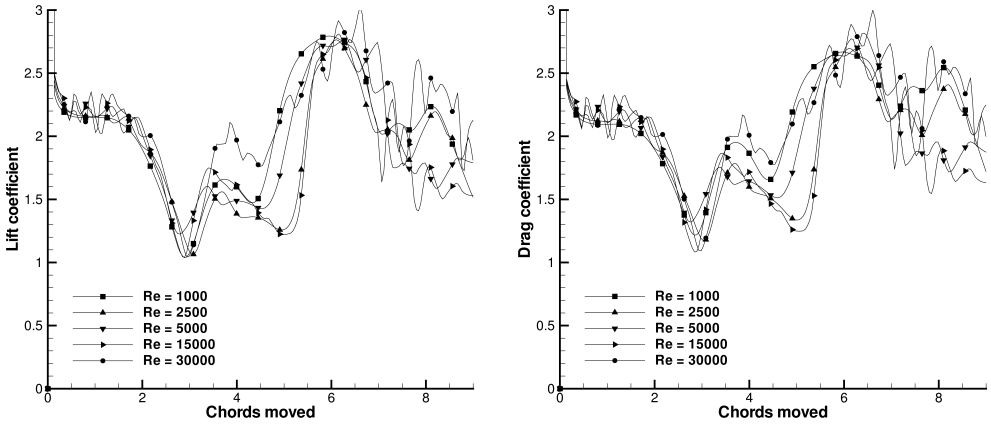

(a) Lift (b) Drag

Figure 5.30: Lift and drag coefficients vs. chords moved for a range of high Reynolds numbers. Angle of attack is 45°. 1% thick elliptical aerofoil.

$Re = 5\,000$ is more complex — the leading-edge vortex sheet breaks down readily, so that the area of vorticity at the leading edge is composed of a central vortex and a number of associated smaller vortices. These smaller vortices rotate in the same direction as the primary LEV and eventually merge with it. In this work, these small vortices will be denoted "breakdown vortices"; the term "secondary vortex" (which could be used) has already been used to refer to those vortices which are formed by the induced velocities of the primary vortices.

There has been some controversy in the literature over the origin of these breakdown vortices. One of the first to note their formation was Prandtl (1904), in his seminal paper on boundary layer theory, but the first detailed photographic images of the phenomenon were captured by Pierce (1961). An example of his work is given in Figure 5.32. Later, Koumoutsakos and Shiels (1996) investigated the phenomenon computationally and concluded that the breakdown vortices appeared only when the plate was uniformly accelerated, not when it was impulsively started. However, the highest Reynolds number they simulated for the impulsively-started case was $Re = 1\,000$, at which Reynolds number the current results indicate that the instability is only just appearing. Their conclusion — that the instability "depends on the acceleration of the plate" — therefore seems unfounded, as the current results (and others) show that the instability occurs even when the plate

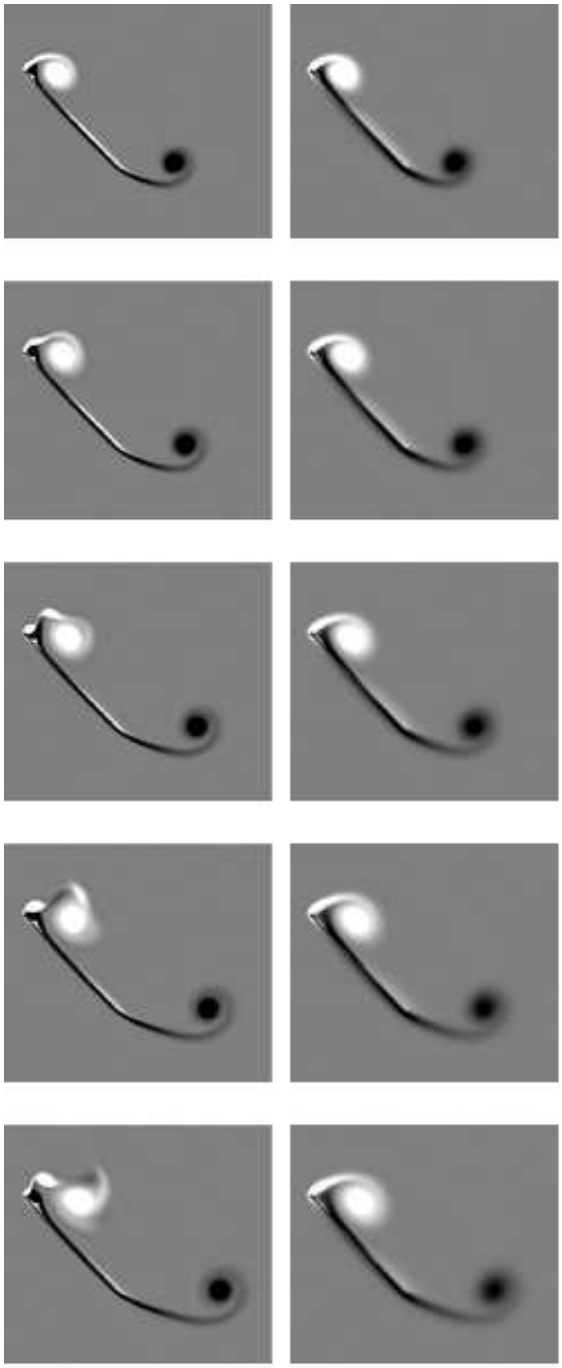

Figure 5.31: Comparison of flow evolution for two Reynolds numbers — $Re = 500$ (right) and $Re = 5\,000$ (left). Light areas show clockwise vorticity, dark areas show anti-clockwise vorticity. The impulsively-started 1% thick elliptical aerofoil has travelled around 0.5 chord lengths at the start of the sequence (top of page) and about 1 chord length at the end of the sequence. Angle of attack is 45°.

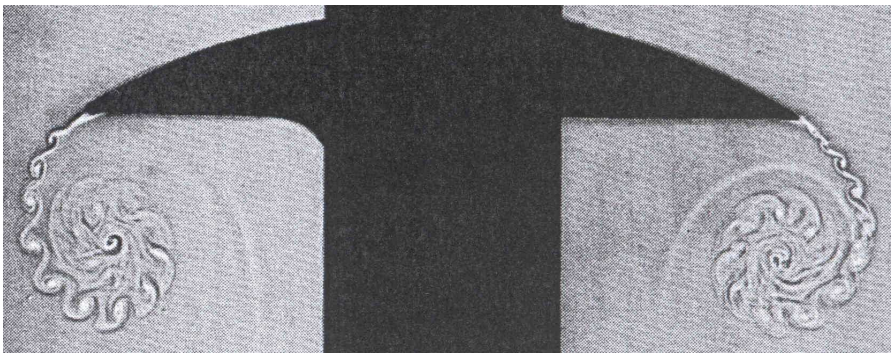

Figure 5.32: Example of the results of Pierce (1961). The D-shaped plate is moving upwards. Primary vortices have been shed from both edges and (what have been called here) breakdown vortices are clearly visible around them. The Reynolds number in this case is approximately 38 000 (based on instantaneous velocity and plate width).

is moving at constant speed, providing that Reynolds number is high enough.

This breakdown of the vortex sheet also occurs in the trailing-edge sheet (see Figure 5.33). However, trailing-edge vortices generally have less impact on forces because they move away from the aerofoil more quickly than leading-edge vortices. The leading-edge vortex, as mentioned above, is one of the primary causes of enhanced lift, and it might be intuitively supposed that this breakdown of the leading-edge vortex could be a problem for FMAVs, which are likely to operate in the region of $Re = O(10\,000)$. Later, it is demonstrated that in fact this is not the case.

What is the cause of this vortex sheet breakdown? The fact that the phenomenon becomes more apparent as Reynolds number increases indicates that it is at least affected by viscosity. A number of clues indicate that this breakdown is caused by Kelvin-Helmholtz instability (KHI). It is known that two-dimensional vortex sheets are susceptible to this type of instability (Kim et al., 2003).

KHI occurs over a wide range of Reynolds numbers and situations. It can occur anywhere where there is a shear layer within the fluid or between two different fluids — that is, a discontinuity in velocity, density, or viscosity[4]. For example, it is due to KHI that wind blowing over water causes waves. The effects of KHI can occasionally be seen in cloud formations (see e.g. Figure 5.34), and signs of KHI

[4]For a detailed discussion of KHI, see Drazin and Reid (1982, §4).

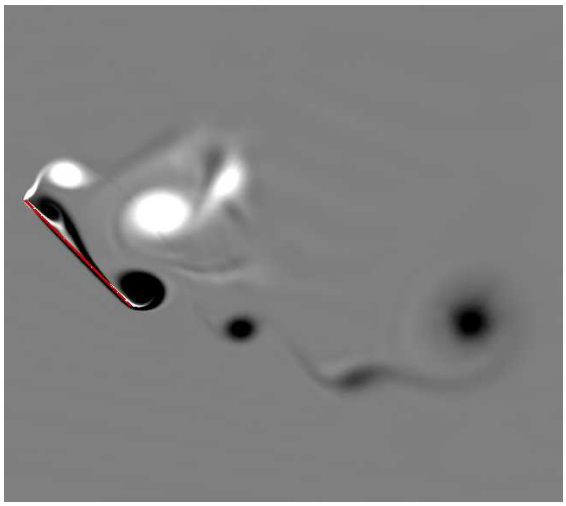

Figure 5.33: Contours of vorticity for $Re = 5\,000$; shaded as in Figure 5.31. The initial trailing-edge vortex is on the right and two smaller trailing-edge vortices can be seen forming in the trailing-edge vortex sheet. The second primary trailing-edge vortex can also be seen building up over the aerofoil's trailing edge. The 'untidy' nature of the leading-edge vortex is apparent. Angle of attack is 45°.

Figure 5.34: KHI in clouds, from Pretor-Pinney (2007).

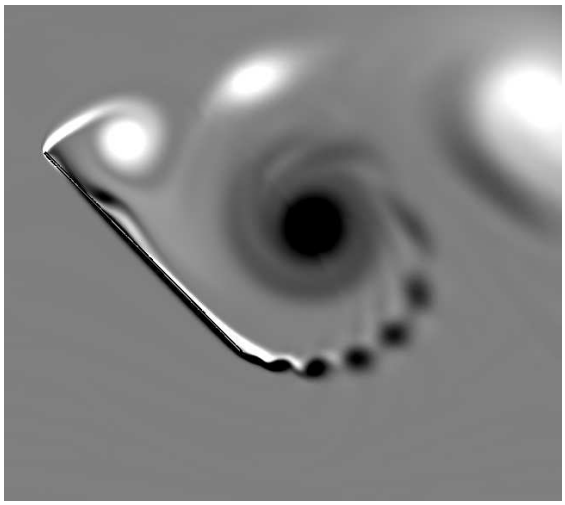

Figure 5.35: Contours of vorticity for $Re = 5\,000$; shaded as in Figure 5.31. The trailing-edge vortex sheet shows signs of KHI — 'bunching' of vorticity at points along the sheet. Angle of attack is 45°.

have even been identified far distant from the earth (see e.g Lobanov and Zensus, 2001).

A significant sign of KHI is a vortex sheet 'bunching' into areas of vorticity (breakdown vortices). This can be seen to some extent in the trailing-edge vortex sheet in Figure 5.33, and to a greater extent in Figure 5.35. It does not occur around the initial (starting) trailing-edge vortex (for reasons that will be explained later) but becomes evident in all subsequent trailing-edge vortices (provided that Reynolds number is sufficiently high).

The susceptibility to KHI of a vortex sheet depends on three factors; firstly, the ratio of densities of the fluids on either side of the sheet; secondly, the ratio of viscosities of the fluids on either side of the sheet, and, thirdly, the gradient of tangential velocity of the fluids across the sheet. The first two of these three factors, in this case, are irrelevant, because in all cases the viscosity and density of the fluid are equal on either side of the sheet[5]. It is safe, therefore, to assume that the KHI in this case is caused solely by the velocity difference across the sheet. At low Reynolds numbers, the vortex sheets are thickened due to the increased dominance of viscosity, meaning that the velocity gradient decreases; so that the

[5] The fluid is assumed to be incompressible — widely accepted as a reasonable assumption at these low Reynolds numbers. However, see discussion on p. 97.

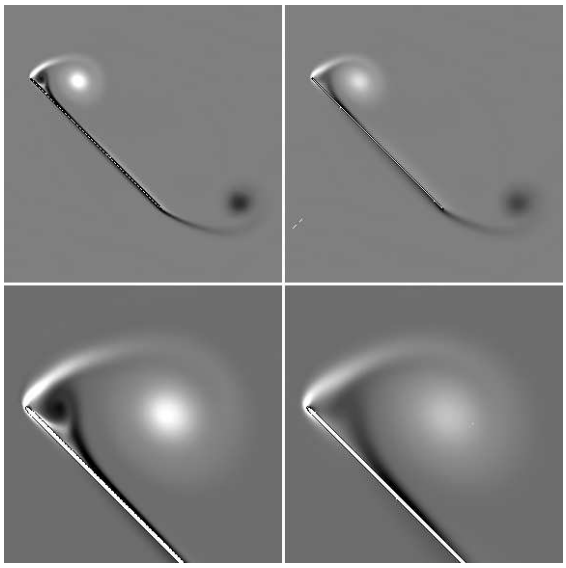

Figure 5.36: Contours of vorticity for $Re = 1\,000$ (right) and $Re = 5\,000$ (left); shaded as in Figure 5.31. Lower frames are enlargements of upper frames. Reynolds number is varied by changing fluid viscosity — freestream velocity is equal in both cases. Angle of attack is 45° and 1% thick elliptical aerofoil has moved around 0.5 chords since an impulsive start.

sheet is less susceptible to KHI.

It is easy to jump to the conclusion that increasing Reynolds number means that velocity has been increased, and therefore of course KHI will occur more readily. However, it is important to realise that the susceptibility of a sheet to KHI depends on the velocity *gradient* across the sheet, not simply the *magnitude* of the velocities on either side of the sheet. KHI also occurs when Reynolds number is increased by other means — for example by increasing fluid density or chord length, or by decreasing fluid viscosity. It is not immediately obvious how taking one of these steps increases the velocity gradient across the vortex sheets. It is clear that as Reynolds number is increased, the vortex sheets will become thinner and therefore the velocity gradient will increase, but the results presented here indicate that the situation is in reality more complex than this.

To investigate this, Figure 5.36 shows the flow field for two Reynolds numbers — 1 000 and 5 000. Here, the Reynolds number is varied by changing fluid viscosity, so that the velocity of the free-stream is equal in both cases. It can be seen that the higher Reynolds number flow produces stronger leading- and trailing-edge vortices

(this is shown by the centres of the vortices being lighter and darker respectively), and this is as would be expected — at higher Reynolds numbers the viscous forces are lower in proportion to the inertial forces, so that vortices develop and strengthen more readily. This alone, however, does not directly explain the increased KHI at higher Reynolds numbers[6].

Looking at the leading-edge vortex structures in Figure 5.36 more closely reveals the secondary vortex at the leading edge which was discussed in §5.3.2.1. This is of opposite sign to the leading-edge vortex — i.e. it rotates anti-clockwise in Figure 5.36. Figure 5.36 also shows that the magnitude of this vortex depends on the Reynolds number of the flow — higher Reynolds numbers produce stronger secondary vortices. This is what would be expected, as at higher Reynolds numbers vortices are created more readily due to the reduced importance of viscosity.

Because the secondary vortex at the leading edge is rotating in the opposite direction to the main leading-edge vortex, there is a velocity at the leading edge of the aerofoil which is almost opposite in direction to the flow that is separating from the leading edge. The magnitude of this velocity is proportional to the strength of the secondary vortex.

This is seen in Figure 5.37, where the velocity of the free stream is the same for both Reynolds numbers (as in Fig. 5.36). The velocity on the left of the leading-edge vortex sheet is therefore equal for both cases. However, for the higher Reynolds number case, because the secondary vortex is stronger, there is a larger velocity difference across the leading-edge vortex sheet, and the sheet is therefore more susceptible to KHI.

The TEV sheet also breaks down due to KHI, but in this case the KHI can stem from either of two causes. The TEV sheet is initially stable, because the presence of the starting vortex ensures that there is very little velocity gradient across the trailing-edge sheet. However, as the starting vortex moves away from the aerofoil, and the LEV grows in size, the trailing-edge sheet becomes unstable — because the LEV induces velocities *above* the trailing-edge sheet that are in the opposite

[6] KHI is not evident in Figure 5.36 for either Reynolds number, but it becomes evident for both later in time — sooner for $Re = 5\,000$ than for $Re = 1\,000$.

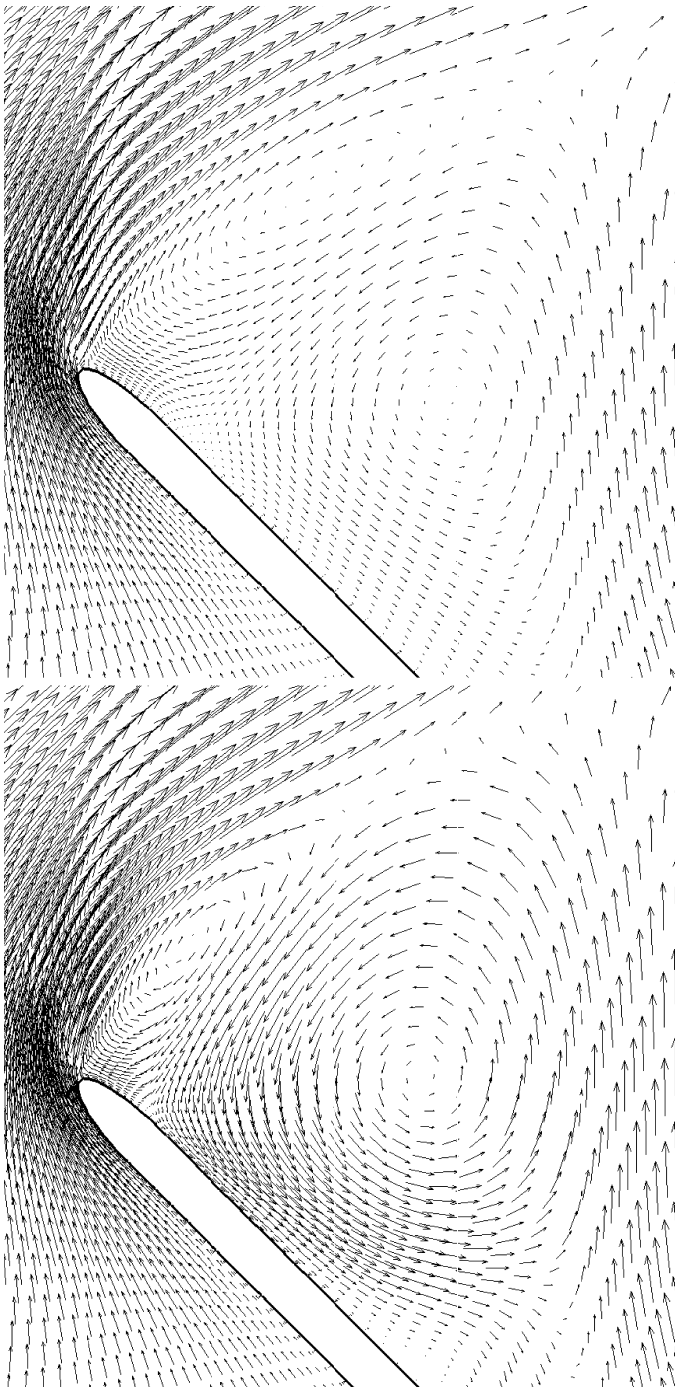

Figure 5.37: Velocity vectors for $Re = 1\,000$ (top) and $Re = 5\,000$ (bottom). Both frames are further enlargements of the data in Figure 5.36. **Note:** the *primary* leading-edge vortex lies to the right of each frame — the vortex seen here is the *secondary* vortex (see text), as can be seen by examining its direction of rotation. Angle of attack is 45°.

direction to those *below* the trailing-edge sheet. The velocity difference is therefore increased and the stability of the trailing-edge sheet decreases.

Subsequent TEVs are unstable (at higher Reynolds numbers) due to a secondary vortex that is produced at the trailing edge of the aerofoil (which can be seen in Figure 5.35 as a light coloured area above the trailing edge). This does not occur with the initial TEV (the starting vortex) because the first TEV moves quickly away from the aerofoil. Subsequent trailing-edge vortices, however, remain above the aerofoil's trailing edge for longer and therefore a secondary TEV is created.

It is worth noting that many inviscid models (such as that of Ansari (2004)) cannot capture any secondary vortices — vorticity is only released from the leading and trailing edges. Some KHI in the trailing-edge vortex sheet *is* captured due to the interaction between the leading-edge vortex and the trailing-edge vortex, but the leading-edge vortex breakdown is not captured, and the KHI in the trailing-edge vortex sheet, seen in Figure 5.35, is also not reproduced. This explains the smoothness of Ansari's data in Figure 5.9 when compared to the $Re = 200\,000$ CFD data.

The occurrence of KHI complicates matters when Strouhal number is considered. At lower Reynolds numbers, vortices are shed in turn from the leading and trailing edges, so that Strouhal number is easy to calculate. When KHI starts to occur, vortices are shed more regularly — Fig. 5.35 shows that the trailing-edge sheet is actually made up of a line of discrete vortices (although it could be argued that this is always the case and that any vortex sheet could be thought of as made up of discrete vortices). There are, therefore, two mechanisms of vortex shedding at higher Reynolds numbers — one dealing with the large-scale shedding that is seen at lower Reynolds numbers, and the other dealing with the small-scale shedding (due to KHI) that is seen only at higher Reynolds numbers. Therefore, in effect, two distinct Strouhal numbers exist at higher Reynolds numbers.

This phenomenon has been noted in the wake of spheres by Sakamoto and Haniu (1990). They found that below a Reynolds number of 800 (based on sphere diameter) only large-scale shedding was observed. However, above $Re = 800$ they found that "the higher and lower frequency modes of the Strouhal number coexist"

(Sakamoto and Haniu, 1990, p. 386). Perhaps not surprisingly it seems that this phenomenon also occurs in the flow around a flat plate at high angles of attack. The lowest Reynolds number at which KHI is seen in the current study is $Re = 1\,000$.

5.3.3.2 Primary vortex shedding frequency

Figure 5.30 is somewhat difficult to interpret due to the high-frequency fluctuations that have already been discussed. However, it is possible to determine that the frequency of primary vortex shedding does remain virtually constant over this range of Reynolds numbers. This is important to note, as it indicates that the occurrence of KHI does not affect the shedding of primary vortices.

Another notable feature of Figure 5.30 is the large magnitude of the peak at around 4 chords travelled in the $Re = 30\,000$ case when compared to the results for lower Reynolds numbers. The reason for this is unclear, but inspection of the CFD data indicates that it is due to a fortuitous occurrence of KHI, which is particularly dominant at this highest Reynolds number. The process of vortex shedding has been described in detail for the $Re = 500$ case above. For higher Reynolds numbers the situation is more complicated — the LEV sheet breaks down due to KHI more readily. If this breakdown happens at the right moment, it can result in the next primary LEV forming slightly earlier than it would if KHI did not occur. In turn, this can mean that a primary LEV and primary TEV both lie above the aerofoil simultaneously, leading to their lift-enhancing effects being combined. This is interesting, but it is important to realise that it is merely due to KHI occurring at a particular moment. In fact, this effect probably accounts for the different magnitudes of peaks for all of the force/time histories in Figure 5.30. It is important to emphasise that although KHI can cause LEVs and TEVs to form slightly earlier than would otherwise be expected, it does not alter the average primary vortex shedding frequency.

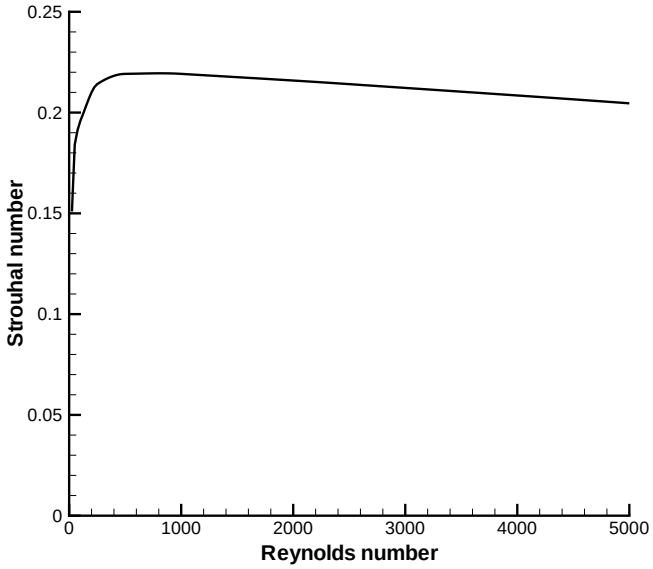

Figure 5.38: Strouhal number vs. Reynolds number for a 1% thick elliptical aerofoil in steady motion at 45° angle of attack.

5.3.4 The relationship of Strouhal number to Reynolds number

It has already been shown (§5.2) that Strouhal number is dependent on Reynolds number only. However, how this relationship 'works' has not been determined — how does Strouhal number change as Reynolds number is increased? From the data above, it is clear that at higher Reynolds numbers Strouhal number remains constant — in Figure 5.25, for example, the peaks and troughs (which relate to the shedding of vortices) lie at about the same positions for most of the different Reynolds numbers. It is only at low Reynolds numbers that notable variation in Strouhal number are seen. This is illustrated by Figure 5.38.

It is clear that Strouhal number can be considered roughly constant when $Re > 500$, and that the constant value lies close to 0.21; although there is a slight drop in St as Reynolds number is increased up to $Re = 5\,000$. This value is close to that determined by others. For example, Chen and Fang (1996) gave a Strouhal number of around 0.22 for a flat plate at an angle of attack of 45° and Reynolds numbers of 11 000 to 32 000. However, they did not investigate lower Reynolds numbers. The current results indicate a sharp decrease in Strouhal number as Re

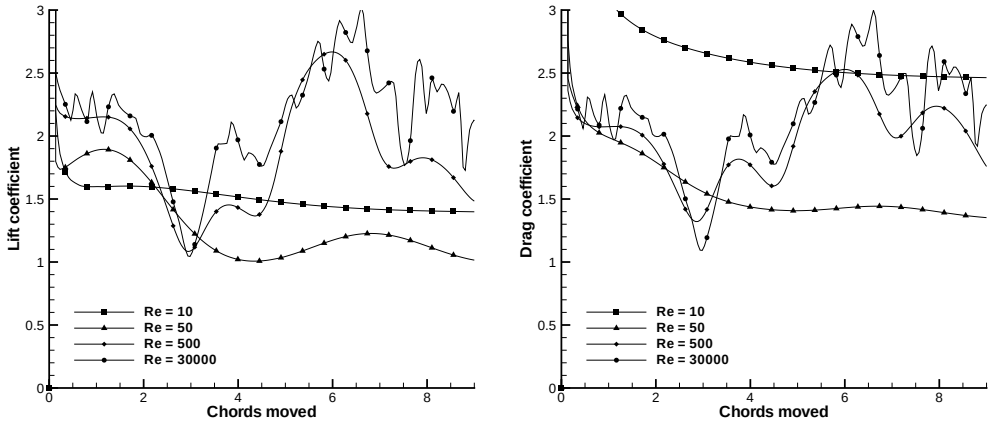

(a) Lift (b) Drag

Figure 5.39: Lift and drag coefficients vs. chords moved for an impulsively-started 1% thick elliptical aerofoil for a range of Reynolds numbers. Angle of attack is 45°.

decreases below $Re = 500$. This indicates that vortices are shed less frequently at lower Reynolds numbers, and this assertion is supported by the changing shape of the curves in Figure 5.21. Later, it is shown that Strouhal number is dependent on angle of attack (§5.4).

Because Strouhal number remains roughly constant for $Re > 500$, and an LEV is only shed once it reaches a certain size, it is possible to conclude that the rate at which an LEV grows is roughly independent of Reynolds number for $Re > 500$. In other words, the size of the LEV will not depend on Reynolds number, but only on the distance that the aerofoil has travelled since that LEV started to form. This becomes important 3D flows are considered.

5.3.5 Summary of Reynolds number effects

Looking now at the entire range of Reynolds numbers — from 5 to 30 000 — a summary of what has been found is given. Firstly, it has been seen that for a 1% thick elliptical aerofoil at 45° angle of attack and low Reynolds numbers ($Re < 25$) vortices are not shed. If $Re > 5$ a stable 'bubble' of recirculating flow is formed above the wing. At $Re = 25$ this bubble becomes unstable and separates. This leads to a recurring pattern of LEV and TEV shedding. From $Re = 25$ to $Re = 1\,000$, this pattern remains fairly similar, although the frequency of vortex

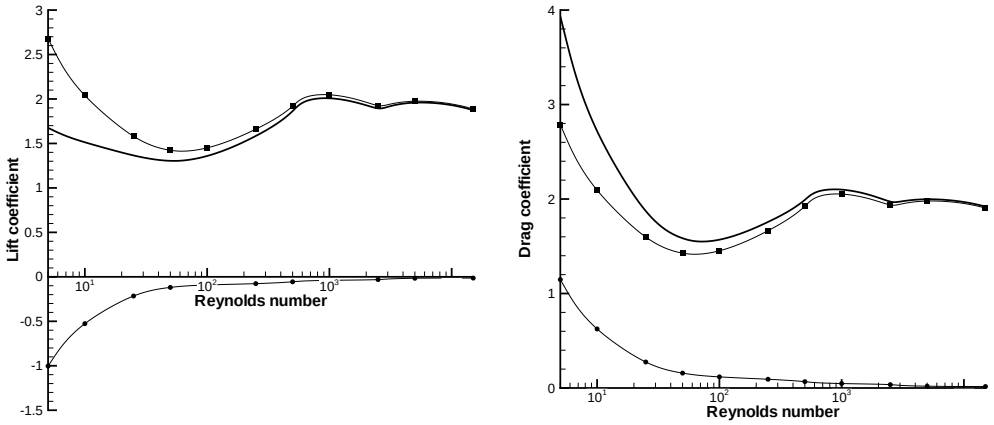

(a) Lift (b) Drag

Figure 5.40: Average pressure (squares), viscous (circles), and total (thick line) lift and drag coefficients for an impulsively-started, 1% thick elliptical aerofoil for a range of Reynolds numbers. Angle of attack is 45°. Note the log scale on the x-axis.

shedding does increase between $Re = 25$ and $Re = 500$. At $Re = 1\,000$, KHI starts to appear in the leading- and trailing-edge vortex sheets, leading to high-frequency fluctuations in lift. These changes are manifest in Figure 5.39.

It is interesting to examine a plot of average lift coefficient (lift coefficient averaged over the first 9 chords of travel after an impulsive start, but ignoring the peak due to added mass) against Reynolds number (Figure 5.40). Here, a decline in this average is seen, until vortex shedding starts to occur at $Re = 50$, and the average then increases as the shed vortices increase in strength. After this the average lift remains almost constant. It is also clear that, as expected, viscous force coefficients decrease as Reynolds number increases; in fact, the variation can be approximated fairly well by a power relationship (as in Figure 5.41). At $Re = 30\,000$, average viscous drag accounts for less than 0.4% of average total drag, meaning that inviscid models can safely be used here. At lower Reynolds numbers (particularly below $Re = 50$) the validity of the inviscid assumption, made in many analytical models, is called into question by the current results.

It has been noted already that as Reynolds number is increased, the strength of the shed vortices increases. This leads to a relationship between Reynolds number and vortex core pressure, with higher Reynolds numbers leading to vortices with

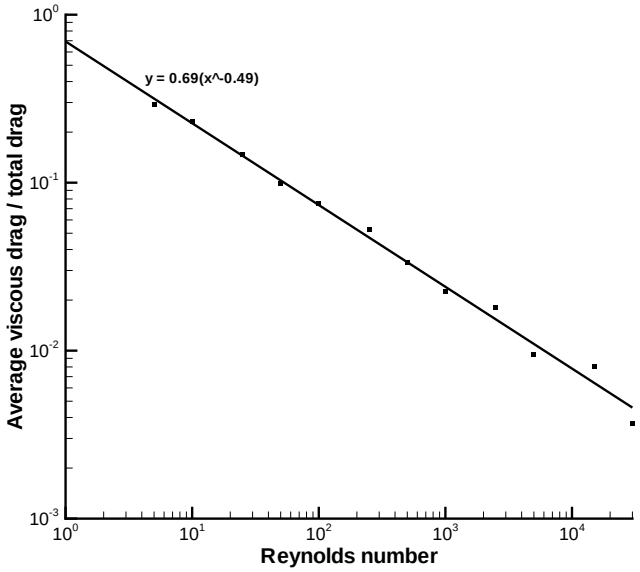

Figure 5.41: Average proportion of drag due to viscous drag vs. Reynolds number for an impulsively-started, 1% thick elliptical aerofoil at an angle of attack of 45°. Note the log scales.

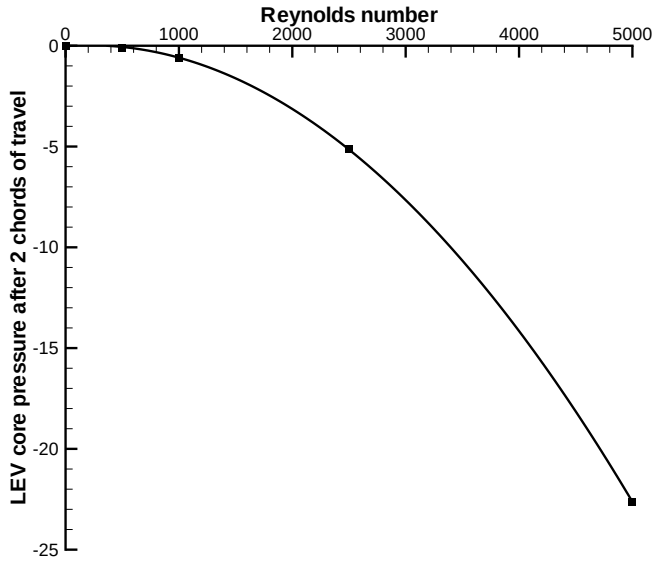

Figure 5.42: LEV core pressure vs. Reynolds number for an impulsively-started, 1% thick elliptical aerofoil, two chords of travel after an impulsive start. Angle of attack is 45°.

lower core pressures. This is shown in Figure 5.42. This relationship is almost exactly a quadratic one — if the Reynolds number is doubled, there is a four-fold decrease in LEV core pressure. This is exactly as would be expected, due to the link that exists between pressure and velocity squared[7].

5.4 Effect of aerofoil angle of attack

Some insight into the effect of angle of attack was gained from the comparison of results from the current CFD model with the results of Dickinson and Götz (1993) above (§5.1.1). This was at a Reynolds number of 192. The relevant CFD results are presented again in Figure 5.43. Recall that in this case the aerofoil was uniformly accelerated to a constant velocity. This explains the initial peak (between 0 and 0.5 chords of travel), caused by added-mass forces.

After the initial added-mass peak (which exists from zero to 0.5 chords of travel), the plot for 45° angle of attack resembles those seen when examining the effect of Reynolds number (particular in §5.3.2.2), as expected, because the Reynolds number here (of around 200) is in the 'medium' range as defined above. There is a plateau of constant lift force until around 2 chords moved, due to the combination of delayed leading-edge separation and the Wagner effect, as explained above (§5.3.2.2). However, it is apparent that for angles of attack above 45°, the lift coefficient during the first two chords of travel (but after the initial added-mass peak) has a downwards trend, whereas for angles of attack below 45° it has an upward trend.

At low angles of attack, the initial bound circulation that instantaneously develops during the 'delayed leading-edge separation' phase of motion (i.e. the initial phase when separation has occurred at the trailing edge but not the leading edge) is reduced (relative to higher angles of attack), because the starting vortex is weaker due to the lower angle of attack (a weaker starting vortex means less positive circu-

[7] Bernoulli's equation, in the cases under consideration here, can be written as

$$p + \frac{1}{2}\rho V^2 = constant,$$

as gravity is ignored and incompressible flow is assumed.

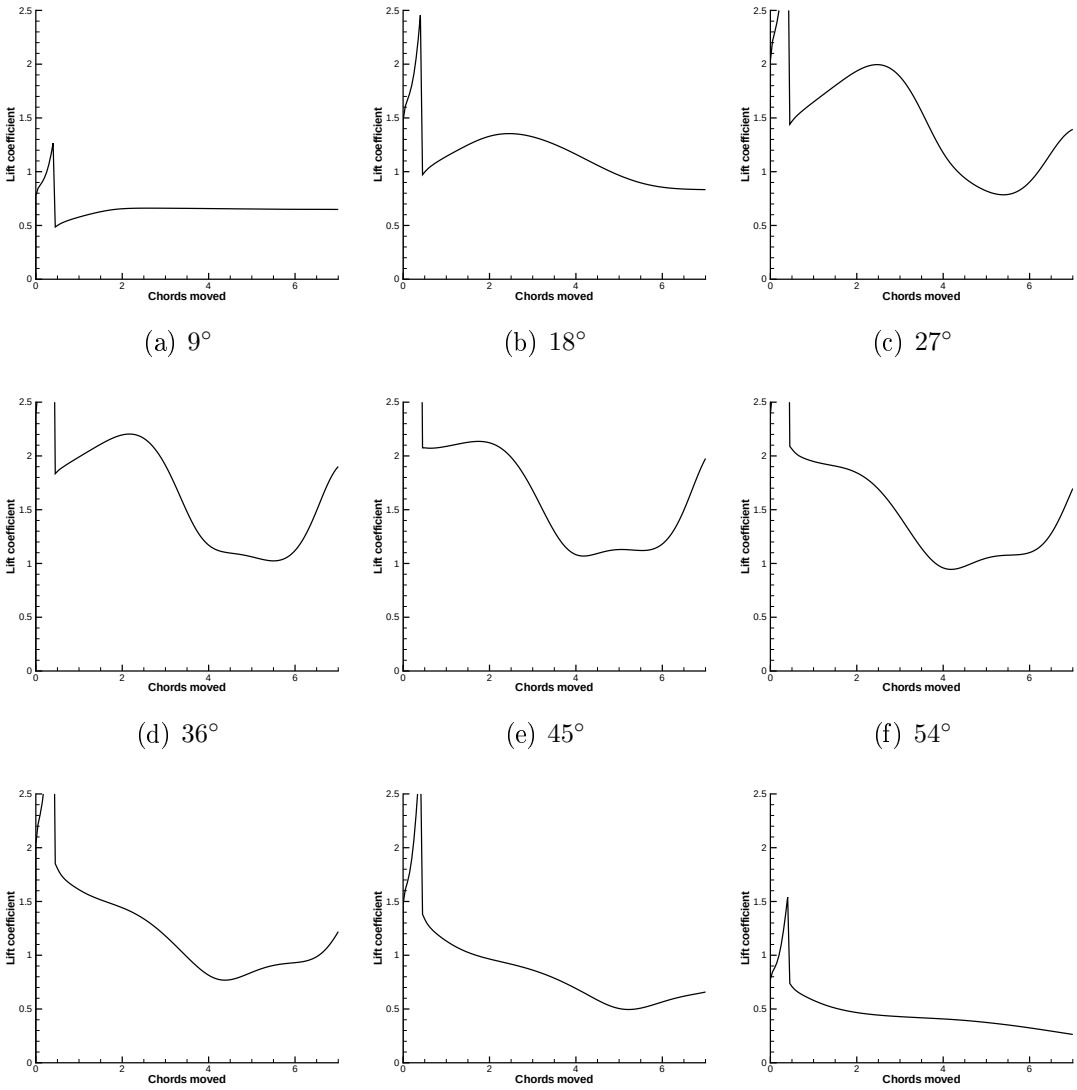

(a) 9° (b) 18° (c) 27°

(d) 36° (e) 45° (f) 54°

(g) 63° (h) 72° (i) 81°

Figure 5.43: Lift coefficient vs. chords moved for a uniformly-accelerated flat-plate aerofoil at various angles of attack. $Re \approx 200$.

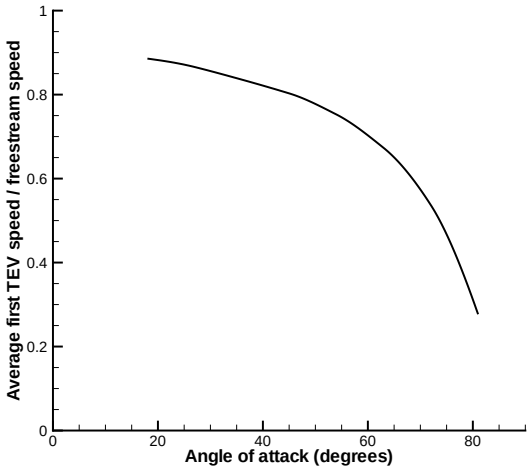

Figure 5.44: Speed of first TEV (averaged over first 7.5 chords of travel and relative to freestream speed) vs. angle of attack for a uniformly-accelerated flat-plate aerofoil. $Re \approx 200$.

lation bound to the aerofoil). At the same time, the rate of growth of the strength of the leading-edge vortex is also reduced due to the fact that the separation angle at the leading edge is reduced, so that the rate at which the initial bound circulation is fed into the LEV is reduced.

So as angle of attack (α) is decreased from the 45° baseline case, two things happen. Firstly, the strength of the starting vortex decreases (due to the lower angle of attack), so that the initial bound circulation (and therefore the initial jump in lift) is reduced — it can clearly be seen that the lift coefficient (immediately after the initial added mass peak, at around 0.5 chords of travel) decreases as α decreases. The value at an angle of attack of 18° is around 1, whereas the value at 9° is around 0.5.

Secondly, this initial bound circulation is shed into the LEV sheet more slowly at lower angles of attack, because the LEV is weaker due to the lower angle of attack.

As mentioned in §5.3.2.2, at the same time as the initial bound circulation is being fed into the LEV, the Wagner effect is tending to increase the bound circulation and therefore the lift. However, the initial TEV moves away from the aerofoil more quickly at lower angles of attack than at higher angles of attack, as

is shown in Figure 5.44. At an angle of attack of 45° the velocity of the starting vortex (averaged over the first 7.5 chords of travel) is around 80% of the freestream velocity. At 18° the corresponding ratio is almost 90%. Therefore as angle of attack is decreased, the rise in circulation due to the Wagner effect is steeper with respect to time.

At low angles of attack, therefore, the *reduction* in lift due to the initial bound circulation reducing happens more slowly than the *increase* in lift that is due to the Wagner effect, and consequently the net lift *rises*. At 45° the initial plateau is roughly flat; the two effects practically balance each other out, as discussed above.

At higher angles of attack (between 45° and 81°), initial bound circulation is still created (as separation still occurs at the trailing edge before the leading edge), but it appears that the magnitude of the initial bound circulation does not increase relative to the 45° case — in other words, the initial bound circulation reaches a maximum at 45°. The amount of initial bound circulation depends on two things — firstly, the strength of the starting vortex, and secondly the time delay between separation at the trailing edge and separation at the leading edge. As angle of attack is increased, the strength of the starting vortex will increase due to the change in the separation angle at the trailing edge, and this will tend to *increase* the initial bound circulation. But also, the time delay between trailing- and leading-edge separation will decrease, and this will tend to *decrease* the initial bound circulation. At 90° angle of attack, the time delay between trailing- and leading-edge separation will be zero and therefore no initial bound circulation will be created.

At these higher angles of attack ($\alpha > 45°$), the LEV that forms is comparatively strong (due to the large separation angle at the leading edge) and therefore the initial bound circulation quickly decreases. At the same time, the initial TEV moves away rather slowly — Figure 5.44 shows that at an angle of attack of 81° the average velocity of the TEV is less than 30% of the freestream velocity. This means the Wagner effect is more prolonged, so that the Wagner effect-induced circulation *rise* happens more slowly. Therefore, at high angles of attack, the *reduction* in lift (with respect to time) due to the reduction in the initial bound circulation

happens more quickly than the *increase* in lift that is due to the Wagner effect, and consequently the net lift *falls*. In addition, at these high angles of attack, the LEV itself has less of a lift-enhancing effect (even though it is stronger) because the relative magnitude of the component of the force due to the LEV in the vertical direction is smaller.

After the first two chords of travel for most cases, a drop in lift is seen that is due to the LEV being shed, as described above. However, for 9° angle of attack, this drop does not occur, and instead the lift remains almost constant (actually continuing to rise slightly due to the Wagner effect). Examination of the flow-visualisation data reveals that the flow becomes steady at this low angle of attack, with no separation bubble formed. At an angle of attack of 18°, the flow also eventually stabilises, but in this case a large separation bubble is formed. At an angle of attack of 27° the flow is unsteady, with alternate shedding of LEVs and TEVs.

It was noted above that at an angle of attack of 45°, the flow was unsteady if $Re \geq 25$. Now it has been seen that when $Re \approx 200$, the flow is unsteady if the angle of attack exceeds 18°. This suggests that whether a flow is steady depends on two factors: the Reynolds number and the angle of attack of the aerofoil. If Reynolds number is low enough, the flow will be stable even if the angle of attack is 90°. Conversely, at higher Reynolds numbers the angle of attack must be low if the flow is to be stable. Van Dyke (1982) shows an image of a flat plate at an angle of attack of 2.5° and Reynolds number of 10 000 which shows a stable laminar separation bubble. However, as noted above, very little work seems to have been carried out at these low Reynolds numbers ($Re = O(10\,000)$ or lower). For the most part, when there is a reference in the literature to a 'laminar separation bubble', what is actually meant is that the flow separates while laminar, undergoes transition to turbulence, and then reattaches (see e.g O'Meara and Mueller, 1987). Potentially (if enough CFD calculations were run) it would be possible formulate some empirical equation involving Re and angle of attack, the result of which would accurately predict whether a particular case was steady or unsteady. But for the purposes of this thesis it is sufficient to know that a stable 2D LEV is *possible*, but

the higher the Reynolds number, the lower the angle of attack at which the flow will become unsteady. This conclusion is supported by the experimental results of Huang et al. (2001).

Changing angle of attack has an impact on vortex shedding frequency. From Figure 5.43, it appears that as angle of attack is increased, the peak due to the second TEV becomes later, indicating that vortex shedding frequency decreases as angle of attack increases. This is not especially surprising, because as angle of attack is increased, the width of the plate *as seen by the flow* is increased. At 0° angle of attack, the flow effectively 'sees' the *thickness* of the plate, whereas at 90° angle of attack the flow 'sees' the *chord length* of the plate. Between the two extremes there is a gradual increase in the effective width of the obstruction in the flow.

This is in agreement with the experimental results of Chen and Fang (1996). They found that Strouhal number decreased as they increased the angle of attack of a flat plate, and proposed a modified Strouhal number St^*, which, instead of being based on the chord of the plate, was based on the effective width of the plate; defined as "the transverse projection of the distance between the upper and lower separation points on the edges of the plate." In other words, they suggested, if Strouhal number were based on the projected width of the plate rather than its actual length, such a Strouhal number would remain constant with changing angle of attack. They assessed this constant value to be around 0.16.

If St is based on projected length (i.e. $c \times sin\ \alpha$), the result is a value of around 0.15 — close to the 0.16 of Chen and Fang[8]. At an angle of attack of 90° (once vortex shedding has started to occur) the mean vortex shedding frequency is therefore around 71% of the mean vortex shedding frequency for the 45° angle of attack case (because $sin\ 45/sin\ 90 \approx 0.71$); for an angle of attack of 27°, the ratio is 155%.

Plotting lift coefficient (averaged over the first 7.5 chords of travel) against angle of attack, as in Figure 5.45, reveals that, as might be predicted, the angle

[8] The difference can be explained by considering that the calculated Strouhal number here was for a Reynolds number of 500, whereas Chen and Fang studied Reynolds numbers ranging from 3 500 to 32 000.

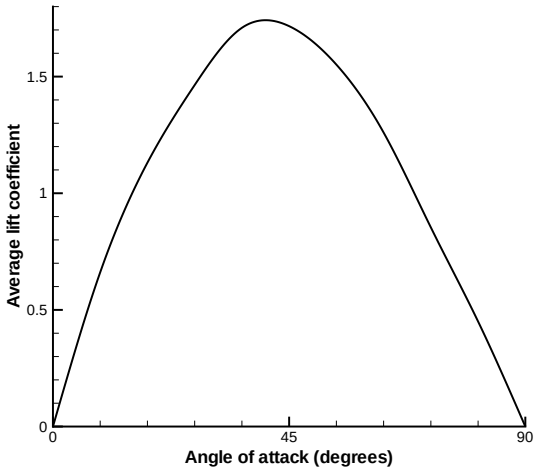

Figure 5.45: Lift coefficient vs. angle of attack for a uniformly-accelerated, flat-plate aerofoil. Lift coefficient is averaged over the entire simulation time (i.e. 7 chords of motion). $Re \approx 200$.

of attack for maximum average lift coefficient is around 45°. In fact, a value of exactly 45° would be expected if viscous forces were excluded from the calculation. Because the aerofoil is very thin, the pressure force on it is almost exactly normal to the chord. The average normal force increases with angle of attack, but lift is the component of this force in the vertical direction; and the relative size of the component of the normal force in the vertical direction will increase up to an angle of attack of 45°, but then decrease if angle of attack is increased beyond 45°. Viscous forces tend to decrease lift so that the angle of attack for maximum lift is shifted away from 45°. The size of the shift will depend on Reynolds number.

Plotting drag coefficient vs. chords moved (as in Figure 5.46) shows, that, as would be expected, drag force generally increases as angle of attack is increased. There is a large initial peak in the drag force (due to added mass), and this peak grows as angle of attack increases. This is because as angle of attack is increased, the width of the aerofoil *as seen by the flow* increases, and at the same time the component of the added-mass force in the drag direction is increasing, because the added-mass force acts in a direction normal to the aerofoil.

Figure 5.47(a) plots average drag coefficient against angle of attack. This confirms the fact that increasing angle of attack generally increases drag force. How-

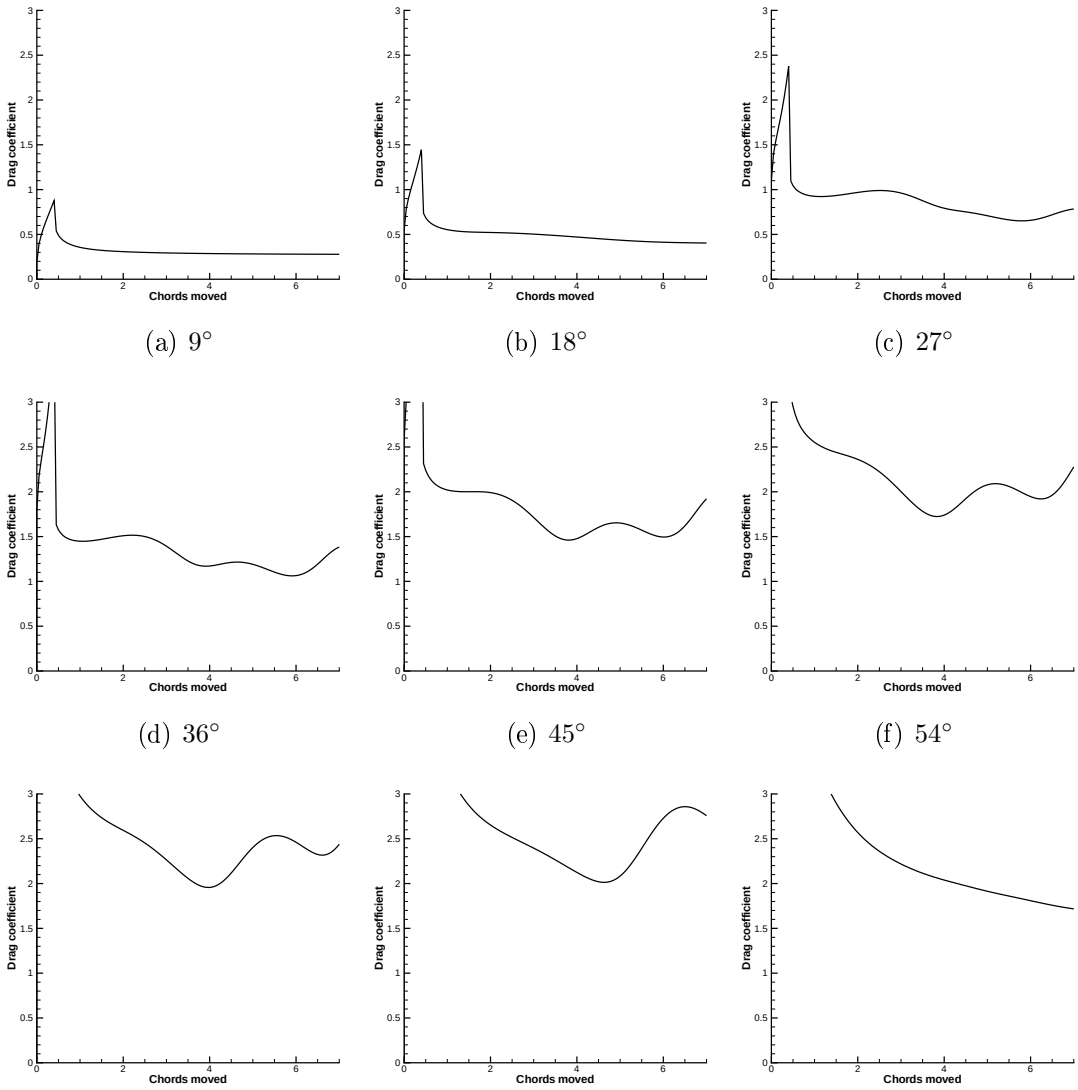

(a) 9° (b) 18° (c) 27°

(d) 36° (e) 45° (f) 54°

(g) 63° (h) 72° (i) 81°

Figure 5.46: Drag coefficient vs. chords moved for a uniformly-accelerated, flat-plate aerofoil at various angles of attack. $Re \approx 200$.

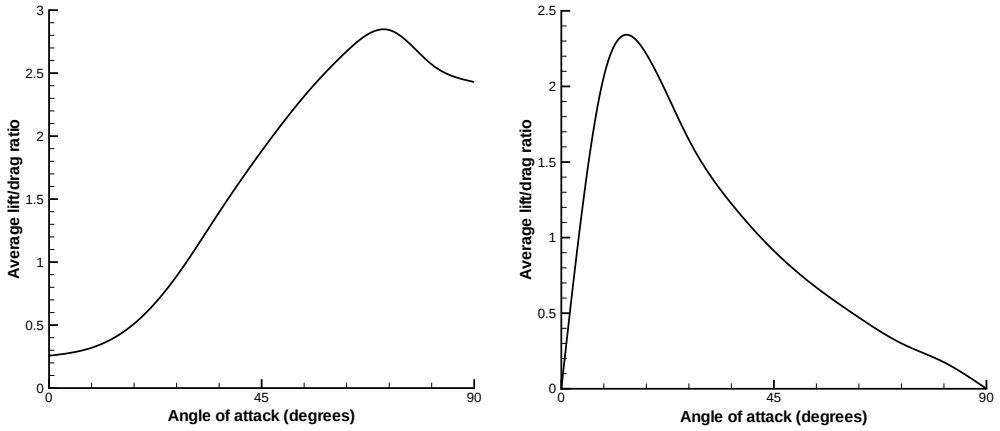

(a) C_D (b) L/D

Figure 5.47: Drag coefficient and lift/drag ratio (both averaged over entire simulation time) vs. angle of attack for a uniformly-accelerated, flat-plate aerofoil. $Re \approx 200$.

ever, at 72° angle of attack this trend reverses, so that increasing angle of attack decreases drag force. It is suggested here that this anomaly is simply a result of the fact that, during the time period over which the average has been taken (the first 7.5 chords of travel) vortex shedding does not occur for the 81° and 90° angle of attack cases, as can be seen from Figure 5.46. It is suggested that when vortex shedding does start to occur in all cases, the average drag force will increase up to a maximum at 90° angle of attack. It has already been noted that vortex shedding occurs more slowly at higher angles of attack.

In traditional analysis of aerofoil performance, the primary measure is often lift/drag ratio, L/D. Plotting the average value of this ratio against angle of attack for the current case (Figure 5.47(b)) reveals an angle of attack for maximum average L/D of somewhere between 9° and 18°. This is where separation starts to occur at the leading edge and a leading-edge vortex is created, leading to a reduction in viscous drag (see p. 155) and an increase in lift (relative to a slightly lower angle of attack where an LEV is not formed). Increasing angle of attack further increases the normal force on the aerofoil, but the component of this force in the vertical direction decreases whereas the component in the horizontal direction increases, leading to a reduction in L/D. Later it is shown that this effect also occurs for 3D

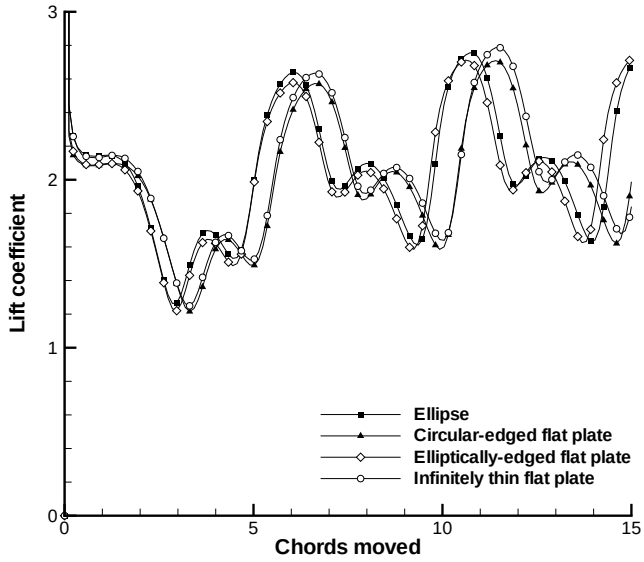

Figure 5.48: Section Comparison at $Re = 500$. Angle of attack is 45° and aerofoil is impulsively started.

cases (§6.6.2).

5.5 Effect of aerofoil cross-section

The above results have used a variety of different aerofoil sections. Here, the effect of changing aerofoil section is investigated. A total of four aerofoil sections have been tested: a 1% thick elliptical aerofoil, a flat plate of zero thickness, and two other flat plates — one with semicircular leading and trailing edges and one with elliptical leading and trailing edges, where each edge is one half of an ellipse with length:thickness ratio 4 : 1. Both of these latter shapes were defined so as to have the same cross-sectional area as the elliptical aerofoil. Details of the exact dimensions of all aerofoils are contained in Appendix B.

Figure 5.48 shows that, at $Re = 500$, the performance of the aerofoil is only slightly affected by its shape (within the range of shapes tested). If the graph suggests anything, it is that the most important aspect of an aerofoil is the shape of its leading and trailing edges — it can be seen that the two aerofoils with elliptical leading and trailing edges (and therefore a continuously varying surface

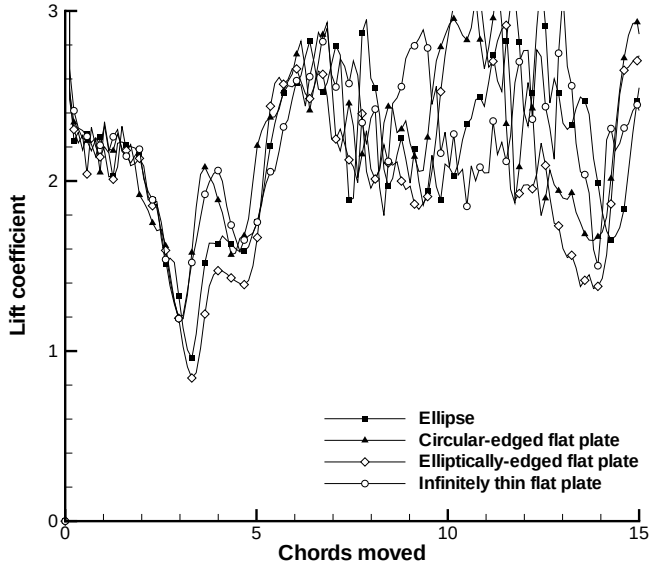

Figure 5.49: Section Comparison at $Re = 15\,000$. Angle of attack is 45° and aerofoil is impulsively started.

curvature) are similar. Equally, the infinitely-thin flat plate and the semicircular-edged flat plate (which have a surface curvature which changes suddenly) are close in performance. This is as would be expected, because the separation point will vary slightly according to the shape of the leading edge (Chen and Fang, 1996).

When Reynolds number is increased, the force/distance histories for the different sections become much more disparate — see Fig. 5.49. This is predominantly due to the occurrence of KHI, as explained in §5.3.3.1; the instability means that the force/time histories are less smooth. The four graphs are similar in shape over the first 5 chords lengths travelled, but they then quickly become very different, and in fact almost unrecognisable as representing similar situations. The graph does prompt a couple of tentative suggestions, though — firstly, the first trough seems later and lower for sections with elliptical edges. This indicates that the second trailing-edge vortex takes longer to start forming, so that the initial leading-edge vortex has moved further from the aerofoil before the 2nd trailing-edge vortex starts to enhance lift. Secondly, the trailing-edge vortex seems to enhance lift to a lesser extent for the elliptically-edged shapes than for the other two sections. This may be related to the first difference — it is possible that because the second

trailing-edge vortex starts to form sooner for the non-elliptical-edged sections, it is able to grow larger before being shed, therefore having a greater effect on lift.

It has already been noted (§2.1.3.4) the comparisons that have been drawn between the LEVs that are formed during insect-like flapping and those formed over delta wings at high angles of attack and the validity of these comparisons is discussed in more detail later (§6.4.5). Lowson and Riley (1995) found that, in the case of delta wings, the *sharpness* of the leading edge (not its shape) was important in determining the structure of the LEV. The results here (and those below, §5.6) suggest that the same is true for this case — the 'sharpness' of the leading edge is much more important than the shape of the leading edge. A similar finding was reported by Ohmi et al. (1990).

The most important conclusion that can be drawn at this stage is that the shape of the section (within the range considered here) has little effect on the phenomenology of the flow. This is in accordance with expectations. If separation occurs in the type of situation under investigation here, it is certain to be at the leading and trailing edges, and no differences in the phenomenology of the flow post-separation would be expected (Koumoutsakos and Shiels, 1996). Therefore, changing the aerofoil section of any eventual FMAV is unlikely to have much of an impact on the aerodynamic performance of the vehicle, provided the section is still 'thin'.

5.6 Effect of aerofoil thickness/chord ratio

All of the above results deal with comparatively thin aerofoil sections (with thickness/chord ratios of 2% or less). Insect wings *are* very thin, and the wings of any eventual FMAV will probably also be thin; but it might provide additional insight if the effect of increasing the thickness/chord ratio of the aerofoil is examined. To do this an elliptical aerofoil section is used at a Reynolds number of 500. This choice of Reynolds number — approximately midway between $Re = 25$ (where vortex shedding first occurs) and $Re = 1\,000$ (where KHI is first seen) — should eliminate the effects that occur at very low and very high Reynolds numbers which

were seen earlier.

Figures 5.50 and 5.51 show the results of this study. It is immediately evident that as the thickness of the aerofoil is increased, the average lift it produces decreases, and this is confirmed in Figure 5.52. This drop in average lift is due to two factors. Firstly, the lift-enhancing effect of LEVs decreases as thickness is increased, and secondly, the lift-enhancing effect of TEVs also drops and eventually reverses (as shown in Figure 5.50).

The first of these two effects appears to be due to a combination of two factors. Firstly, as the thickness/chord (t/c) of the aerofoil increases, its edges by necessity become less sharp, leading to a decrease in vortex strength and vortex core pressure — the angle through which the flow would have to turn to follow the aerofoil's surface will decrease as t/c is increased. Secondly, the location at which the vortex forms moves as t/c is increased. Both of these changes are illustrated in Figure 5.53, where it can be seen that the component of the force due to the LEV in the vertical direction will be smaller for the $t/c = 50\%$ case than for the $t/c = 1\%$ case, because the point on the aerofoil's surface above which the LEV lies becomes more vertical as t/c is increased.

A similar reason can be given for the reduced lift-enhancing effect of TEVs at higher t/c ratios. As t/c increases, TEVs tend to form behind the aerofoil rather than above it. This means that, whilst drag is still increased by the presence of a TEV, lift is not. In fact, once t/c reaches 50%, TEVs actually cause a decrease in lift of such magnitude that the net 'lift' is negative. This is as expected, because an 'aerofoil' of t/c ratio 100% (i.e. a circle) would produce a mean lift of zero, with vortices being shed from opposite sides of the circle producing lift forces in opposite directions.

Figures 5.50, 5.51 and 5.52 also reveal that as t/c is increased, the magnitude of the component of the skin-friction force in the drag direction increases, whilst the magnitude of the component in the lift direction decreases (this leads to an increase in lift because the component of skin-friction force in the lift direction is negative). This is because for thin aerofoils, the skin-friction force must act parallel to the chord of the aerofoil (so that the component in the lift direction is

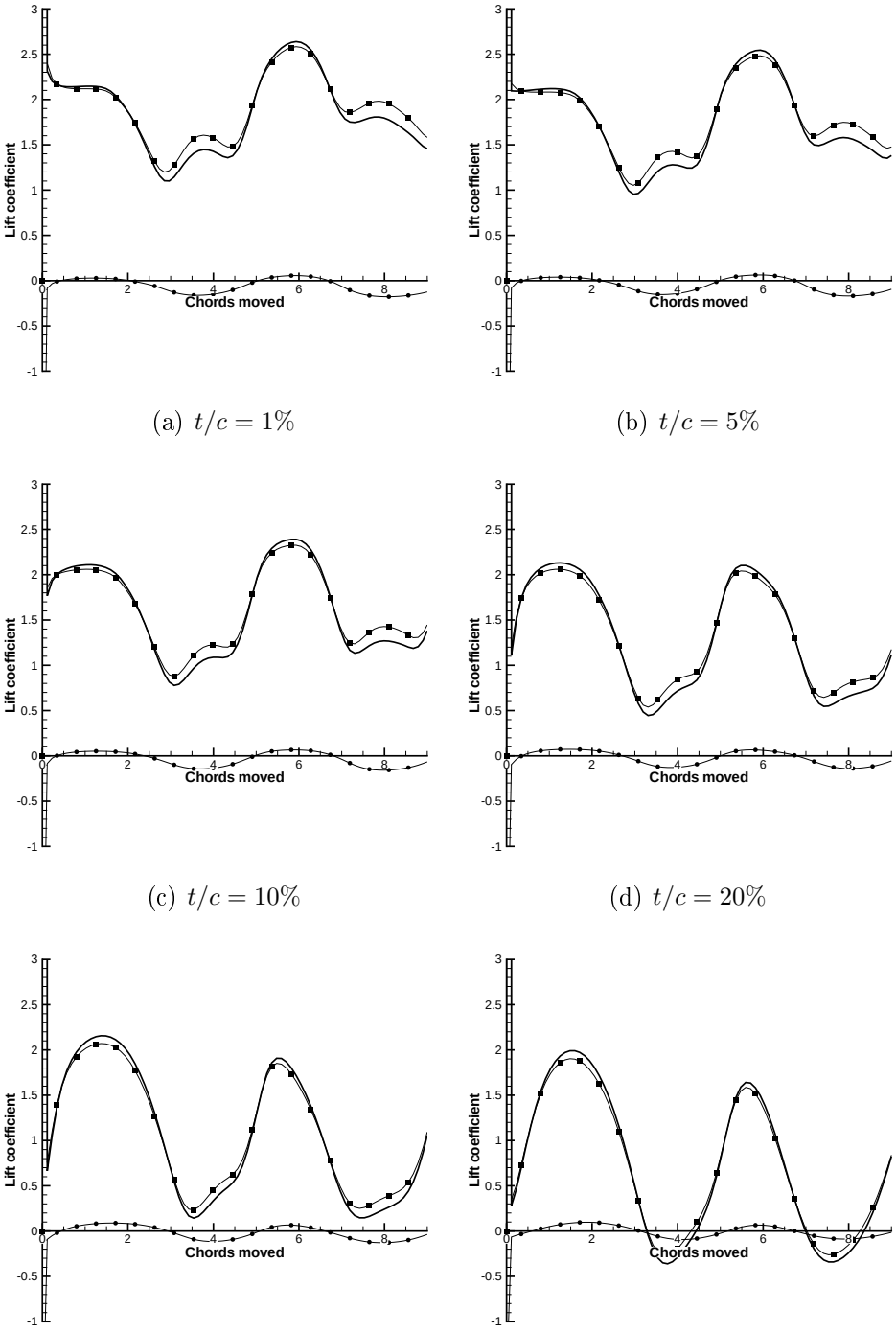

(a) $t/c = 1\%$ (b) $t/c = 5\%$

(c) $t/c = 10\%$ (d) $t/c = 20\%$

(e) $t/c = 30\%$ (f) $t/c = 50\%$

Figure 5.50: Pressure (squares), viscous (circles) and total lift coefficient vs. chords moved for impulsively-started elliptical aerofoils with various thickness/chord ratios. $Re = 500$ and angle of attack is 45°.

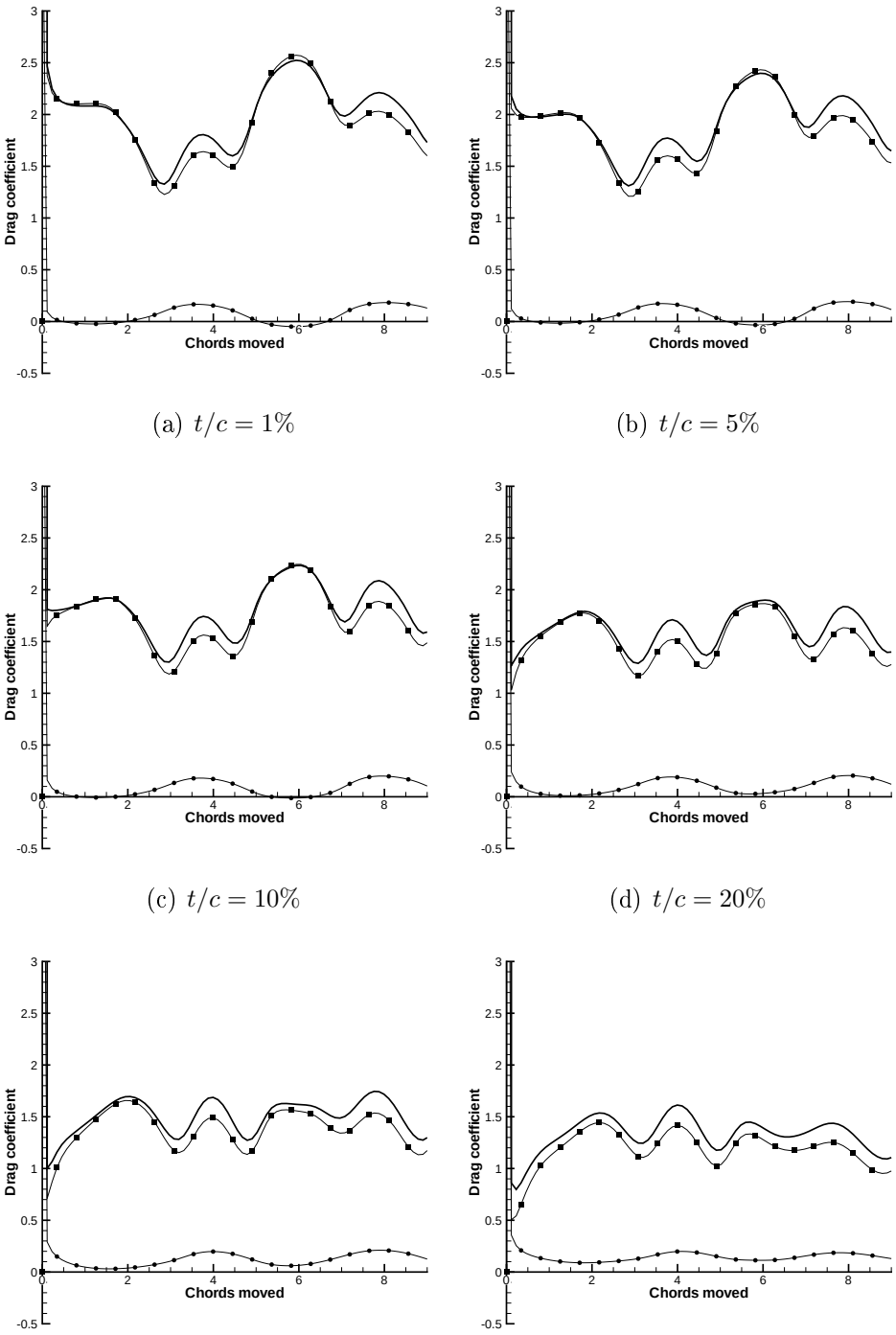

(a) $t/c = 1\%$ (b) $t/c = 5\%$

(c) $t/c = 10\%$ (d) $t/c = 20\%$

(e) $t/c = 30\%$ (f) $t/c = 50\%$

Figure 5.51: Pressure (squares), viscous (circles) and total drag coefficient vs. chords moved for impulsively-started elliptical aerofoils with various thickness/chord ratios. $Re = 500$ and angle of attack is 45°.

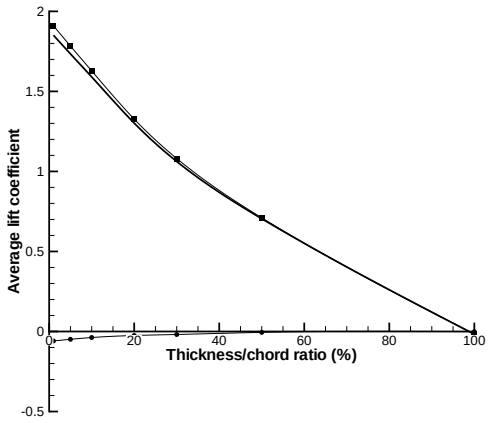

(a) Lift

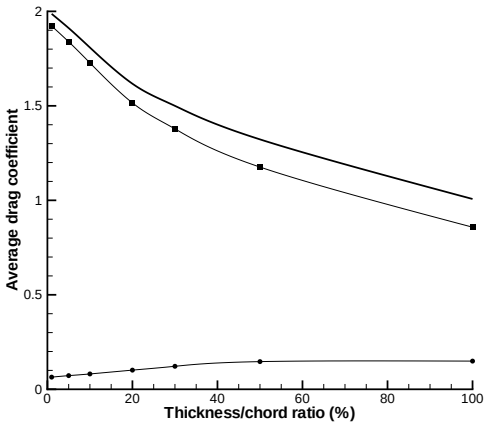

(b) Drag

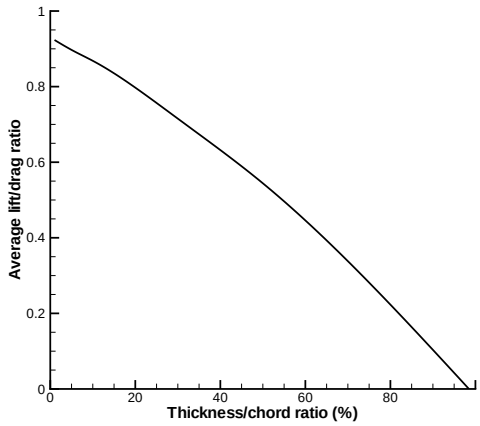

(c) Lift/drag ratio

Figure 5.52: Average lift coefficient, drag coefficient, and lift/drag ratio vs. thickness/chord ratio for impulsively-started elliptical aerofoils. $Re = 500$ and angle of attack is 45°. Averages are over first 9 chords of travel, excluding initial added-mass peak. In (a) and (b), square symbols represent pressure forces and circular symbols represent viscous forces; thick line is total force.

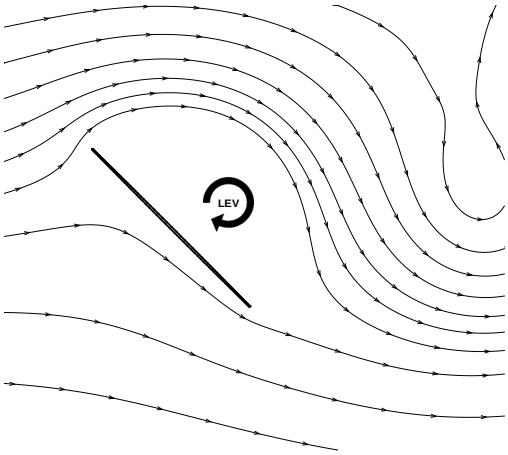

(a) $t/c = 1\%$

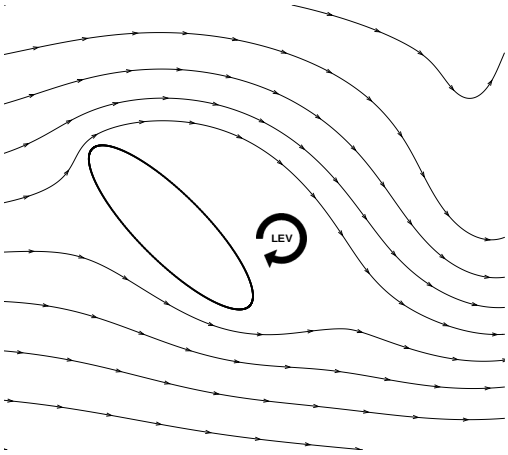

(b) $t/c = 30\%$

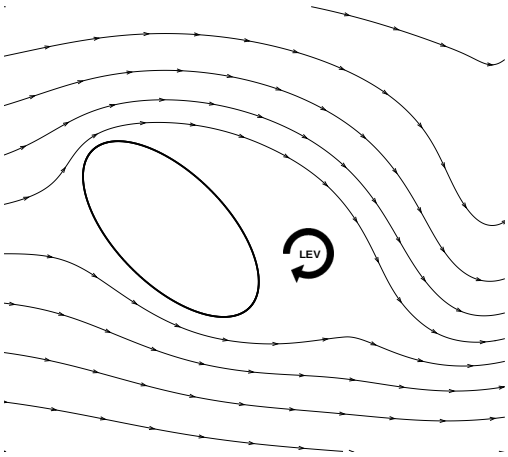

(c) $t/c = 50\%$

Figure 5.53: Schematic showing position of 2nd LEV after 6 chords of travel for impulsively-started elliptical aerofoils of various t/c ratios. $Re = 500$ and angle of attack is 45°.

equal to the component in the drag direction at 45° angle of attack). As t/c is increased, the mean skin-friction force acts increasingly in the drag direction. A similar change occurs in the case of pressure forces. For a very thin aerofoil, the pressure force must act perpendicular to the aerofoil. For a very thick aerofoil, the mean pressure force will increasingly act in the direction of the freestream flow. Thus, for a 100% thick aerofoil, the mean lift force is zero, whereas the mean drag force is not.

Overall, then, these results are as expected. As t/c is increased, the shed vortices decrease in strength, and increasingly form *behind* the aerofoil rather than *above* it. These changes, coupled with the differences in skin-friction and pressure forces outlined above, mean that the aerodynamic performance of the aerofoil (in terms of lift/drag ratio) decreases as its thickness/chord ratio increases. This is consistent with findings regarding delta wings — the lift produced by a delta wing is larger when the leading edge is sharper (Katz and Plotkin, 2001, p. 518).

5.7 Accelerating aerofoils

All of the results above deal with the case of an aerofoil translating with fixed angle of attack and fixed velocity (after an impulsive start). It has been seen that there are a number of important effects that occur even for this apparently simple scenario. It is important to bear in mind, however, that insect-like flapping involves almost constantly-varying velocities and accelerations. It may be enlightening to investigate what differences there are between an aerofoil moving at constant speed and one that is accelerating. An accelerating aerofoil should produce 'extra' lift due to added-mass forces (see §2.1.3.2).

Figure 5.54(a) reveals that, if lift coefficient is calculated using the original steady velocity, the instantaneous lift coefficient rises as the acceleration is increased. However, it is important to bear in mind that, for $a = 0.01m/s^2$, the aerofoil's instantaneous velocity after 10 chords of travel is around $0.2m/s$. For $a = 0.5m/s^2$, the corresponding velocity is around $0.5m/s$. Plotting the results in this way is unhelpful because it is not possible to distinguish between the 'extra'

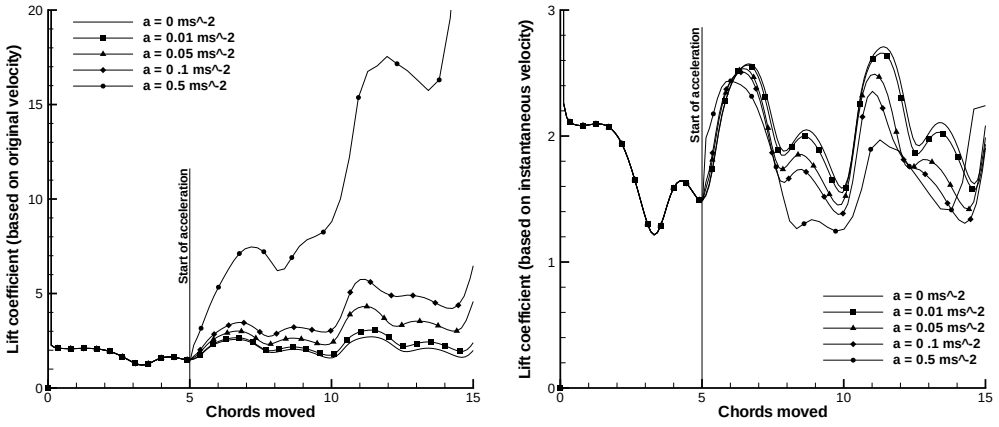

(a) (b)

Figure 5.54: Lift coefficient vs. chords moved for an impulsively-started, flat-plate aerofoil which moves with constant velocity for the first 5 chords and then accelerates at a constant rate. a is the rate of acceleration. Angle of attack is 45° and initial Reynolds number is 500. Final Reynolds numbers are approximately 560, 750, 920 and 1 800 (for $a = 0.01$, 0.05, 0.1 and $0.05 m/s^2$ cases respectively).

force that is due to added mass and the 'extra' force that results from the aerofoil's increased velocity. Intuitively, then, one might try plotting a similar graph but calculate lift coefficient using the instantaneous velocity, as in Figure 5.54(b). This produces results which might be counter-intuitive — generally, the instantaneous lift coefficient seems to *decrease* as the acceleration rate is increased.

Closer inspection reveals that, as the acceleration phase of motion begins (after 5 chords of motion), there is a rapid increase in lift, the magnitude of which depends on the rate of acceleration (Figure 5.55). At 5 chords of travel, before the acceleration begins, the lift coefficient is the same for all 5 cases. At the next time step in the simulation (after around 5.15 chords of travel) the lift coefficient for the accelerating cases is higher than for the non-accelerating case. Because this 'jump' in lift occurs as soon as acceleration begins, it seems reasonable to assume that it is due to added mass (particularly as lift coefficient is calculated using instantaneous velocity). Plotting the magnitude of the 'jump' in lift against acceleration (Figure 5.56) confirms this — it is clear that the magnitude of the lift increase is almost exactly proportional to acceleration, as would be expected (Duncan et al., 1970, p. 152).

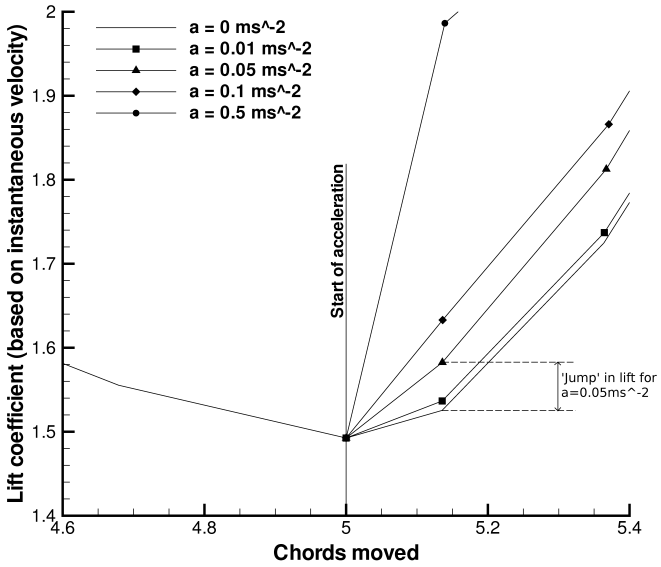

Figure 5.55: Enlargement of portion of Figure 5.54(b), showing 'jump' in lift coefficient at start of acceleration.

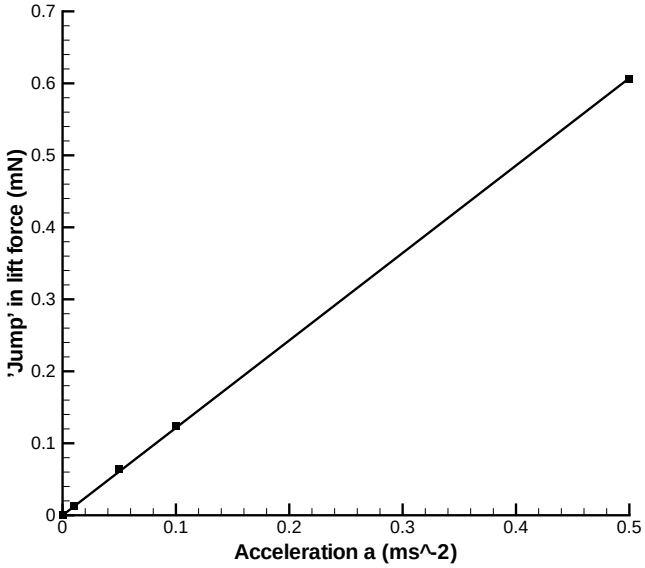

Figure 5.56: Magnitude of added-mass 'jump' in lift vs. acceleration. Angle of attack is 45° and initial Reynolds number is 500.

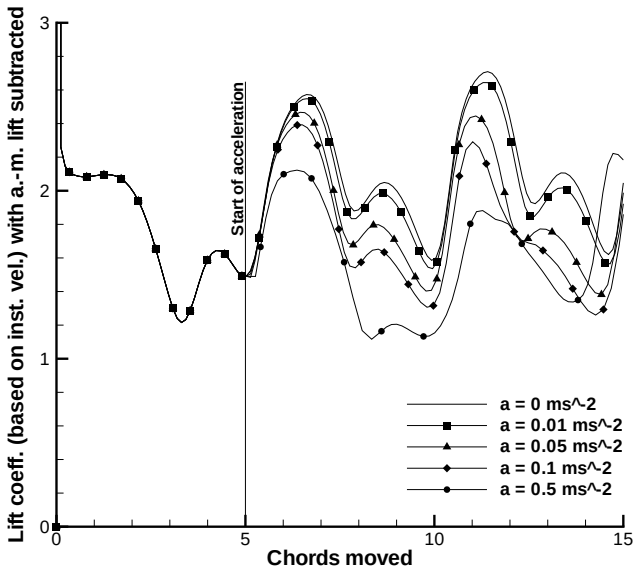

Figure 5.57: As Figure 5.54(b), but with added-mass lift subtracted at each time step.

Because the acceleration in each case is constant, the added-mass lift force will remain constant. If this constant value (the value in Figure 5.56) is subtracted from the lift force at each time step, this should remove the added-mass forces in Figure 5.54(b). The result of this is shown in Figure 5.57. It is clear that after the initial 'jump' in lift, the added-mass force *appears* to be cancelled out by other factors such that the acceleration actually leads to a *decrease* in lift coefficient. It is suggested here that this is predominantly because, in Figure 5.57, the lift coefficient at each time step has been calculated using the velocity of the aerofoil at that time step. However, it is known from the discussion of the Wagner effect earlier that instantaneous changes in aerofoil velocity will not lead to instantaneous changes in lift. Bearing this in mind, it is inappropriate to calculate the lift coefficient using the instantaneous velocity, because the lift is dependent on the *time history* of the velocity, not just the velocity at the current time.

Another complication is introduced by plotting instantaneous lift coefficient vs. velocity. If the quasi-steady assumption (see §2.2.1.1) were made, the aerofoil would be expected to produce the same amount of lift, regardless of its history of motion. In fact, Figure 5.58 reveals that the force on the aerofoil depends not

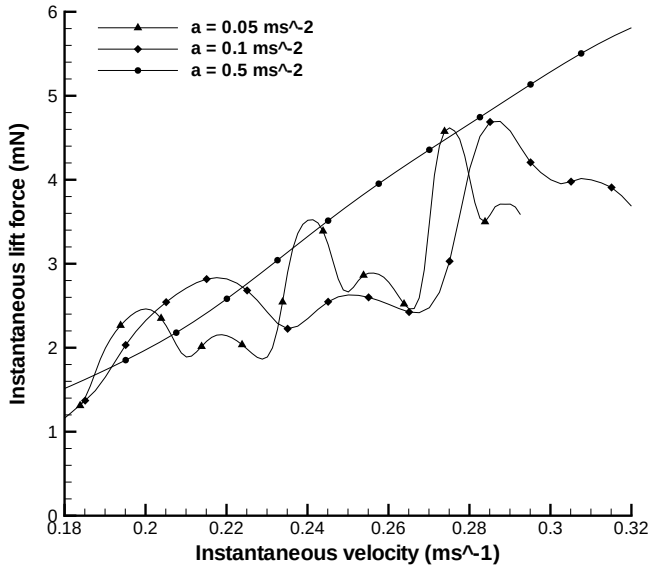

Figure 5.58: Lift force vs. instantaneous velocity for three difference accelerations. Angle of attack is 45° and initial Reynolds number is 500.

just on the instantaneous velocity, but on acceleration *and* on the current phase of vortex shedding. For example, at a velocity of around $0.24m/s$, the aerofoil in the $a = 0.05m/s^2$ case is producing more lift than in the $a = 0.1m/s^2$ case. But this is merely because it so happens that just as the aerofoil in the former case is passing through this velocity, it is experiencing a lift peak because of an LEV. In contrast, when the aerofoil in the latter case is passing through this velocity, its lift is *not* being enhanced by the presence of an LEV.

It is also clear that as acceleration is increased, the magnitude of the lift-enhancing effect of vortices decreases. It has already been noted that for an impulsively-started aerofoil, the initial TEV (or starting vortex) has little lift-enhancing effect because it does not form above the aerofoil but behind it; however, for each subsequent TEV (which forms while the aerofoil is moving with constant velocity), the induced velocity due to the LEV tends to cause the TEV to move forward and it therefore forms above the aerofoil, enhancing lift. In an accelerating case, each LEV does tend to induce the subsequent TEV to move forward to a position above the aerofoil, but because the aerofoil is accelerating as this happens, the TEV does not approach as close to it, and therefore its lift-enhancing effect is

reduced. A similar effect occurs for LEVs — if the wing is accelerating, the vortex that is shed lies further from it, and the lift-enhancing effect is reduced.

It is evident that the lift/time history for $a = 0.5m/s^2$ begins to show some signs of the high-frequency fluctuations that were seen earlier (in §5.3.3.1), particularly once the aerofoil has travelled 10 chords. This is because at this point the speed of the aerofoil has increased to such an extent that the instantaneous Reynolds number exceeds the critical value at which KHI starts to appear in the vortex sheets. The fact that the aerofoil is now accelerating does not seem to mean that KHI occurs at a lower Reynolds number. These results therefore contradict the conclusion of Koumoutsakos and Shiels (1996), who stated that KHI occurred only when the plate was uniformly accelerated, not when it was translated at constant velocity. As was noted in §5.3.3.1, this conclusion was unwarranted because Koumoutsakos and Shiels studied aerofoils in uniform motion only up to a Reynolds number of 1 000. Indeed, there is no reason why an accelerating aerofoil should be more susceptible to KHI than an aerofoil in steady motion — as was stated above, the stability of a vortex sheet depends on the velocity gradient across it, not on the acceleration of the aerofoil from which it stems.

Finally, it is evident that the fact that the aerofoil is accelerating does not have a noticeable impact on the Strouhal number — Figure 5.54(b) shows that an LEV is shed around every 5 chords of travel, regardless of the rate of acceleration. It was seen in §5.3.4 that, for an angle of attack of 45° Strouhal number is approximately constant if $Re > 500$, and in the accelerating cases presented here, the initial velocity is such that $Re = 500$. The fact that Strouhal number remains unchanged as the aerofoil is accelerated indicates that acceleration has no impact on Strouhal number. This is as would be expected, because it has already been confirmed that Strouhal number is dependent on Reynolds number only.

5.8 2D flows — closing remarks

It has been seen that 2D flows are not as simple as might be supposed. In order to predict the force on a given aerofoil at a given point, it is necessary to know

the aerofoil's angle of attack, current velocity, current acceleration, motion history, and the current phase of vortex shedding. Therefore, the quasi-steady approach, which bases force predictions solely on aerofoil shape, orientation, and velocity, is inadequate for this kind of flow, and this goes some way to explaining the fact that, for most situations, the quasi-steady approach cannot account for the high lifts that insect wings produce.

These results also call into question the validity of the assumption of inviscid flow, which is made in many (if not most) analytical models of insect-like flapping (e.g. Jones, 2003). The current CFD results indicate that at a Reynolds number of 50, viscous force can reduce the average lift coefficient by more than 30% and, on average, account for almost 25% of the drag coefficient. Even at a Reynolds number of 250, viscous force accounts for around 5% of the total force. It is suggested here, therefore, that inviscid models should not be used to predict forces at Reynolds numbers below 50; or, if they are, the predictions must be corrected to account for the missing viscous forces. If the model is intended for analysing the aerodynamics of FMAVs (which will probably operate at Reynolds numbers of $O(10\,000)$), viscous forces are insignificant (§5.3.5) and the assumption of inviscid flow can safely be made.

However, all these results are two-dimensional. It has already been mentioned (§2.1.3.4) that experiments with mechanical flappers and propellers (see e.g. Nolan, 2004; Ramasamy et al., 2007) have revealed a highly-3D flow structure. It is therefore imperative to attempt to understand how this 3D structure comes about; and how the move to a 3D wing from a 2D aerofoil affects the pattern of vortex shedding which is seen to occur in 2D cases and the resulting forces.

Chapter 6

3D Results

> *"The outcome of any serious research can only be to make two questions grow where only one grew before."*
>
> — Thorstein Veblen

In this chapter, results pertaining to 3D wings are presented. After discussing the validation of the current 3D CFD model, the differences between 2D and 3D flows are discussed. The chapter continues to examine the effect on 3D flows of Reynolds number, angle of attack, wing planform, aspect ratio, and wing/wake interaction. Finally, the model of Ansari (2004) is discussed.

6.1 Comparison with existing data

Having moved from studying 2D flows to 3D flows, it is important to again try to validate the current CFD model by comparing it to experimental data. In this case, there are two main sources of such data: Firstly, the current 3D force measurements, which were described in §4.5, and secondly, 3D PIV data gathered by Nolan (priv. comm., 2004) using the method described in Nolan (2004).

6.1.1 Comparison with current force measurements

It is shown later (§6.4) that, whereas for 2D flows the force produced by the aerofoil was unsteady for most Reynolds numbers, for 3D cases the force actually becomes

steady. For the CFD case, the lift force becomes steady after around 90° of sweep[1] (after an impulsive start). In the experimental case, however, the lift force did not become steady until the wing had swept through a number of complete revolutions, although a lift plateau did occur at around 90° of sweep. It became clear that this difference (between results from the CFD model and those from experiments) was due to the returning wake, which was not included in the CFD results at this stage[2]. Because the experimental rig consisted of two wings mounted 180° apart (i.e. a propeller) as each wing approached 180° of sweep it started to encounter the wake of the other wing. This tended to affect the lift produced.

The same effect was noted by Usherwood and Ellington (2002a), who performed similar experiments. They grouped their lift coefficient data into 'early' (between 60 and 120° of sweep) and 'steady' (between 180 and 450°). They found that the 'early' lift coefficients tended to be higher than the 'steady' coefficients.

This comparison, therefore, uses the experimental lift coefficient measured during the period of sweep of (approximately) 20° to 120°. This avoids the high transient forces associated with the starting acceleration of the wing and also the effect of the wake of the opposing wing. Force measurements were taken over a range of rotational speeds which translate into a Reynolds number[3] range of approximately 3 000 to 17 000. Force measurements could not be taken below $Re_{3D} = 3\,000$ as the resulting forces were too small to register on the force balance available.

In order to calculate the CFD-predicted lift, the data that are presented later were used to formulate a relationship between lift coefficient and Reynolds number. In fact, as is shown later, the CFD model predicts that lift coefficient remains almost constant as Reynolds number is increased, so that lift force is almost proportional to Ω^2 (all other factors, such as wing shape and size, being equal) where Ω is the rotational speed of the wing. Therefore, because Re_{3D} is proportional to

[1] Recall that sweep is defined as the rotation of the wing in the horizontal plane.
[2] The impact of the returning wake is examined in §6.9.
[3] For 3D cases, Reynolds number is defined as

$$Re_{3D} = \frac{\rho V_{tip} \bar{c}}{\mu},$$

where V_{tip} is tip velocity and $\bar{c}$ is mean aerodynamic chord.

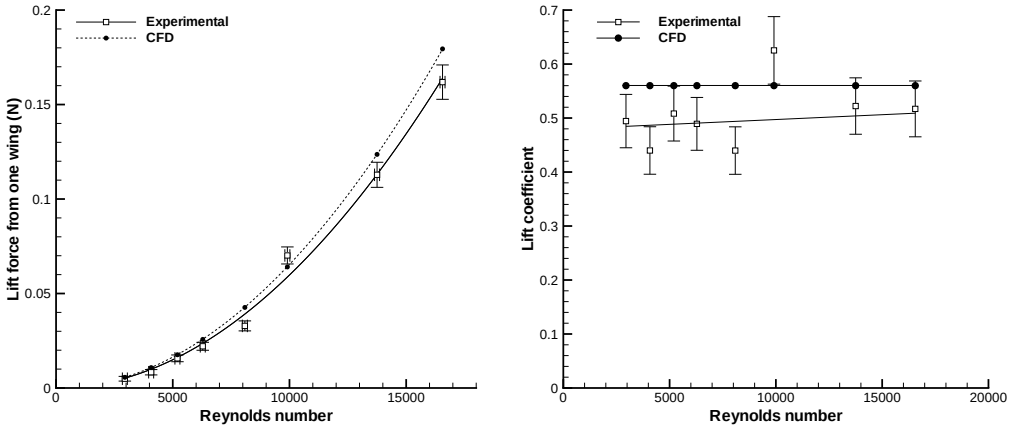

(a) Lift force (b) Lift coefficient

Figure 6.1: Comparison of CFD lift predictions with experimental measurements for 45° angle of attack. Wing is elliptical (see §6.7). A polynomial curve of order 2 has been fitted to both sets of results in (a).

V_{tip}, which is proportional to Ω, the lift force (according to the CFD predictions) is almost proportional to $(Re_{3D})^2$.

At first glance, the results (presented in Figure 6.1(a)) look promising. As expected, the CFD results lie almost exactly on the curve so that lift force is proportional to $(Re_{3D})^2$. The experimental results show more scatter, but this is most likely to be due to experimental errors rather than changes in the phenomenology of the flow. The differences are emphasised if lift coefficient is plotted against Reynolds number, as in Figure 6.1(b), where it is clear that the CFD model predicts an average lift coefficient around 16% higher than that measured in the experiments.

There are a number of possible reasons for this discrepancy. Firstly, in the experimental case, the flow around the wing would have been affected to some extent by the presence of the driveshaft and mounting bracket, which were not modelled in the CFD case. Secondly, the water in the tank used for the experiments might not have been completely stationary before the wing started moving, although precautions were taken to try and prevent this — a relatively long time was allowed between runs to allow the water to settle. Thirdly, there may have been some friction in the lever arm pivot (see §4.5) which would affect the measured force in

the experimental case.

Given this error between the two sets of results, it might be questioned whether the model has been proved to be accurate. The answer to this is that, although the CFD model predicted somewhat higher lift forces than were measured in the current experiments, the two sets of results are broadly in agreement. This indicates that the model is capturing the relevant phenomena, and it is phenomena which are of most interest (rather than the accuracy of the model when predicting forces). In fact, given the differences between the CFD and experimental set-ups, the agreement is encouraging.

The present experimental results also show that there is no dramatic decrease in lift coefficient as Reynolds number is increased, indicating that the LEV is stable and does not 'break away' at higher Reynolds numbers. Nolan (2004), who examined Reynolds numbers from 140 and 6 500, suggested that there may be a "critical range of Re where a stable spiral LEV is manifest"; this may well be the case, but the current results indicate that the phenomenology of the flow remains approximately constant from $Re = 120$ right up to $Re = 20\,000$. Others have reported similar findings up to $Re = 26\,000$ (Usherwood and Ellington, 2002b).

6.1.2 Comparison with the PIV data of Nolan

Nolan used PIV (particle image velocimetry) to obtain details of the 3D flow produced by a rotating wing. In this section these data are compared to data from the current CFD model.

One of the disadvantages of the available PIV data is that the resolution is relatively poor, as shown in Figure 6.2. This means that, when comparing the two vector fields, it is difficult to get any quantitative idea of how big the differences between the two sets of data are. It is apparent that there *are* differences, however. In order to gain a better appreciation of these it is possible to compare line plots of, for example, x-velocity (u) against u-coordinate for a certain x-coordinate. Since the leading-edge vortex (LEV) is thought to be the most notable feature of this type of flow, it seems sensible to choose coordinates that pass through the LEV. Figure 6.3 shows that when examined in this way, the overall agreement is good,

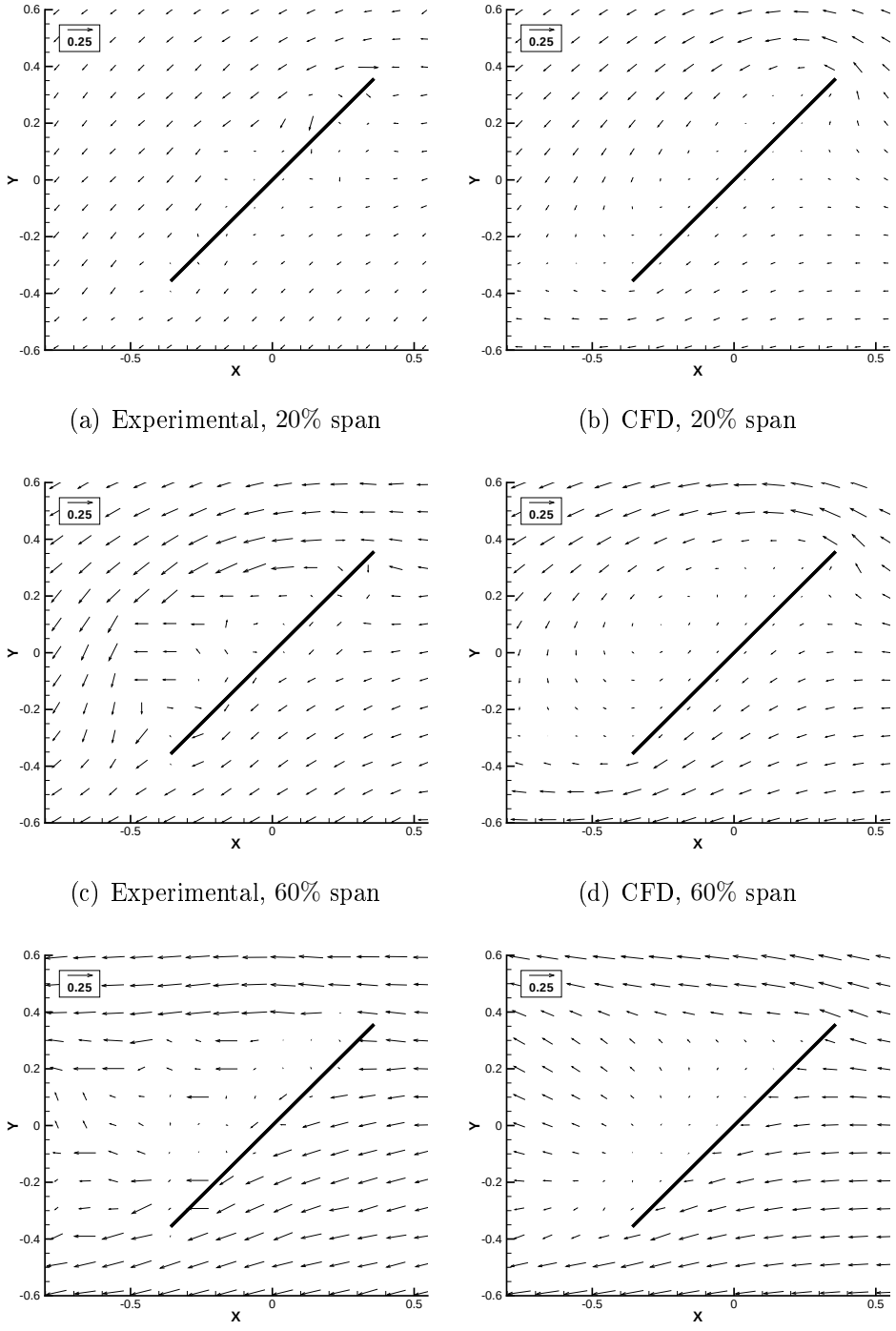

(a) Experimental, 20% span

(b) CFD, 20% span

(c) Experimental, 60% span

(d) CFD, 60% span

(e) Experimental, 100% span

(f) CFD, 100% span

Figure 6.2: Comparison of vector fields from Nolan (priv. comm., 2004) (left) with those from the current CFD model (right) for different spanwise positions. Angle of attack is 45° and Reynolds number is 2 500. The mid-chord of the rectangular wing lies at $(0, 0)$.

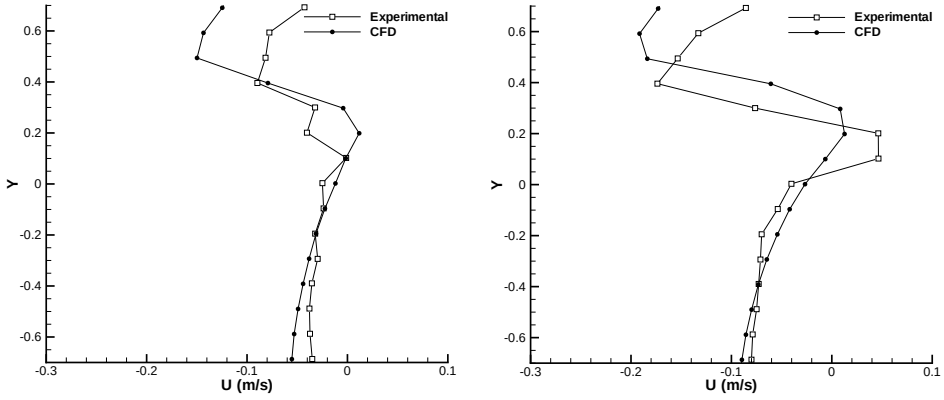

(a) 20% span

(b) 40% span

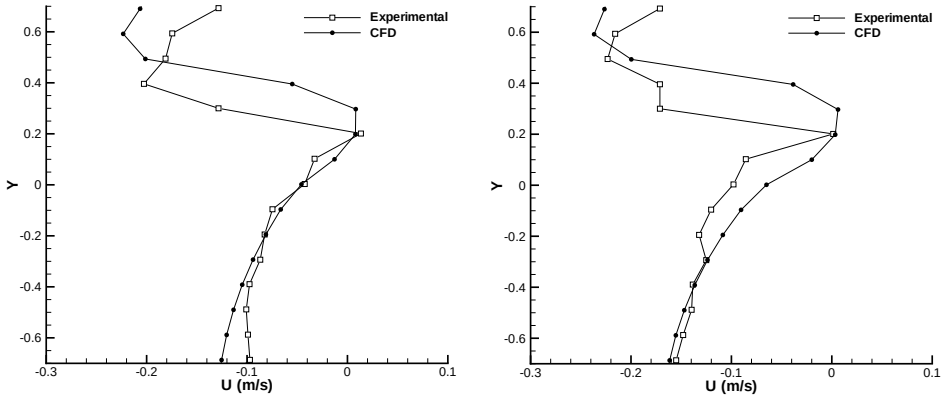

(c) 60% span

(d) 80% span

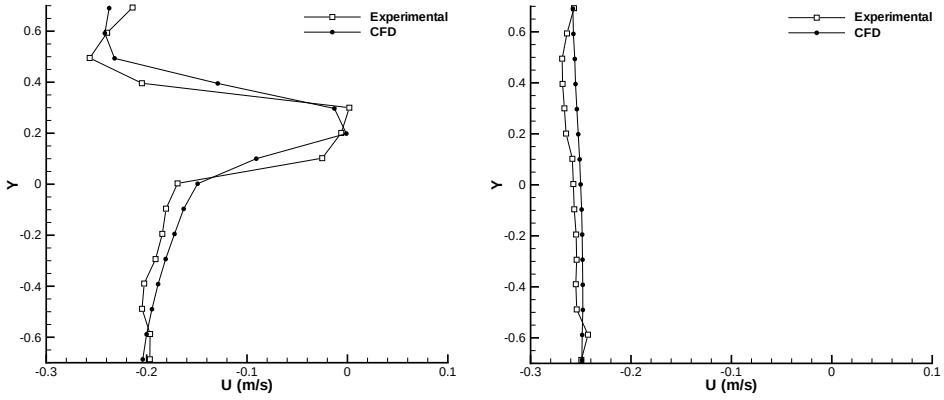

(e) 100% span

(f) 120% span

Figure 6.3: Plots of Y against u (u is x-velocity) at $X = 0.14$. Some of these data are shown in Figure 6.2. u is in wing-fixed coordinates (the wing is stationary, and the fluid is moving past it).

albeit with some significant differences in places. It is clear by the rapid change in u at around $Y = 0.3$ that, for both experimental and CFD cases, the plots pass through the LEV. In general, the CFD results seem to predict that the LEV lies slightly higher than the experimental data would suggest, but when the obviously anomalous data points seen in the experimental data are taken into account (see, for example, the vector above the leading edge of the wing in Figure 6.2(a)) the agreement is quite encouraging. In particular, the plots at the wing tip are very similar, despite the fact that this is where the tip vortex would occur and therefore where the flow might be expected to be most complex.

There are a number of possible explanations for the differences between the current CFD results and the experimental data. The wing that was used by Nolan was thicker than the infinitely-thin wing used here, with a thickness-to-chord ratio of around 3%. However, it was seen in §5.6 that the differences between a 1% thick and a 5% thick aerofoil were small. It is unlikely that the difference in wing thickness can be used to explain the differences between the current results and Nolan's, although it may have had some small impact.

A more important issue is that Nolan's experiments were carried out in a water tank with dimensions $0.60 \times 0.60 \times 0.60m$. The wing was $75mm$ long (with chord $25mm$) and its root was offset $5mm$ from the centre of the tank, meaning that there was a distance of $520mm$ (20 chords) between the wing tip and the tank wall. More critically, though, there was only $300mm$ (12 chords) between the wing and the bottom of the tank. Two issues may have been important in the experimental case — firstly, the downwash from the wing would have set up a recirculation in the tank, with fluid being forced down the centre of the tank and flowing upwards at the sides. It is not clear what precautions were taken to avoid this recirculation affecting the results. Secondly, if the wing was in motion for a long period of time, it would have acted as a 'stirrer', setting up a circulation in the tank in the horizontal plane. Again, it is not clear whether this was accounted for.

An even more important question is what account has been taken of the returning wake. Nolan does not mention at what point the PIV measurements were taken, and it is shown later that if the wing encounters its own wake (or the wake of

the other wing, if there is one) it has a dramatic impact on the flow. It is possible that the PIV data of Nolan were obtained after the wing had rotated through a complete revolution or more. In order to investigate this a CFD simulation was run with a pair of wings, so that each wing encounters the wake of the other after around 180° of sweep (details of this are contained in §6.9). Comparing these data with the experimental data might give some clue as to whether the experimental PIV results are for a wing unaffected by its own wake or for a wing which is passing through its own wake.

Figure 6.4 shows the results of this study, which are somewhat perplexing. On inboard sections of the wing (up to 80%), the inclusion of the preceding wing improves the correlation between the two sets of results. In fact, at 60% span, the agreement between the CFD results (with the wake included) and the experimental data is particularly good, whereas for the case without the wake included, the agreement is significantly worse. On outboard sections, however, the inclusion of the wake makes the agreement worse. This is particularly evident at the 120% span position, though it can also be seen at the 80% and 100% span locations.

One answer could be that some of the PIV data were captured before the wing had travelled far enough to interact with the wake, and some were captured once the wing had entered the wake of the preceding wing. This explanation is, however, rather simplistic and unconvincing. It is possible to conceive, on the other hand, of there being some dependency on how far the wing has travelled. The CFD data were captured when the situation had become fully steady (based on the predicted lift force). In the experimental case, it is not known whether this was true, or whether the flow was still developing. It seems obvious that because of the nature of the experiments, a recirculation would be set up in the tank, and this recirculation would get stronger (up to a limit) as the wings continued to rotate. It is suggested here, therefore, that the PIV data were captured before the flow in the tank had reached a steady state.

This tentative conclusion is supported by the graph for the 100% span position in Figure 6.4(e). Here it is seen that, in the experimental case, the freestream flow value of u (the x-velocity of the flow well below the wing tip) is around $-0.2m/s$.

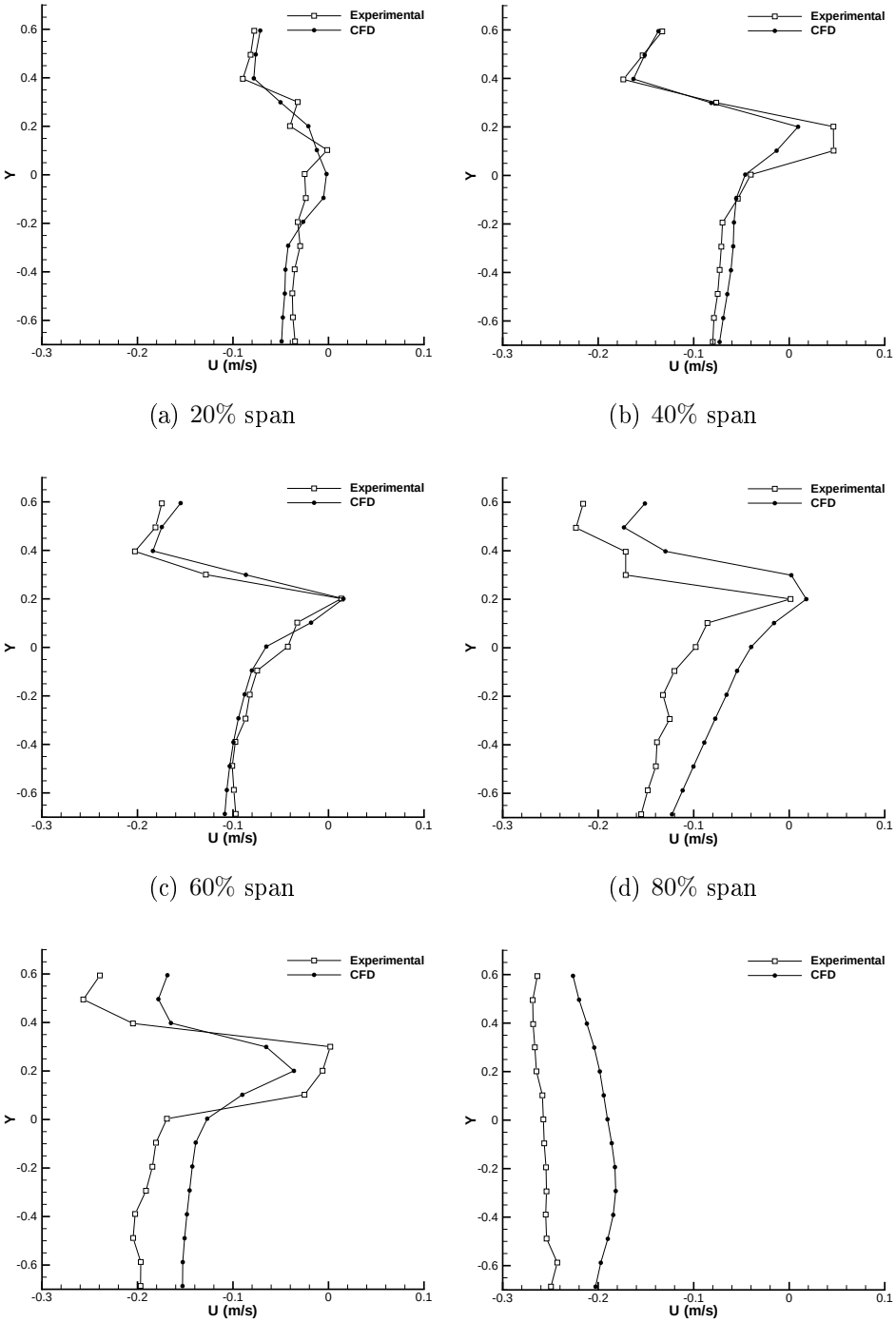

(a) 20% span

(b) 40% span

(c) 60% span

(d) 80% span

(e) 100% span

(f) 120% span

Figure 6.4: Plots of Y against u at $X = 0.14$, as in Figure 6.3 — but in this case, two wings are simulated so that the flow around each wing is affected by the wake of the other wing.

In an absolute frame of reference, the wing tip itself was moving at $0.214m/s$, so in the experimental data the fluid is approximately stationary with respect to the tank. In the CFD case, however, the corresponding fluid velocity is around $-0.15m/s$, meaning that the fluid is moving in the direction of the wing motion with a velocity of around $0.05m/s$ with respect to an absolute frame of reference. In other words, the CFD results indicate a recirculation set up within the fluid, whereas the experimental results show no such recirculation. It is suggested here that the PIV data were captured before this recirculation had time to develop. The same conclusion can be drawn from the graph for the 120% span position.

Despite the differences between the current CFD data and the experimental data, there is much agreement, and overall the comparison is encouraging. Certainly it seems clear that the CFD model is capturing the relevant phenomena, and so it now seems reasonable to use the model to investigate these phenomena.

6.2 3D LEVs

As has already been emphasised, the leading-edge vortex (LEV) is generally thought to be the most important lift-enhancing phenomenon that is involved in insect-like flapping. However, even almost 30 years after the LEV was first identified, there is still controversy as to its exact nature. Broadly speaking, the dispute centres on two questions; firstly, is the LEV stable? and, secondly, if it is stable, why? These questions arise partially because of what was seen in the previous, 2D results, section. There, it was concluded that, for 2D flows, the LEV is unstable for all but the very lowest Reynolds numbers, and this was explained in terms of vorticity balance.

It has also been noted that some insects do operate at Reynolds numbers as low as of $O(1)$ (see §2.1.3). At $Re = 1$, a leading-edge vortex would not be expected to occur at all — but whether this is the case or not has not been determined, and perhaps never will be, given the difficulties of visualising the flow around the wings of these tiny insects or carrying out experiments at these extremely low Reynolds numbers. At slightly higher Reynolds numbers, an LEV would be expected, but

would be 'naturally' stable, because for Reynolds numbers up to $Re = 25$ the LEV remained in place even for the 2D case.

Many insects, as well as FMAVs of the size envisaged, will operate at Reynolds numbers well in excess of 25. Based on the current 2D results, the LEV would be expected to be unstable. On the other hand, a great deal of evidence suggests that this is not the case (see §2.1.3.4) and that the LEV is not shed. However, as already mentioned, there are a number of different definitions of stability. Some work has suggested only that the LEV remains attached for the entire half-stroke, not that it is fully stable (e.g. Dickinson and Götz, 1993); whereas others have indicated that the LEV is stable for all time (e.g. Usherwood and Ellington, 2002b). Here a stable LEV is defined as one that remains attached to the wing no matter how far the wing sweeps. Therefore if the LEV is unstable in the 2D case, and stable in the 3D case, there must be some fundamental cause for this change. One principle aim of this chapter is to determine this cause. The other major question that needs to be answered is does increasing Reynolds number affect the stability of the LEV? If so, scaling up from insect to FMAV might be unfeasible.

6.3 Purely-translating 3D wing

It is possible that the apparent stability of the LEV for 3D wings is due in some way to the tip vortices. In order to investigate this a 3D wing was subjected to a linear motion (as opposed to sweeping it about its root) at 45° angle of attack. This, as might be expected, led to separation at the leading edge, and an LEV developed as for 2D flows. This LEV was connected to the TEV via the tip vortex, as shown in Figure 6.5(a). The TEV quickly detached, and the LEV also proved unstable, just as was seen in the 2D case. The flow in this case was not entirely 2D — there was some spanwise flow within the LEV, from the tips toward the mid-span position. The LEV, together with the tip vortex, remained attached at the leading edge of the tip — leading eventually to a pair of vortices attached at the tip, one of which extended downstream (the tip vortex) and the other of which extended in the spanwise direction (the LEV). The LEV shed from the inboard

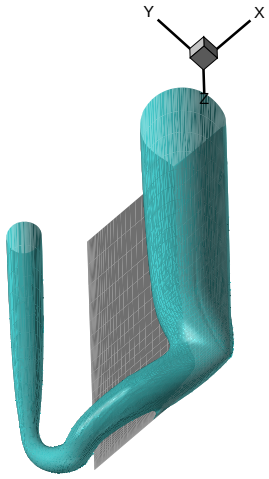

(a) After around 0.5 chords of travel

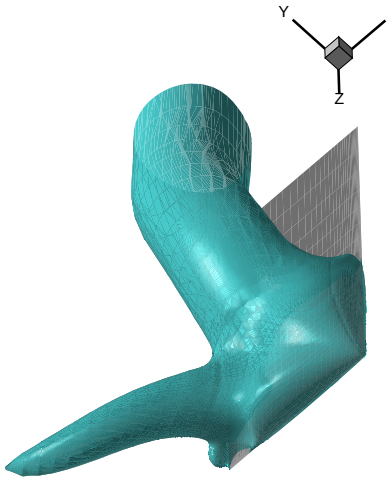

(b) After around 2 chords of travel

Figure 6.5: Showing the vortex system for a 3D wing which is being translated at an angle of attack of 45°. Only half of the wing is shown. Figure 6.5(a) shows the LEV, TEV and tip vortex forming one continuous vortex loop; in Figure 6.5(b), the TEV has diffused, as has much of the tip vortex. In reality, of course, the tip vortex will always extend to the starting vortex so that a continuous vortex loop remains. The LEV can be seen to have separated from the wing on inboard sections, whilst remaining attached at the tip. Vortical structures are visualised by iso-surfaces of pressure. In this case, $Re = 500$ based on wing chord and velocity; wing is moving from left to right in each case.

sections of the wing after around 2 chords of travel (as shown in Figure 6.5(b)) and caused another trailing-edge vortex to form. At the tip, the LEV remained in place longer due to the fact that it grew more slowly (because of the tip vortex) — but in the end, it separated there also. Another LEV formed, and the cycle repeated, just as for 2D flows. So for a purely-translating 3D wing the LEV is generally unstable — although at very low Reynolds numbers ($Re < 25$) a stable LEV may be created as for 2D flows.

6.4 Sweeping 3D wing — development of the LEV

The major difference between 2D cases and 3D cases is that the wing sweeps about its root. This means that the velocity of the wing is not constant along its span, with outboard sections moving faster than inboard sections. This section examines the impact of this change. The wing used here is rectangular (with aspect ratio 2.5) and infinitely-thin, and is impulsively started at an angle of attack of 45°. It is swept about the mid-chord of the root.

6.4.1 A conical LEV

It has already been stated (§5.3.4) that the size of an LEV depends on the distance travelled since it began to form. Therefore, for a 3D sweeping wing, at a given time after motion has started, the LEV will be larger on outboard sections than on inboard sections, since outboard sections have travelled a greater distance. This is shown in Figure 6.6, where the growth of the LEV is shown for different spanwise locations. For example, it is clear that at 5° of sweep[4], the LEV at the 25% span position is hardly noticeable, whereas at the 75% span position the LEV is obvious.

The LEV that forms is therefore conically shaped, as shown in Figure 6.7. This shape is not (at least initially) due to spanwise flow or any other such phenomenon — it comes about merely because of the sweeping motion of the wing and because the vortex at a given spanwise position grows at a rate which depends on the

[4]Note that for 3D sweeping wings distance travelled cannot be defined in terms of chords travelled, but degrees of sweep are used instead. Recall that 'sweep' is defined as the rotation of the wing about its root in the horizontal plane.

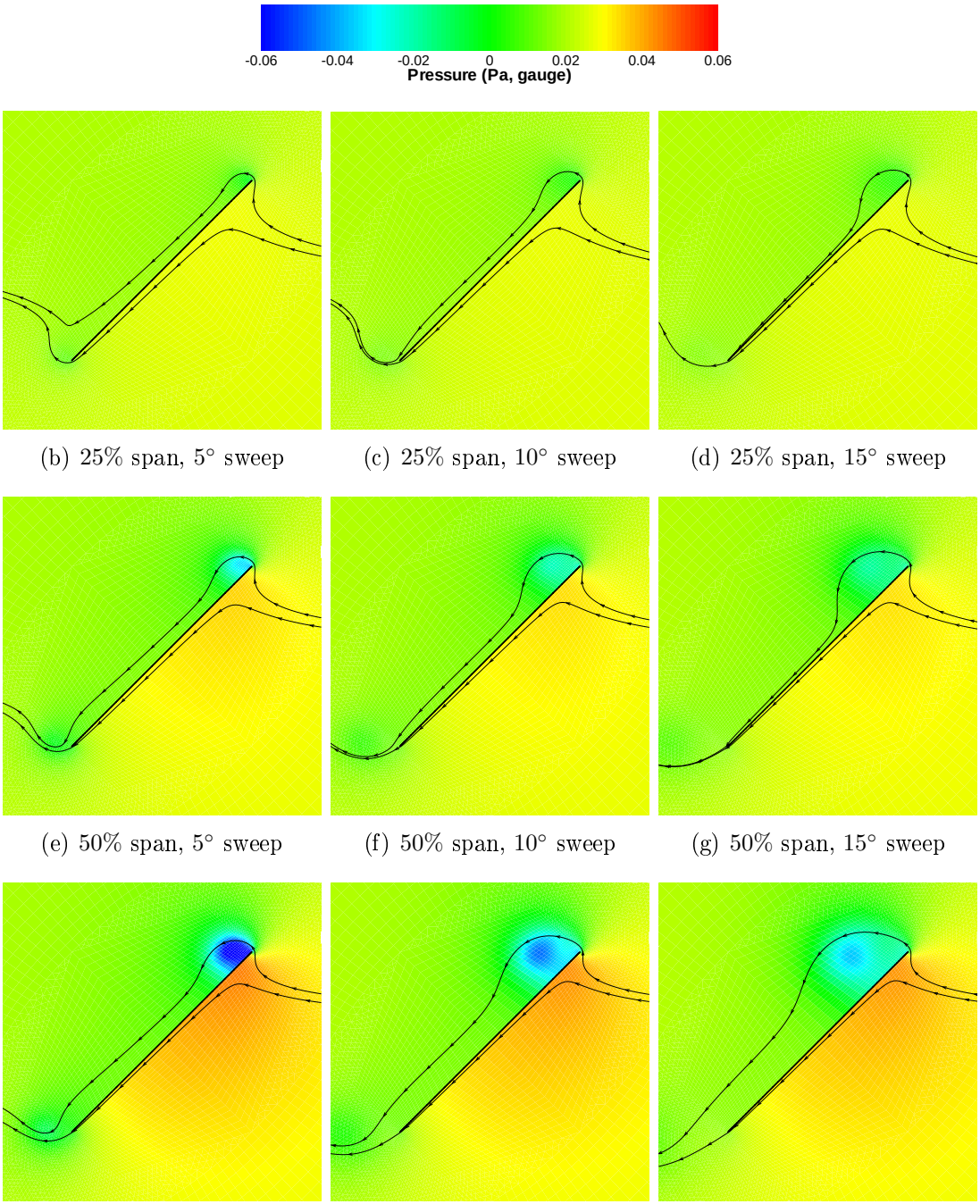

(b) 25% span, 5° sweep (c) 25% span, 10° sweep (d) 25% span, 15° sweep

(e) 50% span, 5° sweep (f) 50% span, 10° sweep (g) 50% span, 15° sweep

(h) 75% span, 5° sweep (i) 75% span, 10° sweep (j) 75% span, 15° sweep

Figure 6.6: Showing growth of LEV for a sweeping, rectangular wing at various spanwise location. Contours of pressure (blue areas are low pressure) and instantaneous 2D streamlines. $Re_{3D} = 500$, angle of attack is 45°, wing length is $0.1m$ and angular velocity is $1.82592 rad/s$.

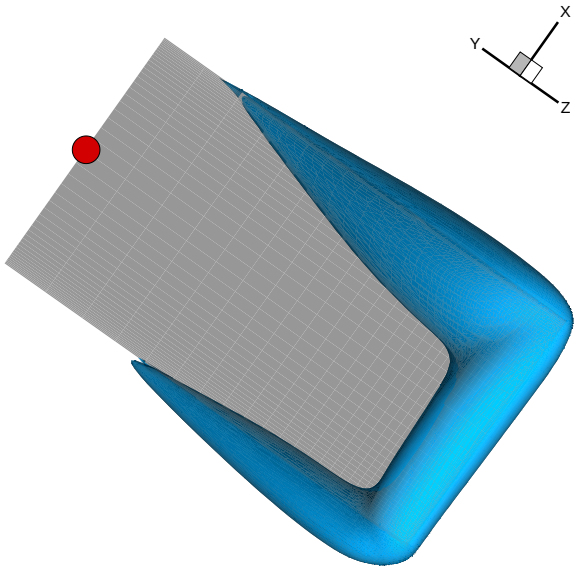

Figure 6.7: Showing vortex system for a 3D wing which has been swept through 5° (about the red dot) at an angle of attack of 45°. As in Figure 6.5(a), the LEV, TEV and tip vortex form one continuous vortex 'loop'; but the conical shape of the LEV (and of the TEV) is clear. Vortical structure is visualised by iso-surfaces of pressure. $Re_{3D} = 500$.

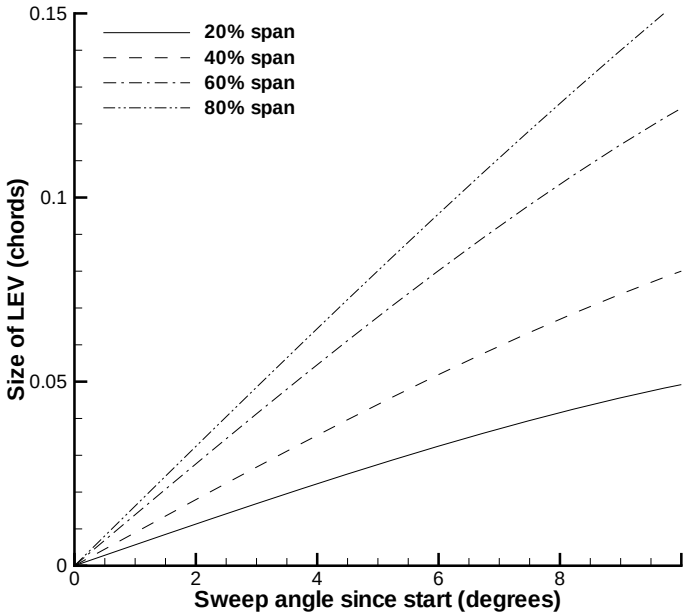

Figure 6.8: Showing growth of LEV at different spanwise positions. $Re_{3D} = 500$. Size of LEV is defined in caption of Figure 5.6.

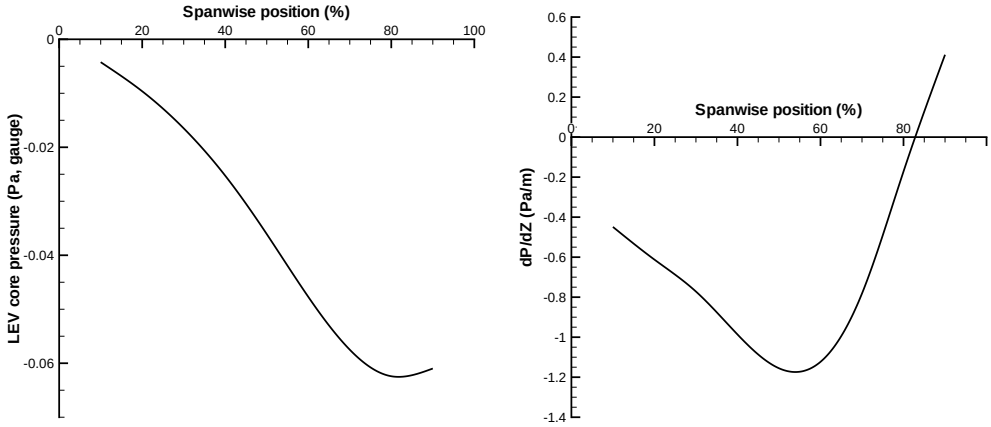

(a) Pressure vs. spanwise position (b) Pressure gradient vs. spanwise position

Figure 6.9: Pressure gradient within 3D LEV. Angle of attack is 45°, $Re_{3D} = 500$, and the wing has swept about the mid-chord of the root through an azimuth of 5° since being impulsively started. Wing length is $0.1m$ and angular velocity is $1.82592rad/s$.

distance to the root. This is clearly illustrated in Figure 6.8 where it is seen that over the first 10° of sweep, the growth of the LEV at each spanwise position is roughly linear.

6.4.2 A spanwise pressure gradient

The spanwise velocity gradient caused by the sweeping motion of the wing not only leads to a conical LEV, but also leads to the LEV on outboard portions of the wing being stronger than that on inboard sections. This is what would be expected, based on the 2D results in §5.3.5, where it was seen that increasing velocity led to an increase in vortex strength and a decrease in vortex core pressure. This is also supported by the experimental results of Nolan (2004). So, the sweeping motion of the wing leads to two separate phenomena — firstly, a conical LEV, and secondly a spanwise pressure gradient within that LEV, as shown in Figure 6.9(a).

The magnitude of the pressure gradient will depend on the velocity gradient along the wing. §5.3.5 showed that for 2D cases the LEV's core pressure fell as a function of velocity squared. In these 3D cases, the rate at which velocity increases along the wing is equal to the angular velocity of the wing, because the speed of a

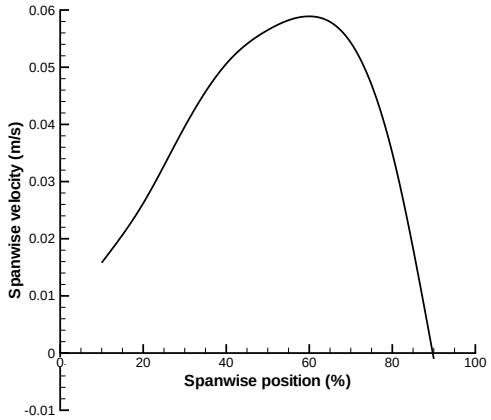

Figure 6.10: Spanwise flow in 3D LEV. Angle of attack is 45°, $Re_{3D} = 500$, and the wing has swept about the mid-chord of the root through an azimuth of 5° since being impulsively started. Wing length is $0.1m$ and angular velocity is $1.82592rad/s$.

given spanwise location is equal to the angular velocity of the wing (Ω) multiplied by the distance of the section from the rotation point. So the spanwise pressure gradient will automatically increase in magnitude if Reynolds number is increased by changing the angular velocity of the wing.

The effect of the tip vortex is apparent in Figure 6.9(b). It can be seen that the rate of change of LEV core pressure is negative until around the 80% span location, but then reverses so that the pressure gradient for the last 10% of span is actually in the direction of tip to root. This is because the tip vortex induces a downwards velocity on the upper surface of the wing, which reduces the effective speed of spanwise locations near the tip. The vortex therefore develops as though it is further inboard — it grows more slowly, is weaker, and has a higher core pressure. Over the majority (80%) of the wing, however, the pressure within the LEV decreases in an outboard direction.

6.4.3 Spanwise flow

The spanwise pressure gradient described above induces spanwise flow, from root to tip. Figure 6.10 shows that the fluid within the LEV accelerates towards the tip up to around the 60% span position, but then begins to decelerate as the pressure gradient starts to become less negative, and, eventually, positive. The tip velocity

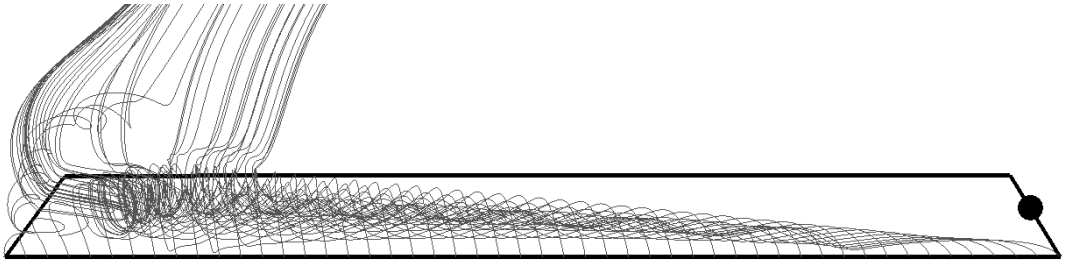

Figure 6.11: Leading-edge vortex structure (shown by instantaneous streamlines originating at leading edge) for a rotating rectangular thin flat plate. The wing is rotating around the point marked with a black dot at angle of attack of 45°and $Re_{3D} = 500$. Here, the wing has rotated through a sweep angle of 10° since being impulsively started. LEV is visualised by instantaneous streamlines originating at leading edge.

for this $Re_{3D} = 500$ case is around $0.2m/s$ so that the peak spanwise velocity at this time (after 5° of sweep) is around one third of tip velocity. As the wing continues to sweep, the spanwise flow increases in magnitude, eventually reaching values of the same order of magnitude of the tip velocity.

It can be seen that outboard of the 90% span position, there is spanwise flow from the tip towards the root (due to the tip vortex) but the flow within the LEV is predominantly towards the tip. Thus a spiral LEV is formed, similar in form to the LEVs seen on a delta wing at high angles of attack. This is shown in Figure 6.11, where it can be seen that a streamline originating from the leading edge at the root leaves the trailing edge at around 75% span.

Because the wing is swept about the mid-chord of the root, there is a small component of velocity at the leading edge toward the tip. In order to test whether this might be responsible for the spanwise flow within the LEV, a simulation was run with the wing rotation about the leading edge of the root. There was virtually no change in the structure of the LEV. Therefore, it is safe to conclude that the spanwise component of velocity at the leading edge cannot be held solely responsible for the spanwise flow within the LEV. In any case, the velocity within the LEV core has a far greater component in the spanwise direction than the corresponding component of the velocity of the oncoming flow at the leading edge.

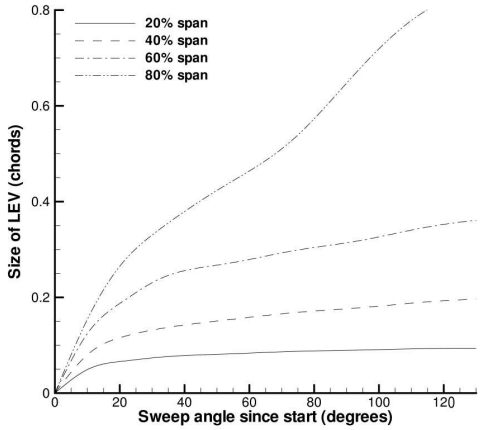

Figure 6.12: Showing growth of LEV at different spanwise positions. $Re_{3D} = 500$. Size of LEV is defined in caption of Figure 5.6.

6.4.4 The development of the LEV

It has been demonstrated that, initially, the LEV that forms over a sweeping 3D wing is conical in shape and contains significant spanwise flow. As the wing continues to sweep, the spanwise pressure gradient remains and the spanwise velocities continue to increase. Thus, not only is vorticity generated and diffused within the LEV, but it is also transported outboard by the spanwise flow. As the wing continues to sweep, the LEV grows, as shown in Figure 6.6. Figure 6.6 also shows that the core pressure within the LEV increases (i.e. becomes less negative) as the vortex grows, but the spanwise pressure gradient remains.

It has already been shown (Figure 6.7) that in reality the LEV, tip vortex, and TEV form a continuous vortex loop. This is fundamental to the development of the vortical system. For the rectangular wing used here, the tip vortex and the LEV might be expected to be separate entities, but in reality there is just one continuous vortex, which dominates the flow around the wing. Vorticity is extracted from the LEV into the tip vortex via the spanwise flow identified above, and is left behind in the wake. This same structure has been noted in experimental work (see e.g van den Berg and Ellington, 1997b).

Because of this spanwise extraction of vorticity, the LEV at a given spanwise location eventually reaches a stable size. At this point, at a given section, the total

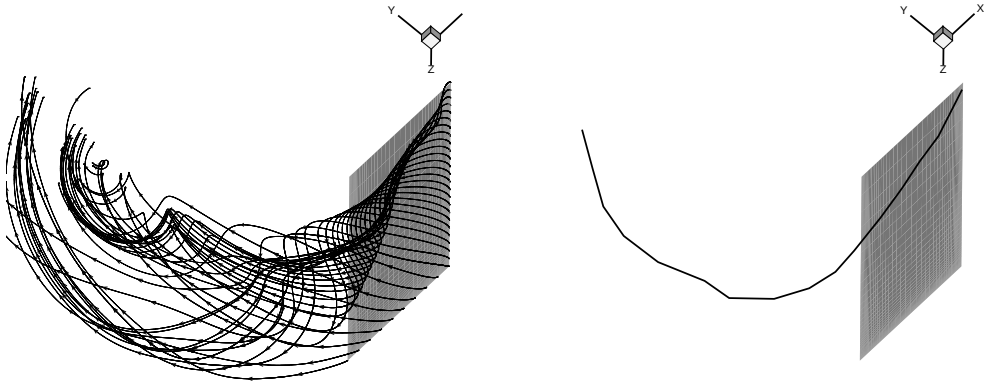

(a) Instantaneous streamlines (b) Vortex core

Figure 6.13: Eventual stable 3D LEV. $Re_{3D} = 500$, $\alpha = 45°$, and wing has swept around 600° since an impulsive start.

vorticity being generated at the leading edge, *plus* the vorticity that is entering that section from inboard sections, is equal to the sum of the vorticity that is being diffused and the vorticity that is leaving that section to outboard sections. This is shown in Figure 6.12. At the 80% span position, the LEV appears to grow indefinitely, but this is due to the fact that at this location the LEV eventually becomes indistinguishable from the tip vortex; after around 180° of sweep, the flow becomes fully stable and the LEV/tip vortex takes a form like that shown in Figure 6.13. Figure 6.13(b) shows that the vortex core has one end attached to the leading edge near the root, as the other end extends to the initial trailing edge vortex, as might be expected from Helmholtz's vortex theorem (see e.g. Kundu and Cohen, 2004, p. 138).

It is important to realise that the creation of an LEV does not 'create' vorticity; if an LEV exists, the net amount of vorticity in the system is still zero, as discussed in §5.3.2.2 (assuming that the flow started from rest). Therefore if vorticity exists in the LEV, there must either be an equal amount of vorticity of the opposite sense either in the trailing-edge vortex sheet or bound to the wing itself. The situation is complicated by the fact that the trailing-edge and leading-edge vortex sheets are in reality parts of the same vortex sheet, along with the tip vortex sheet.

It is clear that when using the phrase 'spanwise flow' care must be taken to

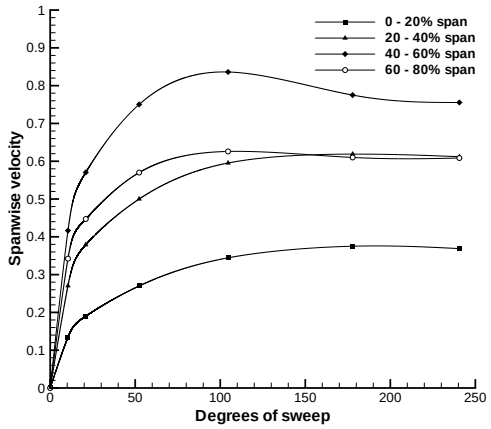

Figure 6.14: Showing spanwise flow within LEV (non-dimensionalised by tip speed), averaged over spanwise positions (the method involved releasing a particle at the inner position and tracking the time taken to reach the outer position). $Re_{3D} = 500$ and angle of attack is 45°. Wing length is $0.1m$ and angular velocity is $1.82592rad/s$.

define exactly what is meant. Generally, 'spanwise flow' is used to mean flow in the direction from root to tip — i.e. in the $+z$ direction in Figure 6.13. However, because the LEV eventually stabilises with its core as shown in Figure 6.13(b), axial flow (that is, flow within the LEV in the direction of the LEV core) is not actually in the spanwise direction. Here, spanwise is used in its conventional sense, so that it is really only sensible to use spanwise velocities to analyse the axial flow within the LEV near the root (where the axial flow will be roughly spanwise).

It has been seen that when the wing begins to rotate, the LEV grows until it becomes stable. The spanwise velocities within the LEV increase until the rate at which vorticity is being created at the leading edge is equal to the rate at which it is leaving the LEV and being shed into the wake. Figure 6.14 shows that the magnitude of the spanwise velocity increases up to around the 60% span position, decreasing near the tip due to the fact that the LEV near the tip is no longer orientated parallel to the leading edge. By the time the wing has swept around half a revolution, the LEV has stabilised. At this point, the peak spanwise velocity with the LEV is around 80% of the tip velocity, which compares well to previous experimental measurements; see, for example, van den Berg and Ellington (1997a).

Experiments were carried out (see §4.5) to verify the existence and nature of

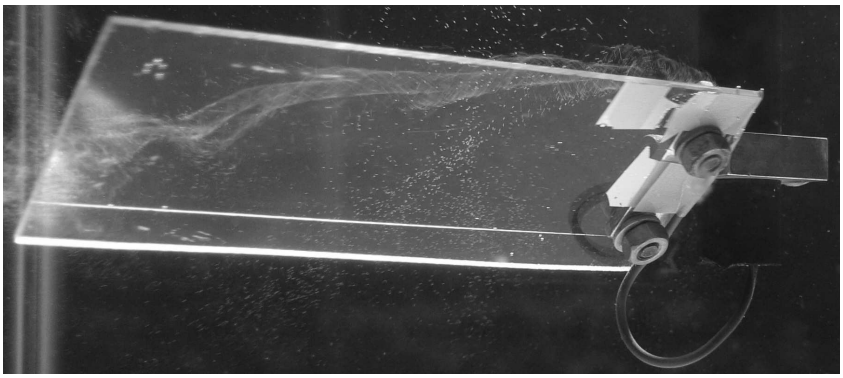

Figure 6.15: Spanwise flow within LEV, shown by hydrogen bubbles released at leading edge near root. Wing is rotating with $Re_{3D} = 2\,500$ and angle of attack 45°.

the 3D LEV, and an example of the structure that was seen is shown in Figure 6.15. The conical shape of the LEV and the spanwise flow within it are evident.

A stable LEV is not dependent on the shape of the wing. Insect wings are not rectangular, but the current results suggest that the complex shape of an insect's wing is not required in order for the LEV to exist and be stable. No doubt insect wings are designed as they are for other reasons; perhaps aerodynamic, perhaps structural, perhaps merely for mimicry. Later, it is shown that planform does have an impact on wing performance, as would be expected; but the wing of an FMAV does not necessarily have to replicate that of an insect in order to produce a stable, lift-enhancing LEV.

6.4.5 Delta-wing LEVs

The conical shape and spiral form of the LEV mean that it is similar in appearance to the LEVs formed over delta wings at high angles of attack, as is demonstrated by Figure 6.16. This has led many to suggest that there may be some link between the two phenomena (e.g. van den Berg and Ellington, 1997a; Shyy and Liu, 2007). It is true that the vorticity balance approach used above has also been extensively used to analyse delta-wing LEVs (see e.g. Lee and Ho, 1990), but it is also the case that although the *appearance* of the LEV is similar to that of a delta-wing LEV, there are major differences in the way it forms.

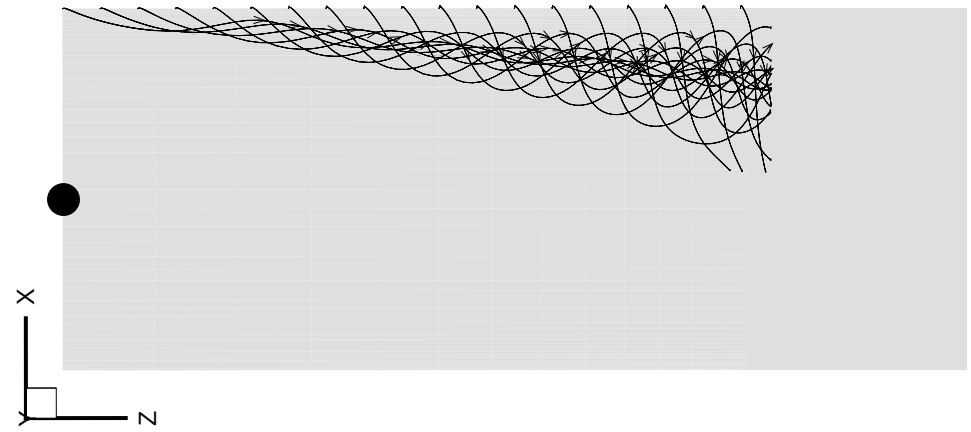

(a) Sweeping wing LEV — rectangular wing is seen from above and is sweeping about point marked by black circle at angle of attack of 45° and $Re_{3D} = 500$.

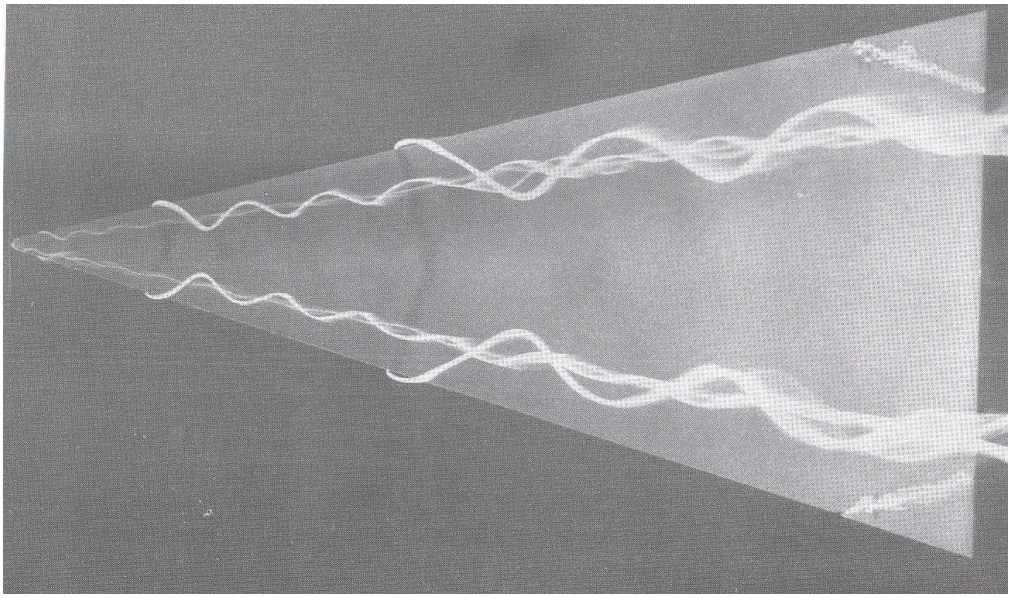

(b) Delta wing LEV, from Houghton and Carpenter (2003), Figure 5.41 after Werlé. Angle of attack is 20° and $Re = 20\,000$.

Figure 6.16: Comparison of sweeping wing LEV and LEV formed over delta wing at high angle of attack.

For a delta wing, a stable, lift-enhancing LEV only forms when the sweep-back angle exceeds a certain value[5]. To understand this it is helpful to think of the oncoming flow at the leading edge as being divided into two components — the component *normal* to the leading edge, and the component *parallel* to the leading edge. A stable LEV will only occur if the latter component is sufficiently large (i.e. only if the sweep-back angle is sufficiently high). This is because the high tangential velocity tends to convect the shed vorticity downstream. In other words, the vorticity generated near the apex of the delta wing is convected downstream because of the high tangential velocity. As Visbal (1995) notes; "these longitudinal vortices [the LEVs] are the mechanisms for the downstream convection of vorticity shed at the edge."

Further downstream, the LEV grows, because its size is enhanced by the vorticity that is being carried downstream by the high tangential velocity. For example, the LEV near the base of the wing contains not only vorticity that is created near the base, but also all the vorticity that was created nearer the tip but was convected towards the base because of the tangential velocity. A conical LEV therefore forms, but this is solely due to the high tangential velocity of the freestream flow at the leading edge (which in turn is a result of the high sweep-back angle).

In the sweeping-wing case, the tangential component of velocity at the leading edge is roughly zero — flow approaches the leading edge approximately normal to it. It is clear, therefore, that the LEV seen in this case is not truly analogous to the LEV seen over a delta wing. In both cases, the LEV is initially created by separation at the leading edge (and, just like for the 2D cases examined earlier, there is no need to use the term 'dynamic stall' to explain this separation), and in both cases the LEV is stabilised by spanwise flow; however, for the delta wing, the spanwise flow is a result of the high sweep angle of the wing; for the current sweeping wing, the spanwise flow is a result of the pressure gradient caused by the sweeping motion of the wing. This fundamental difference — which was noted by

[5] There is potential for confusion here. The sweep-back angle of a delta wing refers to the angle between the wing leading-edge and the normal to the flight velocity vector. 'Sweep', with regard to the current CFD work, refers to the angle through which the entire wing has rotated about its root, as a helicopter rotor blade 'sweeps' through the air.

Maxworthy (2007) — means that care must be taken when comparing the LEV seen here with the LEV formed by a delta wing. A similar conclusion was reached by Shyy and Liu (2007).

6.4.6 Lift distribution

It is interesting to investigate how it might be possible to use a 2D model to predict the lift produced by a 3D wing. This is not merely of academic interest — 2D models are notably faster to run than 3D models (in the current work, a 2D unsteady RANS simulation might take a couple of days, whereas a 3D simulation would take up to two weeks). The 2D model of Ansari (2004) uses, essentially, a 'blade element' approach to analyse 3D wings and is significantly faster than an unsteady RANS CFD model, taking only minutes to calculate several flapping cycles. In this model the wing is divided into a number of chordwise elements and each element is analysed in 2D. Such an approach assumes that there is no spanwise flow — or at least, if there is, it is of negligible impact. Current results demonstrate that this assumption is, strictly speaking, incorrect. The spanwise flow within the LEV is vital to its stability, and in addition the tip vortex has a large impact on the LEV.

It is helpful, however, to try to understand the lift produced by sections of a 3D wing by referring to the 2D results. Figure 6.17(a) shows that, soon after the wing has started motion, the lift distribution is approximately linear, with outboard sections producing more lift. This is as would be expected, firstly because on outboard sections the LEV is larger and secondly because outboard sections are travelling faster. The peak near the wing tip is due to the tip vortex; Figure 6.7 shows that the tip vortex creates an area of low pressure over the entire chord near the tip, at least until it separates as described above (§6.4).

Once the LEV has stabilised, the lift distribution is more complex, as shown in Figure 6.17(b) after around 600° of sweep. There is a gradual build up in lift between the root and the 60% span position, but after this the lift decreases, falling especially sharply near the tip. This is due to the fact that outboard of the 60% span position, the LEV has separated from the wing and is trailing into the wake,

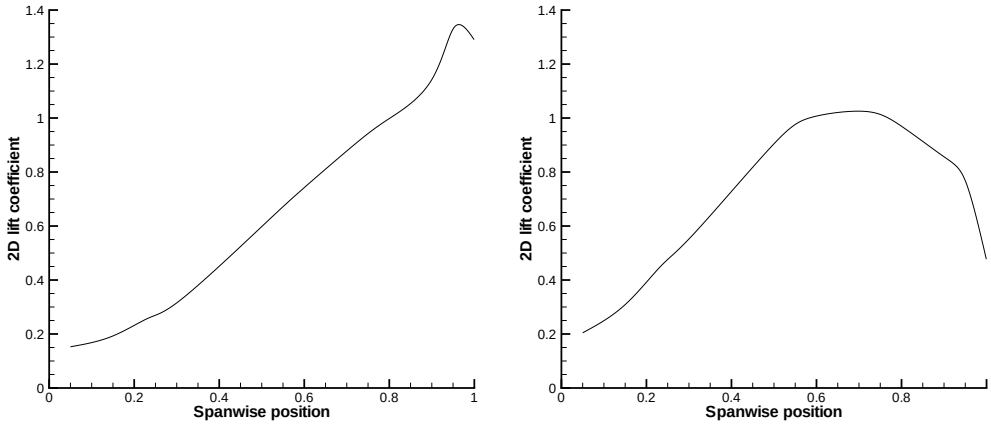

(a) After 5° of sweep

(b) After vortex has stabilised (after around 600° of sweep).

Figure 6.17: Lift distribution for an $AR = 2.5$ rectangular wing at 45° angle of attack and $Re_{3D} = 500$. Lift is non-dimensionalised by tip velocity and mean aerodynamic chord.

as seen in Figure 6.13.

Figures 6.18 and 6.19 show that most of the lift on the wing is caused by upper surface suction. At the root, the LEV is very small and weak, and therefore produces only a small low pressure peak, close to the leading edge ($X = +0.5$). Inboard, the LEV remains relatively small but the core pressure reduces as described above. Past the 30% span position, the peak pressure on the wing surface due to the LEV remains fairly constant (because although the LEV still grows stronger, it is situated further from the wing) until around 60% span. However, the LEV grows, so that the low pressure region spreads over the upper surface of the wing — at 60% span, the LEV lies over almost the entire forward half of the chord. As the LEV begins to turn into the tip vortex (between 60 and 70% span) the pressure on the surface falls. At 80% span and outboard, the effect of the LEV is not seen.

These results indicate that the lift produced by a particular section will not simply be dependent on that section's local velocity and local chord, but will depend also on the local strength and orientation of the LEV. Outboard sections do not benefit from the LEV, because the LEV separates from the wing at around 60 to 70% span. Inboard sections also produce relatively low lift, because the low local velocity means that the LEV formed is small.

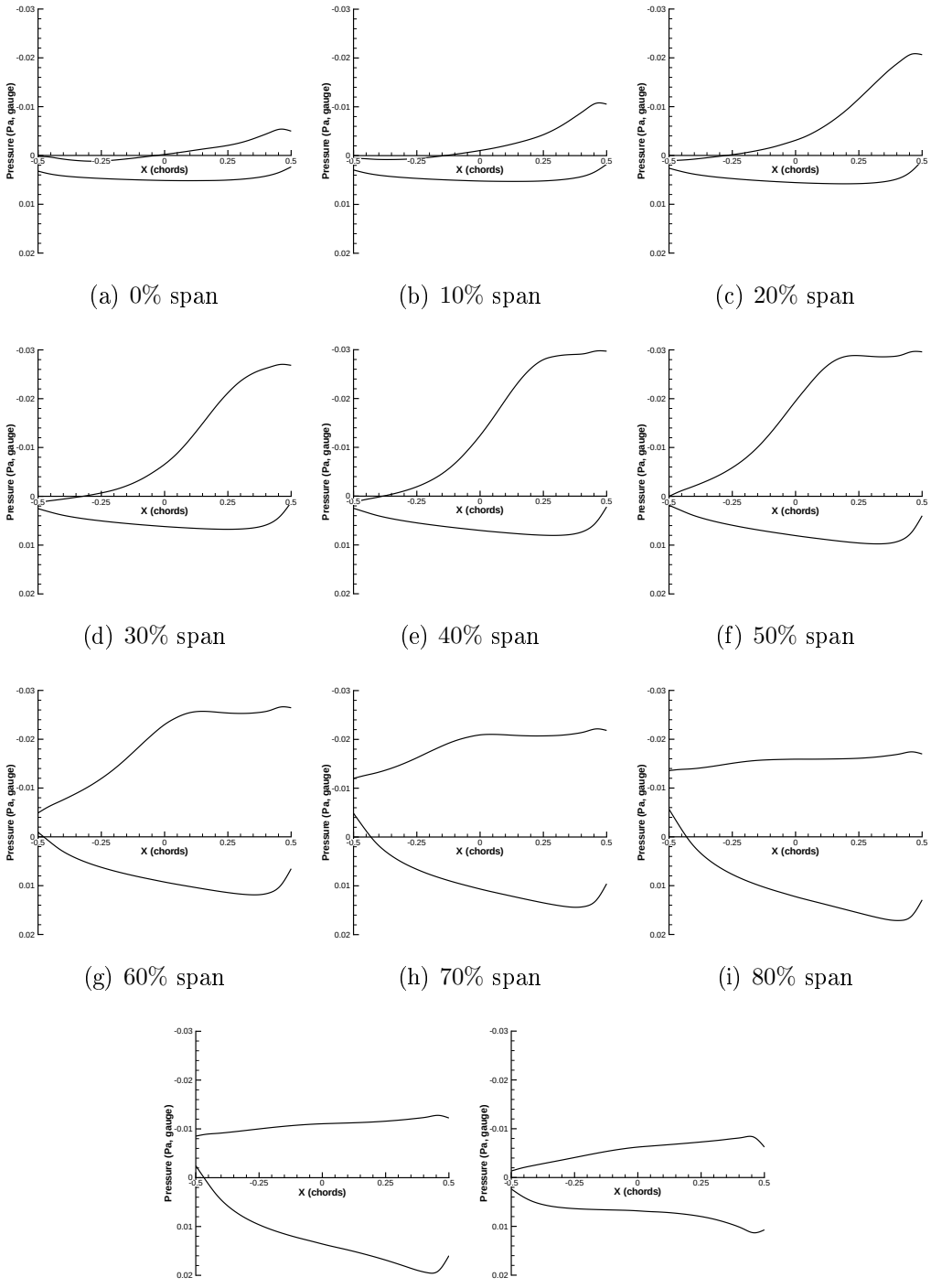

(a) 0% span (b) 10% span (c) 20% span

(d) 30% span (e) 40% span (f) 50% span

(g) 60% span (h) 70% span (i) 80% span

(j) 90% span (k) 100% span

Figure 6.18: Chordwise pressure distributions at various spanwise locations for an $AR = 2.5$ rectangular wing at 45° angle of attack and $Re_{3D} = 500$, once the LEV has reached a stable size. The top line represents the pressure on the upper surface of the wing in each case. Wing length is $0.1m$ and angular velocity is $1.82592rad/s$.

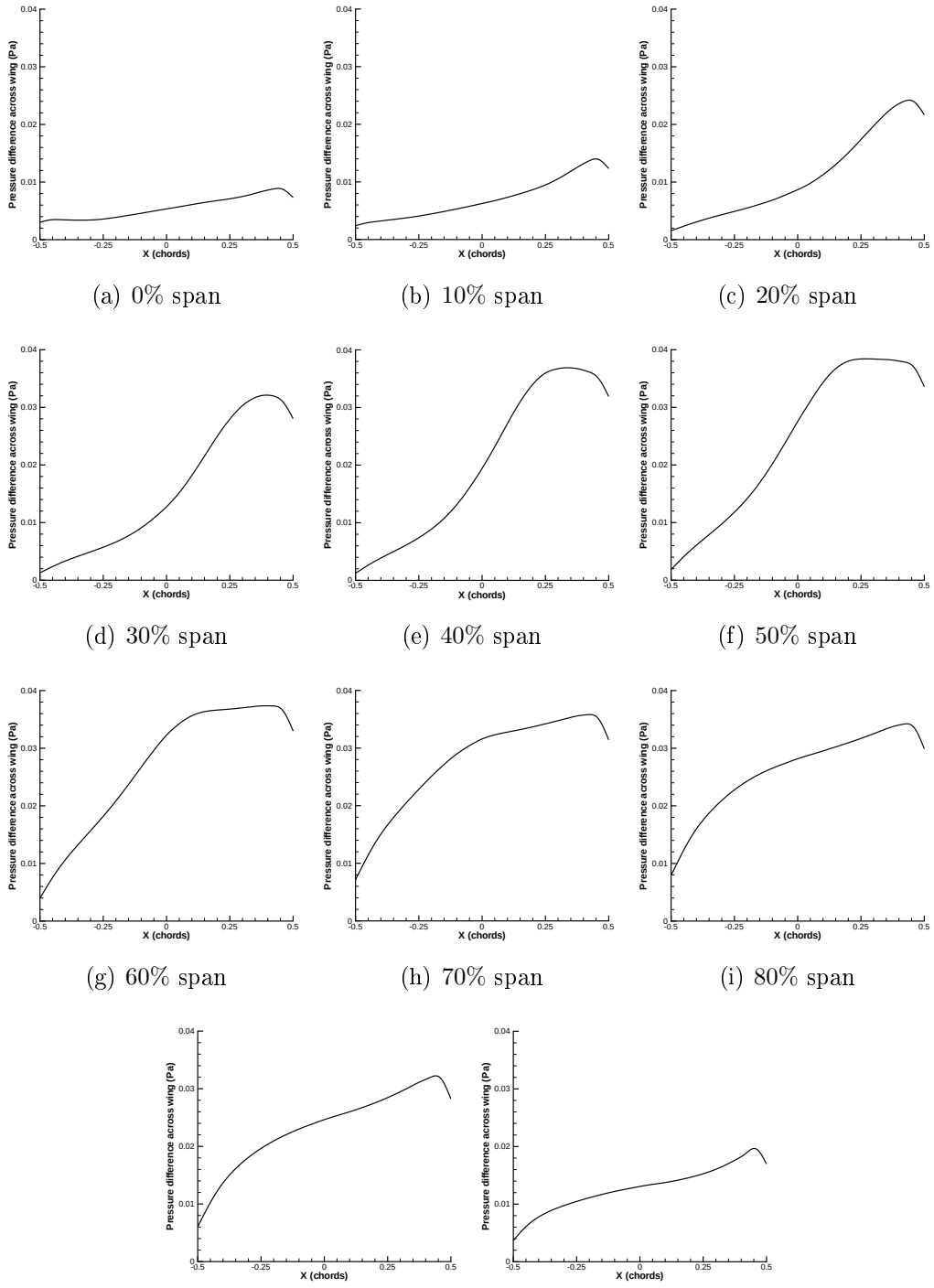

(a) 0% span (b) 10% span (c) 20% span

(d) 30% span (e) 40% span (f) 50% span

(g) 60% span (h) 70% span (i) 80% span

(j) 90% span (k) 100% span

Figure 6.19: Pressure difference across wing against chordwise location at various spanwise positions for an $AR = 2.5$ rectangular wing at 45° angle of attack and $Re_{3D} = 500$, once the LEV has reached a stable size. Wing length is $0.1m$ and angular velocity is $1.82592rad/s$.

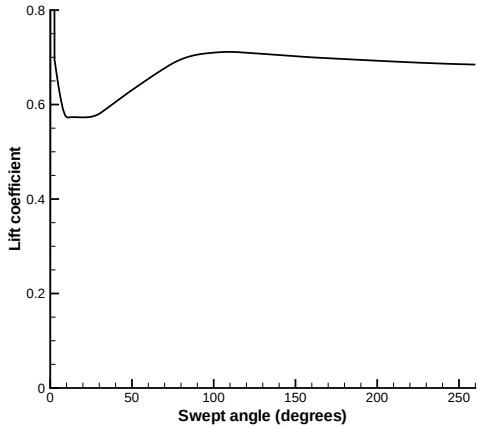

Figure 6.20: 3D lift coefficient vs. swept angle for an $AR = 2.5$ rectangular wing at 45° angle of attack and $Re_{3D} = 500$.

The overall lift coefficient produced by the wing eventually stabilises, as shown in Figure 6.20, at a value of around 0.7. There is a large initial peak, due to added-mass forces, just as seen for the 2D aerofoils earlier. The lift then falls sharply as the added-mass forces disappear, and then slowly increases as the LEV enlarges to its stable size and the TEV moves away from the wing.

6.4.7 2D vs. 3D LEVs

It has been shown that the LEV created by a sweeping 3D wing is a highly 3D structure, containing significant (both in magnitude and importance) spanwise flow. It has also been seen that this LEV is stable — that it grows to a certain size before remaining that size for all time (ignoring for the moment the effect of the returning wake). As seen earlier, for 2D cases the LEV generally grows until it is shed, and that the ensuing flowfield is time-varying.

It could be argued that it might be reasonable to use a 2D approach to model a 3D LEV, provided that the wing does not travel far enough for the LEV to shed in the 2D case. In other words, during the time when the 3D LEV is growing, it might be acceptable to approximate the growth of the LEV using results from a 2D model, and if the wing does not move far enough for the LEV to reach its stable size, the 2D model might give valid predictions of the size of the vortex at

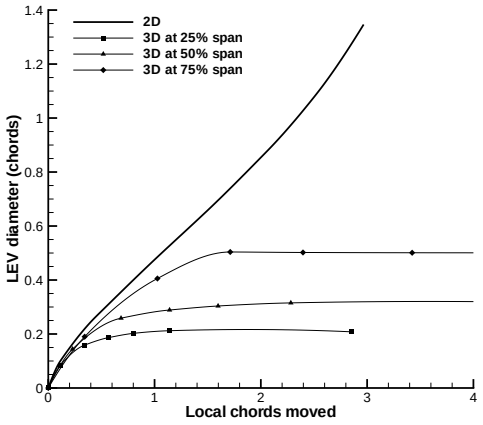

Figure 6.21: Comparison of rate of vortex growth for a 2D wing at 45° angle of attack and $Re = 250$, and various spanwise position of an $AR = 2.5$ rectangular wing at 45° angle of attack and $Re_{3D} = 500$. Size of LEV is defined in caption of Figure 5.6.

a given moment. In order to investigate this, it is possible to analyse the rate of growth of the LEV for 2D cases and for different spanwise locations for a 3D case.

Figure 6.21 compares the size of the LEV against the number of chords moved for a 2D case, and for a 3D case at the 25%, 50%, and 75% span positions. The effective Reynolds number will differ for the three spanwise locations of the 3D wing, but in Chapter 5 it was demonstrated that the rate of vortex growth is almost constant once $Re > 100$. A 2D Reynolds number of 250 was used for the purposes of this comparison as this was the effective 2D Reynolds number for the 3D wing at 50% span.

It can be seen that the initial growth rate is approximately equal in each case. However, after only around 0.4 chords of travel, the 2D model over-predicts the size of the LEV by around 70% at the 25% span position, 25% at the 50% span position, and 10% at the 75% span position. The corresponding errors after 2 chords of travel are 325%, 180%, and 70%. According to Wang et al. (2004), most insect wings travel around 4 chords between stroke reversals at 50% span. Figure 6.22 shows that for the wing used here, the tip has moved around 4 chords after only 90° of sweep. Unless the 3D wing is travelling less than (at most) 0.2 chords at a given spanwise location, using 2D results to predict the growth of the 3D LEV

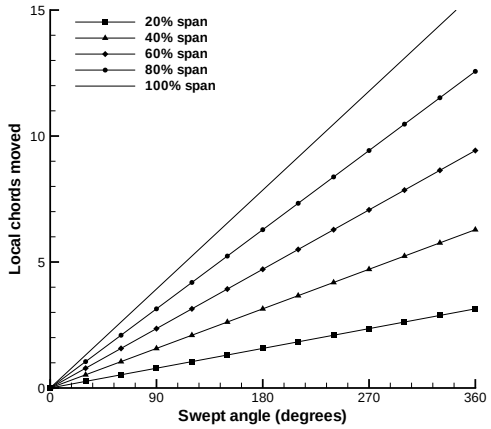

Figure 6.22: Comparison of local chords moved for various spanwise sections of an $AR = 2.5$ rectangular wing of length $0.1m$.

is not sensible. In practice, this means that (for the rectangular planform) the wing can sweep through an angle of around 5° before the 2D vortex size prediction becomes inaccurate.

Figure 6.23 shows that as a result of the difference between 2D and 3D flows, the effective 2D lift coefficient for a given spanwise section of a 3D wing cannot generally be accurately predicted using a 2D model. Figure 6.23 compares the 2D lift coefficient from the present 2D CFD model with effective 2D lift coefficients for various spanwise locations of a 3D wing — the effective 2D lift coefficient is calculated by non-dimensionalising the lift produced by a small spanwise section of the wing by the area of that section and its local velocity. Inboard sections actually produce very high lift coefficients when lift coefficient is calculated in this way.

Two-dimensional models assume that the phenomenology of the flow at each spanwise location is identical, and that there is no spanwise flow — in other words, that the flow is 2D. This assumption is more reasonable at some sections that at others. At the 70% span location, the flow *is* approximately 2D (the LEV has separated from the wing at this point and there is little flow in the spanwise direction). Here, the 2D model predicts lift coefficients of the right order of magnitude. However, at sections near the root, the flow is highly-3D. The assumption that the flow is 2D therefore introduces large errors.

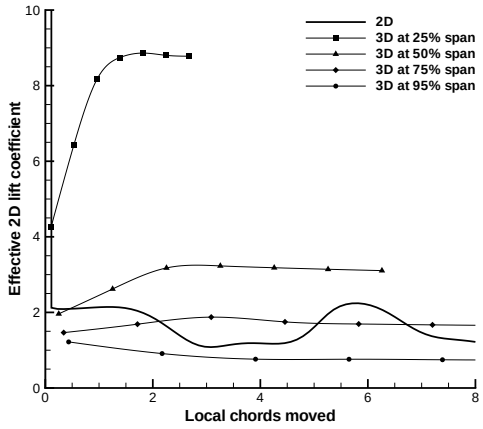

Figure 6.23: Comparison of lift coefficient for a 2D wing at 45° angle of attack and $Re = 250$, and the effective lift coefficient for various spanwise positions of an $AR = 2.5$ rectangular wing at 45° angle of attack and $Re_{3D} = 500$.

Errors are also introduced near the tip (Figure 6.23). Here, spanwise flow occurs due to the tip vortex structure and the 2D lift coefficient is reduced. 2D models cannot account for this, and therefore tend to over-predict the lift. These results, then, suggest that essentially-2D models (like that of Ansari (2004)) will under-predict the lift coefficient for inboard sections. However this is not likely to produce significant errors because these inboard sections contribute little to the overall lift force produced by the wing, due to their low local velocity. In addition, 2D models will over-predict the lift coefficient for outboard sections slightly, but this may well be balanced to some extent by the under-prediction on inboard sections. In fact, it is shown later (§6.10.2.1) that Ansari's model (which is essentially two-dimensional) predicts the total force produced by a 3D wing to be close to the total force predicted by the current CFD model.

These results show that 2D models cannot accurately predict the size of the LEV or the instantaneous effective 2D lift coefficient of a given spanwise section. However, it is important to realise that although the 3D vortical structure is the most dominant phenomenon in the flows examined *here*, the effects of wing reversal or wake capture are not included in the current model. These may well prove to be more important in an analytical model than the ability to accurately predict the size of the LEV. In fact, 2D models have been seen to produce good results

(§3.1.2). Therefore 2D models should not be dismissed as a means of analysing insect-like flapping.

6.5 Effect of changing 3D Reynolds number

Because of the dramatic effect of moving from a 2D aerofoil to a 3D wing, it makes sense to investigate the effect of increasing Reynolds number on these 3D flows, just as was done for 2D flows. Of course, the main concern is to investigate whether the stable, lift-enhancing LEV is a phenomenon that appears only at low Reynolds number (i.e. Reynolds numbers relevant to insect flight). In the worst-case scenario, if the LEV does not exist (or is not stable and lift-enhancing) at higher Reynolds numbers, scaling up insect-like flapping to create an FMAV might not be possible.

It has already been seen that, for $Re_{3D} = 500$, the LEV eventually becomes stable and remains in position for as long as the wing sweeps. This stability has been shown to be due to spanwise flow within the LEV, which extracts vorticity radially and prevents it building up and shedding. This idea is not new, having been suggested by Ellington et al. (1996), but has been widely disputed. Birch and Dickinson (2001) did not detect any spanwise flow at a Reynolds number of around 100 and postulated that some kind of wake capture was responsible for the LEV's stability. Later still, Wang (2005) suggested another hypothesis — that the LEV is stable because the "vortex line is pinned to the root and cannot shed" due to the fact that the velocity is zero at the root. The current results conflict with both of these latter suggestions — firstly, the wing does not interact with its own wake here (although this later is introduced later) so wake capture cannot be responsible for the stability of the LEV; and secondly, the velocity at the leading edge of the root of the wing used here is not zero, because the wing rotates around the mid-chord of the root.

Figure 6.24(a) shows that for all Reynolds numbers tested here, the lift force eventually becomes roughly stable. The final stable lift force increases as Reynolds number is increased, although this increase happens at a decreasing rate, as is

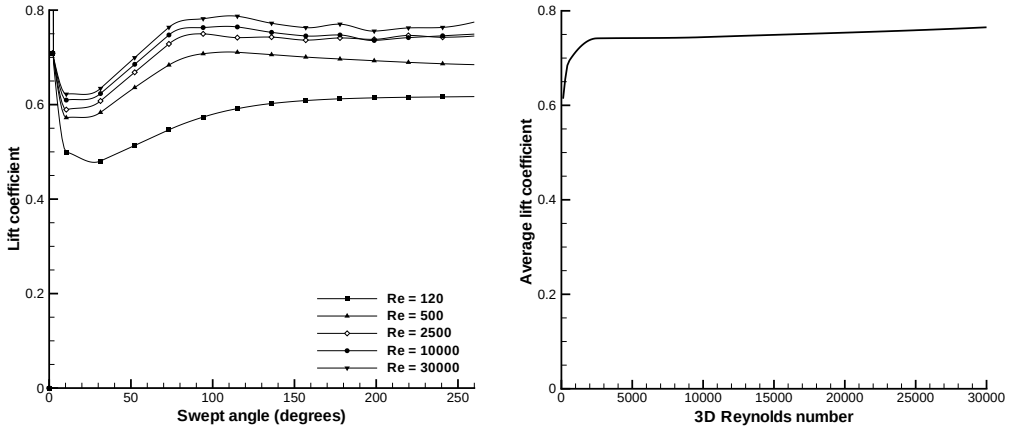

(a) Lift/rotation angle history (b) Average lift coefficient vs Re_{3D}

Figure 6.24: Lift vs. swept angle and average lift coefficient (over 150 to 260° of sweep) vs. Re_{3D} for $AR = 2.5$ rectangular wing at 45° angle of attack.

evident in Figure 6.24(b), and in fact the eventual stable lift coefficient remains almost constant from $Re_{3D} = 2\,500$ to $Re_{3D} = 30\,000$. Some high frequency, low amplitude fluctuations in lift force appear at 3D Reynolds numbers of 2 500 and above (which is why Figure 6.24(b) plots *average* lift coefficient over a time period when the lift coefficient has stabilised).

These results suggest two things. Firstly, because there is no large amplitude fluctuation in lift coefficient, it is reasonable to conclude that large-scale vortex shedding is not occurring (this conclusion is supported examination of the resulting flow-visualisation data, and by the current experiments; see Figure 6.15). For the 2D cases earlier it was seen that the shedding of an LEV (and, to a lesser extent, a TEV) led to a large drop in lift coefficient. For these 3D cases, no such large drop occurs, and therefore it appears that the LEV is stable. There are low amplitude fluctuations in lift at higher values of Re_{3D}, and these are explained later.

The second conclusion that can be drawn from the results in Figure 6.24 is derived from the fact that, from $Re_{3D} = 2\,500$ to $Re_{3D} = 30\,000$, the eventual steady lift coefficient is roughly constant. This suggests that the phenomenology of the flow is unchanged over this range of 3D Reynolds number. In other words, the LEV which was noted above for the $Re_{3D} = 500$ case appears to exist at higher Reynolds numbers also. However, there is a drop in the eventual steady lift

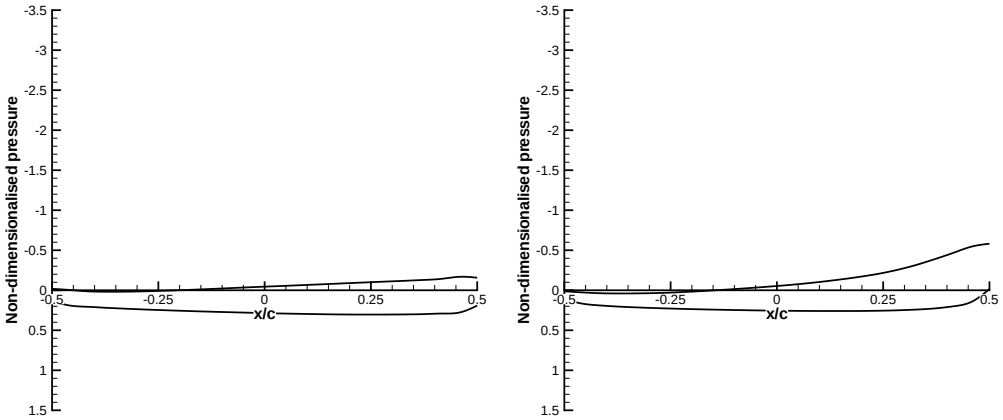

(a) $Re_{3D} = 120$, 10% span (b) $Re_{3D} = 500$, 10% span

Figure 6.25: Normalised pressure ($p/0.5\rho {V_{tip}}^2$) distributions for 3D, $AR = 2.5$, sweeping rectangular wing. Upper curve represents upper wing surface. Angle of attack is 45°.

coefficient at lower Reynolds numbers. There are two reasons for this drop.

Firstly, the current 2D results showed that for very low Reynolds numbers ($Re < 5$) separation did not occur at the leading edge and an LEV did not form. For the 3D case, the effective Reynolds number of a given spanwise position depends on the velocity of that position. Sections near the point of rotation (the root) effectively operate at much lower Reynolds numbers than sections near the tip. Therefore, separation would not be expected to occur at sections very near the root. In other words, for low values of Re_{3D}, there will be a spanwise area near the root where an LEV will not form; and this area will decrease in size as Re_{3D} increases. In fact, for $Re_{3D} = 120$ (the lowest value of Re_{3D} investigated here) the LEV does not form inboard of the 20% span position. But when $Re_{3D} = 500$, separation occurs even at the root, so that the LEV extends over the whole span — at least at an angle of attack of 45°. This effect is demonstrated in Figure 6.25, where it can be that for the $Re_{3D} = 500$ case (Figure 6.25(b)) there is a marked peak in the pressure distribution near the leading edge, which is due to the presence of the LEV. For the $Re_{3D} = 120$ case (Figure 6.25(a)), there is no such peak.

Secondly, outboard of 20% span, where an LEV does form for the $Re_{3D} = 120$

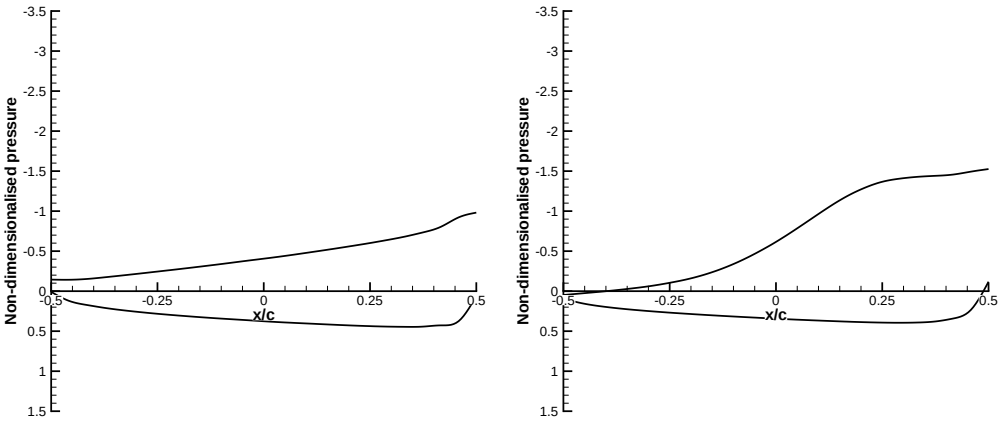

(a) $Re_{3D} = 120$, 40% span (b) $Re_{3D} = 500$, 40% span

Figure 6.26: Normalised pressure ($p/0.5\rho {V_{tip}}^2$) distributions for 3D, $AR = 2.5$, sweeping rectangular wing. Upper curve represents upper wing surface. Angle of attack is 45°.

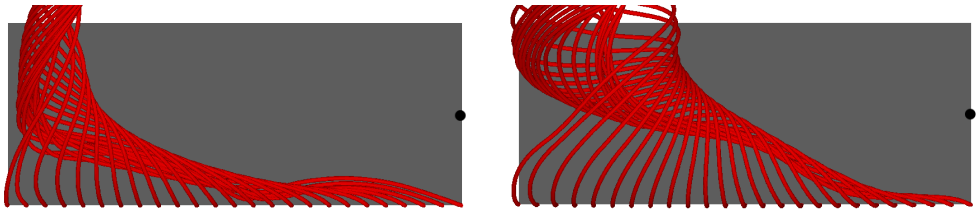

(a) $Re_{3D} = 120$ (b) $Re_{3D} = 500$

Figure 6.27: Structure of stable LEV, visualised by instantaneous streamlines released from leading edge. Angle of attack is 45° and view is from directly above wing. Rotation point is at mid-chord of root, marked with black circle.

case, this LEV is much smaller than for higher 3D Reynolds numbers. This is seen in Figure 6.26, where, for $Re_{3D} = 120$ (Figure 6.26(a)), the peak at the leading edge is much narrower than for $Re_{3D} = 500$ (Figure 6.26(b)). It is also evident in Figure 6.27, where it is clear that the LEV in the $Re_{3D} = 120$ case is much more compact. The reason for this change is, once again, viscosity. At $Re_{3D} = 120$, viscosity is comparatively important. The rate of vorticity production is decreased due to the lower Reynolds number, whereas the rate of vorticity diffusion is increased. The LEV grows more slowly at low Reynolds numbers, as was seen in §5.3.4, but spanwise flow still occurs within the LEV due to the spanwise pressure gradient. As a result, the LEV's stable size is much smaller at this lower Reynolds number than at higher Reynolds numbers.

To summarise: the lift coefficient for a 3D wing is lower at low Reynolds numbers than at higher Reynolds numbers. This is because, firstly, the LEV does not form over inboard sections of the wing at very low Reynolds numbers; and secondly, the size of the stable LEV decreases as Reynolds number is reduced (due to the increasing importance of viscosity).

As Reynolds number is increased, viscous diffusion becomes negligible, and the rate of vortex growth becomes independent of Reynolds number, as was seen in §5.3.4. However, increasing Reynolds number continues to increase the strength of the LEV, particularly on outboard sections, and therefore continues to increase the magnitude of the spanwise pressure gradient. This leads to an increase in the velocity of the spanwise flow within the LEV, and therefore an increase in the rate at which vorticity is extracted from the LEV into the wake. Thus the LEV, in general, remains balanced, and therefore stable, up to $Re_{3D} = 30\,000$. The lift coefficient therefore remains almost constant. This is in agreement with the experimental findings of Usherwood and Ellington who reported an almost constant force coefficient up to a Reynolds number of 26 000. They argue that it is not surprising that the LEV appears so insensitive to Reynolds number, given that LEVs over thin delta wings are "effective lift-producers" over "a vast range of *Re*" (Usherwood and Ellington, 2002b, p.1574).

6.5.1 KHI for 3D cases

The low-amplitude, high-frequency fluctuations in lift that are seen at 3D Reynolds numbers of 2 500 and above are reminiscent of the high-frequency fluctuations that were seen for 2D cases, which were attributed to Kelvin-Helmholtz instability (KHI). There is no reason why KHI should not occur in these 3D cases. For a 2D case it is caused by a velocity gradient across a vortex sheet, as discussed in §5.3.3.1. There, it was noted that it affects both leading- and trailing-edge sheets in the 2D case. The causes of the 2D KHI were also listed, and it was seen that in the case of the leading-edge sheet KHI was caused by the production of secondary vortices at the leading edge which created a large velocity gradient across the sheet.

A secondary leading-edge vortex is also formed in 3D cases, and strengthens as Reynolds number is increased. This is shown in Figure 6.28. For $Re_{3D} = 120$, the primary LEV is very weak and there is no secondary LEV, just as was seen for 2D cases earlier. At $Re_{3D} = 500$, the primary LEV is stronger, but there is still no secondary LEV at this spanwise location. A secondary LEV is first seen at $Re_{3D} = 2\,500$, and increases in strength as Reynolds number is increased further. Compare these plots to Figure 5.37 on p. 186.

Figure 6.29 compares the instantaneous structure of the LEV for a range of Reynolds numbers. It was noted above that the LEV increases in size as Re_{3D} is increased between 120 and 500, and it is clear that there is a further (though small) increase if Re_{3D} is increased to 2 500. After this, though, the size of the LEV remains roughly constant as Re_{3D} is increased further — at least up to $Re_{3D} = 30\,000$.

Figure 6.29 also shows clear breakdown of the leading-edge vortex sheet, particularly at $Re_{3D} = 15\,000$ and 30 000. At about the 60% span position, the LEV sheet is no longer smooth and continuous. The breakdown appears to happen in a similar way to the breakdown that occurs in 2D cases — a 'breakdown vortex' (see p. 179) forms at the leading edge. This breakdown tends to propagate in the spanwise direction, as evident in Figure 6.29(c) at $Re_{3D} = 15\,000$ (and, to a lesser extent, at $Re_{3D} = 30\,000$ in Figure 6.29(d)), leading to a breakdown LEV which may extend over a considerable spanwise portion of the wing. Perhaps the presence

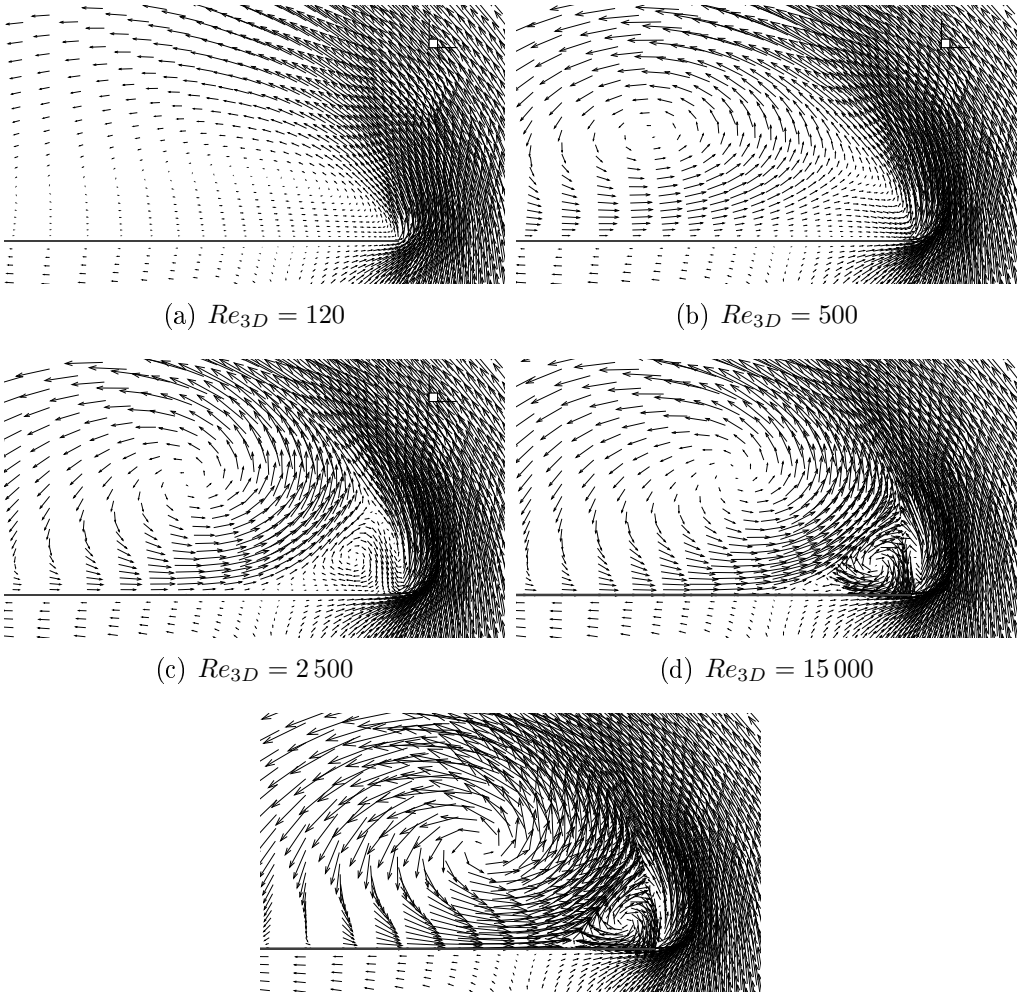

(a) $Re_{3D} = 120$ (b) $Re_{3D} = 500$

(c) $Re_{3D} = 2\,500$ (d) $Re_{3D} = 15\,000$

(e) $Re_{3D} = 30\,000$

Figure 6.28: Instantaneous vectors on 2D slice at 50% span for various 3D Reynolds numbers. The vector field is coarsened for clarity and the lengths of the vectors are normalised with respect to V_{tip} so that the freestream vectors are the same length in each case. The black line is the wing section, with the leading edge on the right. The angle of attack is 45°.

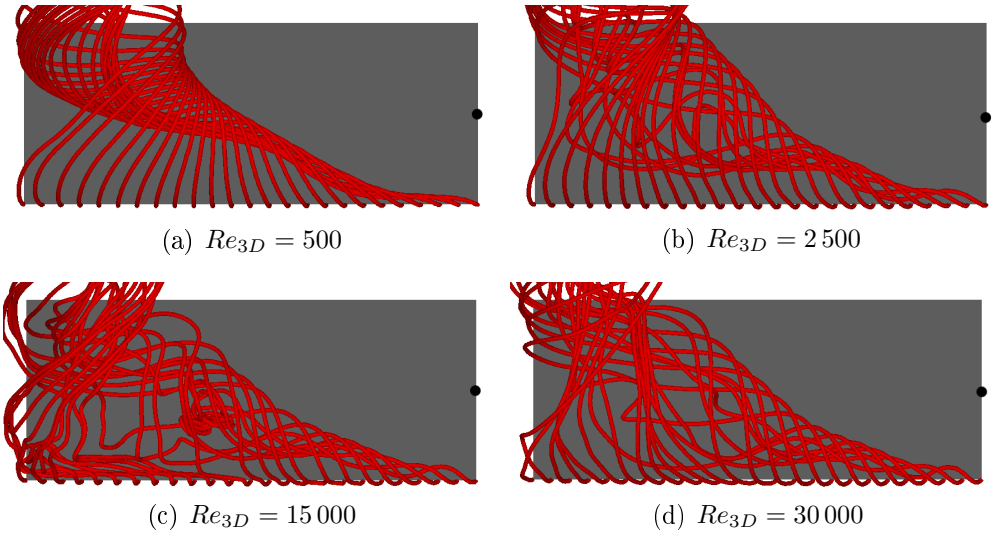

(a) $Re_{3D} = 500$ (b) $Re_{3D} = 2\,500$

(c) $Re_{3D} = 15\,000$ (d) $Re_{3D} = 30\,000$

Figure 6.29: Structure of stable LEV, visualised by instantaneous streamlines released from leading edge. Angle of attack is 45° and view is from directly above wing.

of the breakdown LEV explains the results of Lu et al. (2006), who examined the flow around dragonfly wings and noticed a *pair* of LEVs near the leading edge (see p. 48).

For a 2D case it was seen that the breakdown LEVs which form at the leading edge are immediately shed and encircle the primary LEV, as seen in Figure 5.31 on p. 180, but do not affect the shedding frequency of primary LEVs. The same is true for the 3D cases seen here; the breakdown has a negligible impact on lift production as it does not cause the primary LEV to shed from the wing. However, it does cause the LEV to become less coherent and more 'disorganised'.

The same phenomenon was noted by Nolan (2004), who found that at $Re_{3D} = 6\,500$, the LEV "lost coherency". She suggested that this might be due to the LEV beginning the transition to turbulence, or that it might be the result of vortex bursting (see below). However, she stated that, based on the current state of knowledge, it was "not possible to do more than speculate" about these phenomena (Nolan, 2004, p. 77).

The effect of KHI is less pronounced for 3D cases than for 2D cases. This is simply because for a 2D case, KHI occurs across the whole 'span' instantaneously. For a 3D case, the effect is 'averaged' over much of the span. It is notable that

KHI does not seem to occur inboard of around the 50% span position, even at $Re_{3D} = 30\,000$. It is suggested here that at these inboard sections the size of the secondary LEV is limited (because the primary LEV does not become very large) so that the velocity gradient across the leading-edge vortex sheet does not become steep enough to produce KHI.

6.5.2 Vortex burst

The similarity between the LEVs that form above a delta wing at high angles of attack and the LEV seen on the 3D sweeping wings here has already been observed. Some important differences have also been highlighted. One phenomenon that could be important in the current context is 'vortex burst'[6]. It is well known that the LEVs above a delta wing often experience "a dramatic form of flow disruption" (Visbal, 1995) which results in a reduction of the axial flow velocity and an increase in the size of the vortex core (Bova et al., 2001). If vortex burst occurs above the delta wing, it leads to a dramatic decrease in lift, analogous to stall on a conventional wing (Bertin and Smith, 1998; Katz and Plotkin, 2001). If the LEV seen here is similar to the LEV seen over a delta wing, it is logical to consider whether vortex burst might occur in this case; and, if so, what effect it might have.

Figure 6.30 suggests that vortex burst is occurring in the LEV. There appears to be a sudden increase in the width of the LEV core — a classical sign of vortex burst (Mitchell and Délery, 2001). However, there is no corresponding decrease in lift coefficient, as would be expected if vortex breakdown were present.

Vortex burst can occur whether the vortex is initially laminar or turbulent, but the process of burst invariably leads to turbulent flow (Hall, 1972). In the current simulations, laminar flow has been assumed throughout (see §4.2.1). Therefore it is possible that vortex burst is *starting* to occur; but the fact that transition cannot occur means that the process cannot be completed, so that the loss of lift that is usually associated with vortex burst is not seen. Equally it is possible that vortex burst is *not* occurring; that the phenomenon seen in Figure 6.30 is not vortex

[6] Vortex burst is also occasionally referred to in the literature as vortex breakdown. But because the term 'breakdown' has already been used to refer to the effect of KHI, the term 'vortex burst' is used in this section.

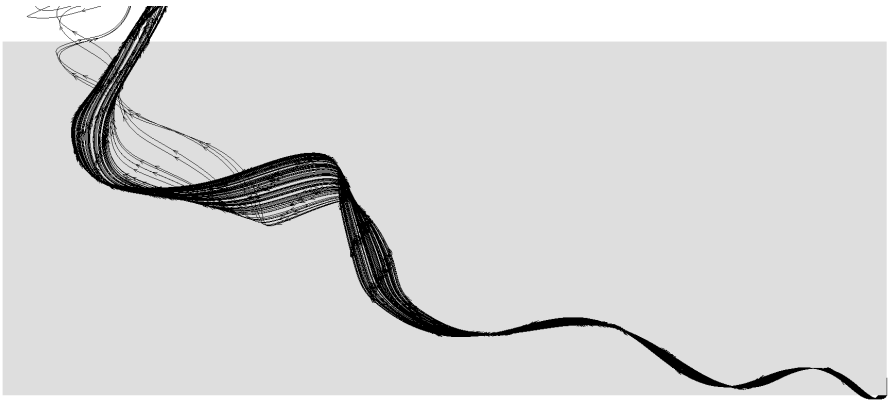

Figure 6.30: Suggestion of vortex burst for $Re_{3D} = 30\,000$ and angle of attack of 45°. View is from directly above wing. Core of LEV (visualised by instantaneous streamlines released from leading edge near root) is tightly wound until the 50% span position, where it enlarges considerably. Compare this Figure with classical images of delta-wing LEV burst, (e.g. Robinson et al. (1994, Figure 4) (reproduced in Figure 6.31)).

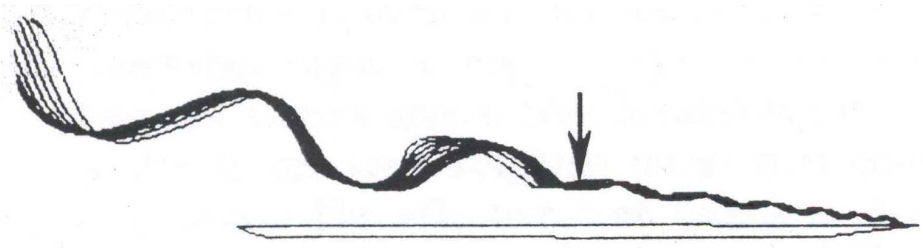

Figure 6.31: Classical image of delta-wing LEV burst, from Robinson et al. (1994, Figure 4). The position of vortex burst is marked by the arrow. In this case the Mach number is 0.30, giving a chord Reynolds number of 10^6. The angle of attack is 30°.

burst, but simply looks like it.

This potential confusion is increased by the fact that even in the case of delta wings, where vortex burst is a well-known phenomenon, the actual process of burst is not well-understood. Mitchell and Délery (2001) speak of the "strong need" for better understanding of the phenomenon, and there appears to be some controversy in the literature as to what is required for vortex burst to occur. Hall (1972) states that it is necessary for an adverse pressure gradient to exist in order for burst to occur; if this is true, it would not be expected in the cases under consideration here because the sweeping motion of the wing leads to a favourable pressure gradient. However, Mitchell and Délery (2001) suggest that although vortex burst is highly sensitive to pressure gradient, an adverse pressure gradient is not absolutely necessary for burst to occur.

One point on which the literature seems to agree is that vortex breakdown will only occur if the helix angle of the vortex exceeds a critical value of around 50° (helix angle being equal to $tan^{-1}(V_\theta/V_Z)$, where V_θ and V_Z are the tangential velocity and axial velocity within the vortex respectively). In the current case, V_θ will increase both as the distance outboard increases and as Reynolds number is increased. V_Z will also increase as Reynolds number is increased, and, generally speaking, will increase with z position; but when the tip vortex starts to influence the LEV, V_Z decreases. Therefore, if vortex burst does occur, it would be expected to occur more readily near the tip.

Another complication is Reynolds number itself. Mitchell and Délery (2001) state that "Reynolds number has nearly no direct effect on the phenomenon [of vortex burst], except at very low Reynolds numbers well below any practical value." Unfortunately they do not state what they mean by "very low" Reynolds numbers, and in fact the Reynolds numbers which they consider to be "well below any practical value" are probably those Reynolds numbers which are of interest to us. Nor do they state what the effect of Reynolds number is at these "very low" Reynolds numbers. Ol and Gharib (2003) studied delta wings at Reynolds numbers between 6 000 and 15 000, but were more concerned with the impact of increasing angle of attack than the effects of changing Re. Van Dyke (1982, Figures 125 & 126) shows

that the vortex burst position for a delta wing does move upstream as Reynolds number is increased from $Re = 5\,000$ to $Re = 10\,000$.

In addition, there are complications when discussing the definition of Reynolds number. In the current case, it is defined using mean wing chord. In the case of a delta wing it is usually defined using wing root chord. For the case of a delta wing the LEV is roughly aligned with the root; for the current case, it is roughly perpendicular to it. Perhaps Reynolds number should be defined using wing length, then, instead of mean chord. Similarly, in the current case Reynolds number is defined using wing tip velocity. In the case of a delta wing it is usually defined using freestream flow velocity. But, again, in the case of a delta wing the freestream flow velocity is roughly aligned with the LEV; in the current case, the wing tip velocity is roughly perpendicular to the LEV.

Therefore it is not immediately clear whether any of the data relating to delta-wing LEV bursting are directly relevant to the current case; and even if they are, the bursting of delta-wing LEVs is still not well understood. Although further work is needed before it is possible to confidently assess the importance of vortex burst in insect-like flapping, the current results indicate that it does not occur at the Reynolds numbers and wing geometries covered here.

6.5.3 Summary of Reynolds number effects

It has been seen that the current model predicts the LEV to be stable and lift-enhancing over the whole range of Reynolds numbers from 120 to 30 000. This is important, as it means that, if this prediction is correct, it should be possible to scale up insect-like flapping to create a functional FMAV, without losing the important lift-enhancing LEV. Perhaps this explains the fossils mentioned earlier (p. 39) — the fossils of dragonfly-like creatures with wingspans of up to 70cm (Dudley, 1998). There is little evidence to suggest that these creatures flew using the same aerodynamic mechanisms as present-day insects, apart from the fossils themselves, which suggest that these large insects had the same biological layout as present-day insects. The atmosphere in which these large insects flew might well have been different to the present-day atmosphere.

Increasing Reynolds number in the 3D cases causes some increase in lift coefficient. The increase is mainly between $Re_{3D} = 500$ and $Re_{3D} = 2\,500$ — from $Re_{3D} = 2\,500$ to $Re_{3D} = 30\,000$ the lift coefficient is roughly constant. In the 2D cases examined earlier it was found that increasing Reynolds number up to $Re = 1\,000$ caused an increase in mean lift coefficient, but any further increases in Re did not cause a further increase in lift (§5.3.5). The findings presented here are therefore not surprising. The occurrence of KHI at higher Reynolds numbers is also not surprising, given the results of the 2D studies earlier (§5.3.3.1).

6.6 Effect of changing angle of attack

All of the above simulations have been for a rectangular wing of $AR = 2.5$ at an angle of attack of 45°. The impact of changing this angle of attack is now considered. In §5.4, it was noted that higher angles of attack produced stronger LEVs for a 2D case. In a 3D case, a similar relationship would be expected to exist between vortex strength and angle of attack, and therefore it might be justifiable to ask whether, at higher angles of attack, the rate of vorticity generation will be high enough to make the 3D LEV unstable. It has been seen that at 45° angle of attack, vorticity is drained from the LEV via spanwise flow at a rate equal to the rate at which it is generated at the leading edge. If higher angles of attack lead to higher rates of vorticity generation, is it possible for the rate of vorticity extraction (via spanwise flow) to rise to the required magnitude to keep the LEV stable?

6.6.1 Lift

Figure 6.32(a) shows that, at a 3D Reynolds number of 500, the lift coefficient eventually stabilises, even at an angle of attack of 81°. This indicates a lack of vortex shedding, which is confirmed by inspection of the resulting flow-field data.

At a 3D Reynolds number of 30 000, Figure 6.32(b) shows that the lift coefficient stabilises at an angle of attack of 9°. At 27° angle of attack, some small-scale fluctuations are evident, and the magnitude of these fluctuations increases as angle of attack increases. This is consistent with the discussion of KHI above; higher

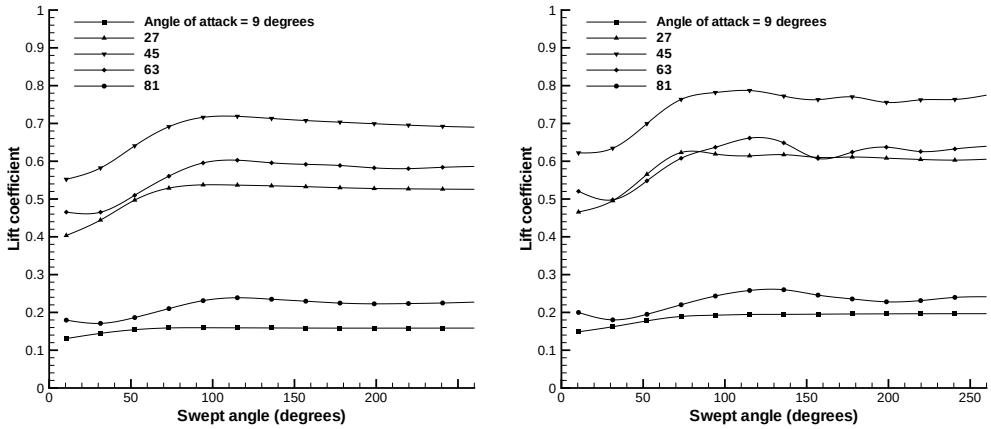

(a) $Re_{3D} = 500$ (b) $Re_{3D} = 30\,000$

Figure 6.32: Lift coefficient vs. swept angle for various angles of attack for a rectangular, $AR = 2.5$, impulsively-started wing.

angles of attack lead to a stronger primary vortex, leading to a stronger secondary vortex. As a result, the velocity gradient across the leading-edge vortex sheet increases, and the sheet becomes more susceptible to KHI.

Plotting lift coefficient (averaged over the range 150 to 250° of sweep angle) against angle of attack, as in Figure 6.33(a), reveals that, for both Reynolds numbers, maximum lift occurs at around 45° angle of attack. Even for $Re_{3D} = 500$, virtually all of the force on the wing is due to pressure[7] and because the wing is infinitely thin, the net force acts roughly perpendicular to the wing. Figure 6.33(b) plots average normal force coefficient against angle of attack. As angle of attack is increased from zero up to 45°, the net force increases to such an extent that even though the *relative* magnitude of the component of force in the vertical direction is *decreasing*, the *absolute* magnitude of the vertical force (i.e. the lift force) *increases*. Once the angle of attack exceeds 45°, the normal force continues to grow, but the rate of growth decreases. In addition the relative magnitude of the component of the normal force in the vertical direction continues to decrease, and as a result the lift force decreases, reaching zero, as would be expected, at 90° angle of attack.

[7]At $Re_{3D} = 500$ and an angle of attack of 45°, the magnitude of the lift due to viscous forces is around 0.8% of the magnitude of the lift due to pressure forces. Viscous forces are more important at lower angles of attack, as is shown later.

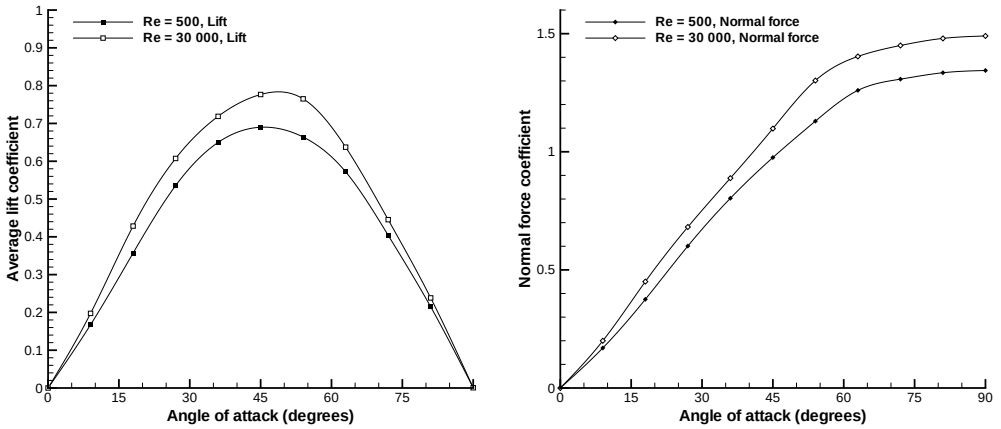

(a) Average lift coefficient (b) Average normal force coefficient

Figure 6.33: Average lift and normal force coefficients vs. angle of attack for a rectangular wing of $AR = 2.5$ between 150° and 250° swept angle.

What has been seen is that, for the situation under consideration here, stall occurs at around 45° angle of attack, if stall is defined as the point of maximum lift. Stall is sometimes defined as the condition in which flow separates from the leading edge (see e.g. Massey and Ward-Smith, 1998) but this definition should be avoided here, because separation occurs at angles of attack much lower than the angle of attack for maximum lift. In the cases under consideration here, there is no dramatic change in the phenomenology of the flow at the stall point, as there is for conventional wings and aerofoils; the fact that lift then starts to drop off is due to the fact that the component of the force on the aerofoil in the vertical direction starts to decrease.

At 90°, the CFD model predicts two stable vortices, one emanating from the leading edge and the other from the trailing edge. These remain in place, at least for as long as the simulation was allowed to run. For 2D cases at the same angle of attack, two vortices are also produced, and grow at the same rate; but generally speaking some instability will eventually cause vortex shedding to occur alternately from each side of the plate. It is not possible to say with certainty whether the same thing would eventually happen for the 3D situations examined here, but in any case the question is of little interest.

These results allow us to gain some idea of the effect of an LEV. In §5.3.2.2, it

was noted that many of the current estimates of the effect of the LEV are based on the logic that the lift due to an LEV can be calculated using the circulation within the LEV. It was stated there that this view is simplistic as it does not take into account the *position* of the LEV. Current results give an eventual steady lift coefficient of around 0.16 for the $Re_{3D} = 500$ case at 9° angle of attack (where there is no LEV). The corresponding lift coefficient for the $Re_{3D} = 30\,000$ case is around 0.2 — an increase of 25%. However, it is important to take account of the fact that there is a rise in lift coefficient when Re_{3D} is increased, even if an LEV is formed in both cases. For example, at 45° angle of attack, the lift coefficients for the $Re_{3D} = 500$ and 300 000 cases are around 0.69 and 0.78 respectively; a rise of around 13%, even though an LEV is present in both cases. It is quite possible that if it were possible to create a case with an angle of attack of 45° but without an LEV (by decreasing Re_{3D} sufficiently) and then compare it to the 45° cases where an LEV is present, a larger difference than 25% might be seen, because in the case without an LEV there would be a large skin-friction force in the negative vertical direction. However these results do question the accuracy of the claim of van den Berg and Ellington (1997a), who stated that the LEV can supply "up to two-thirds of the required lift during the upstroke." In fact it is reasonable to question whether it is possible or sensible to break down the lift force in this way. It is possible to gain the impression that the LEV is something that an insect actively 'creates' by some special mechanism, whereas in fact it is clear that the LEV is simply a perfectly logical result of the kinematics of the wing.

It is important to bear in mind the fact that part of the reason why the lift coefficient is relatively low for the $Re_{3D} = 500$ case at 9° angle of attack is that viscous forces have a component in the negative vertical direction. This component is quite large because of the low Reynolds number. If Reynolds number were increased to $Re_{3D} = 30\,000$, viscous forces would be expected to become less important. Therefore if it were possible to have a wing at an angle of attack of 9° and $Re_{3D} = 30\,000$ *without* an LEV some rise in lift coefficient might be expected. However, it is not possible for such a situation to exist; just as for 2D cases, the LEV cannot be 'turned on' and 'turned off' at will.

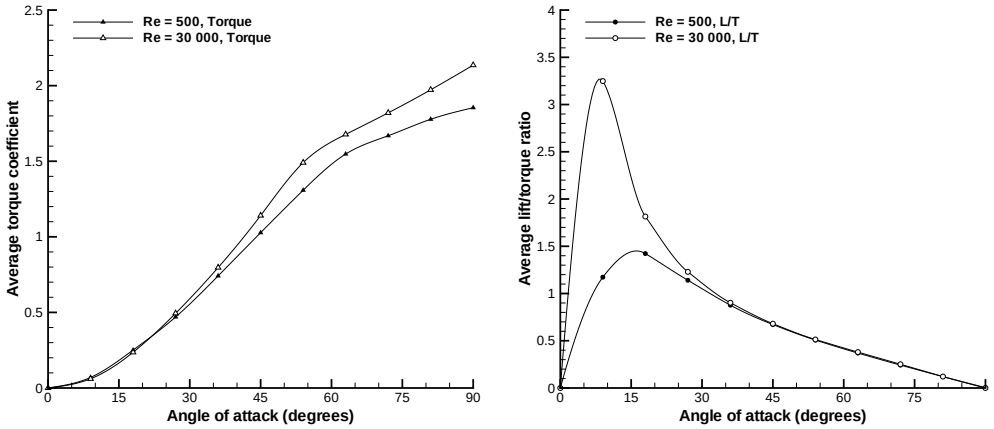

(a) Average torque coefficient (b) Average lift/torque ratio

Figure 6.34: Average torque and lift/torque ratio vs. angle of attack at two different Reynolds numbers for a rectangular wing of $AR = 2.5$ between 150° and 250° swept angle. Lift/torque ratio is non-dimensionalised by multiplying by mean aerodynamic chord.

6.6.2 Lift-to-torque ratio

.

Figure 6.33(a) tells us that maximum lift is produced at 45° angle of attack, but it does not enable us to identify the most *efficient* angle of attack — that is, the angle of attack at which maximum lift is produced *per unit torque* on the motor or mechanism driving the wing. Figure 6.34(a) confirms that the torque coefficient[8] increases as the angle of attack is increased, just as would be expected — the drag force will rise with angle of attack, reaching a maximum at 90° angle of attack, and of course torque is directly related to drag.

Figure 6.34(b) reveals that, for $Re_{3D} = 500$, the angle of attack for maximum lift/torque ratio (L/T) is around 15°. For $Re_{3D} = 30\,000$, it is even lower, at around 10°. This may seem counter-intuitive, but in fact is quite logical. Because the net force on the wing is roughly normal to the wing, as angle of attack is increased the component of the net force in the horizontal direction increases as the component in the vertical direction decreases, so that increasing angle of attack

[8] Torque coefficient is defined as

$$C_T = \frac{T}{\frac{1}{2}\rho V_{tip}^2 A\bar{c}}.$$

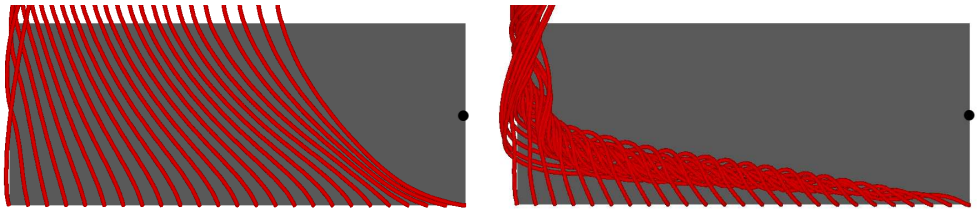

(a) $Re_{3D} = 500$ (b) $Re_{3D} = 30\,000$

Figure 6.35: Eventual steady flow structure, visualised by instantaneous streamlines, for 9° angle of attack. View is from directly above wing. Wing has swept through an angle of around 250° about the mid-chord of the root (marked with a black circle) and lower edge is leading.

tends to decrease L/T. Similar findings were reported for lift/drag ratio in 2D cases (see §5.4).

The reason for the large difference in L/T (between the two Reynolds numbers) at low angles of attack lies in a combination of two factors: the magnitude of viscous forces, and the development of the LEV. For $Re_{3D} = 500$, no LEV is formed at 9° angle of attack, as shown in Figure 6.35(a). The flow simply rounds the leading edge and flows down the upper surface of the aerofoil; as was seen for the 2D case earlier (see Figure 5.13, p. 151). There is some outboard flow on the upper surface due to the pressure gradient, but generally the viscous force on the wing is in a direction which lies parallel to the wing chord and towards the trailing edge. This tends to increase the drag and reduce the lift produced by the wing — in fact, viscous forces account for over 70% of the torque on the wing at this Reynolds number and angle of attack.

At $Re_{3D} = 30\,000$, an LEV *is* formed at 9° angle of attack, as seen in Figure 6.35(b). Just as for the 2D flows earlier (see p. 155), there is a decrease in viscous drag; firstly because viscous forces are less important due to the Reynolds number increase, and secondly because the flow on the upper surface is now not exclusively towards the trailing edge. At $Re_{3D} = 30\,000$, viscous forces account for only 15% of the torque on the wing at 9° angle of attack. The presence of the LEV also enhances lift. As a result of these changes, the torque coefficient at 9° angle of attack is 0.14 at $Re_{3D} = 500$ but only 0.06 at $Re_{3D} = 30\,000$, and the corresponding lift coefficients are 0.17 and 0.20 respectively; hence the large increase in L/T. At

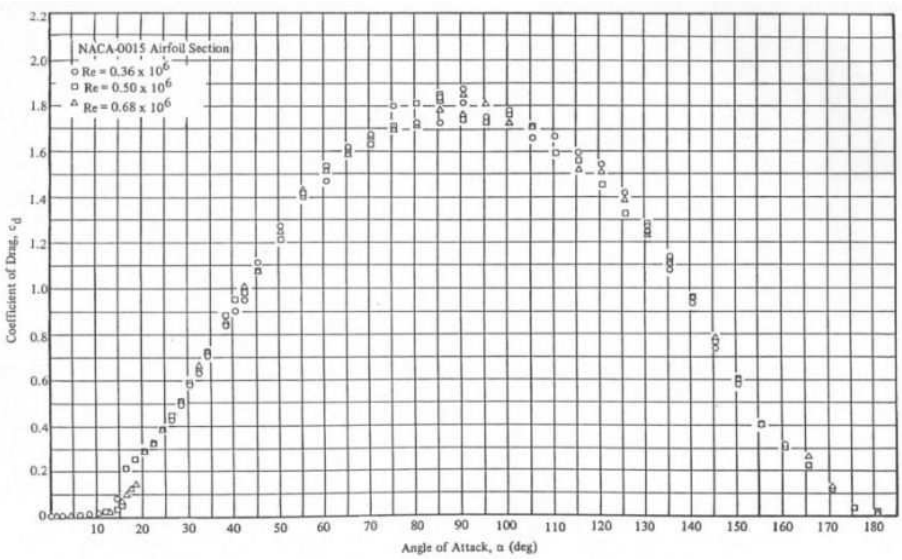

Figure 6.36: Drag coefficient vs. angle of attack for conventional aerofoil, from Sheldahl and Klimes (1981).

higher angles of attack, the change in importance of viscous forces does not have such a dramatic impact because an LEV is formed even at $Re_{3D} = 500$; so that the flow field shown in Figure 6.35(a) does not occur. At angles of attack of 45° and above, L/T is independent of Reynolds number (within the range of Reynolds numbers examined here).

6.6.3 Pressure distribution

It has already been seen (Figure 6.34(a)) that the torque on the wing increases as angle of attack is increased. Of course, this is not surprising, as the same relationship applies for a conventional aerofoil; see Figure 6.36. However, in the case of a conventional aerofoil or wing, there is a sudden jump in drag coefficient at the stall angle of attack, caused by the flow separating from the wing. In the current case there is no such sudden jump because separation actually has a beneficial effect on drag (and therefore torque), due to the low Reynolds numbers used here.

Figure 6.37(a) reveals the causes of the increase in normal force. Generally speaking, the LEV becomes stronger as angle of attack is increased, exactly as would be expected based on the 2D results presented earlier. This is manifested in

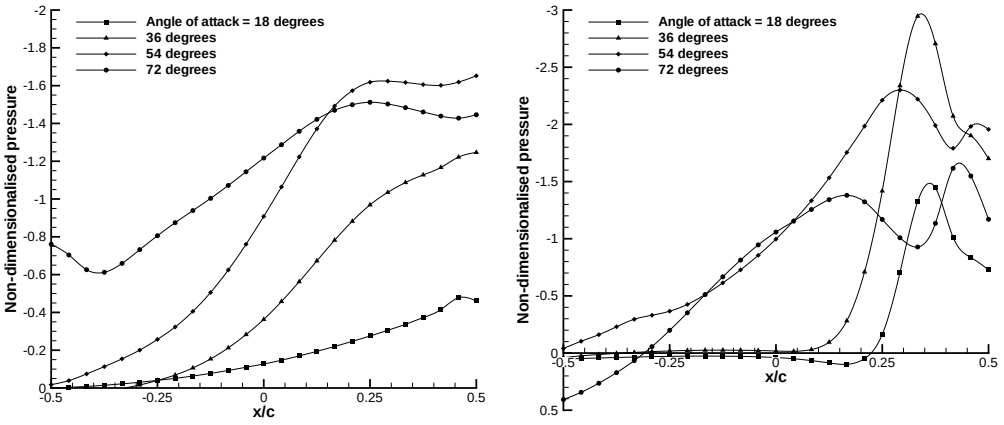

(a) $Re_{3D} = 500$ (b) $Re_{3D} = 30\,000$

Figure 6.37: Non-dimensionalised pressure distribution on wing upper surface at 40% span.

Figure 6.37(a) by a marked increase in the magnitude of the pressure peak near the leading edge. However, once the angle of attack exceeds around 54°, the magnitude of this peak decreases. This is because at these higher angles of attack the LEV is larger, so that its core lies further above the wing. As a result, the magnitude of the pressure drop seen on the wing's surface is decreased.

This increase in the size of the LEV as the angle of attack is increased is also evident in Figure 6.37(a). The area of low pressure due to the LEV spreads over the chord as angle of attack increases, until at 54° the pressure is significantly negative over the entire chord. If angle of attack is increased beyond this point, the pressure at the trailing edge falls further as the LEV continues to grow.

Figure 6.38 visualises the pressure on the upper surface of the aerofoil. For $Re_{3D} = 500$, the LEV is relatively diffused (as is also indicated by the width of the low pressure region at the leading edge in Figure 6.37(a)). As angle of attack is increased, the LEV spreads over the wing. At an angle of attack of 54°, the low pressure due to the LEV core is clearly visible at around 40% span, indicating that the LEV at this angle of attack is stronger than for lower angles of attack.

The plots for $Re_{3D} = 30\,000$ (Figure 6.39) show significant differences from those at the lower Reynolds number. The LEV is more concentrated. Even at an angle of attack of 18°, the line of low pressure due to the LEV is obvious,

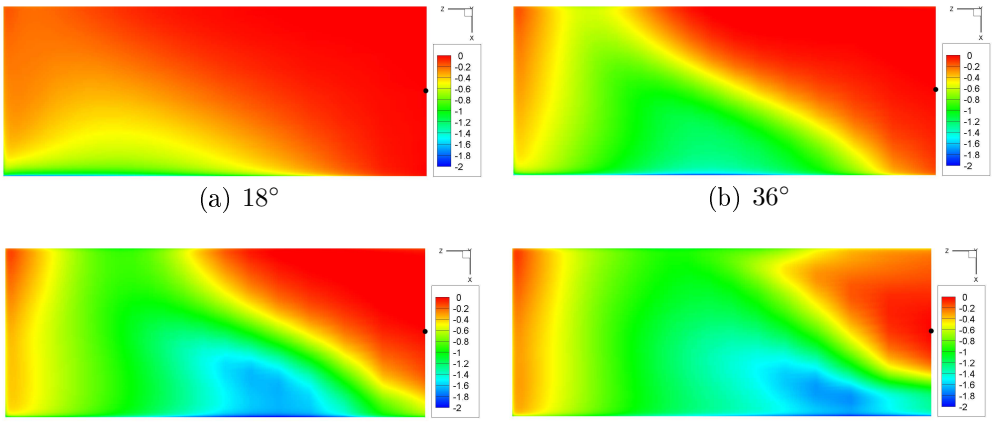

(a) 18° (b) 36°

(c) 54° (d) 72°

Figure 6.38: Contours of non-dimensionalised pressure on wing upper surface for $Re_{3D} = 500$ and various angles of attack. Rectangular, $AR = 2.5$, wing has swept about the mid-chord of the root (black circle) at an angle of attack of 45° through approximately 250° since impulsive start. The leading edge is at the bottom of each image.

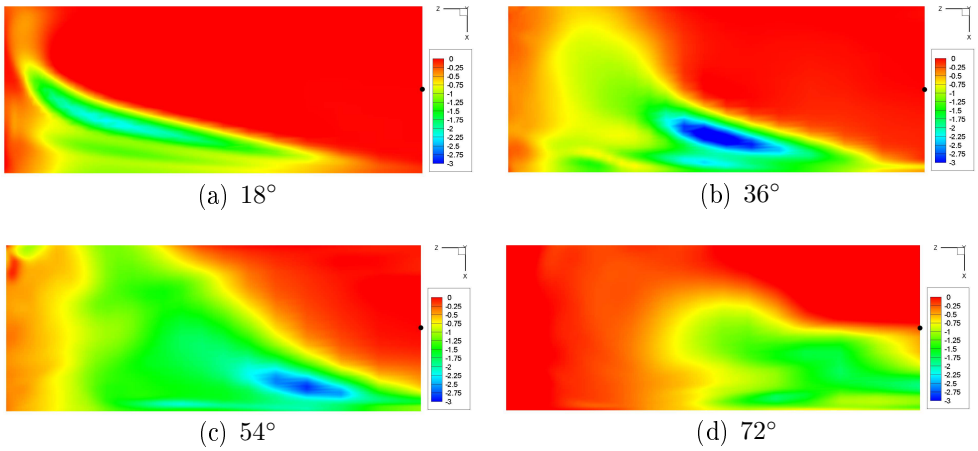

(a) 18° (b) 36°

(c) 54° (d) 72°

Figure 6.39: Contours of non-dimensionalised pressure on wing upper surface for $Re_{3D} = 30\,000$ and various angles of attack. Rectangular, $AR = 2.5$, wing has rotated about the mid-chord of the root (black circle) at an angle of attack of 45° through approximately 250° since impulsive start. The leading edge is at the bottom of each image.

and at 36° the effect of the low pressure core of the LEV is clearly visible. The fact that the LEV becomes more concentrated at higher Reynolds numbers is in agreement with the experimental results of Nolan (2004), who noted that the LEV was comparatively diffused at lower Reynolds numbers. The LEV is also stronger at $Re_{3D} = 30\,000$, as can be seen from the lower pressure on the aerofoil surface.

Also evident in Figure 6.39 is another line of low pressure between the main LEV and the leading edge, particularly at 36° angle of attack. This is the result of the secondary LEV discussed above, and explains the 'twin-peaked' shape of some of the plots in Figure 6.37(b).

6.6.4 Summary of angle of attack effects

It has been seen that the current results suggest that the 3D LEV is a stable phenomenon at all angles of attack up to 81° (at least over the Reynolds number range examined here). As angle of attack is increased, the stable size of the LEV increases, leading to an increase in the normal force on the wing. Both primary and secondary vortices strengthen as angle of attack increases, meaning that the leading-edge vortex sheet is more liable to KHI at higher angles of attack. However, at no angle of attack does KHI cause the LEV to shed from the wing.

6.7 Effect of changing wing planform

All calculations presented so far have been for a rectangular planform wing of $AR = 2.5$. Simulations have also been carried out for an elliptical-planform wing, with the same total area and wing length as the rectangular wing used above. Figure 6.7 compares the lift coefficient for the two shapes. As expected, both planforms eventually produce a stable lift coefficient when the LEV has grown to a stable size. It is clear that the rectangular planform creates more lift than the elliptical wing. However, this does not tell the whole story, as the elliptical planform actually produces a lift-to-torque ratio of around 20% *more* than the rectangular wing (0.80 as opposed to 0.67 — both value non-dimensionalised by mean chord).

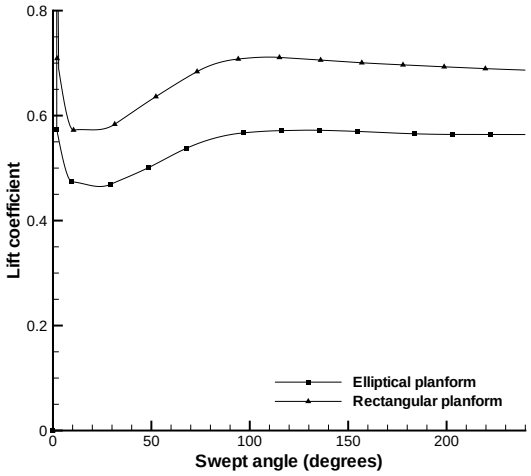

Figure 6.40: Comparison of lift/swept angle history for two wing planforms at $Re_{3D} = 500$ and angle of attack of 45°.

The reason for the difference in lift and lift/torque ratio lies in the area distribution of the wings. The lift produced by a particular section will depend on that section's local velocity and local chord, as well as on the local strength and orientation of the LEV. Increasing the local velocity (by moving towards the tip) would tend to increase lift if there were no tip vortex, but it has also been seen (§6.4) that the interaction of the LEV with the tip vortex (and the consequent separation of the LEV from the wing) mean that sections that are near the tip produce less lift than those further inboard. Increasing the local chord at a given spanwise location would tend to increase the lift produced by that section; however, this relationship is also affected by the local size of the LEV. A small local chord with a large local LEV might produce a higher local 2D lift coefficient than a large local chord with a small local LEV.

The elliptical planform has large chord length on inboard sections (Figure 6.41). These sections do not produce much lift, because the local velocity is low and the LEV is small. The local lift for a given section will tend to increase outboard, because the LEV will become larger and the local velocity will increase. However, at the same time, the local chord is decreasing and this will tend to reduce the local lift. At a certain spanwise location, the combination of the decrease in local chord length and the separation from the wing of the LEV will lead to a decrease

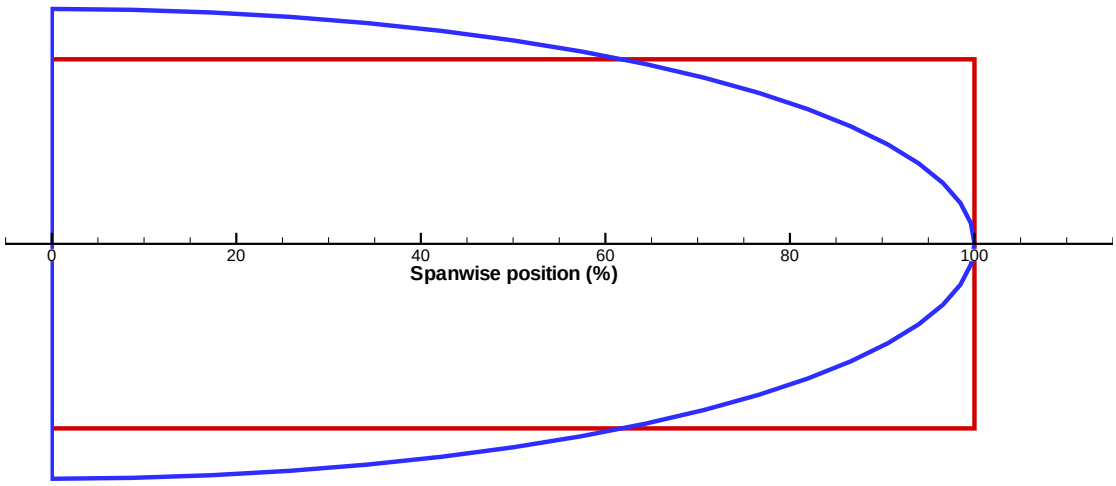

Figure 6.41: Comparison of rectangular and elliptical planforms.

in local lift.

Examination of the lift distributions for the two planforms supports this reasoning. Figure 6.42 shows that the lift distribution over the first 20% of the span is approximately the same for both planforms. Over this first 20%, the LEV is comparatively small, and thus does not greatly enhance lift. Outboard of this point, the elliptical wing starts to produce less lift at a given section than the rectangular wing. Up to around the 60% span position, the local chord for the elliptical wing is greater than for the rectangular wing, but the LEV is smaller (in proportion to the local chord) as is shown later. Therefore the LEV has less of a lift-enhancing effect.

At around the 60% span position, both wings have the same local chord (Figure 6.41), but the LEV is smaller on the elliptical wing than on the rectangular wing (probably because the flow approaches the leading edge with a greater component of velocity towards the tip — see below) so that the elliptical wing produces less lift at this section. Further outboard, the elliptical wing starts to decrease quite rapidly in local chord length, leading to a drop in local lift. At the same time the LEV is tending to separate from the wing, which also leads to a lift decrease. The combination of these two factors leads to a steep decline in the local lift towards the tip, which continues until the tip is reached. For the rectangular wing, the

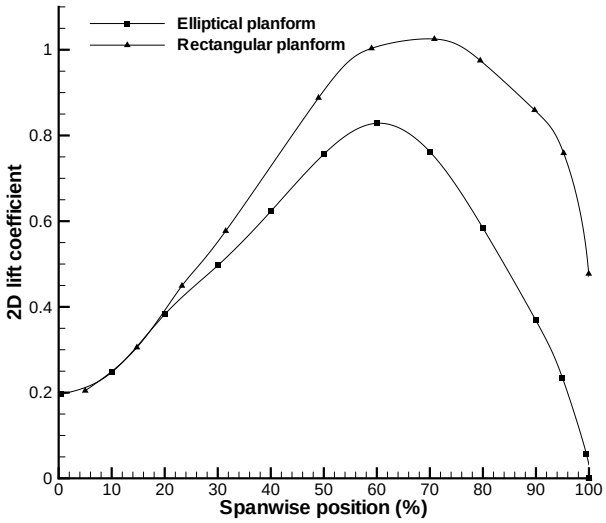

Figure 6.42: Comparison of spanwise lift distributions for elliptical and rectangular planform wings at $Re_{3D} = 500$ and angle of attack 45°. Wings have swept through an angle of around 250° and LEV has stabilised. 2D lift coefficient is based on section chord and wing tip velocity, hence the low values of 2D lift coefficient near the root.

decline does not start until later (because the local chord remains constant) and is less steep; at least until very close to the tip, where the local lift drops suddenly as was seen earlier.

The change in planform has a subtle effect on the size of the eventual stable LEV. Figure 6.43 reveals that the elliptical planform produces an LEV which is smaller in proportion to the local chord. This explains why the elliptical section produces less lift at a given spanwise section, as described above. There are two reasons for this change. Firstly, until the 60% span position, the elliptical wing has a larger local chord than the rectangular wing (Figure 6.41), so that even if the LEV were the same size in absolute terms, it would still be smaller when compared to the local chord. Secondly, though, the LEV is actually smaller in absolute terms — at the 40% span position, the local diameter of the LEV is around $1mm$ greater for the rectangular wing than for the elliptical wing. This small difference is likely to be a result of the fact that, for the elliptical case, the flow approaches the leading edge at a different angle than for the rectangular case, due to the curved shape of the leading edge, and has a larger component of velocity parallel to the leading

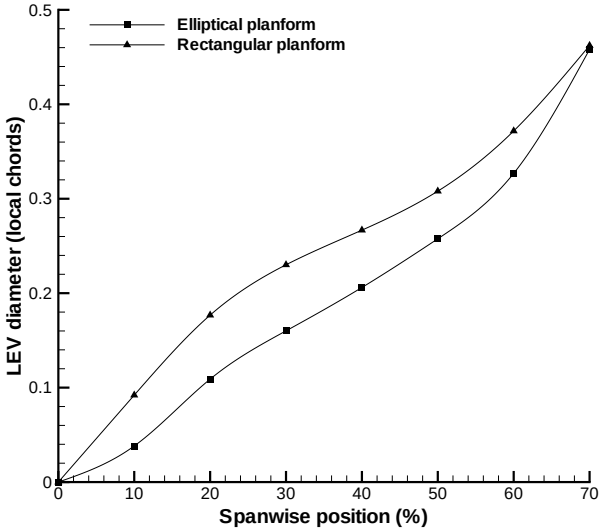

Figure 6.43: Comparison of local size of LEV against spanwise location for elliptical and rectangular planform wings at $Re_{3D} = 500$ and angle of attack 45°. Wings have swept through an angle of around 250° and LEV has stabilised. Figure 6.12 (p. 235) explains how LEV size is defined.

edge.

Another change that occurs within the LEV is that, outboard of 25% span, the core pressure at a given spanwise location is lower for the rectangular wing than for the elliptical wing, as shown in Figure 6.44. The exception is near the root, where the elliptical wing produces an LEV with lower core pressure. This is because the leading edge of the wing has higher local velocity in the elliptical planform case, because the local chord is greater and therefore there is a greater distance from the leading edge to the rotation point (the mid-chord of the root). Thus the LEV that is created is slightly stronger in the elliptical case and therefore has lower core pressure. Outboard of the 20% span position, the LEV core pressure is lower for the rectangular planform than for the elliptical wing. The local chord of the elliptical wing is still higher than for the rectangular wing (up to approximately the 60% span position), so the local incident velocity will still be higher and therefore a stronger LEV might be expected. However, the leading edge of the elliptical wing is curved, so that the oncoming flow meets the leading edge at a different angle. This leads to a smaller and weaker LEV which, consequently, has lower core pressure.

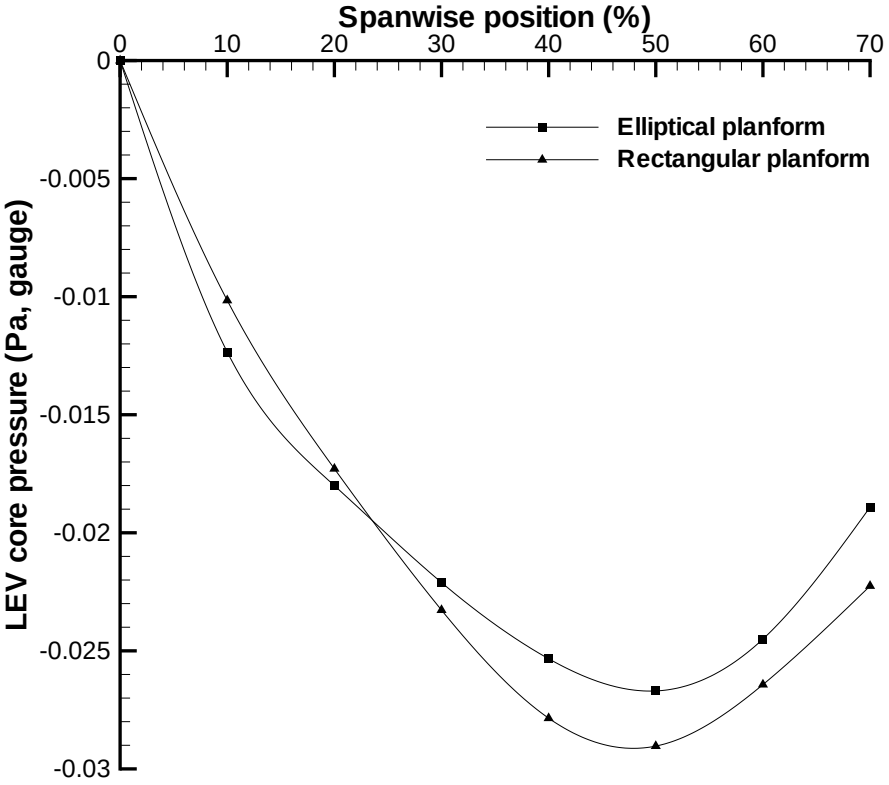

Figure 6.44: Comparison of LEV core pressure against spanwise location for elliptical and rectangular planform wings at $Re_{3D} = 500$ and angle of attack 45°.

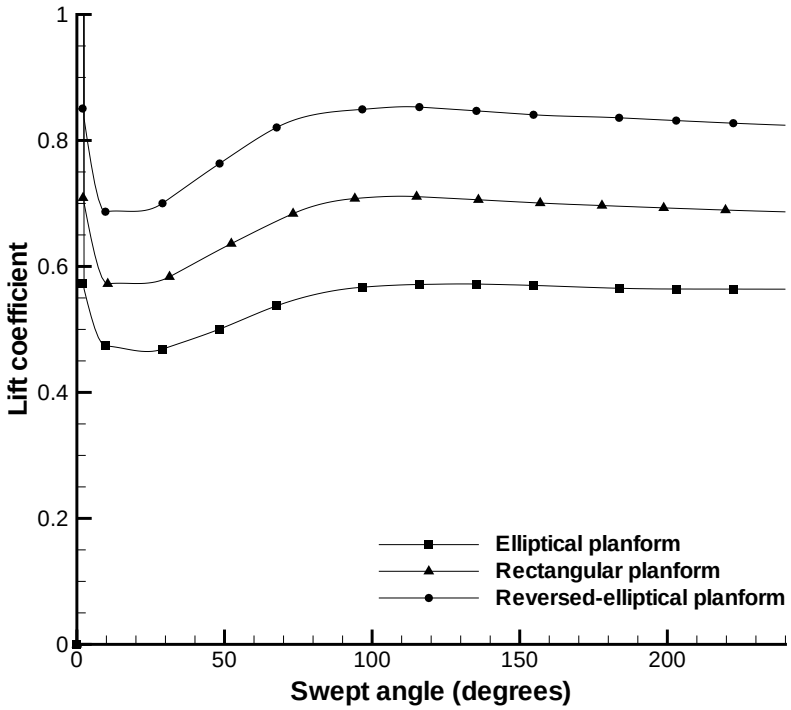

Figure 6.45: Comparison of lift/swept angle history for three wing planforms at $Re_{3D} = 500$ and angle of attack of 45°.

Ansari (2004) reported (based on results from his quasi-2D model — see §3.1.2) that it was preferable to use a wing with a planform such that area was concentrated on outboard sections, in order to take advantage of the high local velocities there. In order to test this simulations were run using the same elliptical-planform wing as above, but reversed so as to sweep around the tapered end of the wing. For a Reynolds number of 500, the CFD model predicted an eventual steady lift coefficient for the reverse-ellipse wing of around 0.83 — almost 20% more than the rectangular-planform wing, and almost 50% more than for the elliptical wing above (Figure 6.7). These changes are of the same sign as reported by Ansari (2004) and of roughly the same magnitude. However, in terms of lift/torque ratio, the reverse-elliptical wing was outperformed by the elliptical wing; the latter produced an eventual steady lift/torque ratio around 13% higher than the former.

Both of these results are to be expected. The reverse-elliptical wing has a larger area outboard, where velocities are higher and the LEV is larger. Therefore the reverse-ellipse produces more lift. However, because a greater proportion of this

lift is produced far from the root, the torque on the wing also increases and there is a net reduction in lift/torque ratio (compared to the elliptical wing case). To maximise lift/torque ratio, therefore, the current results indicate that a planform with large areas near the root would be optimum. However, this would be likely to produce very low lift. The optimum design will depend on the required lift force as well as on the kinematics of the wings.

The phenomenology is essentially the same in the cases which have been tested, but there are subtle changes in the strength and position of the LEV. These changes, along with the more obvious factors of local wing chord and velocity, lead to some changes in the lift distribution along the wing. This confirms what was said earlier; the lift produced by a 2D spanwise section of a wing depends on local chord, local velocity, and the strength, size, and position of the local LEV. Since any 2D model cannot accurately predict the last three of these, it seems clear that 2D models are inadequate for analysing 3D flows of this nature. It is important to emphasise again, however, that other aspects of the aerodynamics of insect-like flapping (such as stroke reversal and wake capture) may well prove more important than the factors investigated here. A 2D model which captures these phenomena (e.g. the model of Ansari) may well prove adequate for investigating flapping wing performance, even though it is not able to predict a stable LEV. The results presented in §3.1.2 and §6.10.2.1 support this assertion.

6.7.1 Summary of effects of changing wing planform

It has been seen that the shape of the wing has a significant impact on its aerodynamic performance, and have highlighted the main factors that affect the lift distribution for a given wing. It is not as simple as supposing that wings with large areas outboard will produce more lift than those with larger areas inboard — the lift produced by a given section is dependent not only on local chord and velocity, but also on the local position and strength of the LEV.

The shapes of insects' wings vary widely (see e.g. Ellington, 1984b). This seems likely to be due to the fact that the wings of a specific insect would be suited to that insect's size, weight, and flight patterns. Dragonflies, which are highly

manoeuvrable, tend to have high aspect ratio wings (the effect of changing aspect ratio is examined in §6.8). Other insects have wings which are designed to fold when not in use (e.g. ladybirds). This would obviously place some limitations on the wing shape. However, in general, the current results suggest that although the planform of the wing will affect the aerodynamic performance, the phenomenology involved seems likely to be fairly consistent across the range of insects.

6.8 Effect of changing aspect ratio

6.8.1 The stability of the LEV

Stable LEVs are not seen on helicopter rotor blades or the blades of wind turbines at high angles of attack. Given that these blades sweep like the wings examined above, it is logical to ask why a stable LEV is *not* seen. There are two possible explanations; either the change is due to the increase in aspect ratio (helicopter rotor blades have aspect ratios of up to 25, whereas insect wings have aspect ratios generally of less than ten) or it is due to the increase in Reynolds number (helicopter rotor blades generally operate at chord Reynolds numbers of $O(10^6)$).

Nolan (2004), in her experimental work, found that "at equivalent low Re, a spiral LEV forms more readily on a higher aspect ratio wing" (Nolan, 2004, p. 75). This is somewhat surprising given that LEVs apparently do not form on high-aspect-ratio helicopter rotor blades.

It has already been noted that for the $AR = 2.5$ rectangular wing examined above, the LEV separates from the wing at around the 70% span position, combining with the tip vortex (§6.4.6). This is supported by various experimental results (see e.g. van den Berg and Ellington, 1997a). For the $10cm$ span wing above, this equated to a distance of about $7cm$ from the wing root. The question is, why does this separation occur — would the LEV still separate at the 70%-span position if the wing were twice as long? Or is the separation due to the fact that the LEV has reached a certain size by this point, and would the LEV therefore still separate around $7cm$ away from the root even if the wing were twice as long?

In order to investigate this, results for the aspect ratio 2.5 wing are compared

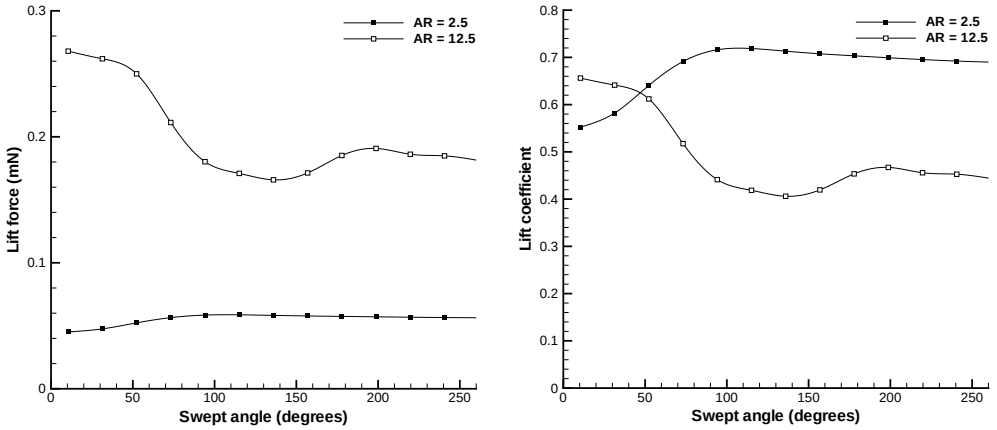

(a) Lift force (b) Lift coefficient

Figure 6.46: Lift force and lift coefficient vs. swept angle for rectangular wings of two aspect ratios. Angle of attack is 45° and $Re_{3D} = 500$ for both cases.

with results for a wing with the same chord length but an aspect ratio of 12.5. Figure 6.46(a) reveals that, as might be expected, the higher aspect ratio wing produces more lift; it has 5 times the area. However, when lift coefficients are compared, it is seen that the lower aspect ratio wing actually produces a significantly higher figure. In addition, there are significant fluctuations in lift coefficient for the higher aspect ratio case, indicating that large-scale vortex shedding is occurring.

Inspection of the flow visualisation data for the two cases indicates that, as the above results suggest, there is an obvious change in phenomenology when aspect ratio is increased. For both cases, the LEV originally extends over the entire span of the wing (Figure 6.47(a)). For the aspect ratio 2.5 case, the LEV continues to extend over the whole span for all time. However, for the higher aspect ratio, the LEV separates near the tip, and another LEV forms on the outboard section (Figure 6.47(b)). The separation point moves inboard and the second LEV appears to cause the first to shed. In the same way, the second LEV also separates near the tip and a third LEV appears (Figure 6.47(c)). The simulation was stopped here, but it is likely that this process would repeat, leading to periodic shedding of LEVs.

In 2D cases, it was seen that the LEV separated once it had formed a new

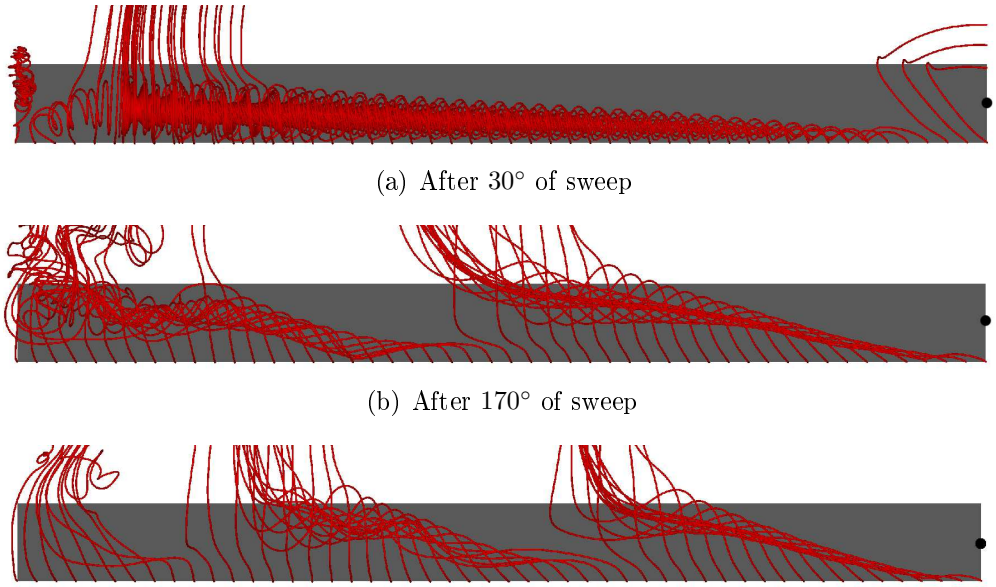

(a) After 30° of sweep

(b) After 170° of sweep

(c) After 260° of sweep

Figure 6.47: Instantaneous LEV structure for $AR = 12.5$, rectangular, flat-plate wing at various sweep positions. Angle of attack is 45° and $Re_{3D} = 500$. Wing is rotating about the mid-chord of the root (marked with black circle) and leading edge is at bottom of figure.

TEV. This new TEV was 'sucked forward' by the LEV, causing the LEV to lift off the aerofoil. The results suggest that a similar process occurs in 3D cases. If the 3D LEV at a given spanwise location grows large enough to produce a new TEV, that new TEV will cause the LEV to shed. The LEV grows fastest on outboard sections, so that shedding of the LEV starts near the tip and then propagates inboard. The stability of an LEV will also therefore depend on wing planform — reducing the wing chord at a given location increases the likelihood of a new TEV being created there.

For the aspect ratio 2.5 wings above, the LEV does grow comparatively large near the tip (see Figure 6.29), and it is logical to ask why a new TEV is not created in this case. The answer lies in the tip vortex, which causes the LEV to turn through 90° near the tip so that the induced velocities at the trailing edge are parallel to the trailing edge rather than normal to it. Thus the situation depicted in Figure 5.22 (p. 163) does not occur and no new TEV is formed.

However, for the aspect ratio 12.5 case under consideration here, the LEV

becomes large on outboard sections *before* it starts to interact with the tip vortex. Thus the induced flow at the trailing edge produces a new TEV. These results suggest, therefore, that in order for an LEV to be stable the aspect ratio of the wing must be such that the LEV merges with the tip vortex (and is therefore turned through 90°) before it affects the flow at the trailing edge.

Where shedding of the LEV does occur, the flow structure is similar to that seen for 2D cases, with LEVs and TEVs being shed alternately. Perhaps, then, it might be possible to use 2D models to analyse the flow in these cases. In fact, the shape of the curve for the aspect ratio 12.5 case in Figure 6.46(b) is remarkably similar to the shape of the curve for results from Ansari's (2D) model, as is shown later (see Figure 6.54, p. 295). But 2D models cannot capture the tip vortex, which, as has been seen, is fundamental in preventing the formation of a new TEV and therefore in preventing shedding of the LEV.

It has been seen, however, that a stable LEV is essential for maintaining a high lift coefficient — once vortex shedding starts to occur in the 3D case the lift coefficient drops dramatically (Figure 6.46(b)). This is to be expected, based on the 2D results presented earlier. A logical question, given this fact, is to what extent aspect ratio can be increased whilst a stable LEV is still created? It has been seen that the LEV is unstable for an aspect ratio 12.5 wing and stable for an aspect ratio 2.5 wing. In fact, though, the critical value of aspect ratio will depend on wing planform, as mentioned above. Since any eventual FMAV is unlikely to have exactly-rectangular wings, there seems little purpose in locating the precise aspect ratio above which a stable LEV is not possible. A quick simulation (with a relatively coarse grid) indicates that, for a rectangular wing, a stable LEV is possible at an aspect ratio of 10. Insect wings generally have aspect ratios of between 1 and 10 (Dudley, 1999), and the preceding results may well explain why this is — above this value of AR, a stable LEV is not possible.

6.8.2 Is wing length more important than aspect ratio?

Nolan (2004) suggests, based on her PIV results, that the creation of a stable LEV is dependent primarily on the velocity of the leading of the wing relative to the

fluid. She then suggests that chord length will not have much of an impact on this velocity, so that it might not be sensible to base Reynolds number on chord length, and states that an LEV is created "only when flow passes the leading edge at a certain speed" (Nolan, 2004, p. 76). It is clear that there is potential for confusion here.

For a given 3D case, there are two questions to be answered. Firstly, is an LEV created at all: in other words, is the Reynolds number/angle of attack combination such that separation occurs at the leading edge? Secondly, if an LEV is created, will it be stable?

Intuitively, it might seem reasonable to expect that the answer to the first of these two questions would depend on the speed and angle of the incident flow at the leading edge, and it might also seem reasonable to expect that this velocity would *not* depend on the chord length of the wing. Nolan (2004) suggests that this might be the case; that the creation of an LEV is dependent on the velocity of the leading of the wing relative to the fluid. She then suggests that because chord length will not have much of an impact on this velocity, it might not be sensible to base Reynolds number on chord length.

The problem with this logic can be summarised by referring back to the 2D, $Re = 5$ case in Figure 5.13 (p. 151). It was noted that there was no separation at the leading edge for this case. If the chord length of the aerofoil were increased by a factor of 10, the Reynolds number (as defined for 2D flows) would increase to 50. At $Re = 50$ it was noted that separation did occur. However, as only the chord of the aerofoil has been changed, the speed and direction of the flow at the leading edge is unchanged — at least, according to the reasoning outlined above. Therefore, based on the reasoning of Nolan (2004), separation would *not* be expected to occur, *even though* the Reynolds number is now 50.

If this were true, it would undermine the whole process of dynamic scaling (see Appendix A), because if a scaled-down model of an aircraft was built and the airspeed was increased to keep Re constant, separation might occur on the model where on the full-scale aircraft it would not occur. It would also undermine the conclusion reached earlier that Strouhal number is dependent on Reynolds number,

implying that leading-edge separation *will* occur at $Re = 50$, *no matter how* that Reynolds number is obtained.

Fortunately the current results show that the suggestion of Nolan is without foundation. If Re is increased by increasing chord length, it has the same impact as increasing Re by any other means. Leading-edge separation does not occur when $Re = 5$; but if chord length is increased by a factor of 10 (so that $Re = 50$), leading-edge separation does occur, even though the speed or direction of the flow at the leading edge has not been actively changed. The fact is the separation is caused by an adverse pressure gradient, which is not simply dependent on the speed and direction of the oncoming flow.

The second of the two questions (regarding the stability of an LEV) is also answered by current results. The stability of the LEV at a given point is critically dependent on the chord length of the wing. To put it simply, if the local LEV grows enough to cause a new TEV to form, the LEV at that location is shed.

6.8.3 Summary of effects of changing aspect ratio

It has been seen that aspect ratio is one of the more important parameters affecting the stability of a 3D LEV. This result is not especially surprising. The LEV grows with outboard location along a 3D wing, and the current 2D results showed that if an LEV grows large enough to create a new TEV, the LEV is shed. Therefore, in order for the LEV to be stable, the local chord length at each spanwise location must be such that the local LEV does not grow large enough to induce flow around the trailing edge. Based on this conclusion, it is evident that helicopter rotor blades (which have aspect ratios much higher than 10) will not benefit from a stable LEV.

6.9 Effect of a returning wake

A major simplifying assumption that has been made in all simulations presented thus far is that the wing or aerofoil operates in undisturbed air. In fact, because insect wings move back and forth through the same volume of air (at least whilst the insect is in the hover) the wing will encounter the wake of previous strokes and

this is certain to have some impact on the forces produced and the phenomenology of the flow.

The potential effects of this wing-wake interaction were discussed in §2.1.3.1. The lack of consensus on this point was also highlighted, with many authors asserting that wake capture *enhances* lift (see e.g. Dickinson, 1994; Sane and Dickinson, 2001; Birch and Dickinson, 2003), some that the presence of the wake *does not affect* lift production (see e.g. Sun and Tang, 2002; Aono and Liu, 2006), and a few that wake capture has a *detrimental* effect on lift production (see e.g. Wu and Sun, 2005).

§6.1.1 mentioned that, whereas for the CFD case the lift force becomes stable after around 90° of sweep, the experiments carried out as part of this work found that the force on a 3D wing did not stabilise until the wing had swept through a number of complete revolutions. However it was noted that a lift plateau did occur at around 90° of sweep. It became clear that this difference was due to the returning wake, which was not included in the CFD results at this stage. Because the experimental rig consisted of two wings mounted 180° apart, as each wing passed 180° of sweep it started to encounter the wake of the other wing.

The experimental results indicated that the effect of the wake was to reduce lift. At around 90° of sweep (when there was a short lift plateau, before the wing encountered the wake of the opposite wing) the average measured lift coefficient was around 0.50. The average eventual steady lift coefficient was close to 0.32 — a reduction in lift of more than a third due to the wake.

6.9.1 CFD method — and a caution

A returning wake can be simulated using periodic boundary conditions within the 3D CFD model. In effect, this means that the flow which leaves the domain downstream of the wing immediately re-enters the domain at the upstream boundary, so that any wake shed by the wing eventually returns to the wing. This is equivalent to having a CFD model of two wings but uses the mesh for only one wing, thereby saving resources and decreasing runtime.

Care must be taken, however, when interpreting these results. It has already

been mentioned that the mesh (for both 2D and 3D cases) is coarsened in areas far from the wing. This means that the shed wake becomes less well resolved downstream, so that the fine detail of the wake will be lost. Although the mesh was refined for the results in this section, it is unlikely that this eliminated this concern.

This problem is common in rotorcraft CFD analysis. Brown and Line state that the effectiveness of CFD models for this kind of flow "is often limited ... by difficulties in retaining the structure and form of the rotor wake that result from their tendency to dissipate vorticity" (Brown and Line, 2005, p. 1434). The vorticity transport model of Brown (2000) might be a suitable way to avoid this problem — the model "addresses the problem of vorticity diffusion by solving the fundamental fluid dynamic equations in vorticity conservation form" (Brown and Line, 2005, p. 1). Further work will be required to understand how this model can be applied to simulations of insect-like flapping. The assumption of inviscid flow made in the model (Brown, 2000, p. 58) would have to be removed in order for the model to be applied; at least if it is intended to be used to model the flight of small insects rather than FMAVs.

This concern appears not to have been addressed in most of the 'full flapping' CFD models. For example, Sun and Tang (2002) use a RANS CFD model to examine the aerodynamics of an insect wing undergoing flapping motion and do not mention this possible disadvantage of their method. For most of the current work, the diffusion of vorticity should not be an issue; it is only in this section that the results should be treated with some caution.

Despite this warning, it appears that the model gives the correct *qualitative* idea of the effect of the wake, though the *quantitative* results may be inaccurate. In fact, comparison with the current experimental results indicates that the *quantitative* results are of the right order of magnitude.

6.9.2 Results

Figure 6.48 shows that the CFD model predicts that a returning wake causes a reduction in lift of about 50%. This is a larger reduction than the $\sim 30\%$ implied by

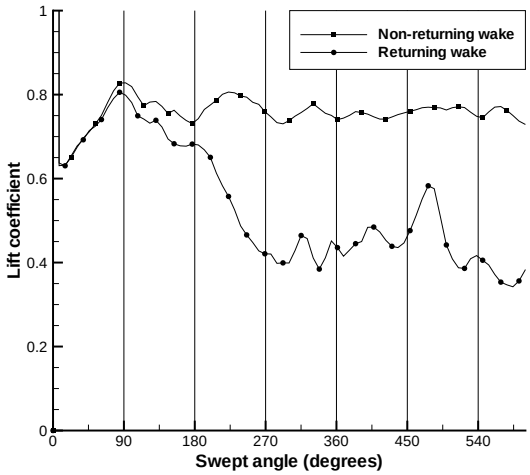

Figure 6.48: Lift coefficient vs. swept angle for a flat-plate, rectangular wing of aspect ratio 2.5 at 45° angle of attack, both ignoring and including the effect of the returning wake. $Re_{3D} = 5\,000$.

current experiments. For the non-returning case, the lift becomes comparatively steady after around 270° of sweep (the small-amplitude, high-frequency fluctuations are due to KHI, as discussed in §6.5.1). For the returning-wake case, the lift starts to drop below the non-returning case at around 90° of sweep, but the two plots diverge most significantly after 180° of sweep. Because two wings are effectively being modelled, this is as expected — at 180° of sweep, the wing has entered the wake from the opposite wing.

The plots diverge before the 180° of sweep position, because the chord of the wing is not zero. It takes 180° of sweep for the centre-chord line of the wing to reach the original position of the centre-chord line of the opposite wing; but the leading edge of the root of the wing will encounter the wake from the trailing edge of the other wing before 180° of sweep.

The reason for the decrease in lift is evident from Figure 6.49. The non-returning wake case produces a large, strong LEV which forms across virtually the entire span of the wing (Figure 6.49(a)). By contrast, the LEV for the returning wake case is significantly smaller and weaker (Figure 6.49(b)). In fact, the effect of the returning wake appears to be similar to the effect of reducing the angle of attack of the wing. The LEV shrinks and weakens, and as a consequence its lift-

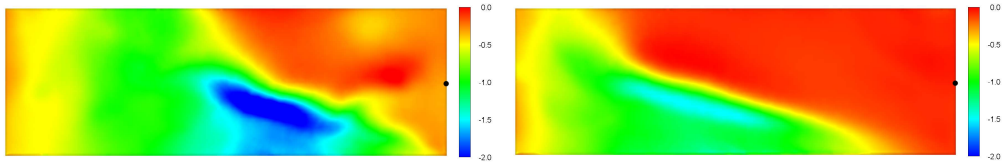

(a) Non-returning wake (b) Returning wake

Figure 6.49: Contours of non-dimensionalised pressure ($p/0.5\rho {V_{tip}}^2$) on wing upper surface for returning and non-returning wake cases after 400° of sweep about mid-chord of root (black circle). $Re_{3D} = 5\,000$ and angle of attack is 45°. Leading edge is at bottom of figure.

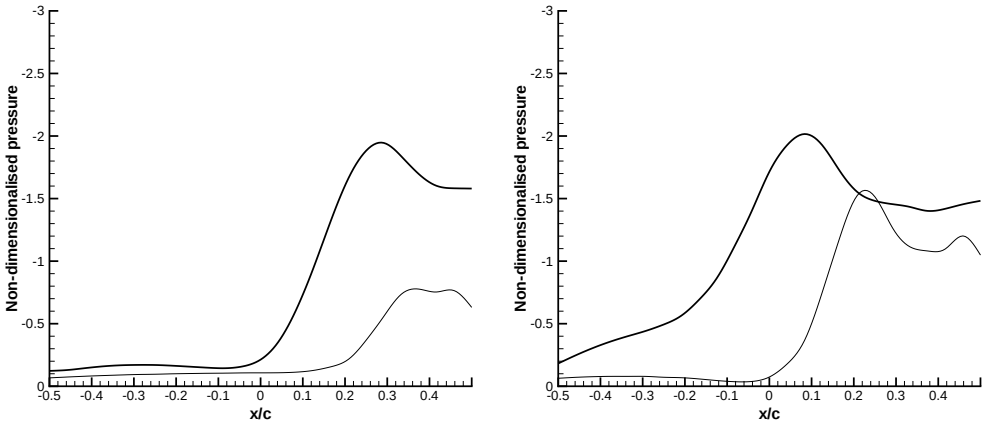

(a) 30% span (b) 50% span

Figure 6.50: Non-dimensionalised pressure ($p/0.5\rho {V_{tip}}^2$) on wing upper surface vs. chordwise position for non-returning (thick line) and returning wake cases after 400° of sweep. $Re_{3D} = 5\,000$ and angle of attack is 45°.

enhancing effect is reduced. This is also demonstrated by Figure 6.50, where it is clear that the pressure on the upper surface is increased (i.e. the LEV core pressure is not so low) if the effect of the returning wake is included in the simulation.

Given the nature of the trailing vortex system behind the wing, it is not surprising that the effect of the returning wake is to decrease the effective angle of attack of the wing. Viewed from ahead of the wing, the trailing vortex (the combined LEV/tip vortex) induces a downward velocity inboard of itself. Thus, when the wing enters this wake, the wake will induce a downward velocity ahead of the wing. This is demonstrated in Figure 6.51. It is clear that for the non-returning wake case, the flow far ahead of the wing is at 45° to the wing chord. The same cannot be said for the returning wake cases.

The lift force for the returning wake case continued to fluctuate until the end of the simulation. This is expected. The wing sheds a wake at time t_1. When it encounters this wake at time t_2, the wake that is being shed at time t_2 is affected. At t_3, the wing encounters the wake that was shed at t_2, which has an impact on the wake that is shed at t_3. The actual value of these times is unimportant; it is simply suggested that one revolution will not be long enough for the flow to reach a steady state. The current experiments suggested that it takes a number of complete revolutions before a steady-state lift force is realised.

6.9.3 Summary of effects of a returning wake

These results suggest that wing/wake interaction can have a significant effect on force production, causing a change in lift of between 30 and 50%. It is important to realise that, although in the case of a sweeping wing this change will always be negative, in the case of insect-like flapping the wing/wake interactions will be much more complex, and the effect of the wake on force production could be either positive or negative. The experimental results of Dickinson, shown in Figure 3.3(a) on p. 83, give some idea of the effect of the wake in a 3D, flapping case.

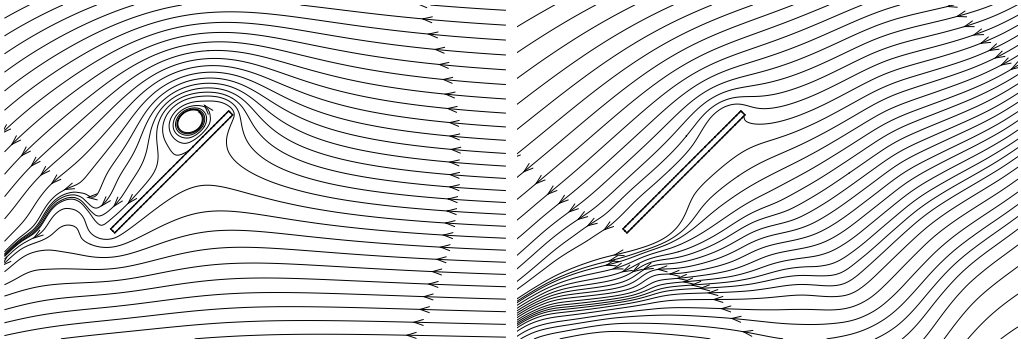

(a) 25% span, non-returning wake

(b) 25% span, returning wake

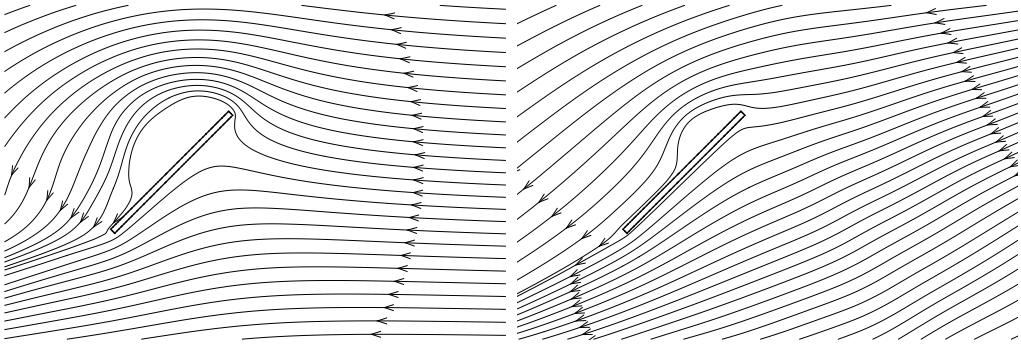

(c) 50% span, non-returning wake

(d) 50% span, returning wake

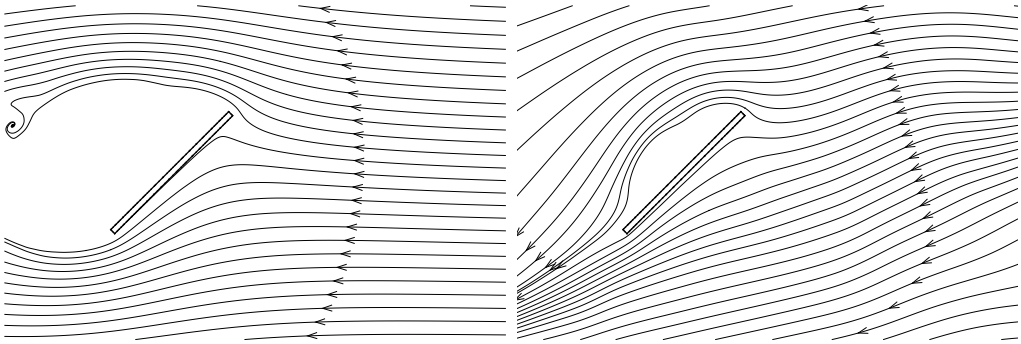

(e) 75% span, non-returning wake

(f) 75% span, returning wake

Figure 6.51: Instantaneous streamlines after 400° of sweep showing effect of returning wake on the effective angle of attack of wing sections. $Re_{3D} = 5\,000$ and angle of attack is 45°.

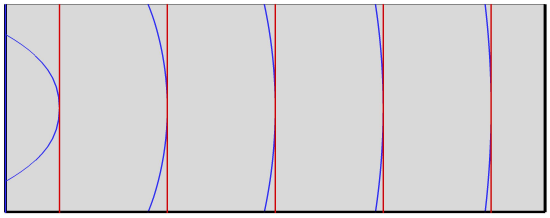

Figure 6.52: Comparison of radial (blue) and straight (red) chords for a rectangular, aspect ratio 2.5 wing.

6.10 Comparison with the model of Ansari (2004)

6.10.1 Flow visualisation

As mentioned in §3.1.3, flow visualisation from the model of Ansari (2004) does not compare well with that from physical, 3D experiments. There has been some suggestion that this is because in experimental cases, flow visualisation is captured over straight chords, whereas the model of Ansari visualises the flow on curved radial chords in an attempt to account for the sweeping motion of the wing (see Figure 6.52). Using the current CFD data, both situations can be investigated; and by comparing the results, the validity of these suggestions can be examined.

Intuitively, the difference would be expected to be greatest near the root of the wing, where the difference between a flat and a curved plane is greatest, as shown in Figure 6.52. Figure 6.53 shows that there are indeed significant differences between the two planes for the 10%-span case.

There are a few features of Figure 6.53 which warrant some explanation. Firstly, for the flat planes, there is a large velocity component normal to the visualisation plane ahead of and behind the wing. This is to be expected because of the sweeping motion of the wing — if the wing were not present, there would be a smooth change from positive normal velocities to negative normal velocities. Conversely, for the radial chord case, if the wing were not present the normal velocity would be zero everywhere, because the flow would follow the curve of the plane.

Secondly, the length of a radial chord is proportional to its distance from the point of rotation. Therefore, the radial chord at 10% span is very short; see Figure 6.52. The length of a straight chord is constant along the span. The 'bent' shape

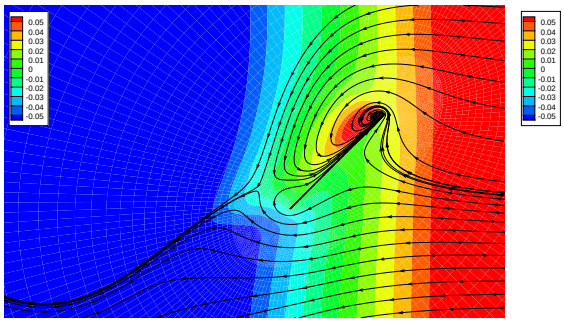

(a) Flat plane, 10% span

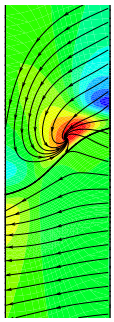

(b) Curved plane, 10% span

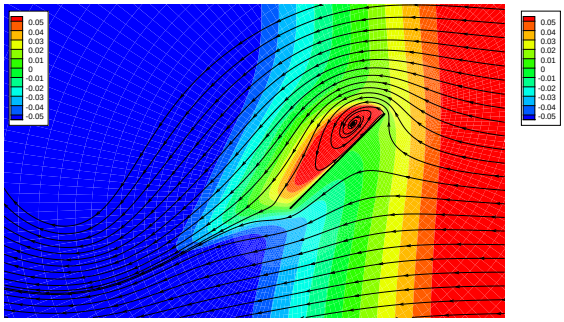

(c) Flat plane, 30% span

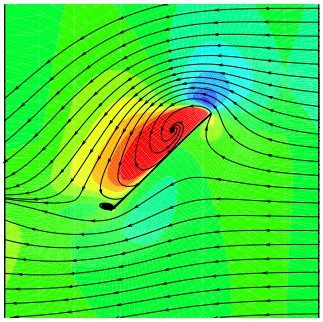

(d) Curved plane, 30% span

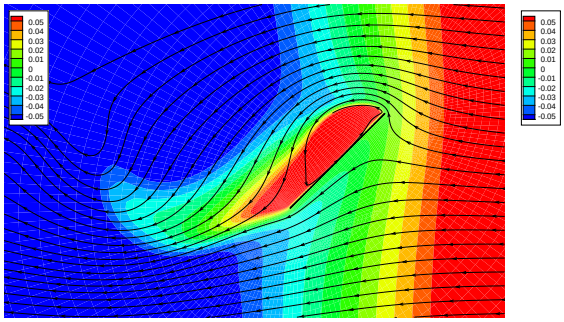

(e) Flat plane, 50% span

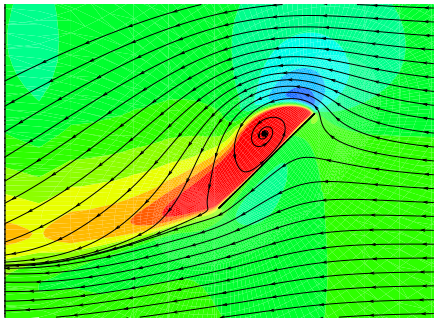

(f) Curved plane, 50% span

Figure 6.53: Comparison of straight- and radial-chord flow visualisation for flat-plate wing of $AR = 2.5$. Angle of attack is 45° and $Re_{3D} = 500$. Instantaneous streamlines show velocities parallel to plane while contours show velocity normal to plane in m/s.

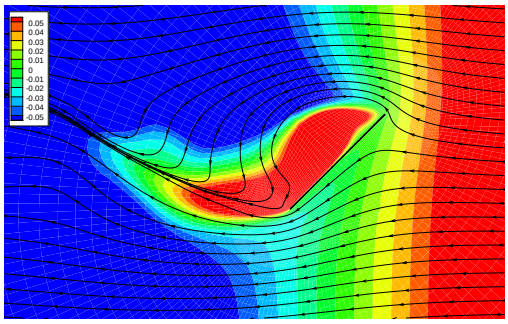

(g) Flat plane, 70% span

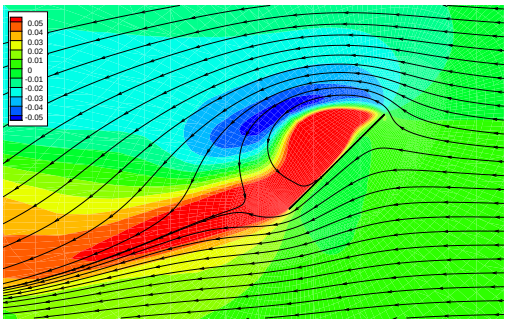

(h) Curved plane, 70% span

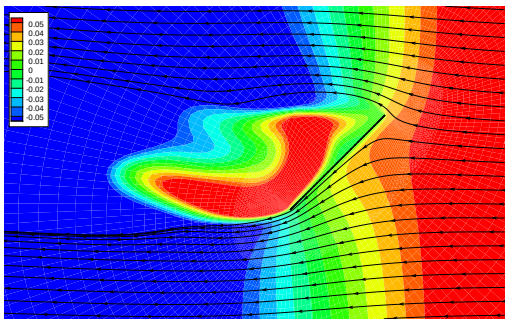

(i) Flat plane, 90% span

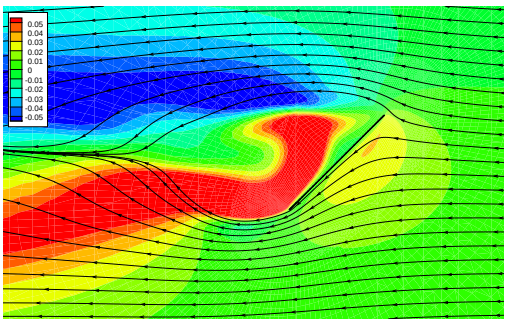

(j) Curved plane, 90% span

Figure 6.53: Comparison of straight- and radial-chord flow visualisation for flat-plate wing of $AR = 2.5$. Angle of attack is 45° and $Re_{3D} = 500$. Instantaneous streamlines show velocities parallel to plane while contours show velocity normal to plane in m/s (continued).

of the wing section for the radial-chord case at the 10%-span position is the result of the 45% angle of attack — at 0° angle of attack the wing would appear straight in both cases.

At all spanwise positions, the two methods produce identical results at the mid-chord of the wing, as should be the case. The first notable difference is seen most clearly at the 70%-span position. Here, a large area of positive normal velocity is visible behind the wing in the radial-chord visualisation. In the straight-chord visualisation, this area does not extend so far downstream. This difference is due to the fact that the radial chord is following the tip vortex, which induces a flow which is normal to the curved plane. For the straight-chord cases, the tip vortex leaves the plane of visualisation a short distance behind the wing and the tip vortex from outboard sections passes through the visualisation plane.

The second difference that is notable is shown by the streamlines behind the wing. At the 90%-span position, the radial-chord visualisation shows the streamlines converging behind the wing. The straight-chord visualisation does not show this convergence. Similarly, at the 70%-span position, the streamlines behind the wing are generally in an upwards direction in the straight-chord visualisation, but in a downwards direction for the radial-chord view. The radial-chord cases resemble more closely the kind of flow structure that is seen in 2D flows; and this is exactly as would be expected, because the radial chords follow the general path of the flow more closely than the straight chords.

It is clear, however, that all the above differences cannot be held responsible for the discrepancies between the predictions of Ansari's model and flow visualisation from 3D experiments. The primary reason is that Ansari's model predicts vortex shedding to occur, just as it does for 2D cases, when in reality, as has been seen, the LEV does not shed for 3D cases. Although Figure 6.53 may be helpful in understanding the structure of the flow, and also useful in comparing flow visualisation from 2D models to that from 3D models or experiments, it is clear that if no vortex shedding occurs when the flow is observed using straight-chord flow visualisation, it will not occur if the flow is examined using radial-chord flow visualisation. What has been seen is that for the flow visualisation from a 3D

model or experiment to be similar to that from a 2D model or experiment, the 3D flow must be visualised using curved planes. Of course, in reality this is difficult; PIV, for example, as used by Nolan (2004), needs a laser light sheet, and creating a curved light sheet (although possible) would involve the use of complex lenses. In addition, the sensor used to record the flow-visualisation images would also have to be curved.

6.10.2 Forces

6.10.2.1 Comparison with current CFD force predictions

It has been noted already (§3.1.2) that Ansari's model produces results which are very close to 3D experimental force measurements for a flapping wing. This section examines how results from his model compare with results from the current 3D CFD simulations for the case of an impulsively-started sweeping wing.

Ansari's model is inviscid (i.e. independent of Re), so that the lift coefficient produced by an aerofoil depends only on the angle of attack and the distance travelled — for example, an aerofoil which has travelled two chord lengths at an angle of attack of 45° will produce a lift coefficient of around 2.14, regardless of the velocity of the aerofoil. This is useful, because it means that 3D wings can be analysed using the results from only a single 2D simulation, as described below. According to Ansari's model, the lift coefficient produced by a particular section of the wing will depend only on the local chord, the local angle of attack, and the distance through which the wing has swept. Therefore it is possible to divide the wing spanwise into chordwise elements, and predict the lift coefficient for each element using the local chord and the local distance travelled. In this section the wing was divided spanwise into 20 sections[9] and the lift coefficient is estimated for each section using 2D results from Ansari (priv. comm., 2006) for an infinitely-thin flat plate at 45° angle of attack.

Figure 6.54 compares results from Ansari's model to results from the current CFD model. Because of the inviscid nature of Ansari's model two Reynolds num-

[9] Ansari (2004) found that the mean force on the wing converged once the number of sections exceeded 20.

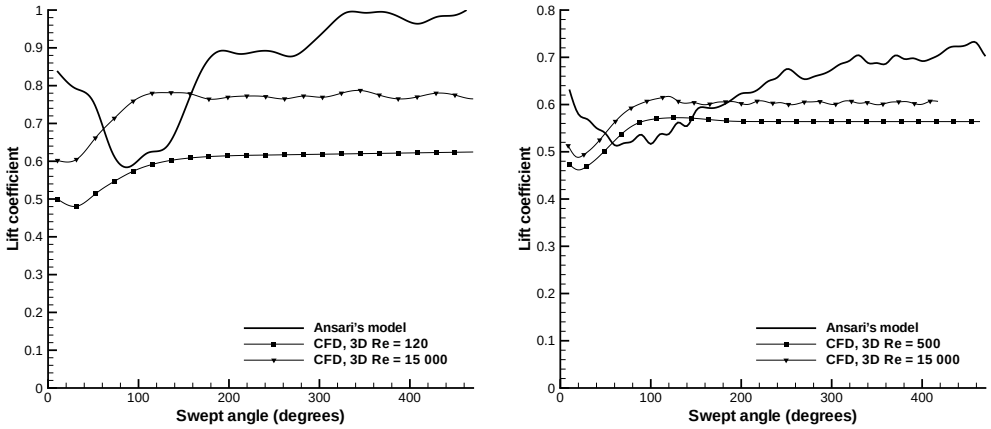

(a) Rectangular planform wing (b) Elliptical planform wing

Figure 6.54: Comparison of results from Ansari's model with results from the current CFD model. $\alpha = 45°$.

bers are plotted for the CFD cases. The lift coefficient predicted by Ansari's model is of the same order of magnitude as that predicted by the current CFD model, but it is immediately obvious is that, whereas the CFD model predicts an eventual steady value of lift, Ansari's model does not. This is expected — it was seen in §6.4 that the CFD model predicts that the LEV grows to a stable size and then remains at that size. Ansari's model, being essentially two-dimensional, does not predict a stable LEV — the LEV for a given section is shed and a new LEV grows.

It is possible to see the effects of the essentially-2D nature of Ansari's model in the comparison presented in §3.1.2 (between experimental results for a flapping wing and results from Ansari's model). In Figure 3.3(b) (p. 83), it was seen that for the initial half-stroke (which begins at $t = 0s$ and ends at around $t = 2.5s$) Ansari's model initially over-predicted the lift force compared with experimental results for a flapping wing; the lift prediction from Ansari's model then dipped, to under-predict the lift force, before rising sharply to over-predict it again, just before stroke reversal. Meanwhile, the experimental data showed a lift force which, after an initial peak, rose gradually to an almost-steady value before stroke reversal. Subsequent strokes are more difficult to interpret due to the effect of the wake from previous strokes, but it is clear that Ansari's model shows a significantly higher degree of lift force fluctuation than is seen in the experimental results, which is

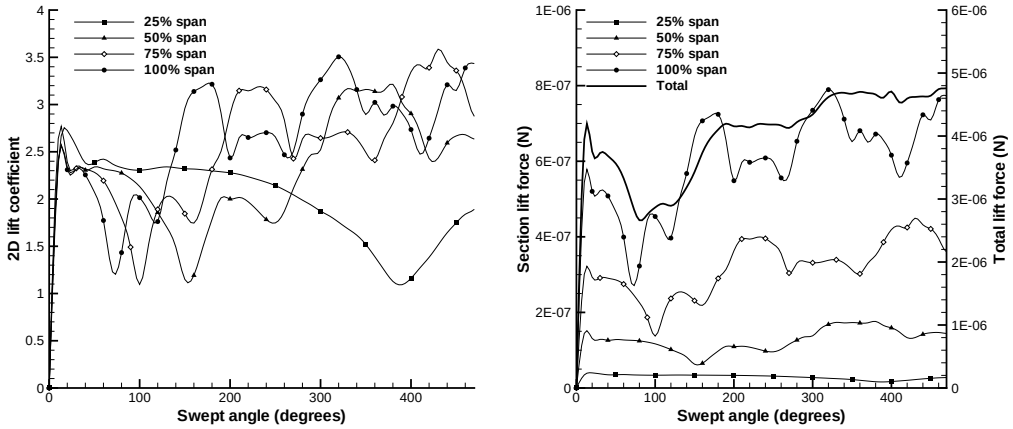

(a) Section lift coefficient

(b) Lift force

Figure 6.55: Lift vs. swept angle for various spanwise sections and total wing; results from Ansari's model. Rectangular $AR = 2.5$ planform, $\alpha = 45°$.

consistent with the fact that (for 3D cases) Ansari's model predicts vortex shedding where in reality none occurs.

It is interesting to break down the force prediction of Ansari's model to compare the force contribution from different sections of the wing. The lift coefficient vs. distance moved plot for each spanwise section will naturally be identical, so if lift coefficient vs. swept angle is plotted for the different sections, as in Figure 6.55(a), the effect is simply to compress or stretch the graph. After 100° of sweep, the section at 25% span has travelled only around 0.8 chords, whereas the section at 100% span has travelled 4.2 chords[10].

Figure 6.55(b) reveals that the *shapes* of the lift vs. sweep angle plots are also identical for all spanwise locations, as would be expected. However, because outboard sections are travelling faster, the actual *lift* (as opposed to the lift *coefficient*) produced by an outboard section is higher than that produced by an inboard section. It is clear that Ansari's model predicts shedding of the LEV at every spanwise location; although the total lift does appear to stabilise for a time at around 200° (and again at around 320°) of sweep, this is simply because during

[10]It might be expected that the 100%-span position would have moved four times as far as the 25%-span position; it *has* moved four times as far in *absolute* terms, but because curved chords are used, the chord length at the 25%-span position is longer than that at the 100%-span position.

this time, the lift from some wing sections is rising, whereas the lift from others is falling, leading to a net change in total lift of approximately zero.

Also worth noting is that Ansari's model cannot take account of the tip vortex, which is probably why his model generally predicts a higher total lift coefficient than the current CFD model. The current model predicted the 2D lift coefficient to peak at around 60% span, and then fall sharply towards the wingtip (see Figure 6.17(b), p. 242) whereas the model of Ansari predicts the average lift coefficient at the tip to be higher than at any other spanwise location.

It is clear, then, that although Ansari's model predicts wing lift coefficients of the same order of magnitude as the current CFD model, there is a large difference in the actual phenomenology between the two models. However, this may not be important. The effects of wing reversal have not been considered, which may well be more important than the effects of predicting vortex shedding where in reality it does not occur. It has been seen that Ansari's model does in fact predict forces on 3D wings with a high degree of accuracy (Figure 3.3(b)), and so it would be highly premature to dismiss all 2D models as worthless; particularly when one takes into account the speed of Ansari's model when compare to the CFD simulations carried out here.

6.10.2.2 The impact of using curved chords

Ansari's model is essentially two-dimensional in nature, but uses curved chords in the analysis in an attempt to account for the sweeping motion of the wing. Ansari et al. (2006a) state that the use of flat chords is less tenable than the use of curved chords for these comparatively low aspect ratio wings. In this section the effect on lift of using flat or curved chords is examined, in an attempt to establish whether the change actually makes a tangible difference. By taking data from Ansari's model, it is possible to analyse a 3D wing using both straight and curved chords and examine the impact of the change. This section, therefore, does not use any results from the current CFD model.

The same number of sections is used for both cases, and compare the total predicted lift in Figure 6.56. The difference is very small — the difference in the

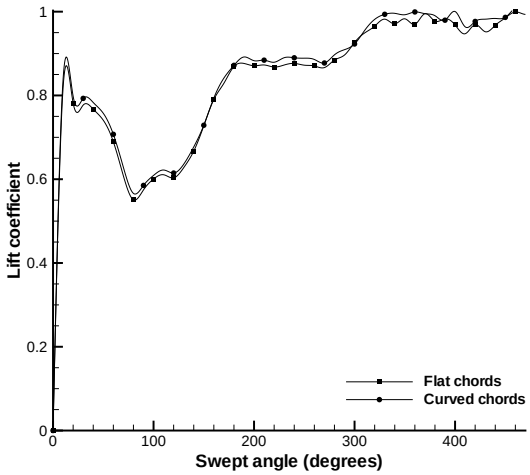

Figure 6.56: Comparison of predicted lift coefficient using curved and straight chords for a rectangular, $AR = 2.5$ wing at 45° angle of attack.

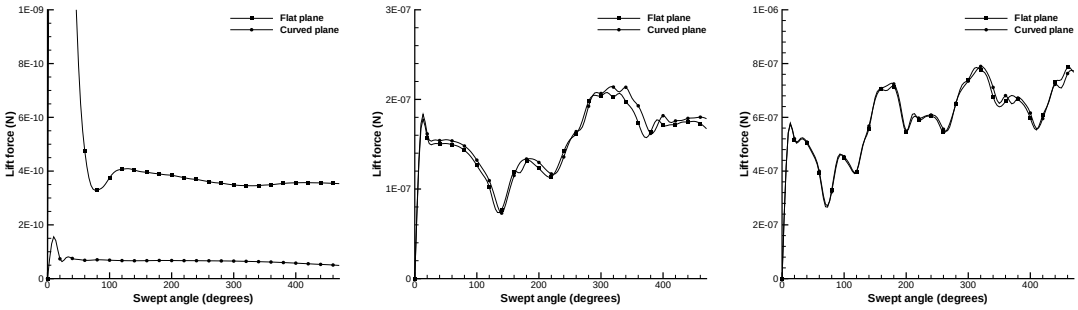

(a) 2.5% span (b) 52.5% span (c) 97.5% span

Figure 6.57: Comparison of section lift predictions using flat and curved chords at various spanwise locations. Rectangular $AR = 2.5$ planform, $\alpha = 45°$.

average lift coefficients is around 1.5% of the curved chords average — with the curved-chords simulation predicting a lift force slightly higher than the straight-chords simulation.

To explain this, Figure 6.57 shows the section lift prediction at various spanwise locations using straight and curved chords. At the root, the straight-chords model predicts a much higher lift coefficient, whereas at positions further outboard, the curved-chord model predicts a very slightly higher lift coefficient. Figure 6.58 confirms that the difference is large near the root, and that, inboard of the 12.5%-span position, the straight-chords prediction is higher than the curved-chords prediction. Outboard of this position, the situation is reversed. The difference decreases fur-

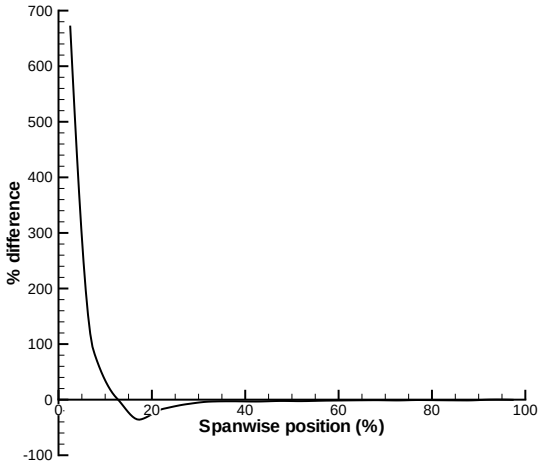

Figure 6.58: Average difference between 2D lift predictions using curved and flat chords vs. spanwise location. Expressed as percentage of curved-chords lift force. Rectangular $AR = 2.5$ planform, $\alpha = 45°$.

ther outboard; at the tip, the difference is less than 0.5%.

The reason for the reversal at 12.5%-span is that, up until this point, a curved chord is shorter than a straight chord passing through the same spanwise position; see Figure 6.52. Outboard of the 12.5%-span position, the situation is reversed, so that a curved chord is longer than a straight chord, but the difference decreases further outboard. This is demonstrated in Figure 6.59.

The difference in chord length also means that, for a given swept angle, the curved chord at a given spanwise location has travelled slightly less or more chord lengths than the straight chord. Thus the plot of lift coefficient vs. swept angle is slightly compressed or stretched, depending on the sign of the difference in chord length between the curved and straight chord.

Overall, however, the difference in lift for a given section is very small, apart from at the root; and because the root sections do not produce much lift anyway, large changes here result in only small changes in the overall lift on the wing.

6.10.3 Ansari's model — conclusions

It has been seen that the fact that flow visualisation from Ansari's model does not agree with that from 3D experiments is less to do with the curved/straight chords

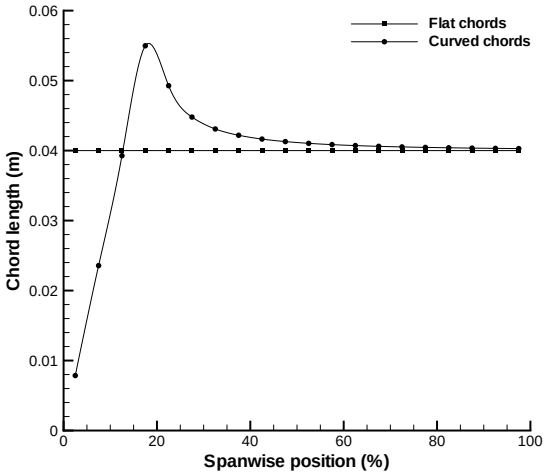

Figure 6.59: Lengths of curved and straight chords vs. spanwise location. Rectangular planform.

issue, and more to do with the fact that Ansari's model cannot predict a stable LEV. In other words, Ansari's model predicts vortex shedding where the current CFD results predict (and the experimental results of Nolan (2004) and others show) that in reality vortex shedding does not occur. The same reason accounts for the discrepancies between lift predictions from the current CFD model and those from Ansari's model.

The current results question the conclusion of Ansari that "a quasi-3D ... model is capable of reproducing well the flow and associated forces for insect-like flapping wings at low Reynolds numbers" (Ansari, 2004, §7.1). In particular, the implication that essentially-2D models can be used to visualise 3D flows is inaccurate; it has been shown that 2D and 3D flows are fundamentally different in terms of phenomenology and force production. However, Ansari's model has been shown to be able to predict the force produced by a flapping wing with a surprising degree of accuracy (see Figure 3.3(a) on p. 83). This indicates that other factors, apart from the stable LEV, are important in force production — for example, stroke reversal and wake capture. Ansari's model is also much quicker to run than the current RANS CFD simulations.

The case for using curved chords as opposed to straight chords has been examined. The change does make a difference, especially at the root; but it has a

negligible impact on the overall lift that is predicted. In any case, it is not possible, based on currently-available data, to assess which system (curved or straight chords) produces the more *accurate* results. The assumption that using curved chords will increase accuracy (because the flow will follow the chords) is not supported by the current results, as there is significant spanwise flow within the LEV.

Again, however, it is important to emphasise that the fact that results from Ansari's model do not agree with results from the current CFD model may not be important. Ansari's model is designed for flapping wings and includes the effects of wing reversal and wake capture. These two effects may well prove to be of much greater importance than the fact that Ansari's model cannot predict a stable LEV. The current results do suggest that flow visualisation data for 3D cases from Ansari's model will not be realistic, but again this may not be an issue when the model is used for its intended purpose (i.e. when the swept distance between stroke reversals is small). Ansari's model does predict forces of the right order of magnitude; and though the instantaneous force at a given time may not be accurate, the mean force may be.

6.11 3D flows — closing remarks

It has been seen that there is a fundamental difference between 2D flows and 3D flows. Whereas 2D flows reveal an unstable flow structure, with vortices continually being shed and created (apart from at very low Reynolds numbers), 3D flows produce a stable LEV and there is no vortex shedding, providing that aspect ratio is below a critical value (of around 10, for a rectangular wing).

It has been demonstrated that this LEV is stable because of spanwise flow within it. This extracts vorticity and 'balances' the vorticity being fed into the LEV from the leading edge separation. The spanwise flow is, in turn, a result of the pressure gradient that exists within the LEV due to the sweeping motion of the wing. The LEV merges with the tip vortex and separates from the wing near the tip.

This phenomenon appears resilient to changes in Re. The current CFD results

show a stable LEV at Reynolds numbers from 120 up to 30 000, and the current experimental results support the assertion that the LEV continues to exist at these higher Reynolds numbers.

Many of the other findings presented in this chapter — relating to the effect of changing Re or changing angle of attack — closely correlate with the 2D findings earlier. Because of this it is reasonable to investigate the possibility of using a 2D model to analyse 3D wings. Ansari's model has demonstrated that this is possible and that good results can be obtained. However, it must be borne in mind that the phenomenology of the flow (as predicted by 2D models) will probably not correlate with reality. Flow visualisation for 3D cases produced using 2D models should be examined with this in mind.

Chapter 7

Conclusions

> *"Simple models that provide useful insights are often to be preferred to models that get so close to the real world that the mysteries they intend to unravel are repeated in the model and remain mysteries."*
>
> — Frederick W. Lanchester

The primary aim of the current study has been to provide insight into the LEV seen to exist during insect-like flapping, mainly using a CFD approach. The RANS CFD models used were validated against existing and new experimental data. The problem was simplified by breaking down the complex kinematics of insect-like flapping into its constituent parts and analysing one of these parts — translation at high angles of attack. Starting with 2D flows, the effects of various parameters, including Reynolds number, angle of attack, acceleration, and aerofoil cross-section and thickness, have been examined in detail. The 2D results were then used in conjunction with 3D results to explain the stability of 3D LEVs and to examine the impact of parameters such as angle of attack and Reynolds number for 3D wings.

This closing chapter summarises what has been learnt from the present study. As the current results naturally fall into two categories — 2D and 3D flows — the same layout is followed here.

7.1 2D flows

Strouhal number Strouhal number is dependent on Reynolds number. At Reynolds numbers of 1 000 or above, there are two Strouhal numbers; one relating to the frequency of primary vortex shedding, and one relating to the frequency of breakdown vortex shedding (breakdown vortices being the result of Kelvin-Helmholtz instability). When $Re > 500$, the former of these two is constant, at around 0.22. When $Re < 500$, the frequency of primary vortex shedding is reduced relative to the $Re = 500$ case.

Reynolds number The phenomenology of a 2D flow is highly dependent on Reynolds number if Reynolds number is very low. For a 1% thick elliptical aerofoil at 45° angle of attack, there is no LEV for Reynolds numbers up to 5. For $5 < Re < 25$, a stable LEV (or separation bubble) exists above the aerofoil. For $Re \geq 25$, the LEV is unstable and regular vortex shedding occurs. The Reynolds numbers at which these changes occur will depend on angle of attack; if angle of attack is lower than 45°, the values will be increased, and conversely if angle of attack is higher than 45°, these values of Re will be decreased.

If the Reynolds number/angle of attack combination is sufficiently high for vortex shedding to occur, the flow is relatively insensitive to further increases in Reynolds number. For example, for a 45° angle of attack, the phenomenology of the flow is almost identical whether $Re = 25$ or $Re = 500$.

At another, higher, critical Reynolds numbers (1 000 for an angle of attack of 45°), Kelvin-Helmholtz instability occurs in the leading- and trailing-edge vortex sheets. This causes low-amplitude, high-frequency fluctuations in the force on the aerofoil, but does not alter the frequency of primary vortex shedding.

At a Reynolds number of 10, viscous force accounts for around 25% of total force. At $Re = 30\,000$ the corresponding figure is less than 1%. This enables us to assess the validity of the assumption of inviscid flow made in many analytical models and judge when this assumption is reasonable.

Vortex shedding It is misleading to use the term 'dynamic stall' or 'delayed stall' to explain the cause of the LEV. Dynamic stall only occurs when an aerofoil undergoes an increase in angle of attack whilst translating, but an LEV is formed even if both angle of attack and velocity are constant.

Vortex growth occurs when the combination of angle of attack and Reynolds number result in a vortex experiencing a net increase in circulation. Vortices grow more readily at high angles of attack and high Reynolds numbers. If a vortex grows beyond a critical size, it induces the creation of another TEV which eventually causes the LEV to shed.

Both leading- and trailing-edge vortices increase the force on the aerofoil. The size of the increase depends on vortex strength and position. As a vortex moves away from the aerofoil, its impact on force production decreases.

Angle of attack The initial lift plateau that results when an aerofoil starts motion at 45° angle of attack is due to a combination of the initial bound circulation (due to delayed leading-edge separation) being shed into the leading-edge vortex sheet and the Wagner effect (i.e. the effect of the starting vortex, see p. 57). At low angles of attack, the Wagner effect dominates and (after the initial added-mass peak) the lift rises. At high angles of attack, the decrease in lift (due to the shedding of the initial bound circulation into the LEV sheet) dominates and the lift falls. At 45°, the two balance out and the lift remains constant until the initial LEV begins to move away from the aerofoil.

Vortices are shed more frequently at lower angles of attack (provided that the angle of attack is high enough for vortex shedding to occur at all). If Strouhal number is based on the effective width of the aerofoil (i.e. the width as seen by the flow upstream) then Strouhal number is roughly constant for all angles of attack.

Aerofoil section & thickness The cross-sectional shape of the aerofoil has little impact on the phenomenology of the flow, provided that the aerofoil remains thin. This is because separation is enforced at the leading and trailing edges.

The thickness/chord ratio has more of an impact, because this determines the 'sharpness' of the leading and trailing edges. Thin aerofoils outperform thick ones

in terms of lift and lift/drag ratio.

Aerofoil acceleration Accelerating aerofoils experience additional force due to added mass. The acceleration does not affect the Strouhal number relating to primary vortex shedding frequency, provided that Reynolds number does not fall below 500.

7.2 3D flows

3D LEV development A 3D wing which undergoes pure translational motion at a high angle of attack experiences separation at the leading edge, resulting in the creation of a large LEV which grows until it is shed, as for 2D cases. The tip vortices limit the growth of the LEV near the tip.

A 3D sweeping wing also experiences separations at the leading edge (provided that the local Reynolds number is sufficiently high). The LEV that forms is stronger on outboard sections (due to the higher local Reynolds number) and therefore a spanwise pressure gradient is created within the LEV. This leads to spanwise flow, which extracts vorticity from the core of the LEV and leads to an eventual stable LEV. In reality, there is just one vortex involved in the flow; the leading-edge, tip, and trailing-edge vortices are in fact all parts of the same continuous vortex line. In other words, it is not the case that the LEV and tip vortex are two vortices both extending downstream; in fact, they are both part of the same vortex line, as would be expected from Helmholtz's vortex theorem (see e.g. Kundu and Cohen, 2004, p. 138).

Although the LEV that forms is similar in appearance and structure to the LEV formed over a delta wing at high angle of attack, there are important differences in the way that the two LEVs form. A delta-wing LEV forms due to the large component of the freestream velocity which is tangential to the leading edge. For a rotating wing at high angle of attack, the LEV is conical (and spanwise flow is present within the LEV) due to the sweeping motion of the wing. Therefore comparisons of the two, though such comparisons may be valid, should be carried

out with care.

3D wing lift distribution The lift produced by a particular spanwise section will not simply be dependent on that section's local velocity and local chord, but will depend also on the local strength and orientation of the LEV. Outboard sections do not benefit from the LEV, because the LEV separates from the wing at around 60 to 70% span (for low aspect ratio wings). Inboard sections also produce relatively low lift, because the low local velocity means that the LEV formed is small.

2D vs. 3D LEVs Using a 2D model to analyse the growth of a 3D LEV (using a blade element approach), if it is possible at all, is sensible only for the initial few degrees of wing sweep (up to 5°). After this point, the 2D model will predict the LEV to continue growing whereas in reality the rate of growth of a 3D LEV reduces as the LEV approaches its stable size. At a sweep angle of 90°, the error in the predicted size of the LEV at the 50% span position will be of $O(100\%)$.

Effect of changing Reynolds number The LEV seen here is stable for Reynolds numbers from 120 to 30 000. The LEV formed at low Reynolds numbers is smaller than that formed at higher Reynolds numbers, meaning that the lift coefficient increases as Reynolds number is increased.

If the local Reynolds number for a given section exceeds a critical value (which depends on the angle of attack, as for the 2D flows above) Kelvin-Helmholtz instability occurs in the leading-edge vortex sheet. This leads to small-amplitude, high-frequency fluctuations in lift coefficient but does not cause the LEV to shed from the wing.

The LEV itself is more concentrated at higher Reynolds numbers ($Re > 1\,000$), having a distinct low pressure core. At lower Reynolds numbers ($Re < 500$) the core is more diffuse.

Effect of changing angle of attack The stall angle of attack for 3D wings (that is, the angle of attack for maximum lift) is around 45°. However, the angle

of attack for maximum lift/torque ratio is much smaller, and appears to be the lowest angle of attack at which an LEV is formed.

Increasing angle of attack increases the steady size of the LEV and therefore increases the normal force on the wing.

Effect of changing wing planform Changes in wing planform have little impact, broadly speaking, on the phenomenology of the flow, but do affect the lift produced and the lift/torque ratio. The ideal wing for a given case will depend on the required lift force as well as the kinematics of flapping. This may be a clue as to why insect wings are varied and relatively complex in planform.

Effect of changing aspect ratio Aspect ratio is one of the more important parameters affecting the stability of a 3D LEV. The LEV grows with distance outboard along a 3D wing, and the current 2D results showed that if an LEV grows large enough to create a new TEV, the LEV is shed. Therefore, in order for the LEV to be stable, the local chord length at each spanwise location must be such that the local size of the eventual stable LEV is not large enough to induce the creation of a new TEV. The current results indicate that a stable LEV is possible for aspect ratios of up to 10, although this will depend on wing planform. This may be a hint as to why most insect wings have aspect ratios less than 10 and also explains why stable LEVs are not formed by helicopter rotor blades at high angles of attack.

Effect of a returning wake Based on the current results (noting the caution on p. 284), wing/wake interaction can have a significant effect on lift production, decreasing lift by around 40%. The direction and magnitude of the lift change will depend on the exact kinematics of the wing. These results support the conclusion that wake capture may play an important role in explaining insect flight.

Ansari's model The fact that flow visualisation from Ansari's model does not agree with that from 3D experiments is less to do with the curved/straight chords issue (i.e. the fact that Ansari's model produces visualisation on radial rather than

flat surfaces in an attempt to account for the sweeping motion of the wing), and more to do with the fact that Ansari's model cannot predict a stable LEV. The same reason probably accounts for the discrepancies between lift predictions from the current CFD model and those from Ansari's model. However, Ansari's model is still successful at predicted the lift on a flapping wing, because it captures the important phenomena of wing reversal and wake capture.

7.3 Overall conclusions

In §3, a series of questions were posed relating to insect-like flapping, all of which have now been answered. The topics to be addressed were:

- the relevance of Strouhal number;
- the effect of Reynolds number;
- the effect of aerofoil section;
- the impact of angle of attack;
- the importance of wing kinematics, including acceleration;
- the effects of moving from a 2D aerofoil to a purely-translating 3D wing;
- the effects of wing sweeping motion;
- the stability of the LEV for sweeping wings;
- the effect of wing planform;
- the effect of wing aspect ratio.

Important insight into the phenomenology of the flow around an insect's (or FMAV's) wings has been gained. This insight should be valuable in designing further experiments to investigate the practicability of building a functional FMAV and also gives pointers as to future directions for research in this field (see below).

The principle conclusions of the current work are that 2D and 3D flows are fundamentally different; that 3D LEVs are generally stable; that this stability is not affected by increasing Reynolds number (at least up to $Re = 30\,000$); but that the stability of the LEV is critically dependent on the aspect ratio of the wing.

7.4 Further work

There are four main areas suggested for further work in this field.

7.4.1 Transition and turbulence

All of the current CFD simulations were carried out under the assumption that flow is laminar. It is known that transition occurs in the wake of circular cylinders at Reynolds numbers as low as 200, although transition only occurs far downstream. As Reynolds number is increased, the transition point will move upstream. Here, it has been assumed that even at the highest Reynolds numbers examined here, transition will occur far enough downstream not to affect the flow near the aerofoil. In fact, although this assumption is made in all the CFD studies (as well as all of the analytical models) of insect flight extant, it may not be valid.

However, predicting and modelling transition is still at the cutting edge of CFD capabilities. The basic problem is that, as noted by Versteeg and Malalasekera, there is "no comprehensive theory regarding the path leading from initial instability to fully turbulent flows" (Versteeg and Malalasekera, 2007, p. 46). Some CFD codes require the user to specify the transition location, but if this is not known from physical experiments it is not possible to determine it exactly using analytical methods, although there are empirical or semi-empirical methods for predicting the point of transition (see e.g. Arnal and Casalis, 2000). The predicted transition point can then be fed into a CFD code. However the prediction is only an estimate, and in many cases the resulting flow will be highly dependent on the location specified (Kusunose and Cao, 1994). Menter et al. (2006) reviewed current models and presented their own, which they stated was "a significant step forward in engineering transition modeling," but the field is still in its infancy.

In any case, even if some method of transition prediction were incorporated into the CFD model, the problem of modelling the resulting turbulence would remain. There are a number of turbulence models; for example the well-known $k-\varepsilon$ model. But all these models are statistical approximations and therefore introduce errors. An alternative method is direct numerical simulation (DNS), where the Navier-Stokes equations are solved numerically without any turbulence model — so that the only error is introduced by the discretisation process. However, DNS is computationally extremely expensive even at low Reynolds numbers and becomes more so as Reynolds number is increased, because the mesh must be fine enough to capture all of the spatial scales within the flow. Writing in 2000, Mathieu and Scott stated that "it is currently very expensive to conduct a DNS calculation at even moderately high Reynolds numbers" (Mathieu and Scott, 2000, p. 327) — for unsteady flows it will be even more expensive. The technique may be valuable for low Reynolds number cases, but it is highly unlikely ever to be a practical solution at the Reynolds numbers relating to FMAVs (Bradshaw, 2008).

Further experimental work might help to confirm whether (or perhaps more importantly, where) transition occurs. Introducing the possibility of transition into the current CFD model might then be possible; but if it is required to model full insect-like flapping, the problem returns (see below).

7.4.2 Full insect-like flapping

This thesis has provided insight into the LEV by looking only at the translational phases of motion. It is accepted that this is in reality only part of the picture. In order to fully determine the relative importance of all the potentially-lift-enhancing phenomena mentioned in §2.1.3, it will be necessary to model full insect-like flapping. In order to do this with the current model, extensive modification will be required in three main areas.

Firstly, as mentioned in §6.9.1, RANS CFD models tend to dissipate vorticity. It may be possible to address this using the vorticity transport model of Brown (2000), but further work is required to investigate the feasibility of this.

Secondly (and related to the first point) the mesh will need to be refined far

from the wing in order to avoid losing the details of the vortices that will be shed during pronation and supination. This will greatly increase simulation run times which may in fact result in CFD being an unsuitable tool for investigating this type of flow; perhaps an analytical model like that of Ansari (2004) (but including the effects of spanwise flow) would be more viable.

Thirdly, it is suggested some account will need to be taken of transition in the wake. It is unclear what effect including transition will have even for the non-returning wake cases (see above). For a full-flapping case, when the wing passes repeatedly through its own wake, the effects of ignoring transition may be even more important.

7.4.3 Experimental data

The lack of experimental data at the low Reynolds numbers which are of interest has already been noted. There is a need for further experimentation in order to confirm or deny the results presented here; in particular, the results concerning the existence of a stable laminar separation bubble at low Reynolds numbers and high angles of attack. In addition, considering the inconsistencies in the experimental data of Dickinson and Götz (1993) (against which the current 2D CFD model and many other CFD and analytical models are validated) there is a need for force measurements on 2D wings at low Reynolds numbers and high angles of attack.

Further 3D experimental work could also be valuable; particularly to confirm the growth in lift coefficient as Reynolds number is increased from $O(100)$ to $O(1\,000)$. Further PIV measurements on the 3D LEV (particularly stereoscopic PIV) could be valuable in confirming the structure of the LEV. It is clear that there is a lack of consensus on whether the LEV is stable, let alone why it is stable. Without further experimental evidence, reaching this consensus may prove difficult. Based on the findings in §6.1.2, it is important that if such experiments are carried out, care is taken to avoid problems with recirculation being set up by the wing. If a tank is used, it must be large enough to avoid this problem; or alternatively, the experiments should be carried out in free air.

7.4.4 Analytical modelling of insect-like flapping

It is clear that there is a fundamental difference between 2D and 3D flows. It is suggested here that any future analytical model of insect-like flapping needs to incorporate 3D effects — most importantly, spanwise flow within the LEV, and the tip vortex. It is also suggested that, if such a model is intended to analyse the flight of very small insects, some account needs to be taken of viscosity. Conversely, if the model is intended to analyse the flight of FMAVs, it may need to include a facility for modelling transition and turbulence. Most current analytical models are both inviscid and laminar, and this may explain some of the error seen when results from these models are compared to the very limited number of experimental data available. Nevertheless, it is undeniable that some existing analytical models (especially that of Ansari (2004)) do compare favourably to experimental data.

7.5 Summary

In this work, the flow around an aerofoil or wing at high angles of attack has been studied over a range of Reynolds numbers. A number of important insights have been obtained regarding 2D flows, 3D flows, and the differences between them. It is hoped that the results presented will enable future models of insect-like flapping to capture the relevant phenomena, as well as enable the design of future experimental work. Based on the current results, there appears to be no reason why the lift-enhancing LEV seen to occur during insect flight will not occur if an FMAV is based on a scaled-up insect. Therefore, an insect-based FMAV should be a viable prospect.

References

AeroVironment, Inc., 2007a. *AeroVironment, Inc.: Innovation at Work.* World Wide Web, www.aerovironment.com. Accessed: 02/11/2007.

AeroVironment, Inc., 2007b. *U.S. Air Force takes delivery of BATMAV micro unmanned aircraft systems from AeroVironment.* World Wide Web, investor.avinc.com/phoenix.zhtml?c=203794&p=irol-newsArticle&ID=1036868. Accessed: 02/11/2007.

J. D. Anderson, 1995. *Computational Fluid Dynamics — the basics with applications.* McGraw-Hill.

S. A. Ansari, 2004. *A Nonlinear, Unsteady, Aerodynamic Model for Insect-like Flapping Wings in the Hover with Micro Air Vehicle Applications.* PhD thesis, Cranfield University, Shrivenham.

S. A. Ansari, R. Żbikowski, and K. Knowles, 2006a. Aerodynamic modelling of insect-like flapping flight for micro air vehicles. *Progress in Aerospace Sciences*, 42:129–172.

S. A. Ansari, R. Żbikowski, and K. Knowles, 2006b. A nonlinear unsteady aerodynamic model for insect-like flapping wings in the hover: Part 1: methodology and analysis. *Proceedings of the Institute of Mechanical Engineering, Part G: Journal of Aerospace Engineering*, 220(2):61–83.

S. A. Ansari, R. Żbikowski, and K. Knowles, 2006c. A nonlinear unsteady aerodynamic model for insect-like flapping wings in the hover: Part 2: implementation and validation. *Proceedings of the Institute of Mechanical Engineering, Part G: Journal of Aerospace Engineering*, 220(3):169–186.

O. A. Antonova, A. K. Brodsky, and V. D. Ivanov, 1981. Wing kinematics in five insect species. *Zoologicheskii Zhurnal*, 60:506–518. In Russian.

H. Aono and H. Liu, 2006. Vortical structure and aerodynamics of Hawkmoth hovering. *Journal of Biomechanical Science and Engineering*, 1(1):234–245.

D. Arnal and G. Casalis, 2000. Laminar-turbulent transition prediction in three-dimensional flows. *Progress in Aerospace Sciences*, 36:173–191.

S Avadhanula, R. J. Wood, E. Steltz, J. Yan, and R. S. Fearing, 2003. Lift force improvements for the Micromechanical Flying Insect. *IEEE International Conference on Intelligent Robots and Systems, October 2003, Las Vegas, NV, USA*.

A. Azuma, 1992. *The Biokinetics of Flying and Swimming*. Springer-Verlag.

A. Azuma, M. Okamoto, and K. Yasuda, 2001. Aerodynamic characteristics of wings at low Reynolds number. In T. J. Mueller, editor, *Fixed and Flapping Wing Aerodynamics for Micro Air Vehicle Applications*, pages 341–398. AIAA.

R. Barrett, R. McMurtry, R Vos, P. Tiso, and R. De Breuker, 2006. Post-buckled precompressed piezoelectric flight control actuator design, development and demonstration. *Smart Materials and Structures*, 15(5):1323–1331.

I. K. Bartol, M. Gharib, D. Weihs, P. W. Webb, J. R. Hove, and M. S. Gordon, 2003. Hydrodynamic stability of swimming in ostraciid fishes: role of the carapace in the smooth trunkfish *Lactophrys triqueter* (Teleostei: Ostraciidae). *Journal of Experimental Biology*, 206(4):725–744.

G. K. Batchelor, 2000. *An introduction to fluid dynamics*. Cambridge University Press.

L. Bennett, 1977. Clap and fling aerodynamics — an experimental evaluation. *Journal of Experimental Biology*, 69:261–272.

J. J. Bertin and M. L. Smith, 1998. *Aerodynamics for Engineers*. Prentice-Hall.

J. M. Birch and M. H. Dickinson, 2001. Spanwise flow and the attachment of the leading-edge vortex on insect wings. *Nature*, 412:729–733.

J. M. Birch and M. H. Dickinson, 2003. The influence of wing-wake interactions on the production of aerodynamic forces in flapping flight. *Journal of Experimental Biology*, 206:2257–2272.

J. M. Birch, W. B. Dickson, and M. H. Dickinson, 2004. Force production and flow structure of the leading edge vortex on flapping wings at high and low Reynolds numbers. *Journal of Experimental Biology*, 207:1063–1072.

G. A. Bird, 1994. *Molecular Gas Dynamics and the Direct Simulation of Gas Flows*. Oxford University Press.

R.J. Bomphrey, N.J. Lawson, N.J. Harding, G.K. Taylor, and A. L. R. Thomas, 2005. The aerodynamics of Manduca Sexta: digital particle image velocimetry analysis of the leading-edge vortex. *Journal of Experimental Biology*, 208(6): 1079–1094.

A. S. Bova, R. M. Lang, G. L. Blaisdell, J. Gibson, and T. Niessen, 2001. Investigation of vortex bursting at a low Reynolds number using a schlieren visualization scheme. *International Journal of Fluid Dynamics*, 5:31–40.

J. Brackenbury, 1995. *Insects in Flight*. Cassell.

P. Bradshaw, 2008. Review of "*Prediction of Turbulent Flows, ed. G. F. Hewitt & J. C. Vassilicos, Cambridge University Press* ". *AIAA Journal*, 46:796–797.

M. Braun, 1995. *Picturing Time: The Work of Etienne-Jules Marey (1830-1904)*. University of Chicago Press.

A. K. Brodsky, 1991. Vortex formation in the tethered flight of the Peacock butterfly *Inachis io* L. (Lepidoptera, Nymphalidae) and some aspects of insect flight evolution. *Journal of Experimental Biology*, 161:77–95.

A. K. Brodsky and V. D. Ivanov, 1984. The role of vortices in insect flight. *Zoologicheskii Zhurnal*, 63:197–208. In Russian.

R. E. Brown, 2000. Rotor wake modeling for flight dynamic simulation of helicopters. *AIAA Journal*, 38:57–63.

R. E. Brown and A. J. Line, 2005. Efficient high-resolution wake modeling using the vorticity transport equation. *AIAA Journal*, 43:1434–1443.

B. H. Carmichael, 1982. Low Reynolds number airfoil survey. Contractor Report 165803, NASA.

C.-C. Chang, Y.-C. Hsiau, and C.-C. Chu, 1993. Starting vortex and lift on an airfoil. *Physics of Fluids*, 5:2826–2830.

J. M. Chen and Y-C. Fang, 1996. Strouhal numbers of inclined flat plates. *Journal of Wind Engineering and Industrial Aerodynamics*, 61:99–112.

A. Conn, S. Burgess, and C. Ling, 2007. An insect-inspired micro air vehicle flapping mechanism. *Comparative Biochemistry and Physiology — Part A: Molecular & Integrative Physiology*, 146(4, Supplement 1):S140.

A. T. Conn, S. C. Burgess, C. S. Ling, and R. Hyde, 2006. An insect-inspired MAV flapping mechanism based on parallel crank-rockers with phase control. *European Micro Air Vehicle Conference, July 2006, Braunschweig, Germany.*

J. L. R. d'Alembert, 1844. *Traité de l'Equilibre et du Mouvement des Fluides.* David.

DARPA, 2000. *DARPA Micro Vehicle Program.* Defense Advanced Research Projects Agency Fact Sheet.

M. Dickinson, 2006. Insect flight. *Current Biology*, 16(9):R309–R314.

M. H. Dickinson, 1994. The effects of wing rotation on unsteady aerodynamic performance at low Reynolds number. *Journal of Experimental Biology*, 192: 179–206.

M. H. Dickinson, 1996. Unsteady mechanisms for force generation in aquatic and aerial locomotion. *American Zoologist*, 36(6):537–554.

M. H. Dickinson and K. G. Götz, 1993. Unsteady aerodynamic performance of model wings at low Reynolds numbers. *Journal of Experimental Biology*, 174: 45–64.

M. H. Dickinson, F. O. Lehmann, and K.G. Götz, 1993. The active control of wing rotation by *Drosophila*. *Journal of Experimental Biology*, 182:173–189.

M.H. Dickinson, F. Lehmann, and S. P. Sane, 1999. Wing rotation and the aerodynamic basis of insect flight. *Science*, 284(5422):1954–1960.

Die Raven, 2005. *Galerie: Unbemannte Flugmaschinen für Kampf & Überwachung*. World Wide Web, hp.kairaven.de/bigb/mav.html. Accessed: 03/12/2007.

Y. F. Dong, Z. L. Wei, and C. Xu, 1997. Transition of separated shear layer from order to chaos. *Physics of Fluids*, 9:2580–2584.

P.G. Drazin and W. H. Reid, 1982. *Hydrodynamic Stability*. Cambridge University Press, 1st paperback edition.

R. Dudley, 1998. Atmospheric oxygen, giant paleozoic insects and the evolution of aerial locomotor performance. *Journal of Experimental Biology*, 201:1043–1050.

R. Dudley, 1999. *The biomechanics of insect flight*. Princeton University Press.

R. Dudley and C. P. Ellington, 1990. Mechanics of forward flight in Bumblebees. II. Quasi-steady lift and power requirements. *Journal of Experimental Biology*, 148:53–88.

W. J. Duncan, A. S. Thom, and A. D. Young, 1970. *Mechanics of Fluids*. Edward Arnold.

F. F. C. Duval, S. A. Wilson, G. Ensell, N. M. P. Evanno, M. G. Cain, and R. W. Whatmore, 2007. Characterisation of PZT thin film micro-actuators using a silicon micro-force sensor. *Sensors and Actuators A: Physical*, 133:34–44.

C. P. Ellington, 1984a. The aerodynamics of hovering insect flight. I. The quasi-steady analysis. *Philosophical Transactions of the Royal Society of London B*, 305:1–15.

C. P. Ellington, 1984b. The aerodynamics of hovering insect flight. II. Morphological parameters. *Philosophical Transactions of the Royal Society of London B*, 305:17–40.

C. P. Ellington, 1984c. The aerodynamics of hovering insect flight. III. Kinematics. *Philosophical Transactions of the Royal Society of London B*, 305:41–78.

C. P. Ellington, 1984d. The aerodynamics of hovering insect flight. IV. Aerodynamic mechanisms. *Philosophical Transactions of the Royal Society of London B*, 305:79–113.

C. P. Ellington, 1984e. The aerodynamics of hovering insect flight. V. A vortex theory. *Philosophical Transactions of the Royal Society of London B*, 305:115–144.

C. P. Ellington, 1984f. The aerodynamics of hovering insect flight. VI. Lift and power requirements. *Philosophical Transactions of the Royal Society of London B*, 305:145–181.

C. P. Ellington, 1995. Unsteady aerodynamics of insect flight. In C. P. Ellington and T.J. Pedley, editors, *Biological Fluid Dynamics*, pages 109–129. Society for Experimental Biology.

C. P. Ellington, 2006. Insects versus birds: The great divide. *44th AIAA Aerospace Sciences Meeting and Exhibit, January 2006, Reno, NV, USA*.

C. P. Ellington, C. van den Berg, A. P. Willmott, and A. L. R. Thomas, 1996. Leading-edge vortices in insect flight. *Nature*, 384:626–630.

C.P. Ellington, 1999. The novel aerodynamics of insect flight: applications to micro-air vehicles. *Journal of Experimental Biology*, 202:3439–3448.

A. R. Ennos, 1989a. Inertial and aerodynamic torques on the wings of Diptera in flight. *Journal of Experimental Biology*, 142:87–95.

A. R. Ennos, 1989b. The kinematics and aerodynamics of the free flight of some Diptera. *Journal of Experimental Biology*, 142:49–85.

Epson, 2003. *Epson Develops World's Smallest Flying Microbot.* World Wide Web, www.epson.co.jp/e/newsroom/news_2003_11_18_2.htm. Accessed: 02/11/2006.

Epson, 2004. *Epson Announces Advanced Model of the World's Lightest Micro-Flying Robot.* World Wide Web, www.epson.co.jp/e/newsroom/news_2004_08_18.htm. Accessed: 02/11/2006.

A. Fage and F. C. Johansen, 1927. On the flow of air behind an inclined flat plate of infinite span. *Proceedings of the Royal Society of London A*, 116(773):170–197.

R. S. Fearing, 2007. *Micromechanical Flying Insect (MFI) Project.* World Wide Web, robotics.eecs.berkeley.edu/ ronf/MFI/. Accessed: 07/11/2007.

Fluent Inc., 1998. *Fluent 5 User's Guide.* Fluent Inc.

C.M. Friend, A. Kaley, and A. Hameed, 2003. Shape-memory alloy actuation of insect-like flapping wings. *Journal de Physique IV*, 112:1193–1196.

C. Galiński and R. Żbikowski, 2007. Materials challenges in the design of an insect-like flapping wing mechanism based on a four-bar linkage. *Materials and Design*, 28(3):783–796.

I. E. Garrick, 1937. Propulsion of a flapping and oscillating airfoil. Technical Report TR-567, NACA.

E. W. Geller, 1955. An electrochemical method of visualizing the boundary layer. *Journal of the Aeronautical Sciences*, 22:869–870.

H. Glauert, 1929. The force and moment on an oscillating aerofoil. Reports and Memoranda 1242, Aeronautical Research Council.

G. Goebel, 2006. *Unmanned Aerial Vehicles.* World Wide Web, www.vectorsite.net/twuav.html. Accessed: 02/11/2007.

K. G. Götz, 1987. Course-control, metabolism and wing interference during ultra-long tethered flight in *Drosophila melanogaster*. *Journal of Experimental Biology*, 128:35–46.

J. M. Grasmeyer and M. T. Keennon, 2001. Development of the Black Widow micro air vehicle. In T. J. Mueller, editor, *Fixed and Flapping Wing Aerodynamics for Micro Air Vehicle Applications*, pages 519–535. AIAA.

K. E. Gustafson and J. A. Sethian, editors, 1991. *Vortex methods and vortex motion*. Society for Industrial Mathematics Publications.

M. G. Hall, 1972. Vortex breakdown. *Annual Review of Fluid Mechanics*, 4: 195–218.

M. Hamamoto, Y. Ohta, K. Hara, and T. Hisada, 2007. Application of fluid-structure interaction analysis to flapping flight of insects with deformable wings. *Advanced Robotics*, 21(1-2):1–21.

Harvard Microrobotics Laboratory, 2007. *Welcome to the Harvard Microrobotics Lab*. World Wide Web, micro.seas.harvard.edu/index.html. Accessed: 02/11/2007.

S. Hawker and C. Soanes, 2005. *Compact Oxford English Dictionary of Current English*. Oxford University Press.

F. S. J. Hollick, 1940. The flight of the Dipterous fly *Muscina Stabulans* Fallén. *Philosophical Transactions of the Royal Society of London, Series B, Biological Sciences*, 230(572):357–390.

Honeywell, 2004. *Honeywell Micro Air Vehicle*. World Wide Web, www.defensereview.com/stories/honeywell/Honeywellta Accessed: 13/03/2008.

E. L. Houghton and P. W. Carpenter, 2003. *Aerodynamics for Engineering Students*. Butterworth-Heinemann, 5th edition.

F. Hsiao, C. Liu, and Z. Tang, 1989. Aerodynamic performance and flow structure studies of a low Reynolds number airfoil. *AIAA Journal*, 27(2):129–137.

R. F. Huang, J. Y. Wu, J. H. Jeng, and R. C. Chen, 2001. Surface flow and vortex shedding of an impulsively started wing. *Journal of Fluid Mechanics*, 441: 265–292.

Institution of Mechanical Engineers, 2007a. *Western Aerospace Centre Prize*. World Wide Web, imeche.org/industries/aero/prizeaward/Western-Aerospace-Centre-Prize/western-aerospace-centre-prize.htm. Accessed: 22/02/2008.

Institution of Mechanical Engineers, 2007b. *Whittle Reactionaries Prize*. World Wide Web, imeche.org/industries/aero/prizeaward/whittle/Whittle-Reactionaries-Prize.htm. Accessed: 22/02/2008.

Israel Aerospace Industries, 2007. *Israel Aerospace Industries*. World Wide Web, www.iai.co.il/Default.aspx?FolderID=18892&lang=EN. Accessed: 02/11/2007.

M. Jensen, 1956. Biology and physics of locust flight. III. The aerodynamics of locust flight. *Proceedings of the Royal Society B*, 239:511–552.

R. W. Johnson, editor, 1998. *The handbook of fluid dynamics*, chapter 38. CRC Press.

K. D. Jones, C. J. Bradshaw, J. Papadopoulos, and M. F. Platzer, 2003. Development and flight testing of flapping-wing propelled micro air vehicle. *2nd AIAA Unmanned Unlimited Systems, Technologies, and Operations (Aerospace, Land, and Sea) Conference and Workshop, September 2003, San Diego, CA, USA*.

K. D. Jones, C. J. Bradshaw, J. Papadopoulos, and M. F. Platzer, 2004. Improved performance and control of flapping-wing propelled micro air vehicles. *42nd AIAA Aerospace Sciences Meeting and Exhibit, January 2004, Reno, NV, USA*.

K. D. Jones, C. M. Dohring, and M. F. Platzer, 1998. Experimental and computational investigation of the Knoller-Betz effect. *AIAA Journal*, 36:1240–1246.

K. D. Jones, T. C. Lund, and M. F. Platzer, 2001. Experimental and computational investigation of flapping wing propulsion for micro air vehicles. In T. J. Mueller, editor, *Fixed and Flapping Wing Aerodynamics for Micro Air Vehicle Applications*, pages 307–339. AIAA.

M. A. Jones, 2003. The separated flow of an inviscid fluid around a moving flat plate. *Journal of Fluid Mechanics*, 496:405–441.

R. T. Jones, 1990. *Wing Theory*. Princeton University Press.

J. Katz and A. Plotkin, 2001. *Low-Speed Aerodynamics*. Cambridge University Press.

J. Katz, S. Yon, and S. E. Rogers, 1996. Impulsive start of a symmetric airfoil at high angle of attack. *AIAA Journal*, 34:225–230.

M. T. Keennon and J. M. Grasmeyer, 2003. Development of the Black Widow and Microbat MAVs and a vision of the future of MAV design. *AIAA/ICAS International Air and Space Symposium and Exposition: The Next 100 Years, July 2003, Dayton, OH, USA*.

T. Keuter, D. Hermans, D. Jerome, R. Decuypere, and G. Boyet, 2002. Aerodynamic research on lifting surfaces and performance for micro & mini UAV. *UAV Systems Conference, April 2002, Bristol, UK*.

S.-C. Kim, J.-Y. Lee, and S.-I. Sohn, 2003. Long time computation of two-dimensional vortex sheet by point vortex method. *Journal of the Physical Society of Japan*, 72:1968–1976.

P. Koumoutsakos and D. Shiels, 1996. Simulations of the viscous flow normal to an impulsively started and uniformly accelerated flat plate. *Journal of Fluid Mechanics*, 328:177–227.

M. Kramer, 1932a. Die Zunahme des Maximalauftriebes von Tragflügeln bei plötzlicher Anstellwinkelvergrösserung (Böeneffekt). *Zeitschrift für Flugtechnik und Motorluftschiffahrt*, 23(7):185–189.

M. Kramer, 1932b. Increase in the maximum lift of an airplane wing due to a sudden increase in its effective angle of attack resulting from a gust. Technical Report TM-678, NACA.

I. Kroo and P. Kunz, 2001. Mesoscale flight and miniature rotorcraft development. In T. J. Mueller, editor, *Fixed and Flapping Wing Aerodynamics for Micro Air Vehicle Applications*, pages 503–517. AIAA.

P. K. Kundu and I. M. Cohen, 2004. *Fluid Mechanics*. Academic Press.

D. F. Kurtulus, L. David, A. Farcy, and N. Alemdaroglu, 2007. Aerodynamic characteristics of flapping motion in hover. *Experiments in Fluids*, 44:23–36.

H. G. Küssner, 1936. Zusammenfassender Bericht über den instationären Auftrieb von Flügeln. *Luftfahrtforschung*, 13(12):410.

K. Kusunose and H. V. Cao, 1994. Prediction of transition location for a 2-D Navier-Stokes solver for multi-element airfoil configurations. *25th AIAA Fluid Dynamics Conference, June 1994, Colorado Springs, CO, USA*.

C-M. G. Lam, 1989. Nonlinear wake evolution of Joukowski aerofoils in severe maneuver. Master's thesis, Massachusetts Institute of Technology.

T. Lawson, 2001. *Building Aerodynamics*. Imperial College Press.

M. Lee and C-M. Ho, 1990. Lift force of delta wings. *Applied Mechanics Reviews*, 43(9):209–221.

N. K. W. Lee, 1991. *Evolution and Structure of Leading Edge Vortices over Slender Wings*. PhD thesis, Massachusetts Institute of Technology.

F.-O. Lehmann, 2004. The mechanisms of lift enhancement in insect flight. *Naturwissenschaften*, 91:101–122.

F.-O. Lehmann and S. Pick, 2007. The aerodynamic benefit of wing-wing interaction depends on stroke trajectory in flapping insect wings. *Journal of Experimental Biology*, 210:1362–1377.

J. G. Leishman, 2000. *Principles of Helicopter Aerodynamics*. Cambridge University Press.

M. J. Lighthill, 1973. On the Weis-Fogh mechanism of lift generation. *Journal of Fluid Mechanics*, 60:1–17.

L. Lipera, 2000. Micro Craft ducted air vehicle. *International Powered Lift Conference, November 2000, Arlington, VA, USA*.

L. Lipera, J. Colbourne, M. Tischler, M. Mansur, M. Rotkowitz, and P. Patangui, 2001. The Micro Craft iSTAR micro air vehicle: Control system design and testing. *American Helicopter Society 57th Annual Forum, May 2001, Washington DC, USA*.

H. Liu, C. P. Ellington, K. Kawachi, C. van den Berg, and A. P. Willmott, 1998. A computational fluid dynamic study of Hawkmoth hovering. *Journal of Experimental Biology*, 201:461–477.

H. Liu and K. Kawachi, 1998. A numerical study of insect flight. *Journal of Computational Physics*, 146:124–156.

A. P. Lobanov and J. A. Zensus, 2001. A cosmic double helix in the archetypical quasar 3c273. *Science*, 294(5540):128–131.

Lockheed Martin, 2000a. MicroSTAR being designed for tomorrow's battleground. *AeroStar (LM internal news journal)*, 1(5):46.

Lockheed Martin, 2000b. MicroSTAR vehicles soar over Quantico. *AeroStar (LM internal news journal)*, 1(9):51.

R. G. Loewy, 1957. A two-dimensional approximation to the unsteady aerodynamics of rotary wings. *Journal of the Aeronautical Sciences*, 24(2):81–92.

M. V. Lowson and A. J. Riley, 1995. Vortex breakdown control by delta wing geometry. *Journal of Aircraft*, 32:832–838.

Y. Lu, G. X. Shen, and G. J. Lai, 2006. Dual leading-edge vortices on flapping wings. *Journal of Experimental Biology*, 209:5005–5016.

H. J. Lugt, 1995. *Vortex Flow in Nature and Technology*. Krieger Publishing Company.

A. Magnan, 1922. Les caracteristiques des oiseaux suivant le mode de vol. *Annales des Sciences Naturelles*, 10(5):125–334.

A. Magnan, 1934. *La Locomotion chez les Animaux*. Hermann et Cie.

J. H. Marden, 1987. Maximum lift production during takeoff in flying animals. *Journal of Experimental Biology*, 130:235–258.

E. J. Marey, 1868. Determination experimentale du mouvement des ailes des insectes pendant le vol. *Les Comptes rendus de l'Académie des Sciences*, 67: 1341–1345.

B. Massey and J. Ward-Smith, 1998. *Mechanics of Fluids*. Stanley Thornes, 7th edition.

J. Mathieu and J. Scott, 2000. *An Introduction to Turbulent Flow*. Cambridge University Press.

T. Maxworthy, 1979. Experiments on the Weis-Fogh mechanism of lift generation by insects in hovering flight. Part 1: Dynamics of the 'fling'. *Journal of Fluid Mechanics*, 93:47–63.

T. Maxworthy, 2007. The formation and maintenance of a leading-edge vortex during the forward motion of an animal wing. *Journal of Fluid Mechanics*, 587: 471–475.

W. J. McCroskey, 1981. The phenomenon of dynamic stall. Technical Memorandum 81264, NASA.

G. B. McCullough and D. E. Gault, 1951. Examples of three representative types of airfoil-section stall at low speed. Technical Note TN-2502, NACA.

J. E. McCune, C-M. G. Lam, and M. T. Scott, 1990. Nonlinear aerodynamics of two-dimensional airfoils in severe maneuver. *AIAA Journal*, 28(3):385–393.

J. E. McCune and T. S. Tavares, 1993. Perspective: Unsteady wing theory — the Kármán/Sears legacy. *Journal of Fluids Engineering*, 115:548–560.

F. R. Menter, R. Langtry, and S. Völker, 2006. Transition modelling for general purpose CFD codes. *Flow, Turbulence and Combustion*, 77:277–303.

W. Merzkirch, 1987. *Flow Visualization*. Academic Press.

L. A. Miller and C. S. Peskin, 2004. When vortices stick: an aerodynamic transition in tiny insect flight. *Journal of Experimental Biology*, 207:3073–3088.

L. M. Milne-Thomson, 1973. *Theoretical Aerodynamics*. Dover, 4th edition.

F. O. Minotti, 2002. Unsteady two-dimensional theory of a flapping wing. *Physical Review E*, 66(5):1–10.

A. M. Mitchell and J. Délery, 2001. Research into vortex breakdown control. *Progress in Aerospace Sciences*, 37:385–418.

R. Mittal, V. Seshadri, and H. S. Udaykuma, 2004. Flutter, tumble and vortex induced autorotation. *Theoretical and Computational Fluid Dynamics*, 17:165–170.

H. K. Moffatt, 1964. Viscous and resistive eddies near a sharp corner. *Journal of Fluid Mechanics*, 18:1–18.

B. Mols, 2005. Flapping micro plane watches where it goes. *Delft Outlook*, 22(4): 3–7.

R. M. Morris, 1937. The two-dimensional hydrodynamical theory of moving aerofoils — I. *Proceedings of the Royal Society of London, Series A*, 161(906):406–419.

T. J. Mueller and S. M. Batill, 1982. Experimental studies of separation on a two-dimensional airfoil at low Reynolds numbers. *AIAA Journal*, 20(4):457–463.

F. T. Muijres, L. C. Johansson, R. Barfield, M. Wolf, G. R. Spedding, and A. Hedenström, 2008. Leading-edge vortex improves lift in slow-flying bats. *Science*, 319:1250–1253.

P. Muren, 2005. *Proxflyer*. World Wide Web, www.proxflyer.com. Accessed: 02/11/2006.

Natural History Museum, 2005. *Mass migration at the Museum.* World Wide Web, www.nhm.ac.uk//about-us/news/2005/august/news_6158.html. Accessed: 24/08/2006.

G. Nolan, 2004. *Aerodynamics of Vortex Lift in Insect Flight.* PhD thesis, University of Cambridge.

K. Ohmi, M. Coutanceau, T. P. Loc, and A. Dulieu, 1990. Vortex formation around an oscillating and translating airfoil at large incidences. *Journal of Fluid Mechanics*, 211:37–60.

K. Ohmi, M. Coutanceau, T. P. Loc, and A. Dulieu, 1991. Further experiments on vortex formation around an oscillating and translating airfoil at large incidences. *Journal of Fluid Mechanics*, 225:607–630.

M. V. Ol and M. Gharib, 2003. Leading-edge vortex structure of nonslender delta wings at low Reynolds number. *AIAA Journal*, 41:16–26.

M. M. O'Meara and T. J. Mueller, 1987. Laminar separation bubble characteristics on an airfoil at low Reynolds numbers. *AIAA Journal*, 25(8):1033–1041.

ONERA, 2004. *Micropropulsion and Microcombustion.* World Wide Web, www.onera.fr/conferences/micropropulsion/. Accessed: 03/12/2007.

M. F. M. Osborne, 1951. Aerodynamics of flapping flight with application to insects. *Journal of Experimental Biology*, 28:221–245.

R. L. Panton, 1996. *Incompressible Flow.* John Wiley & Sons, 2nd edition.

A. Pascua, C. Pérez, and F. J. Serón, 1996. A comparison of segregated and coupled methods for the solution of the incompressible Navier-Stokes equations. *Communications in Numerical Methods in Engineering*, 12:617–630.

S. V. Patankar, 1980. *Numerical Heat Transfer and Fluid Flow.* Hemisphere.

C. B. Pedersen, 2003. *An indicial-Polhamus model of aerodynamics of insect-like flapping wings in hover.* PhD thesis, Cranfield University, Shrivenham.

C. B. Pedersen and R. Żbikowski, 2006. An indicial-Polhamus aerodynamic model of insect-like flapping wings in hover. In R. Liebe, editor, *Flow Phenomena in Nature: A Challenge to Engineering Design*. WIT Press.

D. Pierce, 1961. Photographic evidence of the formation and growth of vorticity behind plates accelerated from rest in still air. *Journal of Fluid Mechanics*, 11 (3):460–471.

D. J. Pines, 2007. *Challenges Facing Small Scale Flight*. World Wide Web, www.aaicorp.com/New/AUVSI/AUVSI_pines43007.pdf. Accessed: 03/12/2007.

Plantraco, 2007. *Plantraco Microflight*. World Wide Web, www.microflight.com. Accessed: 02/11/2007.

M. F. Platzer and K. D. Jones, 2006. Flapping wing aerodynamics — progress and challenges. *44th AIAA Aerospace Sciences Meeting and Exhibit, January 2006, Reno, NV, USA*.

C. Poelma, W. B. Dickson, and M. H. Dickinson, 2006. Time-resolved reconstruction of the full velocity field around a dynamically-scaled flapping wing. *Experiments in Fluids*, 41:213–225.

E. C. Polhamus, 1966. A concept of the vortex lift of sharp-edge delta wings based on a leading-edge suction analogy. Technical Note D-3767, NASA.

E. C. Polhamus, 1971. Predictions of vortex-lift characteristics by a leading-edge suction analogy. *Journal of Aircraft*, 8(4):193–199.

L. Prandtl, 1904. Über Flüssigkeitsbewegung bei sehr kleiner Reibung. *Verhandlungen des III. Internationalen Mathematiker-Kongresses*, 1:484–491.

L. Prandtl, 1928. Motion of fluids with very little viscosity. Technical Memorandum TM-452, NACA.

G. Pretor-Pinney, 2007. *The Cloud Appreciation Society photo gallery*. World Wide Web, cloudappreciationsociety.org/gallery. Accessed: 15/01/2008.

D. I. Pullin and Z. J. Wang, 2004. Unsteady forces on an accelerating plate and application to hovering insect flight. *Journal of Fluid Mechanics*, 509:1–21.

M. Raffel, C. E. Willert, and J. Kompenhans, 1998. *Particle Image Velocimetry — A Practical Guide*. Springer-Verlag.

R. Ramamurti and W. C. Sandberg, 2002. A three-dimensional computational study of the aerodynamic mechanisms of insect flight. *Journal of Experimental Biology*, 205:1507–1518.

M. Ramasamy, T. E. Lee, and J. G. Leishman, 2007. Flowfield of a rotating-wing micro air vehicle. *Journal of Aircraft*, 44:1236–1244.

M. Ramasamy and J. G. Leishman, 2006. Phase-Locked Particle Image Velocimetry Measurements of a Flapping Wing. *Journal of Aircraft*, 43(6):1867–1875.

RC-Helicopters.net, 2004. *What is the Best Remote Control Helicopter to Buy?* World Wide Web, www.rc-helicopters.net/remote-control-helicopter.htm. Accessed: 03/12/2007.

D. Rempfer, 2006. On boundary conditions for incompressible navier-stokes problems. *Applied Mechanics Reviews*, 59:107–125.

O. Reynolds, 1883. An experimental investigation of the circumstances which determine whether the motion of water shall be direct or sinuous, and of the law of resistance in parallel channels. *Proceedings of the Royal Society of London*, 35: 84–99.

W. C. Reynolds and L. W. Carr, 1985. Review of unsteady, driven, separated flows. *AIAA Paper 85-0527*.

B. A. Robinson, R. M. Barnett, and S. Agrawal, 1994. Simple numerical criterion for vortex breakdown. *AIAA Journal*, 32:116–122.

W. Roos, 2007. *DelFly*. World Wide Web, www.delfly.nl. Accessed: 07/11/2007.

A. Roshko, 1955. On the development of turbulent wakes from vortex streets. Technical Report TR-1191, NACA.

V. J. Rossow, 1978. Lift enhancement by an externally trapped vortex. *Journal of Aircraft*, 15:618–625.

H. Sakamoto and H. Haniu, 1990. A study on vortex shedding from spheres in a uniform flow. *Journal of Fluids Engineering*, 112:386–392.

S. P. Sane, 2003. The aerodynamics of insect flight. *Journal of Experimental Biology*, 206:4191–4208.

S. P. Sane and M. H. Dickinson, 2001. The control of flight force by a flapping wing: Lift and drag production. *Journal of Experimental Biology*, 204(15):2607–2626.

S. P. Sane and M. H. Dickinson, 2002. The aerodynamic effects of wing rotation and a revised quasi-steady model of flapping flight. *Journal of Experimental Biology*, 205:1087–1096.

T. Sarpkaya, 1979. Vortex induced oscillations: a selective review. *Journal of Applied Mechanics*, 46:241–258.

J. A. Schetz and A. E. Fuhs, editors, 1999. *Fundamentals of fluid mechanics*, chapter 11, pages 671–696. John Wiley & Sons.

F. W. Schmitz, 1940, translated 1967. Aerodynamik des Flugmodells: translated as "Aerodynamics of the model airplane. Part I. Airfoil measurements". Technical Report 721, Originally published in book form (in German) by Carl Lange: translated into English and published as technical report by Redstone Scientific Information Center.

M. T. Scott, 1987. Nonlinear airfoil-wake interaction in large amplitude unsteady flow. Master's thesis, Massachusetts Institute of Technology.

C. T. Shaw, 1992. *Using Computational Fluid Dynamics*. Prentice Hall.

R. E. Sheldahl and P. C. Klimes, 1981. Aerodynamic characteristics of seven symmetrical airfoil sections through 180-degree angle of attack for use in aerody-

namic analysis of vertical axis wind turbines. Technical report, Sandia National Laboratories.

W. Shyy and H. Liu, 2007. Flapping wings and aerodynamic lift: The role of leading-edge vortices. *AIAA Journal*, 45:2817–2819.

S. P. Singh and S. Mittal, 2005. Flow past a cylinder: shear layer instability and drag crisis. *International Journal for Numerical Methods in Fluids*, 47:75–98.

J. Skeen, 2000. Spy plane almost child's play. *Daily News (Los Angeles, CA), September 17.*

SRI International, 2007. *SRI International.* World Wide Web, www.sri.com. Accessed: 06/11/2007.

R. B. Srygley and A. L. R. Thomas, 2002. Unconventional lift-generating mechanisms in free-flying butterflies. *Nature*, 420:660–664.

Stanford University, 1999. *The Mesicopter: A Meso-Scale Flight Vehicle.* World Wide Web, aero.stanford.edu/mesicopter/mesicopter.html. Accessed: 06/11/2007.

E. Steltz, S. Avadhanula, and R. Fearing, 2007. High lift force with 275 hz wing beat in mfi. *2007 IEEE/RSJ International Conference on Intelligent Robots and Systems, October 2007, San Diego, CA, USA.*

R. L. Street, G. Z. Watters, and J. K. Vennard, 1996. *Elementary Fluid Mechanics.* John Wiley & Sons, 7th edition.

V. Strouhal, 1878. Über eine besondere Art von Tonerregung. *Ann. Phys. und Chemie, Neue Folge*, 5:216–251.

M. Sun, 2005. High-lift generation and power requirements of insect flight. *Fluid Dynamics Research*, 37:21–39.

M. Sun and S. L. Lan, 2004. A computational study of the aerodynamic forced and power requirements of dragonfly (*Aeschne juncea*) hovering. *Journal of Experimental Biology*, 207:1887–1901.

M. Sun and J. Tang, 2002. Unsteady aerodynamic force generation by a model fruit fly wing in flapping motion. *Journal of Experimental Biology*, 205:55–70.

M. Sun and J. H. Wu, 2003. Aerodynamic force generation and power requirements in forward flight in a fruit fly with modeled wing motion. *Journal of Experimental Biology*, 206:3065–3083.

M. Sun and Y. Xiong, 2005. Dynamic flight stability of a hovering bumblebee. *Journal of Experimental Biology*, 208:447–459.

M. Sun and X. Yu, 2006. Aerodynamic force generation in hovering flight in a tiny insect. *AIAA Journal*, Vol. 44:1532–1541.

Q. Sun and I. D. Boyd, 2003. Simulation of gas flow over micro-scale airfoils using a hybrid continuum-particle approach. *33rd AIAA Fluid Dynamics Conference and Exhibit, June 2003, Orlando, FL, USA*.

Q. Sun and I. D. Boyd, 2004. Flat-plate aerodynamics at very low Reynolds number. *Journal of Fluid Mechanics*, 502:199–206.

S. Sunada and C. P. Ellington, 2000. Approximate added-mass method for estimating induced power for flapping flight. *AIAA Journal*, 38(8):1313–1321.

S. Sunada, A. Sakaguchi, and K. Kawachi, 1997. Airfoil section characteristics at low Reynolds numbers. *Journal of Fluids Engineering*, 119:129–135.

J. Tang, D. Viieru, and W. Shyy, 2008. Effects of Reynolds number and flapping kinematics on hovering aerodynamics. *AIAA Journal*, 46:967–976.

T. S. Tavares, 1990. *Aerodynamics of Maneuvering Slender Wings with Leading-Edge Separation*. PhD thesis, Massachusetts Institute of Technology.

T. S. Tavares and J. E. McCune, 1993. Aerodynamics of maneuvering slender wings with leading-edge separation. *AIAA Journal*, 31(6):977–986.

G. K. Taylor, R. L. Nudds, and A. L. R. Thomas, 2003. Flying and swimming animals cruise at a Strouhal number tuned for high power efficiency. *Nature*, 425: 707–711.

Teal Group Corporation, 2006. *Teal Group Predicts Worldwide UAV Market Will Top $54 Billion.* World Wide Web, www.tealgroup.com/releases/2006-10-9.htm. Accessed: 02/11/2007.

TechLink, 2006. *BITE-Wing Micro Air Vehicle (UAV).* World Wide Web, www.techlinkcenter.org/cgi-bin/techlink/01014.html. Accessed: 07/11/2007.

T. Theodorsen, 1935. General theory of aerodynamic instability and the mechanism of flutter. Technical Report 496, N.A.C.A.

R. Thirumalainambi, J. Bardina, and O. Miyazawa, 2005. Nonintrusive techniques of inspections during the pre-launch phase of space vehicle. *Proceedings of the SPIE — Modeling, Simulation, and Verification of Space-based Systems II*, 5799: 92–99.

Thumbs Up (UK) Ltd, 2007. *BladeRunner iVAMP.* World Wide Web, www.thumbsupuk.com/products/BladeRunner-iVAMP.htm. Accessed: 03/12/2007.

L. W. Traub, 2004. Analysis and estimation of the lift components of hovering insects. *Journal of Aircraft*, 41(2):284–289.

US Air Force Special Operations Command, 2007. *Fact Sheet: BATMAV Micro Unmanned Aircraft System.* World Wide Web, www2.afsoc.af.mil/library/factsheets/factsheet.asp?id=9114. Accessed: 02/11/2007.

US Naval Research Laboratory, 2007. *BITE-Wing: Biplane Insectoid Travel Engine.* World Wide Web, www.nrl.navy.mil/techtransfer/exhibits/pdfs/Info0Sheets/BITE-Wing.pdf. Accessed: 07/11/2007.

US Patent Office, 2004. *Dual wing-pair air vehicle.* US Patent No. 6 959 895.

J. R. Usherwood and C. P. Ellington, 2002a. The aerodynamics of revolving wings. I. Model hawkmoth wings. *Journal of Experimental Biology*, 205:1547–1564.

J. R. Usherwood and C. P. Ellington, 2002b. The aerodynamics of revolving wings. II. Propeller force coefficients from mayfly to quail. *Journal of Experimental Biology*, 205:1565–1576.

A. Van de Rostyne, 2006. *Piccolino: 1.69 gram RC helicopter*. World Wide Web, www.rcgroups.com/forums/showthread.php?p=5378631. Accessed: 03/12/2007.

C. van den Berg and C. P. Ellington, 1997a. The three-dimensional leading-edge vortex of a "hovering" model Hawkmoth. *Philosophical Transactions of the Royal Society B*, 352(1351):329–340.

C. van den Berg and C. P. Ellington, 1997b. The vortex wake of a "hovering" model Hawkmoth. *Philosophical Transactions of the Royal Society B*, 352(1351): 317–328.

B. G. van der Wall and J. G. Leishman, 1994. On the influence of time-varying flow velocity on unsteady aerodynamics. *Journal of the American Helicopter Society*, 39(4):25–36.

M. Van Dyke, 1982. *An Album of Fluid Motion*. The Parabolic Press.

H. K. Versteeg and W. Malalasekera, 2007. *An Introduction to Computational Fluid Dynamics — The Finite Volume Method*. Pearson Education, 2nd edition.

M. R. Visbal, 1995. Computational and physical aspects of vortex breakdown on delta wings. *33rd AIAA Aerospace Sciences Meeting, January 1995, Reno, NV, USA*.

S. Vogel, 1967a. Flight in *Drosophila*: II. Variations in stroke parameters and wing contour. *Journal of Experimental Biology*, 46:383–392.

S. Vogel, 1967b. Flight in *Drosophila*: III. Aerodynamic characteristics of fly wings and wing models. *Journal of Experimental Biology*, 46:431–443.

S. Vogel, 1994. *Life in Moving Fluids: The Physical Biology of Flow*. Princeton University Press.

T. von Kármán and W. R. Sears, 1938. Airfoil theory for non-uniform motion. *Journal of the Aeronautical Sciences*, 5(10):379–390.

H. Wagner, 1925. Über die Entstehung des dynamischen Auftriebes von Tragflügeln. *Zeitschrift für Angewandte Mathematik und Mechanik*, 5(1):17–35.

D. Walker, 2007. *PicooZ — world's smallest radio-controlled helicopter*. World Wide Web, techdigest.tv/2007/02/picooz_worlds_s.html#more. Accessed: 03/12/2007.

J. A. Walker, 2002. Rotational lift: something different or more of the same? *Journal of Experimental Biology*, 205:3783–3792.

J. A. Walker and M. W. Westneat, 2000. Mechanical performance of aquatic rowing and flying. *Proceedings of the Royal Society B*, 267:1875–1881.

J. A. Walker and M. W. Westneat, 2002. Kinematics, dynamics, and energetics of rowing and flapping propulsion in fishes. *Integrative and Comparative Biology*, 42:1032–1043.

J. K. Wang and M. Sun, 2005. A computational study of the aerodynamics and forewing-hindwing interaction of a model Dragonfly in forward flight. *Journal of Experimental Biology*, 208:3785–3804.

Z. J. Wang, 2000. Vortex shedding and frequency selection in flapping flight. *Journal of Fluid Mechanics*, 410:323–341.

Z. J. Wang, 2005. Dissecting insect flight. *Annual Review of Fluid Mechanics*, 37:183–210.

Z. J. Wang, J. M. Birch, and M. H. Dickinson, 2004. Unsteady forces and flows in low Reynolds number hovering flight: two-dimensional computations vs robotic wing experiments. *Journal of Experimental Biology*, 207:449–460.

P. P. Wegener, 1997. *What Makes Airplanes Fly?* Springer.

T. Weis-Fogh, 1972. Energetics of hovering flight on Hummingbirds and *Drosophila*. *Journal of Experimental Biology*, 56:79–104.

T. Weis-Fogh, 1973. Quick estimate of flight fitness in hovering animals, including novel mechanisms for lift production. *Journal of Experimental Biology*, 59:169–230.

T. Weis-Fogh and M. Jensen, 1956. Biology and physics of Locust flight. I. Basic principles in insect flight: A critical review. *Philosophical Transactions of the Royal Society of London B*, 239:415–458.

P. Wilkins and K. Knowles, 2007. Investigation of aerodynamics relevant to flapping-wing micro air vehicles. *37th AIAA Fluid Dynamics Conference and Exhibit, June 2007, Miami, FL, USA*.

P. Wilkins, K. Knowles, and R. Żbikowski, 2006. CFD investigation of aerodynamics relevant to flapping-wing micro air vehicles. *European Micro Air Vehicle Conference, July 2006, Braunschweig, Germany*.

C. H. K. Williamson, 1996. Vortex dynamics in the cylinder wake. *Annual Review of Fluid Mechanics*, 28:477–539.

A. P. Willmott and C. P. Ellington, 1997. The mechanics of flight in the Hawkmoth, *Manduca sexta*: II. Aerodynamic consequences of kinematic and morphological variation. *Journal of Experimental Biology*, 200:2723–2745.

A. P. Willmott, C. P. Ellington, and A. L. R. Thomas, 1997. Flow visualization and unsteady aerodynamics in the flight of the Hawkmoth, *Manduca sexta*. *Philosophical Transactions of the Royal Society of London B*, 352:303–316.

R. Wood, 2007. Liftoff of a 60mg flapping-wing MAV. *2007 IEEE/RSJ International Conference on Intelligent Robots and Systems, October 2007, San Diego, CA, USA*.

M. I. Woods, J. F. Henderson, and G. D. Lock, 2001. Energy requirements for the flight of micro air vehicles. *Aeronautical Journal*, 105:135–149.

J. Wu and M. Sun, 2005. The influence of the wake of a flapping wing on the production of aerodynamic forces. *Acta Mechanica Sinica*, 21(5):411–418.

T. Wu, 2001. On theoretical modelling of aquatic and aerial animal locomotion. In E. van der Giessen, T. Wu, and H. Aref, editors, *Advances in Applied Mechanics, Vol. 38*, pages 291–353. Academic Press.

Y. Yu, B. Tong, and H. Ma, 2003. An analytical approach to theoretical modeling of highly unsteady viscous flow excited by wing flapping in small insects. *Acta Mechanica Sinica*, 19(6):508–516.

R. Żbikowski, 2002a. On aerodynamic modelling of an insect-like flapping wing in hover for micro air vehicles. *Philosophical Transactions of the Royal Society of London A*, 360:273–290.

R. Żbikowski, 2002b. Red admiral agility. *Nature*, 420:615–618.

R. Żbikowski, 2004. Sensor-rich feedback control: A new paradigm for flight control inspired by insect agility. *IEEE Instrumentation and Measurement Magazine*, 7:19–26.

R. Żbikowski, C. Galiński, and C. B. Pedersen, 2005. Four-bar linkage mechanism for insect-like flapping wings in hover: Concept and an outline of its realisation. *Journal of Mechanical Design*, 127(4):817–824.

P. Zdunich, D. Bilyk, M. MacMaster, and D. Loewen, 2007. Development and testing of the Mentor flapping-wing micro air vehicle. *Journal of Aircraft*, 44(5): 1701–1711.

Appendices

Appendix A

Dynamic scaling of insect-like flapping

It was mentioned in §2.1.2 that some concerns have been expressed (see e.g. Galiński and Żbikowski, 2007) about the validity of using scaled-up mechanical 'flappers' to emulate insect-like flapping. Because many of the current analytical and computational models have been validated against or compared to data from mechanical 'flappers', it is important to investigate these concerns and whether they are valid.

A.1 Dimensional analysis of insect like flapping

Non-varying terms do not need to be considered during dimensional analysis. This makes dimensional analysis of insect-like flapping much more viable — in reality, the force on an insect wing depends on stroke plane, angle of attack, and other kinematic parameters, as well as wing planform and cross-section. If it is assumed that the wing kinematics and wing shape are fixed it may be possible to analyse insect-like flapping dimensionally[1]. The aim, of course, is to determine what dimensionless parameters need to be kept constant when using a scaled-up mechanical 'flapper' to analyse insect aerodynamics. It is also assumed that the fluid

[1] It should be noted that 'wing kinematics' are kept constant in this section, flapping frequency is excluded.

is incompressible. The relevant parameters are listed below.

Mean force $\overline{F}$. The mean force on a wing is of interest, not the instantaneous force. This removes the complication of time-dependence. The mean force has dimensions of $[MLT^{-2}]$.

Wing size. As mentioned above, a fixed wing shape is assumed, so that the size factor can be represented by a single typical dimension, which will be denoted in this case by L. Its dimensions are $[L]$.

Flapping frequency f. f is the number of complete cycles per second — each cycle made up of downstroke and upstroke. Dimensions, $[T^{-1}]$.

Fluid density ρ and dynamic viscosity μ. Dimensions, $[ML^{-3}]$ and $[ML^{-1}T^{-1}]$ respectively.

Vortex shedding frequency f_{vs}. Insect wings translate at high angles of attack and *may* shed vortices. There is plenty of evidence that vortex shedding occurs only at stroke reversal, in which case $f_{vs} = f$. But for the moment this evidence is ignored and it is supposed that vortex shedding can occur during the upstroke and downstroke. f_{vs} has dimensions of $[T^{-1}]$.

Velocity V_i. This is the speed of the insect relative to the air, and has dimensions of $[LT^{-1}]$.

In other words, $\overline{F}$ is a function of the preceding 6 parameters, thus:

$$\begin{aligned} \overline{F} &= f\left[L, f, \rho, \mu, f_{vs}, V_i\right] \\ &= \sum C L^a f^b \rho^c \mu^d f_{vs}^e V_i^h, \end{aligned}$$

Where C is a constant. In terms of the fundamental dimensions (mass M, length L and time T) this becomes;

$$\left[\frac{ML}{T^2}\right] = \left[(L)^a \left(\frac{1}{T}\right)^b \left(\frac{M}{L^3}\right)^c \left(\frac{M}{LT}\right)^d \left(\frac{1}{T}\right)^e \left(\frac{L}{T}\right)^h\right]. \qquad \text{(A.1)}$$

The dimensions of both sides of this equation must be the same, so that the indices of M, L and T can be equated to give three simultaneous equations:

$$\begin{aligned} 1 &= c + d \\ 1 &= a - 3c - d + h \\ -2 &= -b - d - e - h \end{aligned}$$

$$\begin{aligned} \therefore \quad c &= 1 - d \\ a &= 1 + 3c + d - h \\ &= 1 + 3(1 - d) + d - h \\ &= 4 - 2d - h \\ b &= 2 - d - e - h. \end{aligned}$$

Substituting these into Equation A.1 gives:

$$\begin{aligned} \overline{F} &= \left[L^{4-2d-h} f^{2-d-e-h} \rho^{1-d} \mu^d f_{vs}^e V_i^h\right] \\ &= \rho L^4 f^2 \left(\frac{\mu}{\rho f L^2}\right)^d \left(\frac{f_{vs}}{f}\right)^e \left(\frac{V_i}{Lf}\right)^h. \end{aligned} \tag{A.2}$$

If wing semi-span (defined as the distance from centre of rotation to wing tip) is taken as the representative length L, then some of these expressions become more familiar. The distance that the wing tip travels with each stroke is proportional to L, with the constant of proportionality (denoted P in this case) dependent on the kinematics of the wing. The wing tip travels through this distance (PL) at $2f$ times a second (the 2 occurs because f is the frequency of flapping, i.e. the number of complete upstroke-downstroke cycles per second). The mean wing tip velocity $\overline{V_{tip}}$ is therefore equal to $2PLf$, or alternatively

$$Lf = \frac{1}{2P}\overline{V_{tip}}.$$

Substituting this into Equation A.2 gives

$$\begin{aligned}
\overline{F} &= \rho\left(\frac{1}{2P}\overline{V_{tip}}\right)^2 L^2 \left(\frac{\mu}{\rho\frac{1}{2P}\overline{V_{tip}}L}\right)^d \left(\frac{f_{vs}}{\frac{1}{2P}\frac{\overline{V_{tip}}}{L}}\right)^e \left(\frac{V_i}{\frac{1}{2P}\overline{V_{tip}}}\right)^h \\
\frac{\overline{F}}{\rho\overline{V_{tip}}^2 L^2} &= \frac{1}{4P^2}\left(2P\frac{\mu}{\rho\overline{V_{tip}}L}\right)^d \left(\frac{2PLf_{vs}}{\overline{V_{tip}}}\right)^e \left(\frac{V_i}{\frac{1}{2P}\overline{V_{tip}}}\right)^h \\
&= function\left(\frac{\mu}{\rho\overline{V_{tip}}L}, \frac{f_{vs}L}{\overline{V_{tip}}}, \frac{V_i}{\overline{V_{tip}}}\right). \qquad \text{(A.3)}
\end{aligned}$$

The LHS of Equation A.3 is the force on the wing, non-dimensionalised by mean wing tip speed and wing length. The first term on the RHS is the inverse of Reynolds number and the second term is vortex shedding frequency, non-dimensionalised by mean tip speed and wing length — usually called Strouhal number St. In fact, Strouhal number is dependent on Reynolds number only (for a given shape at a given incidence), as was shown in §5.2, and so this latter term can be ignored — providing the Reynolds numbers for the insect and 'flapper' are equal, force coefficients (and flow structure) should match. The third term on the RHS is the ratio of the speed of the insect through the air to the mean velocity of the wing tip relative to the insect body, and is usually called *reduced frequency*. In much of what follows the insect is assumed to be in hover, so that this third term becomes irrelevant.

Equation A.3 provides insight into this problem, but Equation A.2 is a more compact expression, and can be written as

$$\frac{\overline{F}}{\rho L^4 f^2} = function\left(\frac{\mu}{\rho f L^2}, \frac{f_{vs}}{f}, \frac{V_i}{Lf}\right). \qquad \text{(A.4)}$$

What this shows is that for a 'flapper' to be scaled so that the mean force on the wing and the flow around it to be equivalent to the insect case, the RHS bracketed terms must be kept constant during the scaling process. If they are, then the LHS term will be the same for the 'flapper' as for the original insect.

The first term on the RHS is modified Reynolds number $\hat{Re}$; so that

$$\hat{Re} = \frac{\mu}{\rho f L^2}. \qquad \text{(A.5)}$$

The second term on the RHS is equivalent to the number of vortices shed per flapping cycle. In general, the frequency of vortex shedding is not something that can be controlled — for example, a sphere in a flow will shed vortices at a rate which depends only on the dimensions of the sphere and the velocity of the flow. What this second term means is that if the flapping of an insect generates (for example) 5 shed vortices per flapping cycle, the flapping of the 'flapper' must also shed 5 vortices per flapping cycle.

There are two possible types of vortex shedding involved in insect-like flapping. Firstly, there is *forced* shedding, where vortices are shed due to the flapping motion of the wings. It is well known that a wing will shed vortices whenever its velocity or angle of attack changes. Because this forced shedding is dependent on the kinematics of the wing, the frequency of forced shedding will be preserved between insect and 'flapper', provided that the kinematics and Reynolds number are preserved.

The second possible source of vortex shedding is *natural* vortex shedding. However, there is a possible source of confusion here. It was seen that for Reynolds numbers of less than 1 000, an aerofoil at a high angle of attack will shed vortices. For a Reynolds number higher than 1 000, the aerofoil will still shed these vortices but in addition, Kelvin-Helmholtz instability will appear in the vortex sheets, forming smaller vortices within the sheets. Thus, there are two Strouhal numbers — one relating to the shedding of the large vortices (which are seen at all Reynolds numbers above $Re = 25$) and one relating to the smaller vortices (which are the result of KHI and are only seen at $Re > 1\,000$). However, Sakamoto and Haniu (1990) have shown that *both* these Strouhal numbers are dependent on Reynolds number.

What has been shown is that the frequency of vortex shedding is dependent on two factors — kinematics (which affect the frequency of forced shedding) and Reynolds number (which affects the frequency of both forced and natural shedding). Therefore, provided that kinematics and Reynolds number are preserved when moving from insect to 'flapper', the second term on the RHS of Equation A.4 will be preserved and so the term on the LHS of Equation A.4 (and the dy-

namics of the flow) will also be preserved.

This information can be used to test some of the 'flappers' that have been used in the literature and check that they are dynamically scaled.

A.2 Are 'flappers' dynamically scaled?

A.2.1 Ellington's 'flapper'

Ellington's 'flapper' is described in Ellington et al. (1996). It was modelled on *Manduca sexta*, a moth with a wingspan of around $10cm$ which has a flapping frequency of around $26Hz$. The 'flapper' itself is 10 times larger than the insect and has a flapping frequency of $0.3Hz$. The analysis is carried out assuming hover conditions, so reduced frequency is zero in both cases. Therefore, in order for the model to be valid, $\hat{Re}_1$ must be equal to $\hat{Re}_2$, where the subscripts 1 and 2 refer to the 'flapper' and insect respectively. In other words it is necessary to calculate the ratio of $\hat{Re}_1$ to $\hat{Re}_2$;

$$\begin{aligned}\frac{\hat{Re}_1}{\hat{Re}_2} &= \frac{\frac{\mu_1}{\rho_1 f_1 L_1^2}}{\frac{\mu_2}{\rho_2 f_2 L_2^2}} \\ &= \frac{\mu_1}{\mu_2}\frac{\rho_2}{\rho_1}\frac{f_2}{f_1}\frac{L_2^2}{L_1^2}.\end{aligned}$$

Ellington's 'flapper' operates in air, so $\mu_1 = \mu_2$ and $\rho_1 = \rho_2$. Therefore

$$\begin{aligned}\frac{\hat{Re}_1}{\hat{Re}_2} &= \frac{f_2}{f_1}\frac{L_2^2}{L_1^2} \\ &= \frac{26}{0.3}\frac{0.1^2}{1.0^2} \\ &= 0.867,\end{aligned}$$

which is probably close enough to one to be acceptable. It is possible that the flapping frequency for the 'flapper' of 0.3 is rounded; if f_1 were 0.26, the result would be exactly unity. Equally, the full-size value of $26Hz$ is presumably an average for the species (*Manduca sexta*).

In Ellington et al. (1996), the authors stated "another similarity condition [apart

from Reynolds number] was also met." They observe that during a stroke the high angle of attack *might* cause vortex shedding. They noted that the frequency of this *natural* vortex shedding (as opposed to the *forced* vortex shedding caused by the starting and stopping motion of the wings) is determined by the Strouhal number. They then use the fact that Strouhal number is dependent on Reynolds number to state that, for a given Reynolds number, the frequency of free vortex shedding is proportional to flapping frequency. Thus, they argue, the vortex shedding patterns for their 'flapper' should be similar to those of the insect. In other words, they argue, Strouhal number may be important, but because it is dependent on Reynolds number, it is necessary only to match Reynolds number and Strouhal number will be matched automatically. In a later paper, van den Berg and Ellington (1997b) reiterated this view, once again stating that St is "constant for a given Re."

Based on the analysis above, it is possible to state that Ellington's 'flapper' *is* dynamically scaled. Reynolds number is preserved, and Strouhal number is not important because natural vortex shedding does not occur — only forced shedding. In any case, even if free vortex shedding *did* occur, it would occur at a rate determined by Strouhal number, which is itself dependent on Reynolds number.

A.2.2 Dickinson's 'flapper'

Dickinson's 'flapper' (known as 'Robofly') is described in Dickinson et al. (1999). It is modelled on a much smaller insect than Ellington's — the fruit fly *Drosophila melanogaster*. *Drosophila* has a typical wingspan of $2.5mm$ and the 'flapper' is scaled up by a factor of 100. Frequency was scaled down by a factor of 1320, and the 'flapper' operates in mineral oil, with density $880kg/m^3$ and dynamic viscosity $0.1012kg/ms$. Once again the insect is assumed to be hovering. Using the same approach as for Ellington's 'flapper' above:

$$\begin{aligned}\frac{\hat{Re}_1}{\hat{Re}_2} &= \frac{\mu_1}{\mu_2}\frac{\rho_2}{\rho_1}\frac{f_2}{f_1}\frac{L_2^2}{L_1^2} \\ &= \frac{0.1012}{1.7895e^{-5}}\frac{1.225}{880}\frac{1320}{1}\frac{1^2}{100^2} \\ &= 1.04,\end{aligned}$$

which is again close to 1.

Later, Sane and Dickinson (2001) described the scaling process in more detail and noted that there were two parameters to match — Reynolds number and reduced frequency. However, they noted that because the body velocity is zero, reduced frequency is also zero for both insect and 'flapper'. Later still, Poelma et al. (2006) conceded that "the Reynolds number is not the only dimensionless number that is relevant in flapping flight," commenting that Strouhal number was also important. However, using the relationship between flapping frequency and tip velocity (described above), they concluded that Strouhal number scales with Reynolds number, so that it is not necessary to match them both individually.

A.3 Forward flight

If using a 'flapper' to analyse forward flight, reduced frequency (V_i/Lf) becomes a second non-dimensional parameter to be matched. Fortunately this will not prove difficult. The value of L is prescribed during the scaling-up process — usually a decision will be made to scale up by a factor of 10, or 100, or some other number. Once this is done, the required value of f can be determined using the equation for modified Reynolds number $\hat{Re}$;

$$\begin{aligned} \frac{\hat{Re}_1}{\hat{Re}_2} &= 1 = \frac{\mu_1}{\mu_2}\frac{\rho_2}{\rho_1}\frac{f_2}{f_1}\frac{L_2^2}{L_1^2} \\ \therefore \quad \frac{f_1}{f_2} &= \frac{\mu_1}{\mu_2}\frac{\rho_2}{\rho_1}\left(\frac{L_2}{L_1}\right)^2. \end{aligned}$$

All the variables on the RHS will be fixed, so f_1/f_2 can be calculated. (V_{i1}/V_{i2}) can then be calculated using the definition of reduced frequency:

$$\begin{aligned} \frac{\frac{V_{i1}}{L_1 f_1}}{\frac{V_{i2}}{L_2 f_2}} &= 1 \\ \therefore \quad \frac{V_{i1}}{V_{i2}} &= \frac{L_1 f_1}{L_2 f_2} = \frac{L_1}{L_2}\frac{\mu_1}{\mu_2}\frac{\rho_2}{\rho_1}\left(\frac{L_2}{L_1}\right)^2 = \frac{\mu_1}{\mu_2}\frac{\rho_2}{\rho_1}\frac{L_2}{L_1}. \end{aligned}$$

So if the scale factor is 10 (i.e. the 'flapper' is 10 times larger than the insect)

then V_i must be 10 times smaller for the 'flapper' than for the insect (provided the 'flapper' operates in air).

A.4 Conclusion

It has been shown that for 'flappers' in hover, there is only one dimensionless parameter that needs to match that of the original insect. This parameter is Reynolds number, which can be expressed in terms of L (a representative length) and either mean tip velocity $\overline{V_{tip}}$ or flapping frequency f (as well as the density and viscosity of the fluid). It is generally easier to use flapping frequency, since this is usually programmed into the 'flapper', whereas $\overline{V_{tip}}$ depends on wingtip path and has to be calculated.

All this is assuming that the kinematics are preserved when moving from insect to 'flapper'. If this is not the case, then even if the frequency of flapping and wing dimensions are preserved, the aerodynamics and the force coefficients will not be.

Appendix B

CFD model details

B.1 Meshes

Here, details are presented of the meshes that were used for the CFD analysis. Coordinates and lengths in this section are given in arbitrary units simply to describe the relative positions of the points. When grids were imported into Fluent, the grids were scaled such that the aerofoil or wing size was as required.

2D cases

Elliptical aerofoils

A number of elliptical aerofoil sections were used of different thickness/chord ratios. However, they all took the same form, and here details are given for the 1% thick aerofoil.

As shown in Figure B.1, an O-grid is used close to the aerofoil, which transitions to a triangular unstructured grid about 0.5 chords from the aerofoil. The grid is symmetrical both horizontally and vertically.

In Figure B.2, the mid-chord of the aerofoil lies at $(0, 0)$. Point A is at $(0, 4000)$, C is at $(0, 200)$, and E is at $(0, 2)$. The aerofoil chord length is 400. A series of cell layers was created on the surface of the aerofoil with initial cell thickness 0.01, growth factor 1.61, and number of rows 7, in order to capture the boundary layer.

The mesh is symmetrical in horizontal and vertical planes and the mesh parame-

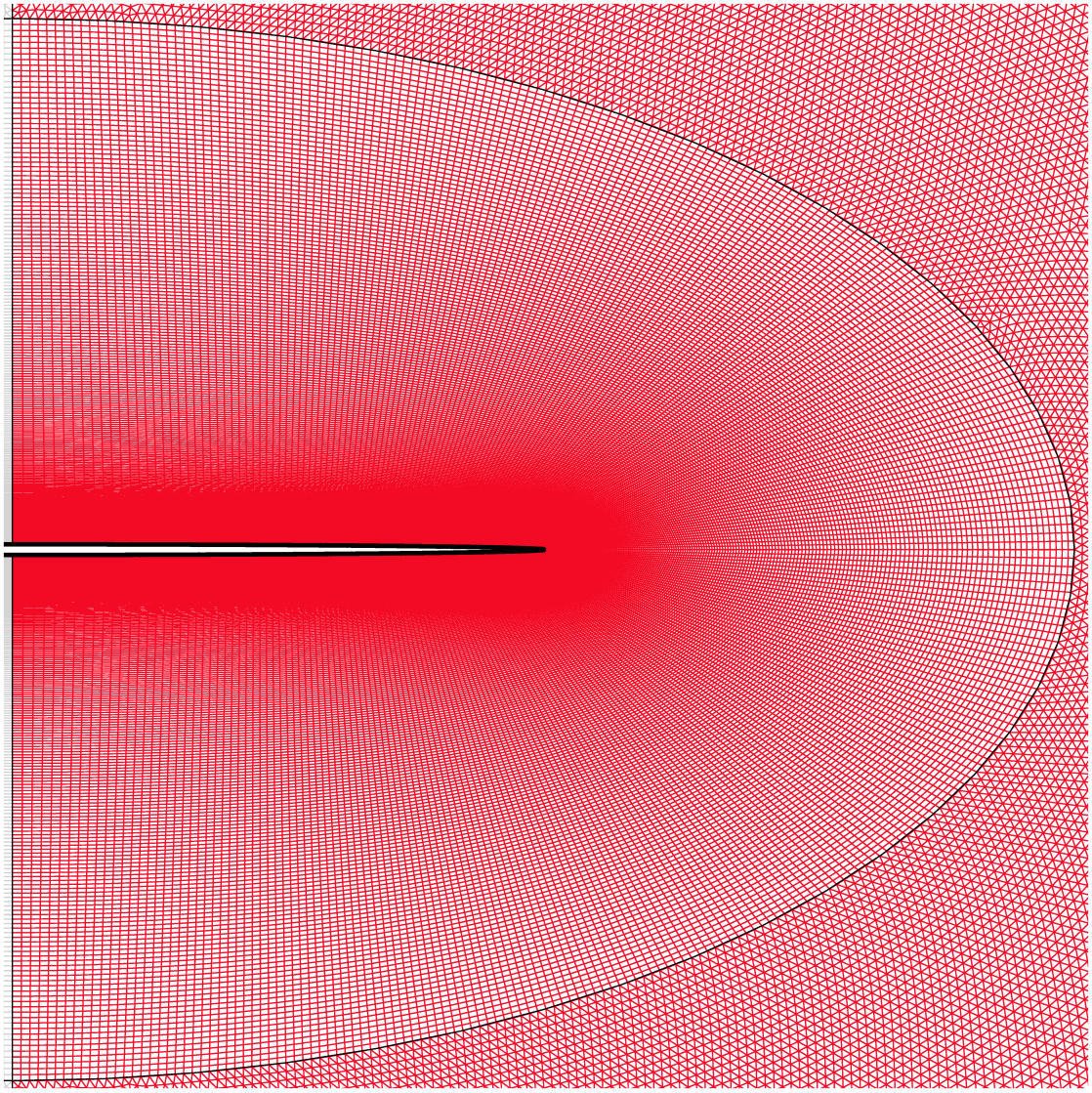

Figure B.1: Mesh for 1% thick elliptical aerofoil. One half of the mesh close to the aerofoil is shown.

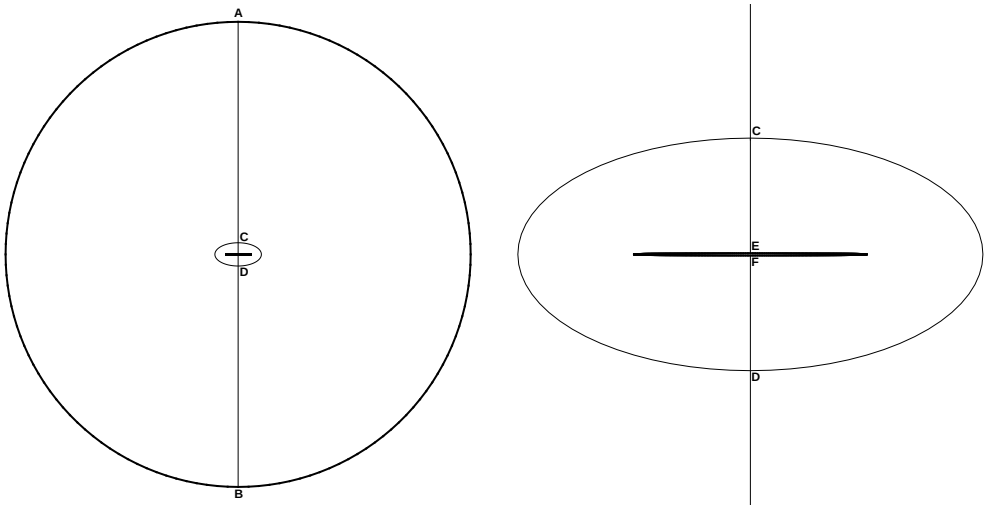

(a) Full mesh (b) Centre section

Figure B.2: Vertex labels for Table B.1.

Line	Interval count	Successive ratio
AB	70	1
AC	50	1.08
CD	145	1
CE	75	1.04
EF	145	1.06^a

Table B.1: Mesh parameters for 1% thick elliptical aerofoil. "Interval count" is the number of mesh intervals on the specified line; "successive ratio" gives the rate of growth of the intervals (e.g. if the successive ratio is 1.01, each interval will be 1% larger than one of its neighbours). The successive ratios are such that the end of the line where the intervals are *smallest* lies closest to the aerofoil. Note (a): this successive ratio is double-sided, so that the mesh density is closest at the leading edge.

t/c	Successive ratio for line EF
1	1.06
5	1.06
10	1.04
20	1.03
30	1.02
50	1.01
100	1

Table B.2: Successive ratio for cells on aerofoil perimeter for elliptical aerofoils of varying thickness to chord ratio. See note (a), Table B.1.

Line	Interval count	Successive ratio
AB (& DC)	60	1.05
BC	25	1

Table B.3: Mesh parameters for flat plate with elliptical edges. The successive ratios are given such that the end of the line where the intervals are smaller always lies closest to the aerofoil.

ters are given in Table B.1. The total number of cells for this mesh is approximately 1×10^5.

For the investigation of aerofoil thickness (§5.6) the number of cells on the aerofoil surface was kept constant as the thickness of the aerofoil was increased so that the total number of cells around the aerofoil's perimeter remained fixed at 290. However, the successive ratio was varied as t/c was increased, as shown in Table B.2. All other parameters were kept constant, apart from for the 100% thick case. In this case point C (in Figure B.2) had to be moved away from the aerofoil. Meshes for the thicker ellipses are shown in Figure B.3.

Flat plate with elliptical edges

Most of the mesh parameters for this aerofoil are identical to those for the 1% thick elliptical aerofoil above; the only thing that changes is the shape of the curve from E to F in Figure B.2 (i.e. the shape of the aerofoil). For this case, each half of the aerofoil was divided into three sections; the upper surface, the curved end portion, and the lower surface, as in Figure B.4. The sections were then meshed using the parameters given in Table B.3. The total number of intervals around the aerofoil's

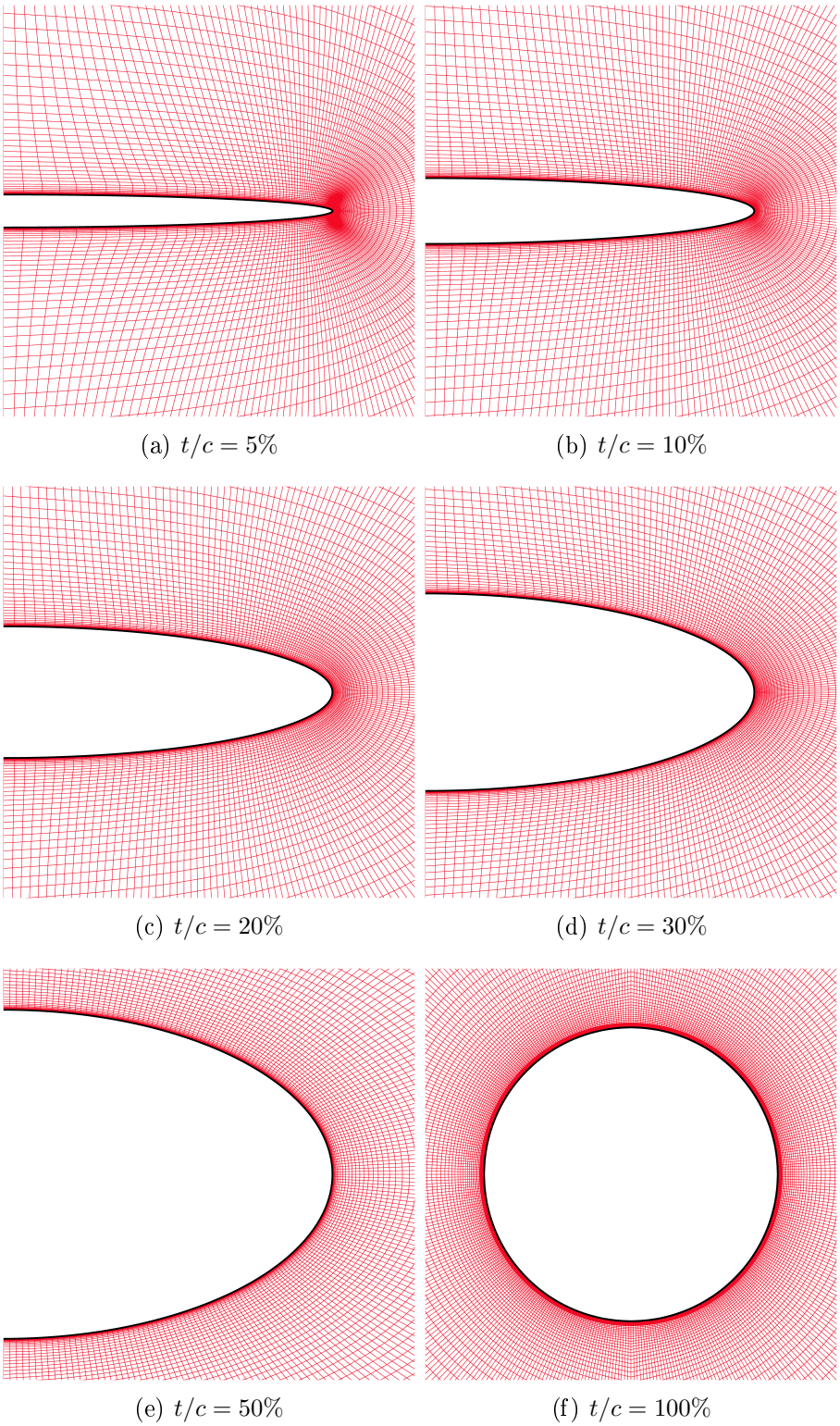

(a) $t/c = 5\%$ (b) $t/c = 10\%$

(c) $t/c = 20\%$ (d) $t/c = 30\%$

(e) $t/c = 50\%$ (f) $t/c = 100\%$

Figure B.3: Meshes for elliptical aerofoils of various thickness/chord ratios.

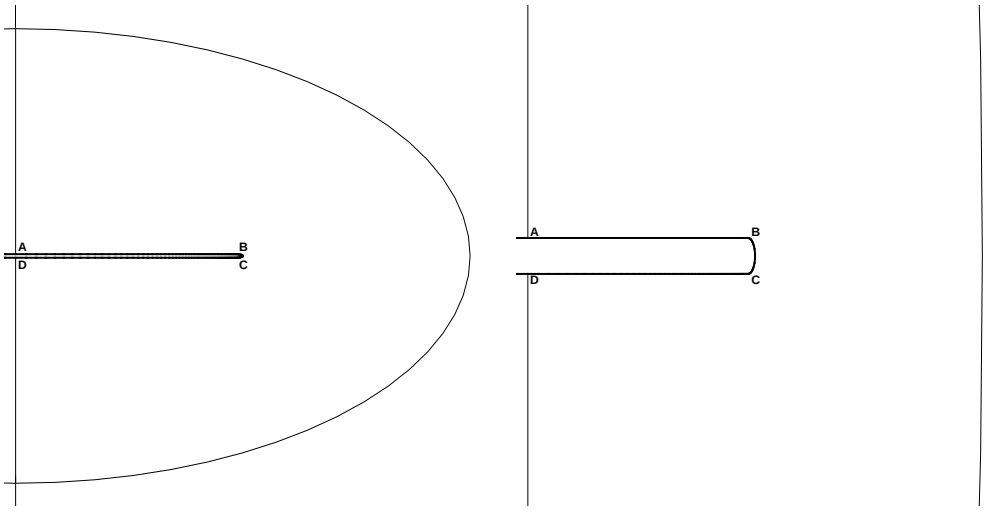

(a) To scale (b) Vertically-stretched

Figure B.4: Shape of aerofoil. Figure B.4(b) is vertically stretched with scale factor 10 for clarity.

perimeter was therefore 290.

A series of cell layers was created on the surface of the aerofoil, with initial cell thickness 0.01, growth factor 1.61, and number of rows 7, in order to capture the boundary layer. The total number of cells for this grid was approximately the same as for the 1% thick elliptical aerofoil above.

This aerofoil shape was used for the mesh-sensitivity analysis in §4.3.4.1. To refine the mesh, the number of intervals around the aerofoils surface was increased, and the number of intervals on other edges was increased by the same factor.

Flat plate with semicircular edges

Exactly the same procedure was followed with this aerofoil shape as for the elliptically-ended flat plate above. Therefore the mesh parameters are identical for the two grids.

Infinitely-thin flat plate

For this aerofoil, an O-grid could not be used to the aerofoil as it could for the aerofoils above, and instead the domain was meshed as shown in Figure B.5.

In Figure B.6, the mid-chord of the aerofoil lies at $(0, 0)$ and point A is at

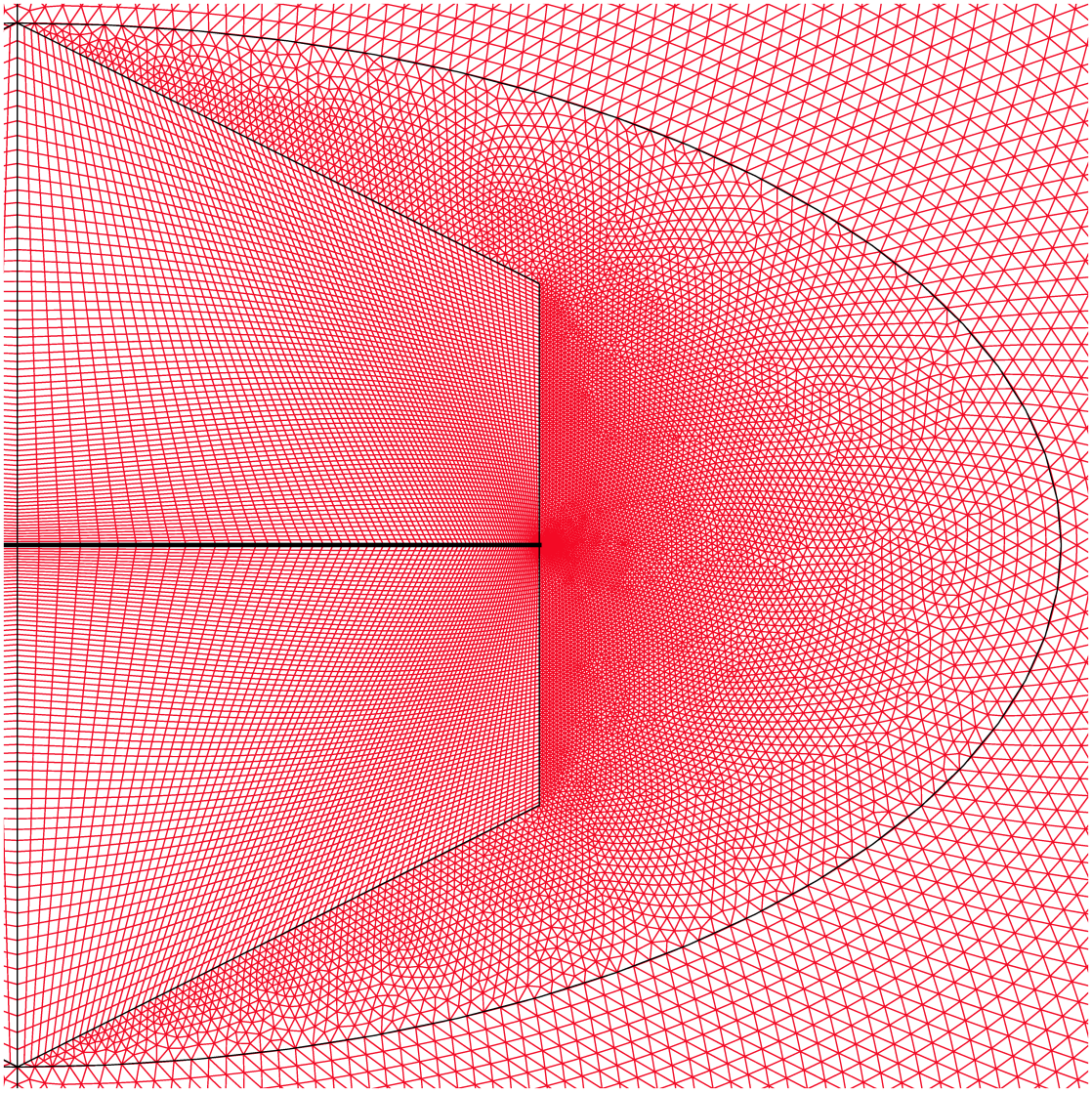

Figure B.5: Mesh for infinitely-thin flat-plate aerofoil. One half of the mesh close to the aerofoil is shown.

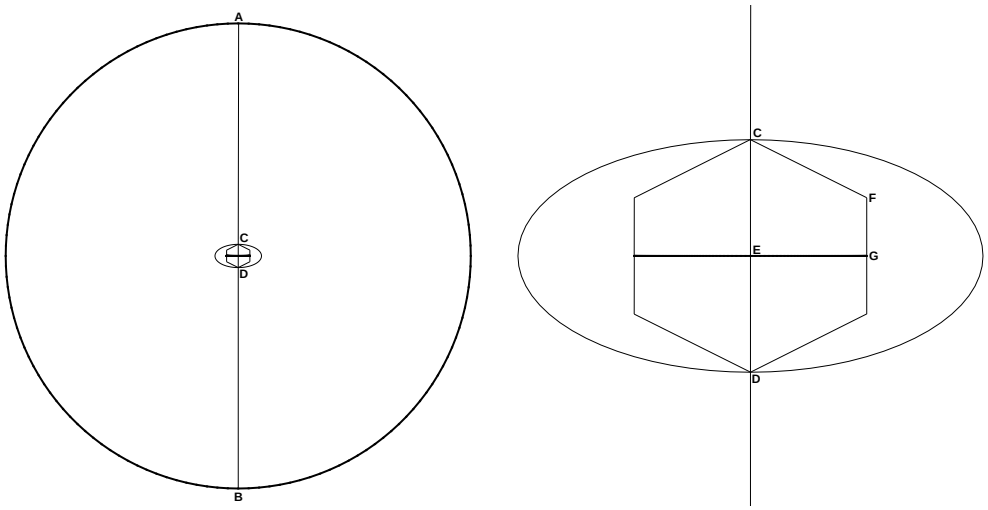

(a) Full mesh (b) Centre section

Figure B.6: Vertex labels for Table B.4.

Line	Interval count	Successive ratio
AB	70	1
AC	50	1.08
CD	145	1
CE	75	1.03
CF	75	1
EG	75	1.04
FG	75	1

Table B.4: Mesh parameters for infinitely-thin flat-plate aerofoil. The successive ratios are given such that the end of the line where the intervals are smaller always lies closest to the aerofoil.

$(0, 4000)$. The aerofoil chord length is 400. A series of cell layers was created on the upper and lower surfaces of the aerofoil, with initial cell thickness 0.01, growth factor 1.61, and number of rows 7, to capture the boundary layer.

The mesh is symmetrical in horizontal and vertical planes and the mesh parameters are given in Table B.4. The total number of cells for this mesh is approximately 1.3×10^5.

3D cases

Rectangular planform

As discussed in §4.3.4.2, it seemed sensible to use as much information as possible from the 2D meshes when drawing 3D meshes. Therefore, 3D meshes have used extruded 2D meshes. §4.3.4.2 also discusses the work that was done to ensure the 3D results were mesh-independent.

All 3D wings were infinitely thin, in order to remove the complication of wingtip shape. Therefore, to produce rectangular-planform 3D wings, a mesh based on the mesh for the infinitely-thin aerofoil, described above, was simply extended out of the plane of the 2D mesh (in the $+z$ direction). Before the extrusions was carried out, the mesh was coarsened in the region far from the wing in order to decrease the total number of grid cells and reduce the simulation times to a practical level. The outer portion of the grid was also meshed using an O-grid scheme in order to make the extrusion easier and reduce the cell count further. The 3D grid therefore took a form like that shown in Figure B.7.

The number of 2D slices of which the wing was composed was set at 40 (for the aspect ratio 2.5 case), in accordance with the results shown in Figure 4.5(a), with a successive ratio of 0.9, such that the 2D slices were narrower at the wingtip than at the root. It was thought reasonable to assume that the area of most rapid change in fluid properties in the Z direction would be near the tip, as the flow is very much slower near the root. This assumption is supported by the results presented in §4.3.4.2. For wings of higher aspect ratio, the number of slices was increased proportionally.

The distance between the wing tip and the $+z$ boundary was set at 1 chord, in accordance with the results presented in Figure 4.5(b), and the number of slices between the wing tip and this boundary was also set at 40, with a successive ratio of 0.93 (such that the interval size was smallest near the wingtip). This number of slices could possibly have been reduced, but it was thought important to try and capture the tip vortex in as great detail as practical.

The structure of the mesh as it appears in the xy, xz and yz planes is shown

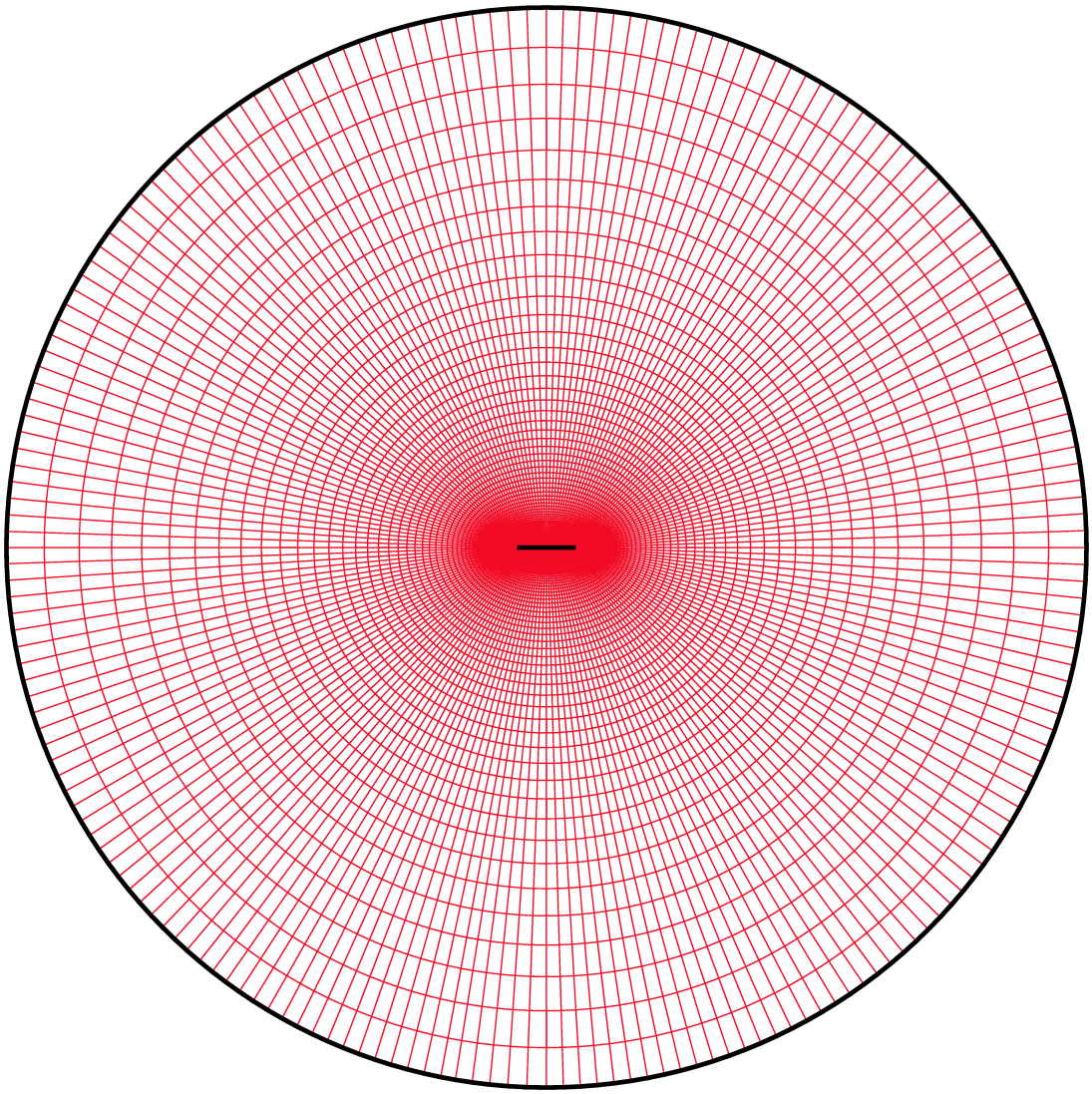

(a) xy plane

Figure B.7: Grid structure for 3D rectangular-planform, infinitely-thin section wing.

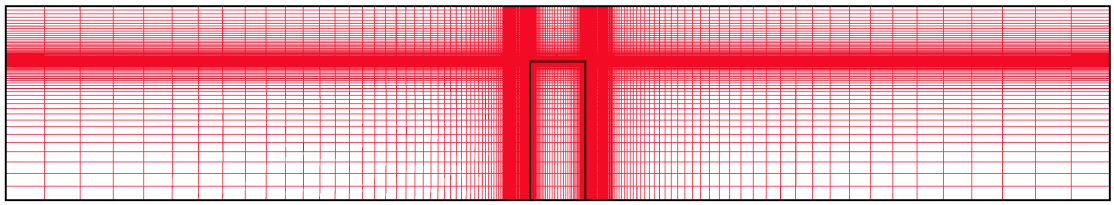

(b) xz plane

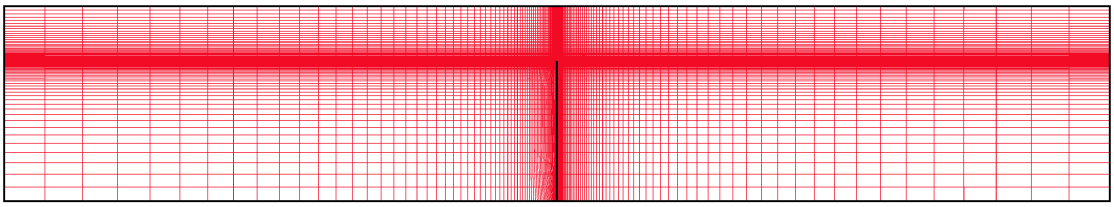

(c) yz plane

Figure B.7: Grid structure for 3D rectangular-planform, infinitely-thin section wing (continued).

Line	Interval count	Successive ratio
AB	59	1.11
AJF	80	1
BC	58	0.95
BHE	80	1
CD	12	1
CGD	80	1

Table B.5: Mesh parameters for 3D elliptical wing. Successive ratios are given such that the smallest intervals lie close to the *edges* of the wing.

in Figure B.7. An alternative view of the mesh is given in Figure 4.4 on p. 113.

Elliptical planform

To create the mesh for the elliptical-planform wing (used in §6.1.1 and §6.7) a 2D mesh was created in the xz plane and then extended in the y direction. The wing was defined to have the same length and area as the rectangular wing described above. The layout of the 2D grid is shown in Figure B.8(a) and has a vertical line of symmetry. The wing is the area $BHEB$. The root chord is of length 509.2, and the wing length is 1 000. Point A is at $(-1\,200, 0)$, J is at $(0, 2\,000)$, C is at $(-50, 0)$, and G is at $(0, 300)$. The area $CGDC$ is meshed using an unstructured triangular grid whereas the rest of the domain uses an O-grid. Grid parameters

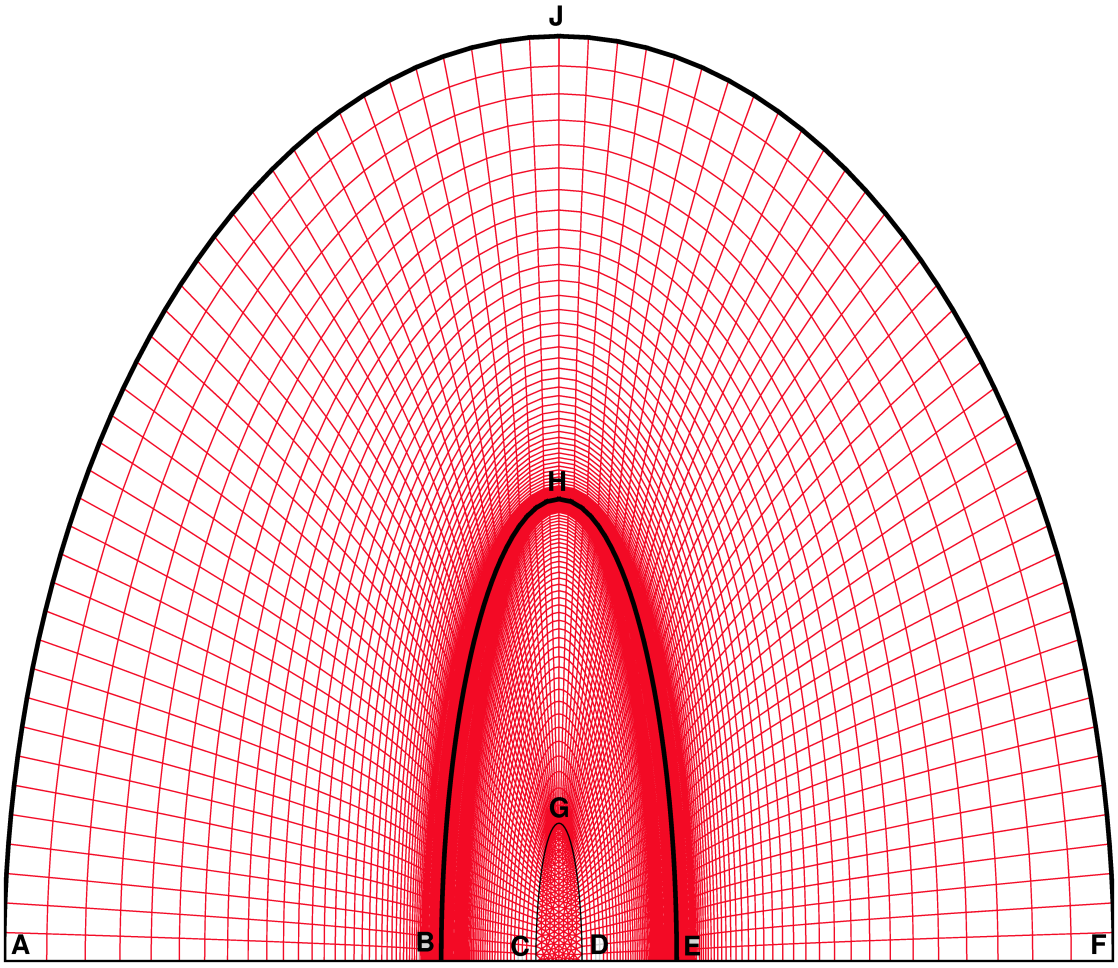

(a) xz plane at $y = 0$

Figure B.8: 3D mesh for elliptical wing.

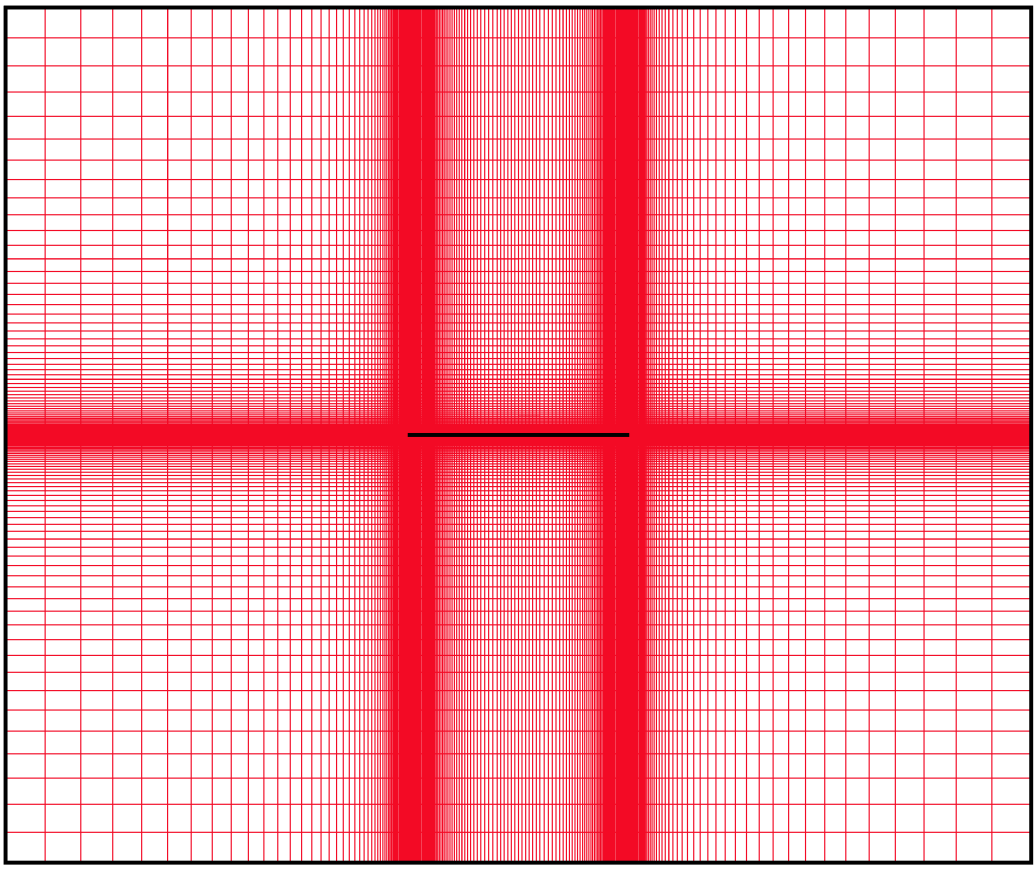

(b) xy plane at $z = 0$

Figure B.8: 3D mesh for elliptical wing (continued).

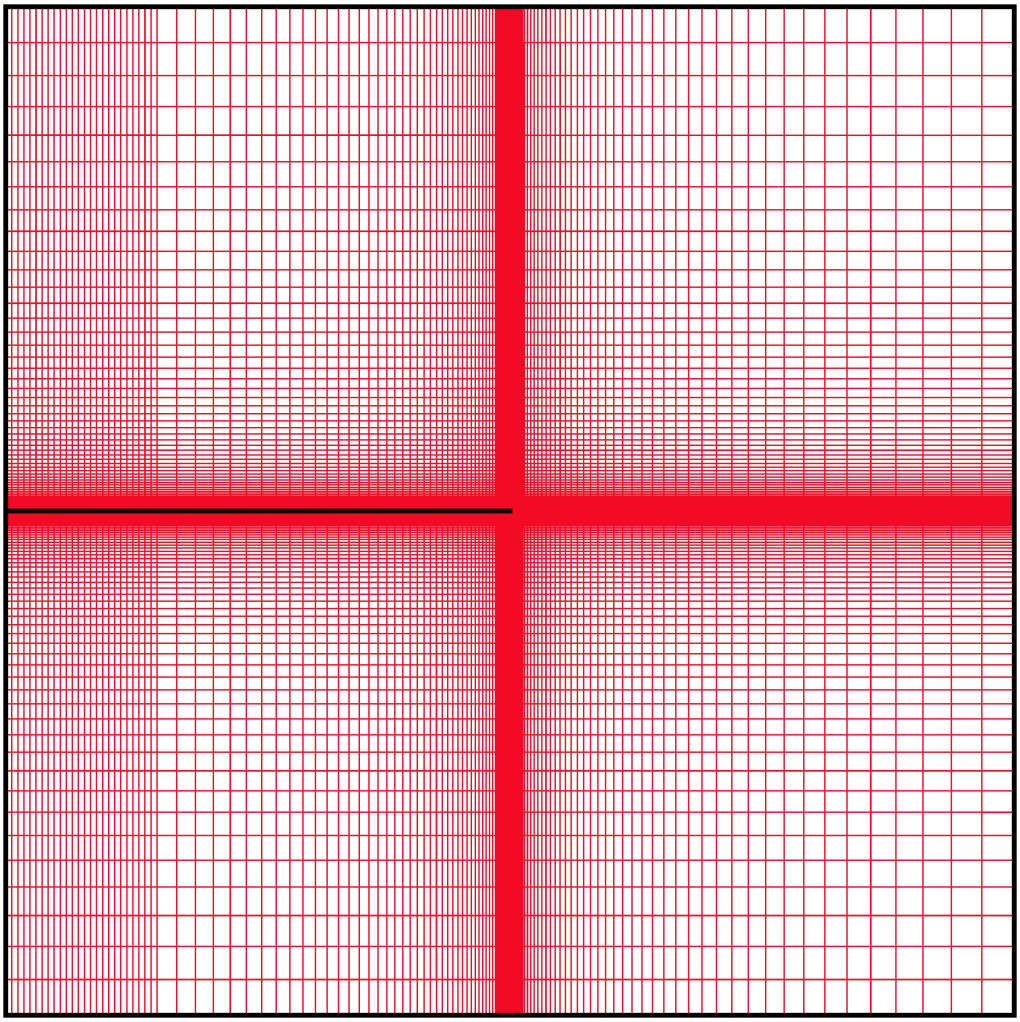

(c) yz plane at $x = 0$

Figure B.8: 3D mesh for elliptical wing (continued).

are given in Table B.5.

The boundaries for this case are close to the wing — around 1.5 root-chords away at the root. Based on the results presented in Figure 4.2, it might be expected that the predicted force on the wing would be too high. But in fact the results presented in §6.1.1 indicate that, although the CFD model does indeed over-predict the lift force, the error is small. It is likely that due to the fundamentally-different nature of 3D flows relative to 2D flows, the results are not so sensitive to boundary distance. It might therefore be possible in any future work to reduce the boundary distance in the x and y directions for the rectangular wing discussed above.

The 2D grid shown in Figure B.8(a) was extruded in the $\pm y$ directions to create the 3D grid for this wing. 60 slices were created in each direction with a successive ratio of 1.075 (such that slices close to the wing were more refined than those further away). The boundary in the y direction was at a distance of 1 000 from the wing. The mesh at the root, viewed from the $+z$ direction, is shown in Figure B.8(b) and the mesh on the wing centreline viewed from the $-y$ direction is shown in Figure B.8(c).

A reverse-elliptical planform was also investigated. This was identical to the elliptical wing above, but reversed (so that the tapered end of the wing lay at the origin). The mesh parameters used for this reverse-elliptical wing were identical to those used for the elliptical wing above, but the whole grid was meshed using a triangular unstructured grid.

B.2 Fluent parameters

This section presents the parameters and settings that were used in the CFD simulation. These are presented in sections, according to where they are located within the Fluent CFD software used, to enable the results to be reproduced easily. Any parameters or settings that are not included here were left at default settings.

Solver

Solver Fluent offers two solvers; segregated, and coupled. In the most recent versions of Fluent these are renamed pressure-based and density-based respectively. As this study deals with low-speed, incompressible flows, and the coupled solver was originally designed for high-speed, compressible flows, the former (segregated) solver was exclusively used in the current study.

Both processes are iterative, and both require a set of 'initial conditions' to be supplied, so that the solver has a 'starting point'. Here, these initial conditions are set to assume a uniform flow — in other words, flow as though the aerofoil or wing were not present. The simulation will then progress as though the aerofoil or wing has suddenly been placed in the flow. In other words, it is as if the aerofoil or wing has been impulsively started.

The coupled approach was originally designed for high-speed compressible flows and involves solving the momentum and continuity equations simultaneously (i.e. coupled together) (Fluent Inc., 1998). This process requires more memory than the segregated approach (Pascua et al., 1996), and for the types of flow which are of interest here (i.e. low-speed incompressible flows) is unlikely to provide any performance benefit. A segregated approach has therefore been used throughout this work, despite the performance benefit that can be achieved using a coupled approach.

A segregated approach takes the linearised continuity and momentum equations and solves them sequentially. The pressure field is used to calculate an updated velocity field, and the momentum equation is used to correct this velocity field. An updated pressure field is then produced, and the process is repeated until convergence is achieved (i.e. until the solution stabilises and does not change significantly with each iteration). The exact procedure for solving the system of equations, using a Gauss-Seidel method, is covered in Shaw (1992); Patankar (1980); Fluent Inc. (1998).

Time For all cases (apart from for some of the comparisons with the results of Sun and Boyd (2003, 2004) — see §5.1.3) the simulation was defined as unsteady.

Velocity formulation For 2D cases, where the motion of the aerofoil was imposed by simple velocity-inlet boundary conditions, the **absolute** velocity formulation was used. For 3D cases, where the wing motion was simulated using a rotating reference frame, the **relative** formulation was used.

Unsteady formulation Fluent offers first- or second-order discretisation with respect to time. **First order** was used exclusively here. A quick comparison revealed no noticeable change in either the phenomenology of the flow or the forces predicted when the second-order scheme was used; however, there was a noticeable increase in simulation time.

Gradient option It is necessary to calculate gradients of the various flow parameters in order to construct the variable values at cell faces. Fluent offers three methods of calculating gradients; for unstructured meshes, the **Green-Gauss Node-Based** method is known to be more accurate and stable than the alternatives. This method was used here since a relatively large proportion of the grids were unstructured.

Energy

The energy equation is required only in cases where the flow is compressible or where heat transfer is important. In the present cases, therefore, the energy equation is not used.

Viscous

Laminar flow is assumed throughout this work, as discussed in §4.2.1. Therefore no turbulence model is needed and the **laminar** viscous model is used.

Materials

For most of the simulations, air was used as the working material, with density and viscosity assumed **constant** at ISA sea level values. However, for some of the 2D

results, one or both of these attributes was changed in order to change Reynolds number. In addition, some of the 3D results were carried out using water as the working material in order to match experiments. Density and viscosity for water were assumed to be $998.2 kg/m^3$ and $1.003 \times 10^{-3} kg/ms$ respectively. For the comparison with the results of Dickinson and Götz (1993) (§5.1.1), the fluid properties were set equal to those of the 54% sucrose solutions used by Dickinson and Götz — they give an average kinematic viscosity of $2.35 \times 10^{-5} m^2/s$. In fact, the exact values of these properties are unimportant, as long as Reynolds number is the required value.

Boundary conditions

Aerofoils & wings Aerofoil and wings were defined as stationary **walls**, with the no-slip condition enforced on the surface. Sun and Boyd (2003) suggested that the no-slip condition is not valid at very low Reynolds numbers, as discussed in §5.1.3, but their conclusion seems likely to be due to the very small scale of the flows they investigated.

Outer boundary The boundaries of the domain (including the boundary at the wing root for 3D cases — see §4.3.4.2) were set as **velocity inlets**. For 2D cases the velocity of the aerofoil was imposed at the boundaries. For 3D cases the velocity at the boundaries was set to zero and the motion of the wing was imposed using a rotating reference frame for the fluid (see below). For some 3D cases, periodic boundary conditions were used to include the effect of a returning wake — see §6.9.1.

Fluid For 3D cases, a rotating reference frame was defined for the fluid. The origin and direction of the rotation axis and the rotational velocity were defined to give the required angle of attack and Reynolds number.

Solution controls

Under-relaxation factors The under-relaxation factors control the convergence of the solution and prevent instabilities building up in the model by limiting the changes in fluid properties between iterations. For many of the simulations it was found to be essential to reduce some of the factors (notably those for pressure and momentum) to reach a converged solution.

Pressure-velocity coupling Fluent offers three methods of pressure-velocity coupling. The default method, **SIMPLE**, was found to produce reasonably quick convergence and good accuracy and was therefore used in all simulations. Fluent suggest the use of the PISO algorithm for transient flows (Fluent Inc., 1998), as it can produce faster convergence, but this was found to be less reliable (i.e. it frequently diverged) than the SIMPLE method. The SIMPLEC algorithm was also not found to produce any real advantage.

Further work to establish the reasons for the frequent lack of convergence when using the PISO algorithm could be carried out, but the SIMPLE algorithm has proved adequate.

Discretisation Because of the unstructured nature of parts of the grids used here, **second-order** schemes were used for both pressure and momentum.

Multigrid controls

In order to accelerate convergence, Fluent computes corrections on a series of coarse grid levels. For unstructured grids, it is not trivial to create these coarse grid levels, as it is for structured grids. For 2D cases, default settings produced good convergence, but for 3D cases use of the default cycles often led to divergence. It was necessary to use a 'Flexible' cycle for pressure in order to overcome this. The differences between the various cycle types, and the methods used, are complex; but are detailed in Fluent Inc. (1998, §17.5).

Initialisation

For 2D cases, the initial solution was defined by setting the velocity everywhere in the domain to the freestream velocity. This is equivalent to defining the aerofoil at 0° angle of attack and then instantaneously increasing its angle of attack, or to impulsively starting the aerofoil.

For 3D cases, the initial solution was defined by setting the absolute velocity to zero within the domain. Because the fluid was defined using a rotating reference frame, this is again equivalent to suddenly introducing the wing into the flow or to impulsively starting the wing.

In other words, for both 2D and 3D cases, the initial solution was defined as though the aerofoil or wing were not present. Once the simulation started it was as if the wing or aerofoil had suddenly 'appeared' in the flow.

Monitoring convergence

For each time step, it was necessary to iterate the solution until convergence was obtained, before advancing to the next time step. In order to assess convergence, the residuals were monitored. For 2D cases, typical values at which the solution was deemed converged were of $O(10^{-6})$. Even at this low value, the solution converged quickly, provided that the time step was set to be small.

For 3D cases, time constraints meant that such stringent convergence criteria could not be used, and instead, values of $O(10^{-4})$ were used. The residuals generally levelled out at around this value, meaning that further run times did not result in better convergence.

Forces were also monitored during the simulation to ensure that the predicted forces had converged for each time step. It was usually found that by the time the residuals had fallen to the required level, forces had stabilised to 5 significant figures.

Time stepping

For simplicity, a fixed time step size was used for each simulation. The size of the time step was varied according to the velocity of the aerofoil or wing, ranging from $0.0001s$ for the highest velocity 2D cases to around $0.04s$ for the lowest velocity 3D cases. The size of the time step did not affect the solution, but small time steps meant that the solution converged more quickly for each time step. If the time step was too large, divergence occurred. There was therefore a balance between having a large number of small time steps and a small number of large time steps. In general, the former option was found to produce shorter *total* simulation times and better convergence.

Appendix C

Tabulation of CFD cases run

Here, the cases that were run using the CFD models are outlined.

2D cases

Aerofoil section	Re	Angle of attack	Notes
Thin flat plate	192	$-9°$	§5.1.1
"	"	$9°$	"
"	"	$18°$	"
"	"	$27°$	"
"	"	$36°$	"
"	"	$45°$	"
"	"	$54°$	"
"	"	$63°$	"
"	"	$72°$	"
"	"	$81°$	"
"	"	$90°$	"
Thin flat plate	500	$45°$	§5.1.2
Thin flat plate	1.357	$0°$	§5.1.3
"	"	$10°$	"
"	"	$20°$	"
"	"	$30°$	"
"	"	$40°$	"
"	"	$50°$	"
"	13.57	$0°$	"
"	"	$10°$	"
"	"	$20°$	"
"	"	$30°$	"
"	"	$40°$	"
"	"	$50°$	"
"	135.7	$0°$	"
"	"	$10°$	"
"	"	$20°$	"
"	"	$30°$	"
"	"	$40°$	"
"	"	$50°$	"
Thin flat plate	120	$45°$	§5.1.4
"	200 000	"	"
1% thick ellipse	500	$45°$	§5.2
"	"	"	"
"	"	"	"

2D cases (cont.)

Aerofoil section	*Re*	Angle of attack	Notes
1% thick elliptical	5	45°	§5.3
"	10	"	"
"	14	"	"
"	18	"	"
"	22	"	"
"	25	"	"
"	50	"	"
"	100	"	"
"	250	"	"
"	500	"	"
"	1 000	"	"
"	2 500	"	"
"	5 000	"	"
"	15 000	"	"
"	30 000	"	"
Circ.-edged	500	45°	§5.5
"	15 000	"	"
Ellip.-edged	500	"	"
"	15 000	"	"
Thin flat plate	500	"	"
"	15 000	"	"
5% thick elliptical	500	45°	§5.6
10% thick elliptical	"	"	"
20% thick elliptical	"	"	"
30% thick elliptical	"	"	"
50% thick elliptical	"	"	"
100% thick elliptical	"	"	"
Thin flat plate	500	45°	§5.7
"	"	"	§5.7
"	"	"	§5.7
"	"	"	§5.7

3D cases

Planform	AR	Re_{3D}	Angle of attack	Notes
Rectangular	3	2 500	45°	§6.1.2
"	3	"	"	§6.1.2 (ret. wake)
Rectangular	2.5	500	45°	§6.3 (pure translation)
Rectangular	2.5	500	45°	§6.4
Rectangular	2.5	120	45°	§6.4
"	"	2 500	"	"
"	"	15 000	"	"
"	"	30 000	"	"
Rectangular	2.5	500	9°	§6.6
"	"	"	27°	"
"	"	"	63°	"
"	"	"	81°	"
"	"	30 000	9°	"
"	"	"	27°	"
"	"	"	63°	"
"	"	"	81°	"
Elliptical	2.3	500	45°	§6.7
Reversed-ellip.	2.3	"	"	"
Rectangular	12.5	500	45°	§6.8
"	10	500	45°	"
Rectangular	2.5	500	45°	§6.9 (ret. wake)

Appendix D

Publications generated by the current work & prizes won

The three publications listed below were generated by the work presented in this thesis:

P. Wilkins, K. Knowles, and R. Żbikowski, 2005. Some non-linear aerodynamics relevant to flapping-wing MAVs. *International Powered Lift Conference, October 2005, Dallas, TX, USA.*

P. Wilkins, K. Knowles, and R. Żbikowski, 2006. CFD investigation of aerodynamics relevant to flapping-wing micro air vehicles. *European Micro Air Vehicle Conference, July 2006, Braunschweig, Germany.*

P. Wilkins and K. Knowles, 2007. Investigation of aerodynamics relevant to flapping-wing micro air vehicles. *37th AIAA Fluid Dynamics Conference and Exhibit, June 2007, Miami, FL, USA.*

In addition, two other papers (reproduced here in full) were written by the author and submitted for IMechE prize competitions. Both were awarded first prize.

D.1 Western Aerospace Centre prize winner 2007

The Western Aerospace Centre (WAC), a regional group of the Institution of Mechanical Engineers (IMechE), awards the WAC prize (Institution of Mechanical Engineers, 2007a) annually. Papers are invited from practising graduate engineers and post-graduate engineering students who are living, studying or working in the western regions of the UK. A short-list of up to four papers is selected and the authors of those papers are invited to present their paper to an audience of IMechE members. The prize is awarded to the best combined paper and presentation. The following paper was the winning entry for 2007.

Investigation of aerodynamics relevant to flapping-wing micro air vehicles*

Peter Wilkins
Department of Aerospace, Power and Sensors, Cranfield University
Defence Academy of the UK, Shrivenham

Supervisor: Dr. K. Knowles

Abstract

This paper explores results from an investigation of aerodynamics relevant to flapping-wing micro air vehicles. The work has used a computational fluid dynamics model which has been validated against both experimental data and existing analytical models. Results show that these relatively low-Reynolds-number flows are usually vortex-dominated, and that the exact phenomenology of the flow depends on Reynolds number. For 3D flows, the rotation of the wing produces a conical leading-edge vortex (LEV). There is therefore a spanwise pressure gradient, which produces spanwise flow. This extracts vorticity from the LEV and stabilises it. The exact form of the LEV is seen to be dependent on Reynolds number and angle of attack.

1 Introduction

There are two main motivations for developing micro air vehicles (MAVs). Firstly, their small size would allow them to be easily transported, along with the associated control equipment, by a single person, and deployed quickly on demand. The second motivation is the potential ability of an MAV to fly in confined spaces, which could be useful in a variety of scenarios, e.g. to infiltrate a hostile environment such as an enemy-held building or a contaminated industrial plant.

An MAV must possess a number of attributes in order to be successful. Firstly and by definition, they must be **small in size**. Because of this only a small amount of energy can be stored onboard, so that an MAV must be **highly power efficient**. The MAV must be able to **carry a payload** of at least one sensor. Because of the requirement for indoor flight, the MAV must be **highly manoeuvrable** at low speeds, and preferably at zero speed, and needs to have **vertical flight** and **hover** capabilities. It must also be **stable** even when flying close to surfaces such as walls. Finally, any MAV should preferably be **autonomous**.

These criteria are stringent, and most possible solutions for an MAV fail to meet at least one of them. Fixed wing aircraft lack manoeuvrability and efficiency at lower speeds. Rotary winged aircraft pass the manoeuvrability test and can hover, but again are generally inefficient.

An alternative is a flapping-wing micro air vehicle (FMAV) based on insect-like flapping. It is evident from the superb designs which are found in nature that this is an excellent way of lifting and propelling aerial vehicles of this size. In fact, analysis has suggested that this type of aircraft would be more efficient than both fixed- and rotary-wing aircraft at typical MAV speeds (Woods et al., 2001).

The model of Ansari et al. (2006a,b) has proved accurate when results from it are compared to experimental data. However, because of the nature of the model (essentially 2D and inviscid) it is unable to provide insight on a number of issues. Firstly, what role does spanwise flow have in stabilising the leading-edge vortex seen to be involved in insect-like flapping? Secondly, how does increasing Reynolds number affect the aerodynamics involved?

*This paper is entirely the work of its author and is based on current and recent activities in the field of aerospace engineering. This paper has not been previously submitted for any other prize competition, published in the proceedings of professional bodies, or publicly presented.

We have used CFD to study the aerodynamics of insect and FMAV wings and explain some of the phenomenology involved. In this paper, we report on the effects of Reynolds number for 2D flows and the stability of the leading-edge vortex (LEV) when the problem is extended to 3D.

2 The aerodynamics of insect-like flapping

Because insects are small in size and their wings move at relatively low speeds, the Reynolds numbers at which they operate are small — for the smallest flying insects, $Re = O(1)$ (that is, of the order of 1). FMAVs are likely to be larger than the average insect, and so will operate at higher Reynolds numbers — probably in the region of $Re = 30\,000$. This is still much lower than the Reynolds numbers for conventional aircraft, which generally operate at $Re = O(10^6)$.

In addition to this Reynolds-number-related issue, there are a number of other important differences between insect aerodynamics and those of more conventional aircraft. Firstly, an insect wing stops and starts whilst the insect is in flight (see Fig. 1). Secondly, an insect wing interacts to a large extent with its own wake from previous strokes. Thirdly, insect wings can be observed to operate at angles of attack in excess of 45°, but there appears to be no catastrophic stall.

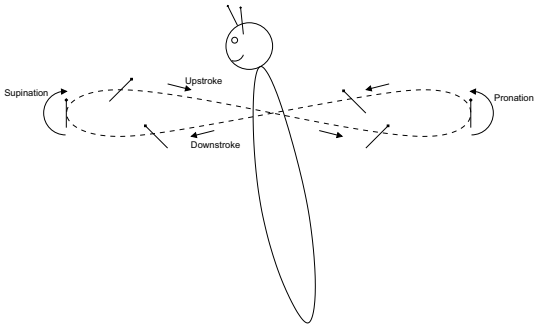

Figure 1: Typical insect wing kinematics. The wing tip is shown moving in a figure-of-eight pattern. The leading edge of the wing is marked by the black circle

Because of these important differences, attempts to analyse insect flight using techniques developed for conventional aircraft have generally proved unsuccessful. One of the first to experience this was Magnan, who said "I have applied the laws of air resistance to insects, and have arrived...at the conclusion that their flight is impossible" (author's translation of Magnan, 1934). In fact, the failure of these methods, which were developed for analysing the flight of fixed-wing aircraft, is unsurprising, given the fundamental differences between insect-like flapping and the flight of conventional aircraft.

3 The leading-edge vortex

One of the most important phenomena involved in insect flight is the stable leading-edge vortex or LEV. Flow is seen to separate from the leading edge and form a spanwise leading-edge vortex (LEV) above the wing. This generates low pressure above the wing, increasing lift. The LEV, which is similar in form to those seen on slender delta wings at high incidences, is the main focus of the current CFD investigation and of the results presented here.

One possible explanation for the stability of the LEV was given by Willmott et al., who suggested that this stability could be "explained by the spanwise flow, which transports vorticity out towards the wingtip before it can roll up and become unstable" (Willmott et al., 1997, p. 314). This explanation was generally accepted for some time. However, Birch and Dickinson (2001) later reported that "at the Reynolds numbers matching the flows relevant for most insects, flapping wings do not generate a spiral vortex akin to that produced by delta-wing aircraft". They found that "limiting spanwise flow with fences and edge baffles does not cause detachment of the leading-edge vortex", and put forward an alternative explanation — that "downward flow induced by tip vortices limits the growth of the leading-edge vortex". Later on, Birch et al. (2004) conceded that "spiral flow [within the LEV] is a conspicuous feature of flapping wings at Reynolds numbers (Re) of 5 000" but also stated that "similar experiments at $Re = 100$ failed to identify a comparable structure" (Birch et al., 2004, p. 1063), indicating that the phenomenology involved in the LEV varies with Reynolds number.

There are a number of questions relating to the LEV that therefore remain unanswered. To list a few; why is it that the LEV appears to be stable at low Reynolds numbers even when spanwise flow is prevented?

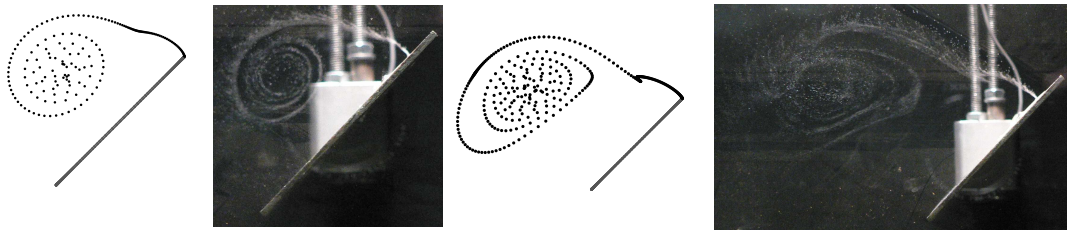

(a) After 2 chords travelled

(b) After 4 chords travelled. The second LEV is just beginning to form for both experimental and CFD cases

Figure 2: Comparison of 2D CFD flow visualisation (left of each figure) with that from 2D experiments (right of each figure) at $Re = 1000$. The aerofoil is moving left to right. The leading-edge vortex sheet does not appear to be emanating from the leading edge in the experimental case; this is due to the perspective

What are the reasons for the changes in the phenomenology involved in the LEV as Reynolds number is increased? And will a stable LEV still exist when Reynolds number is scaled up to match the Reynolds number of an FMAV, or will the LEV detach from the wing? This project aims to answer these and other questions using a predominantly CFD approach.

4 Method

The present work has adopted a CFD approach using the Fluent 6 commercial code together with the grid-generating software Gambit 2. Mesh sensitivity has been addressed and the results presented here are grid-independent. Validation has been carried out by comparing CFD results with experimental data, both existing (from Dickinson and Götz (1993)) and new, with encouraging results. Fig. 2 shows the agreement between the current CFD model and experimental flow-visualisation conducted by the author — the LEV is of very similar size, shape, and location in both cases. The CFD results have also been compared to those from the model of Ansari et al. (2006a,b), as this model has been shown to agree well with data from other experiments, again with encouraging agreement.

5 Results

5.1 2D results — effect of Reynolds number

Here we examine the geometrically simple case of a flat plate aerofoil set suddenly into constant-speed motion at 45°angle of attack. The aim is to take a step back from the full flapping 3D CFD simulations that have

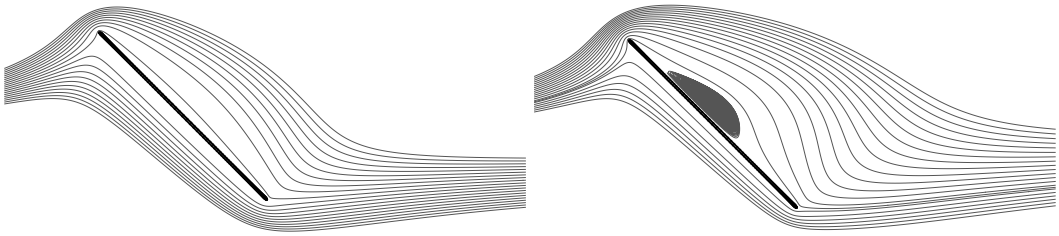

(a) $Re = 5$

(b) $Re = 10$, showing stable separation bubble

Figure 3: Streamlines for steady-state flows

been carried out by others (e.g. Ramamurti and Sandberg, 2002) and to isolate 2D effects from 3D effects.

These 2D results can be divided by Reynolds number into three sections — low ($Re = O(10)$), medium ($Re = O(100)$) and high ($Re = O(1\,000 - 10\,000)$). We are most interested in the last two of these categories, as the second is the region in which most insects are found, and the third is the region in which FMAVs will probably operate.

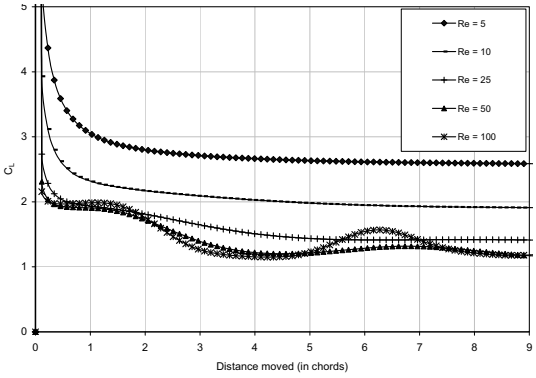

Figure 4: Lift coefficient vs. chords moved for a flat plate aerofoil over a range of low Reynolds numbers

At very low Reynolds numbers ($Re < 10$), the flow separates from the trailing edge but not from the leading edge — it simply runs down the upper surface of the wing, parallel to it (Fig. 3(a)). This flow pattern produces relatively high lift, with lift coefficient eventually settling at around 2.6 (Fig. 4).

For $10 < Re < 25$, a separation bubble occurs at about the mid-chord position on the upper surface, but the flow remains steady (Fig. 3(b)). The size of this bubble increases with Re. This bubble was seen by Sun and Boyd (2004) using a different computational method, but there are no experimental results extant at these very low Reynolds numbers which can verify this finding. It may be that this stable separation bubble, which is similar to an LEV in shape, also occurs on 3D wings at low Reynolds numbers. This may then explain why the LEV seen by Birch and Dickinson (2001) remained attached to the wing even when spanwise flow was prevented — perhaps at these very low Reynolds numbers, the vorticity within the LEV dissipates naturally at a rate equal to its generation at the leading edge, so that the LEV is stable even without spanwise flow occurring.

If Re is increased further ($Re > 25$), the phenomenology of the flow changes slightly again. Instead of the LEV initially starting as a separation bubble, the flow separates at the leading edge almost as soon as the aerofoil starts moving, creating a LEV which then grows (indicating that the rate of generation of vorticity at the leading edge is higher than the rate at which vorticity can be dissipated naturally) until it eventually sheds from the aerofoil. A new trailing-edge vortex (TEV) then builds up and is shed, followed by a new LEV forming and subsequently shedding. The cycle repeats, forming a von Kármán street-like structure in the wake (Fig. 6). At $Re = 25$ the shed vortices are very weak and have little effect on the lift produced by the aerofoil. However as Re is increased the shed vortices become stronger and the lift becomes less steady (see Fig. 4). For $Re > 100$ the fluctuation in lift force can be easily explained by considering the shedding of LEVs and TEVs (see Fig. 7) — both LEVs and TEVs augment lift while they remain attached, though LEVs have a larger effect than TEVs.

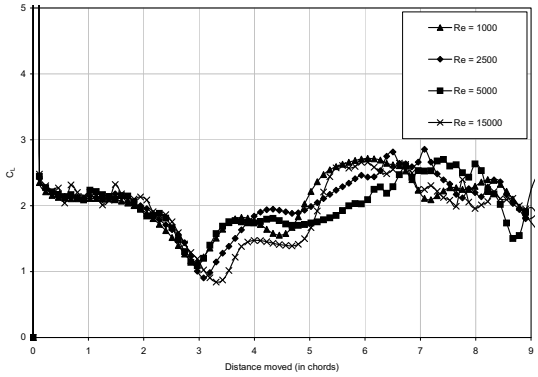

Figure 5: Lift coefficient vs. chords moved for a flat plate aerofoil over a range of high Reynolds numbers

For $Re > 1000$ another phenomenon is seen. This can be identified in Fig. 5. It manifests itself as relatively high-frequency unsteadiness in the lift/time history, which increases with Re. Examining the flow field reveals the source of the increasing unsteadiness. As Reynolds number increases, the vortex sheets become less stable and break up more readily. This is illustrated in Fig. 8, which compares the evolution of the flow field for two Reynolds numbers (500 and 5 000). This breakdown is caused by Kelvin-Helmholtz instability, which is in turn caused by the increase in velocity gradient across the vortex sheets when Re is increased.

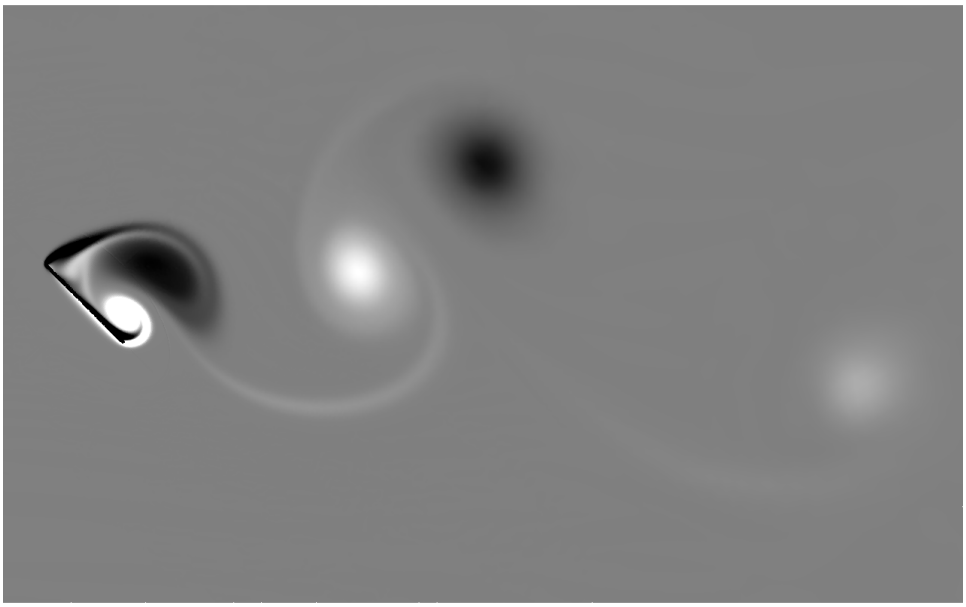

Figure 6: von Kármán street-like wake structure. Contours of vorticity; light areas show anti-clockwise vorticity, dark areas clockwise vorticity. The aerofoil is at 45°angle of attack and $Re = 500$

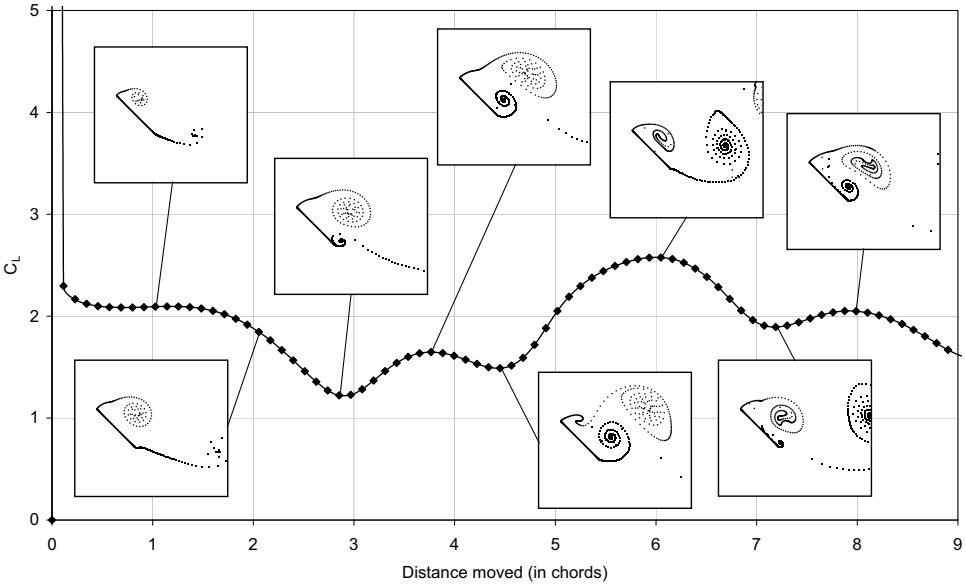

Figure 7: Lift coefficient vs. chords moved for a flat plate aerofoil at $Re = 500$ and 45°angle of attack showing vortical structures at points of interest

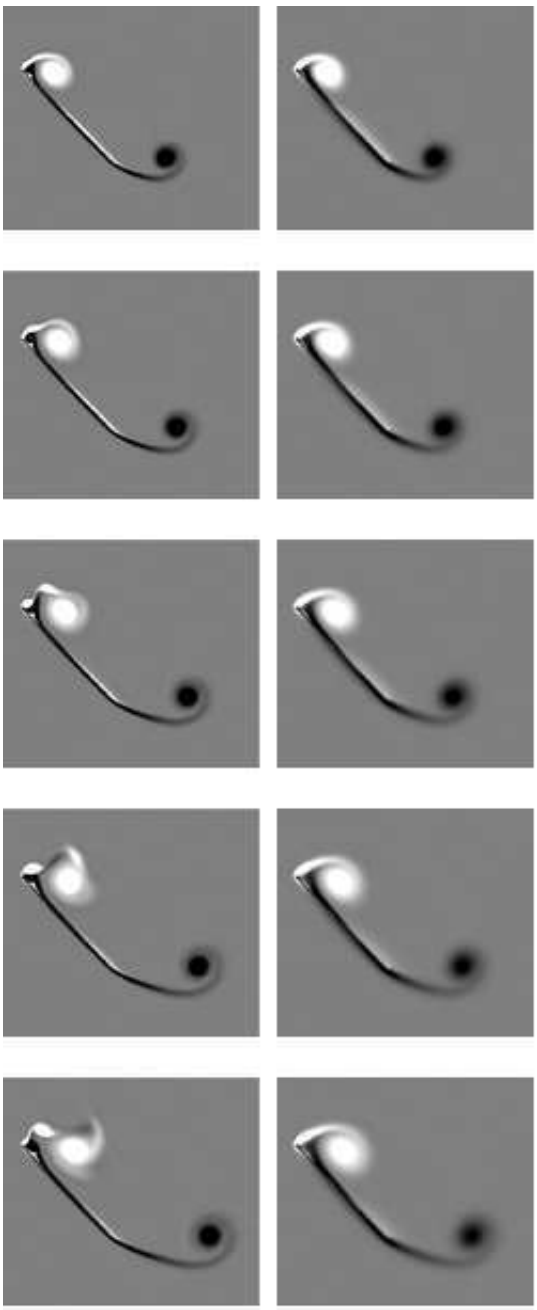

Figure 8: Comparison of flow evolution for two Reynolds numbers — $Re = 500$ (right) and $Re = 5\,000$ (left). Angle of attack is 45°in both cases. Light areas show clockwise vorticity, dark areas show anti-clockwise vorticity. The aerofoil has travelled around 0.5 chord lengths at the start of the sequence (top of page) and about 1 chord length at the end of the sequence. Note the instability in the leading-edge vortex sheet in the $Re = 5000$ case

We have seen that the leading-edge vortex is unstable for 2D flows for all but the very lowest Reynolds numbers — continually growing and breaking away, then re-forming. It seems then that the main reason for the stability of the LEV produced by insect-like flapping is due to a 3D effect, i.e. spanwise flow.

5.2 3D results — spanwise flow within the LEV

The author has used a CFD model to simulate a 3D wing moving in a straight line at 45°angle of attack and $Re = 500$. This shows that the LEV is unstable; it increases in size until it is shed into the wake, as for 2D cases. This indicates that the stability of the LEV in insect flight is a result of the rotary motion of the wing, rather than the presence of a tip vortex. Simulating a rotating wing at 45°angle of attack shows clear spanwise flow within the LEV from root to tip — see Fig. 9, where a streamline originating from the leading edge at the root leaves the trailing edge at around 75% span. Note that we are still not dealing with a flapping wing but simply with a wing rotating around a point at the mid-chord of its root. This motion is a constituent part of full, insect-like flapping wing kinematics.

The LEV formed is similar in appearance to that produced by delta wings at high angles of attack. However, it is postulated here that the mechanism of formation is different: for a delta wing, 'spanwise flow' (that is, flow *tangential* to the leading edge, caused by the wing sweep angle being above a critical value) leads to a conical leading-edge vortex. In the case of an insect wing, a conically-shaped LEV (caused by the sweeping motion of the wing) leads to spanwise flow. If this hypothesis (that spanwise flow is the *result*, not the *cause*, of the conical LEV) were true, spanwise flow would be expected in all cases where a leading-edge vortex is formed. So far in the current work spanwise flow *has* been seen for all Reynolds numbers tested. This appears to contradict the findings of Birch et al. (2004), but more work is needed to gain a comprehensive understanding of the flow field.

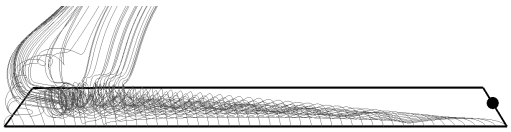

Figure 9: LEV structure (shown by instantaneous streamlines originating at leading edge) for a rotating rectangular thin flat plate. The wing is rotating around the root (marked with black dot) at 45°angle of attack and $Re = 500$. The wing has swept 10°since being impulsively started

The evolution of the leading-edge vortex depends on the Reynolds number. Below a critical Reynolds number the leading-edge vortex grows until reaching a steady state, retaining its conical shape. The resulting leading-edge vortex size is dependent upon the Reynolds number, with higher Reynolds numbers resulting in larger leading-edge vortices. This can be seen by comparing Figs. 11(a) and 11(b).

Increasing Re above a critical value leads to a breakdown of the leading-edge vortex sheet once it has grown to a certain size. This is shown in Fig. 11(c). The mechanism by which the breakdown occurs is similar to that observed for 2D flows; it is caused by Kelvin-Helmholtz instability. The breakdown occurs first on outboard sections, since inboard sections are at a lower local Reynolds number due to the rotational motion of the wing. This agrees with experimental results from Ellington et al. (1996), who reported that the leading-edge vortex broke down at around 65% span on a mechanical, dynamically scaled-up insect wing for $Re = 5000$.

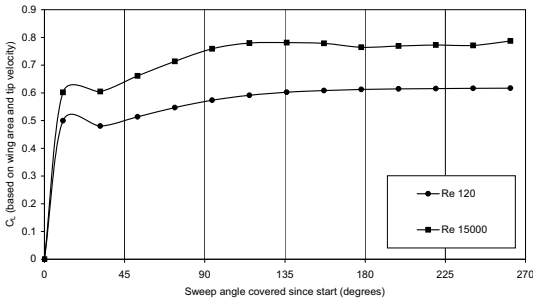

Figure 10: Comparison of lift vs. sweep angle for two Reynolds numbers. The horizontal axis is in terms of the angle that the wing has swept since being started

However, this breakdown has little effect on the overall lift produced by the wing. This is shown in Fig. 10. For the low Reynolds number case, the total lift on the wing increases as the leading-edge vortex develops until it reaches a steady-state condition, at which point the lift stabilises. For the high Reynolds number case, the lift reaches a peak after around 115°of travel, but then fluctuates as the leading-edge vortex in outboard sections breaks down and re-forms. The impact of the breakdown is lessened because although

the leading-edge vortex breaks down in the same way as for 2D flows, it does not shed from the wing — a von Kármán street-like structure is not seen. The lack of such a structure has been observed by others in physical experiments (see e.g. Dickinson et al., 1999). The occurrence of Kelvin-Helmholtz instability does not completely destroy the effectiveness of the LEV as a lift-generating mechanism.

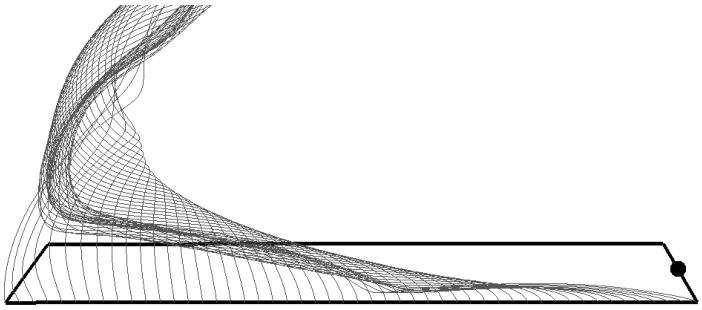

(a) $Re = 120$: the leading-edge vortex has reached a steady-state condition

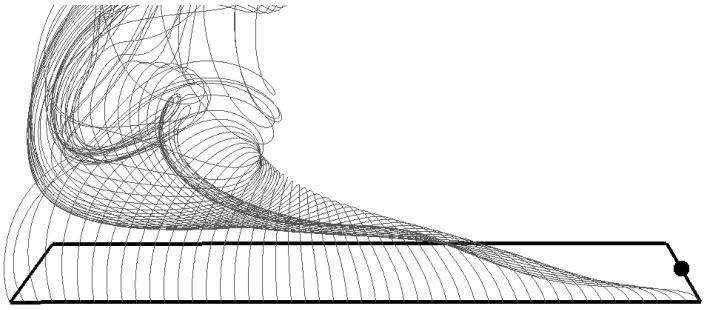

(b) $Re = 500$: the leading-edge vortex has reached a steady-state condition

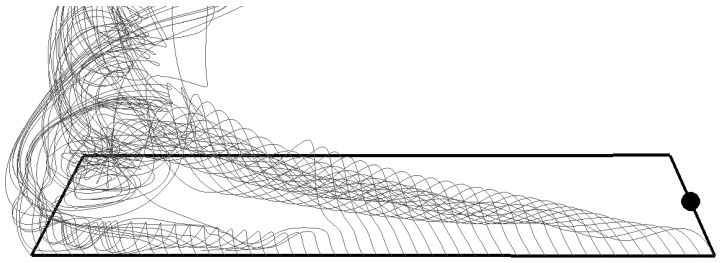

(c) $Re = 15\,000$: the leading-edge vortex sheet can be seen to have broken down outboard of around the 60% span

Figure 11: Leading-edge vortex structure for various Reynolds numbers. The wing is rotating as in Fig. 9 with rotation speed being varied to change Re. (Note that fig c is plotted from a slightly different perspective; the wing is the same size and shape in all cases)

6 Conclusions

In this paper results have been presented which indicate the following;

- For 2D flows of the kind investigated here, the exact phenomenology of the flow depends only on Reynolds number (for constant angle of attack). There are a number of important transition points relating to the formation of a stable separation bubble at $Re \approx 10$; the change to a conventional unstable LEV at $Re \approx 25$; and the introduction of Kelvin-Helmholtz instability at $Re \approx 1\,000$.
- The stability of the LEV produced by insect-like flapping is due to the rotational motion of the wing, which produces spanwise pressure gradients. These in turn produce spanwise flow, which extracts vorticity from the LEV. The LEV is stable when the rate of production of vorticity at the leading edge is equal to the rate at which it is extracted via spanwise flow. Increasing Re results in a higher rate of production of vorticity — therefore the size of the LEV grows as Re is increased. Kelvin-Helmholtz instability occurs at high Reynolds numbers, as for 2D flows, but this does not have a large impact on the lift produced as it does not cause the LEV to detach from the wing.

References

S. A. Ansari, R. Żbikowski, and K. Knowles, 2006a. A nonlinear unsteady aerodynamic model for insect-like flapping wings in the hover: Part 1: methodology and analysis. *Proceedings of the Institute of Mechanical Engineering, Part G: Journal of Aerospace Engineering*, 220(2):61–83.

S. A. Ansari, R. Żbikowski, and K. Knowles, 2006b. A nonlinear unsteady aerodynamic model for insect-like flapping wings in the hover: Part 2: implementation and validation. *Proceedings of the Institute of Mechanical Engineering, Part G: Journal of Aerospace Engineering*, 220(3):169–186.

J. M. Birch and M. H. Dickinson, 2001. Spanwise flow and the attachment of the leading-edge vortex on insect wings. *Nature*, 412:729–733.

J. M. Birch, W. B. Dickson, and M. H. Dickinson, 2004. Force production and flow structure of the leading edge vortex on flapping wings at high and low Reynolds numbers. *Journal of Experimental Biology*, 207: 1063–1072.

M. H. Dickinson and K. G. Götz, 1993. Unsteady aerodynamic performance of model wings at low Reynolds numbers. *Journal of Experimental Biology*, 174:45–64.

M.H. Dickinson, F. Lehmann, and S. P. Sane, 1999. Wing rotation and the aerodynamic basis of insect flight. *Science*, 284(5422):1954–1960.

C. P. Ellington, C. van den Berg, A. P. Willmott, and A. L. R. Thomas, 1996. Leading-edge vortices in insect flight. *Nature*, 384:626–630.

A. Magnan, 1934. *La Locomotion chez les Animaux*. Hermann et Cie.

R. Ramamurti and W. C. Sandberg, 2002. A three-dimensional computational study of the aerodynamic mechanisms of insect flight. *Journal of Experimental Biology*, 205:1507–1518.

V. J. Rossow, 1978. Lift enhancement by an externally trapped vortex. *Journal of Aircraft*, 15:618–625.

Q. Sun and I. D. Boyd, 2004. Flat-plate aerodynamics at very low Reynolds number. *Journal of Fluid Mechanics*, 502:199–206.

A. P. Willmott, C. P. Ellington, and A. L. R. Thomas, 1997. Flow visualization and unsteady aerodynamics in the flight of the Hawkmoth, *Manduca sexta*. *Philosophical Transactions of the Royal Society of London B*, 352:303–316.

M. I. Woods, J. F. Henderson, and G. D. Lock, 2001. Energy requirements for the flight of micro air vehicles. *Aeronautical Journal*, 105:135–149.

D.2 Whittle Reactionaries prize winner 2007

The Whittle Reactionaries prize (Institution of Mechanical Engineers, 2007b) was established in 1998 in memory of Sir Frank Whittle and is awarded annually by the Combined Propulsion Technical Committee of the IMechE and Royal Aeronautical Society. The stated object of the prize is to "stimulate and encourage young engineers to continue to apply innovative and forward-looking thinking to aerospace propulsion problems that demonstrates technical excellence, originality and independent thinking, high-quality presentation and effective communication." All undergraduates and postgraduates studying at UK universities, and recent graduates working in British industry, are eligible to enter. The following paper was awarded the Whittle Reactionaries prize for 2007.

Insect-like Flapping

the propulsion of micro air vehicles

Peter Wilkins
Department of Aerospace, Power and Sensors
Cranfield University, Defence Academy of the UK, Shrivenham

Abstract

This paper examines the motivation for developing micro air vehicles, explores the possibilities for their propulsion, and shows that the optimum solution is the use of flapping wings like those used by insects. The kinematics and aerodynamics of insect-like flapping are then analysed, before the methods used during the current study are outlined. Results from the present work are then given, exploring the stable leading-edge vortex seen to occur during insect flight — a phenomenon which, it is thought, is responsible for a large proportion of the lift produced by insect-like flapping. The stability of the leading-edge vortex is shown to be a result of spanwise flow within the vortex. Results suggest that a stable, lift-enhancing leading-edge vortex will still exist if insect-like flapping is scaled up in order to propel an MAV.

1 Introduction

Motivation for MAVs

Recent world developments have stimulated interest in micro air vehicles, or MAVs. An asset that could be transported by a single soldier and deployed almost instantly to provide short-range airborne surveillance would be extremely valuable — particularly in urban warfare situations.

In addition to this military value, there is significant interest in MAVs from paramilitary and civil organisations. As examples, MAVs could be used for search and rescue operations, for inspecting dangerous areas such as the dome of a nuclear reactor, or to provide building security.

Most of these potential uses are only possible because of the small size of these aircraft. MAVs have only recently become viable due to the progress made in the field of micro-electronics; sensors and their associated processing electronics have decreased in size dramatically over the past couple of decades.

Historically, the general trend has been for UAVs to be larger than their predecessors. This is because the focus has been on long-range surveillance, for which a low wing loading is required. Global Hawk, a modern high-altitude, high-endurance, long-range UAV, has a wing span greater than that of a Boeing 737. These assets have proved tremendously valuable; but there remains a niche in the current marketplace which only MAVs can fill — flight in confined spaces such as inside buildings.

These, then, are the two major motivations for developing MAVs — firstly, the potential for producing a man-portable airborne surveillance platform, and secondly the potential for flight in confined spaces.

Requirements for MAVs

For an MAV to be successful it needs to have certain attributes:

Small size: a maximum dimension in any direction of 6 inches (150mm).

High power-efficiency: a small aircraft can only carry a limited amount of energy.

Ability to carry at least one sensor: for returning information to the outside world.

High manoeuvrability at low speeds: for flying inside confined areas and through narrow openings.

Vertical flight capability: for operating inside vertical shafts and for vertical take-off and landing.

Hover capability: for surveying confined spaces.

Stability when flying close to surfaces: for flying close to walls, ceilings or floors.

High autonomy: for sensing and avoiding obstacles. A communications link could not always be guaranteed if the MAV were inside a building or other structure.

In addition to these criteria there may be other required attributes, depending on the exact role of the MAV. For example, an MAV which is designed to infiltrate enemy held buildings would need to have low aural and visual signatures to avoid detection. This would not be required if the MAV were designed for search and rescue.

MAV options

Because of the unique set of requirements for an MAV listed above, the two traditional design concepts — fixed- and rotary-wing — are both unsuitable. Although it has been shown that MAV-sized fixed-wing aircraft are viable flying machines (see e.g. DARPA, 2000), fixed-wing MAVs become less efficient and less manoeuvrable as speed is reduced, and incorporating a system to allow controllable hover is often problematic.

Again, rotary-wing MAVs have been designed and flown (see e.g. Epson, 2003). However, they also have crucial disadvantages. Small rotors are generally inefficient, and suffer from aerodynamic instability effects when operating close to walls or other surfaces. Rotary-wing MAVs also have significant aural signature, which may be a problem if the MAV is required to be discreet.

A third option that could be considered is a lighter-than-air MAV. However, lighter-than-air vehicles depend on displacing a volume of air to remain in flight, and so reducing the size of the aircraft directly reduces the available lift. At MAV scales, a lighter-than-air vehicle would not be viable, and even if it were it would be very susceptible to air currents and would probably lack the required manoeuvrability due to its inherent bulk.

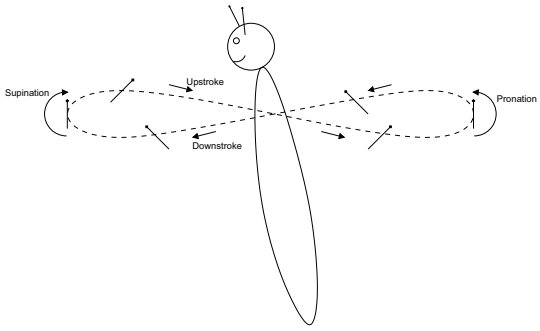

Figure 1: Typical insect wing kinematics. The wing tip is shown moving in a figure-of-eight pattern. The leading edge of the wing is marked by the black circle.

So to design an aircraft for flight in confined spaces it is not sufficient to simply scale down existing UAVs. Due to the unique set of requirements for this type of aircraft — predominantly the need for extreme manoeuvrability and high power efficiency at low speed — a radical new concept is required. As often happens the solution is found in the world around us. There are already an enormous number of MAVs with amazing manoeuvrability and outstanding efficiency — insects. And despite the diversity in design and size, these MAVs all have one thing in common — they all fly using flapping wings. This suggests (if not proves) that flapping wings are an efficient form of propulsion and lift for aircraft at small scales, and, to confirm this suggestion, recent research has indicated that insect-like flapping requires less power at typical MAV (i.e. low) speeds than both rotorcraft and fixed-wing aircraft (Woods et al., 2001).

2 Insect-like flapping

Kinematics

One of the factors which has restricted understanding of insect flight is the speed with which their wings move — the human eye is simply not fast enough to capture the kinematics of insect flight in any great detail. Marey (1868) was one of the first researchers to film tethered insects, but his work did not enable any great

progress to be made. It was the advent of high-speed photography which enabled detailed determination of the kinematics of insects' wings. Jensen (1956) and Weis-Fogh and Jensen (1956) were among the first to describe these kinematics, but by 1984 "relatively few" detailed accounts had been given (Ellington, 1984, p. 43). Since then further research has increased our knowledge of exactly what insects do with their wings (see e.g. Ennos, 1989; Willmott et al., 1997; Dickinson et al., 1999; Srygley and Thomas, 2002; Tammero and Dickinson, 2002; Fry et al., 2003).

It has been shown that, generally, the tips of an insect's wings move in a figure-of-eight pattern (as in Fig. 1)[1], and the entire wing cycle can be broken down into four sections: downstroke, supination, upstroke, and pronation. The downstroke commences with the wing tip above the insect's body. The wing then sweeps forwards and downwards (travelling, typically, around 4 chord lengths), coming to rest below the insect's body. The wing then rotates in pitch (angle of attack) through a large angle (typically around 120°) — this is termed *supination*, and results in the leading edge from the downstroke being also the leading edge for the upstroke. The upstroke then begins, being an approximate 'mirror-image' of the downstroke. At the top of the upstroke the wing rotates again, in the opposite direction (this is termed *pronation*), ready to start the next downstroke.

Aerodynamics

One result of the complex kinematics described above is that it is not possible to accurately predict the lift produced by insect-like flapping using conventional aerodynamics. Because of this, many of the early attempts to analyse insect flight came to an unsatisfactory conclusion — one author wrote *"I have applied the laws of air resistance to insects, and have arrived... at the conclusion that their flight is impossible"* (author's translation of Magnan, 1934). This conclusion was a result of attempting to analyse insect flight using invalid assumptions.

One of the major differences between insects and more conventional 'aircraft' concerns size. Insects are almost without exception smaller than any fixed- or rotary-wing aircraft, and, as a result, insects operate at what most aerodynamicists would call very low Reynolds numbers[2]. Vogel gives the Reynolds number of the smallest flying insects as $O(30)$ (Vogel, 1994, table 5.1), which is extremely low compared to, for example, a conventional aircraft, which might operate at $Re = O(10^6)$. It is not surprising that attempts to analyse insect flight using ideas and techniques that were developed for much higher Reynolds numbers have often failed. Any FMAV is likely to operate at $Re = O(10^3)$.

In addition to this Reynolds-number-related issue, the aerodynamics of insect-like flapping differ from those of more conventional aircraft in three key ways:

- An insect wing stops and starts at the end of each stroke (i.e. when the 'aircraft' is *in flight*), unlike the wings on rotary- or fixed-wing aircraft.
- An insect wing passes through its own wake, which produces complex interactions between the wake and the aerofoil. This happens with a rotary-wing aircraft but to a much lesser degree.
- The angle of attack of an insect wing is often much higher than would normally occur on conventional aircraft (often in excess of 45°), and yet there seems to be no catastrophic 'stall' as we might expect. Instead a stable *leading-edge vortex* (LEV) is formed.

The aerodynamics of insect flight are therefore highly unsteady and quite unlike the aerodynamics of fixed- or rotary-winged aircraft. The most novel and interesting phenomenon involved in insect flight is the stable leading-edge vortex (LEV). This is not seen in either fixed- or rotary-wing flight and it has been postulated that the LEV generates 70% of the lift produced by insect-like flapping (Discover Magazine, 2000).

[1] The actual tip path of insects' wings varies widely (see e.g Ellington, 1984, § 3).

[2] Reynolds number (Re) is an indication of the relative importance of viscous and inertial forces. A high Reynolds number indicates that inertial forces will dominate the flow, whereas a low Reynolds number indicates that viscous forces will be more dominant. Reynolds number is calculated using the formula

$$Re = \frac{\rho V l}{\mu}, \tag{1}$$

where ρ and μ are fluid density and viscosity respectively. In this paper, for 2D cases l is wing chord and V is wing velocity; for 3D cases, l is wing mean aerodynamic chord and V is wing tip velocity.

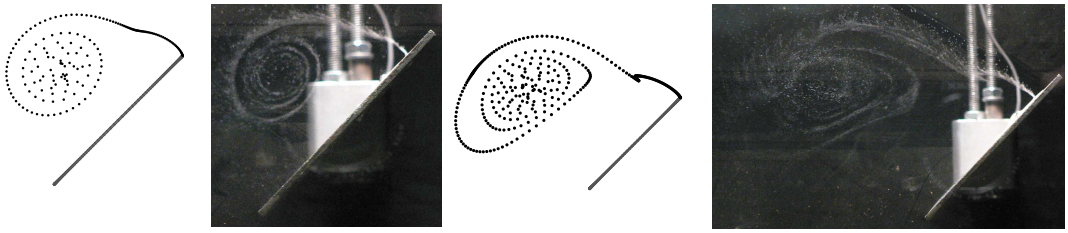

(a) After 2 chords travelled

(b) After 4 chords travelled. The second LEV is just beginning to form for both experimental and CFD cases

Figure 2: Comparison of 2D CFD flow visualisation (left of each figure) with that from 2D experiments (right of each figure) at $Re = 1000$. The aerofoil is moving left to right. The leading-edge vortex sheet does not appear to be emanating from the leading edge in the experimental case; this is due to the perspective.

Because the Reynolds number of an FMAV will be larger than that of insects, one of the most important issues that remains to be addressed is whether the LEV will still exist as a stable, life-enhancing mechanism when Reynolds number is increased. If the increase in Re means that the LEV will not be formed, then insect-like flapping might not be an efficient way of propelling an MAV.

One possible explanation for the perhaps unexpected stability of the LEV is that it can be "explained by the spanwise flow, which transports vorticity out towards the wingtip before it can roll up and become unstable." (Willmott et al., 1997) This explanation has been generally accepted for some time, but more recent work has shown that at low Reynolds numbers the LEV is stable even if spanwise flow is prevented (Birch and Dickinson, 2001). Others have reported that the LEV is *unstable*, asserting that the LEV seen does not stay attached to the wing despite significant spanwise flow (Ramasamy and Leishman, 2006). Here, we investigate this issue using a CFD approach.

3 Method

The present work has used the Fluent 6 commercial code together with the grid-generating software Gambit 2. A Reynolds-averaged Navier Stokes (RANS) formulation is used, with the fluid assumed to be inviscid and incompressible — reasonable assumptions at these low Reynolds numbers. Mesh sensitivity has been addressed and the results presented here are grid-independent. Validation has been carried out by comparing CFD results with experimental data, both existing and new, with encouraging results. Fig. 2 shows the agreement between the current CFD model and experimental flow-vis conducted by the author — the LEV is of very similar size, shape, and location in both cases. A more quantitative validation approach has been to to compare force data from the CFD model with experimental data from Dickinson and Götz (1993), as in Fig. 3. Again, the agreement is good.

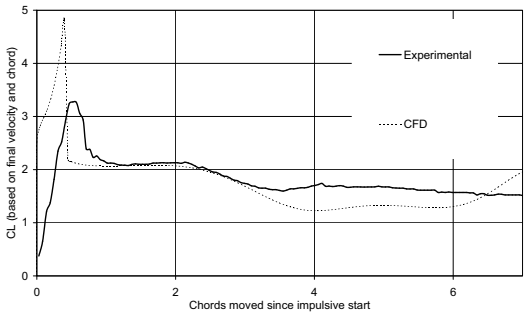

Figure 3: Comparison of CFD results with data from Dickinson and GötzDickinson and Götz (1993). The graph shows lift on an aerofoil impulsively started at 45°angle of attack and $Re = 200$.

4 Results

As mentioned above, the principal question that remains to be answered is whether the stable LEV seen on insect wings will exist on larger FMAV wings at the associated higher Reynolds numbers. In order to address this we need to understand the cause of the stability of the LEV. First we investigate the stability of the LEV formed in 2D flows, in order to establish whether the stable LEV seen in 3D flows is due to a 3D effect (i.e. spanwise flow) or a 2D effect.

2D Flows

Leading-edge vortices are caused by flow separating from the leading edge of an aerofoil or wing. The flow is then 'sucked' into the area of low pressure above the wing, so that if the flow were visualised by particles released near the leading edge a spiral would be seen, as in Fig. 4. This spiral is a vortex.

Because of the relatively high velocities within the vortex, it is an area of low pressure, and since it forms above the aerofoil it increases the lift produced by the aerofoil. The actual pressure within a vortex is inversely proportional to its strength — as the strength of a vortex increases, the pressure at its core drops (Bartol et al., 2003).

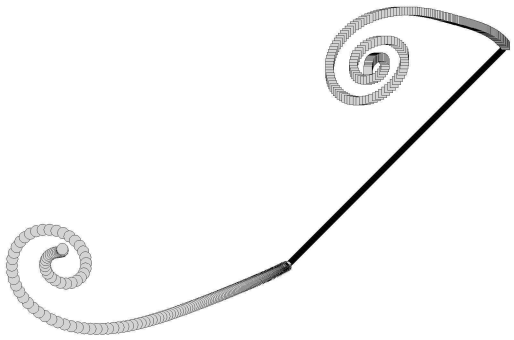

Figure 4: Spiral form of LEV created by aerofoil. Trailing-edge (starting) vortex is also visualised. Aerofoil is moving from left to right.

The evolution of a vortex can be understood using a vorticity balance approach. Vorticity is a measure of the amount of 'swirl' in a region, so a vortex is an area of vorticity. If vorticity is fed into a vortex, the vortex will grow. Conversely, if vorticity is extracted by some means, the vortex will shrink.

In the 2D case shown in Figure 4, vorticity is generated by the interaction of the fluid with the aerofoil. A line of vorticity is generated — a leading-edge vortex sheet — which concentrates into a spiral as discussed above. Because vorticity continues to be fed into the vortex from the leading-edge vortex sheet, the vortex will tend to grow. However, vorticity will also be dissipated within the vortex due to viscosity. Dissipation will tend to make the vortex shrink and will be more dominant in low Reynolds number flows where viscous effects are more important.

Thus the development of any 2D LEV will follow one of three patterns. Either

(A) the rate of vorticity production will be higher than the rate of dissipation, in which case the LEV will grow; or

(B) the rate of vorticity production will equal the rate of dissipation, which case the size of the LEV will remain constant; or

(C) the rate of vorticity production will be lower than the rate of dissipation, in which case the LEV will shrink.

The rate of dissipation will depend on the size of the vortex, with more dissipation occurring in larger vortices than in smaller vortices. Thus if vorticity is fed into a vortex, it will grow — but as it grows, the rate of dissipation will increase. If the rate of dissipation increases to a point where it matches the rate of vorticity addition, the vortex will stabilise and vortex growth will cease.

Based on the reasoning above, we would expect to find a maximum value of Reynolds number at which case (b) can occur — above this Reynolds number, viscous effects become too weak (relative to inertial effects) to stop the LEV growing and case (a) will occur. CFD results indicate that this critical value of Re is around 25.

Figure 5 compares lift coefficient vs. distance travelled for five different Reynolds numbers. The shape of the curve varies as Reynolds number is increased, suggesting that the phenomenology of the flow changes.

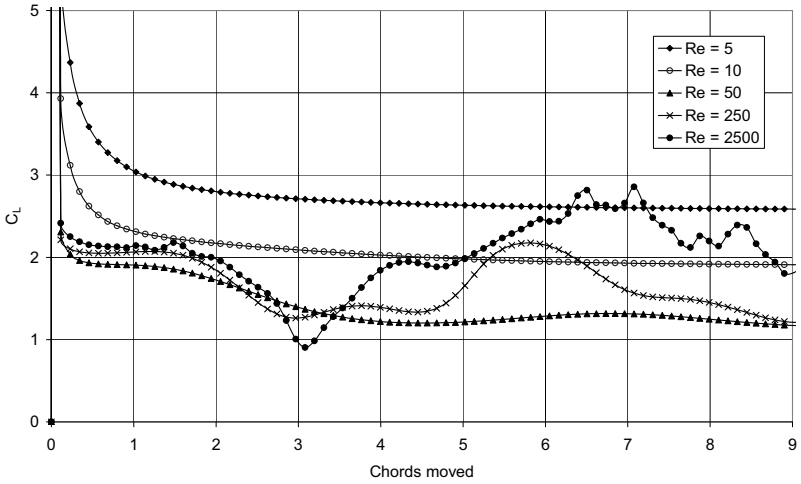

Figure 5: Lift coefficient vs. chords moved for a flat plate aerofoil over a range of Reynolds numbers. The angle of attack is 45°for all cases.

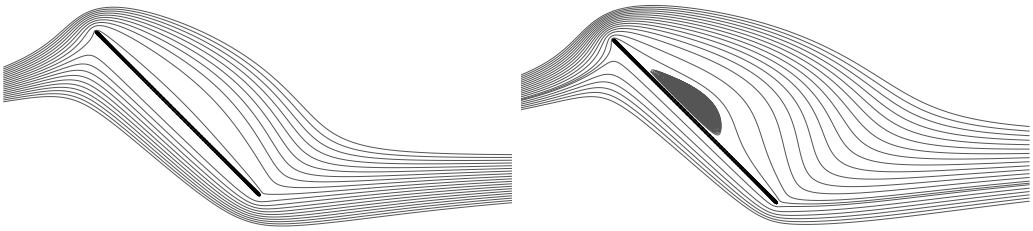

(a) $Re = 5$ (b) $Re = 10$

Figure 6: Streamlines for steady-state flows. Aerofoil is moving from right to left.

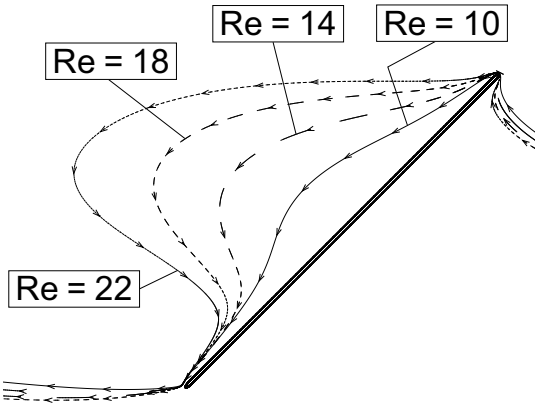

Figure 7: Change in separation bubble for increasing Reynolds number. All four cases shown here are steady. Aerofoil is moving from left to right.

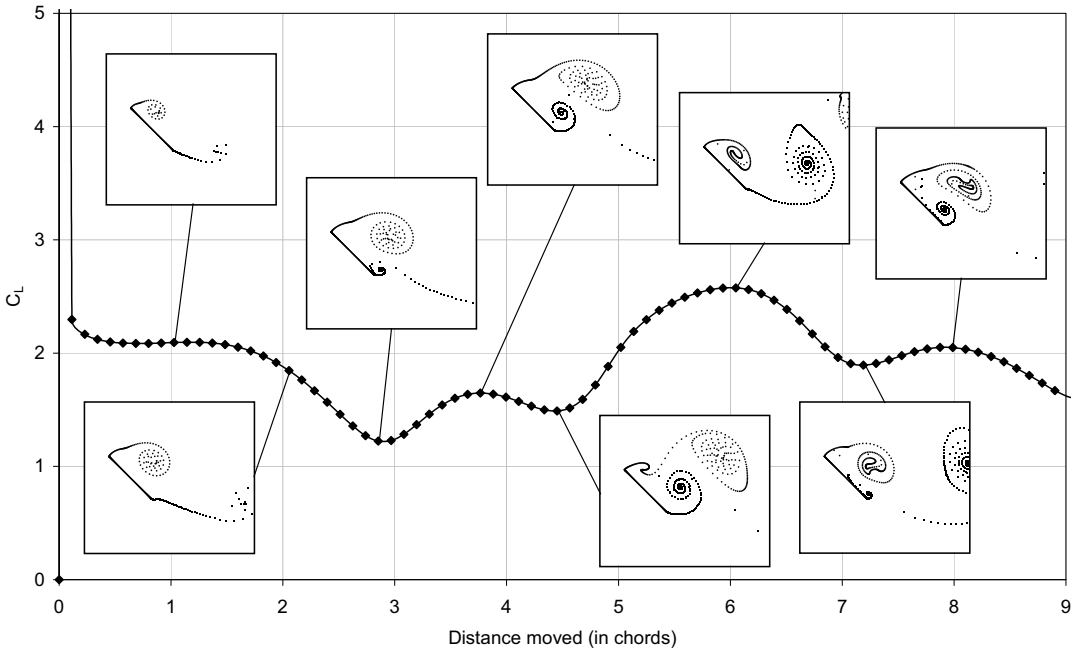

Figure 8: Lift coefficient vs. chords moved for a flat plate aerofoil at $Re = 500$ showing vortical structures at points of interest. The angle of attack is 45°.

Examination of the CFD data shows that this is the case. For a Reynolds number of 5, no leading-edge vortex is formed — viscous effects are so dominant that the flow does not separate from the leading edge. The flow pattern is shown in Fig. 6(a) and is steady; thus the lift coefficient is also steady once the flow has stabilised, as seen in Fig. 5.

If Reynolds number is increased slightly so that $Re > 5$, the flow cannot negotiate the sharp leading edge and separates. A leading-edge vortex is formed and initially grows. However, providing that $Re < 25$, the vortex eventually stabilises because, as explained above, as the vortex grows the rate of vorticity dissipation also grows. An example of the flow pattern is shown in Fig. 6(b). Fig. 7 shows the change in flow pattern as Re is increased — higher Reynolds numbers lead to larger LEVs, consistent with the reasoning above.

This phenomenon (a stable separation bubble) has been noted by others using a different computational method (Sun and Boyd, 2004), but its existence cannot be validated as there are no experimental data available at these extremely low Reynolds number. It is postulated here that this stable bubble is equivalent to the separation bubbles seen behind a sphere or cylinder at low Reynolds numbers (Houghton and Carpenter, 2003), which also grow as Re is increased.

This result is important, as it shows that spanwise flow and other 3D effects are not essential to form a stable LEV. Providing that $5 < Re < 25$, a stable LEV will be formed because vorticity is not generated fast enough to overcome the dissipative influence of viscosity. This is supported by the results of Miller and Peskin (2004), who used a CFD method and found that below $Re = 32$ vortices were not shed by a 2D aerofoil. This may explain the results of Birch and Dickinson (2001), who observed a stable LEV on a 3D wing at low Reynolds numbers even when spanwise flow was prevented.

However, most insects operate at Reynolds numbers in excess of 25, as well any viable FMAV. Therefore it is important to understand what happens to the LEV at higher Reynolds numbers.

If $Re > 25$, viscosity is no longer able to dissipate enough vorticity to keep the LEV stable, and it grows to a point where it is shed from the aerofoil. This results in another trailing-edge vortex (TEV) forming and eventually being shed, and then another LEV. The cycle repeats. Because the flow never stabilises, the forces on the aerofoil also remain unsteady — as shown in Fig. 5. The fluctuations in force can be explained

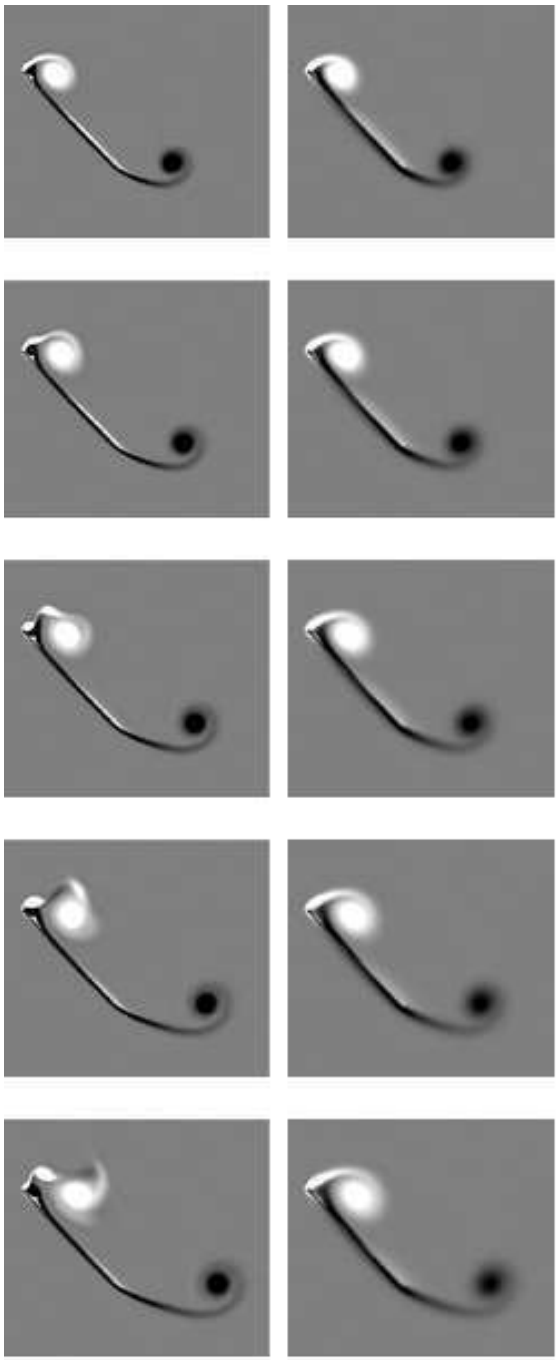

Figure 9: Comparison of flow evolution for two Reynolds numbers — $Re = 500$ (right) and $Re = 5\,000$ (left). Light areas show clockwise vorticity, dark areas show anti-clockwise vorticity. The aerofoil has travelled around 0.5 chord lengths at the start of the sequence (top of page).

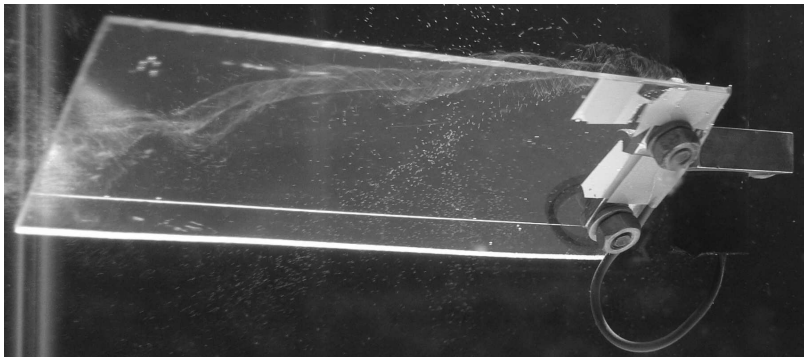

Figure 10: Spanwise flow within LEV, shown by hydrogen bubbles released at leading edge near root. Wing is rotating with $Re_{3D} = 2500$ and angle of attack 45°.

by examining the flow in detail — force peaks can be related to LEVs and TEVs. This is demonstrated in Fig. 8. It can be seen that an LEV results in a larger force peak and a TEV results in a smaller peak — both are areas of low pressure and therefore we would expect both to have a lift-enhancing effect.

The only other phenomenon that is noticeable in Fig. 5 is that for Reynolds number of the order of 1 000 a high-frequency fluctuation in lift is seem, superimposed on the fluctuations described in the previous paragraph. The cause of these high-frequency fluctuations can be discerned by comparing flow visualisation for two Reynolds numbers, as in Fig. 9. It can be seen that whereas for the $Re = 500$ case the vortex sheets shed from leading edge remains smooth and continuous, the $Re = 5\,000$ case shows breakdown of the leading-edge vortex sheet and the formation of small vortices which eventually combine with the primary LEV. This breakdown leads to low-magnitude, high-frequency fluctuations in lift, and is caused by Kelvin-Helmholtz instability (KHI). This kind of instability has been observed in physical experiments in the course of this work and by othersPierce (1961), and also occurs in the vortex sheets emanating from the edges of delta wingsGursul (2005). It may occur anywhere where there is a shear flow, though it appears more readily at higher Reynolds numbers. Viscosity stabilises the flow and can prevent the instability if Reynolds number is lowTritton (1988).

The main conclusions that can be drawn from these 2D results are that (*a*) the leading-edge vortex is unstable for 2D flows, periodically breaking away and re-growing, for all but the very lowest Reynolds numbers, and (*b*) KHI occurs at Reynolds numbers above 1000. It is notable that KHI does not affect the frequency at which the primary leading- and trailing-edge vortices are shed. The occurrence of KHI may be important when we come to consider 3D flows.

3D Flows

When considering 2D flows we used a 'vorticity balance' approach to explain the reasons for the stability of the LEV at very low Reynolds numbers. We can do the same for 3D flows, remembering that now it is possible for vorticity to be removed from the LEV via another mechanism — spanwise flow. This has been noted by others who considered the LEV on delta wings at high angles of attackLee and Ho (1990).

If the LEV seen in insect-like flapping is stable, the total vorticity within the LEV must be constant. Therefore, either vorticity must stop being generated (a possibility which can safely be discounted), or vorticity must be removed from the LEV (by some means or some combination of means) at a total rate equal to the rate at which it is generated at the leading edge.

Vorticity will be dissipated due to viscosity within the LEV, but we have seen from the 2D results above that the rate at which this happens cannot match the rate at which vorticity is generated, except at very low Reynolds numbers. The stability of the LEV seen at higher Reynolds numbers during insect flight must be the result of some other method of vorticity removal. The only method by which the vorticity within a vortex can be reduced, other than by dissipation, is by extraction through spanwise flow. The question is, if

this spanwise flow exists, what causes it?

Because an insect wing rotates around its root, sections near the tip move faster than those near the root. Therefore, the LEV created over outboard sections will be of greater strength than that formed over inboard sections, leading to a pressure gradient along the span, shown in Figure 11. This leads to spanwise flow, which, as already mentioned, has been clearly seen in previous experiments, and has also been seen in experiments conducted as part of the current work — see Figure 10.

This spanwise flow is clearly seen in the 3D CFD results obtained here — see Figure 12, where a streamline originating from the leading edge at the root leaves the trailing edge at around 75% span. Note that we are still not dealing with a flapping wing, but simply with a wing rotating around a point at the mid-chord of its root. This motion is a constituent part of full, insect-like flapping-wing kinematics.

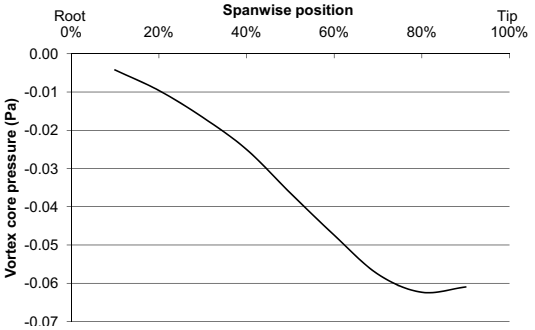

Figure 11: Pressure gradient within a 3D LEV. Angle of attack is 45°, $Re_{3D} = 500$, and the wing has swept through an azimuth of 5° since being impulsive started.

Based on this reasoning we would expect to see spanwise flow within the LEV at all Reynolds numbers (providing the Reynolds number is high enough for an LEV to be formed). In the current work, simulations have been run for a 3D Reynolds number range of 120-30 000 (based on mean chord and tip velocity), and spanwise flow has been seen for all Reynolds numbers tested. This appears to contradict the findings of Birch et al. (2004), who reported that the LEV remained stable even when an attempt was made to eliminate spanwise flow using fences. However, this was reported for a Reynolds number of 120 (calculated using wing mean chord and tip velocity); it is possible that, at these low Reynolds numbers, vorticity is dissipated naturally within the LEV at a rate equal to its generation at the leading edge, so that the vortex is naturally stable even without spanwise flow.

The development of the LEV in 3D cases depends on Reynolds number. For lower Reynolds numbers it is completely stable for all time, with higher Reynolds numbers producing larger LEVs, as can be seen by comparing Figures 13(a) and 13(b). Increasing Re above a critical value leads to a breakdown of the leading-edge vortex sheet once it has grown to a certain size; this is shown in Figure 13(c). The mechanism by which the breakdown occurs is similar to that observed for 2D flows; it is caused by Kelvin-Helmholtz instability. The breakdown occurs more readily on outboard sections, since they are effectively at a higher Reynolds number. This agrees with experimental results given by Ellington et al. (1996), who reported that the leading-edge vortex was seen to break down at around 65% span on a mechanical, dynamically scaled-up insect wing for a Reynolds number of 5000.

This breakdown has little effect on the lift produced by the wing, because the LEV does not break away from the wing completely as it does for 2D flows. This has been noted by others in physical experiments (Dickinson et al., 1999). Instead, the LEV combines with the tip vortex and all that is left behind the wing

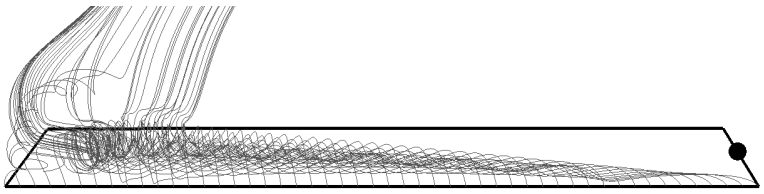

Figure 12: LEV structure (shown by instantaneous streamlines originating at leading edge) for a rotating rectangular thin flat plate. The wing is rotating around the root (marked with black dot) at 45° angle of attack and $Re_{3D} = 500$. The wing has swept 10° since being impulsively started.

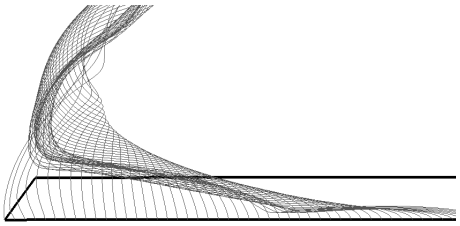

(a) $Re = 120$: the leading-edge vortex has reached a state condition.

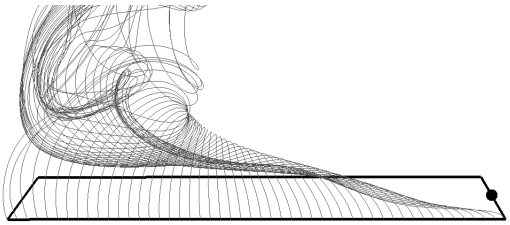

(b) $Re = 500$: the leading-edge vortex has reached a steady-state condition.

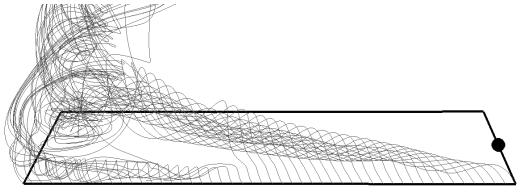

(c) $Re = 15\,000$: the leading-edge vortex sheet can be seen to have broken down due to KHI outboard of around the 60% span.

Figure 13: Leading-edge vortex structure for various Reynolds numbers. The wing is of the same planform in each case; perspective changes are the cause of the differences seen here. The wing rotates at an angle of attack of 45° around the point marked by the black circle.

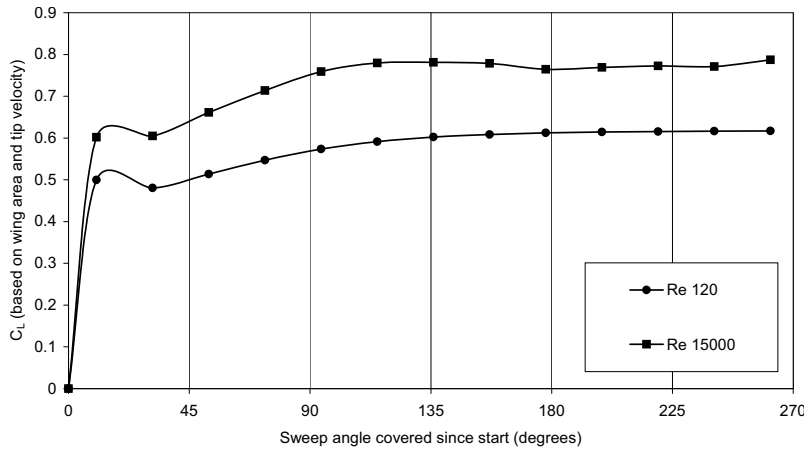

Figure 14: Comparison of lift coefficient vs. rotation angle history for two 3D Reynolds numbers. The horizontal axis is the angle that the wing has swept since being impulsively started. Lift coefficient is calculated using wing area and tip velocity.

is a concentrated area of vorticity trailing from around the tip of the wing. The fact that the LEV does not shed means that the lift produced by a 3D wing is much more stable than that produced by a 2D aerofoil. This is shown in Figure 14, where for the $Re = 120$ case the lift stabilises after around 120° of rotation. For the $Re = 15\,000$ case, the lift never completely stabilises, but fluctuates slightly around the $C_L = 0.8$ mark as the LEV breaks down and reforms over outboard sections of the wing.

5 Conclusion

A RANS CFD approach has been used to attempt to build understanding of and gain insight into the flow around insect wings, with a view to determining whether the lift-enhancing leading-edge vortex seen in insect-like flapping will still occur if the dimensions involved are scaled up to FMAV sizes.

It has been shown that the stability of the 3D LEV is due to spanwise flow, which in turn is due to the sweeping motion of the wing. 2D LEVs are unstable except at very low Reynolds numbers ($Re < 25$). The fact that 2D LEVs are stable at very low Reynolds numbers may explain the result of Birch et al. (2004), who observed a stable LEV at a low Reynolds number even when spanwise flow was prevented. However, any eventual FMAV will rely on spanwise flow to retain a stable LEV. Results presented here indicate that a stable LEV will still occur at the Reynolds numbers that FMAVs will operate at, despite the occurrence of Kelvin-Helmholtz instability in the leading-edge vortex sheet.

The most important conclusion that can be drawn from this work is that, despite the size difference between an insect and a micro-air vehicle, the primary lift-enhancing aerodynamic phenomenon that occurs during insect flight should also occur during the flight of any future FMAV. Therefore, there is no reason to dismiss insect-like flapping as a possible effective and efficient method of propulsion for MAVs.

References

I. K. Bartol, M. Gharib, D. Weihs, P. W. Webb, J. R. Hove, and M. S. Gordon, 2003. Hydrodynamic stability of swimming in ostraciid fishes: role of the carapace in the smooth trunkfish *Lactophrys triqueter* (Teleostei: Ostraciidae). *Journal of Experimental Biology*, 206(4):725–744.

J. M. Birch and M. H. Dickinson, 2001. Spanwise flow and the attachment of the leading-edge vortex on insect wings. *Nature*, 412:729–733.

J. M. Birch, W. B. Dickson, and M. H. Dickinson, 2004. Force production and flow structure of the leading edge vortex on flapping wings at high and low Reynolds numbers. *Journal of Experimental Biology*, 207: 1063–1072.

DARPA, 2000. *DARPA Micro Vehicle Program.* DARPA Fact Sheet.

M. H. Dickinson and K. G. Götz, 1993. Unsteady aerodynamic performance of model wings at low Reynolds numbers. *Journal of Experimental Biology*, 174:45–64.

M.H. Dickinson, F. Lehmann, and S. P. Sane, 1999. Wing rotation and the aerodynamic basis of insect flight. *Science*, 284(5422):1954–1960.

Discover Magazine, 2000. *The Physics of...Insect Flight.* World Wide Web, http://discovermagazine.com/2000/apr/featphysics. Accessed: 19/07/2007.

C. P. Ellington, 1984. The aerodynamics of hovering insect flight. *Philosophical Transactions of the Royal Society of London B*, 305:1–181.

C. P. Ellington, C. van den Berg, A. P. Willmott, and A. L. R. Thomas, 1996. Leading-edge vortices in insect flight. *Nature*, 384:626–630.

A. R. Ennos, 1989. The kinematics and aerodynamics of the free flight of some Diptera. *Journal of Experimental Biology*, 142:49–85.

Epson, 2003. *Epson Develops World's Smallest Flying Microbot.* World Wide Web, http://www.japancorp.net/Article.asp?Art_ID=5967. Accessed: 27/08/2006.

S. N. Fry, R. Sayaman, and M. H. Dickinson, 2003. The aerodynamics of free-flight manuevers in *Drosophila*. *Science*, 300:495–498.

I. Gursul, 2005. Review of unsteady vortex flows over slender delta wings. *Journal of Aircraft*, 42(2):299–319.

E. L. Houghton and P. W. Carpenter, 2003. *Aerodynamics for Engineering Students.* Butterworth-Heinemann, 5th edition.

M. Jensen, 1956. Biology and physics of locust flight. III. The aerodynamics of locust flight. *Proceedings of the Royal Society B*, 239:511–552.

M. Lee and C-M. Ho, 1990. Lift force of delta wings. *Applied Mechanics Reviews*, 43(9):209–221.

A. Magnan, 1934. *La Locomotion chez les Animaux.* Hermann et Cie.

E. J. Marey, 1868. Determination experimentale du mouvement des ailes des insectes pendant le vol. *Les Comptes rendus de l'Académie des sciences*, 67:1341–1345.

L. A. Miller and C. S. Peskin, 2004. When vortices stick: an aerodynamic transition in tiny insect flight. *Journal of Experimental Biology*, 207:3073–3088.

D. Pierce, 1961. Photographic evidence of the formation and growth of vorticity behind plates accelerated from rest in still air. *Journal of Fluid Mechanics*, 11(3):460–471.

M. Ramasamy and J. G. Leishman, 2006. Phase-Locked Particle Image Velocimetry Measurements of a Flapping Wing. *Journal of Aircraft*, 43(6):1867–1875.

R. B. Srygley and A. L. R. Thomas, 2002. Unconventional lift-generating mechanisms in free-flying butterflies. *Nature*, 420:660–664.

Q. Sun and I. D. Boyd, 2004. Flat-plate aerodynamics at very low Reynolds number. *Journal of Fluid Mechanics*, 502:199–206.

L. F. Tammero and M. H. Dickinson, 2002. The influence of visual landscape on the free flight behaviour of the fruit fly *Drosophila melanogaster*. *The Journal of Experimental Biology*, 205:327–343.

D. J. Tritton, 1988. *Physical Fluid Dynamics.* Oxford University Press, 2nd edition.

S. Vogel, 1994. *Life in Moving Fluids: The Physical Biology of Flow.* Princeton University Press, Princeton.

T. Weis-Fogh and M. Jensen, 1956. Biology and physics of Locust flight. I. Basic principles in insect flight: A critical review. *Philosophical Transactions of the Royal Society of London B*, 239:415–458.

A. P. Willmott, C. P. Ellington, and A. L. R. Thomas, 1997. Flow visualization and unsteady aerodynamics in the flight of the Hawkmoth, *Manduca sexta*. *Philosophical Transactions of the Royal Society of London B*, 352:303–316.

M. I. Woods, J. F. Henderson, and G. D. Lock, 2001. Energy requirements for the flight of micro air vehicles. *Aeronautical Journal*, 105:135–149.

Index